Experimental study of fracturing mechanisms in unconsolidated sand reservoirs under fluid injection

Thanh Tung Nguyen

École des Ponts ParisTech

THÈSE DE DOCTORAT

de l'École des Ponts ParisTech

Experimental study of fracturing mechanisms in unconsolidated sand reservoirs under fluid injection

Étude expérimentale des mécanismes de fracturation par injection de fluide dans les réservoirs sableux non consolidés

École doctorale N° 531 Sciences, Ingénierie et Environnement - SIE

Géotechnique

Thèse préparée au sein du laboratoire Navier, équipe Géotechnique – CERMES

Thanh Tung NGUYEN

Composition du jury:

Jianfu SHAO Professeur, Université de Lille	*Président*
Didier MAROT Professeur, Université de Nantes	*Rapporteur*
Panos PAPANASTASIOU Professeur, Université de Chypre	*Rapporteur*
Jalel OCHI Docteur, TotalEnergies	*Examinateur*
Nadia BENAHMED Chargée de recherche, INRAE	*Examinateur*
Jean SULEM Directeur de recherche, École des Ponts ParisTech	*Directeur de thèse*
Jean-Claude DUPLA Chargé de recherche, École des Ponts ParisTech	*Co - Encadrant de thèse*
Jean CANOU Chercheur, École des Ponts ParisTech	*Co - Encadrant de thèse*
Rawaz MUHAMMED Docteur, École des Ponts ParisTech	Invité
Jean-Grégoire BOERO-ROLLO Ingénieur, TotalEnergies	Invité

ACKNOWLEDGEMENT

This work would not be possible without the support of these wonderful people. The short lines below cannot express my gratitude to all of you. Deep down in my heart, I would like to express my sincere thanks to every person who contributed to make this project come true.

Abstract thank

Thanks to such an amazing country, France, for helping me complete my master's degree and now my prestigious PhD.

Thanks to École des Ponts ParisTech for welcoming me and providing me with a quality educational environment.

Thanks to the geotechnical family CERMES/NAVIER for offering me a friendly work environment and great colleagues and friends. If you think of France, you will think of Eiffel Tower, but for me, the symbol of France is CERMES.

Thanks to TotalEnergies for funding this research project.

My friends, my colleagues

Many thanks to Dr. Jalel Ochi and Jean-Grégoire Boero-Rollo, my TotalEnergies co-supervisors, for sharing their practical experiences in petroleum fields and their provided valuable contributions to this work.

I would like to thank Dr. Michel Bornert and Dr. Patrick Aimedieu. Everything I know about X-ray Computed Tomography is nurtured by the precious sharing.

I would like to warmly thank the members of my thesis jury. I particularly thank Prof. Panos Papanastasiou and Prof. Didier Marot for having accepted to review this work. Their very positive comments as well as their remarks and suggestions encouraged me and helped me to better prepare the defense. I also acknowledge the very kind participation of Prof. Jian Fu-shao, president of the examination committee and Dr. Nadia Benahmed, examiner.

Thanks specifically to the entire technical team of CERMES for always being happy to help and tolerate my complaints and requests whenever the experimental device had a problem. Thanks to Manu for all his career dedicated to CERMES. I feel very lucky to be a part of his memories during his last years in CERMES. Thank to Marine (je n'arrive toujours pas à te trouver un nom spécial), Baptiste (Monsieur Bobo), Loic (my beautiful) and Xavier for solving all the troubles I have caused (water leak-off, equipment damage, etc.), and helping me to develop a new device.

Thanks to my CERMES colleagues for such great things we have shared together. Thanks for tolerating me making noise every day.

A few words for some of the most amazing people I work with

First of all, I would like to express my sincere thanks to Prof. Jean Sulem, my thesis director. There are no words to express my admiration and gratitude for you. In the early days of my thesis, facing a respected and distinguished professor, I always felt stressed and scared because of my limited ability in language and expertise. However, the amazing kindness and patience I received from you really surprised me. I appreciate the time you spent working and teaching me even throughout evenings and weekends. Thanks Prof. Jean Sulem, thanks really a lot.

I would like to thank Dr. Jean-Claude Dupla, my co-supervisor, for having followed, supervised and accompanied me during these three years. Thanks for your kind help since I could not even write a complete report in French until I finished this manuscript. I remember that when I was a research intern, 4 years ago, I told you that I would never do a PhD and finally, I finished it under your wonderful guidance.

I am grateful to Dr. Jean Canou, who co-supervised this work and provided precious and rigorous scientific advices. I will never forget your smile and positive encouragement every time we meet.

Dr. Rawar Muhammed, my co-supervisor, my brother and my friend, too many things to thank you for during my thesis. You have carefully guided me and corrected me in detail from how to carry out an experiment in the calibration chamber to how to write a scientific article. You are always by my side whenever I need your help. I hope you will find a new job position worthy of your talents and personality.

For my family

I don’t think it’s enough to thank my family in these few pages because, simply for me, they are everything. My father NGUYEN Thanh Hai, my mother VU Thi Hang, my sister NGUYEN Yen Nhung and the whole family have been and will always be my great encouragement and motivation on my life journey. Thank you, my nephew Hanh Phuc (born September 9, 2021) for coming to this family to make this happiness more complete.

THANKS FOR ALL.

“IF YOUR WHY IS BIG ENOUGH, THE HOW BECOMES EASY”

ABSTRACT

Formation damage and the associated injectivity loss of wells induced by the produced water re-injection can be often overcome by injecting in the fracturing injection regime. Hydraulic fracturing in hard rocks has been extensively studied and well mastered, but the mechanisms of hydraulic fracturing in unconsolidated sand formation, on the contrary, are still an open issue. In this context, the main objective of this thesis is to identify and understand the fracturing mechanisms induced by fluid injection in unconsolidated sand packs. The impact of various parameters (confining pressure, stress ratio coefficient, flow rate, permeability, suspended particles concentration in injection water) on the fracturing process in sand packs is also investigated to encircle the main factors controlling the initiation of the fracturing regime.

For this purpose, an experimental study has been performed in two different setups: the radial injection cell (small scale) and the radial injection chamber (large scale). These setups were designed to simulate the injection wells condition in the sand reservoirs. A central tube, fixed on the lower baseplate of the cell, permits to perform a radial injection through a cylindrical sand specimen under axial and radial confining stresses. The radial injection chamber was developed several years ago within the Geotechnical team of the Navier laboratory (CERMES) while the small cell is a new device that was developed and manufactured at the beginning of this thesis. This cell provides a possibility to analyze the fractures pattern of the whole specimen in 3D using X-ray Computed Tomography (X-ray CT). A testing program has been established based on two injection scenarios in a dense sand pack: pure water and water containing suspended fine particles.

Typical test results exhibit pressure drops during fluid injection corresponding to fracturing of the specimen, and consequently to an increase of the overall permeability. This can be confirmed by the detection of small radial fractures around the injection point either by visual observation when disassembling the specimen or by 3D X-ray CT. Fractures appear as localized zones of higher porosity and larger pore size resulting from dilatant shearing and particles transport. The extension and the opening of the fractures are enhanced by higher flow rate during the fracturing regime. The obtained experimental results suggest that the critical fracturing pressure is mainly controlled by the confining pressure and does not change significantly with other testing parameters. Higher increase of the overall permeability corresponds to the detection of longer and larger fractures along the injection source. Finally, a comparison is established between the results obtained with two different injection scenarios as well as two different injection setups.

Keywords: PWRI **–** Suspended particles injection – Fracturing flow regime – Fracturing mechanisms - Unconsolidated sand reservoirs – Radial injection experimental setup – X-Ray Computed Tomography.

RÉSUME

Le colmatage des réservoirs pétroliers peu consolidés et la perte d'injectivité associée induits par la réinjection d'eau de production peuvent souvent être surmontés en injectant dans le régime de fracturation. La fracturation hydraulique dans les roches dures a été largement étudiée et bien maîtrisée, mais les mécanismes de la fracturation hydraulique dans les formations sableuses non consolidées, restent un problème ouvert. Dans ce contexte, l'objectif principal de cette thèse est d'identifier et de comprendre les mécanismes de fracturation induits par l'injection de fluide dans les réservoirs sableux. L'impact de divers paramètres (pression de confinement, rapport de contraintes, débit, perméabilité, concentration de particules en suspension) sur le processus de fracturation dans les éprouvettes/massifs de sable est également étudié pour mettre en évidence les principaux facteurs contrôlant l'initiation du régime de fracturation.

Dans ce but, une étude expérimentale est réalisée sur deux dispositifs différents : la cellule d'injection radiale (à petite échelle) et la chambre d'injection radiale (à grande échelle). Ces dispositifs ont été conçus pour simuler les conditions d'injection en puits sur une éprouvette de sable. Un tube central, fixé sur l'embase inférieure de la cellule, permet d'effectuer une injection radiale à travers une éprouvette cylindrique sous contraintes de confinement axiale et radiale. La chambre d'injection radiale a été développée, il y a plusieurs années, au sein de l'équipe Géotechnique du laboratoire Navier (CERMES) tandis que la petite cellule est un nouveau dispositif qui a été développé et fabriqué au début de cette thèse. Cette cellule donne la possibilité d'analyser la morphologie des fissures de l'ensemble de l'éprouvette en 3D à l'aide de la tomographie aux rayons X. Un programme d'essais a été établi sur la base de deux scénarios d'injection dans une éprouvette de sable dense : eau pure et eau contenant des particules fines en suspension.

Les résultats typiques des essais montrent des chutes de pression lors de l'injection de fluide correspondant à la fracturation de l'éprouvette, et par conséquent à une augmentation de la perméabilité globale. Ceci peut être confirmé par la détection de petites fractures radiales autour du point d'injection soit par observation visuelle lors du démontage de l'éprouvette, soit par les images de tomographie. Les fractures apparaissent sous forme de zones localisées de porosité plus élevée et de plus grande taille de pores, résultant de la formation des bandes de dilatation et du transport des particules. L'extension et l'ouverture des fractures sont renforcées par un débit plus élevé pendant le régime de fracturation. Les résultats expérimentaux obtenus suggèrent que la pression de fracturation critique est principalement contrôlée par la pression de confinement et ne change pas de manière significative avec d'autres paramètres d'essai. Une augmentation plus élevée de la perméabilité globale correspond à la détection de fractures plus longues et plus grandes le long du tube d'injection. Enfin, une comparaison est établie entre les résultats obtenus avec les deux scénarios d'injection différents ainsi que les deux dispositifs d'injection différents.

Mot clés : PWRI – Particules en suspension – Régime de fracturation – Mécanismes de fracturation – Réservoirs sableux non consolidés – Dispositif d'injection radiale – Tomographie aux rayon X

LIST OF SYMBOLS

D_{50}	µm	Mean particle size
H	m	Height of the injection zone
$I_{D\ NE34}$	-	Density index of the NE34 sand matrix
k	Darcy	Intrinsic permeability
$k_{end,m}$	Darcy	Permeability of the sample at the end of matrix loading phase
k_{int}	Darcy	Initial permeability of the sample at the beginning of matrix loading phase
K_0	-	Stress ratio coefficient (σ_h / σ_v)
k_{unload}	Darcy	Final permeability of the sample at the end of the unload
p	kPa	Pressure
P_1	kPa	Measured pressure by the inlet pressure transducer
P_2	kPa	Measured pressure by the outlet pressure transducer
P_{frac}	kPa	First drop pressure observed during non-matrix regime
P_{in}	kPa	Pressure at the entrance of injection tube
P_{out}	kPa	Pressure at the outlet of injection cell
P_{tr}	kPa	Pressure at the transition point of two injection regime (Matrix and fracturing regime)
q	l/min	Flow rate
Q_{frac}	l/min	Flow rate corresponding to the first drop pressure
Q_{tr}	l/min	Flow rate at the transition point of two injection regime
r_0	m	Radius of the injection tube
r_1	m	Radius of the cell specimen or the internal ring of the chamber sand pack
r_2	m	Radius of the outer ring of the sand pack in the injection chamber
t	min	Time
v_{r0}	m/s	Radial flow velocity at the entrance of the specimen
ΔP_s	kPa	Pressure loss in the specimen
μ	cP	Fluid viscosity
ρ_s	t/m^3	Density
σ_h	kPa	Confining pressure (horizontal stress)
σ_v	kPa	Axial stress

GENERAL INTRODUCTION

In hydrocarbon producing fields, Produced Water Re-Injection (PWRI) is known as an economically attractive and environmentally friendly method for managing produced water. This method has the advantage of pressure maintenance support and sweeping efficiency in order to enhance the hydrocarbon production (Farajzadeh, 2004; Souilah et al., 2014). However, despite many treatment processes, there is always a small amount of impurities, such as solid particles of several micrometers and oil droplets in treated produced water (Mainguy et al., 2020). Once produced water is re-injected through injection wells into reservoirs, the filtration of these components at the entrance of the reservoir leads to the plugging of the medium, and consequently, to the deterioration of the injectivity (Al-Abduwani et al., 2005; Li and Wong, 2008; Feia et al., 2015, 2017). The formation of filter cakes, due to the deposited solid particles in the near-wellbore region, is stated as the dominant mechanism of the formation damage (i.e. permeability decrease) during PWRI (Shutong and Sharma, 1997). Once the formation damage occurs, several treatments can be applied for improving well injectivity in the matrix flow regime such as clean water injection (to flush away a fraction of deposited particles in the near-wellbore region) or chemical additives injection (to destabilize the filter cake and to clean the sand controls screen) (Mainguy et al., 2020; Souilah et al., 2014). Using these techniques may partially restore the injectivity loss but the beneficial effect disappears soon after PWRI resumes and these techniques require a substantial cost compared to the benefits they bring. On the other hand, formation damage and its associated injectivity loss of wells induced by the injection or re-injection of water containing fine particles can be often overcome by injecting in the fracturing regime (or frac-regime) (Ochi et al., 2014; Mainguy et al., 2020). While this operation is possible and widely applied in consolidated rock reservoirs, it is much less obvious in soft/unconsolidated sand reservoirs because fracturing of the granular medium may require a higher injection pressure to reach the frac-regime and the fracturing mechanisms are still an open issue.

This Ph.D thesis has been developed within the framework of a research project in collaboration between the Geotechnical team (CERMES) of Navier laboratory and TotalEnergies. Its main objective is to study the conditions for reaching the frac-regime and explore the fracturing mechanisms in unconsolidated sand reservoirs due to the injection of water with and without suspended particles. The effect of various parameters on the fracturing process in sand specimens is also explored to highlight the main factors controlling the initiation of the frac-regime and the extension of fractures.

In this context, an experimental study has been performed in two different setups which are designed to simulate the injection wells condition in the sand reservoirs. The first is the radial injection chamber (large scale) that was developed several years ago within the Geotechnical team of the Navier laboratory (CERMES) (Feia, 2015; Feia et al., 2017a). The second is the radial injection cell which was developed and manufactured at the beginning of this thesis. The second setup provides a more reasonable testing duration than the first one and a possibility to

analyze the fracture pattern of the whole specimen in 3D using X-ray Computed Tomography (X-ray CT).

These setups have a central tube, fixed on the lower baseplate, which permits to perform a radial injection through a cylindrical sand specimen under axial and radial confining stresses. A lateral drainage system provides a fully radial flow inside the specimen. The experimental tests are completed by additional observations with X-Ray CT and optical microscopy of some typical samples in order to analyze the change of the granular structure after fracturing. At the end of the injection phase, a small volume of a mixture of silica gel and dye will be injected for the purpose of freezing and visualizing fractures or preferential flow paths induced in the frac-regime. A parametric study exploring the influence of some key parameters such as confining pressure, stress ratio coefficient, flow rate, permeability, suspended particles concentration in injection water are performed.

This dissertation consists of four main chapters and additional results and tests details are presented in Appendices.

Chapter 1 presents a literature review related to this work. A brief introduction on the PWRI operation and its associated consequences on the formation damage is first presented. Then, some fundamental mechanisms of hydraulic fracturing in consolidated media are described. Finally, both experimental and numerical studies on hydraulic fracturing in unconsolidated sand formations are reviewed.

Chapter 2 describes the characteristics of the tested materials, experimental setups and testing procedures. The preliminary tests, to validate the choice of the appropriate colored gel to freeze the sand specimen, are presented. Then, the two experimental setups (i.e., radial injection cell and radial injection chamber) as well as the testing procedure for both setups are detailed.

Chapter 3 is devoted to the presentation and analysis of experimental results with injection of pure water in both radial injection setups. First, the preliminary tests to qualify the new injection cell setup and to validate the injection protocol, are presented. Then, typical experimental results of fracturing as well as observations of the sand specimen post-mortem using X-ray CT and optical microscope are presented. A sensitivity analysis is then detailed in order to highlight the effect of various parameters, including confining pressure, stress ratio coefficient, injection flow rate and permeability (i.e., the concentration of particles present in the specimen) on the fracturing process of sand specimens. Finally, a comparison of the results obtained in the two injection setup is presented.

Chapter 4 presents the experimental results with suspended particles in water injection which are performed in both radial injection setups. In this chapter, the preliminary tests are performed to develop an injection protocol that allows to first partially plug the specimen by a cake formation and then to fracture the clogged specimen. The typical injection tests in both setups with additional observations using X-ray CT are described in detail. The results of a sensitivity analysis are then discussed, allowing to investigate the effect of the confining

pressure and the particles concentration on the formation damage and on the fracturing response of sand specimens. Finally, a comparison of the results obtained in two injection scenarios (i.e., injection of water with and without suspended particles) is made.

This manuscript ends with a general conclusion that summarizes the major findings of this work along with the possible perspectives for future research.

CHAPTER 1. BIBLIOGRAPHIC REVIEW

1.1 INTRODUCTION

In hydrocarbon producing fields, formation damage and the associated injectivity loss of wells are commonly observed during Produced Water Re-Injection (PWRI) due to the infiltration/deposition of the suspended impurities (solid particles, oil droplets) carried in produced water. To maintain injectivity, the injection or re-injection of produced water in the so-called 'fracturing regime' could be an option to overcome it (Mainguy et al., 2020).

Hydraulic fracturing is commonly used in petroleum engineering for enhancing oil and gas production. It is the process of creating fractures in the formation by injecting the frac-fluid into a selected section of wellbore under very high pressure. The first experimental fracturing was conducted in the Hogoton field in 1947 (Montgomery et al., 2010). Since that time, hydraulic fracturing has been one of the primary engineering tools for enhancing oil recovery. It is estimated that more than 90% of gas wells and 70% of oil wells throughout the world apply this technique (Economides and al., 2007).

In the case of consolidated and brittle materials (e.g. hard rocks) with low permeability, hydraulic fracturing has been extensively studied (Detournay, 2016). The fracturing mechanism is dominated by tensile failure and conventional modeling is based on Linear Elastic Fracture Mechanics (LEFM) (Fjaer et al., 2008). Fracturing of soft rock formations, on the other hand, results in a higher net fluid pressure, shorter and wider fractures as compared to those obtained in a strong elastic formation because of the development of plastic zones at the fracture tip during fracture propagation and fluid leak off in the porous rock (Papanastasiou, 1997, 1999; Sarris and Papanastasiou, 2013). However, the dominant mechanism of fracturing in soft rocks is also tensile failure and fracture propagation is controlled by the rock toughness.

The mechanisms involved in fracturing of unconsolidated sand reservoirs, which are studied in the present PhD work, are fundamentally different than the ones involved in brittle fracturing. Due to the negligible tensile strength as well as the extremely large fluid leak-off, the possibility of tensile failure is suppressed in favor of shear failure (Zhai and Sharma, 2005; Bohloli and de Pater, 2006), fluidization (Chang, 2004; Wu, 2006) or flow-induced channelization surrounding an injection point (Mahadevan et al., 2012; Ameen and Taleghani, 2015; Bautista and Taleghani, 2018).

In this chapter, a brief review of the PWRI and its associated formation damage are presented. Then, some fundamental mechanisms of hydraulic fracturing in consolidated medium (i.e., rock) is briefly reviewed. Finally, a synthesis of both experimental and numerical research related to the hydraulic fracturing in unconsolidated, granular materials is presented.

1.2 PRODUCED WATER RE-INJECTION

Petroleum is well-known as a major source of energy and it is an important revenue for many countries in the world. Therefore, the production of petroleum is one of the most

important industrial activities since late 1850s when Edwin Drake has successfully drilled the first oil well (Oliveira et al., 2005; Igunnu and Chen, 2014). It should be noted that 60% of the world's oil and gas reserves are in carbonate reservoirs, and that 90% of oil and gas producing wells are drilled in siliciclastic reservoirs. Currently, most of the discoveries have been made in unconsolidated sand formations or weakly consolidated and cemented sandstones (Feia, 2015). Despite its important value, petroleum production faces many difficulties with the production of large volumes of waste including liquid waste, sludge, mineral scales, … in which produced water is the major part accounting for more than 80% of liquid waste (Igunnu and Chen, 2014). Worldwide 75% of the production is water and this rate can be up to 98% (Farajzadeh, 2004; Feia, 2015) depending on the nature of the oilfields, the method of well drilling, the different types of completion, the age of the production well (Reynolds and Kiker, 2003). After water and hydrocarbons are separated, management of the produced water is one of the main issues in the petroleum industry due to the increasing volume of produced water all over the world in the current decade and the expensive treatment costs (Ahmadun et al., 2009). Figure 1.1 presents an estimation of daily global water production since 1990 and forecast until 2015. There are different ways to handle produced water such as discharge to the environment (as long as it meets the environmental regulations); reuse in the industry operations (dust control, vehicle wash water, power generation; agricultural use; Produced Water Re-Injection (PWRI) and even drinking water. The choice of the disposal methods depends on several factors: site location (onshore or offshore), cost-effectiveness, regulatory acceptance, technical feasibility, and availability of equipment.

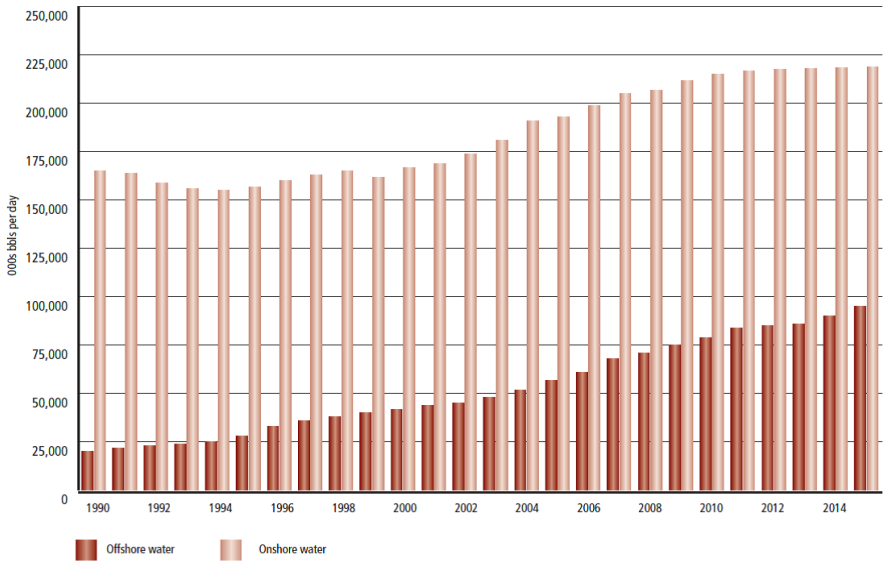

Figure 1.1: Daily global onshore and offshore water production (Dal Ferro and Smith, 2007).

Among these technics, PWRI is known as an economically attractive and environmentally friendly method to manage the produced water (Farajzadeh, 2004; Wong and Mettananda, 2010). This method has the advantage of pressure maintenance support and sweeping efficiency in order to enhance the hydrocarbon production (Farajzadeh, 2004; Souilah et al., 2014). Before PWRI operation, the produced water is treated to eliminate the organic and inorganic

components (heavy metals, dispersed oil, suspended solids, chemical compounds, dissolved gases and bacteria, …) using combined physical, chemical and biological methods (Figure 1.2).

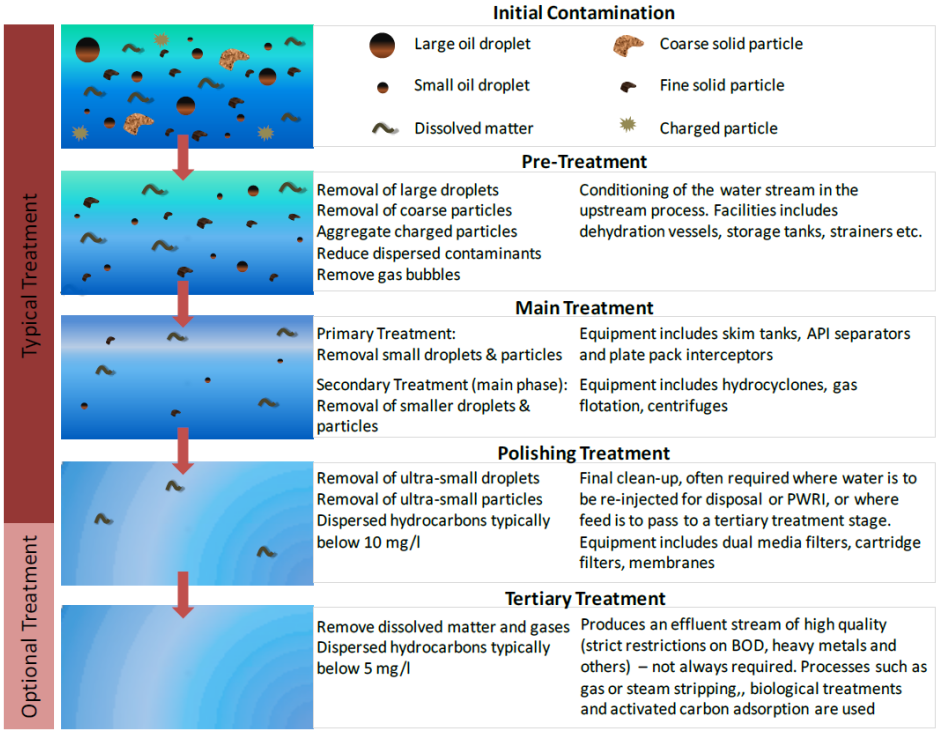

Figure 1.2: Typical water treatment process in the oil and gas industry (modified from Shell, 2009).

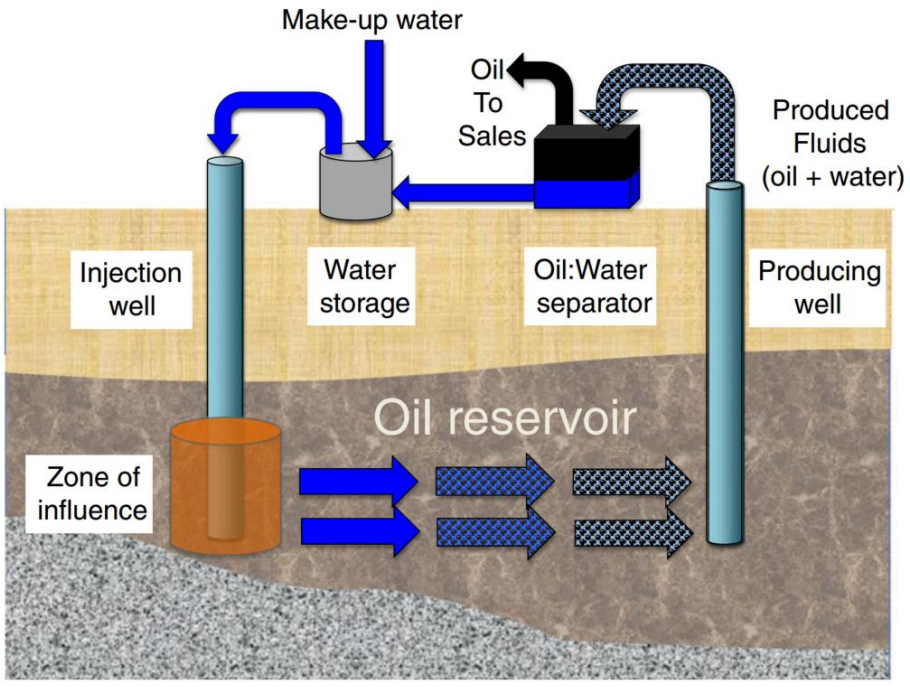

Figure 1.3: Schematic diagram for Produced Water Re-Injection PWRI (Gieg et al., 2011)

However, due to the treatment costs, the technology and equipment requirements, treated produced water contains always a small amount of impurities such as solid particles of several micrometers in size and oil droplets (Mainguy et al., 2020). The re-injection of treated produced water through the injection well into reservoirs leads to the plugging of the medium, consequently, the loss of the injectivity, because of the filtration of these components at the entrance of the reservoir (Al-Abduwani et al., 2005; Li and Wong, 2008; Feia et al., 2015, 2017). Figure 1.3 shows a schematic diagram of PWRI operation commonly used in oilfields, the most influenced zone during reinjection is an area around the injection well.

Sharma et al. (1997) have presented an injection history of a well in the Gulf of Mexico during PWRI (Figure 1.4). An important decline of the injectivity ratio was observed during 400 injection days although many different treatment methods have been applied such as replacing the µm filters twice a month, continuous and batch treatments with sodium hypochlorite to control bacteria as well as adding a scale inhibitor in the water to reduce and/or prevent the deposition of the inorganic scales (e.g., calcium carbonate, calcium sulfate, barium sulfate, …). The authors indicate that the process leading to injectivity decline occurred in the near-wellbore region. Since other damages were effectively controlled in the injection facilities (scale deposition, oxygen corrosion and bacteria), they concluded that low concentration of suspended solids in the injection water was the main cause of the formation damage.

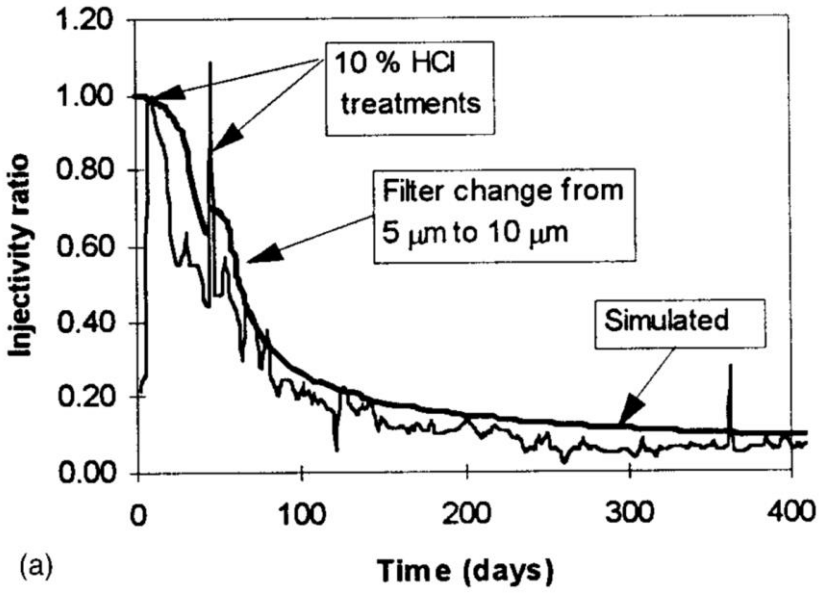

Figure 1.4: Injection history of an injection well A09 at an offshore field in the Gulf of Mexico during PWRI operation ((Sharma et al., 1997).

Mainguy et al. (2020) have presented the PWRI history in two fields from Block 17, deep offshore in Angola. The exploitation is performed in unconsolidated sand reservoir. The injection water during PWRI is a mixture of treated produced water (PW) and desulfated seawater (SRU) and the PW concentration in the mixture generally increases during the lifetime of the project due to its increasing volume during production (Figure 1.5). Consequently, a decreasing trend in injectivity is observed during PWRI. The authors propose several

mechanisms to explain the causes of the injectivity loss such as the formation of the sulfate scales on the surface of the production equipment due to the presence of the sulfate in seawater, the formation damage associated with the different temperature between injected water and reservoirs (thermal-stress influences), clay swelling due to the salinity of the injected water as well as the deposition of the solid particles and oil droplets in the near-wellbore region (cake formation). However, based on the injection results when varying the PW concentration in the injected water, the authors emphasize that the deposition of solids particles and oil droplets is the main cause of the injectivity decline.

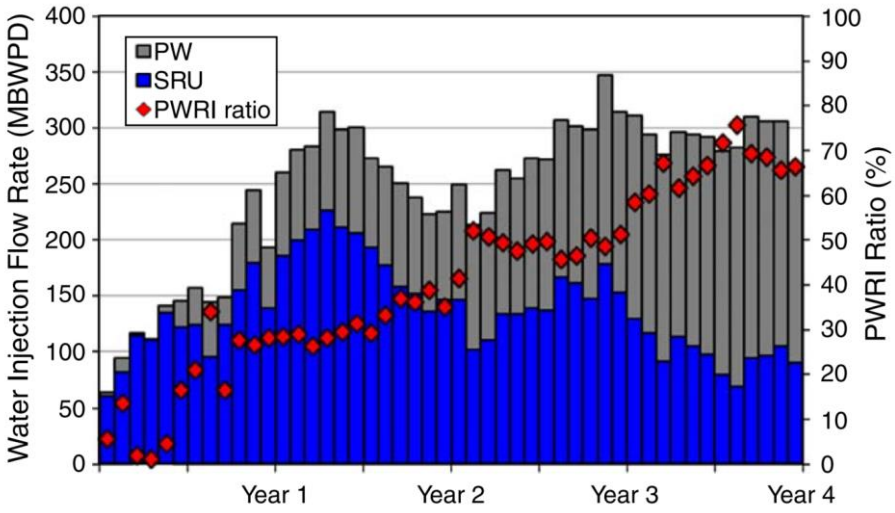

Figure 1.5: Average daily of the injected water for Field A, Offshore Angola. Note: PWRI ratio = PW/(SRU+PW) (Mainguy et al., 2020).

Ochi and Oughanem (2018) have conducted a series of core flooding experiments in laboratory to investigate the effect of water components on the formation damage during PWRI. Water containing suspended particles, oil droplets or both of them are injected in high permeability sand specimens. Based on the experimental results, the authors conclude that the formation damage due to suspended particles is more aggressive as compared to that obtained with oil in suspension (Figure 1.6). The oil in suspension generates only internal formation damage on the entire length of the specimen without formation of the filter cake whereas injection with suspended particles results in the formation of internal and/or external cake by deposition of the particles at the first layer of the specimen. These cakes induce a rapid decrease in overall permeability over time.

The formation damage due to suspended particles injection depends on many factors such as concentration of suspended particles in the injected fluid, particle characteristics (minerals, grain size), flow rate, injected volumes, medium properties (permeability, pore-throat size) as well as nature of the interaction between the injected particles and the porous medium (Saada et al., 2006; Shutong and Sharma, 1997). This phenomenon has been extensively studied for almost 50 years through experiments (Todd et al., 1990; Al-Abduwani et al., 2005; Feia et al., 2015) and modeling approaches (van Oort et al., 1993; Shutong and Sharma, 1997; Al-Abduwani et al., 2005; Zhou et al., 2018).

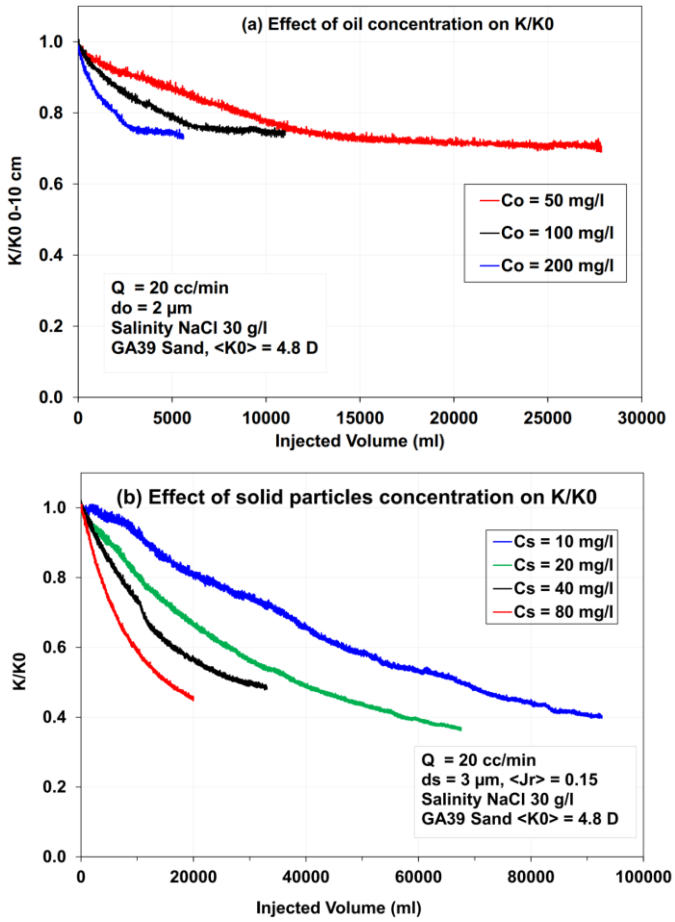

Figure 1.6: Effect of different water components on the formation damage: (a) oil concentration effect; (b) solid particles concentration (Ochi and Oughanem, 2018).

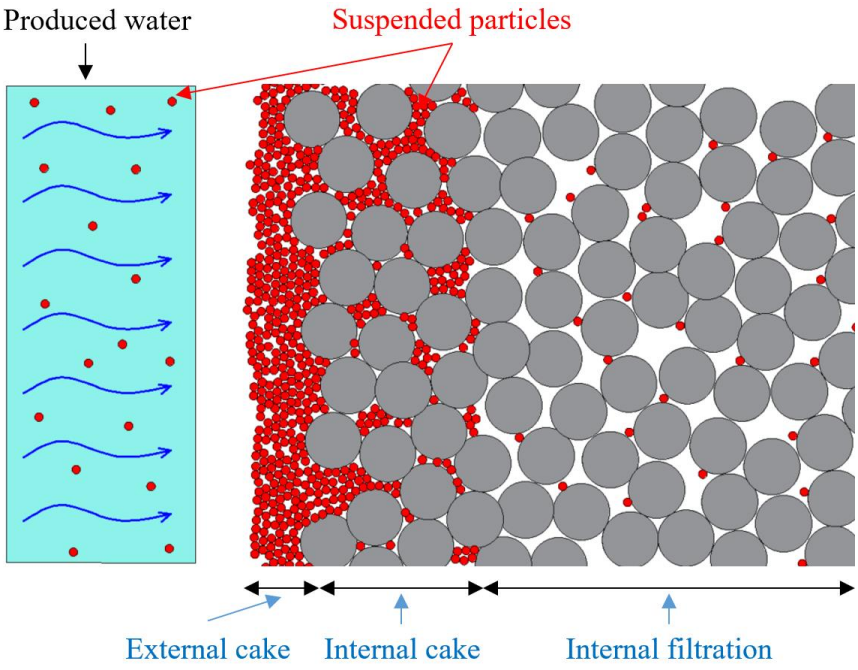

Figure 1.7: Schematic diagram of the filter cakes formation due to deposited particles carried in the injection fluid.

Barkman and Davidson (1972) proposed the four following mechanisms of well and formation impairment due to suspended particles: the invasion of particles into the formation (internal cake), wellbore narrowing (external cake on the face of the wellbore), perforation plugging and wellbore fillup (decrease of the net height of injection zone due to the settlement of particles to the bottom). Therefore, the internal and external cake formation are stated as the dominant mechanisms (Shutong and Sharma, 1997). Figure 1.7 presents a schematic diagram of two different scenarios of the filter cake (internal and external cake).

The re-injection of treated produced water in the matrix regime (i.e., the injection pressure is lower than the horizontal *in-situ* stress) always leads to the injectivity loss because of the cake formation. Some treatments such as cleaner water injection or chemical additives injection can be performed to partially restore the permeability decline, however, these solutions are relatively expensive and provides only temporary results in the short term. On the other hand, the injection or re-injection of treated produced water in the fracturing regime (i.e., the injection pressure is higher than the horizontal *in-situ* stress) could be a reasonable solution to overcome the formation damage and the associated injectivity loss of wells (Ochi et al., 2014; Mainguy et al., 2020). Fracturing hydraulic is widely applied in consolidated reservoirs (i.e, rock) and its associated mechanisms are well-known in the literature, it is much less obvious in unconsolidated sand reservoirs because the frac-regime is more difficult to achieve and not yet well mastered. The section below will present a literature review of hydraulic fracturing in both consolidated and unconsolidated mediums.

1.3 FUNDEMENTAL MECANISMS OF HYDRAULIC FRACTURING FOR CONSOLIDATED ROCK FORMATIONS

On idealized conditions when the rock is assumed elastic, isotropic and homogeneous, hydraulic fracturing takes place when the fluid pressure within the rock exceeds the smallest principle stress plus the tensile strength, this results in tensile failure or splitting of the rock (Fjaer, E. and al., 2008). Theoretically, the idealization of the problem is a two-dimensional hydraulic fracture. The fracture is a bi-wing, vertical fracture and the fracture plane is perpendicular to the minimum horizontal in situ stress (Figure 1.8).

Figure 1.9 presents a typical downhole pressure record during injection at a given flow rate. When pumping start, the downhole pressure increases very quickly until it reaches the maximum pressure P_b corresponding to the initial breakdown pressure. Continue pumping will eventually result in stable fracture growth at the propagation pressure P_{prog}. The real fracture initiation pressure depends on a number of parameters such as stress conditions, rock properties (tensile strength, permeability), fluid properties (viscosity, concentration of suspended particle) and operational procedure (flow rate).

Conventional modeling of hydraulic fracture in the rock is based on the theory of linear elastic fracture mechanic (LEFM) which first assumes that the material is isotropic and linear elastic. The main assumption of LEFM is that the process zone, a region near the fracture tip

where the behavior of the material is not elastic (e.g. region of plastic deformation, micro-cracking, etc.), is negligible as compared to the fracture sizes. This assumption is not valid anymore for fracture tip behavior in soft formations with significant plastic deformation (Sarris and Papanastasiou, 2013).

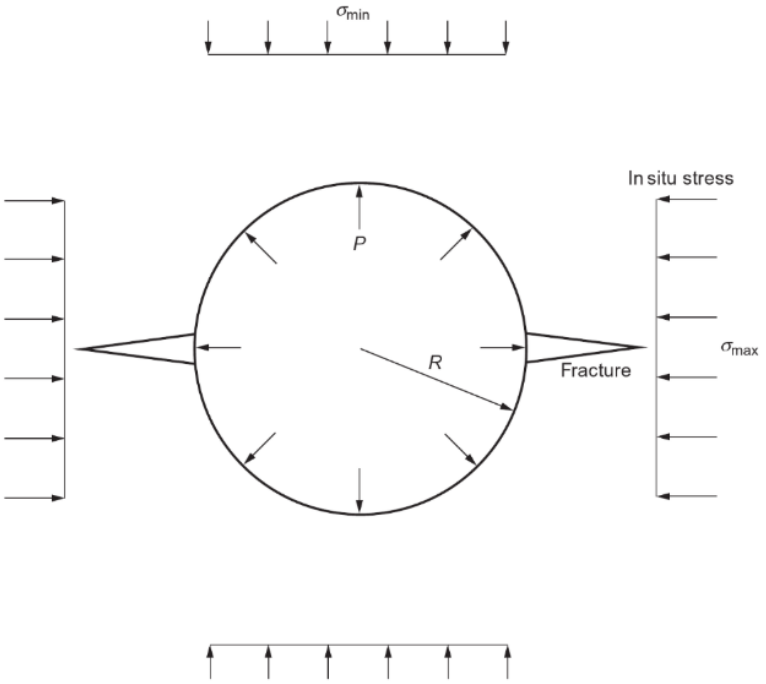

Figure 1.8: Horizontal section of the vertical well under hydraulic fracturing (Yew and Weng, 2014).

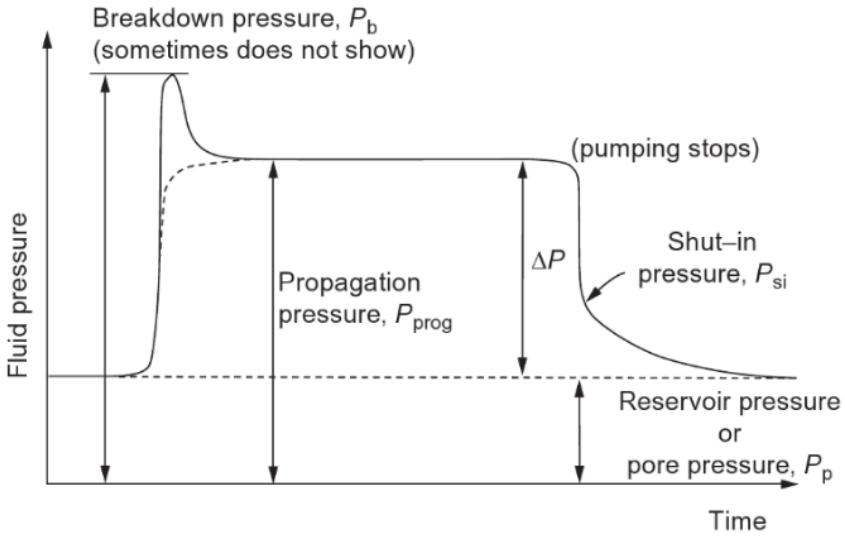

Figure 1.9: Typical downhole pressure – time curve during hydraulic fracturing of conventional rock (Yew and Weng, 2014).

The propagation of the fracture can occur only if the mode I stress intensity factor K_I reaches a critical value K_{Ic}, which is called the fracture toughness.

$$K_I = K_{Ic} \tag{1.1}$$

Modeling the hydraulic fracture in the rock is a challenging problem with a set of nonlinear integro-differential equations, therefore simple fracture geometries have been used. The most widely used ones are presented in Figure 1.10.

The plane strain or KGD model introduced by Khristianovic and Zheltov (1955) and Geertsma and de Klerk (1969), which assumes that fractures propagate under plane strain conditions in a horizontal plane. The KGD model assume an elliptical horizontal cross-section and rectangular vertical cross-section where the fracture length L is much smaller than the constant fracture height H.

Unlike the KGD model, the PNK model presented by Perkins and Kern (1961) and Nordgren (1972) which assumes that the fracture length L are much longer than the constant fracture height H. In this model, a 2D plane-strain model is assumed in the vertical plane where the fracture has an elliptical cross-section shape both in the horizontal and vertical directions.

The third model in 2D plane-strain is the penny-shaped or radial model. The fracture is assumed to be radially symmetric and initiated perpendicular to the injection well. The periphery of the fracture is circular (penny-shaped).

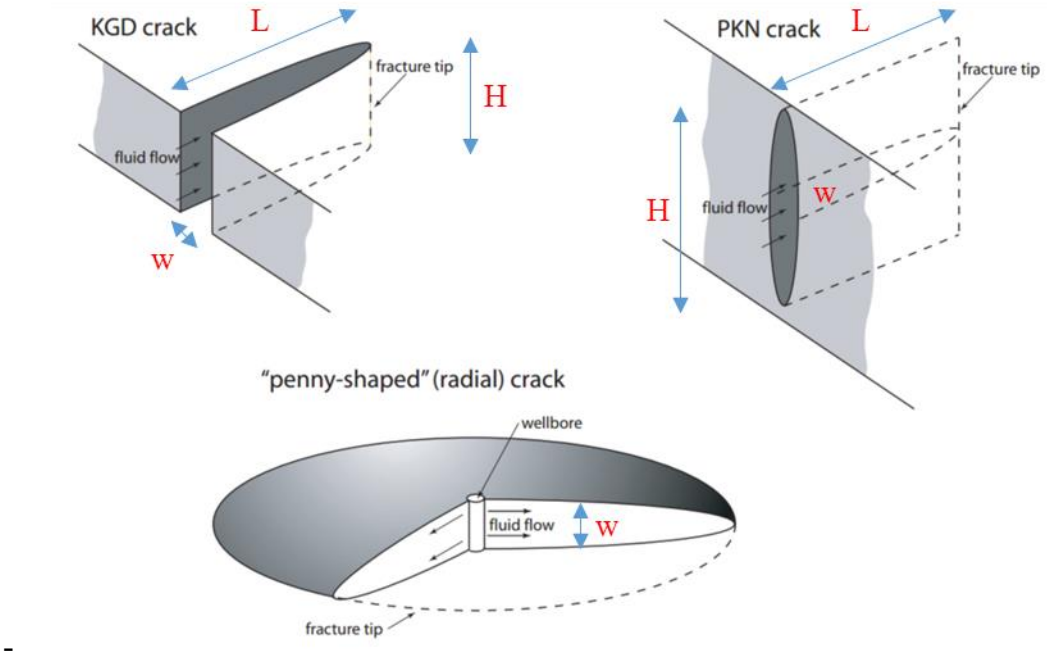

Figure 1.10: Different hydraulic fracture models (Adachi, 2001).

The hydraulic fracturing involves the coupling of four distinct processes: (i) mechanical deformation of the solid medium induced by the fluid pressure acting on the fracture surfaces;

(ii) flow of fluid within the fracture; (iii) propagation of the fracture; and (iv) leak-off of the fracturing fluid into the permeable medium, which is a history-dependent process. Two competing asymptotic dissipation mechanisms and two competing storage mechanisms are highlighted. Energy is dissipated by fracture propagation and by fluid viscous flow in the fracture. Fluid storage processes are fluid leak-off in the porous medium and fluid storage in the crack (Carrier and Granet, 2012). The four following combined asymptotic regimes can be presented from these two sets of mechanisms: storage-toughness (Garagash, 2006), storage-viscosity (Savitski and Detournay, 2002), leak-off-toughness (Bunger et al., 2005) and leak-off-viscosity (Adachi and Detournay, 2008). These competing processes are illustrated by the parametric domain in Figure 1.11. A dimensionless toughness κ describes the relative magnitude of the dissipation processes while a dimensionless leak-off coefficient C, on the other hand, describes the relative magnitude of the storage processes. These parameters are given by (Carrier and Granet, 2012):

$$\mathcal{K} = \frac{4K_{Ic}}{\sqrt{\pi}}\left(\frac{1}{3Q_0E'^3\mu}\right)^{1/4} \quad \mathcal{C} = 2C_L\left(\frac{E't}{12\mu Q_0^3}\right)^{1/6} \tag{1.2}$$

where: K_{Ic} is fracture mode-I toughness; Q_0 is injection rate; t is time; μ is fluid viscosity; C_L is the leak-off coefficient and E' is the plane strain elastic modulus.

Each edge of this domain represents an asymptotic regime. During the injection of a fluid in a plane-strain fracture, the propagation regime evolves from the storage-dominated edge ($\mathcal{C} \ll 1$) to the leak-off-dominated edge ($\mathcal{C} \gg 1$) with time.

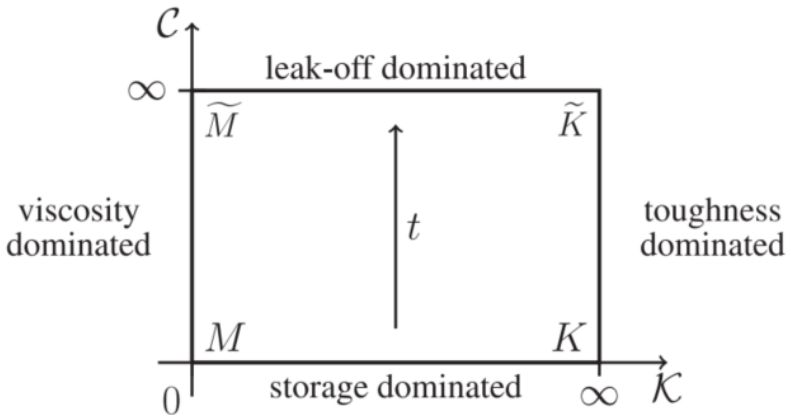

Figure 1.11: Hydraulic fracture parametric space for elastic rocks (Carrier and Granet, 2012).

In soft/weak rock formations, when taking into account the inelastic rock behavior, higher net pressure (i.e., the difference between the borehole fracturing pressure and far-field confining stress) is observed as compared to elastic-brittle formations rocks (Papanastasiou, 1997; 1999). A worldwide survey performed by the Delft Fracturing Consortium shows that net-pressures obtained in the field are commonly 50 to 100% higher than those predicted by the conventional hydraulic fracturing simulator using LEFM and the difference is even higher in the case of weak

formations (Papanastasiou, 1999). The influence of the non-linear mechanisms including plastic yielding, rock dilation, cohesive zone and fluid-lag in hydraulic fracturing propagation within rock formations has been first investigated by Papanastasiou and Thiercelin (1993). Since then, some further research has been conducted to explore the effect of inelastic rock behaviors on hydraulic fracturing using both numerical and experimental methods (Papanastasiou, 1997; 1999; Van Dam et al., 2000; Sarris and Papanastasiou, 2013). Fractures induced in the soft formations are shorter and wider than fractures formed in an elastic medium because of the occurrence of the plastic yielding at the fracture tip (Papanastasiou, 1997). The propagation criterion for non-brittle fracture is usually defined by the cohesive zone model (Figure 1.12). However, as the hard rocks, the dominant fracturing mechanism in soft rocks is also tensile failure and fractures are true opening cracks, resulting from the rock splits and the fracture propagation is in the direction perpendicular to the minimum in-situ stress.

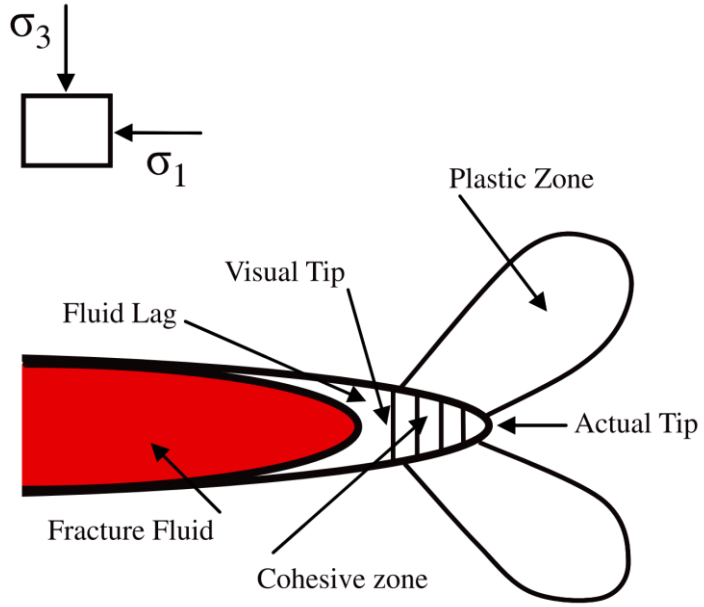

Figure 1.12: Geometry for a plane strain hydraulic fracture in weak rocks (Sarris and Papanastasiou, 2013)

1.4 HYDRAULIC FRACTURING IN UNCONSOLIDATED AND GRANULAR MATERIALS

Since the last two decades, a number of experimental and numerical studies have been dedicated to investigate the mechanisms and to improve the aspects related to the modeling of hydraulic fracturing in unconsolidated or poorly consolidated formations. However, the exact mechanisms of fracturing remain unknown. In this part, a brief summary of the experimental and numerical investigations on hydraulic fracturing in unconsolidated and granular materials will be presented.

1.4.1 Experimental investigations

1.4.1.1 *Injection of polymers in a half-cylindrical setup*

Khodaverdian and McElfresh (2000) have performed a series of tests in a radial flow cell (RFC) to define the fundamental mechanisms controlling fracture propagation in poorly consolidated sand. The RFC consists of a metal half-cylinder, allowing to build a sand specimen of 0.3 m (1-ft) in height and 0.9 m (3-ft) in radius from the center of the injection tube (Figure 1.13).

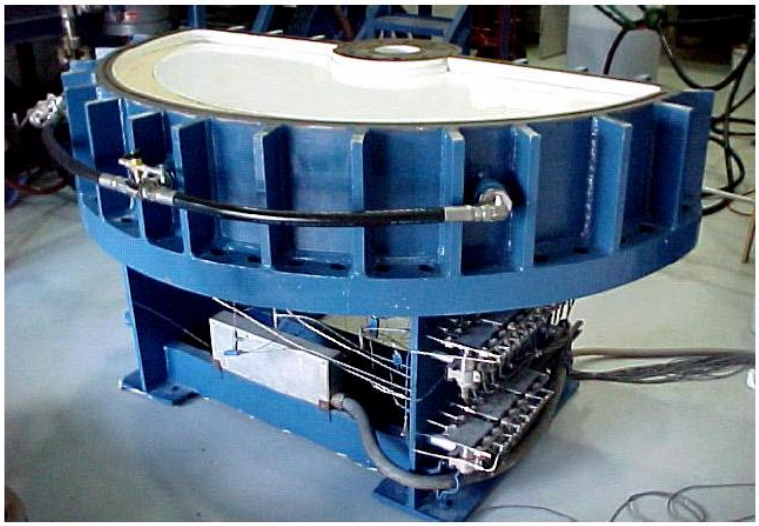

Figure 1.13: Half-cylinder radial flow cell (Khodaverdian and McElfresh, 2000).

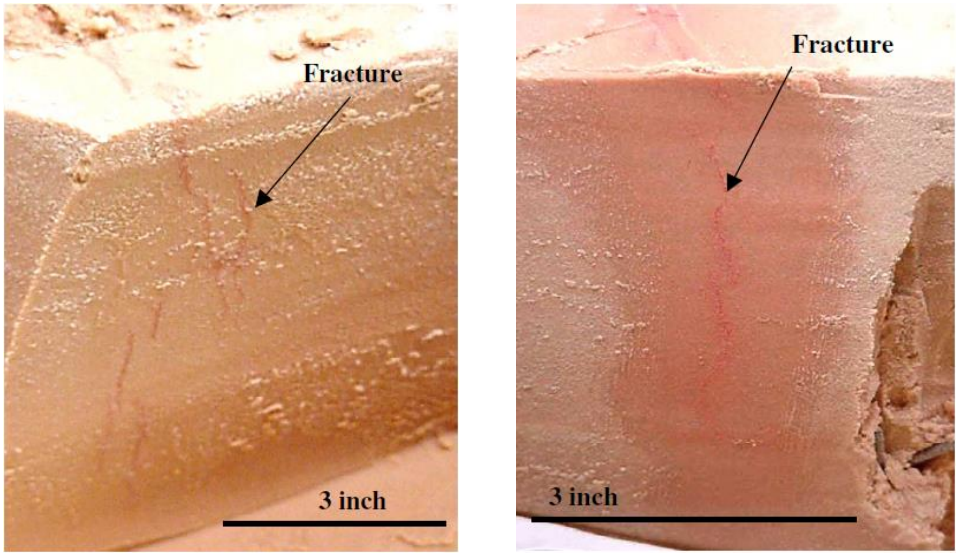

Figure 1.14: (a) sub-parallel vertical fractures; (b) single vertical fracture (Khodaverdian and McElfresh, 2000).

The fluid is injected through a casing having 5 perforated holes, one at the center and four others at ± 45° from the central holes. The confining stress can be applied up to 34.5 MPa. 200-mesh sand (Badger WS-140™) is used to reconstitute the specimen. The frac-fluid is a borate cross-linked guar (XLG) with an apparent viscosity varying between 110 cP (low efficiency) and 1100 cP (high efficiency) at a shear rate of 40 s^{-1}. The results clearly showed that fractures are created within the specimen after injecting the frac-fluid under high pressure, however, the mechanisms of fracturing propagation are not the same as those observed in consolidated material. The authors conclude that fracture propagation in soft sand medium is dominated by shear failure within a process zone ahead of the fracture tip.

These authors also indicate that the rheology of fluids has a pronounced effect on the fracturing mode and the critical fracturing pressure. Multiple sub-parallel fractures were formed (Figure 1.14a) when injecting a low viscosity fluid while for the tests in which, high viscosity fluids were injected, a single vertical fracture propagates (Figure 1.14b). Figure 1.15 presents the evolution of the net injection pressure (the difference between the critical fracturing pressure and the fracture closure stress). We observe that an increase in the fluid viscosity results in a decrease in the net injection pressure.

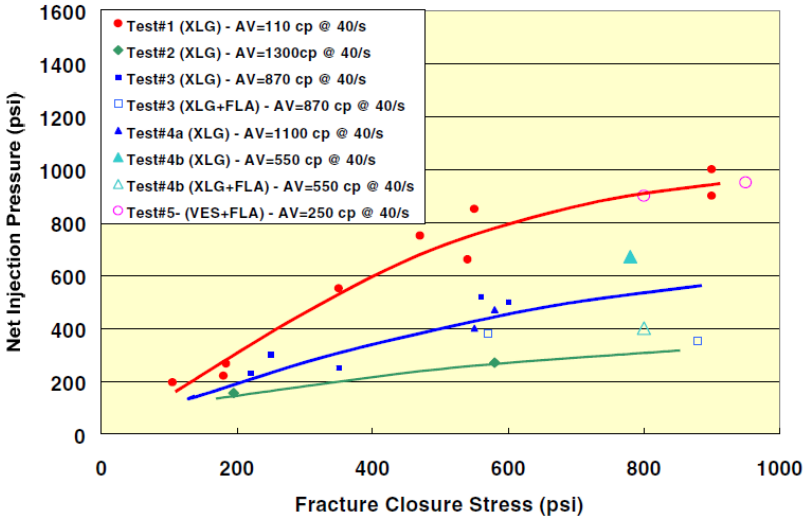

Figure 1.15: Net injection pressure vs fracture closure stress curve (Khodaverdian and McElfresh, 2000).

1.4.1.2 *Injection of high viscosity fluids in a triaxial cylindrical setup.*

a. Research group of Delft University of Technology

One of the most comprehensive experimental programs focusing on hydraulic fracturing in cohesionless sand has been conducted by the group of Delft University of Technology (Bohloli and de Pater, 2006; de Pater and Dong, 2007, 2009; Dong, 2010; Zhou et al., 2010). Experiments have been performed in an axisymmetric triaxial cell containing a central tube

fixed to the lower baseplate (Figure 1.16). Different configurations of injection tube have been used such as the porous tube, the slotted open hole, open-hole interval, depending on the purpose of the research. The applied radial stress is in the range of 0.2 MPa to 20 MPa, and the axial stress is in the range of 1.3 MPa to 28 MPa. Quartz sand is used to prepare the specimen.

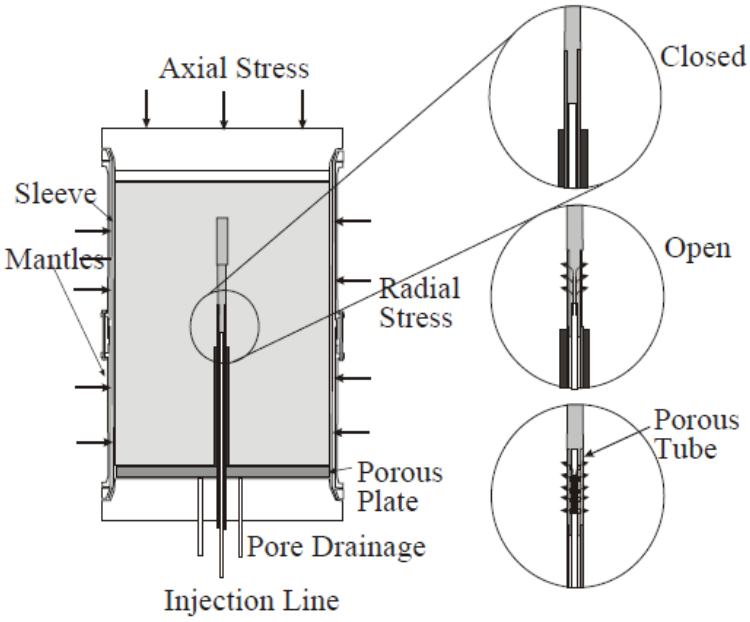

Figure 1.16: Triaxial cell configuration (de Pater and Dong, 2007).

Bohloli and de Pater (2006) have investigated the effect of various parameters on hydraulic fracturing such as the nature of the injection fluid, the confining pressure, the geometry of injection tube. The tests are performed in the large bi-axial cell with the specimen size of 0.4 m in diameter and 0.5 m in length. The results are briefly presented below.

❖ Effect of the injection fluid

Three different fluids are tested: viscous Newtonian fluid (Viscasil oil 500), bentonite slurry, cross-linked gel. The results show a strong influence of the rheology of the fluid on the response to hydraulic fracturing. In the case of Viscasil oil 500 with a viscosity of 6.10^5 cP, high injection pressures can be reached without creating visible fractures. If the fractures are formed, they are very tortuous and branched (Figure 1.17).

For the injection tests with the bentonite slurry, the concentration of bentonite is 100 to 150 g/l of water. The combination of four phenomena, including borehole expansion, fluid infiltration, shear banding and fracturing was observed. However, the expansion and infiltration remain the dominant phenomena. The authors found difficulties to create a fracture, especially in the case of a dense specimen.

Figure 1.18 presents an CT-Scan image of an injection test with bentonite. In this test, the stress conditions are 0.5 MPa of confining pressure and 0.8 MPa of axial stress. The maximum injection pressure is $P_{inj\ max}$ = 7 MPa corresponding to 14 times of the confining pressure, which leads to an expansion of the borehole and the creation of shear bands inside the specimen.

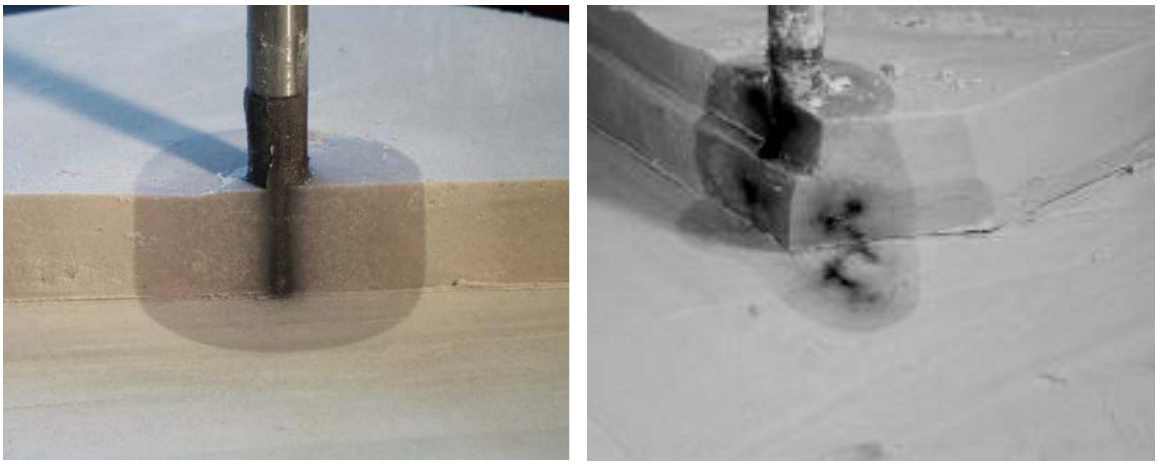

(a) (b)

Figure 1.17: Injection of viscous Newtonian fluid (Viscasil oil 500) in the sand specimen: (a) infiltration only (σ_3 = 20 MPa; σ_1 = 31 MPa; $P_{inj\ max}$ = 38.2 MPa); (b) small fractures creation (σ_3 = 7.5 MPa; σ_1 = 12 MPa; $P_{inj\ max}$ = 27.2 MPa) (de Pater and Dong, 2007).

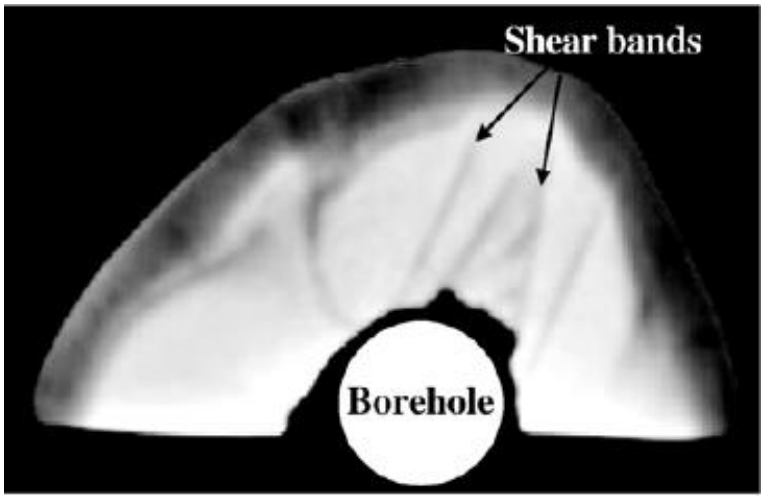

Figure 1.18: Typical CT-Scan horizontal cross-section after injecting the bentonite slurry (σ_3 = 0.5 MPa ; σ_1 = 0.7 MPa ; $P_{inj\ max}$ = 7 MPa): borehole expansion and shear bands (Bohloli and de Pater, 2006)

The gel injection tests with "Borate cross-linked" mainly resulted in fluid infiltration into the formation without fracturing. To increase fluid efficiency, quartz particles (concentration of 4.8 g/l with a $D_{50} \approx 10$ µm) were added to the gel. These particles allow to form the cakes to reduce the gel leak-off into the medium. By using the mixture of gel + quartz particles, fractures have been observed for all the tests, even for a very high confining pressure (Figure 1.19).

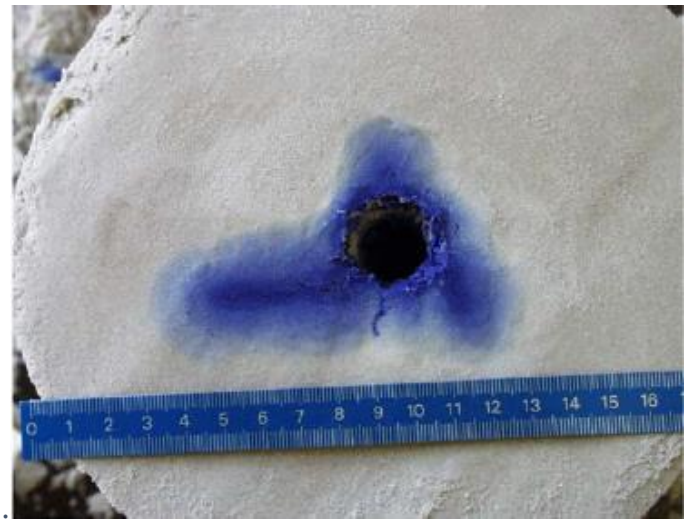

Figure 1.19: Fractures observed while injecting the mixture of borate cross-linked gel and quartz particles (σ_3 = 20 MPa; σ_1 = 28.5 MPa; $P_{inj\ max}$ = 55.5 MPa) (Bohloli and de Pater, 2006).

❖ Effect of the confining pressure

The authors highlight an important effect of the confining pressure on the maximum injection pressure. The higher the confining pressure, the lower the ratio of maximum pressure to confining pressure (Figure 1.20). This ratio decreases from around 12 to 3 with the increase of the confining pressure from 0.5 to 7.5 MPa. It can be also noted that the injection tests with bentonite lead to a higher fracturing pressure at the same magnitude of confining pressure. The authors observe that the fractures obtained at high confining pressure are short, branched and tortuous whereas in the case of low confining pressure, the fractures are longer and straighter (Figure 1.21).

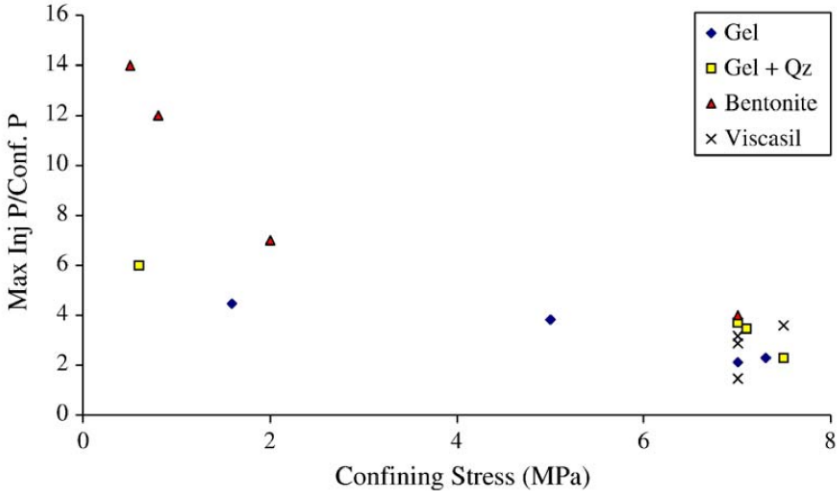

Figure 1.20: Normalized maximum injection pressure by confining pressure vs confining pressure (Bohloli and de Pater, 2006).

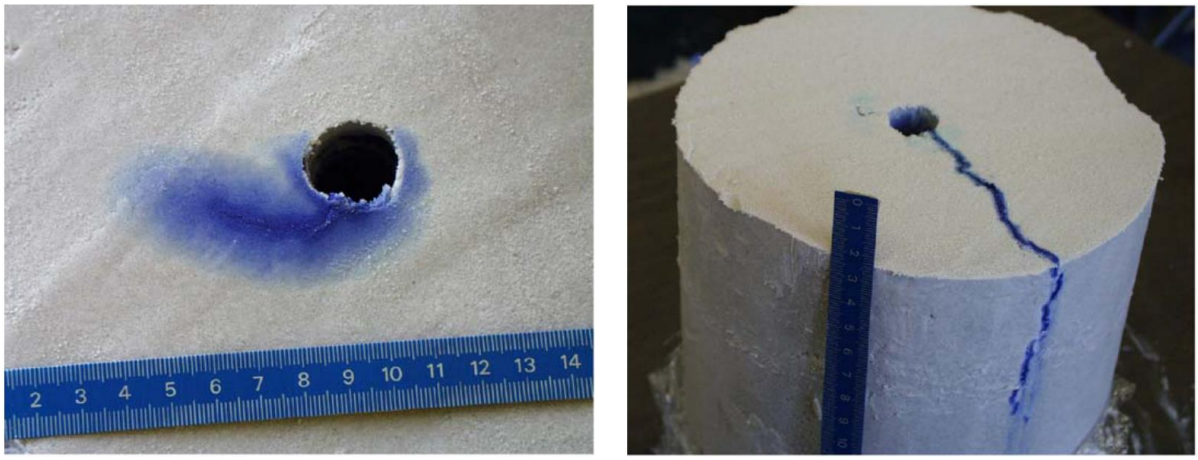

(a) (b)

Figure 1.21: Effect of confining pressure on the fracture shape: (a) high confining pressure (σ_3 = 20 MPa ; σ_1 = 28.5 MPa ; $P_{inj\ max}$ = 55.5 MPa); (b) low confining pressure (σ_3 = 0.6 MPa; σ_1 = 1.3 MPa; $P_{inj\ max}$ = 3.6 MPa) (Bohloli and de Pater, 2006).

❖ Effect of the geometry of the injection tube

The geometry of the injection tube also plays a very important role in the morphology of the fracture. The test with the porous tube mainly resulted in a slight expansion of the area around the tube and infiltration of the fluid into the medium (Figure 1.22a) while for the tubes with open vertical slots (Figure 1.22b,c), the fractures generated at the open slots position.

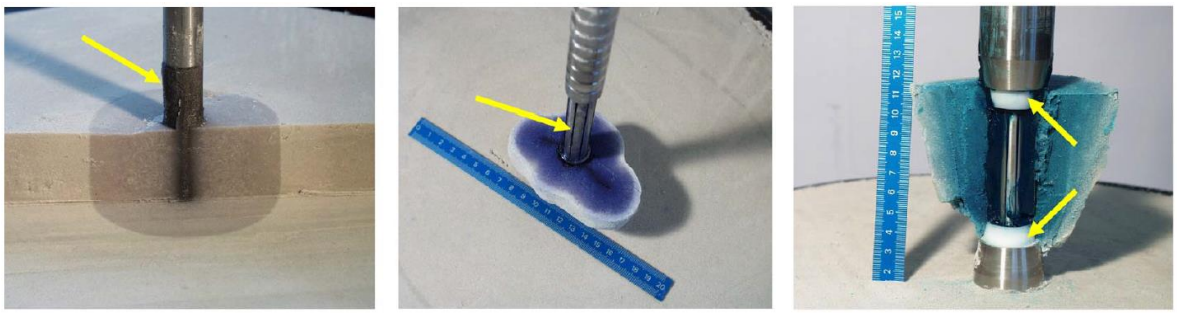

(a) (b) (c)

Figure 1.22: Effect of the tube geometry: (a) porous tube; (b) slotted open hole tube; (c) slotted tube plus PVC end pieces (Bohloli and de Pater, 2006).

Zhou et al., 2010 have performed an experimental investigation on hydraulic fracturing due to polymer injection in the unconsolidated sand specimens. The tests were carried out on a triaxial cylindrical cell (Figure 1.16) with the slotted open hole tube (Figure 1.22b). The specimens were prepared by the mixture of quartz (D_{50} = 105 µm) and silt (D_{50} = 15 µm). The mass ratio of silt to quartz is 10%. The test procedure consists of three principal steps: saturation of the specimen with water to measure the initial permeability (absolute permeability); saturation with oil to simulate an unconsolidated sand reservoir containing viscous oil and final injection phase of a small volume of the polymer to fracture the medium and to study the sweep

efficiency of the polymer injection. The experimental results exhibited two trends corresponding to different geometries of the fractures:

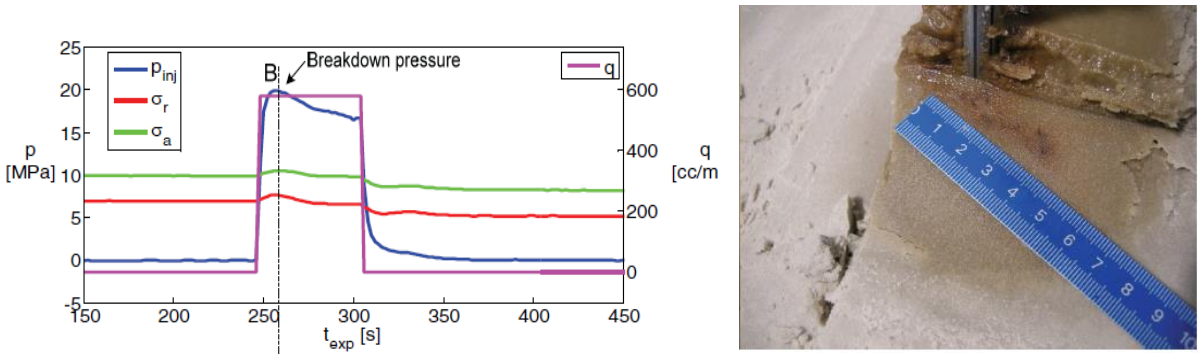

(a) (b)

Figure 1.23: Injection test with high flow rate and high viscosity fluid (q = 0.6 l/min; μ = 10^4 cP): (a) test results during injection; (b) typical photo of the specimen during excavation (Zhou et al., 2010).

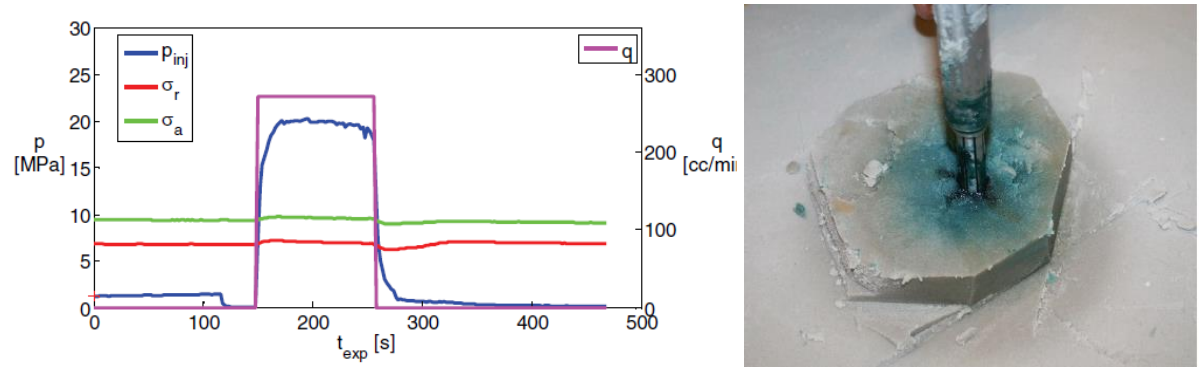

(a) (b)

Figure 1.24: Injection test with low flow rate and low viscosity fluid (*q* = 0.3 l/*min; μ = 3.5*10*^{3} *cP): (a) test results during injection; (b) typical photo of the specimen during excavation* (Zhou et al., 2010).

- By combining both a high flow rate and a high viscosity fluid, a drop in injection pressure is observed; it corresponds to the propagation of a long fracture in the specimen (Figure 1.23).
- In the case of low injection rate and low viscosity, no pressure drop or clear pressure decline tendency is identified and only some small fractures are observed around the injection tube (Figure 1.24).

By performing a series of five injection tests, the authors observed that the injection pressure must exceed the confining pressure by a factor of 2.5 to induce fracturing of the specimen (Figure 1.25). All these tests have been performed at the same stress conditions (7 MPa of confining pressure and 10 MPa of axial stress).

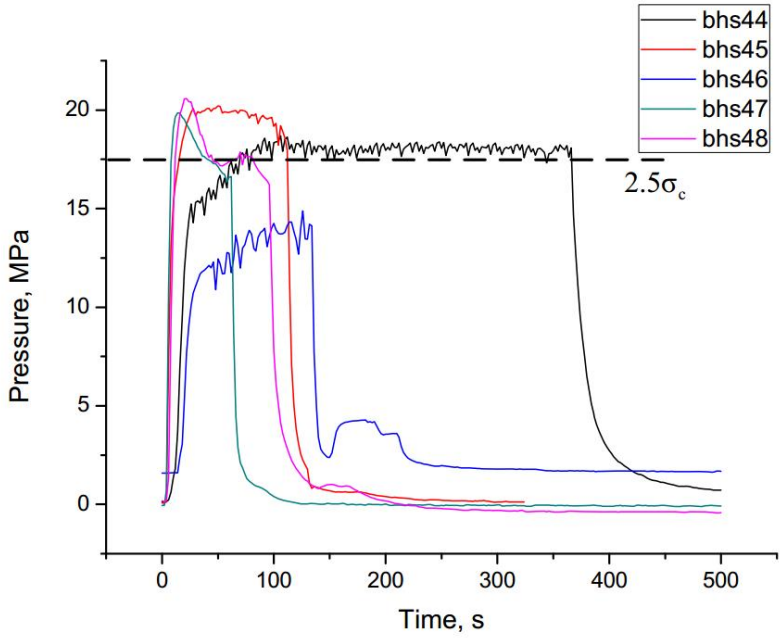

Figure 1.25: Synthesis of all polymer injection tests performed by Zhou et al., 2010.

b. Research group at Georgia Institute of Technology

Another interesting study on hydraulic fracturing in particulate materials has been performed at Georgia Tech (Chang, 2004; Wu, 2006; Germanovich et al., 2012; Hurt, 2012). The schematic diagram of the injection cell is presented in Figure 1.26. The tests are performed on two different scales (small and large cell). For the small-scale experiments, the specimen sizes are about 10 cm (4 in) in diameter and 20 cm (8 in) in height. For the large-scale injection cell, the diameter of the specimen is about 30 cm (12 in) and the height is 46 cm (18 in). The specimens are prepared with a mixture of Ottawa Sand F110 (D_{50} = 110 µm) and silica fine particles (D_{50} = 22 µm). Different configurations of the injection tube are used to favor fracturing of the specimen (Figure 1.27 and Figure 1.28). Chang (2004) and Wu (2006) investigated hydraulic fracturing in dry sand specimen whereas Hurt (2012) performed the tests in saturated sand. The general procedure of the experiments consists of injecting viscous fluid into the specimens at a constant flow rate. The fluid solidifies after injection and the invaded area is extracted for post-test analysis. Fracturing fluids are selected to satisfy various requirements. First, a high viscosity is necessary to reduce the leak-off of the fluid into the medium. Second, the fluid must freeze in the saturated environment. Third, the fluid must be easily drained from the injection line. Finally, the fluid must be immiscible with the fluid in the pores (water). Consequently, two types of fluids have therefore been chosen: silicone adhesives and guar-based fluids which are both non-Newtonian and very viscous fluids.

Various parameters have been studied, such as the specimen properties (permeability, ratio of fines in the mixture sand + fines), fluid rheology, stress conditions, injection rate and volume. In the following, some typical results of the Georgia Tech group are presented.

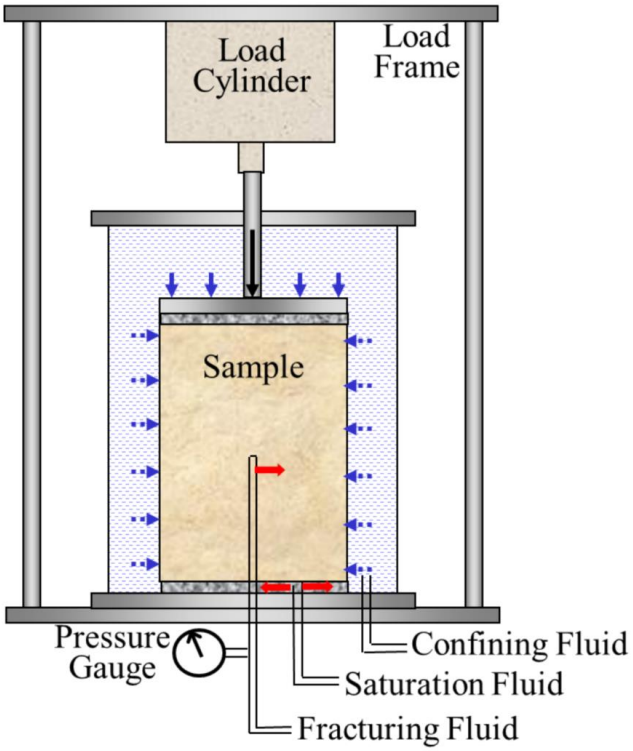

Figure 1.26: Schematic diagram of the injection cell (Hurt and Germanovich, 2012).

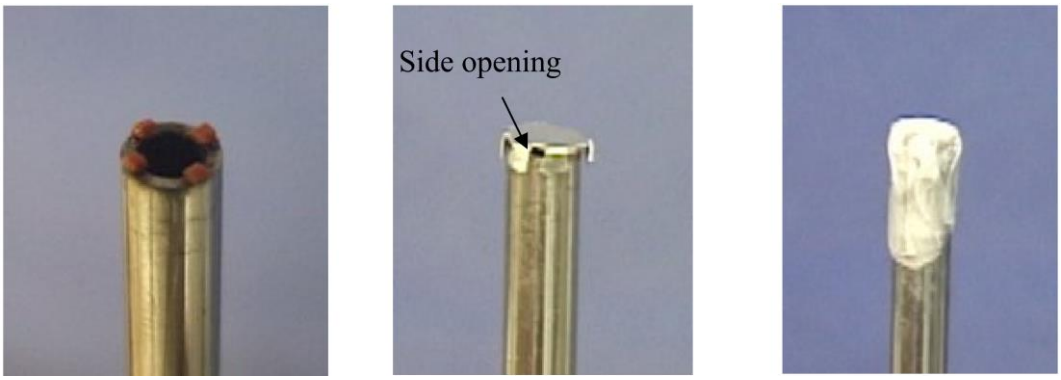

Figure 1.27: Configurations of the injection tube used in the experiment of Chang (2004).

Figure 1.28: Injection tubes used by Hurt and Germanovich, 2012.

Chang (2004) and Wu (2006) found that hydraulic fracturing in granular materials is possible if fluid infiltration in the area around the fracture is minimized (high injection rate, low permeability of the medium, high fluid viscosity). After the observation of the fracture geometry and of the measured pressure curves, the authors suggest that hydraulic fracturing could occur in granular materials according to the following steps:

i. Expansion of the cavity before the injection pressure reaches its maximum value

ii. Initiation of the fracture after expansion of the cavity (near the pressure peak)

iii. Propagation of the fracture in the specimen

Steps (i) and (ii) are the main steps in the fracture initiation process. Figure 1.29 shows a typical injection test result. The pressure *p* represents the pressure at the end of the initiation phase of the fracture.

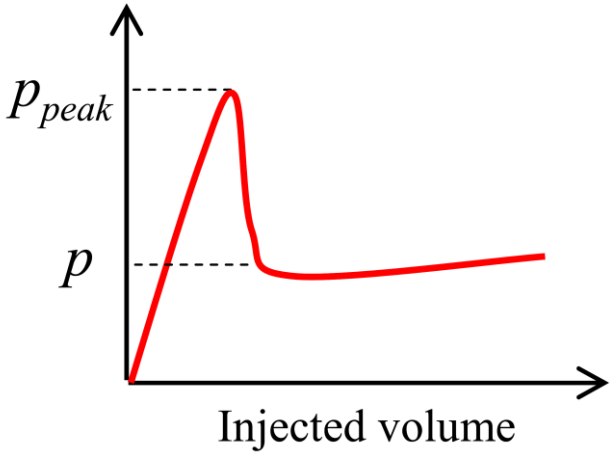

Figure 1.29: An example of pressure – injection volume curve (Chang, 2004).

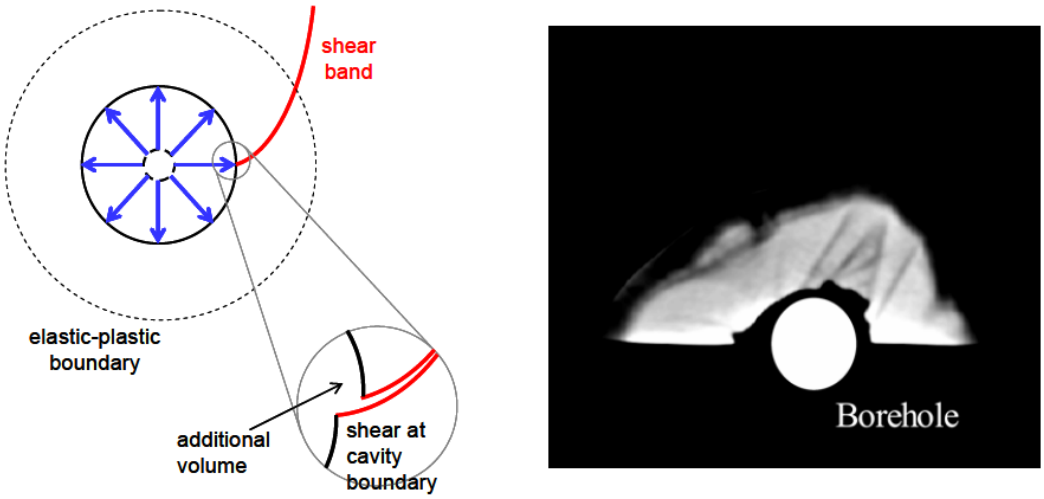

Figure 1.30: (a) Concept of shear band developed around the cavity (Chang, 2004)*; (b) CT scan image of the specimen after injection* (de Pater and Dong, 2007).

Chang (2004) suggested three mechanisms that may explain fracture initiation.

- Formation of shear bands as shown in Figure 1.30, which abruptly affect the shape of the cavity. This mechanism has been also observed by de Pater and Dong (2007) when performing the injection of bentonite slurry into sand specimens and by Alsiny et al. (1992) when studying strain localization in cavity expansion tests.

- Effects of liquefaction caused by the infiltration of pressurized fluid into the dry specimen; thereafter, the effective stress around the cavity decreases to zero (Figure 1.31a).

- Off-shoots from the cavity. This can occur if the pressure required to expand the nearby small cavity is less than the current pressure in the large cavity (Figure 1.31b).

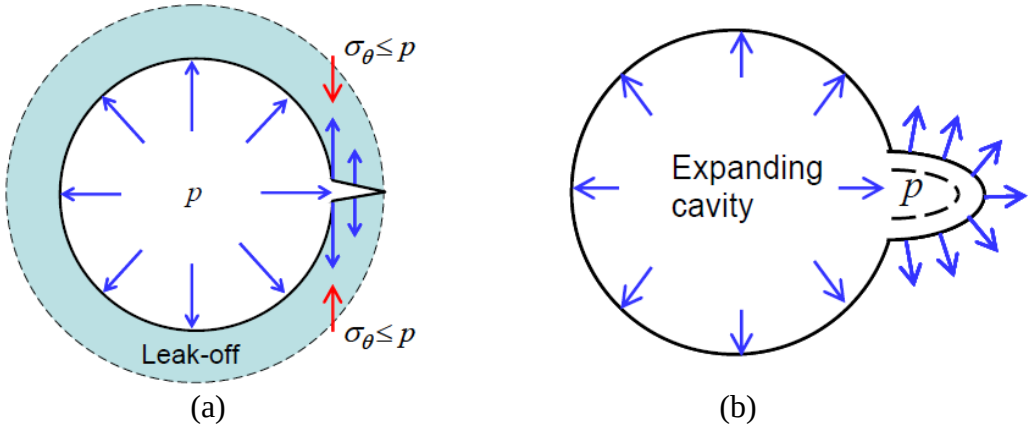

Figure 1.31: Hypothesis of the fracture initiation mechanism: (a) liquefaction-like effect (b) cavity expansion (Chang, 2004).

Germanovich et al. (2012); Hurt (2012) have developed an experimental program to investigate the initiation and propagation of the fractures induced in the saturated granular materials. Four main parameters were studied in these works: confining pressure, fluid rheology, flow rate and the permeability of the medium. The results are briefly presented below.

❖ Effect of different injection fluids

Two non-Newtonian fluids are used: silicone adhesive and guar-based fracturing fluid. They are both the viscous fluids with the apparent viscosity of about 10^4 to 10^5 cP and they solidify after injection.

Figure 1.32a presents the injection results of a test series with silicone adhesives in terms of pressure – time curves. . In this series, all other parameters are fixed (σ_3 = 20 psi, k = 1.3 Darcy, Q = 50 ml/min, τ_o = 457 Pa, K = 123 Pa×sec^n, and n = 0.75) with the exception of the injection volume varying between 100 ml, 200 ml and 400 ml. Qualitatively, the first specimen illustrates the initial phase of fracturing (Figure 1.32b) while two others (Figure 1.32c&d) show the propagation of the fracture. The cross-sections are cut at the height at which the fracture is wider.

In silicone injection tests, the fracture opening is quite large, suggesting that there is significant plastic deformation during fracturing. Many specimens were injected with colored silicone with two different dyes (white and black). The authors observed that when injecting the second dye (black dye), the fluid continues to flow in the direction parallel to the existing fracture and not contributing measurably to the existing leak-off surface elsewhere (Figure 1.33).

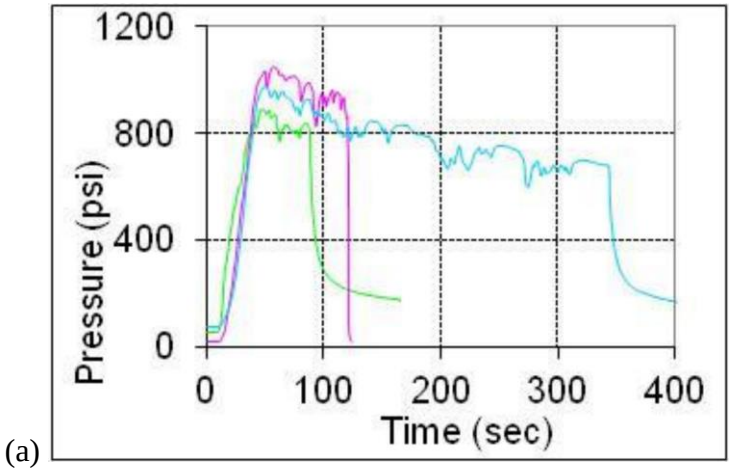

(a)

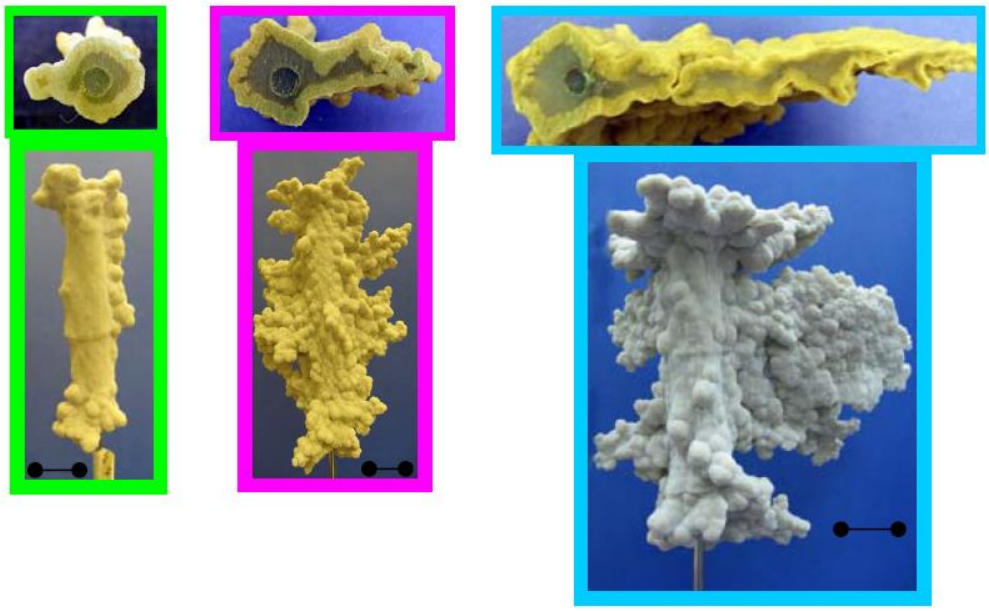

(b) (c) (d)

Figure 1.32: Fractures observed in the tests with different injection volumes of the silicone adhesive under the same testing conditions (σ_3 = 20 psi, k = 1.3 Darcy, Q = 50 ml/min) (a) injection results (100 ml – green curve, 200 ml – pink curve, 400 ml – blue curve); (b), (c), (d) fracture morphology of the tests with the injected volume of 100 ml, 200 ml, 400 ml, respectively (Germanovich et al., 2012).

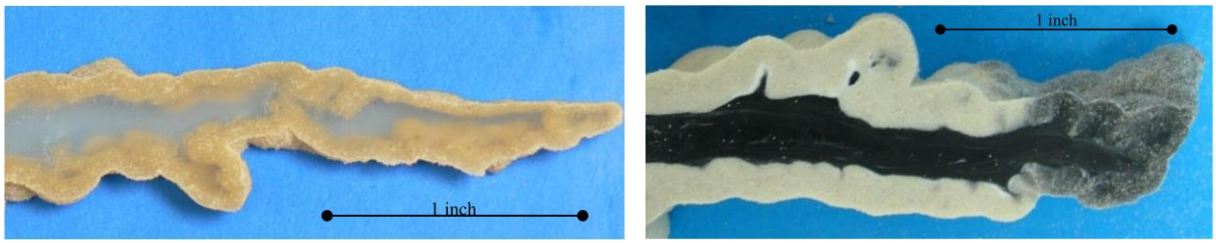

(a) (b)

Figure 1.33: Typical cross-sections with the silicone injection: (a) one injection phase without adding dye; (b) two injection phases with different dyed fluids (black fluid following white) (Hurt, 2012).

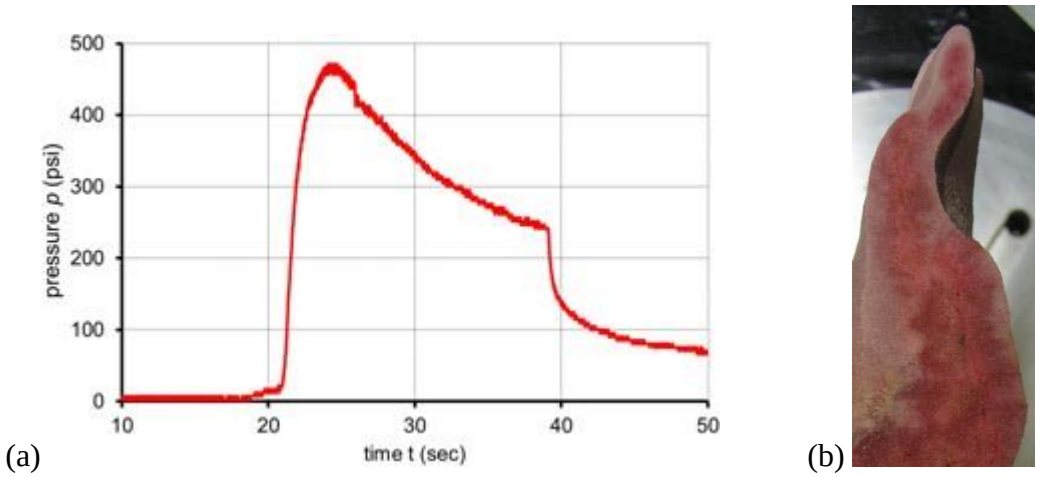

(a) (b)

Figure 1.34: Test result with guar gel injection: (a) pressure – time curve; (b) a typical slide of the specimen after injection (Germanovich et al., 2012).

The fractures induced by the guar gel, under experimental conditions similar to those with silicone, present different morphologies (Figure 1.34b). Nevertheless, the trend in the pressure - time curve observed during these tests is consistent with the results obtained with silicone (Figure 1.34a). The fractures are generated by the guar fluid required a high flow rate to control the leak-off of this gel in the specimen. The existence of a stress threshold for the silicone-based fluid makes it possible to preserve the opening of the fracture after stop pumping and the injection pressure decreases to zero while in the case of the guar fluid, the fracture closes and fluid infiltrates into the formation.

- ❖ Effect of confining pressure

A series of silicone injection tests was performed at the same flow rate of 50 ml/min while changing the magnitude of the confining pressure (Figure 1.35). The authors found that the confining pressure is the primary factor affecting the maximum injection pressure (peak pressure) as well as the fracture aperture. An increase of the confining pressure results in a higher peak pressure, a larger fracture aperture and a thicker leak-off zone.

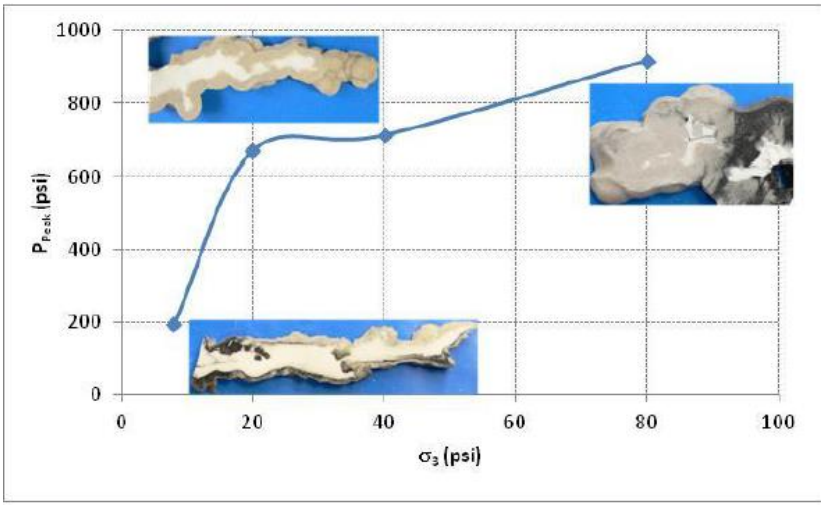

Figure 1.35: Silicone injection tests under different confining pressures (10, 20, 40 and 80 psi) at the same flow rate of 50 ml/min (Hurt, 2012).

❖ Effect of the fluid viscosity

The peak pressure increases slightly by increasing the viscosity of injection fluid (Figure 1.36). It can be seen that the fracture aperture is wider when injecting a higher fluid viscosity. Increasing the viscosity also reduces the leak-off of the silicone fluid into medium.

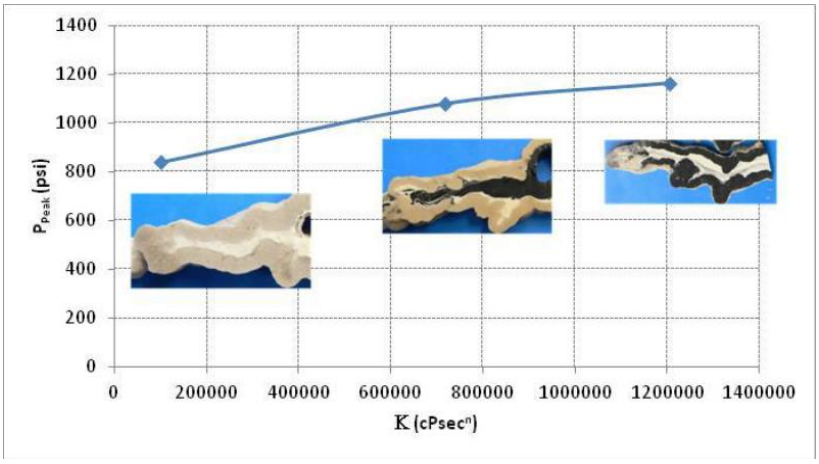

Figure 1.36: Results of two test series at a confining pressure of 80 psi and a flow rate of 1700 ml/min (Hurt, 2012).

❖ Effect of flow rate

The authors observed that the flow rate has no significant effect on the maximum injection pressure however, increase in flow rate leads to the formation of longer and larger fractures within the specimen (Figure 1.37). A significant reduction of the leak-off zone is also observed when the flow rate increases.

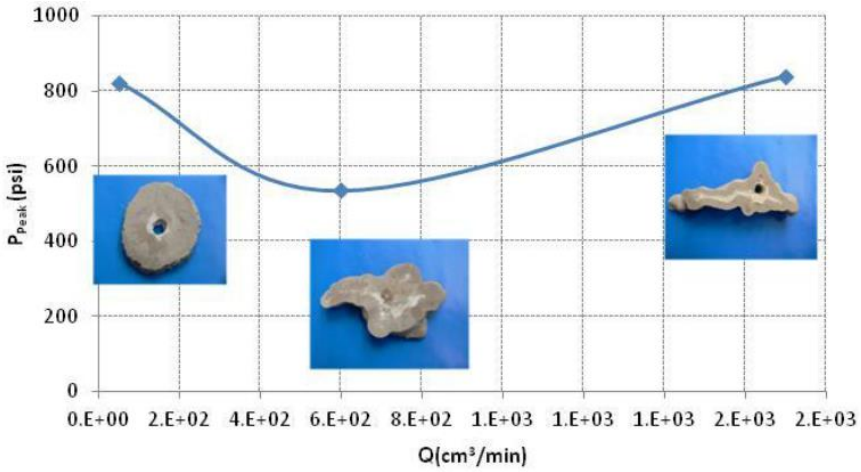

Figure 1.37: Results of three injection tests with different flow rates. k = 1000 mD, σ_c = 80 psi (Hurt, 2012).

❖ Effect of the permeability

The authors found that reducing the permeability significantly reduces the leak-off of the fluid into the medium (Figure 1.38), however, the peak pressures do not appear to be affected.

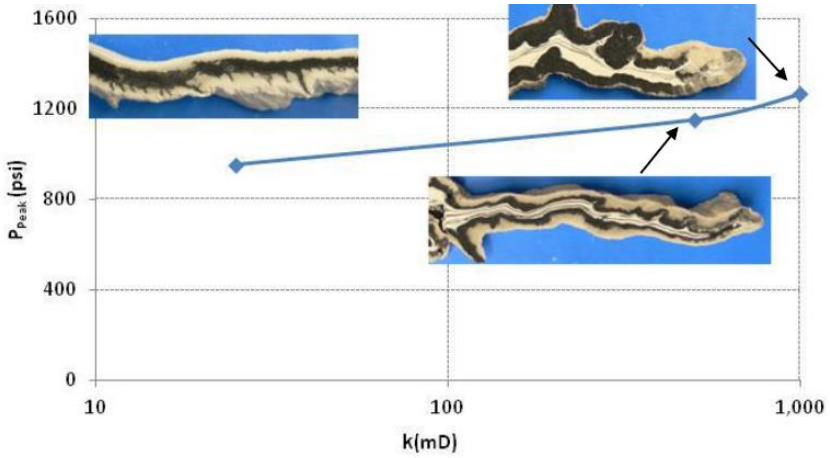

Figure 1.38: Different fracture morphologies when changing the permeability of the specimen. (Q =1700 ml/min and σ_c = 80 psi) (Hurt, 2012).

Hurt (2012) presents an interpretation method that incorporates the impact of the combination of experimental parameters on the maximum pressure value (P_{peak}) using a dimensionless analysis model (Barenblatt, 2003). In fact, the traditional method, which represents the relationship between the confining stress and the normalized maximum pressure, is not efficient, the effects of other experimental parameters being ignored (Figure 1.39). This is why the maximum pressure for tests performed at confining stress of 500 kPa (80 psi) varies considerably. Data from a single vertical line at 80 psi of confining stress represents over 30 tests.

This new model consists in bringing together all the experimental parameters using the dimensionless analysis model (Barenblatt, 2003). The maximum injection pressure depends on the following parameters:

$$P_{peak} = f(K, n, E, v, k, c, \tan\varphi\,, Q, \sigma_{max}\,, \sigma_{min}) \tag{1.3}$$

where K et n are the fluid parameters (Herschel-Bulkley fluid); $E, v, k, c, \tan\varphi$ are the parameters of the material; $Q, \sigma_{max}\,, \sigma_{min}$ are the test conditions.

For all the tests of this work, the injection rate Q, the viscosity of the fluid or the consistency factor K, the intrinsic permeability of the medium k, and the confining stress, σ_o, are the parameters that vary in a wide range during the experiments, while the other parameters vary much less or they are not independent. By choosing Q, K and k, σ_o as the independent parameters, the authors define two dimensionless combinations (i.e., dimensionless peak pressure and dimensionless stress):

$$\frac{P_{peak}}{K}\left(\frac{k^{\frac{3}{2}}}{Q}\right)^{n} = f\left[\frac{\sigma_o}{K}\left(\frac{k^{\frac{3}{2}}}{Q}\right)^{n}\right] \tag{1.4}$$

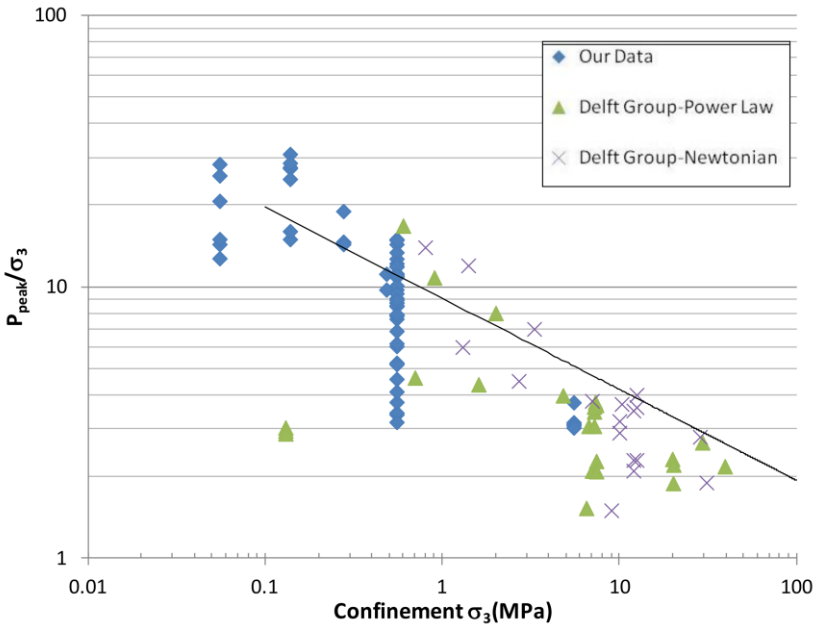

Figure 1.39: Relation between the confining pressure and the normalized peak pressures taken from De Pater and Dong (2007), Dong (2010) *and the results of this research* (Hurt, 2012).

Using this equation, the authors plotted over 60 experimental data points from their studies and by combining those from the literature results at the University of Delft (Figure 1.40). The authors obtain a reasonable fit, although the logarithmic scale limits the precision of the fit. A

simple dimensionless relationship between the confining stress and the maximum injection pressure is used to determine the initiation of hydraulic fracturing.

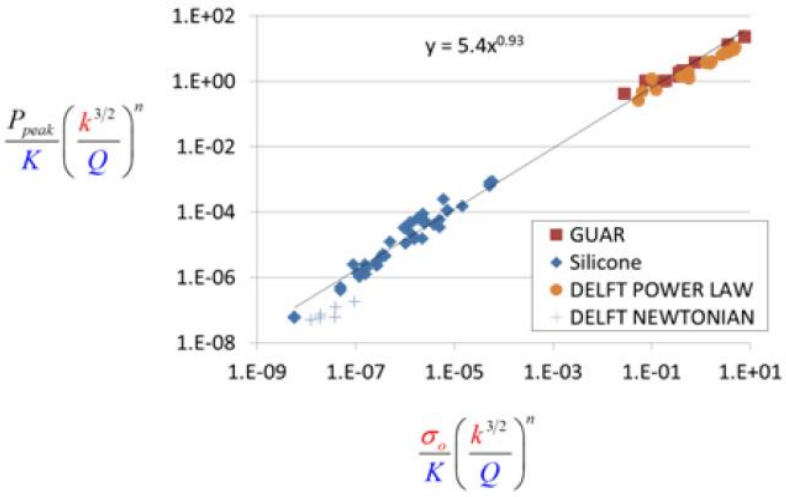

Figure 1.40: Dimensionless relationship between maximum injection pressure and confinement pressure (Hurt, 2012).

1.4.1.3 *Injection of low viscosity fluids in a true triaxial setup*

a. <u>Research group at University of Illinois</u>

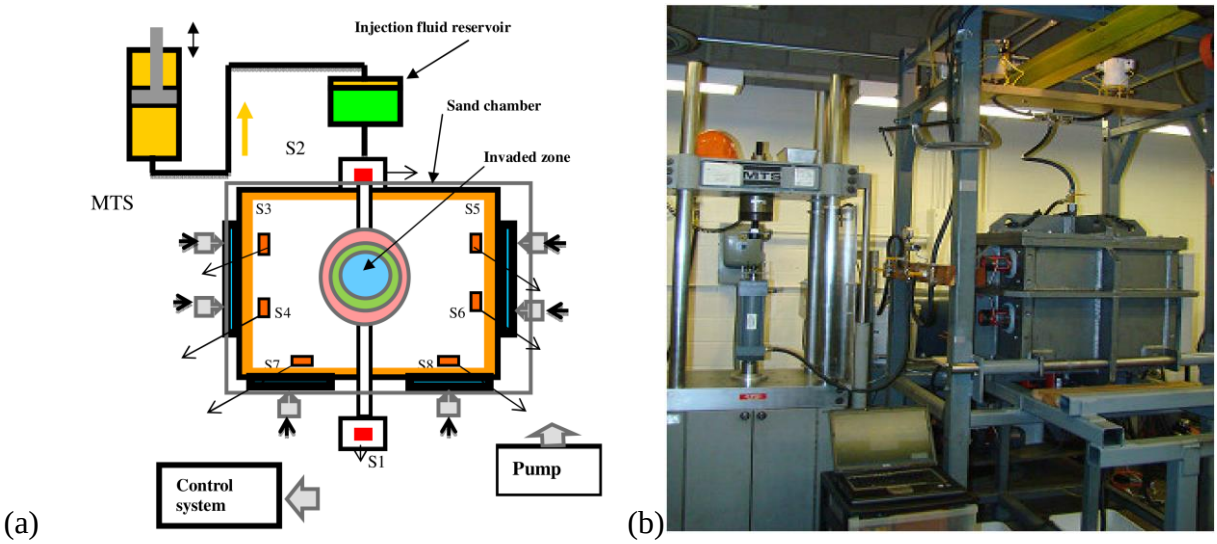

Figure 1.41: (a) schematic diagram of the injection setup; (b) view of the chamber (Golovin et al., 2011).

An interesting work on hydraulic fracturing in cohesionless sand was conducted at the University of Illinois (Golovin et al., 2010, 2011; Chudnovsky et al., 2015; Jasarevic et al.,

2010; Wong et al., 2017). These authors have developed a special device for performing injection tests under 3D stress conditions (i.e., axial stress σ_v, maximum horizontal stress σ_H and minimum horizontal stress σ_h) (Figure 1.41). The chamber has a cubic shape of about 61 cm (2 ft). An aluminum tube (D_{ext} = 12.5 mm and D_{int} = 9 mm) is used as a wellbore. Two opposite open holes are made in the middle of the tube. The material used in this experiment is the arkosic feldspathic sand which is similar in texture and mineralogy as compared to the sand reservoirs in the Gulf of Mexico. The injection fluid is a mixture of gelatin powder dissolved in water. Before the injection, this mixture is heated to 65°C to provide a similar viscosity as water (1 cP). The mixture crosslinks after cooling, thus allowing the injection zone to be solidified. Various concentrations of solids are added to the fracturing fluid to provide a better fracture creation. The dyes (red or blue) are also added to the fluid to increase the contrast of the fracture.

The authors have studied the effect of various parameters such as injection rate, concentration of solid particles, stress conditions on hydraulic fracturing. The results show that, according to these parameters, the process covers matrix injection regime, cavity expansion, creation of a single long fracture or multiple branching and random fractures.

Golovin et al., 2010 have conducted a series of 75 tests for studying the effects of various parameters on the geometry of the fractures after injection. Figure 1.42 presents the observation of the invaded zone after freezing and its corresponding vertical cross-sections. In the sensitivity analysis, the authors have selected the vertical cross-sections at a distance of 25 mm from the injection tube in order to evaluate the effect of various parameters, detailed below, on the fracturing shapes.

(a) (b)

Figure 1.42: (a) invaded zone after solidifying of a typical specimen; (b) verticals cross-sections of the invaded zone chamber (Golovin et al., 2011).

❖ Effect of solid concentration in the injection fluid

A series of tests has been carried out with different concentrations of solids in the fracturing fluid. The added solid is quartz powder with a grain size of around 10 µm. The other parameters are maintained constant during these tests: gelatin concentration of 11.5%; flow rate of 10

cm^3/s; stress conditions σ_v = 275 kPa (40 psi), σ_H = 240 kPa (35 psi), σ_h = 70 kPa (10 psi). Figure 1.43 shows the impact of the solid concentrations on the morphology of the invaded zone, size and shapes of the fracture. Without solid particles in the injection fluid, the invaded zone is almost spherical without any visible created fracture inside this zone. This phenomenon is also observed by Bohloli and de Pater (2006) for the injection tests of the borate cross-linked gel. As the solid concentration increases, the invaded zone becomes more flattened in the direction of the minimum horizontal stress (σ_h) and the fracture is longer and less branching.

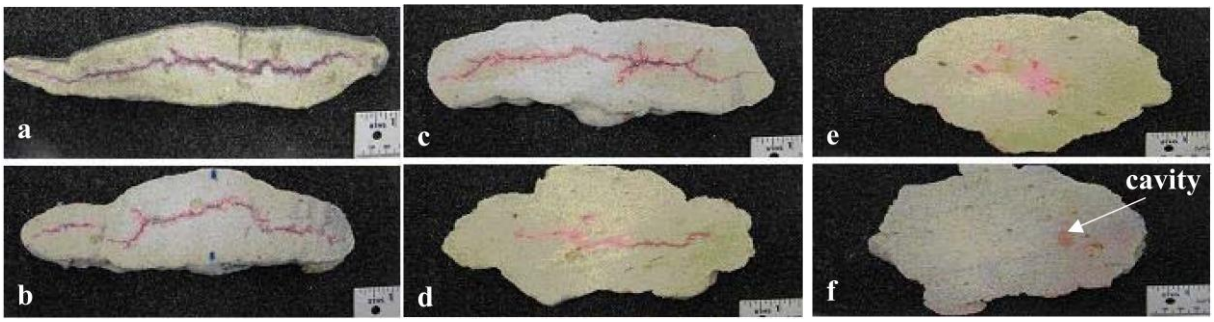

Figure 1.43: Effect of the solid concentration on the fracture morphology (% by mass): a) 11.5%, b) 7.5%, c) 3.75%, d) 2%, e) 1%, f) 0% (Golovin et al., 2010).

❖ Effect of the injection rate

The authors have performed two series of tests with different flow rates varying between 1 and 100 cm^3/s: the first series was carried out with a low solid concentration of 2% and the second with a high concentration of 7.5%. The other parameters are fixed constant: gel concentration of 11.5%; the stress conditions σ_v = 275 kPa (40 psi), σ_H = 240 kPa (35 psi), σ_h = 70 kPa (10 psi).

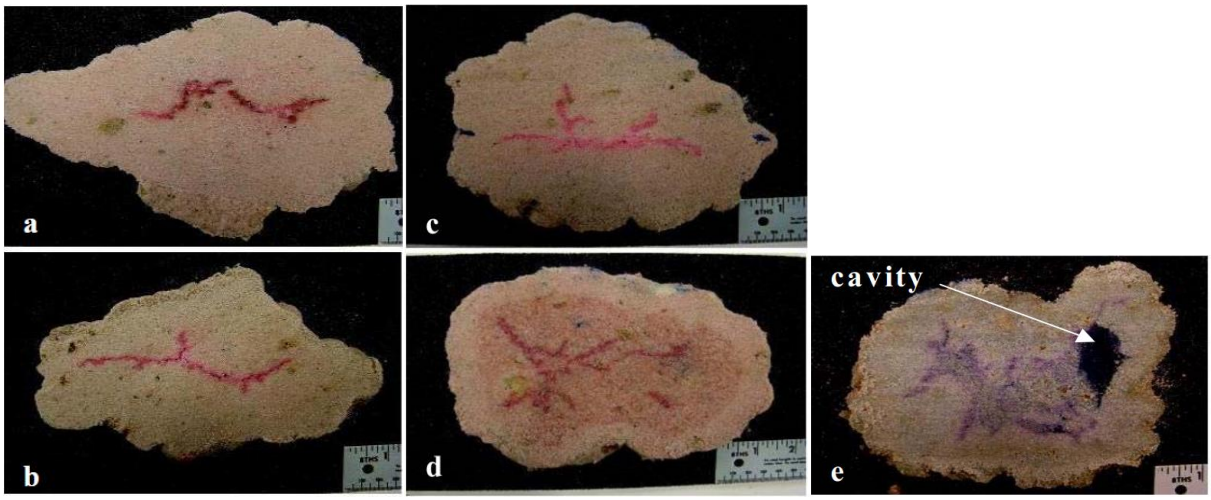

Figure 1.44: Effect of the injection rate on the fracture morphology for low solid concentration of 2%: a) 1 cm^3/s; b) 5 cm^3/s; c) 10 cm^3/s; d) 25 cm^3/s; e) 100 cm^3/s (Golovin et al., 2010).

Figure 1.44 presents the experimental results with the solid concentration of 2%. It can be seen that the injection rate only slightly affects the shape and size of the gelification zone. However, the fracture pattern appears to be highly dependent on the injection rate. At low flow rate, a simple, noticeably straight fracture with small branches is created. As the flow rate increases, the fracture pattern becomes more complex with multiple branches. On the other hand, in the case of the high concentration of solid particles (7.5%), the invaded zone changes significantly as the injection rate increases (Figure 1.45).

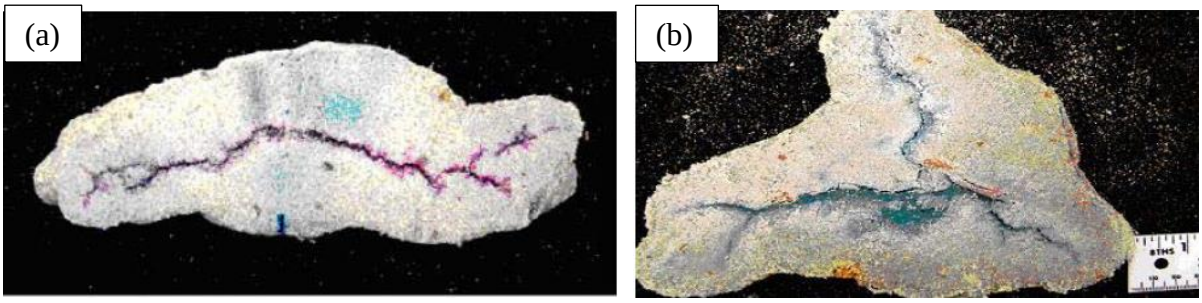

Figure 1.45: Effect of the injection rate on the fracture morphology for high solid concentration (7%): (a) 10 cm^3/s; 100 cm^3/s (Golovin et al., 2010).

❖ Effect of the stress conditions

In order to show the effect of the stress conditions applied to the specimen, the authors have performed a series of tests with the same components of fracturing fluid (water / gel / solid = 82% / 13% / 5%) and an injection rate of 50 cm^3/s. The vertical stress and the maximum horizontal stress are equal ($\sigma_v = \sigma_H > \sigma_h$). Figure 1.46 shows the effect of the stress conditions on the fracturing mode. As the stress conditions increase, the invaded zone becomes more flattened and the fractures becomes less branching. This behavior is similar to the effect of increasing the solid concentration in the injection fluid.

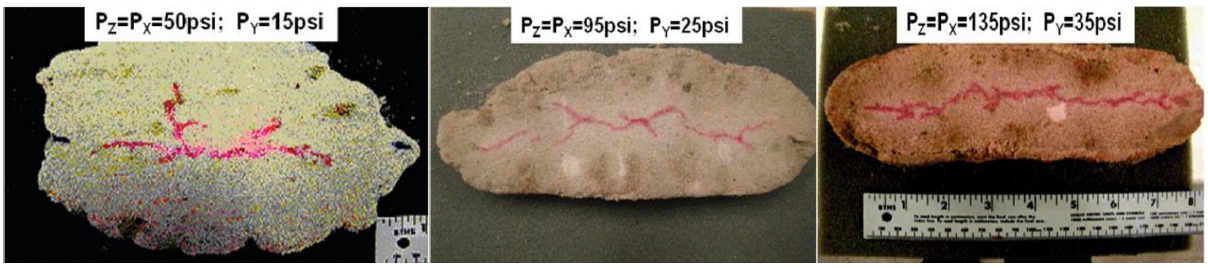

Figure 1.46: Effect of stress conditions on the fracture morphology (Golovin et al., 2010).

❖ Fracture growth in the test with two injection stages.

Figure 1.47 presents a typical injection test with two injection stages at the same injection rate of 50 cm^3/s. For the first injection stage, the red dye is added into the fluid and the blue dye

is used in the second stage. During the first stage, a sharp pressure drop is identified, followed by a gradual decrease of the injection pressure until full stop of the injection (Figure 1.47a). The second stage presents an almost constant value of injection pressure without any pressure drops. Figure 1.47b presents a cross-section of the invaded zone post-test. The peripheral part of the fracture is blue, which implies that during the second injection, the fracture is reopened and then it continues to propagate in the specimen.

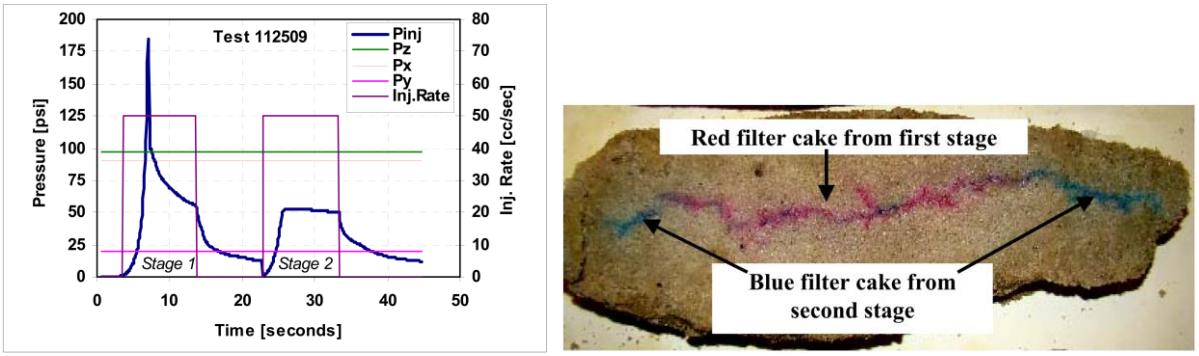

Figure 1.47: Two-injection stages test: (a) pressure – flow rate – time curves, (b) cross-section of the invaded zone (Golovin et al., 2010).

Golovin et al., 2011 have performed an experimental study of injection rate effects on water flooding mechanisms in cohesionless sand. A total of 45 tests are carried out and analyzed in wet and saturated sand specimens. The same preheated solution of gelatin powder dissolved in water is used in this research, but without the solid particles. Each test consists of three injection steps with the use of three different dyes, allowing to better visualize the progress of the fluid at each step.

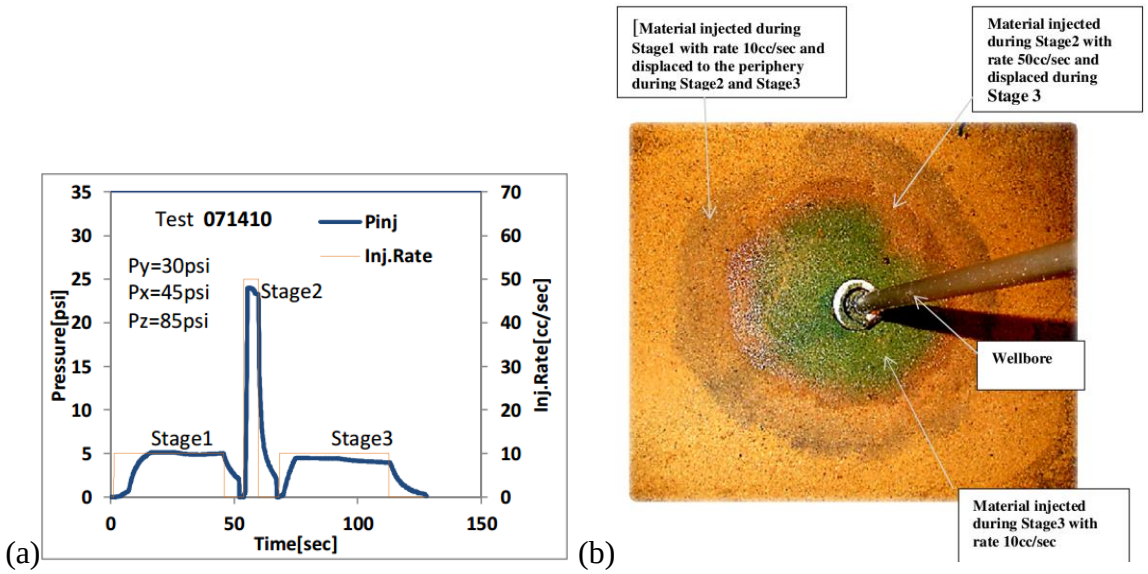

Figure 1.48: Results of a typical injection test in the matrix regime in the wet sand specimen by oil: (a) pressure – flow rate – time curves; (b) horizontal cross-section at the middle of the invaded zone (Golovin et al., 2011).

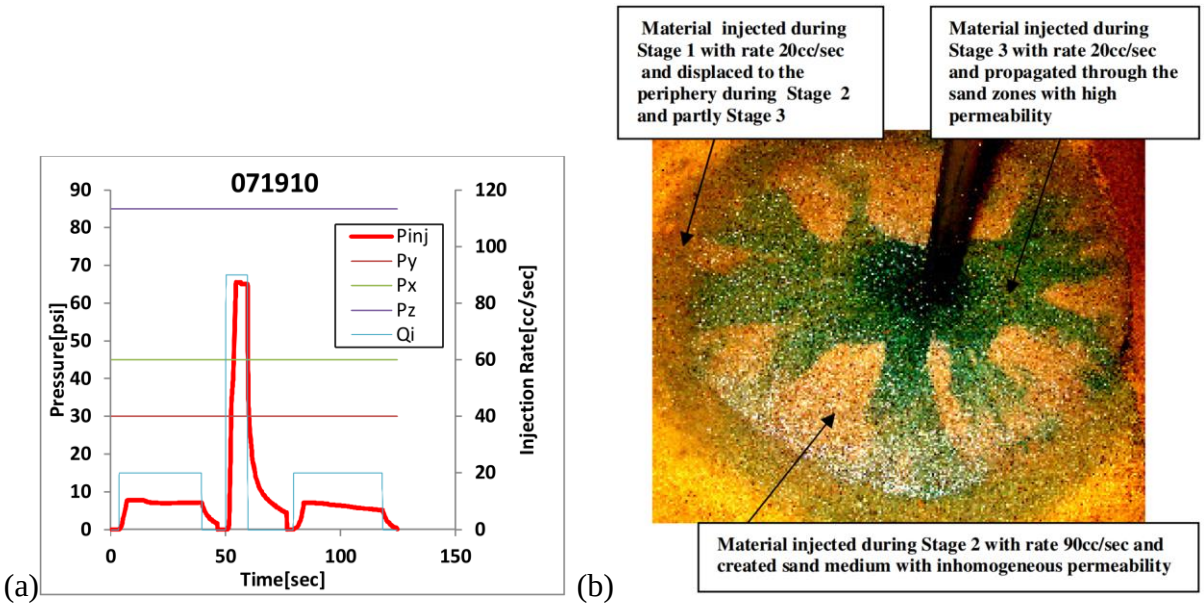

Figure 1.49: Results of a typical injection test in non-matrix regime (fracturing regime) in the wet sand specimen by oil: (a) pressure – flow rate – time curves; (b) horizontal cross-section at the middle of the invaded zone (Golovin et al., 2011).

In the matrix regime (i.e. when the injection pressure is smaller than the minimum stress), called waterflooding, an axisymmetric distribution of the injected fluid is observed without fracturing around an injection point (Figure 1.48). In the non-matrix regime or the fracturing regime (i.e., the injection pressure is greater than the minimum stress), a very heterogeneous flow pattern is observed with clearly visible preferential paths (Figure 1.49). The authors also conclude that increasing injection rate in the fracturing regime increases of the overall permeability and injectivity of the specimen.

b. Other studies

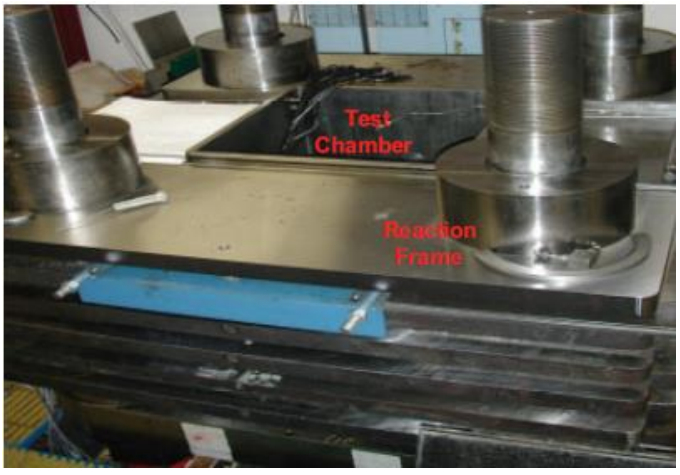

Figure 1.50: True triaxial setup used for polymer-injection testing (Khodaverdian et al., 2010).

Khodaverdian et al., 2010 have performed a test series on the effect of polymer injection in unconsolidated sand reservoirs. Experiments are carried out in a true triaxial cell (a cubic cell of 45 cm each edge) which allows applying the stress in three independent directions (Figure 1.50). Sand pack consists of a central layer of sand of 20 cm in height and two impermeable layers of a mixture of clay and sand that confine the layer in which the injection is performed. The fracturing fluid is polyacrylamide polymer diluted in water which is a non-Newtonian fluid. The apparent polymer viscosity is in the range of 20 to 40 cP corresponding to the shear rates in the range of 100 to 1000 s^{-1}.

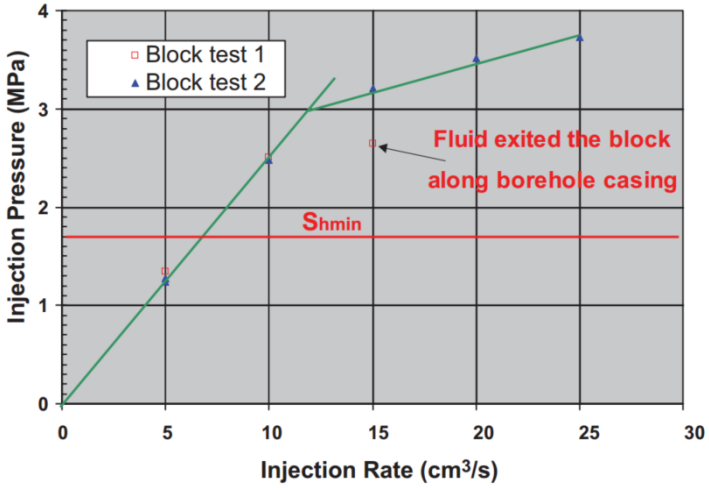

(a)

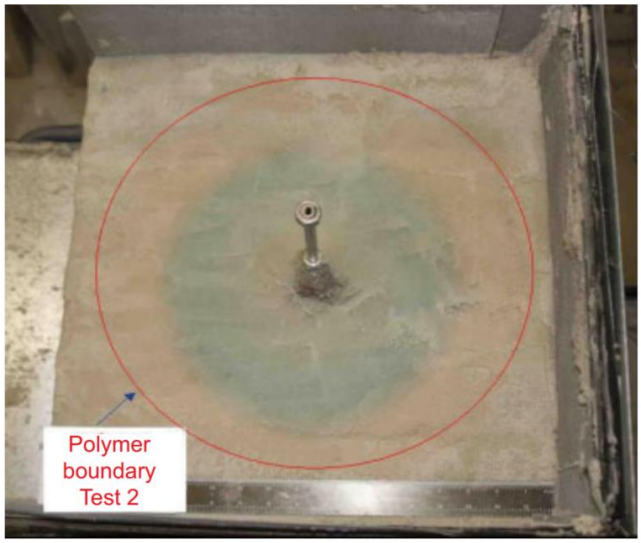

(b)

Figure 1.51: (a) pressure – flow rate test for the tests in poly-axial cell; (b) typical horizontal cross-section during disassembling (Khodaverdian et al., 2010).

Figure 1.51a presents a typical test result in the true triaxial setup. The authors identified a change in the slope of the pressure – flow rate curve for an injection pressure corresponding to approximately 1.5 times the smallest horizontal stress. However, no trace of fractures or preferential paths could be detected during the excavation of the sand pack (Figure 1.51b). The authors propose two additional mechanisms that could explain the increase of the permeability

after injection: shear-induced dilation and effective-stress reduction due to fluid flow in the medium.

Based on previous research, the authors introduce the concept of pseudo-fracture in unconsolidated sand formation encompassing shear failure bands, sub-parallel fractures and permeability-enhanced zones. A pseudo-fracture can be induced by fluid mobility, formation damage or both (Figure 1.52). In the first mechanism, fracturing would be controlled by the fluid leak-off into the formation which leads to a rapid decrease of the effective stress, consequently, the shear bands and the more permeable zones are formed around the injection point (Figure 1.52a). Regarding the second mechanism, the pseudo-fracture is caused by damage in the formation and by the phenomenon of plugging. In this case, when injecting a viscous fluid or a fluid containing solid particles, plugging occurs on both sides of the fracture. By maintaining a constant injection rate, the fracture tends to propagate further into the medium (Figure 1.52b).

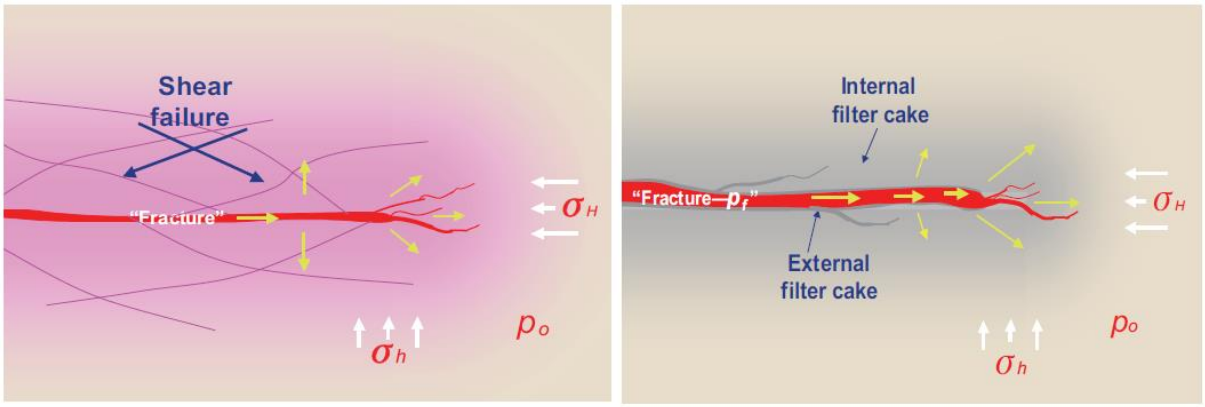

(a) (b)

Figure 1.52: Conceptual scheme of the fracture-tip propagation: (a) pseudo-fracture by shear failure; (b) pseudo-fracture by formation damage (Khodaverdian et al., 2010).

1.4.2 Modeling of hydraulic fracturing in granular materials

It is clear from the experimental results that the hydraulic fracturing in unconsolidated materials is significantly different than fracturing encountered in hard/consolidated rock. Unlike consolidated and brittle reservoirs, unconsolidated formation has little or no tensile strength as well as extremely large fluid leak-off. It is characterized by a low Young's modulus, low cohesion, high permeability and large inelastic deformation caused by slippage and rotation of relative rigid sand grains. Papanastasiou (1997) indicated that net pressure (difference between the fracturing fluid pressure and the far-field stress) encountered in the field of unconsolidated reservoirs commonly are 50% to 100% higher than their corresponding values predicted by conventional fracturing simulators.

Zhai and Sharma (2005) proposed a new approach for fracture propagation in unconsolidated sands. Their model is based on the constitutive relationship of permeability and porosity as a function of effective stress. The coupling of the stress distribution with the pore pressure is used and applying to hydraulic fracturing problems in unconsolidated sands. The

modified Coulomb failure criterion is used to check for formation failure. The simulation is based on 2-D finite difference method. They concluded that shear failure is the dominant failure mechanism when fluids are injected into unconsolidated sands and far-field stress anisotropy contributed an important role in determining the dimensions of the fracture zone. Xu and Wong (2010) presented a similar approach to simulate the hydraulic fracturing process in unconsolidated sand formation. A poro-elasto-plastic constitutive model, with a strain-induced anisotropic full permeable model, are formulated and implemented into a 3D finite element simulation. The Drucker-Prager plasticity model is applied to describe the pressure-sensitive behavior of unconsolidated sands that exhibit dilatancy when sheared. Unlike the conventional modeling in hard rock, the hydraulic fracturing in an unconsolidated sand formation is simulated as a large area of shear dilated plastic zone, inside which the effective stresses are low and the permeability is high. Figure 1.53 shows the evolution of the fractured zones at different injection time. The vertical fractured zone propagates perpendicular with the smallest horizontal stress (noted here that $\sigma_{Hmin} < \sigma_{Hmax} < \sigma_v$).

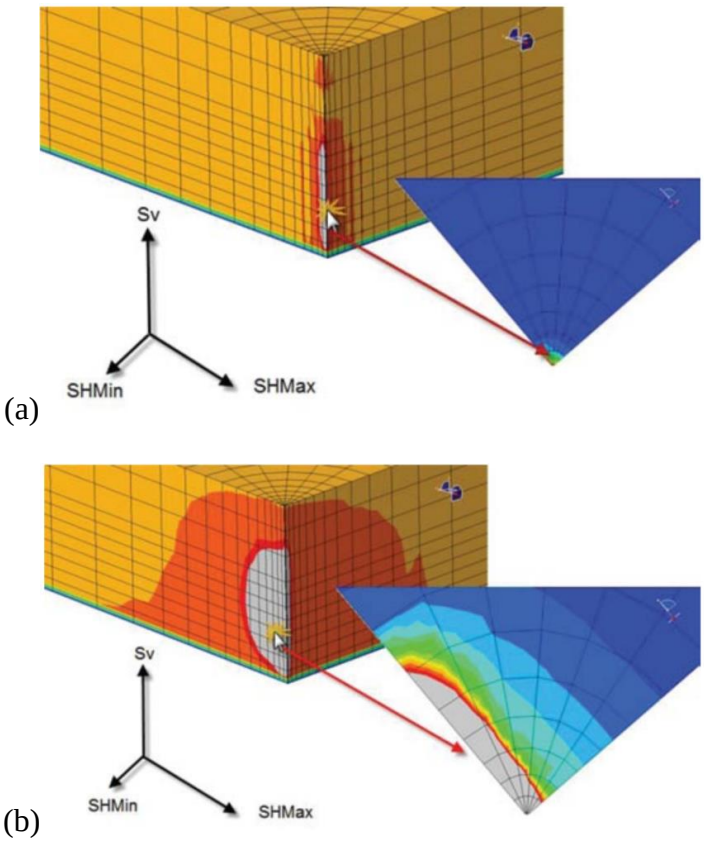

Figure 1.53: 3D shapes of the fractured zones at injection time (a) 0.5 hours; (b) 15 hours (Xu and Wong, 2010).

Agarwal and Sharma (2011) developed a numerical model for fracture growth in unconsolidated sands using a 3D finite difference method (FLAC3D code). In this model, the authors also evaluate the effect of internal and external filter cakes due to plugging by particles

present in the injected fluids on the type of failure and the pore pressure distributions. The theory of poroelasticity (Detournay and Cheng, 1993; Jaeger et al., 2007) is the basis for fluid/solid coupling. Mohr-Coulomb yield criteria are used to model the shear failure with a tension cutoff to determine tensile failure. Post failure elasto-plastic material behavior is modeled using the incremental flow theory of plasticity. Figure 1.54a shows the modeled domain with its boundary conditions and the failure state diagram after running the stimulation presented in Figure 1.54b. Shear failure takes place at the tip due to fluid invasion and pore pressure increase, then the tip may fail in tension and the fracture propagates.

The discrete element method is also used in order to understand the mechanism of hydraulic fracturing in poorly consolidated formations. It is based on the discretization of a solid medium into circular or spherical particles. Gil (2005) conducted discrete element modeling to investigate this phenomenon by combining the mechanical and hydraulic behavior of an unconsolidated rock specimen. The results from all the numerical tests show that shear failure seems to be more important than tensile failure during hydraulic fracturing process.

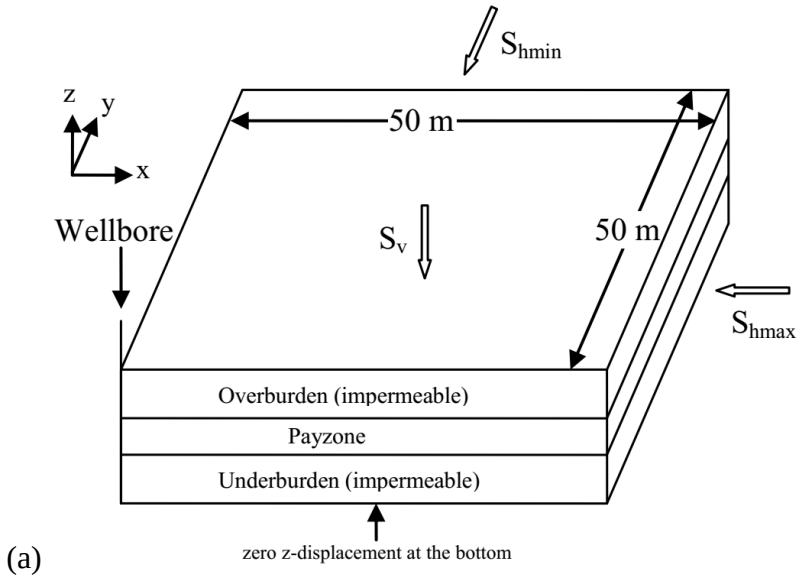

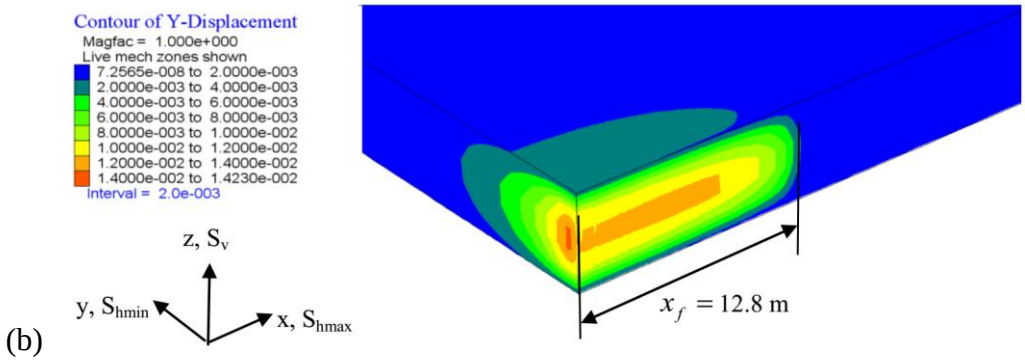

Figure 1.54: (a) Schematic of modeled domain with boundary conditions; (b) Failure state diagram of payzone height H = 5m (Agarwal and Sharma, 2011).

Wu (2006) presented a numerical simulation of water injection into particulate material by using the discrete element code PFC (i.e., Particle Flow code) to investigate the fracture initiation mechanism in water flooding conditions. As an extreme case of hydraulic fracturing, water flooding fracturing exhibits some significant contrasts from the conventional hydraulic fracturing such as very low viscosity of water compared to the typical polymer-based fracturing liquids, very long injection duration, the extremely high level of leak-off. The author observed that "fluidization" of the particulate material due to the water injection results in the initiation of a fracture. The process of fluidization is equivalent to liquefaction in soils mechanics while the effective stress becomes zero, the particles loose contact in all directions. Figure 1.55 shows three stages of cavity propagation corresponding the increase of fluid velocity. The author explained the evaluation of these stages by considering the drag forces exerted on the particles by fluid continuously seeping through the particle assembling. Due to the drag forces, particles tend to move away from the injection point. When the injection rate reaches a critical value, corresponding to the loss of contact between the particles (fluidization), the cavity begins propagating into the medium.

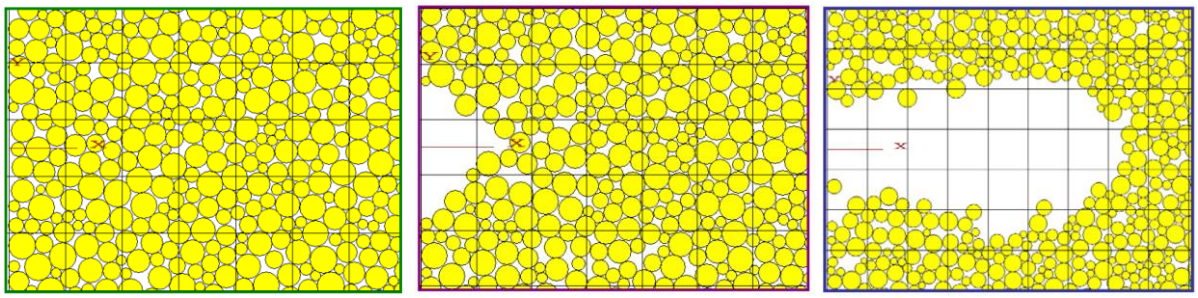

Figure 1.55: Cavity propagation during water injection (a) "fix bed flow" during the cavity initiation stage; (b) stable cavity development; (c) unstable cavity propagation (Wu, 2006).

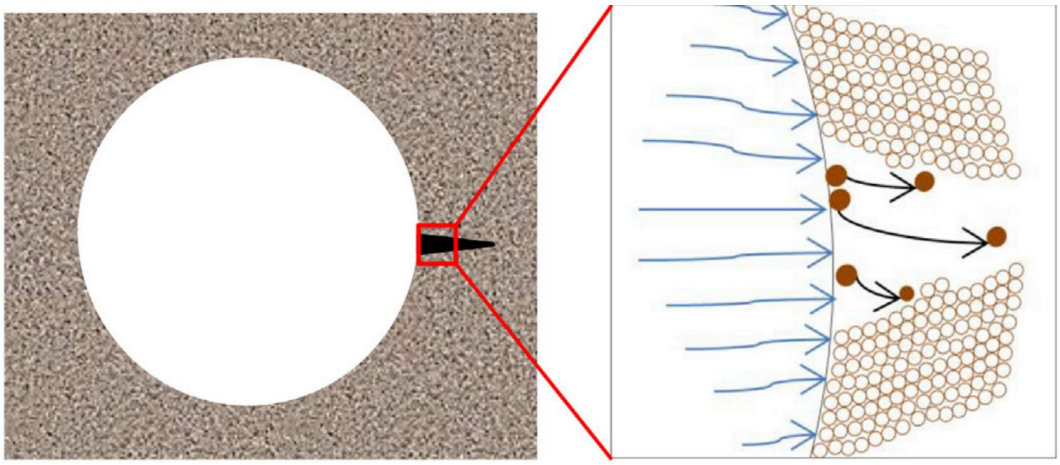

Figure 1.56: Graphical demonstration of detachment and transport during the channelization (Bautista and Taleghani, 2018).

Some researchers applied a concept of flow-induced channelization to explain the formation damage due to fluid injection into unconsolidated formations (Ameen and Taleghani, 2015; Bautista and Taleghani, 2018; Mahadevan et al., 2012). Channelization in the porous medium might occur when the fluid-induced stresses and drag force locally becomes greater than a critical threshold, the smaller grains are assumed to be detached from sand matrix and transported in the flow direction that changes the local porosity and hydraulic conductivity, therefore, erosional channels or preferential paths are created (Figure 1.56).

Ameen and Taleghani (2015) developed a 2D model on the basis of the multiphase-volume-fraction concept proposed by Mahadevan et al. (2012). Rather than considering the interaction between each particle explicitly, they decompose porous medium into mobile and immobile phases by means of their volumetric fractions. The immobile phase represents the fraction of detached grains from matrix and transport away by the fluid. The model is solved in a control volume in space using the finite-volume method (FVM). A series of simulations was performed to investigate the effect of different parameters such as flow rate, formation heterogeneity, initial average porosity and stress distribution on the channel formation. The authors found that injection rate has a crucial effect on the formation of erosion channels. The porosity distribution patterns corresponding to the different injection rates are shown in Figure 1.57. Above a critical injection rate on which the drag force acting on a sand particle is greater than the confining force holding the grains together, the channels will be created around the wellbore. As the injection rate increases, the number of channels as well as the lengths of channel increase.

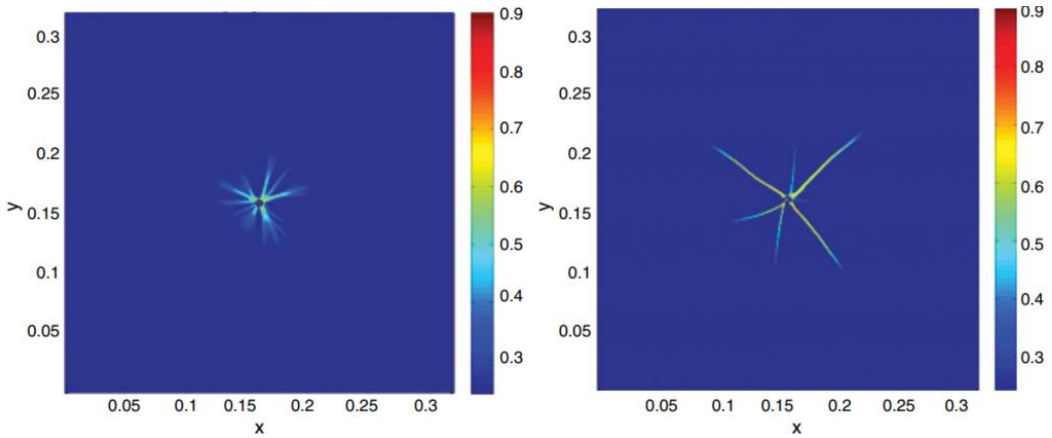

Figure 1.57: Final porosity distribution for different injection rates: (a) q = 0.04 m^3/s, channels initiation; (b) q = 0.4 m^3/s channels propagation (Ameen and Taleghani, 2015).

Based also on the basis of multiphase-volume-fraction, Bautista and Taleghani (2018) presented a three dimensional model using the finite element method (FEM) to predict formation damage by water injection in unconsolidated formation. Figure 1.58a presents the numerical result for a 2D case final porosity distribution after the channelization occurred. The authors observed the similarity of the simulation when compared to the experimental results

from Jasarevic et al. (2010) (Figure 1.58b). Unlike the hydraulic fracture in consolidated materials, multiple small channels are identified with a much more random pattern.

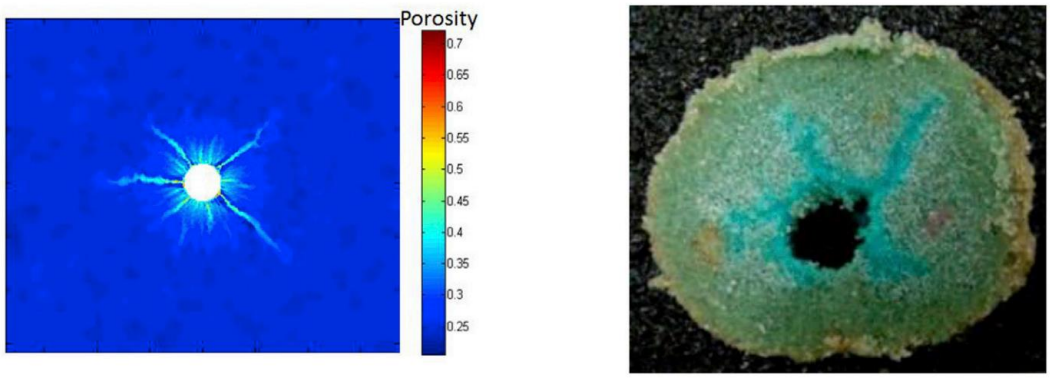

(a) (b)

Figure 1.58: 2D case final porosity distribution after channelization (Bautista and Taleghani, 2018) *comparing with the experimental observation from* Jasarevic et al. (2010).

1.4.3 Summary of the literature review related to hydraulic fracturing in granular materials

Various experimental injection setups and associated results, found in the literature, was presented above. It is found that different sizes and configurations of radial injection setups have been developed, including half cylindrical cell, triaxial cylindrical cells and triaxial cubic chambers. The tube designs are also very different throughout these studies such as slotted open hole tube and porous tube or tube containing some open holes, which provide different flow patterns within the sand specimen.

The parametric study shows a strong sensitivity of the parameters such as stress state, permeability of the medium, fluid rheology (type, viscosity), injection flow rate as well as the injection tube pattern on the critical fracturing pressure and the fracturing pattern. Despite the differences in the experimental setups, test procedures and number of experiments performed in these studies, some main conclusions can be drawn:

- The confining pressure is the main factor affecting the critical fracturing pressure. A higher confining pressure leads to a higher fracturing pressure (i.e., peak pressure), however the ratio of fracturing pressure to confining pressure tends to decrease as the confining pressure increases. At a low confining pressure below 3 MPa, this ratio varies significantly in the range of 3 to 20, depending on injection fluid and injection setup. At high confining pressure, this variation is much smaller on the order of 2 to 4 times.
- A strong impact of the fluid rheology on the morphology and size of the fracture is observed. We distinguish two kinds of the injection fluids tested: a high viscosity fluid and a very low viscosity fluid (similar to water) with and without solid particles. Note that, the experimental protocol of these studies consists in injecting only a small volume of the injection fluid compared to the pore volume of the sand specimen.

  - High viscosity fluid tests: An increase of the fluid viscosity generally leads to higher fracturing pressure, lower fluid leak-off, wider and longer fractures. Different types of the injection fluid also result in different fracture morphologies.
  - Very low viscosity fluid (having a similar viscosity as water): Fractures were not detected in the tests without adding solid particles in the injection fluid (to reduce the leak-off of the fluid into the medium). When injecting at a pressure much larger than the minimum applied stress, a very heterogeneous flow pattern is observed around the injection point with visible preferential paths but no clear fracture induced. The addition of solid particles in the injection fluids allows for the formation of a cake around the injection point, and consequently, leads to a reduction of the leak-off of the fluid into the medium. The experimental results show that a higher concentration of particles leads to longer fractures and smaller leak-off of the fluid.

- The flow rate and the initial permeability of the specimen have a minor impact on the critical fracturing pressure. However, an increase in flow rate and a decrease in permeability both leads to the formation of longer fractures and smaller fluid leak-off.
- The tube geometry also plays an important role in creating fractures. The tube containing a limited number of open holes favors the fracture formation than the one having a long injection interval as the porous tube.

Concerning the modeling approaches developed to study hydraulic fracturing in granular material using different methods, such as finite element method, finite difference method, discrete element method and finite volume method. Three phenomena are proposed in an attempt to explain the fracturing mechanisms in the granular material, including shear dilation bands, fluidization of materials around the injection point and channeling induced by the transport of a fraction of small particles.

1.5 CONCLUSIONS

Although the benefits of Produced-Water Re-Injection are very obvious to minimize environmental impacts and increase production efficiency, this method still faces difficulties in the application process, especially with the formation damage due to the filter cake formations. On the other hand, hydraulic fracturing process can be applied to overcome this challenge. Hydraulic fracturing is widely applied in the oil and gas fields over more than 70 years and its mechanisms in consolidated rock medium has been extensively studied. The simulation in this kind of reservoir is based on the theory of LEFM. However, the mechanisms of hydraulic fracturing in unconsolidated sand medium seem fundamentally different and more difficult to well master it. Some assumptions of shear failure, fluidization or channels formation (preferential path) have been proposed as presented above in Section 1.4, however, the exact mechanisms are still an open issue. Most of the experimental studies in the soft sand formations refer to frac-packing treatment or polymer flooding since they have been performed with very viscous fluids or with fluids containing a high concentration of solid particles with a high flow rate in order to enhance fracturing of the unconsolidated sand. Very few studies focus on the fracturing in the situation of PWRI in which the injected fluid has a very low viscosity (of the order 1 cP) and a low concentration of solid particles and in which the injection is maintained over a long period of time (Onaisi et al., 2011). The purpose of this thesis aims to explore the conditions for reaching the fracturing regime when radially injecting water with or without suspended particles in unconsolidated sand reservoirs and to identify the fracturing mechanism.

CHAPTER 2. TESTED MATERIALS, EXPERIMENTAL SETUPS AND METHODS

2.1 INTRODUCTION

In this chapter, the materials studied are first described with a discussion on the choice of the appropriate colored gel which is injected at the end of the test in order to freeze the specimen and observe the fluid flow pattern. Indeed, an important aspect of this research concerns the analysis of the specimens after fracturing. To achieve this objective, colloidal silica was used to solidify the specimen structure before the disassembling phase. Dyes are also added to the colloidal solution to improve the visibility of the fractures and the fluid flow pattern within the specimen. Preliminary tests were performed to validate the choice of these products. The two experimental setups (radial injection cell and radial injection chamber) as well as the testing procedure for both setups are then presented in detail.

2.2 TESTED MATERIALS DESCRIPTION

2.2.1 Tested soils

In order to represent the clogged area around injection wells due to PWRI, specimens of dense mixture of sand and fine particles are reconstituted by compaction. Fontainebleau NE34 sand and C10 silica particles have been selected in this study. During the tests with suspended solids in injected water, C500 silica particles have been used. A detailed description of these materials is presented below.

2.2.1.1 *Fontainebleau NE34 sand and fine particles*

Fontainebleau NE34 sand has sub-rounded grains (D_{50} = 210 µm) and is composed of 99% of silica. An optical microscope view of NE34 is presented in Figure 2.1. C10 and C500 particles are non-plastic fines composed of silica particles with a mean particle size of 20 µm for C10 and 4.5 µm for C500. The main characteristics of these materials are presented in Table 2.1. The mean particle size D_{50} and the uniformity coefficient C_u is determined based on the grain size curves presented in Figure 2.2 and the other parameters are taken from Feia (2015). The particle size distribution of the different types of materials is established by laser diffraction granulometry. This device allows measuring particle sizes between 0.05 and 900 µm, with a better precision than dry sieving. Moreover, dry sieving is limited to particles size bigger than 80 µm. The principle of this technique is based on the diffraction of a laser beam passing through the particles. The smaller the particle, the larger the diffraction angle (laser beam angle). The grain size distribution curve of NE34 given by the manufacturer confirms the accuracy of the measurement using laser diffraction granulometry (see Figure 2.2).

Table 2.1: Characteristics of the tested materials.

Material	D_{50} (µm)	C_u	e_{min}	e_{max}	Angularity	ρ_s (t/m^3)
Fontainebleau NE34 sand (after Feia, 2015)	210	1.5	0.55	0.88	Sub-rounded	2.65
C10 silica particles	20	11	-	-	-	2.65
C500 silica particles	4.5	5.5	-	-	-	2.65

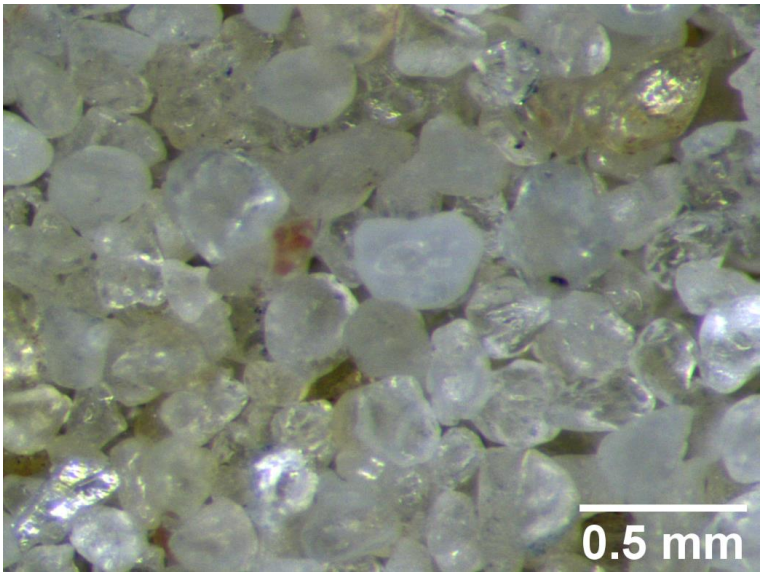

Figure 2.1: Optical microscopy view of Fontainebleau NE34 sand.

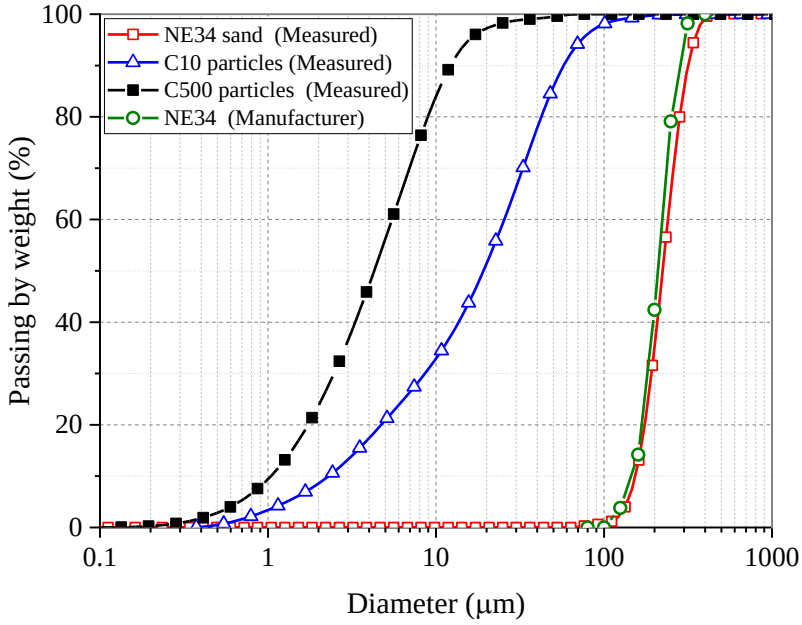

Figure 2.2: Grain size distribution of the tested materials.

2.2.1.2 *Homogeneity of the mixture of sand and fines particles*

The preparation of the mixture (NE34 sand and C10 fines) is carried out using a mixer. The two components are poured into a metal bowl (Figure 2.4). Mixing is maintained for 20 minutes. In order to ensure the homogeneity, three mixtures were prepared with different percentages by mass of C10 (10%, 15%, 20%). For each mixture, two samples were taken and passed through laser granulometer. The particle size curves are presented in Figure 2.3. The results show a very good homogeneity of the mixture of NE34 + C10. This confirms the effectiveness of the method used for the preparation. An optical microscopy view of a mixture of NE34 sand with 22% C10 (reference mixture) is presented in Figure 2.5.

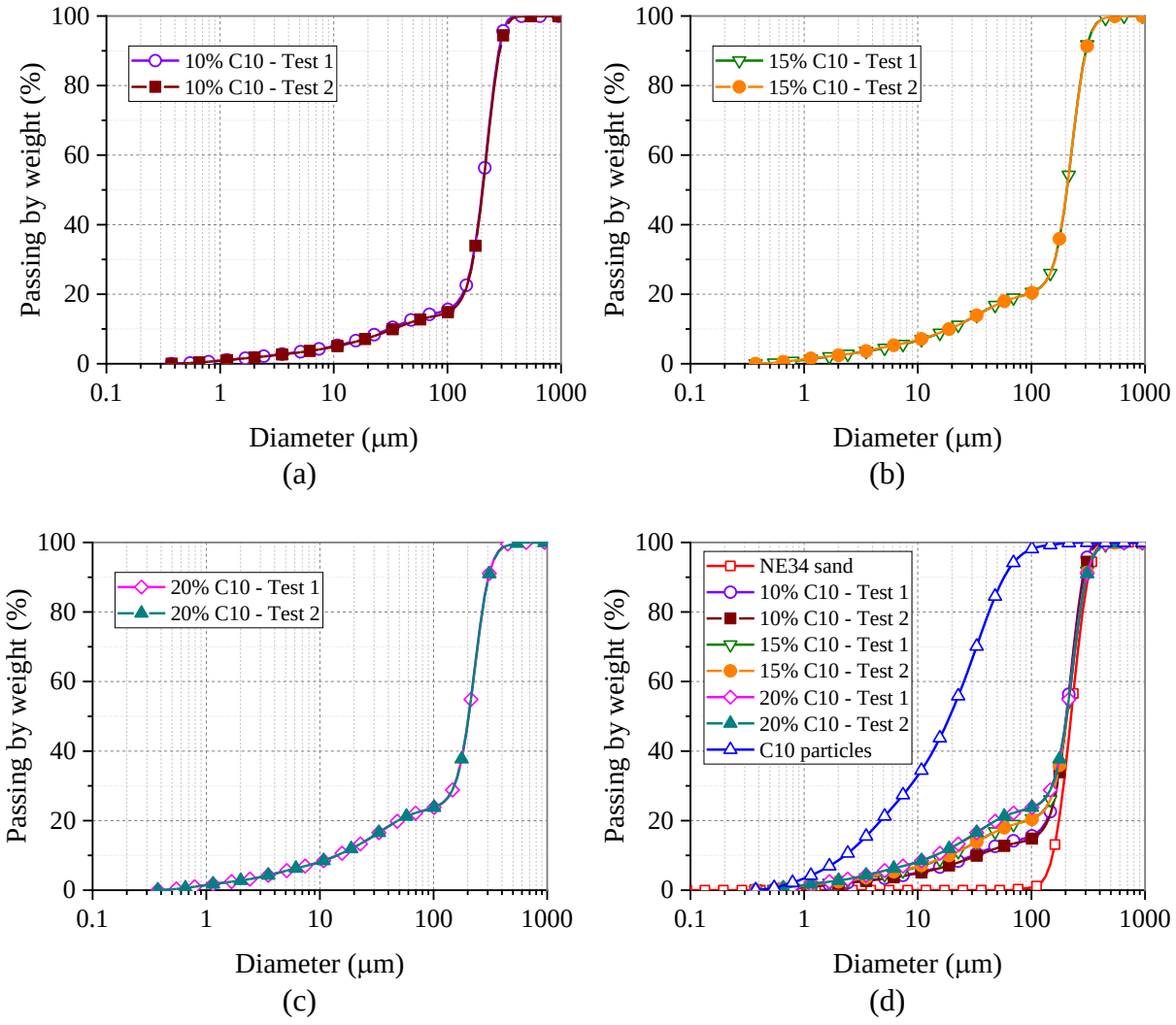

Figure 2.3: Grain size distribution of the mixture of NE34 sand and different percentages of C10 fines: (a) 10% C10; (b) 15% C10; (c) 20% C10; (d) synthesis.

Figure 2.4: Mixer used for preparing the sand and fines mixture.

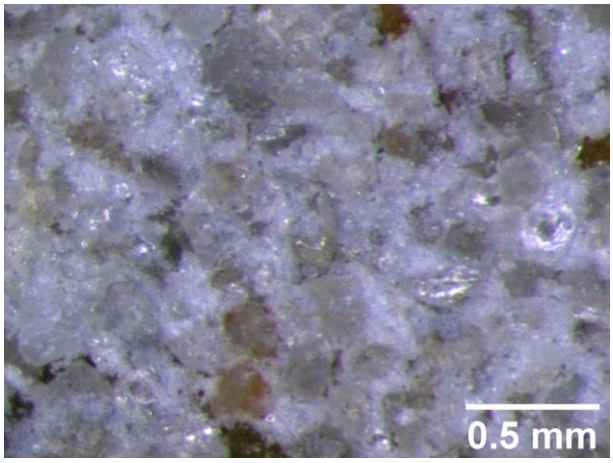

Figure 2.5: Optical microscopy view of a mixture of NE34 sand and 22% of C10.

2.2.1.3 *Permeability tests with different mixtures of NE34 sand and C10 fines*

A series of falling-head permeability tests has been performed in a triaxial cell in order to measure the permeability of different mixtures. The cylindrical specimens have a diameter of 100 mm and a height of 200 mm. They are reconstituted by manual compaction with a density index of the sand matrix $I_{D\ NE34}$ = 0.90. The specimens are fully saturated with de-aired water. These tests are performed under an isotropic consolidation stress of 200 kPa. During the test, water flows through the specimen from a de-aired water tank which provides the water head and allows measuring the injected volume of water. Figure 2.6 presents the results of the measured permeability as a function of the ratio by mass of C10 fines and NE34 sand (0, 10, 15 and 20%). Higher concentration of C10 fines results in lower permeability of the specimen.

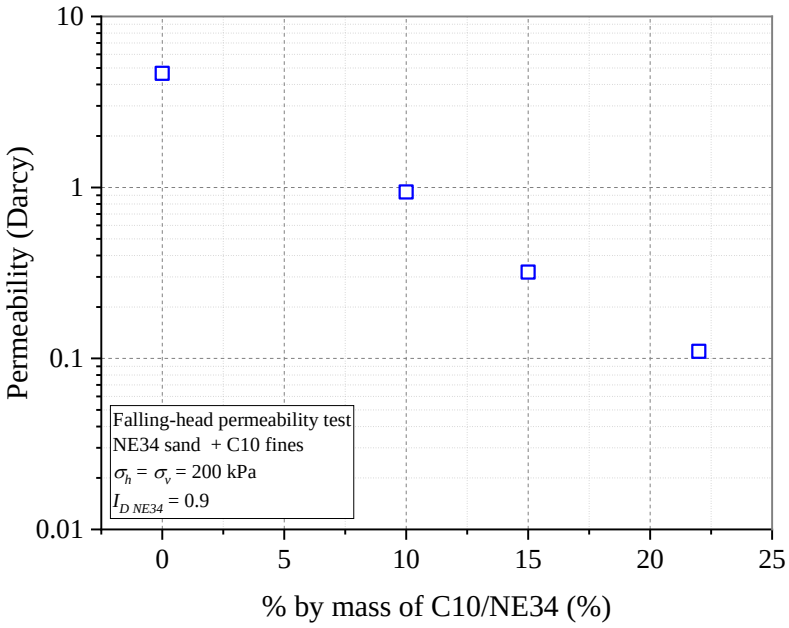

Figure 2.6: Variation of permeability as a function of the percentage of C10 fines in the specimen.

2.2.2 Gelling solution and visualization products

2.2.2.1 *Colloidal silica (MasterRoc MP320)*

a. Properties of the colloidal silica

Colloidal silica is a stable aqueous suspension (colloid) of nanometric silica particles. The particles size is generally between 7 and 22 nm (Gallagher and Lin, 2009). The nanosilica suspension can be gelled by raising the pH or changing ionic strength of the solution. This compresses the double layer of ions between silica particles in order to form interparticle siloxane bonds. The ionic strength is determined by the concentration of the sodium chloride (NaCl). During gelling, the viscosity increases over time until the material becomes solid. The gel time depends on the interaction rate between these particles, which is influenced by many factors such as the concentration of the silica suspension, the silica particle size, the ionic strength, the pH, and the temperature (Persoff et al., 1999). The advantages of silica gel, as compared to others that are presented in the bibliographic review, can be listed below:

- Initial viscosity between 2 and 5 cP, which is similar to water (1 cP at 20°C);
- Adjustable gel time;
- Safe product when handling and injecting;
- Excellent durability characteristics;
- Easy to clean with water;
- No volume change after gelification;

The colloidal silica used in this research is commercially referenced as MasterRoc MP320. It was provided by BASF Construction Chemical Company. A sodium chloride solution (called an accelerator) is added to MasterRoc MP320 at the required ratio to obtain adequate gel times.

The preparation of the accelerator consists of dissolving 10% by mass of salt in water. The characteristics of the product are shown in Table 2.2. The initial properties of colloidal silica are similar to those of water.

Table 2.2: MasterRoc MP320: data of BASF Construction Chemical Company.

-	Colloidal	Accelerator	Mixture of colloidal and accelerator
Color	Translucent white	Translucent	Translucent white
Viscosity (mPa.s)	10	1	5
Density (kg/l)	1.3	1.07	1.25
pH	9.5 to 9.8	7	~9 (depends on the concentration)
SiO_2 concentration	40 ± 1	-	-

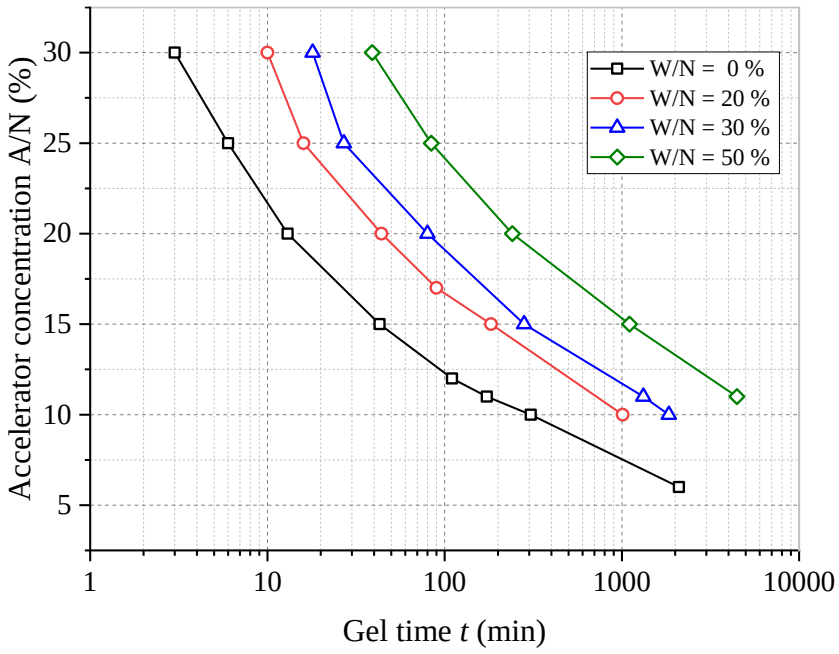

Figure 2.7: Gel time of MasterRoc MP320 with different accelerator concentrations and dilution concentrations.

b. Gel time

The main factors which influence the gel time of colloidal silica are the ionic strength (and the concentration of silica particles in the solution.. Persoff et al. (1999) have presented the evolution of colloidal silica over time until it becomes solid in 11 states (Table 2.3). State 1 corresponds to the period during which the viscosity of the solution remains practically unchanged. The viscosity gradually increases during State 2 and then begins to progress rapidly

through several states until the solution solidifies. In our work, colloidal silica will be injected in the specimen right after adding the accelerator (State 1) in order to avoid any change of the viscosity. The gel time is defined as the moment when the gel surface no longer deforms upon inversion (State 9). Figure 2.7 presents the gel time of MasterRoc MP320 with varying accelerator ratios. The accelerator concentration (A/N) is defined as the percentage by mass of the accelerator (A) to the MasterRoc MP320 colloidal silica (N). It makes evidence that higher concentration of accelerator results in shorter gel time. The results of diluted colloidal silica before adjusting the accelerator are also presented in Figure 2.7. W/N is defined as the mass ratio between added water (W) and the initial MasterRoc MP320 colloidal (N). Gel time increases with the decrease of the silica concentration in the colloid.

In our test protocol, the colloidal silica is injected right after the water injection phase. To optimize the duration of the test and to avoid an undesired increase of the viscosity, the accelerator concentration of 11% is chosen, corresponding to a gel time of approximately 3 hours. The evolution of the viscosity of these mixtures will be presented in the next section.

*Table 2.3: Gel state evolution (*Persoff et al. (1999))

State	Description
1	No detectable gel formed. Gel appears to have same viscosity (fluidity) as original polymer solution and no gel is visually detectable.
2	Highly flowing gel. Gel appears to be only slightly more viscous than initial polymer solution.
3	Flowing gel. Most of obviously detectable gel flows to bottle cap upon inversion.
4	Moderately flowing gel. Small portion (5–15%) of gel does not readily flow to bottle cap upon inversion—usually characterized as ‘‘tonguing’’ gel (i.e., after hanging out of bottle, gel can be made to flow back into bottle by slowly righting it.
5	Barely flowing gel. Gel slowly flows to bottle cap and/or significant portion (>15%) of gel does not flow upon inversion.
6	Highly deformable nonflowing gel. Gel does not flow to bottle cap upon inversion (gel flows to just short of reaching bottle cap).
7	Moderately deformable nonflowing gel. Gel flows about halfway down bottle upon inversion.
8	Slightly deformable nonflowing gel. Only gel surface deforms slightly upon inversion.
9	Rigid gel. There is no gel-surface deformation upon inversion.
10	Ringing rigid gel. Tuning-fork-like mechanical vibration can be felt or tone can be heard after bottle is tapped.
11	Rigid gel no longer ringing. No tone or vibration can be felt or heard, because natural frequency of gel has increased.

c. Viscosity of the silica colloid

The viscosity of the MasterRoc MP320 is measured using a Fann 35 Viscometer of the standard type R1-F1-B1. It is a reference device used for the rheological analysis of fluids

according to American Petroleum Institute standards. The rotor of this viscometer is driven by an electric motor with 6 fixed rotation speeds (3, 6, 100, 200, 300, 600 rpm). For each rotation speed, the reading in degrees is taken on the dial of the viscometer. Figure 2.8 shows a view of the complete device and its principle of operation. The fluid is poured into a stainless steel, then the viscosity measurement is made when the outer cylinder R2, rotating at known speed, causes a viscous drag exerted by the fluid. This force creates a torsion on the inner cylinder "bob" (R1) which is transmitted to the precision spring, and its deflection is measured. The corresponding values are displayed on a dial whose scale is expressed in degrees.

Figure 2.9 presents the rheograms obtained for the colloidal silica MasterRoc MP320 after mixing with different accelerator concentration (11 and 12%). The results make evidence that, initially, the colloid behaves as a newtonian fluid with a linear relationship between shear rate and shear stress (constant viscosity). When the viscosity increases beyond a critical value, it becomes a non-newtonian fluid (type of shear thinning fluid), so its viscosity decreases when subjected to a higher shear rate.

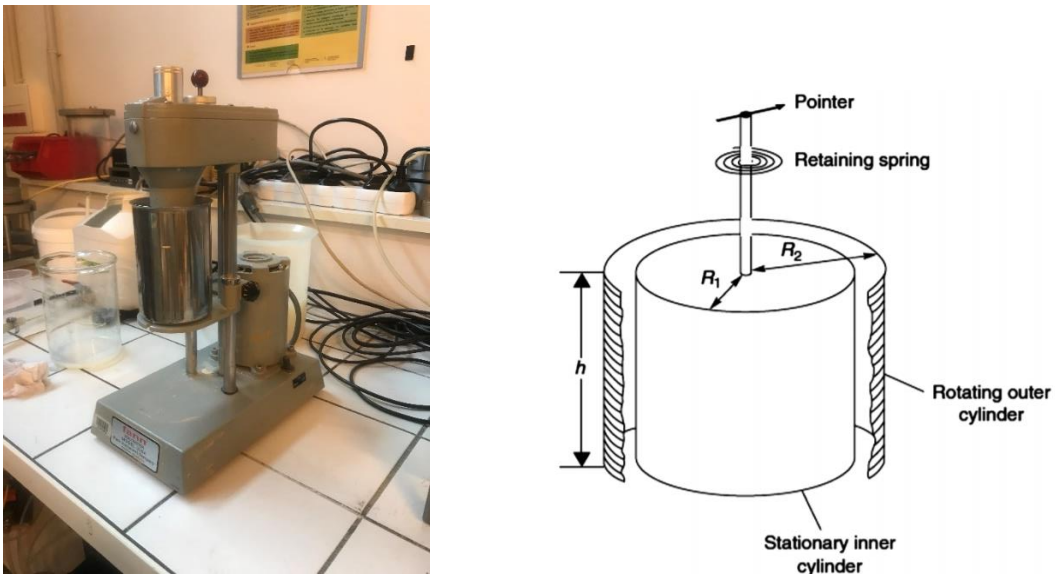

(a) (b)

Figure 2.8: Fann Model 35 Viscometer: (a) view of the device; (b) schematic diagram (Bahrainian et al., 2018).

The apparent viscosity of these colloids during the newtonian fluid phase is presented in Figure 2.10. During the first 30 minutes, the colloidal silica containing 12% accelerator exhibits a faster increase in viscosity than the mixture with 11%. Note that when injecting the colloid into the low permeability specimen, a slight change in viscosity can influence the injection pressure response. Therefore, a concentration of 11% accelerator was chosen for two main

reasons: reasonable gel time (3 hours) and almost constant viscosity of the solution during the first fifteen minutes (about 3 cP).

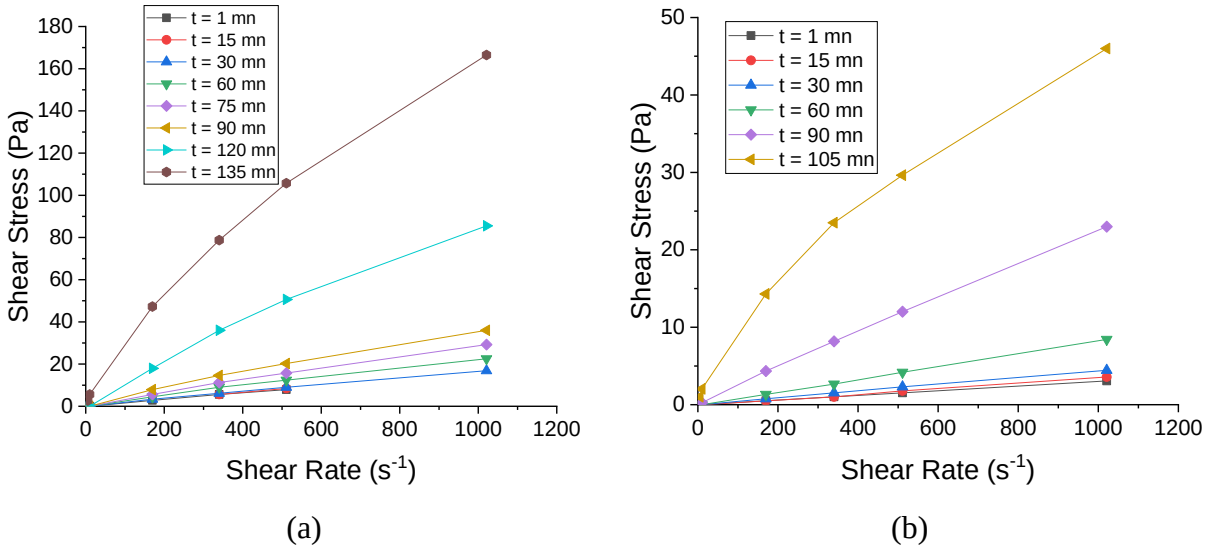

Figure 2.9: Rheograms of the MasterRoc MP320 colloidal silica during gelling: (a) 11% of accelerator concentration; (b) 12% of accelerator concentration.

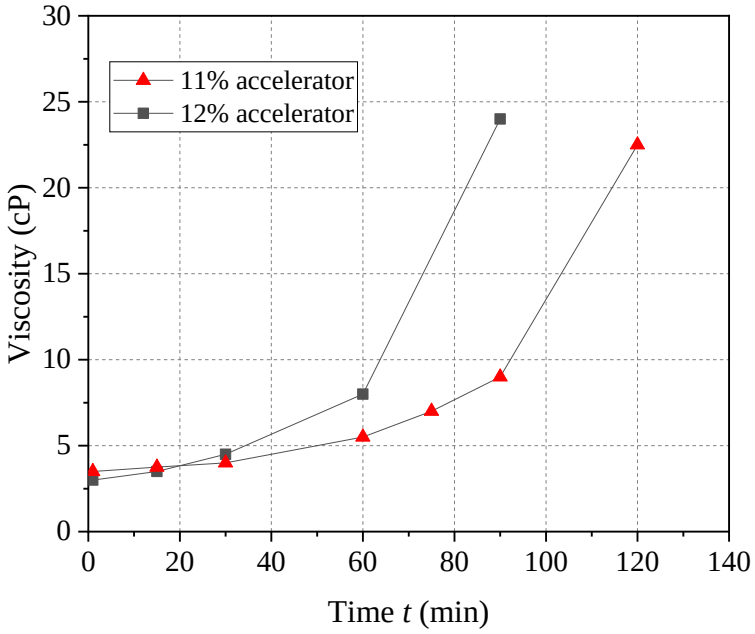

Figure 2.10: Viscosity of MasterRoc MP320 during the newtonian fluid phase.

2.2.2.2 *Validation of the dyes*

A dye can be used to better visualize the fractures or the preferential paths after fracturing. The choice of dye must validate the following criteria:

- The dye must be soluble in colloidal silica and should not affect the gel time

- The dye should be easily cleaned and any deterioration of the pump and of the injection cell must be avoided
- The dye must not be filtered by the low permeable specimen

Based on the recommendations of the supplier of MasterRoc MP320 (BASF), three dyes have been adopted, namely: Basacid® Blue 762 (water based anionic dye solution), Blue Dispers 6900 (pigment preparation in aqueous phase) and Puricolor® Red FRE14 (powder soluble in water) (Figure 2.11).

(a) (b) (c)

Figure 2.11: Different dyes: (a) Puricolor® Red FRE14; (b) Basacid® Blue 762; (c) Blue Dispers 6900.

To validate the choice of these three dyes, a series of four tests was carried out in a uniaxial injection device on specimens of 80 mm in diameter and 40 mm in height (Figure 2.12 and Figure 2.13). The detailed description of this device is presented in Feia et al. (2015).

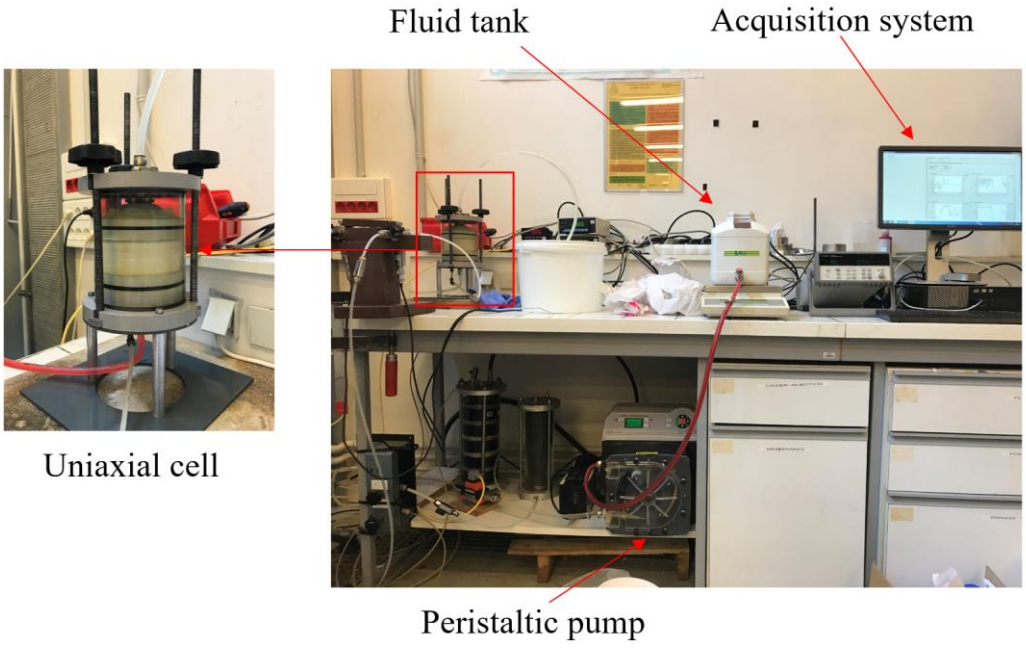

Figure 2.12: View of the uniaxial injection device.

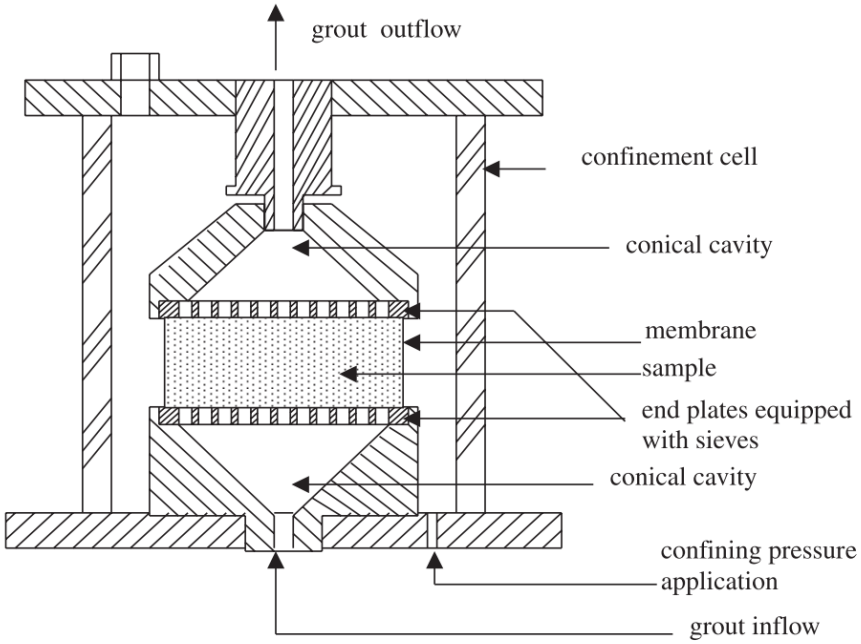

Figure 2.13: Schematic diagram of the uniaxial cell (Saada et al., 2006).

The specimens consist of a mixture of NE34 sand and 22% of C10 fines (reference mixture). The density of the sand matrix (i.e. without fines) $I_{D\ NE34}$ is 0.90. The global porosity n of the specimen is defined as the ratio of voids volume to total volume, according to Equation (2.1). The porosity corresponding to the sand matrix density of 0.90 is equal to 23%.

$$n = \frac{V_v}{V} = \frac{V_v}{V_v + V_{NE34} + V_{C10}} \tag{2.1}$$

where V is the specimen volume; V_v, V_{NE34}, V_{C10} are the volume of voids, volume of NE34 sand and volume of C10 fines, respectively.

The specimen is saturated by injecting water upwards (from the bottom baseplate) at a low constant flow rate for two hours. Then the flow rate is increased by steps to measure the initial permeability of the specimen. Finally, the dye is injected at a constant flow rate of 0.14 l/min. Four tests have been performed with different concentration of dyes diluted in water. Among these three dyes, Basacid Blue 762 (0.2% in concentration) is the best suited to our needs, because it does not filter in the granular medium and it is easy to clean after use. Puricolor® Red remains an acceptable option when injecting a small amount at a low concentration. This dye is filtered at the entrance of specimen in form of an internal cake, and consequently decreases of the permeability of the medium. Dispers Blue 9600 dye is not suitable for our application because of high filtration of pigments within the granular medium and of cleaning difficulty of the device after injection (Dispers Blue adheres tightly to the inner surface of the PVC tube and the injection pump). The results of these validation tests are presented in detail in Appendix A.

2.2.2.3 *Validation of the choice of the mixture of MasterRoc MP320 and dye (colored gel)*

These tests aim at studying the effect of the injection of this colored gel on the pressure response compared to the water injection (different viscosity) and to verify the efficiency of this gelling solution. Before the experiment, a validation test was performed to ensure that the presence of the dye does not affect the gel time of the colloidal silica. Figure 2.14 shows the three different mixtures of these products. The gel time is almost equal (about 110 minutes) for the three mixtures, confirming no effect of these dye on the gel time of the solution. Table 2.4 shows the characteristics of the validation tests. Those were performed in the uniaxial cell using the same protocol as the validation tests of the dyes. The C5 test was performed with the injection of the mixture of gel and Basacid Blue to freeze the whole specimen whereas the red colored gel (test C6) was injected to partially freeze the specimen. This partial injection protocol is similar to the colored gel injection protocol used for the radial injection setups (see Section 3.4.1.2).

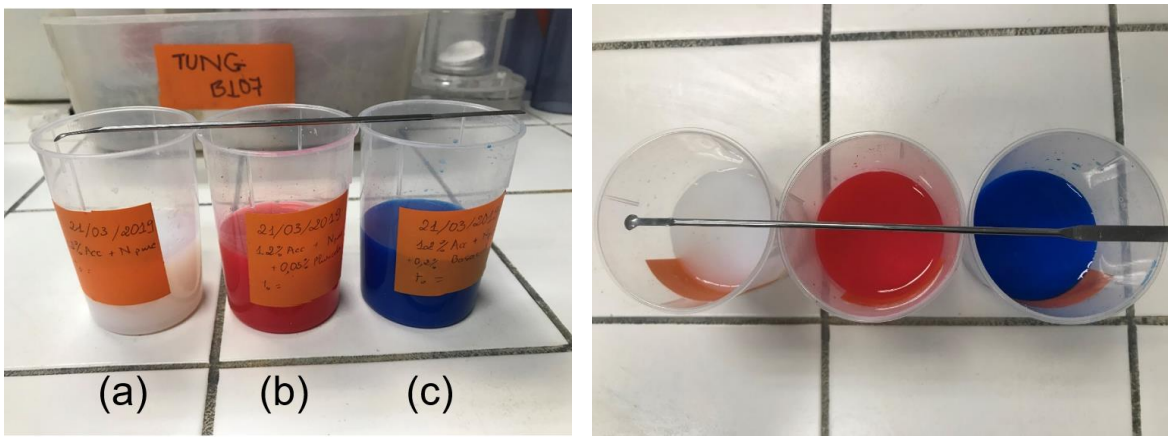

Figure 2.14: Effect of dyes on the gel time of the MasterRoc MP320 with 12% accelerator: (a) gel silica without dye; (b) with 0.05% of Puricolor Red prouder; (c) with 0.2% Basacid Blue 762.

Table 2.4: Characteristics of the validation tests with the mixture of colloid and dye.

Test	Mixture	σ_c (kPa)	Injection protocol
C5	Gel (12% Accelerator)+ 0.2% Basacid® Blue 762	200, 300	Total injection
C6	Gel (12% Accelerator)+ 0.05% Puricolor® Red	300	Partial injection

Results of test C5 are shown in Figure 2.15. The rather significant fluctuations in flow and pressure which are observed is due to the type of operation of the peristaltic pump used here. This pump was initially used in the work of Feia, 2015. To avoid the flow and pressure fluctuations, two new injection pumps will be used for experiments with the radial injection setups which provides a better stabilization of both flow rate and injection pressure. It will be

presented later in Sections 2.3.1.1 and 2.3.2.1 . After the saturation, water was first injected followed by the colored gel injection. During the water injection, the confining pressure is increased from 200kPa to 300 kPa and the induced injection pressure values, for the same flow rate, are quite similar. This result shows the negligible effect of the confining pressure, in this small range, on the permeability of the specimen. When injecting water, the pressure is almost constant at a constant flow rate of 0.1 l/min whereas rapid increase in injection pressure is observed when the dyed colloid begins to penetrate into the specimen. This can be explained by the difference between the viscosity of water and that of the colloidal silica. The viscosity of the colloid (approximately 3 cP) is 3 times greater than that of water (1 cP). To avoid liquefaction of the specimen, the imposed flow rate was reduced from 0.1 l/min to 0.06 l/min. At 0.06 l/min, a continuous increase of the injection pressure was still observed during this stage because of a slight increase in viscosity of the colloid as presented in Figure 2.10. The specimen was excavated two days later. It was well solidified by the gel and could be cut easily (Figure 2.16).

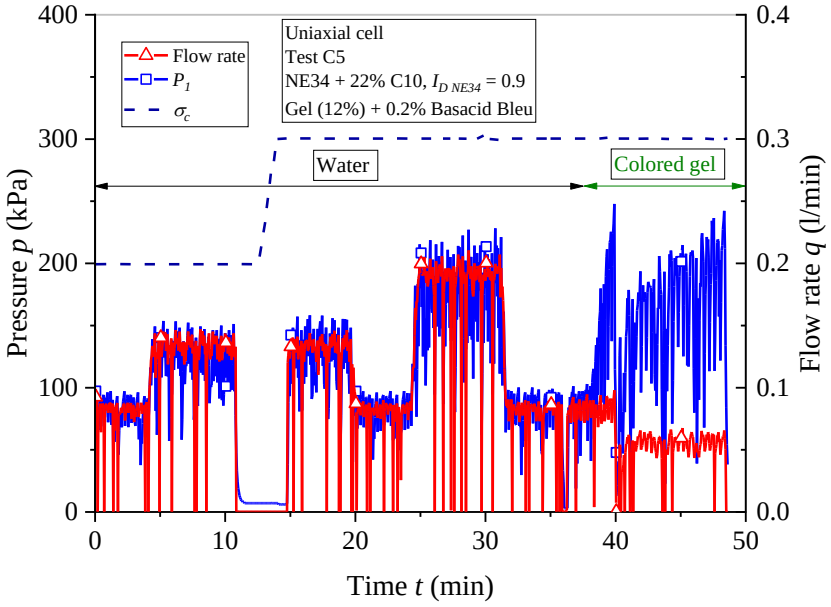

Figure 2.15: Test C5: Injection of the mixture of colloidal silica + 0.2% Basacid.

For the test C6, a small volume of the mixture of colloid + 0.05% Puricolor® Red was injected. This volume corresponds to about 60% of the voids volume of the specimen. The disassembling of test C6 was made one day after injection to freeze the gel invaded part of the specimen. Figure 2.17 shows three different layers of the specimen. The layer close to the injection surface (lower part) is well solidified by the gel, while in the middle layer, the gel has been diluted with water, so that the specimen is colored but not solidified. The upper layer is the wet sand layer. Because of a small injected volume, the Puricolor dye was not filtered at the entrance of the specimen.

Figure 2.16: Disassembling of the test C5.

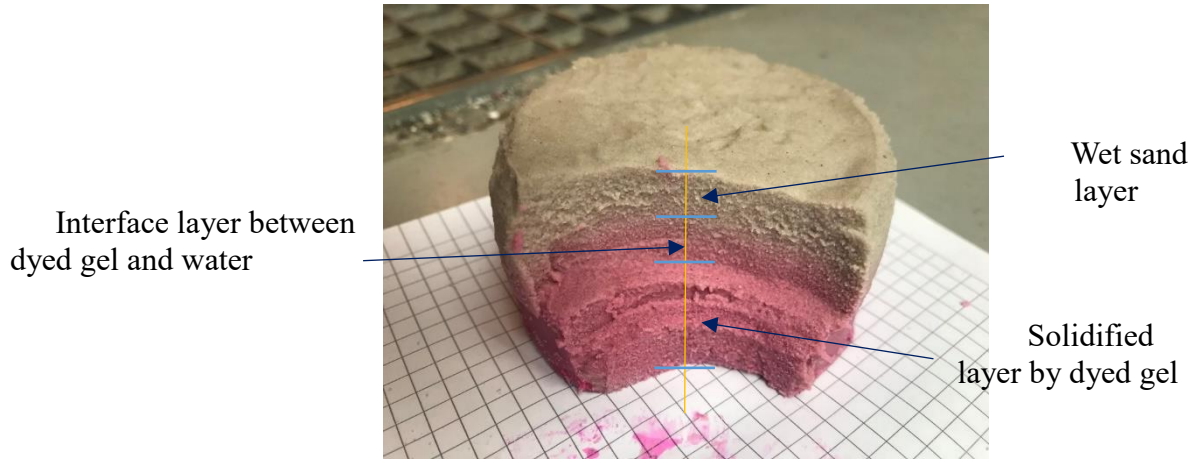

Figure 2.17: Specimen C6 after disassembling.

2.2.2.4 *Validation R-ray CT scans of the colored gel specimen*

X-ray CT is a non – destructive method for reconstructing the 3D images of an object. It will be used in this research to analyze the change of the internal structure of the specimen due to fluid injection. As the colored gel is also injected into the specimen after fracturing, the presence of this gel may affect the contrast of the scanning images due to the difference in chemical composition as compared to the initial state of the specimen without gel. The gel is a silica solution (SiO_2) which results in higher absorption of X-ray beams as compared to air or water. Therefore, preliminary scans need to be performed to validate these products. Five specimens of the mixture of NE34 sand and 22% of C10 fines (reference mixture) have been prepared in a plastic tube (Figure 2.18a). The dimensions of the specimen are 55 mm in diameter and 40 mm in height. The compaction was performed using a metallic cylindrical block (Figure 2.18b). A porous plastic was used as the baseplate of the tube, allowing the fluid to flow through the specimen. The density index of the sand matrix $I_{D\ NE34}$ is 0.6 (corresponds to a global

porosity of 0.29) which is smaller than the reference density of 0.9 due to the difficulty of compaction in the plastic tube. Then, these specimens were saturated with different fluids (Figure 2.19a). The saturation process consists of preparing the fluid in a glass vase and then fixing it at a position higher than the specimen to provide the pressure head (Figure 2.19b). A support was used to connect the glass vase with the specimen (Figure 2.19c). During the saturation of the specimen, a negative pressure was applied at the outlet of the specimen to accelerate the fluid flow and to increase the degree of saturation (Figure 2.19d). A schematic diagram of the saturation system is presented in Figure 2.19e.

In order to estimate the minimum size of the fracture that could be detected using X-ray CT, 4 holes have been made in each specimen using the needle. The position of these holes are presented in Figure 2.20a,b. Two were made immediately after saturation whereas two others were made after the gelification of the colloidal silica. The diameters of the needle are 0.44 and 0.69 mm, respectively which correspond to 2 and 3 times the grain size of the NE34 sand (Figure 2.20).

(a)  (b) 

Figure 2.18: Specimen preparation for R-ray CT scans : (a) different specimens of the mixture of NE34 sand + 22% of C10 fines in the plastic tube. $D_{specimen}$ = 55 mm, $H_{specimen}$ = 40 mm, $I_{D\ NE34}$ = 0.6; (b) compaction tool.

These specimens were then scanned using an UltraTom microtomograph (RX-Solutions, Chavanod, France), available at laboratory Navier. The chosen parameters of the X-ray source are 120 kV in accelerating voltage and 140 µA of the currents. The detector used in this scan measure the intensity of the incident X-rays on a square of 1456 pixels each edge.

The source for this study was a Hamamatsu L10801. Acceleration voltage and current were respectively set at 120kV and 140µA. The imager was a Varian 4343. Every projection was 1456 x 1456 pixels. Figure 2.21 presents the typical X-ray images corresponding with the different scanned specimens. The 3D images have a voxel size of 46 µm which is higher than the particles size C10 (D_{50} = 20 µm). Due to the inclination of the needle, the holes are not exactly at the same positions between these specimens.

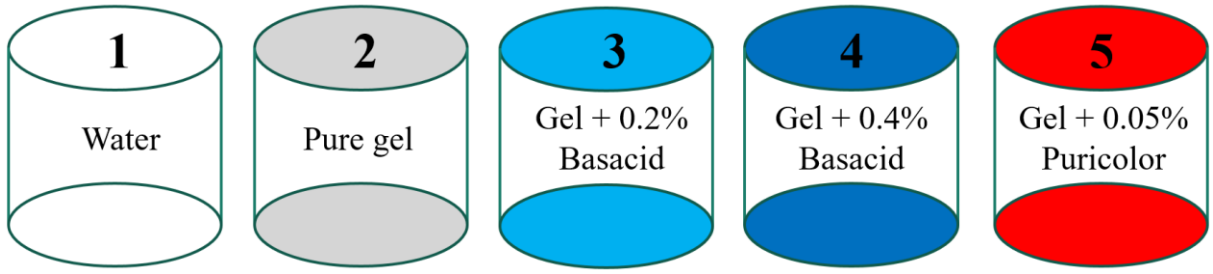

(a)

(b)

(c)

(d)

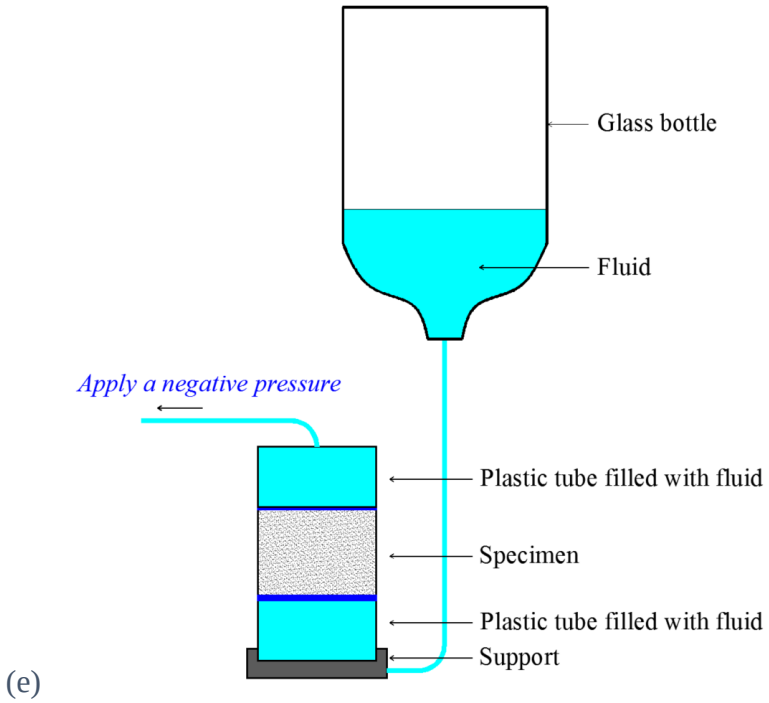

(e)

Figure 2.19: Saturation process of the specimen: (a) different saturation fluids; (b) preparing the fluid in the glass bottle; (c) fixing the specimen on the saturation system; (d) applying the negative pressure on the top of the specimen during saturation; (e) schematic diagram of the system.

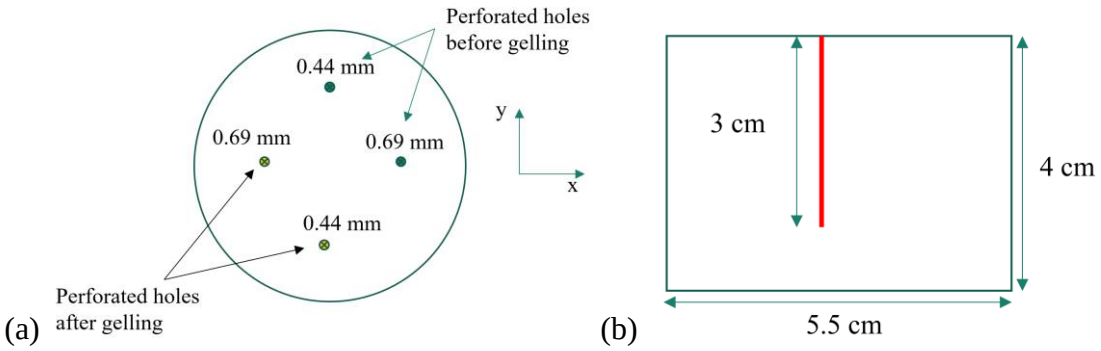

Figure 2.20: Schematic illustration of the holes: (a) horizontal section; (b) vertical section.

The red-dashed rectangular in Figure 2.21 presents the zone in which the histogram is plotted for all specimens. The results are presented in Figure 2.22a. As the voxel size is even bigger than the particles size, the grey value of each voxel is the average of the attenuation coefficients of different phases of the sample (air, fluid, solid). This is called the partial volume effect (PVE) due to the limited CT resolution (Cnudde and Boone, 2013). The mean values and their corresponding standard deviation of the grey level are very close between these specimens which confirm that no evident effect of the colored gel on the image contrast compared to the case with water saturation (Figure 2.22b). The difference of the voxels number, corresponding to each grey level, may be contributed by the degree of saturation, the porosity of the specimen, the internal structure of the specimen and the image artifacts (Figure 2.22a).

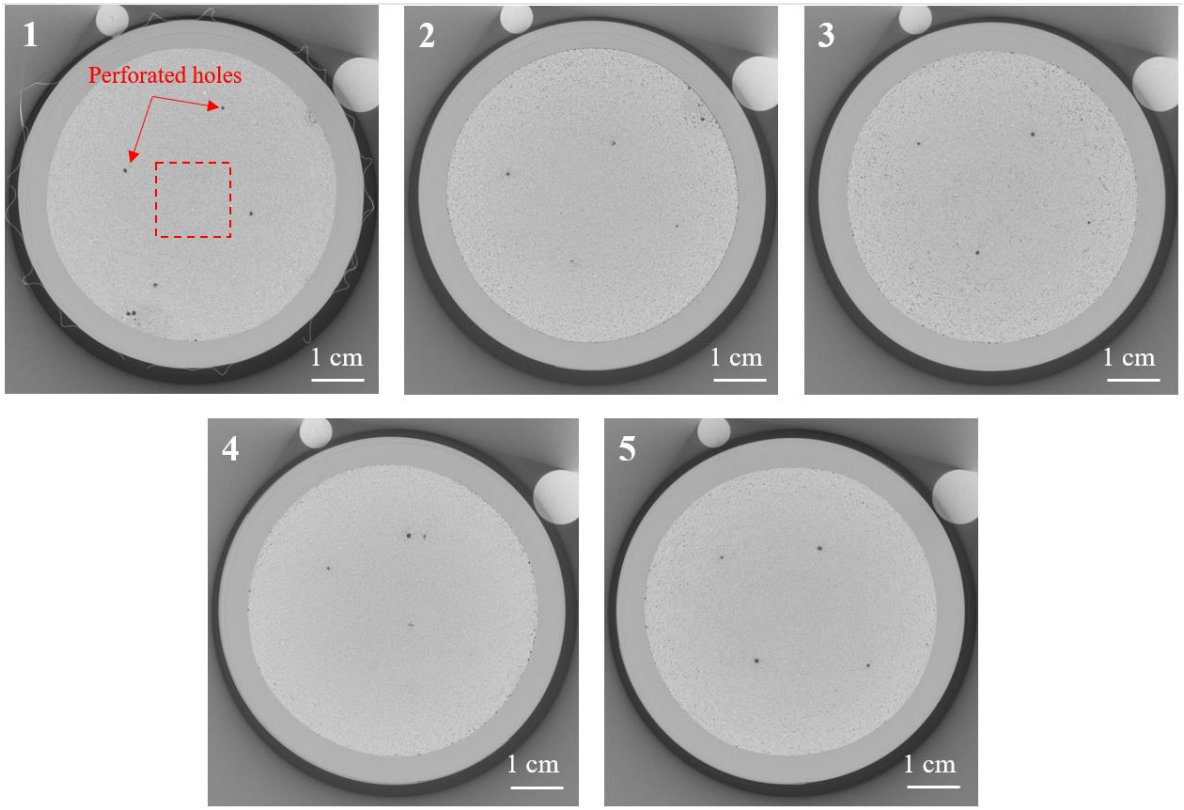

Figure 2.21: Typical X-ray images of the specimens: (1) water, (2) pure gel, (3) gel + 0.2% Basacid, (4) gel + 0.4% Basacid, (5) gel + 0.2% Puricolor.

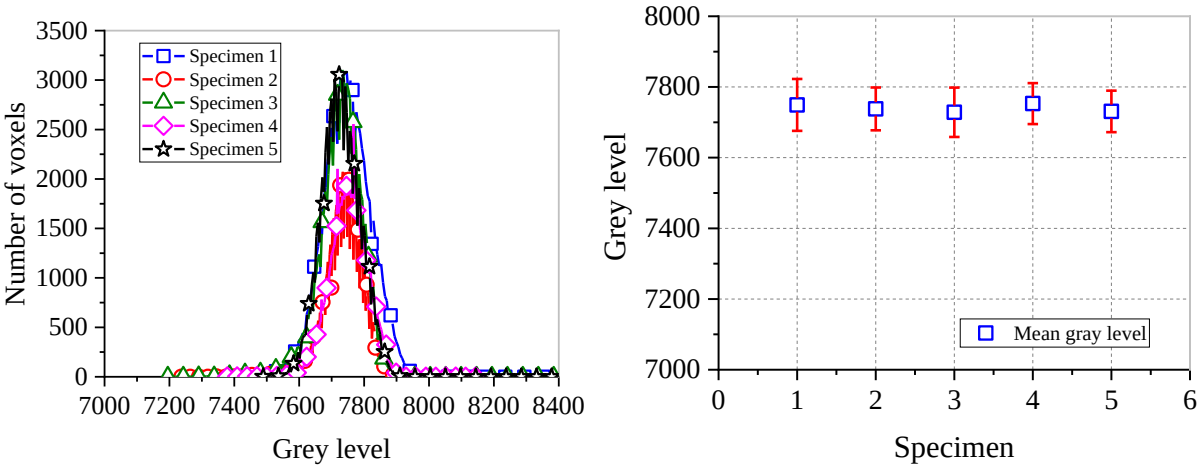

Figure 2.22: (a) histogram and (b) mean grey value + standard deviation of red-dashed rectangular presented in Figure 2.21 for all specimen.

To display the 3D view of the perforated holes in the specimen, the ImageJ 3D Viewer plugin (Schmid et al., 2010), available in FIJI open-source software (Schindelin et al., 2012), is used. The image processing consists of 3 major steps: filtering (reduce the noise), thresholding (segmentation of the perforated holes and the surrounding medium) and volume rendering (render a 3D image). This process will be detailed later in the typical test in the radial injection cell (Section 3.4.1).

Figure 2.23 shows a typical transverse cross-section of Specimen 3. It makes evident that the perforated hole filled with air is darker than one filled with the colored gel. For the considered materials, solids (NE34 sand + C10 fine particles) are the most absorbing objects while air is the least absorbing. The grey level profile presented in Figure 2.24 confirms the visual observation from Figure 2.23. Higher absorbing material results in higher grey value.

The analyzed zone is delimited with the dash rectangular in Figure 2.23 and the image treatment is applied for the whole specimen. After filtering the images with the median filter of 2 voxels, one can easily distinguish the grey level corresponding to different phases of the specimen (Figure 2.24). The choice of the threshold value is based on the grey level profile. As many large pores are also present within the specimen and also considering the effect of imaging artefacts (PVE, noise, limited resolution), this choice has to satisfy two conditions: reducing the noise around the perforated holes and distinguishing the holes (both air-filled hole and gel-filled hole) and the medium. Therefore, the selected value must be in the range of 7450 to 7600. Figure 2.25 shows the image treatment by applying different threshold values (7500, 7550, 7600). High effect of this value on the clarity of the 3D image is observed. The case of 7500 shows a better view as compared to others while keeping the shape of the gel-filled hole (Figure 2.26a&d). The white voxels represent the perforated holes whereas the black ones represent the surrounding medium. Many white voxels also appear around the holes which are the pores having the grey level smaller than the selected threshold. To reduce these noises, another filtering can be applied on the binary images. It may slightly reduce the contour of the hole (Figure 2.26a), however, this treatment gives a better view of the 3D image (Figure 2.26b).

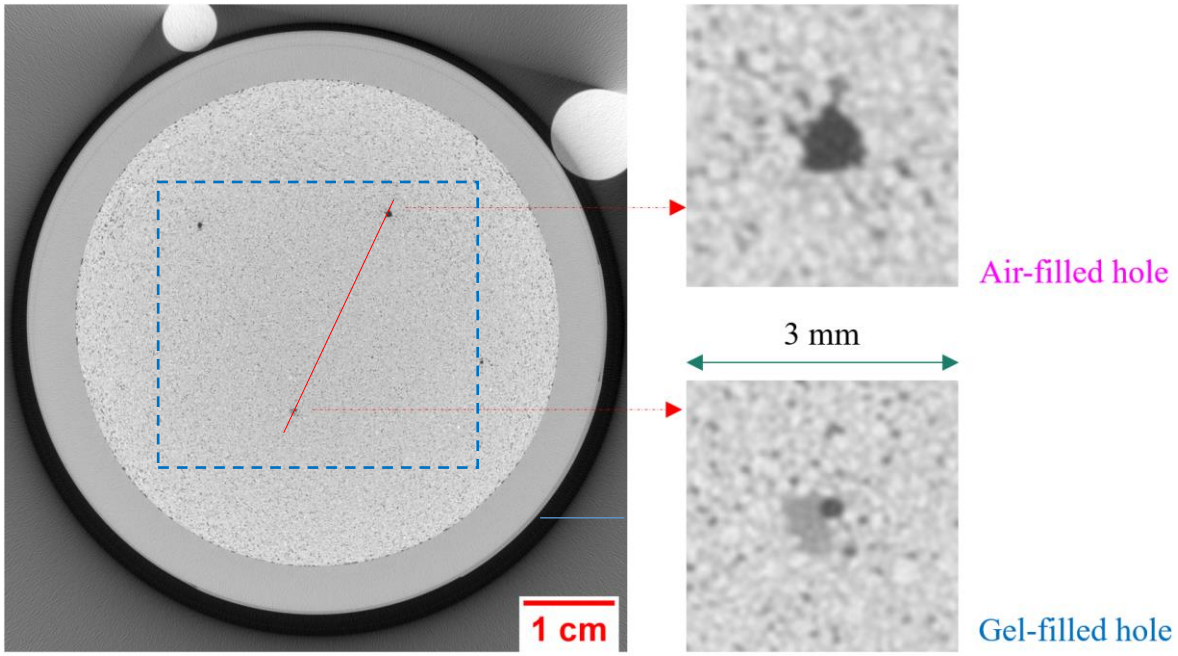

Figure 2.23: Scanning image of Specimen 3 (Gel +0.2 % Basacid) before filtering.

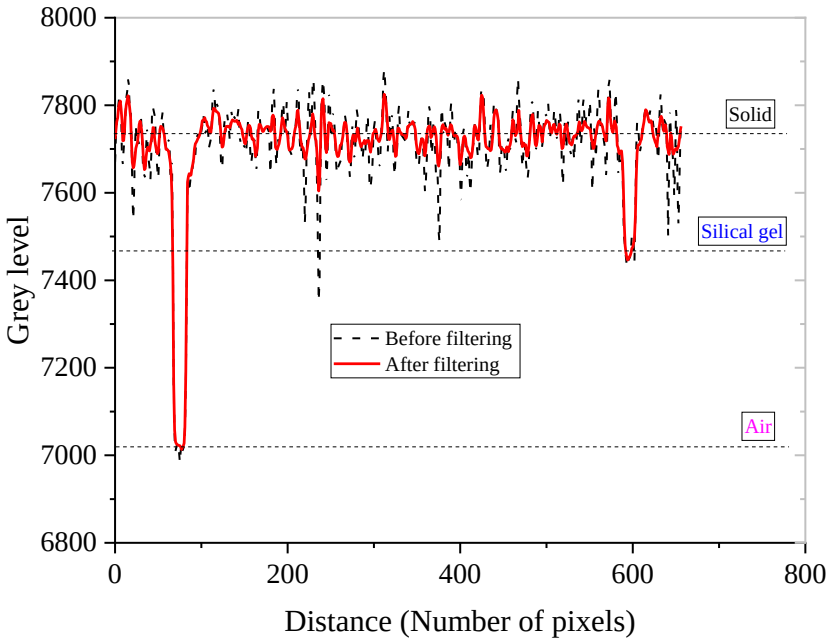

Figure 2.24: Grey level profile before and after filtering over the red line in Figure 2.23.

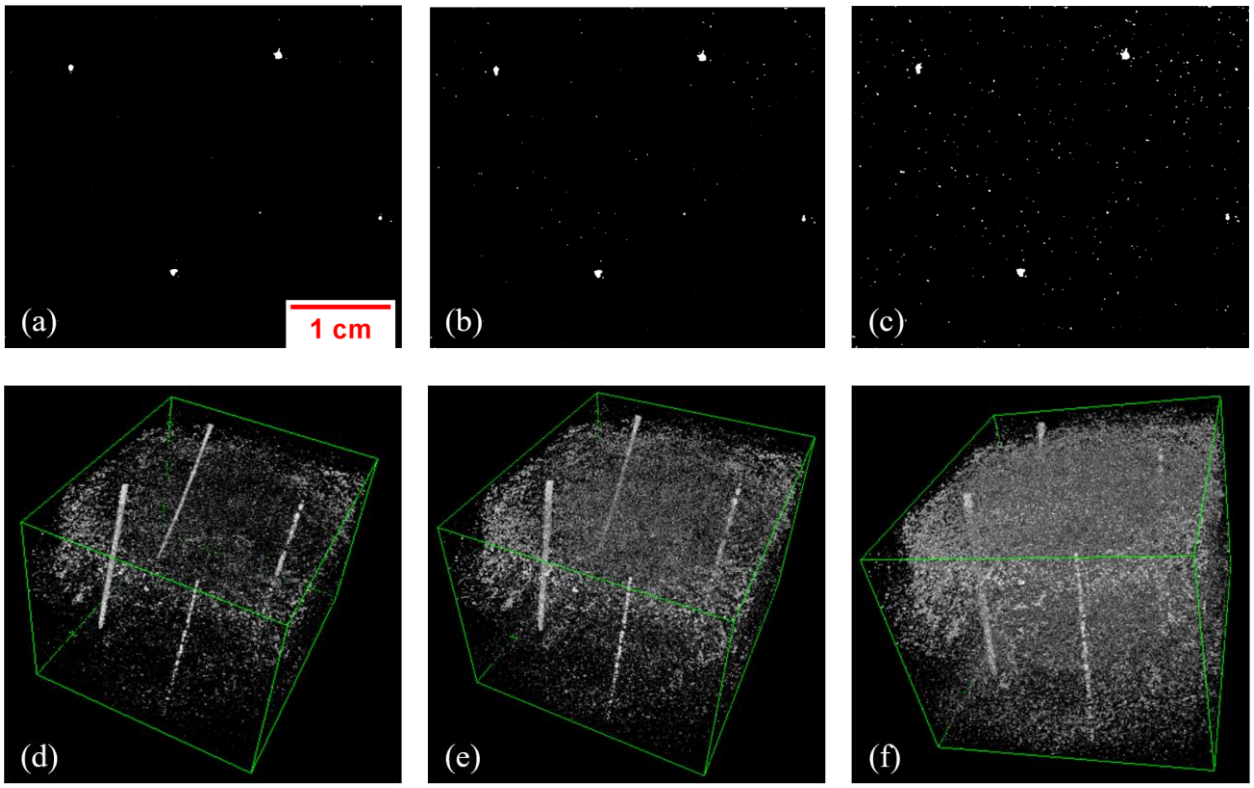

Figure 2.25: Binary image after thresholding and 3D view of the perforated holes with different choices of the threshold value: (a)&(d) 7500; (b)&(e) 7550; (c)&(f) 7600.

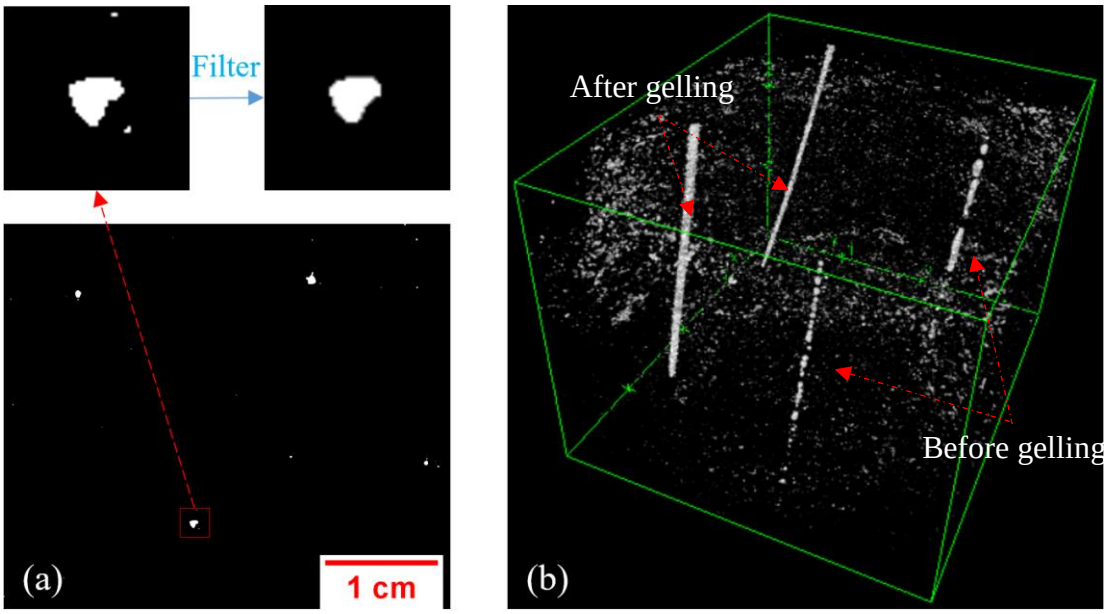

Figure 2.26: (a) applying the second filtering on the binary image; (b) its corresponding 3D view. Thresholding value of 15000.

2.3 EXPERIMENTAL SETUPS AND METHODS

To study fracturing in an unconsolidated sand reservoir subjected to fluid injection, two experimental setups are used: the radial injection cell (small scale) and the radial injection chamber (large scale). These setups were designed to simulate the injection wells condition in the sand reservoirs. A central tube, fixed on the lower baseplate of the cell, allows to perform a radial injection through a cylindrical sand specimen under axial and radial confining stresses. The radial injection chamber was developed several years ago within the Geotechnical team of the Navier laboratory (CERMES) while the small cell is a new device that was developed and manufactured at the beginning of this thesis. In this section, a detailed description of these two experimental setups is presented. Then, we present the experimental procedure as well as the sand pack reconstitution procedure in detail.

2.3.1 Radial injection chamber

2.3.1.1 *Device description*

The calibration chamber of the Geotechnical team of the Navier laboratory (CERMES) was developed as part of a collaboration between the american universities of Clarkson and Louisiana and CERMES in France in 1989. This setup has been used in many projects in relation with sand liquefaction (Dupla (1995) and pile and micropiles behavior ((Francis (1997), Le Kouby (2003), Le Thiet (2005), Tali (2011) and Muhammed (2015)). Regarding the research domain related to injection, this chamber was used by Feia (2015) to study the process of transport and deposition of suspended particles in porous medium. In his research, various developments and modifications were made on the calibration chamber in order to better simulate well conditions by generating a radial flow of a fluid charged with a small quantity of solid particles in a dense sand specimen. Figure 2.27 presents the photos of the radial injection chamber. The description of the device is detailed in Feia et al. (2017). The calibration chamber allows to reconstitute a specimen of 524 mm in diameter and 400 mm in height. This height has been reduced from the maximum height (700 mm) to favor the radial flow and minimize the effect of gravity. Injection is performed through the strainer tube with 200 µm mesh openings (Figure 2.27c). The strainer tube is a real injection tube used in practice and it has an external diameter of 70 mm. In our research, we will use the same chamber configuration as that used by Feia (2015) with some additional modifications (Figure 2.28). A second reservoir is set up for the injection of the colored gel. This device will be called “radial injection chamber” throughout our research to distinguish with the experimental setup called the radial injection cell. A global view of the radial injection chamber is shown in Figure 2.29.

A Hydra-Cell Pump (WANNER manufacturer) of the model G03-S is used to perform the fluid injection (Figure 2.30a). The flow rate can be manually controlled by an adjustment knob in the range of 1.5 l/min to 7 l/min. The injection below the minimum flow rate of the pump (1.5 l/min) can be carried out using a T-shaped split pipe installed at the outlet pipe of the pump. The principle of this pump model is presented in Figure 2.30b. The sequential movement of three diaphragms (forward and backward) provides consistent, low-pulse flow which is

significantly lower than the pulses observed for peristaltic pump used in the colored gel validation tests.

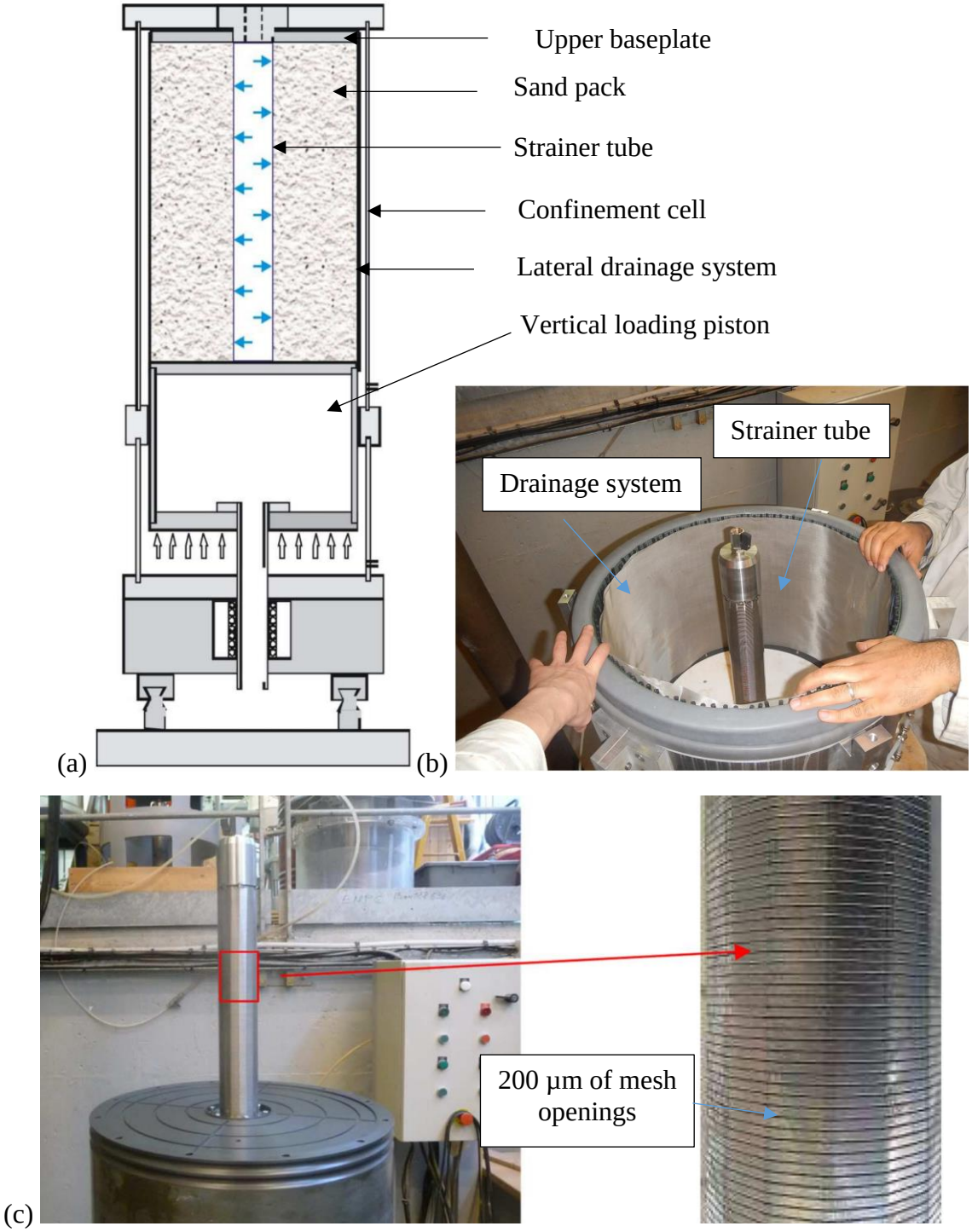

Figure 2.27: (a) 2D schematic diagram of the radial injection chamber; (b) view of the chamber; (c) view of the strainer tube (Feia, 2015, 2017).

In addition, a pulsation dampener is installed at the outlet side of the pump to absorb the pulsations of the flow rate and fluid pressure (Figure 2.30c). Three pressure transducers (MEAS manufacturer) are used to measure the confining pressure σ_h, the axial stress σ_v and the inlet

injection pressure of the sand pack P_1 (Figure 2.30d) up to 1 MPa. The precision of these transducers is 0.5 kPa. The flow rate is measured using a flowmeter ranging from 0.5 l/min to 10 l/min (KOBOLD manufacturer - Figure 2.30e). In the tests with suspended particles injection, a mixture will be used (Figure 2.30f).

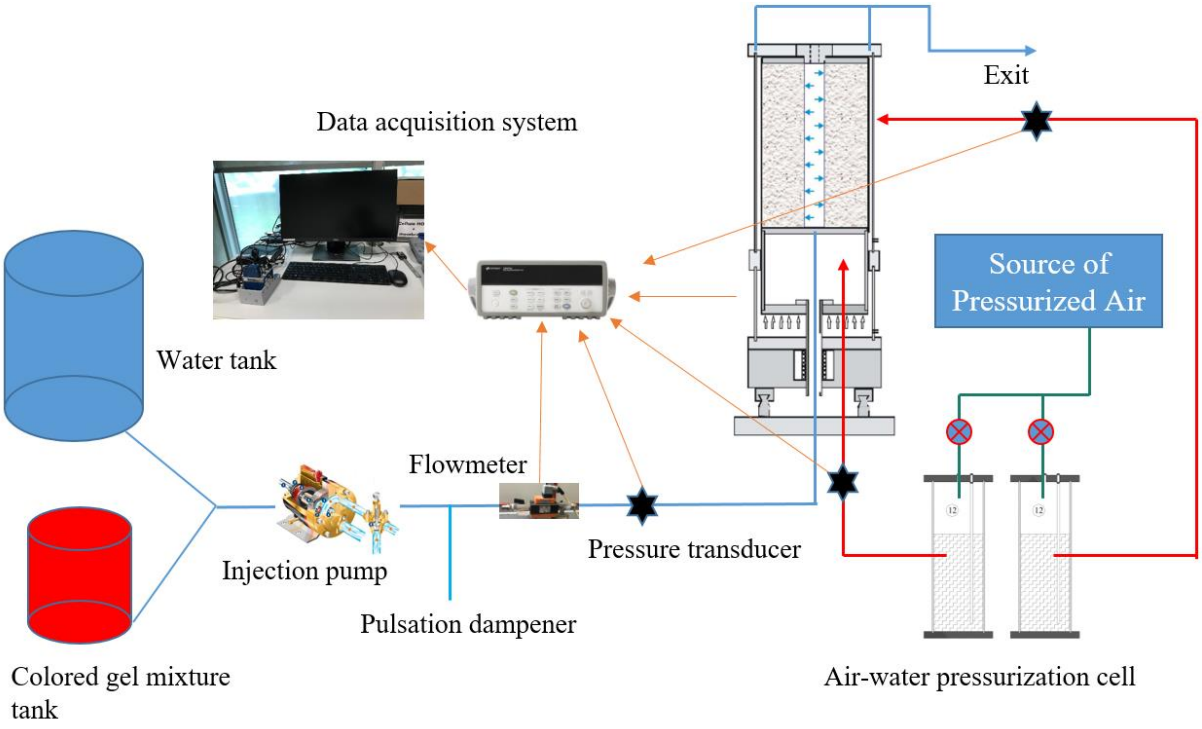

Figure 2.28: Functional scheme of the radial injection chamber setup.

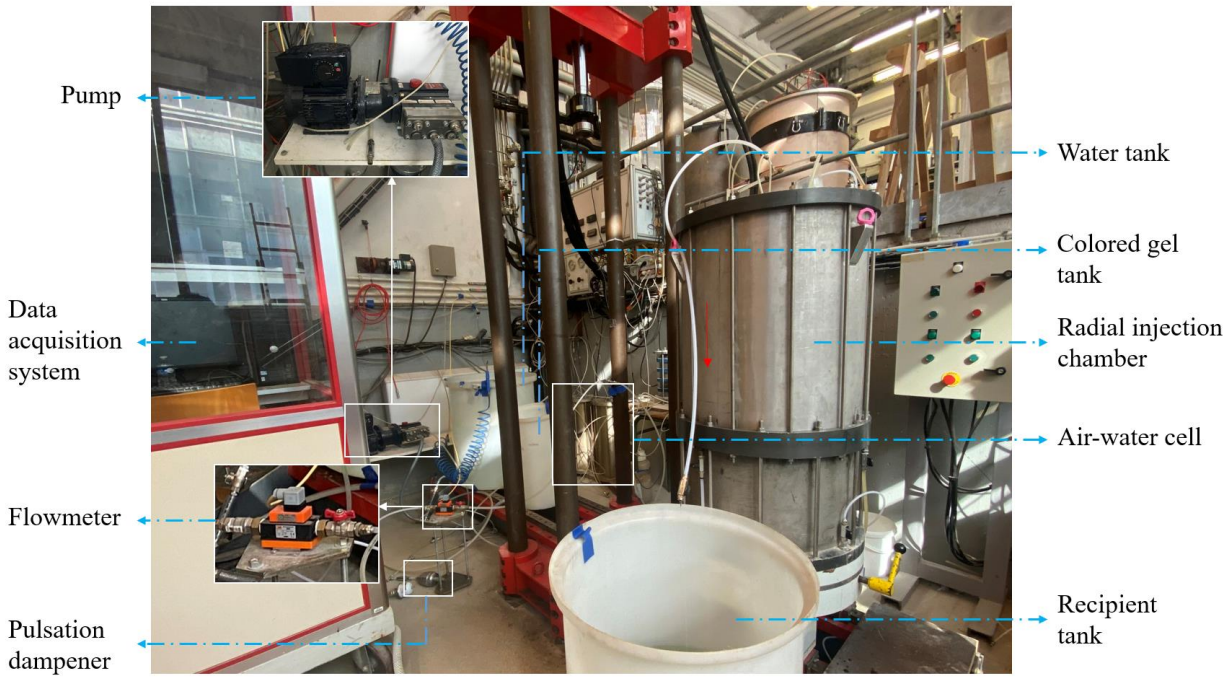

Figure 2.29: Global view of the radial injection chamber setup.

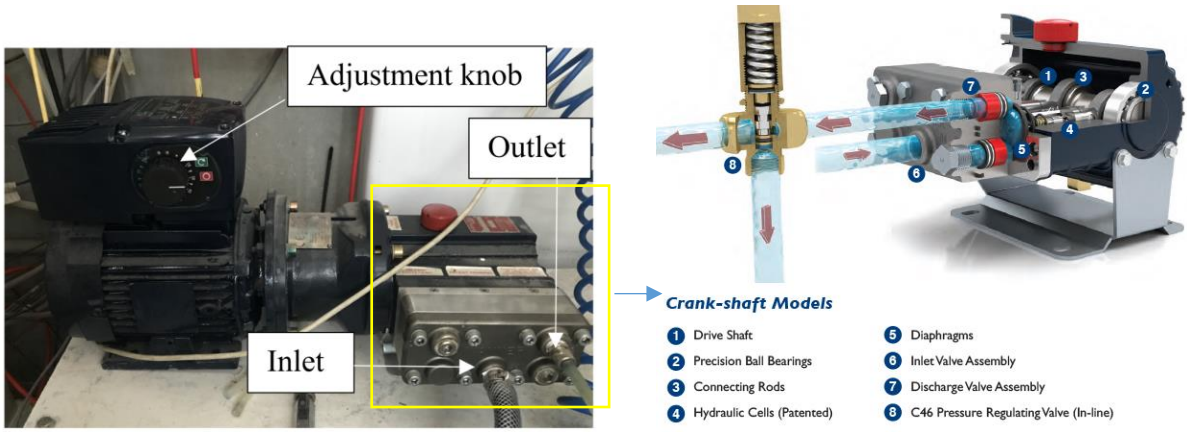

(a) (b)

(c) (d)

(e) (f)

Figure 2.30: Photos of the injection pump and auxiliary parts for the radial injection chamber setup : (a) view of G03-S Hydra-Cell Pump and (b) its principles (ref: https://www.hydra-cell.com/product/positive-displacement-pump.html); (c) pulsation dampener; (d) pressure transducer; (e) flowmeter; (f) mixer of suspended particles in water.

2.3.1.2 *Testing procedure and sand pack preparation*

Figure 2.32 shows the main steps of the experimental procedure developed in order to perform injection tests in the radial injection chamber. The reconstituted sand pack consists, on its lower and upper part of two low permeability layers (H_{layer} = 4 cm) of the mixture of NE34 sand + 32% C10 fines. The fluid is injected at the central zone of the sand pack (H = 32 cm). The representative diagram of the configuration of the sand pack with its corresponding dimensions is presented in Figure 2.31. Two small membranes covered with grease are placed at the interface of these layers (Figure 2.32e,g). The two low permeability layers and the two small membranes act as a barrier that prevents parasitic flow to the two ends of the chamber. These developments are made following the problems encountered by (Feia et al., 2017b) while performing injection tests within the radial injection chamber. These authors has prepared a homogeneous sand pack of NE34 without these two confining layers and membranes. During injection, the vertical parasitic flow was observed, causing the erosion of material at the interface of the sand pack and the upper baseplate.

The injection area consists of a double ring. The idea is to reconstitute around injection tube an inner ring of lower permeability made up of a mixture of NE34 sand + C10 fines in order to represent a damage zone (internal cake) by PWRI. The outer ring is fabricated by pure NE34 sand which represents the initial state of the reservoir before impairment.

The saturation phase consists of radially injecting de-aired water through the sand pack by gravity. A de-aired water tank is positioned higher than the radial injection chamber which provides a water head at the entrance of the sand pack (Figure 2.32p). The saturation is done after one day.

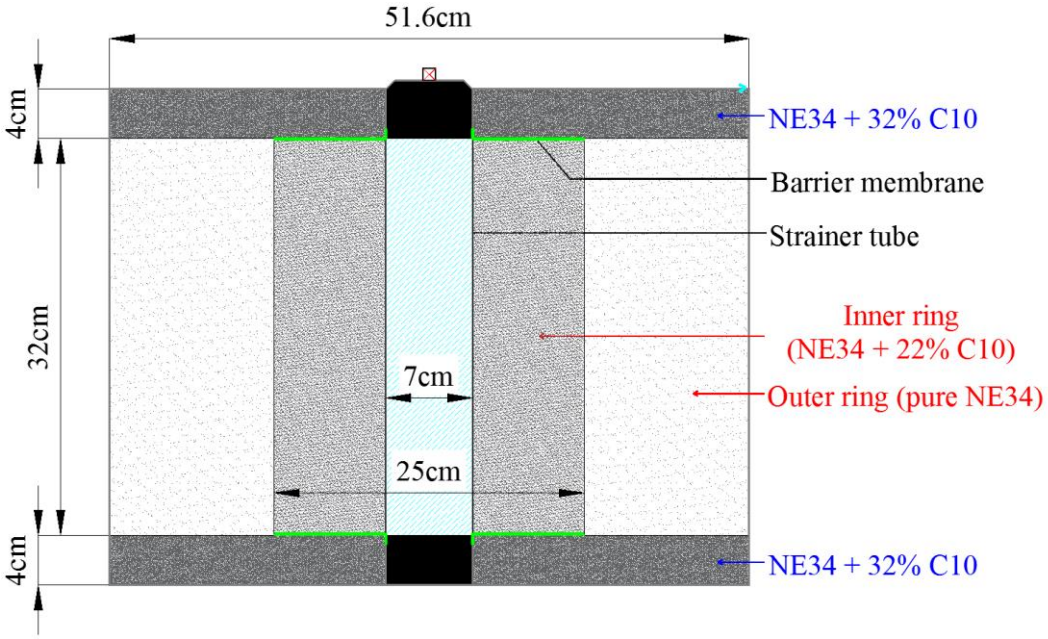

Figure 2.31: Configuration of the sand pack in the radial injection chamber.

a – fixing the membrane onto the lower baseplate

b – installation of the mold

c – installation of the lateral drainage system

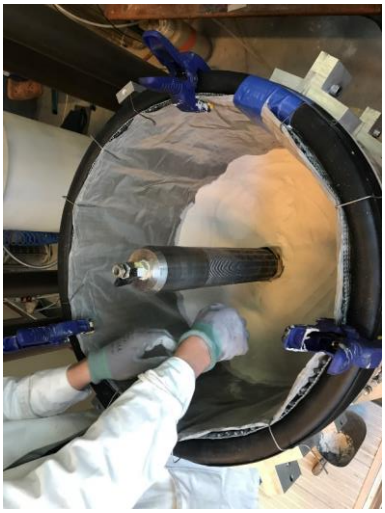

d – compaction of the first low permeability layer

e – setting up a small latex membrane

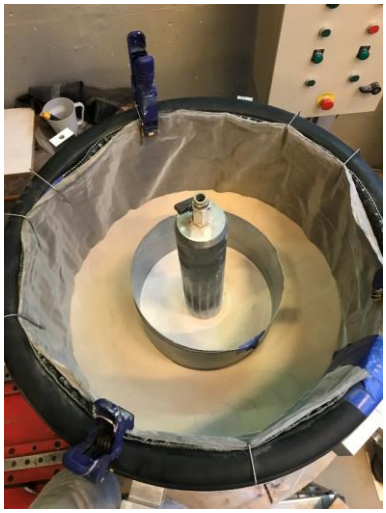

f – compaction of the double rings

g – setting up a small latex membrane

h – compaction of the upper low permeability layer

i – installation of the upper baseplate

k – applying a vacuum in the sand pack and unmolding

l – setting up the lateral confining cell

m –installation of the cell cover

n – fixing the system by using twelve rods

o – saturation of the sand pack

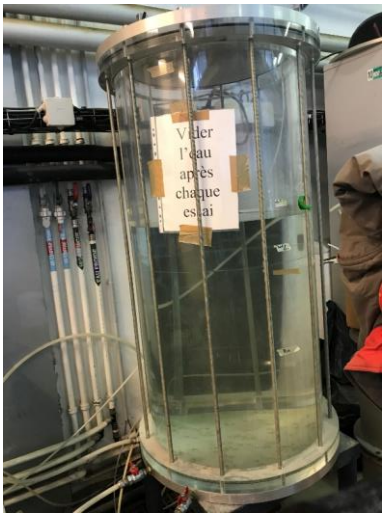

p – de-aired water tank for saturation

Figure 2.32: Experimental procedure for the radial injection chamber test.

Injection tests with pure water injection are performed at controlled flow rate. During the water injection phase, the flow rate is increased until fracturing of the sand pack. The injection rate is gradually increased by steps of 0.2 l/min. Each step is maintained for approximately 5 minutes. When the injection pressure reaches the first pressure drop, the injection rate is maintained constant for 15 minutes. Three subsequent injection steps are carried out before decreasing the injection rate to zero (Figure 2.33).

The colored gel injection phase is performed by injecting a small volume of a mixture of gel MasterRoc MP320 + 0.2% Basacid Blue 762, which corresponds to 50 % of the void volume of the inner ring. Before injecting the mixture, some reloading steps of increasing the flow rate are carried out to confirm the change of the permeability after fracturing.

Once the sand pack is solidified by the injected gel, the applied stresses are released and the disassembling is performed. This phase consists in excavating the first low permeability layer and then excavating the outer ring which contains only Fontainebleau NE34 sand. The membrane and lateral drainage system are removed before the horizontal excavation of inner ring is performed. For some selected tests, several cylindrical samples containing the fractures are carefully extracted from the inner ring and then, they are scanned by X-ray CT and then observed by using optical microscope.

Cleaning of the overall system after the test is an important task that must be carefully done to avoid any damage of the device by colored gel injection. A flow of water needs to be applied immediately after injecting this mixture. The pressure transducer and the pulsation dampener are then removed and rinsed again with water to remove any residual colored gel. At the end of the disassembling, the injection tube is filled by the rigid silica gel. High pressure water pump system needs to be used to clean up this tube.

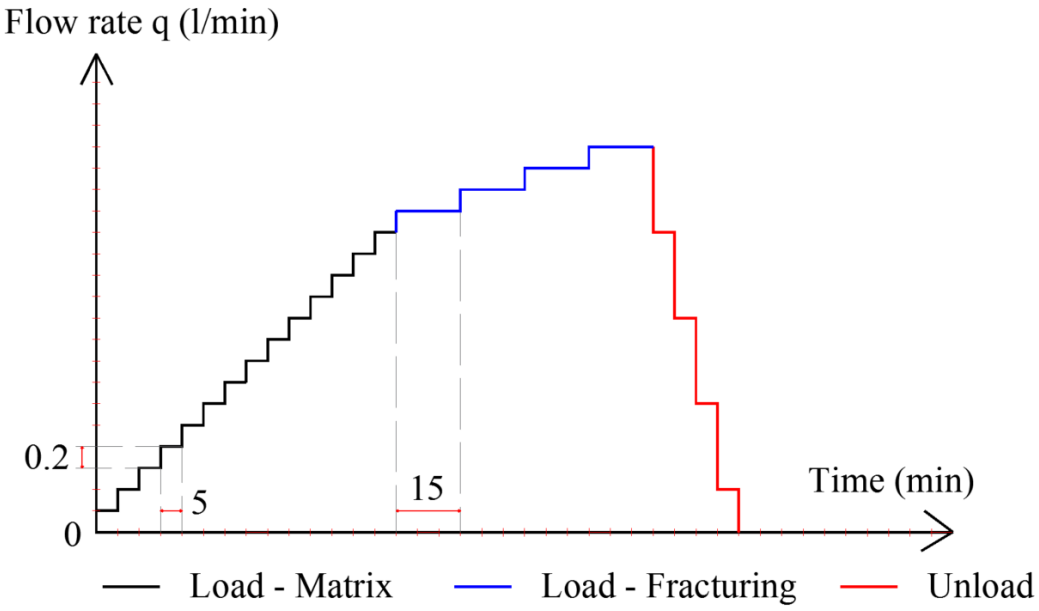

Figure 2.33: Schematic process for the water injection phase in radial injection chamber.

2.3.2 Radial injection cell

2.3.2.1 *Device description*

This new experimental setup, developed within the framework of this thesis, is a radial injection cell, specially designed and built to study fracturing mechanisms in unconsolidated sand specimens under fluid injection. This development is based on the configuration of the radial injection chamber with an important feature of the cell which allows the entire granular structure of the specimen to be observed thanks to X-ray CT. Figure 2.34 shows a schematic cross section of the radial injection cell with some of its major components. The sand specimen has 100 mm in diameter and 200 mm in height. The confining cell is basically a classical triaxial cell with independent application of confining and axial stress. The cell is equipped with a central injection tube attached to the lower baseplate which permits internal radial injection of a fluid. In order to avoid the absorption of X-ray and metal artifacts during the scan of the specimen, the cell is fabricated with a limited number of metallic pieces. In particular, the scanned part (red rectangular in Figure 2.34) is made of the polymethyl methacrylate (PMMA) to facilitate the penetration of X-ray. In order to avoid specimen disturbance during the specimen transportation from the cell to the X-ray CT, additional consideration is taken into account in the design of the cell allowing the specimen to be easily transported.

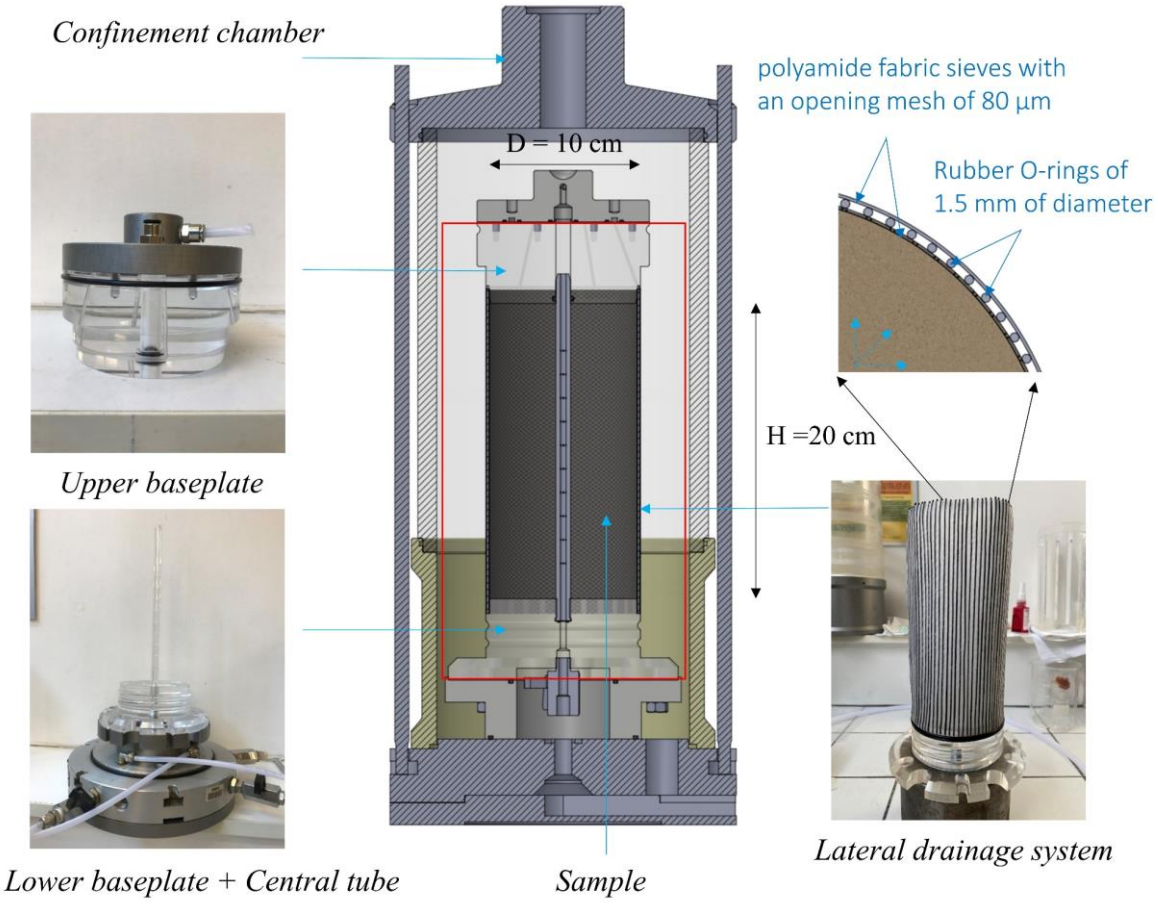

Figure 2.34: 2D cross section of radial injection cell and its corresponding components.

The cell consists of the following major components: an upper baseplate, a lower baseplate, an injection tube, a peripheral drainage system, a lateral latex membrane and a confinement chamber. The upper and lower baseplates both consist of two different pieces: one in PMMA and another one in aluminum. Two rubber O-rings are positioned between the two pieces for sealing. The drainage system consists of two polyamide fabric sieves of cylindrical shape with an opening mesh of 80 μm, which allow for the retention of sand grains and the passage of fine particles. The rubber O-rings are glued between these two sieves for maintaining a sufficient space for drainage and flow out of the fluid. Figure 2.35 shows a 3D schematic cross-section of the upper part of the cell with the drainage system for the fluid flow within the cell. On the upper baseplate, there are one outlet of injection tube and two outlets of lateral drainage. Six small holes of 2 mm in diameter, located symmetrically inside the PMMA piece, allow to link the lateral drainage system with two outlets of the upper baseplate. The configuration of the injection tube, composed of PMMA, is presented in Figure 2.36a. The inner and outer diameter of the injection tube are 4 mm and 10 mm, respectively. Holes have been made in the helical groove, to provide a radial fluid injection along the tube. The injection tube is covered by an 80 µm sieve to prevent the inflow of sand into the injection tube (Figure 2.36b). The choice of the tube configuration among three configurations (Figure 2.37) has been validated by the preliminary tests. The detailed results are presented in Appendix B. The third configuration (with helical groove) has been chosen for the following main reasons: providing a better radial flow though the helical groove, minimizing the localized flow at the open hole levels and ensuring tube rigidity during specimen preparation. Due to the selected material (PMMA) and the tube size, the tube cannot be designed with the strainer configuration as the radial injection chamber.

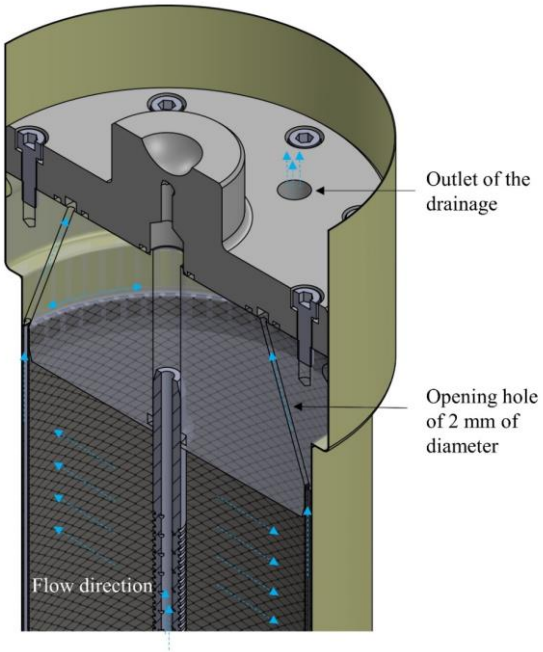

Figure 2.35: 3D schematic cross-section representing the flow direction within the radial injection cell.

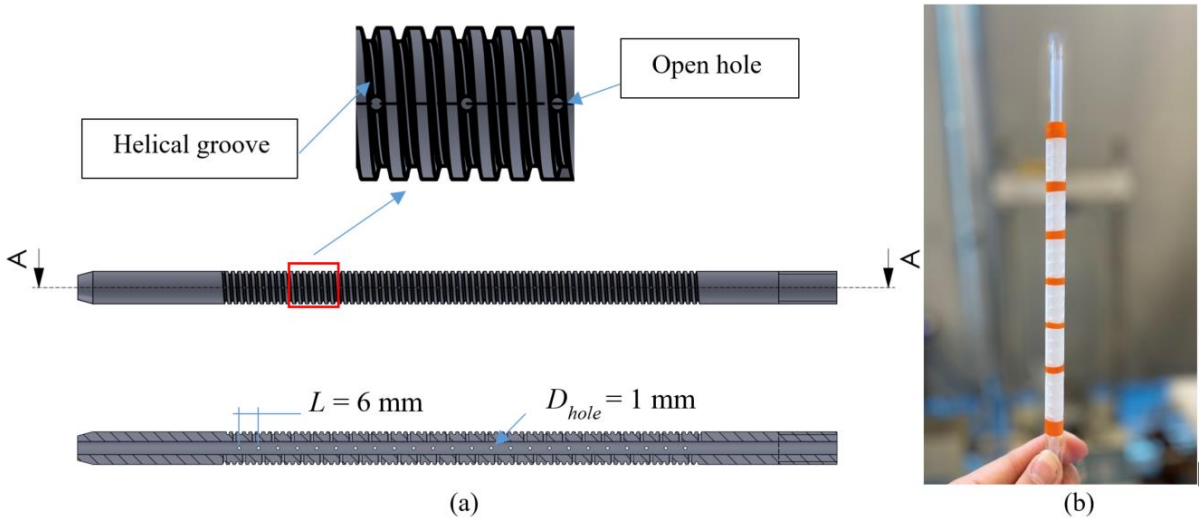

Figure 2.36: Injection tube: (a) configuration of injection tube; (b) view of the tube covered with polyamide sieves.

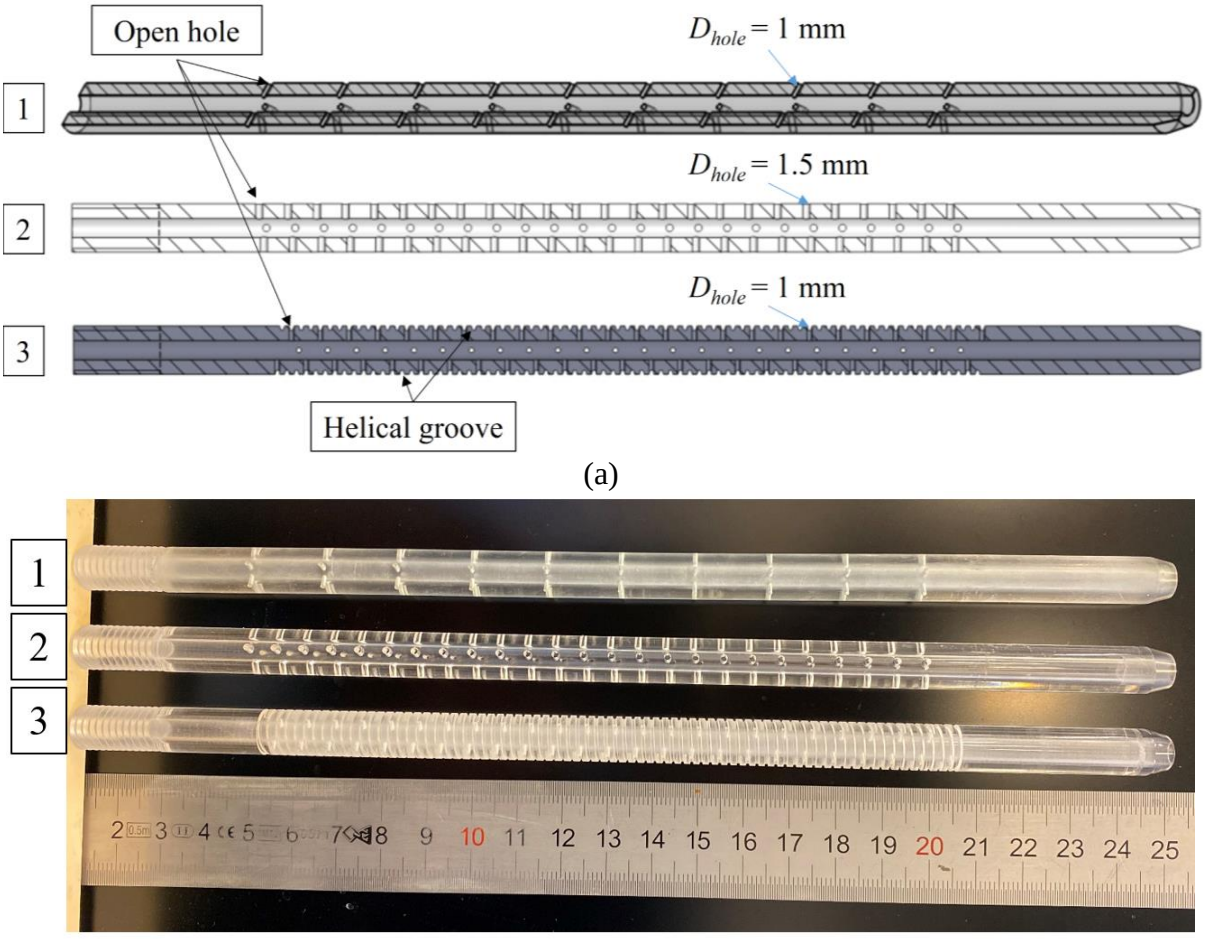

Figure 2.37: Different configurations of the injection tube testing: (a) 2D design view; (b) photo of the tubes.

Figure 2.38 and Figure 2.39 present a functional scheme and a global view of the experimental setup, respectively. Injection was carried out with a G03-G Hydra-Cell Pump at a constant flow rate with a range between 0.1 l/min and 2.3 l/min (Figure 2.40a). A pulsation dampener, installed at the outlet of the pump, is used to reduce the pressure fluctuations and flow pulsation during injection. A same flowmeter as the one used for the radial injection chamber is used with a smaller flow rate range (between 0.2 and 3.2 l/min). The injection rate is measured with a flowmeter installed at the inlet of the specimen.

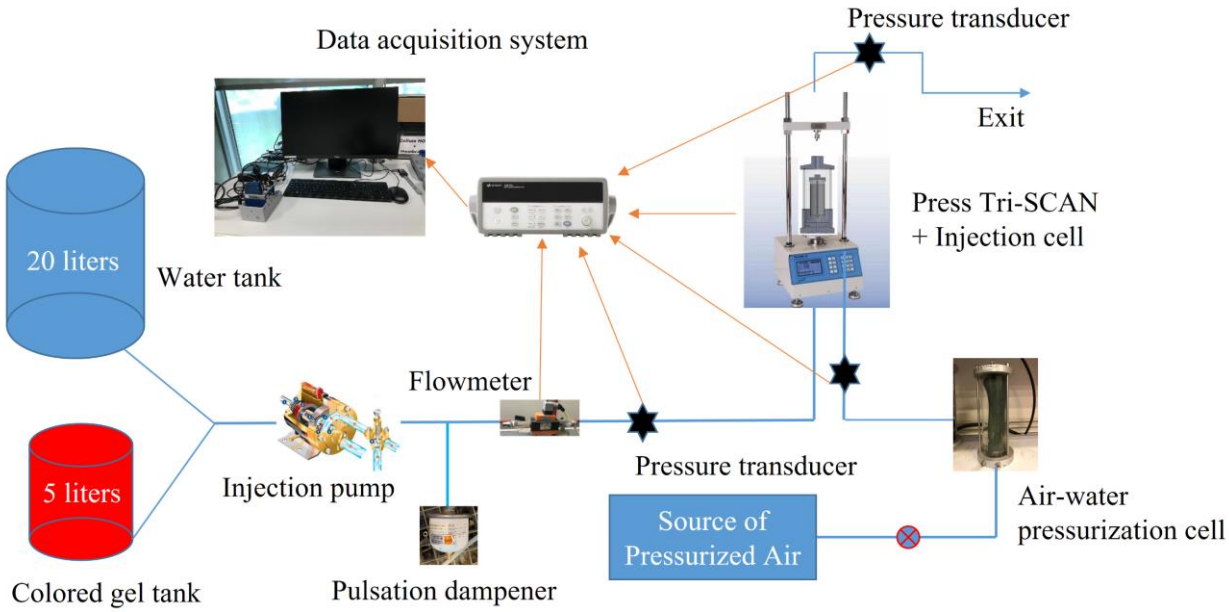

Figure 2.38: Functional scheme of the radial injection cell setup.

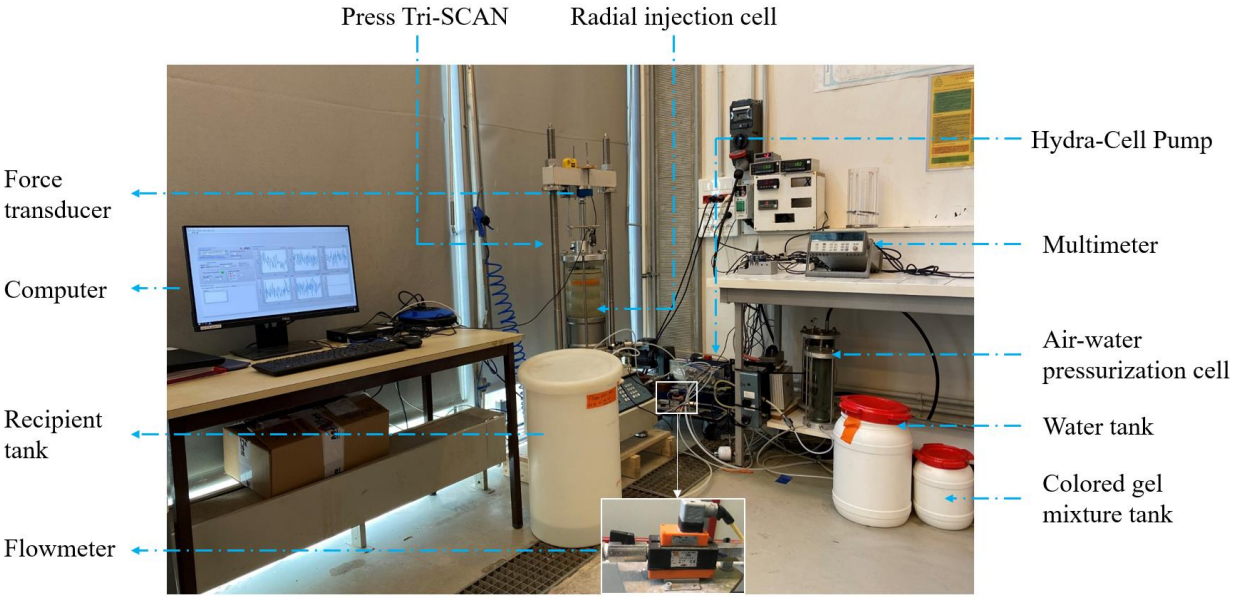

Figure 2.39: General view of the radial injection cell setup.

Three pressure transducers (MEAS manufacturer) are used to monitor the confining pressure, the injection pressure at the inlet and at the outlet of the specimen. The measurement accuracy of these sensors is of 0.5 kPa and the measurement capacity is 1 MPa The vertical stress is applied to the specimen through a 50 kN Mecanical press Tri-SCAN. The axial force is measured using a force transducer (INTERFACE manufacturer) installed on the top of the cell (Figure 2.40b). The maximum capacity of the sensor is 10 kN with a measure accuracy of 0.004 kN. The confining pressure is applied using an air-water cell which has a maximum capacity of 1 MPa. All the measurement systems are connected to a computer through a multimeter (Figure 2.40c,d) for automatic data acquisition and display (LabVIEW). The acquisition frequency is set to one data point per 3 seconds. Figure 2.41 presents a display window of LabVIEW during data acquisition. Because the press TRI-SCAN operate on the principle of controlled displacement, so that a program has been set up in LabVIEW, allowing to control a constant axial stress σ_v within a selected range $\sigma_v \pm \Delta\sigma_v$ (red dash window in Figure 2.41). The axial stress is calculated from the measured force divided by the area of the specimen. In our work, the axial stress tolerance $\Delta\sigma_v$ is about 2% σ_v to minimize the variation of axial stress during the test and to do not damage the presse TRI-SCAN.

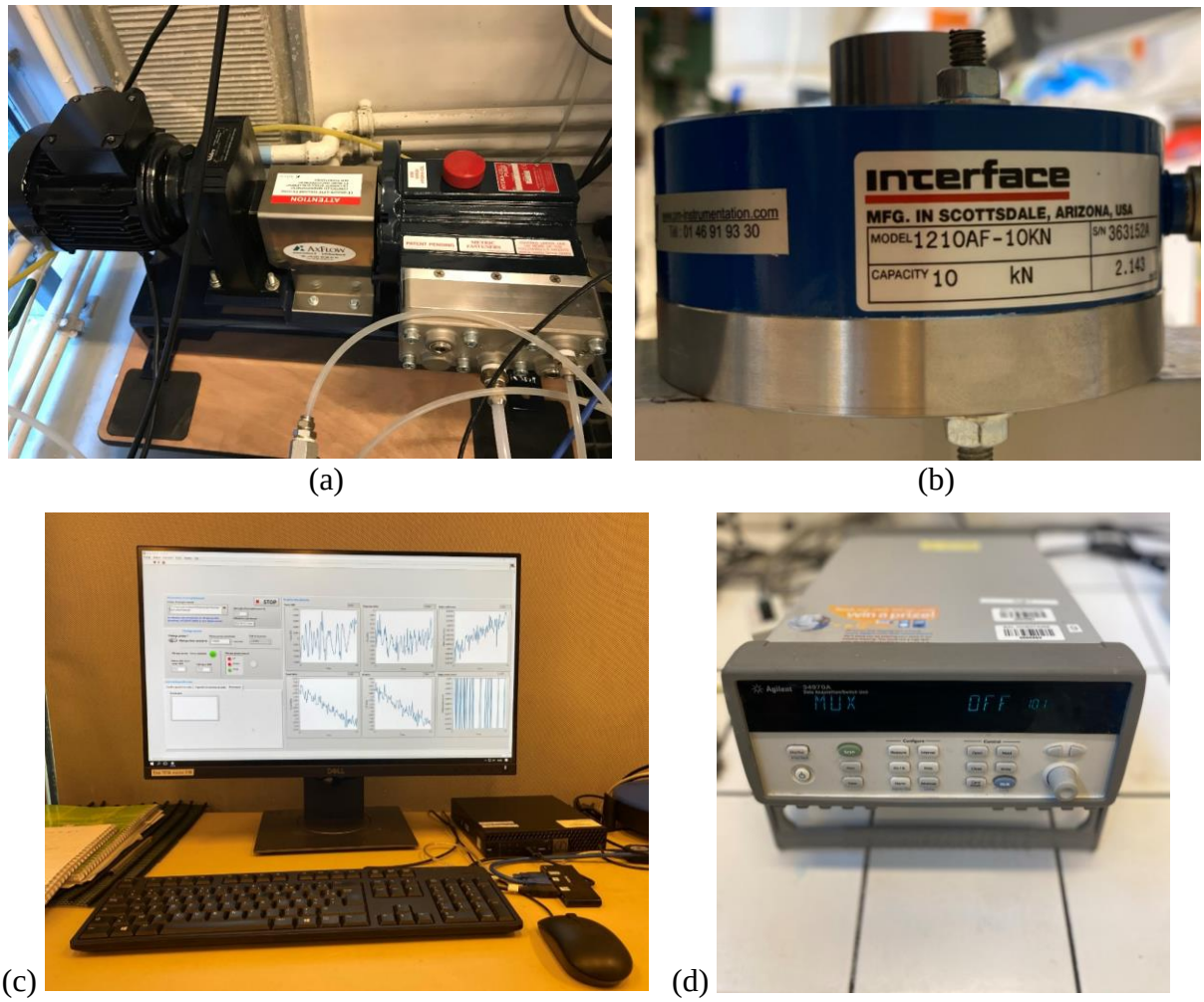

Figure 2.40: Auxiliary parts of the radial injection cell setup: (a) G03-G Hydra-Cell Pump; (b) force transducer; (c) computer; (d) multimeter.

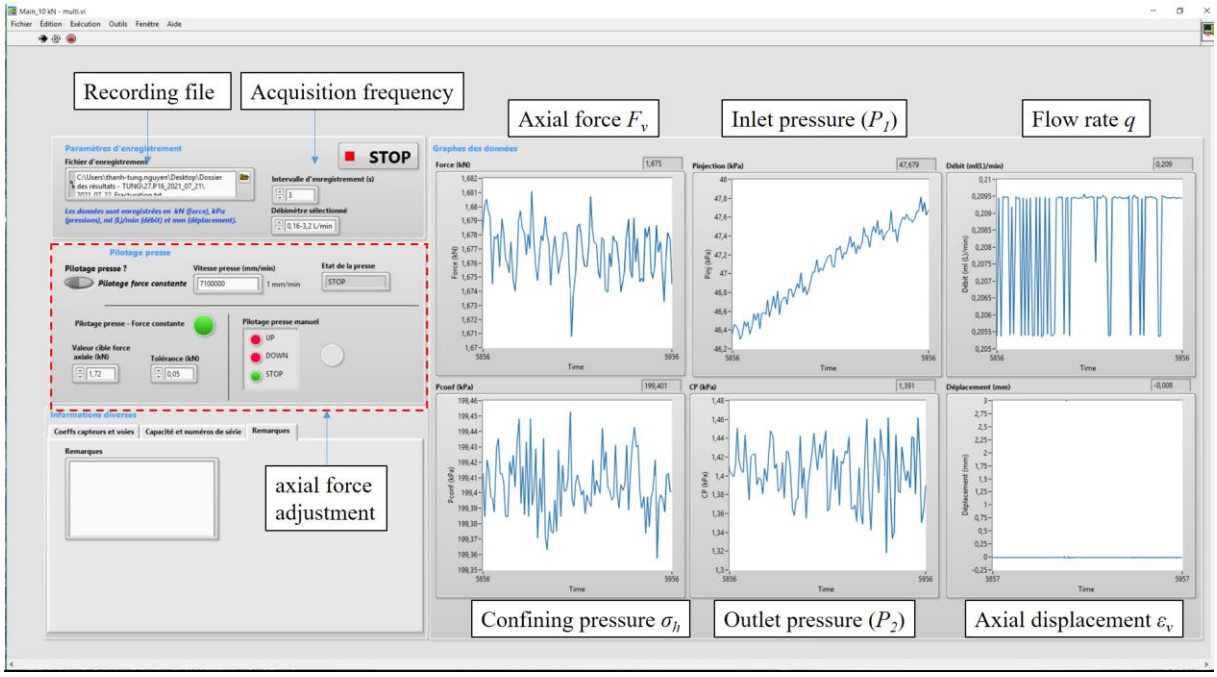

Figure 2.41: View of the data acquisition program under LabVIEW.

2.3.2.2 *Testing procedure and specimen preparation for the radial injection cell*

The complete testing procedure for pure water injection experiments consists of the following operations:

- Fabrication of the specimen
- For some selected tests, initial scan of the specimen with X-ray CT (Scan 1)
- Saturation and application of the initial stress conditions
- Water injection by gradually increasing flow rate by steps until fracturing
- Colored gel injection to solidify the specimen
- For some selected tests, second scan of specimen after fracturing using X-ray CT (Scan 2)
- Visual observation (horizontal excavation) and optical microscopy observation

Figure 2.42 presents the configuration of the reconstituted specimen tested in this research. This configuration is similar to the one used in the radial injection chamber with three distinct zones (i.e. injection zone and two confined layers of lower permeability at the top and the bottom). As for the sand pack in the radial injection chamber, two small membranes are placed between these layers in order to provide full radial flow and to prevent undesired vertical flow out of the injection zone as well as the creation of any preferential flow path.

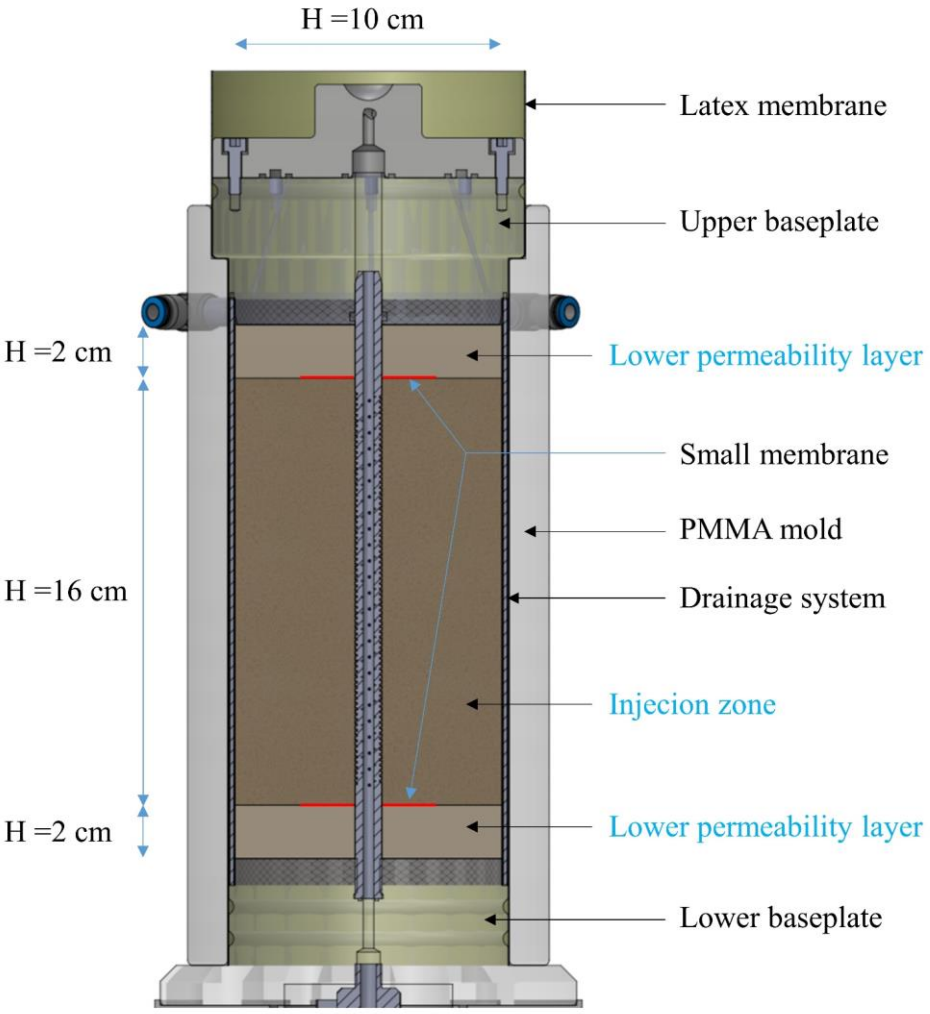

Figure 2.42: Simplified cross section of the specimen during preparation.

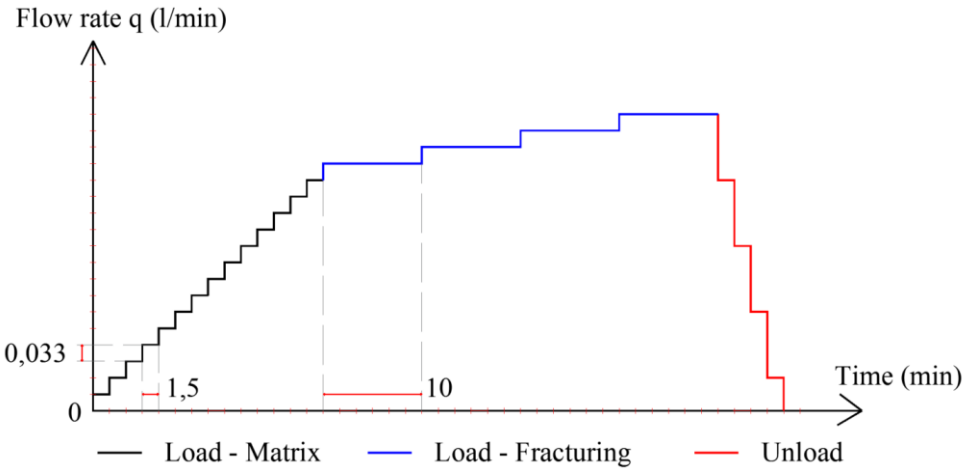

Figure 2.43: Schematic process for the water injection phase in radial injection cell.

Figure 2.44 shows the main steps of the specimen preparation. Firstly, some glass beads are glued to the lower plate as the reference points, allowing to orient the scanned images in initial and post-fracturing states at the same position (Figure 2.44a). The injection tube and drainage system are then fixed on the lower baseplate, followed by the installation of a 0.3 mm thick latex membrane and a cylindrical mold composed of two parts. The vacuum is then applied to press the membrane onto the mold (Figure 2.44b and Figure 2.44c). The mold is also reconstituted by PMMA in order to be compatible with X-ray CT scan (Figure 2.44d). The specimens are reconstructed by dry compaction of ten layers of 2 cm using a groomer, specifically designed for this cell (Figure 2.44e). After compacting the first low permeability layer, a small latex membrane is placed on the top. This membrane is covered with grease to prevent any flow along its surface (Figure 2.44f). Then, the injection zone of the specimen is compacted with eight layers and another small membrane is fixed on the top of injection zone (Figure 2.44g and Figure 2.44h). The compacted surface of each layer is scarified prior to filling the following layer to avoid any artifacts due to manual compaction. When the compaction is done with the upper low permeability layer, a porous plastic is added to maintain the cylindrical shape of the lateral drainage system before setting up the upper baseplate (Figure 2.44i).

Once the specimen has been reconstituted, it is scanned using X-ray CT in order to build a reference 3D image of the specimen. After, the cell is placed on the Tri-SCAN (Figure 2.44k). A vacuum of approximately -20 kPa is then applied to the specimen in order to be able to take the mold out. The specimen is consolidated to an isotropic stress of 50 kPa before saturating (Figure 2.44l). The saturation procedure consists of two steps. First, carbon dioxide (CO_2) is radially percolated under a pressure of 20 kPa for 10 to 15 minutes in order to replace the air present in the pores, then de-aired water is radially injected by gravity through the central tube. After saturation has been completed (Skempton coefficient B value > 0.90), the specimen is loaded to the desired stress conditions (confining pressure and axial stress).

The tests with injection of pure water in the radial injection cell are based on a similar injection protocol as those in the radial injection chamber. Tests are performed at controlled flow rate. This procedure permits to reach the fracturing regime and to pursue the injection beyond the critical threshold corresponding to the maximum injection pressure (fracturing state) by further increase of the flow rate. Various values of the maximum imposed flow rate can be chosen in order to reach various extents of the fractures. During the water injection phase, the flow rate is increased until fracturing of the specimen corresponding to the first sharp drop of the injection pressure measured by the inlet pressure transducer. The injection flow rate is increased by steps of 0.033 l/min. Each step is maintained for approximately 1.5 minutes until the pressure stabilizes. When the injection pressure reaches the first pressure drop, injection step is maintained for 10 minutes before increasing the flow rate. Three more injection steps are carried out before decreasing the injection flow rate to zero (Figure 2.43). The injection protocol of water with suspended fine particles will be detailed later in Chapter 4.

The gelling solution is prepared in the colored gel tank which consists of manually mixing the colloidal silica MasterRoc MP320, the accelerator and 0.2% of Basacid Blue 762 in one minute. Then, the injection of the colored gel is performed immediately to avoid the undesired effect of an increase of viscosity after adding the accelerator. The injected volume is about 50

% of the voids volume of the specimen. The specimen is kept for one week under the stress conditions to solidify.

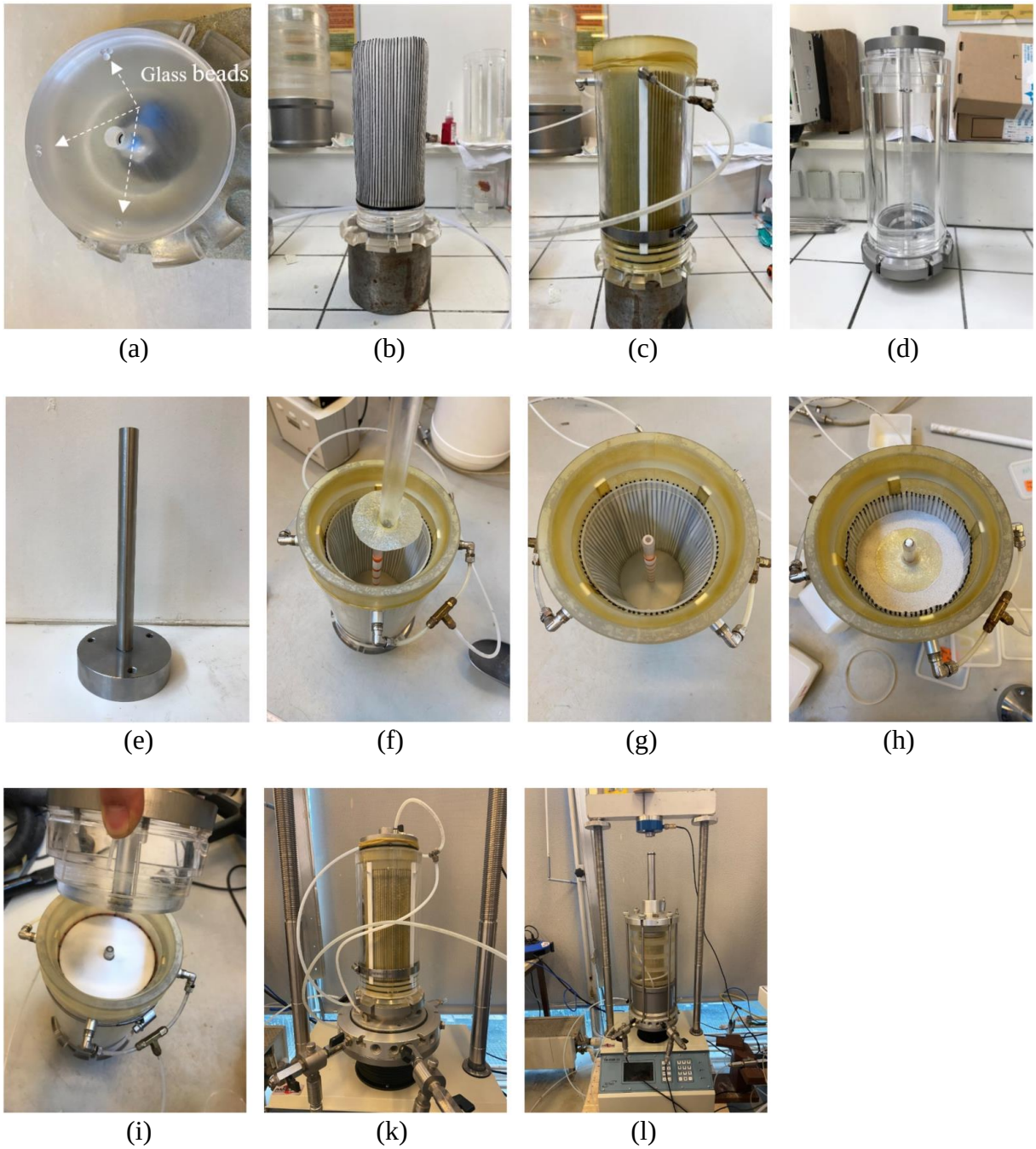

Figure 2.44: Fabrication of the specimen and assembly of the injection cell: (a) glass beads glued to the lower plate; (b) lateral drainage system and injection tube setup; (c) pressing the membrane onto the mold; (d) PMMA mold; (e) groomer; (f) setting up a small latex membrane; (g) compaction of the injection zone; (h) second small membrane; (i) upper base plate; (k) fixing the cell to the Press Tri-SCAN; (l) installation of the confining cell and saturation.

Once the specimen has been solidified by the injected gel, the applied stresses are removed and the mold is reinstalled to protect the specimen. Then, it is transported to X-ray CT for scanning (Scan 2). After scanning the specimen, a second step of disassembling is performed which consists of a horizontal excavation of the specimen. In addition, a small part of the specimen containing the fracture is observed by optical microscopy to characterize the microstructure of the fracture at the grain scale.

2.4 CONCLUSIONS

In this chapter, a detailed presentation of the tested materials, the experimental setups as well as the experimental procedure have been shown. The specimens are manually compacted using the mixture of Fontainebleau sand N34 (D_{50} = 210 µm) with different concentrations of the C10 fines (D_{50} = 20 µm), depending on the clogging scenarios. C500 particles (D_{50} = 4.5 µm) are selected as the suspended particles in the injection fluid. The mixture of colloid MasterRoc MP320 (11% of accelerator concentration) and 0.2% of dye “Basacid® Blue 762” is chosen as the reference colored gel due to a good efficiency of solidification and visualization of the invaded zone as well as a reasonable time gelling. In some tests, higher accelerator concentration is used due to the dilution of this mixture in the saturated medium. The preliminary X-ray scans show no significant effect of the colored gel on the contrast of the X-ray images and the possibility to obtain a 3D image of the fractures even with the size of a few millimeters. Thereafter the description and the test procedure of both two experimental setups are detailed. The sand pack in the chamber consists of two parts: inner ring of the mixture of NE34 sand + C10 fines and outer ring of pure sand whereas the specimen in the cell represents only the internal cake of the NE34 sand + C10 fines mixture. The radial injection chamber permits to use the real *in-situ* injection tube (strainer tube) in practice and larger specimen size whereas the advantage of the radial injection cell is to perform the tests faster than those in the radial injection chamber with additional observations of the entire specimen using X-ray CT.

CHAPTER 3. EXPERIMENTAL RESULTS OF WATER INJECTION TESTS

3.1 INTRODUCTION

After plugging of the medium due to the deposited fine particles carried in produced water, the injection of pure water at a high injection pressure can be applied to restore the permeability loss. This chapter presents an experimental study carried out on two radial injection setups of different sizes (small sand specimen in the injection cell and large sand pack in the injection chamber), aiming at exploring the initiation and development of fracturing in a dense formation containing a mixture of sand and fine particles. We also present the effect of various parameters (stress state, permeability, flow rate, …) on the fracturing phenomenon and on the increase of the permeability of the medium after fracturing. A comparison of the experimental results obtained in the two injection setups is presented in order to explore the effect of the specimen size on the fracturing response.

3.2 EXPERIMENTAL PROGRAMS

3.2.1 Radial injection cell

As the radial injection cell is a new experimental setup, preliminary tests have been performed to qualify this new device and to validate the test procedure. Different configurations of the injection tube have been tested to select the one that best suits the trainer tube used in the radial injection chamber while still ensuring the design capability of the selected fragile material (PMMA). The characteristics of the six preliminary tests are presented in Table 3.1.

Table 3.1: Characteristics of the preliminary tests in the radial injection cell.

Test	Materials		Stress conditions			Density index of the matrix	Tube configuration
	% C10	k (mD)	σ_h (kPa)	σ_v (kPa)	K_0	$I_{D\ NE34}$	
Q1	0	≈ 6 x 10^3	200	200	1	0.90	1
Q2	0	≈ 6 x 10^3	200	200	1	0.90	1
Q3	22		200	200	1	0.60	1
Q4	0	≈ 6 x 10^3	200	200	1	0.90	2
Q5	0	≈ 6 x 10^3	200	200	1	0.90	3
Q6	22	≈ 80	200	400	0.50	0.90	3

To highlight the key factors controlling the initiation of the fracture and the fracturing mode, a series of tests has been carried out in the radial injection cell. The effects of different parameters on the critical fracturing pressure, the increase of the overall permeability as well as the fracture shape were explored. We were particularly interested in the effect of the stress state (confining pressure, stress ratio), the material permeability and the imposed flow rate. These parameters are the main ones which control the fracturing process (Fjaer et al., 2008). The characteristics of the tests performed are summarized in Table 3.2. In these tests, the injected fluid is pure water (without suspended particles). In some selected tests, the specimen was scanned before and after injection using X-ray CT to identify and visualize the induced fractures. Optical microscope observations were also performed to observe the change of the microstructure of the material.

Table 3.2: Characteristics of the tests performed in the radial injection cell

Test	Parameters	Materials		Stress conditions			Number of flow rate steps in the fracturing regime
		% C10	k (mD)	σ_h (kPa)	σ_v (kPa)	K_0	
P1 (*)	Stress conditions	22	≈ 80	200	400	0.50	4
P2 (*)		22	≈ 80	150	450	0.33	4
P3		22	≈ 80	350	700	0.50	4
P4 (*)		22	≈ 80	200	600	0.33	4
P5		22	≈ 80	200	500	0.40	4
P6		22	≈ 80	120	300	0.40	4
P7 (*)	Flow rate	22	≈ 80	200	400	0.50	6
P8	Permeability	19	≈ 150	120	300	0.40	4

(*) with X-ray CT observations

3.2.2 Radial injection chamber

A series of injection tests with pure water has been performed in the radial injection chamber to better understand the fracturing mechanisms in the sand pack having a larger size as compared to the specimen in the injection cell. In particular, by using a real strainer tube, the chamber test allows to more accurately exploit the location of the induced fractures. All tests were carried out with the same configuration of the sand pack as presented in Section 2.3.1.2 . Each test normally takes place over 1 month from the preparation to the disassembling of the sand pack. This experimental campaign started by a validation test N29, with special attention to the reconstitution protocol of the sand pack (very dense structure), the injection protocol as well as the measurement of the sensors (flow rate, inlet pressure, confining pressure and axial stress). Five tests have been carried out to explore the effect of the confining pressure, the stress

ratio and the effect of the injection under several injection cycles. Additional analyses were performed on some typical samples containing the fracture using X-ray CT and an optical microscopy which allows to observe the inter granular change due to fracturing. These samples are easily taken from the sand pack without any significant structure modification, thanks to the efficiency of the silica gel.

Table 3.3: Characteristics of the tests performed in the radial injection chamber

Test	Parameters	Stress conditions			Number of flow rate steps in the fracturing regime	Number of injection cycles/ phases	Observations
		σ_h (kPa)	σ_v (kPa)	K_0			
N29	Validation test	200	400	0.50	-	1	No fracture (Horizontal excavation)
N30	Effect of several injection phases	200	400	0.50	2	3	Flowmeter limitation + different injection time steps (Vertical excavation)
N32		120	360	0.33	4	4	Pump limitation, reducing the applied stresses (Horizontal excavation)
N31	Effect of the stress conditions	150	450	0.33	4	1	Fracturing (Vertical excavation)
N33		120	240	0.50	4	1	Fracturing (Horizontal excavation)
N34		120	360	0.33	4	1	Fracturing (Horizontal excavation)

3.3 PRELIMINARY TESTS FOR VALIDATING THE INJECTION PROTOCOL

In this part, a summary of the preliminary tests in radial injection cell is presented. Details of these tests are presented in Appendix B. During the first three validation tests (Q1, Q2, Q3), we encountered some experimental problems such as pressure pulsations, clogging of the lateral drainage system, limitations of the injection tube and difficulty to achieve a matrix density index ($I_{D\,NE34}$) of 0.9 in the case of the mixture of NE34 + 22% C10 by manual compaction (see Appendix B). In order to solve these problems, we have developed new pieces: injection tube, new drainage system, compaction groomer (Figure 3.1). Then, three new validation tests have been performed (Q4, Q5 and Q6). Tests Q4 and Q5 allowed to validate the choice of the pattern of the injection tube holes - and to verify the accuracy of the measurements (pressure, flow…). Among the three configurations tested, the injection tube with a helical pattern of the groove has been selected for the radial injection cell. Indeed, this configuration provides a good radial injection within the specimen and minimizes the effect of the localized flow (see Appendix B).

We also identified an important effect of the flexible connection tube on the total pressure measured. As the pressure transducers are installed outside of the specimen, one has to account for the hydraulic head loss in the driving line (connection tube of 4 mm in internal diameter, valve, hydraulic tee fitting) to evaluate the pore pressure in the specimen. Thus the pressure loss caused by the driving tube needs to be taken into account when the pressure in the specimen, and so its overall permeability, is evaluated. A series of calibration tests has been performed in order to quantify the pressure loss due to the device. The results of these tests and the process of pressure correction are detailed in Appendix C.

(a)  (b) 

Figure 3.1: New pieces: (a) drainage system containing more O-rings, (b) specific groomer allows protecting the PMMA injection tube during compaction.

Test Q6 was performed to validate the complete protocol before starting the parametric study. Figure 3.2 shows all 5 injection phases for test Q6. The first phase (Phase 1) consists in gradually increasing the flow rate to 0.21 l/min, at an isotropic confining pressure of 200 kPa, to calculate the initial permeability of the specimen. During this phase, we observed a continuous increase in pressure over time at a constant imposed flow rate. This increase in pressure corresponds to a decrease in the overall permeability of the specimen from 89 mD to 78 mD. In Phase 2, the vertical stress was increased up to 400 kPa to provide the anisotropic stress conditions (σ_h = 200 kPa, σ_v = 400 kPa). The permeability was almost unchanged as compared with Phase 1. It can be concluded that for the range of stress conditions tested here, there is no significant effect of the axial stress on the permeability change of the specimen.

During Phase 3, the flow was gradually increased in order to reach the non-matrix regime (i.e., frac-regime). However, at a flow rate of approximately 0.66 l/min, corresponding to an initial pressure of approximately 380 kPa, a rapid increase in pressure was observed. This step was maintained for about 2 hours without pressure stabilization. As during Phase 1, this phenomenon corresponds to the internal erosion of the specimen and a migration of a certain amount of fine particles (C10) within the specimen. These mobilized particles accumulate in the pore throats, causing a local clogging of the specimen, and consequently a decrease of the overall permeability. This phenomenon will be discussed later in Section 3.4.2.2 .

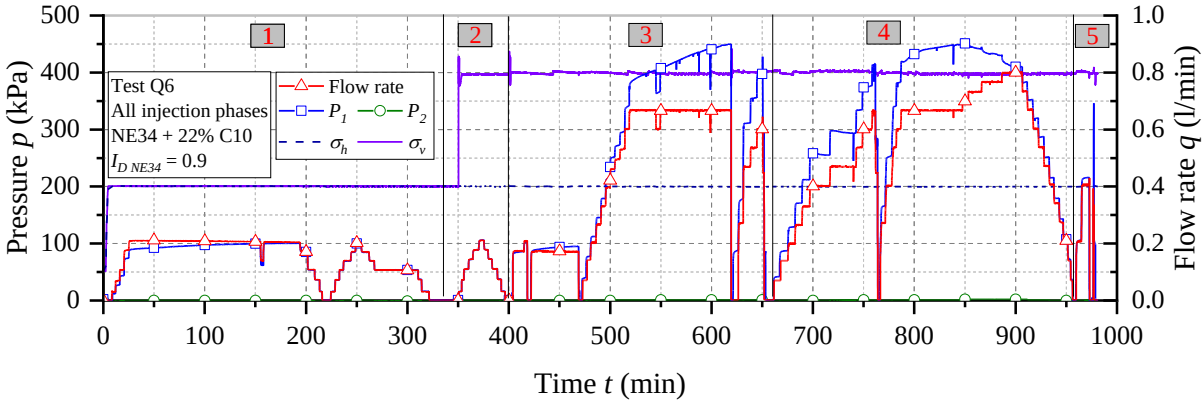

Figure 3.2: Synthesis of the test Q6 results.

Therefore, the injection time in the matrix flow regime needs to be reduced to minimize this internal erosion. Phase 4 corresponds to the continuation of Phase 3, but with a higher flow rate up to 0.8 l/min. During this phase, the non-matrix regime was reached for a flow rate of around 0.7 l/min, corresponding to a critical fracturing pressure around 460 kPa (i.e., 2.3 σ_h). Two more injection steps were carried out before stop pumping (Figure 3.3). As can be seen in Figure 3.4, the permeability decreased from 60.5 mD to 56.4 mD due to the internal erosion in the matrix regime and then increased again up to 73 mD in the fracturing regime.

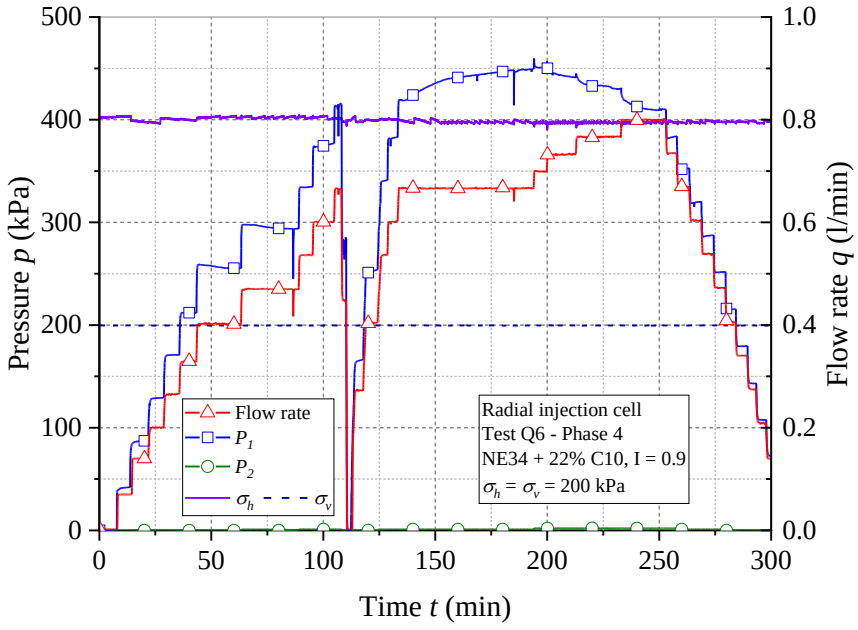

Figure 3.3: Test Q6 – Phase 4: pressure – flow rate – time curves

At the end of the test, a small volume of the mixture of gel + 0.2% Basacid Blue was injected (Phase 5) in order to solidify the specimen. The results obtained during these five phases are described in more detail in Appendix B.4.

During the disassembling of the specimen, the induced fractures were observed along the injection tube. These fractures are responsible for the pressure drops and the increase of the

permeability during the injection phases. They are short and perpendicular to the injection tube (Figure 3.5).

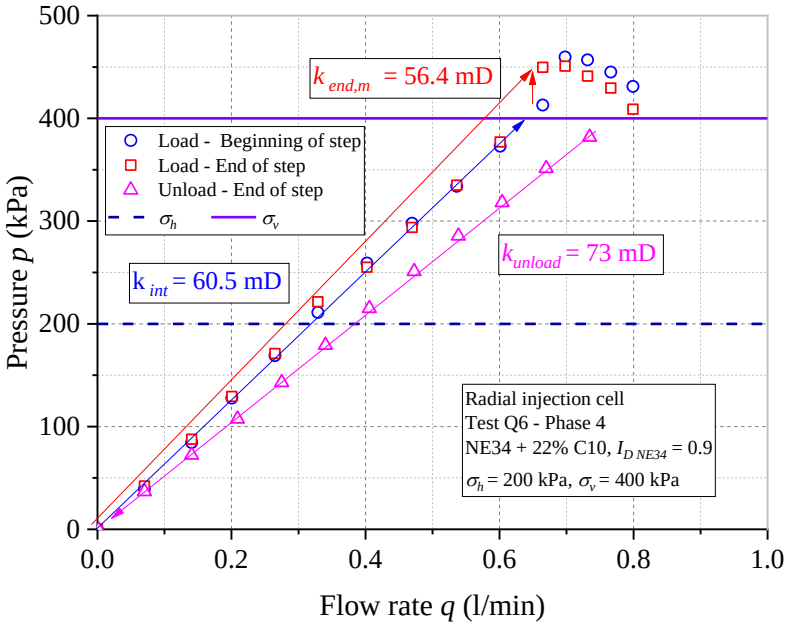

Figure 3.4: Test Q6 – Phase 4: pressure – flow rate curve.

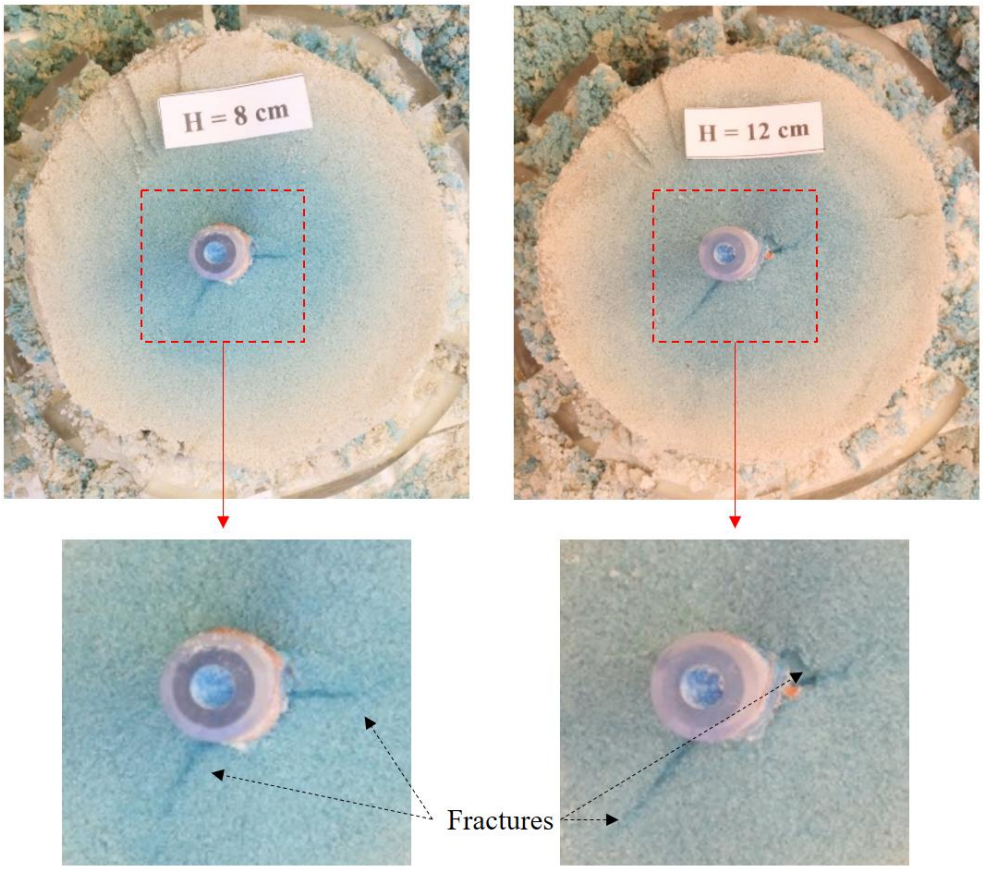

Figure 3.5: Typical horizontal cross-sections observed during the disassembling of the test Q6.

3.4 EXPERIMENTAL RESULTS OF THE TESTS PERFORMED IN THE RADIAL INJECTION CELL

3.4.1 Typical test results

In this section, the results of a reference test carried out (Test P1) in the radial injection cell are presented. First, the results during the injection phase are presented, then, the observations of the specimen using different methods such as X-ray CT, manual excavation and optical microscopy.

3.4.1.1 *Water injection phase*

The pore pressure measurements are shown in Figure 3.6a in which P_1 and P_2 are the measured pressure on the inlet and outlet pressure transducers (T1 and T2), respectively. The injection phase was performed in about 90 minutes. As the outlet pressure transducer was installed at the extremity of the outlet pipe, P_2 corresponds to the atmospheric pressure. During matrix injection regime, we observed a gradual increase of the injection pressure at constant imposed flow rate (Figure 3.6b). This phenomenon can be attributed to internal erosion as for test Q6 (see previous section). Similar results have been also obtained by Xiao and Shwiyhat, 2012. As previously explained, in order to limit this phenomenon, before reaching the fracturing regime, the injection time of each step is fixed to only 1.5 minutes. When the flow rate reached 0.9 l/min, the first pressure drop was observed and the corresponding peak pressure measured by the inlet pressure transducer was 490 kPa. This flow rate step was maintained for 10 minutes, and then the flow rate was further increased with three more steps (0.93 l/min, 0.96 l/min and 1 l/min) before decreasing the flow rate until stop of the pump (Figure 3.6c).

❖ *Corrections of pressure measurements*

As the pressure transducers are installed outside the cell, one has to account for the hydraulic head loss in the driving tube in order to evaluate the pore pressure in the injection zone within the specimen. At a given flow rate, the pressure at the entrance of tube injection P_{in} can be calculated by subtracting the pressure loss of the inlet driving tube from the pressure measured by the inlet pressure transducer P_1. In this device, the inlet pressure transducer was installed at the same vertical position as the cell, therefore the hydrostatic pressure is negligible.

Figure 3.7 presents the test results in terms of pressure versus flow rate. This curve is plotted using the corrected measurements of the pressure at the inlet of the injection tube P_{in}. The fracturing pressure P_{frac} of 484 kPa corresponds to 2.42 σ_h.

The permeability is calculated using Darcy's law in the case of a 2D radial flow, as:

$$k = \frac{\mu . Q}{\Delta P_s . 2 . \pi . H} \ln \frac{r_0}{r_1} \tag{3.1}$$

where : H is the height of the injection zone, r_0 et r_1 are the radius of the injection tube and specimen, respectively, ΔP_s is the pressure drop within the specimen at the injection flow rate Q, μ is the dynamic fluid viscosity.

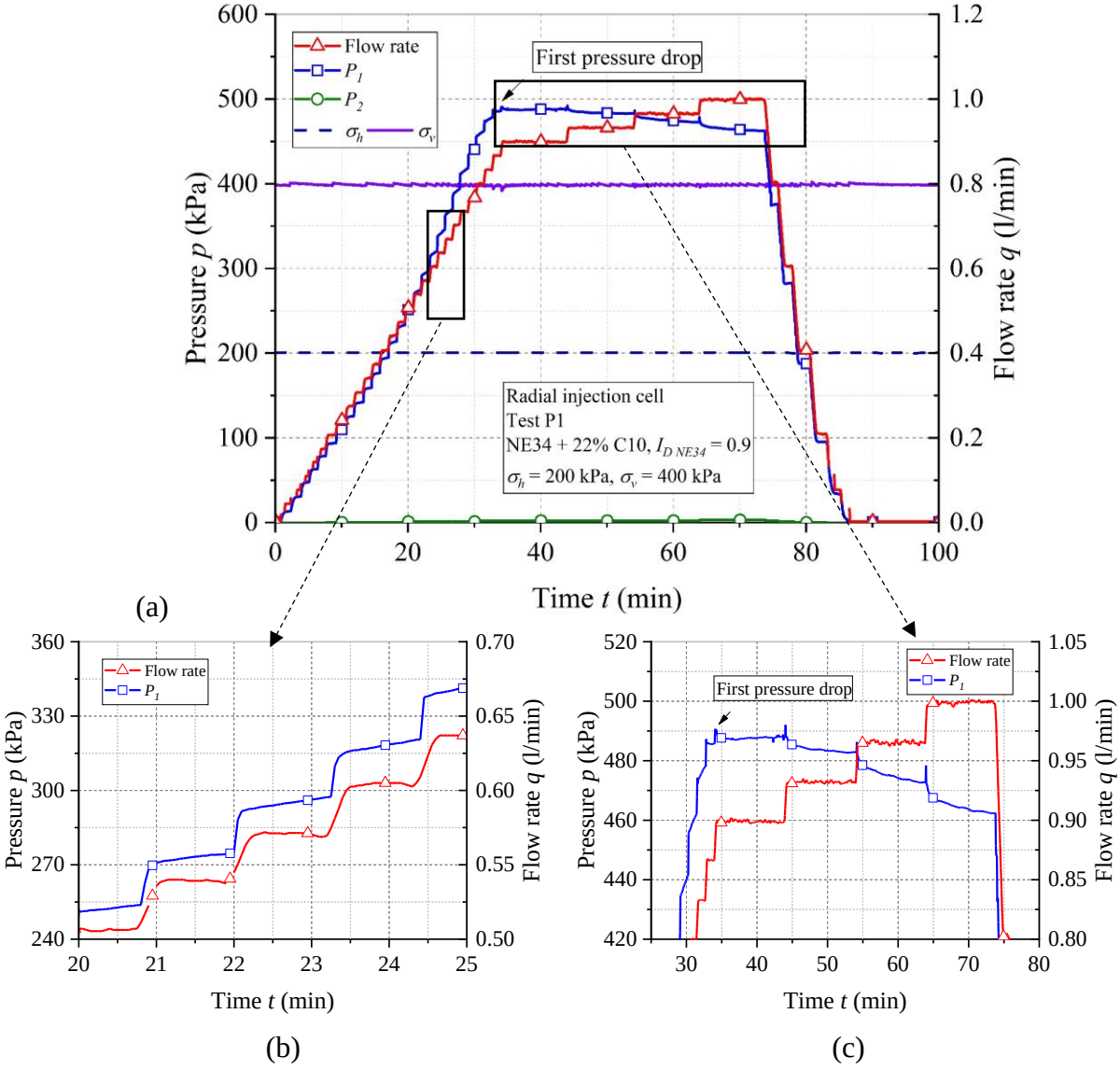

Figure 3.6: Test P1 - (a) evolution of pressure and flow rate versus time during water injection phase; (b) zoom between 20 to 25 minutes showing the injection pressure during matrix regime; (c) zoom between 30 to 80 minutes showing significant pressure drops during fracturing regime.

Due to internal erosion, the overall permeability of the specimen decreases from an initial value k_{int} of 82.8 to 66.6 mD at the end of matrix injection regime ($k_{end,m}$). It was then increased to 87.4 mD after fracturing. Comparing the permeability at the end of the matrix regime $k_{end,m}$ and at the end of the test k_{unload} permits to assess that the gain of permeability due to fracturing is of 31%

It should be noted that we must account for the hydraulic head loss caused by the drainage system. This head loss was determined by performing a calibration test without the specimen. The detail of this calibration is given in Appendix C.

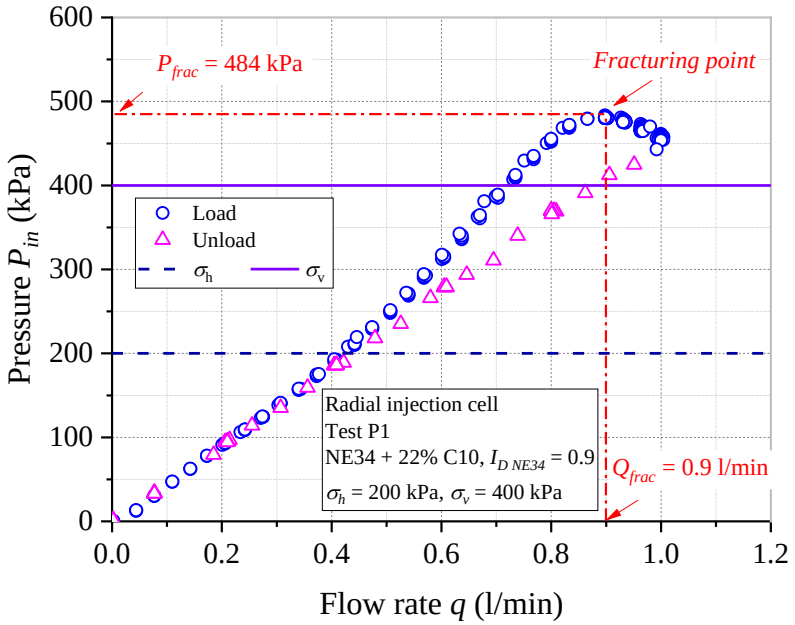

Figure 3.7: Evolution of the injection pressure versus flow rate (Test P1).

3.4.1.2 *Colored gel injection*

Figure 3.8a presents the results obtained during the colored gel injection phase. Before injecting the mixture of MasterRoc MP320 gel and 0.2 % Basacid Blue, two flow rate-hold steps were performed at 0.2 l/min and 0.5 l/min to validate the increase of the overall permeability after fracturing. The colored gel mixture was injected at a flow rate of 0.47 l/min for approximatively 20s. The maximum pressure reached was 420 kPa, which is smaller than the value obtained during the fracturing phase (484 kPa) (Figure 3.8b), ensuring that this phase did not further extend the fracture.

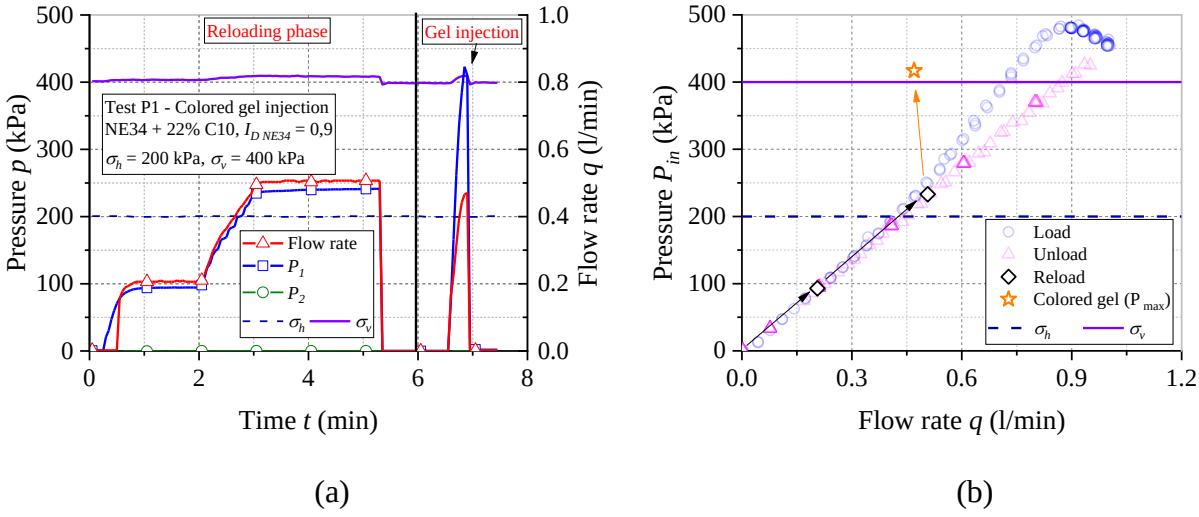

Figure 3.8: Colored gel injection (Test P1): (a) pressure – flow rate – time curves; (b) pressure versus flow rate.

3.4.1.3 *Disassembling phase*

After the specimen was solidified by the colored gel, the applied stresses were released and the mold was reinstalled to protect the specimen. Then, the latter was transported to X-ray CT for scanning. Once the scan had been finished, the second step of disassembling was performed which consists of a horizontal excavation of the specimen. In addition, a small part of the specimen containing the fracture was observed by optical microscopy in order to characterize the microstructure of fracture at the grain scale.

❖ *X-ray CT observations*

The specimen was imaged before injection (Scan 1) and after fracturing (Scan 2). Figure 3.9 presents a view of X-ray CT scanning of specimen P1. The voxels were cubic with a size of 29 µm. The 3D images are reconstructed using X-Act software (RX-Solutions, Chavanod, France). During specimen preparation, some glass balls were glued to the lower plate as the reference points, allowing to orient the scanned images in initial and post-fracturing states at the same position (Figure 3.10). Some typical horizontal slides of the X-ray CT images are presented in Figure 3.11. Compared to the initial state (Scan 1), the scanning images of the fractured specimen (Scan 2) showed some darker bands developed around the injection tube which represent the localized fractures.

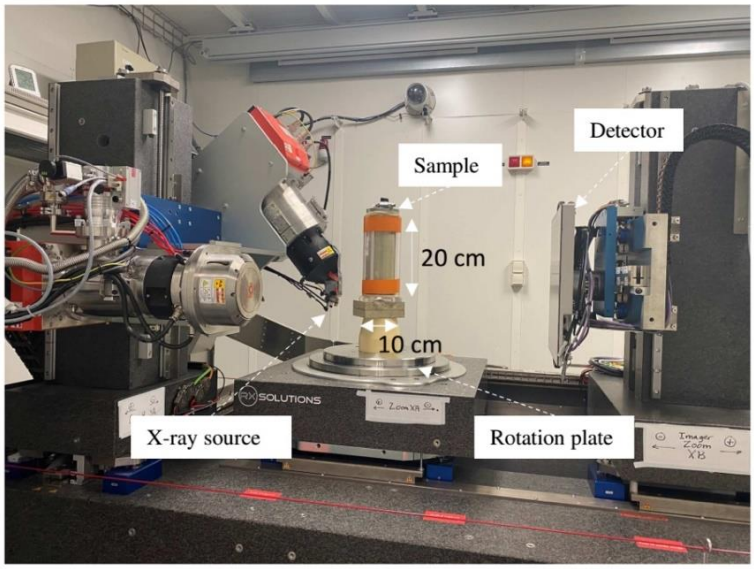

Figure 3.9: View of X-Ray CT of scanning specimen P1.

In order to visualize the 3D shape of the fracture, image processing was applied in the X-ray CT images which is quite similar to the validation test presented in Section 2.2.2.4 . Firstly, the filtering was applied to reduce the noise of the images while keeping the contours between different phases. Then, thresholding was performed to obtain the binary image that distinguishes between the fracture and the surrounding medium. Finally, the volume rendering was made to display a three-dimensional (3D) view of the fracture along the tube by using the ImageJ 3D Viewer plugin. As the fracture was identified only close to the injection tube, this

process was carried out on a volume extracted at the middle of the specimen (Figure 3.11e), which is delimited by the dashed window presented in Figure 3.11d. The treatment is applied to a typical section from H = 10 to H = 12 cm.

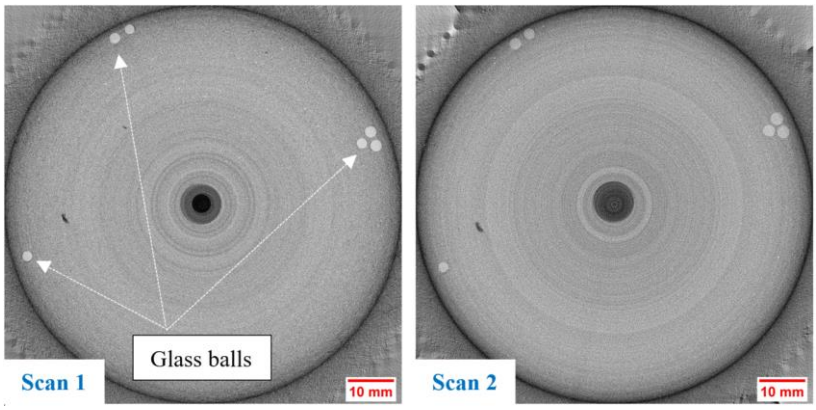

(a) (b)

Figure 3.10: Glass balls glued to the lower plate: (a) scan 1 of specimen P1; (b) scan 2 of specimen P1.

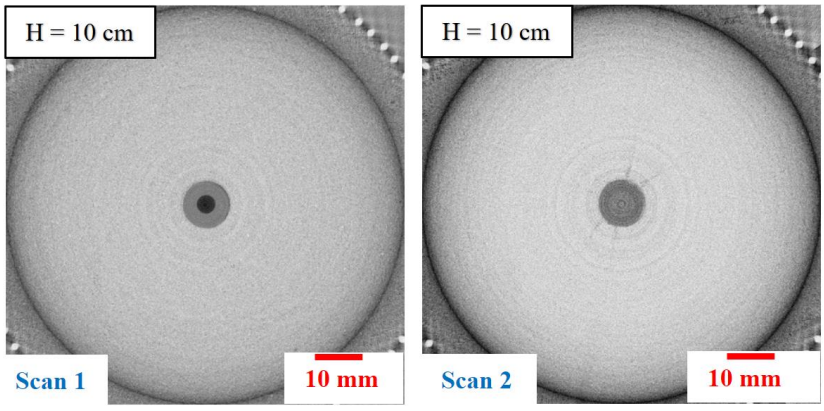

(a) (b)

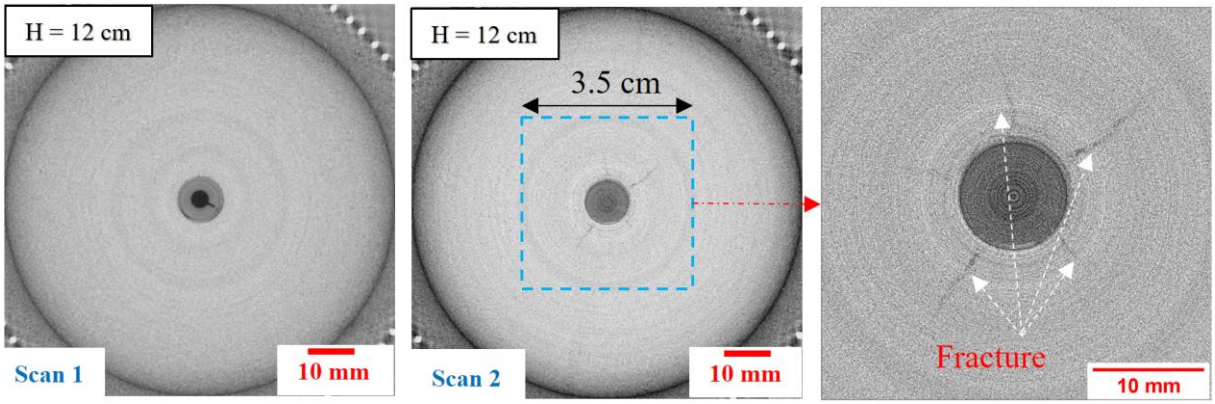

(c) (d) (e)

Figure 3.11: Typical X-Ray CT images of specimen P1 at different heights: (a), (b) at H = 10 cm; (c), (d) at H = 12 cm; (e) magnified zone containing the fractures over which the image treatment process will be applied. Voxel size: 29 µm.

Figure 3.12 shows a typical section after applying the median filter using a radius of 2 pixels. Using FIJI, the profile of the grey level before and after filtering over a typical line can be plotted (Figure 3.12c). It is observed that the fluctuation of the grey value was significantly reduced after filtering.

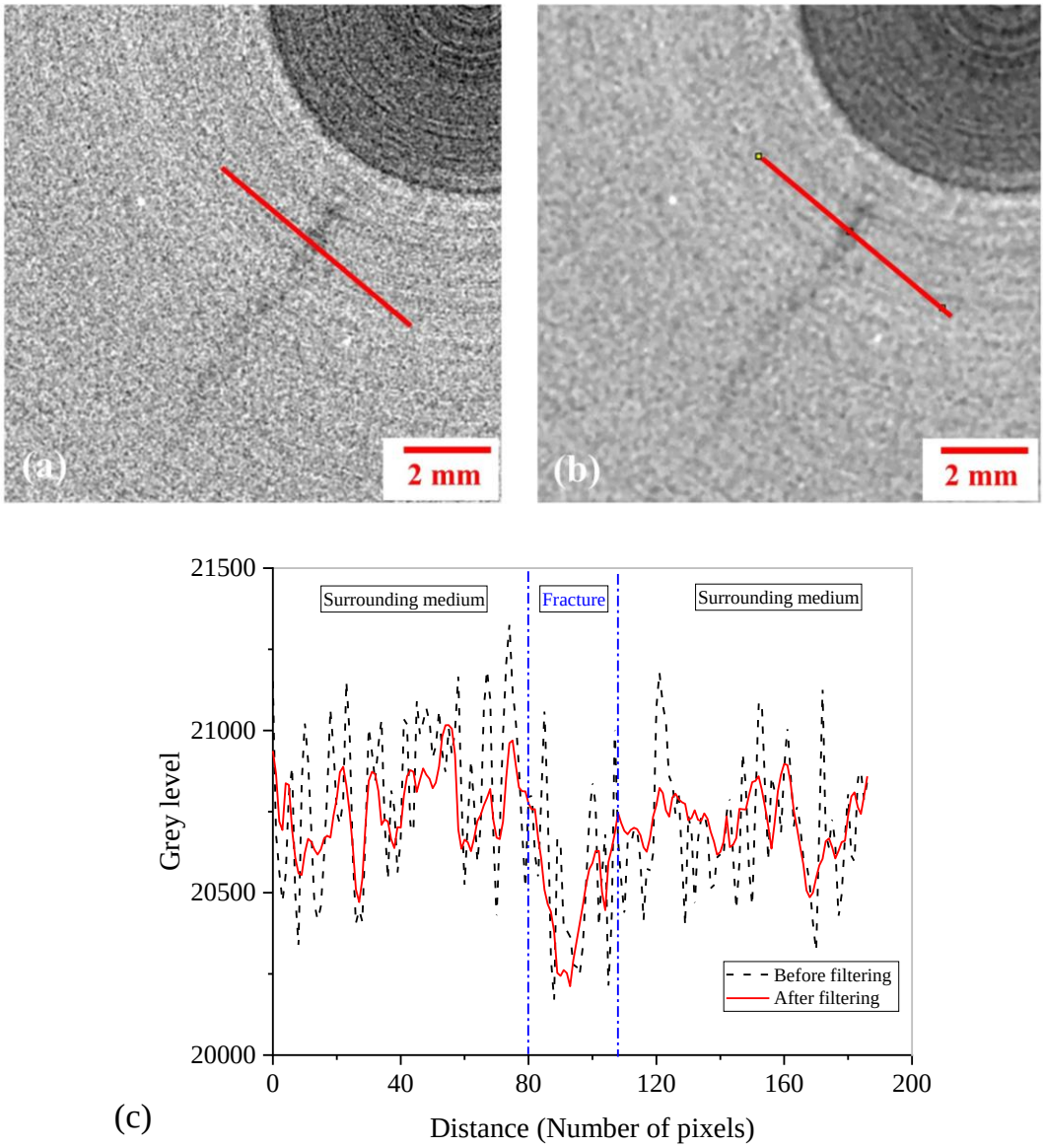

Figure 3.12: Filtering step (specimen P1): (a) typical section taken from the raw image at H = 12 cm; (b) filtered image using median filter of 2 voxels; (c) grey value profiles over the red line before and after filtering.

Figure 3.13 presents the filtered image of the original one shown in Figure 3.11e. As the grey level of the localized fracture zone was very close to the one of the surrounding medium, the choice of grey value threshold used was quite challenging. By testing different values and visualizing the corresponding fracture shape, we selected a grey value of 20440 as the threshold level for the preliminary segmentation. White voxels represent the injection tube and the

localized fracture, whereas the black voxels correspond to surrounding medium (Figure 3.13c). However, due to O-ring artefact of images reconstruction, the white points cannot be removed by thresholding, which introduces some noise around the fracture (Figure 3.14). To limit this effect, a second filtering was applied with the median filter of 2 voxels. This step may reduce the fracture size but gives a better view of the fracture shape (Figure 3.15). Multiple small fractures were observed in several directions around the injection tube which can be related to the pressure drops during the water injection phase.

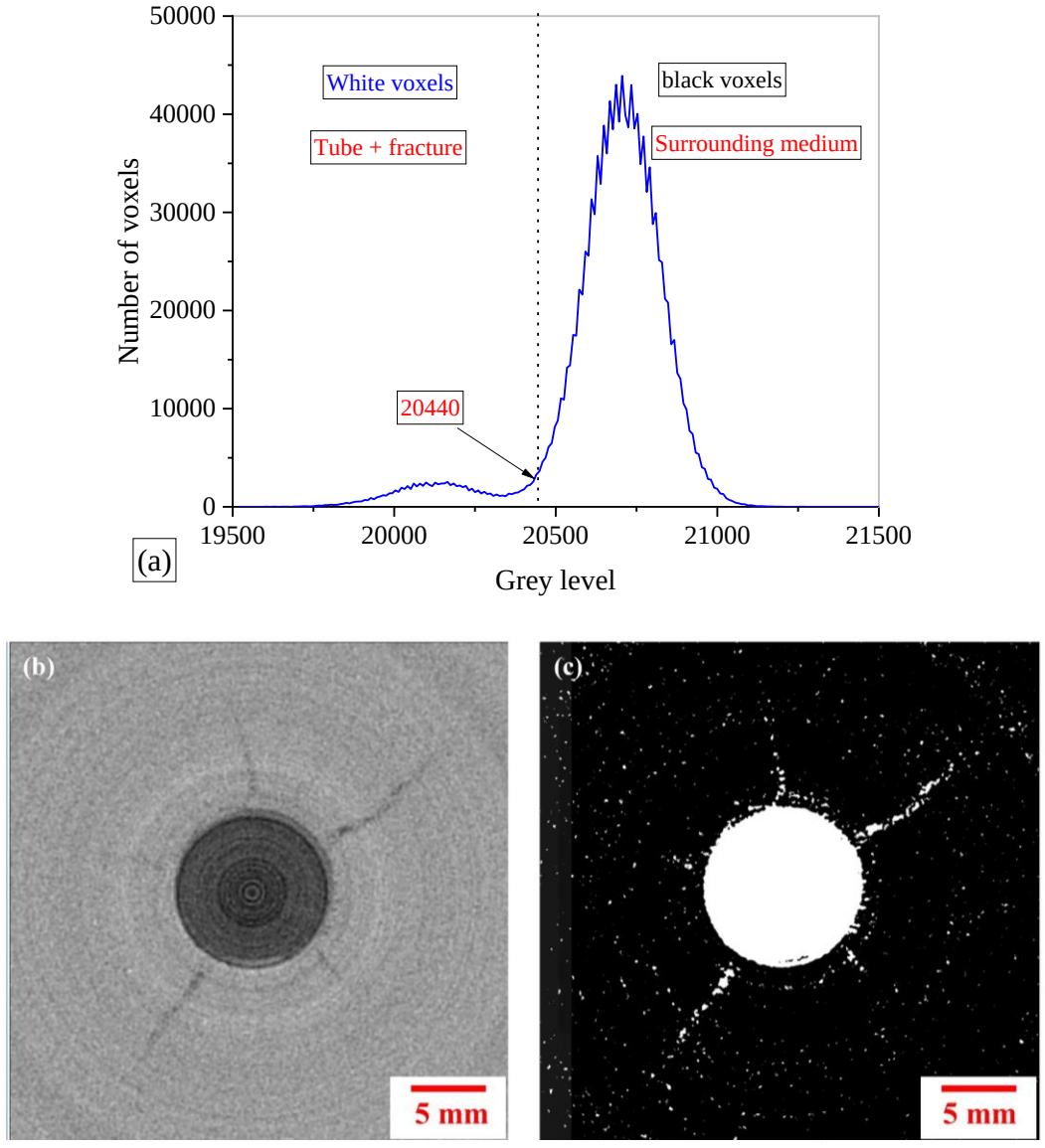

Figure 3.13: Thresholding of the image (specimen P1): (a), (b) filtered image and its associated histogram; (c) binary image after thresholding

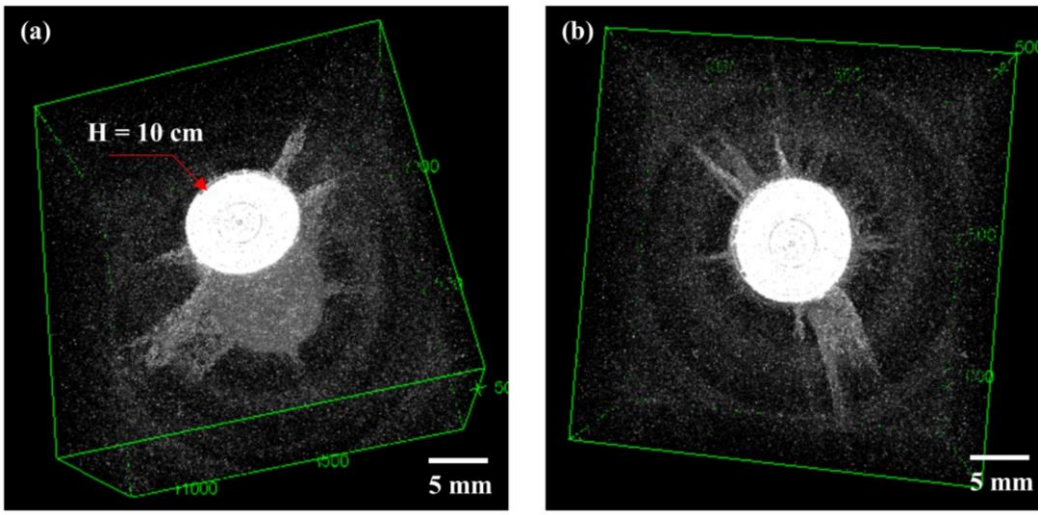

Figure 3.14 : 3D views of fractures developed along the injection tube from H = 10 to H = 12 cm (specimen P1).

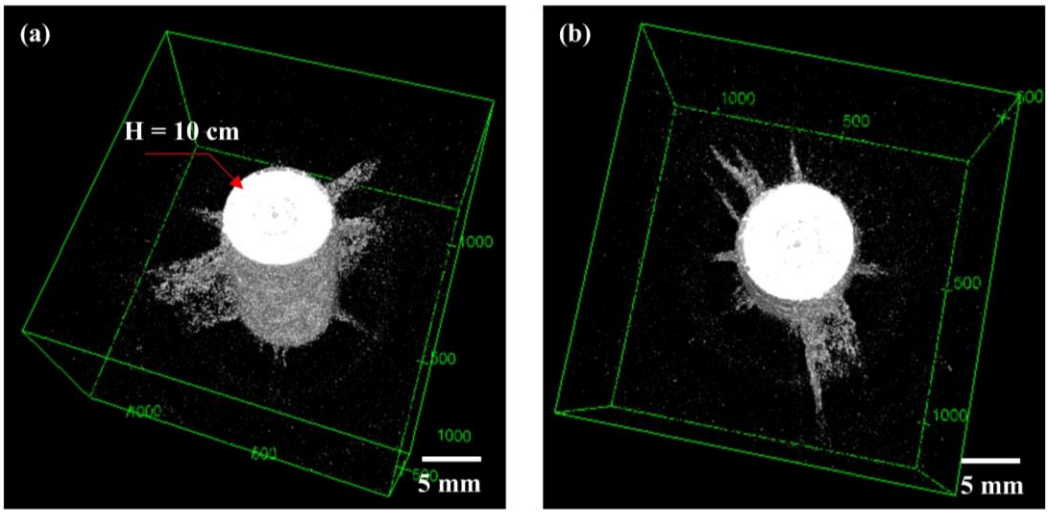

Figure 3.15: The images after the second filtering with the median filter of 2 voxels (specimen P1).

❖ *Horizontal excavation and additional optical microscope observation.*

Figure 3.16 presents a schematic presentation of excavating process from top to bottom of the specimen. A camera was placed above the specimen, allowing photos to be taken every 5 mm of excavation (Figure 3.16b). Some typical photos of the specimen during excavating are presented in Figure 3.17. Small fractures were observed along the injection tube (darker blue). The length of these fractures varies from a few millimeters up to one centimeter. The fractures observed during excavation coincide well with those observed by X-ray CT images (Figure 3.17c,d).

Moreover, in order to identify the change of the granular structure, a typical horizontal cross-section was observed using optical microscopy Leica M80 (Figure 3.18). Figure 3.19 presents the observations of different zones. The localized fracture is clearly identified with a darker blue (Figure 3.19b).

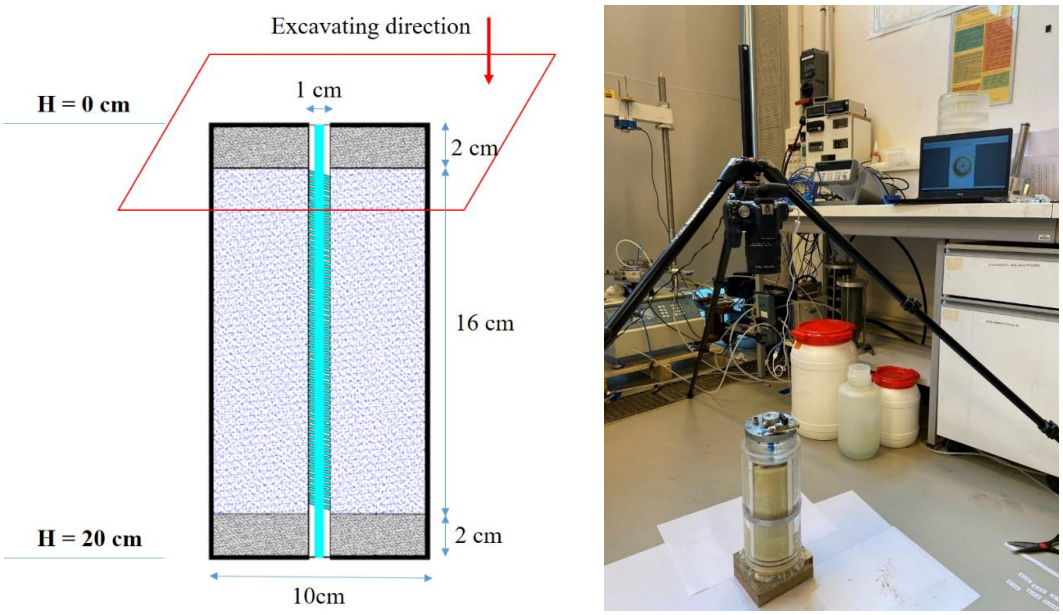

Figure 3.16: Excavating process: (a) schematic representation of excavation; (b) installation of the camera (Specimen P1).

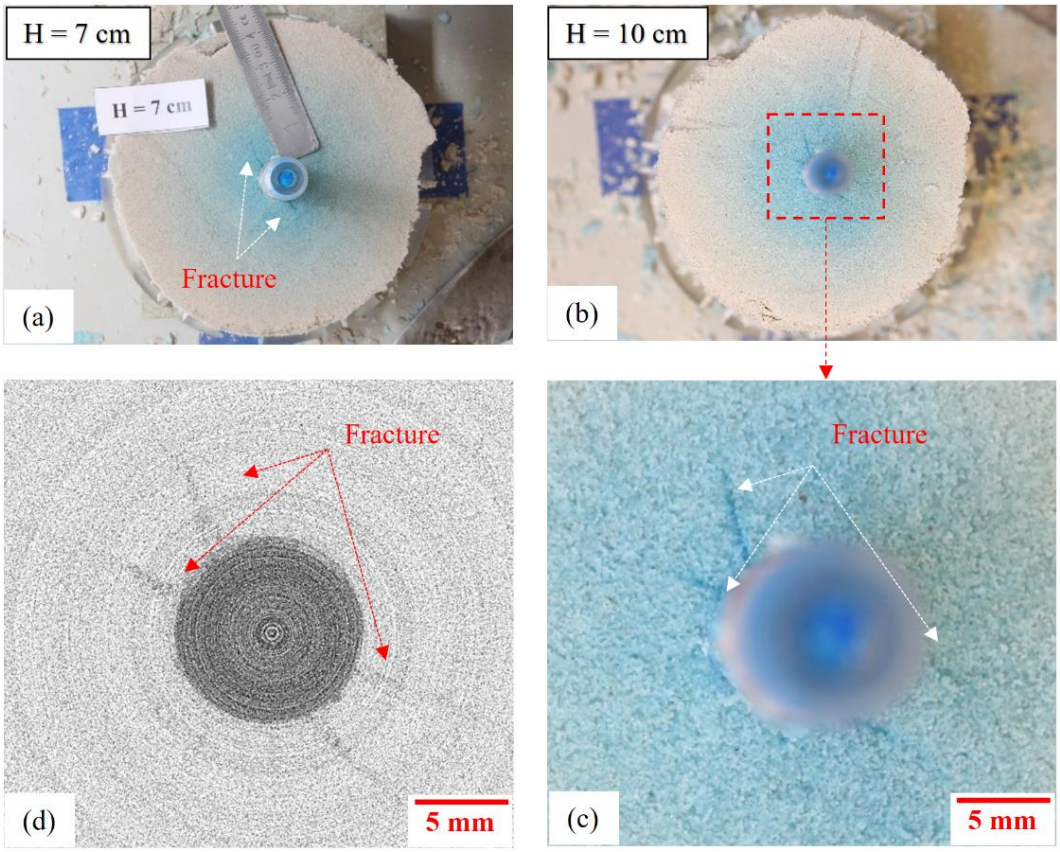

Figure 3.17: Photos of the horizontal cross-sections corresponding to different depths of excavation (specimen P1): (a) at H = 7 cm; (b) at H = 10 cm; (c) magnified zone around the tube at H = 10 cm and (d) its observation from X-ray CT.

As the MasterRoc MP320 silica gel is a transparent gel with nano-particle size between 7 and 22 nm, it allows to observe the sand structure inside the gel. We can clearly observe that the fracture presents fewer C10 fine particles and more porous space as compared to the surrounding medium (Figure 3.19c&d). A higher porosity of these fractures confirms results in terms of overall permeability increase. The fracturing mechanisms will be discussed later in Section 3.5.1.4 of the typical injection test in the injection chamber.

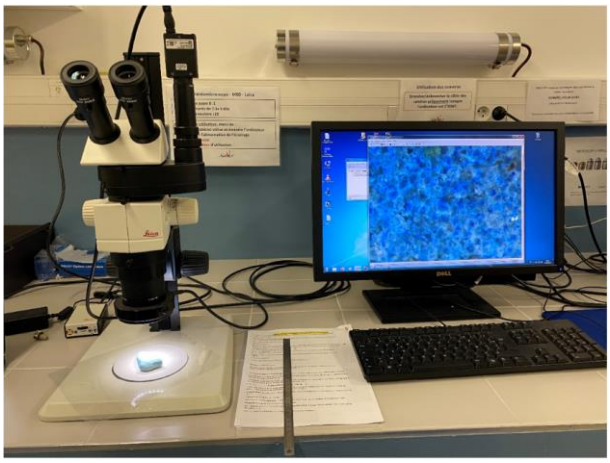

Figure 3.18: Optical microscopy Leica M80

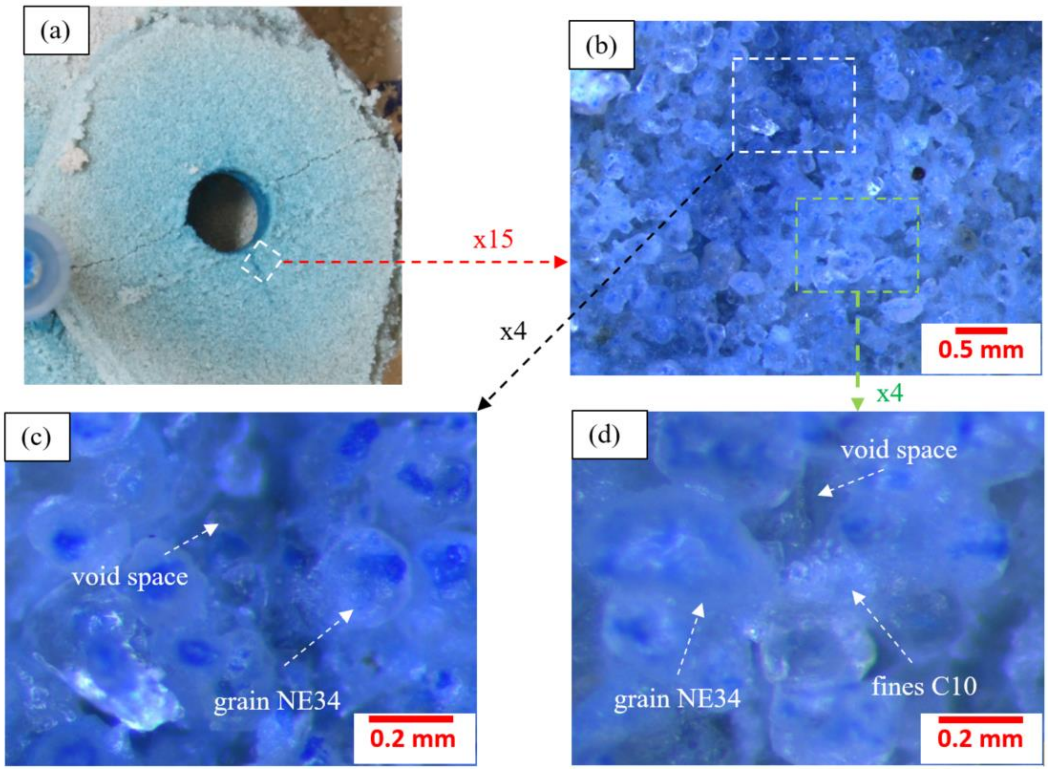

Figure 3.19: Test P1 - Optical microscope observation of a typical transversal cross-section at different zones (specimen P1): (a) a typical cross-section of the specimen; (b) magnified zone containing the fracture; (c) magnified zone inside the fracture; (d) magnified zone at the surrounding medium.

3.4.2 Parametric study

3.4.2.1 *Test repeatability and influence of flow rate during the fracturing regime.*

Test P7 was performed under the same characteristics as the reference test P1. The injection protocol was also similar during the matrix regime with the incremental increase of the flow rates by steps of 0.033 l/min. However, during the fracturing regime, test P7 was carried out with 6 steps, instead of 4 steps as for the reference test P1, to study the impact of flow rate on the fracturing propagation within the specimen. During the PWRI operations, this is one of the most important parameters that the reservoir engineers can control for maintaining injectivity (Ochi et al., 2014). On the other hand, the matrix regime phase of this test allows to evaluate the repeatability of the test in the radial injection cell in terms of the critical fracturing pressure. The detailed results of test P7 are presented in Figure 3.20. The first pressure drop has been identified at a flow rate Q_{frac} of 0.85 l/min (Figure 3.20b) and the corresponding fracturing pressure P_{frac} is 462 kPa (2.3 σ_h). This pressure is about 5% smaller than the critical value obtained for the reference test P1, confirming a very good test repeatability in the radial injection cell.

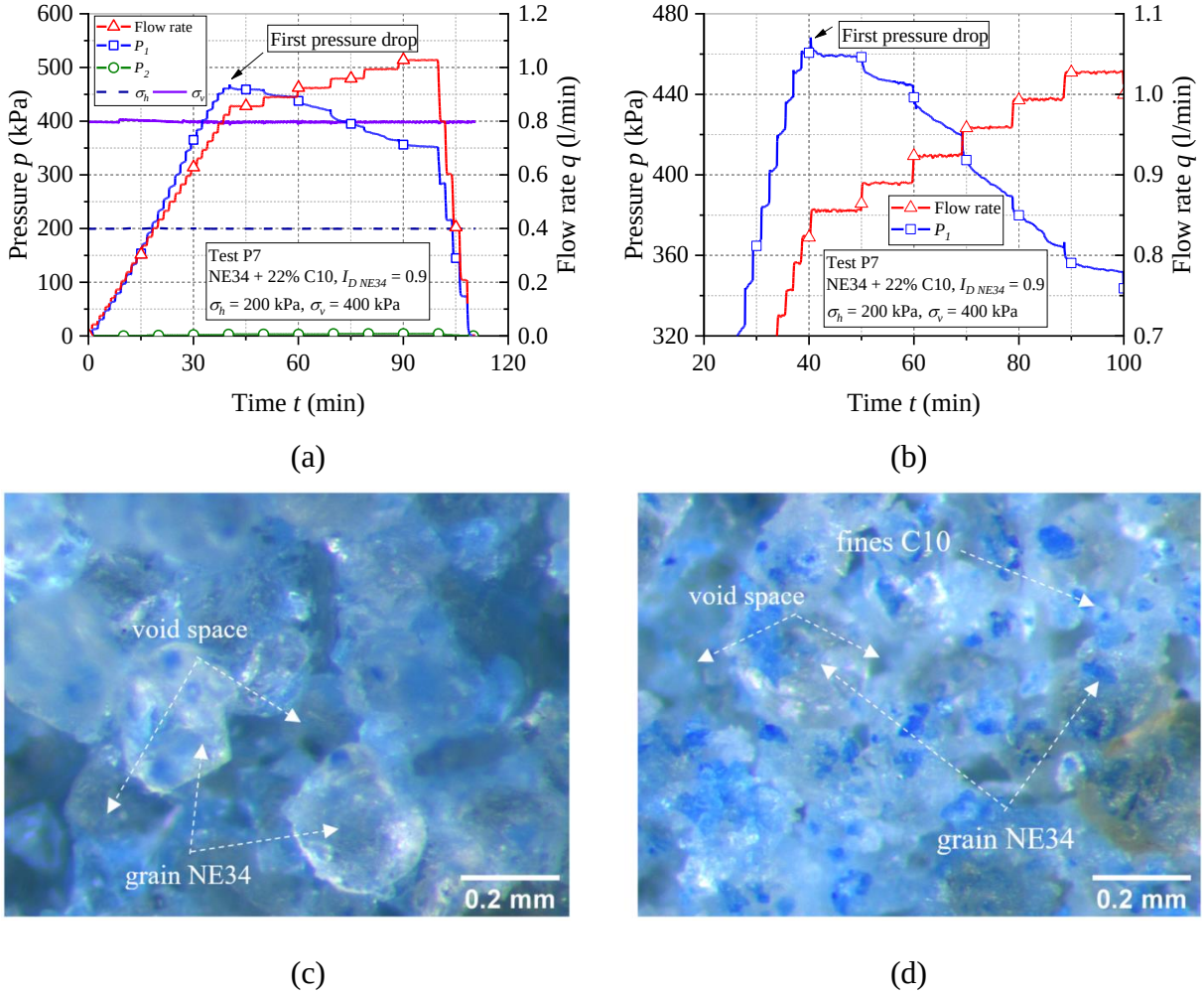

Figure 3.20: Test P7: (a),(b) pressure - flow rate - time curves; (c) magnified zone inside the fracture; (d) magnified zone in the surrounding medium.

Figure 3.21 presents a comparison between tests P1 and P7. A fairly good consistency in terms of pressure – flow rate curve can be observed in the matrix flow regime (before the first pressure drop) (Figure 3.21a). In the fracturing regime, we can observe that increasing further the flow rate results in further propagation and enlargement of the fracture (Figure 3.21c&d). This observation is in accordance with a higher increase of the overall permeability of test P7 as compared to P1 (Figure 3.21b).

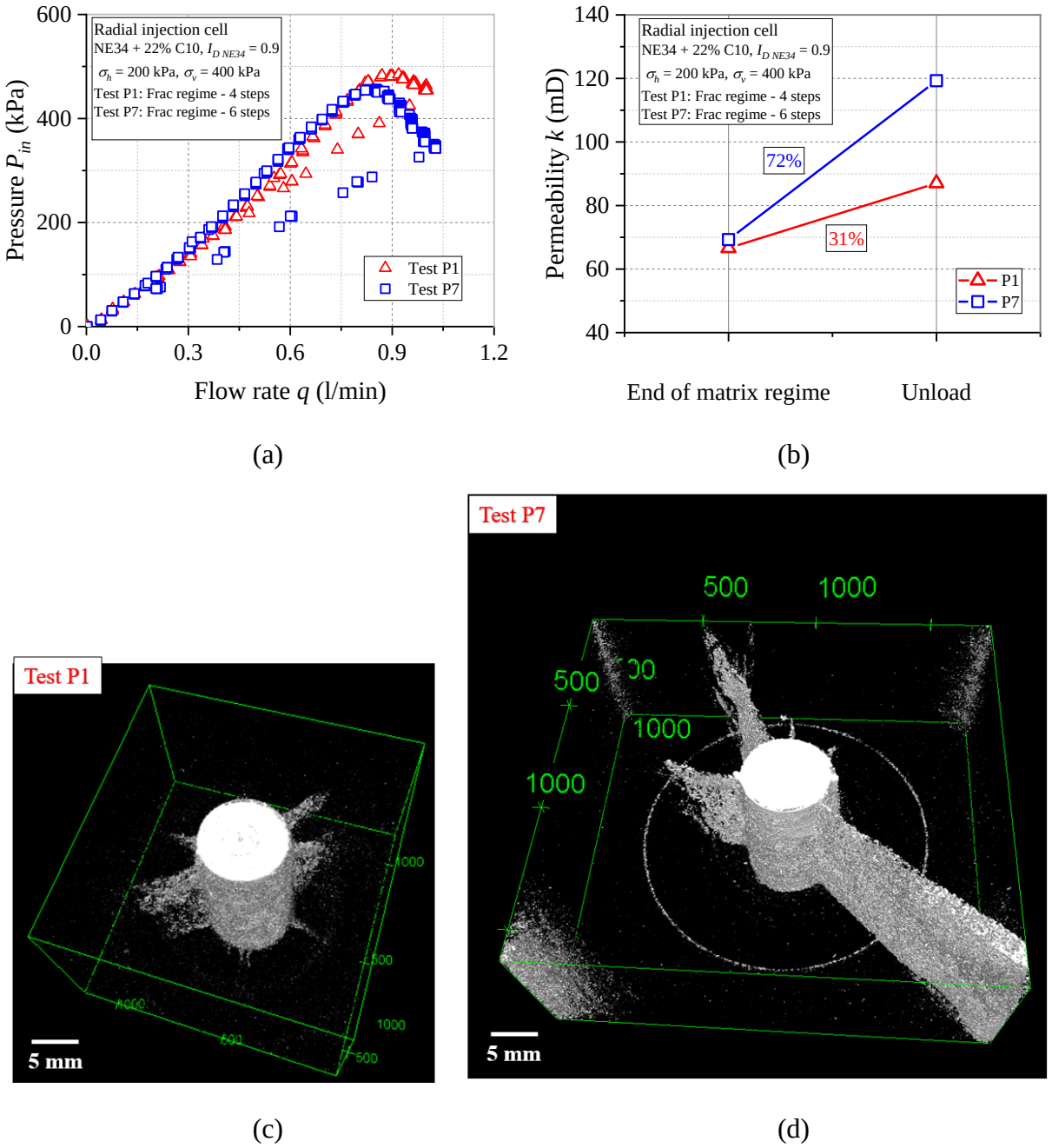

Figure 3.21: Effect of the flow rate: (a) pressure vs flow rate curves; (b) increase of the overall permeability; (c) and (d) 3D views of the fracturation pattern developed along the injection tube from H = 10 to H = 12 cm for test P1 and P7, respectively.

We conclude that, for the radial injection cell, the injection of 4 steps in the fracturing regime is a suitable protocol when performing the parametric study in this setup to avoid the boundary effect as observed in specimen P7.

3.4.2.2 *Effect of stress conditions*

- *Effect of the confining pressure*

The confining pressure is one of the most important parameters controlling the fracturing process. To investigate this effect, six tests have been performed with different values of the confining pressure σ_h (120, 150, 200 and 350 kPa) and different stress ratios $K_0 = \sigma_h/\sigma_v$ (0.33, 0.4 and 0.5). The injection results are presented in Figure 3.22.

Figure 3.22a presents the injection results in the case of K_0 = 0.33. Tests P2 and P4 have been performed under the confining pressures of 150 kPa and 200 kPa respectively. We observe that a higher confining pressure results in a higher critical fracturing pressure. The first pressure drop P_{frac} in test P2 (σ_h = 150 kPa) is 360 kPa and 435 kPa in test P4 (σ_h = 200 kPa). However, the ratio of the fracturing pressure over the confining pressure is very close for both tests (2.4 for test P2 and 2.2 for test P4).

Figure 3.22b shows that a higher increase of the overall permeability is observed at lower confining pressure**.** As the specimen is manually compacted with the mixture of sand and fine particles, the initial overall permeability may be slightly different depending on the compaction process, the homogeneity of the mixture, the distribution of inter-granular porosity…

Similar results are obtained for K_0 = 0.4 (Figure 3.22c&d) and K_0 = 0.5 (Figure 3.22e&f)

During the disassembling phase of the experiment, test P2 with lower confining pressure presents longer fractures as compared to test P4 (Figure 3.23)

Figure 3.24 presents a synthesis of the normalized fracturing pressures (P_{frac}/σ_h) under different stress conditions. For the same stress ratio K_0, there is a decrease tendency for this normalized ratio, however, no definite conclusions can be drawn because of the limited number of tests and the reduced stress range. Futher tests under a higher stress condition should be performed to complement this conclusion. The mean value of this normalized ratio is 2.35 with the corresponding standard deviation of 0.1.

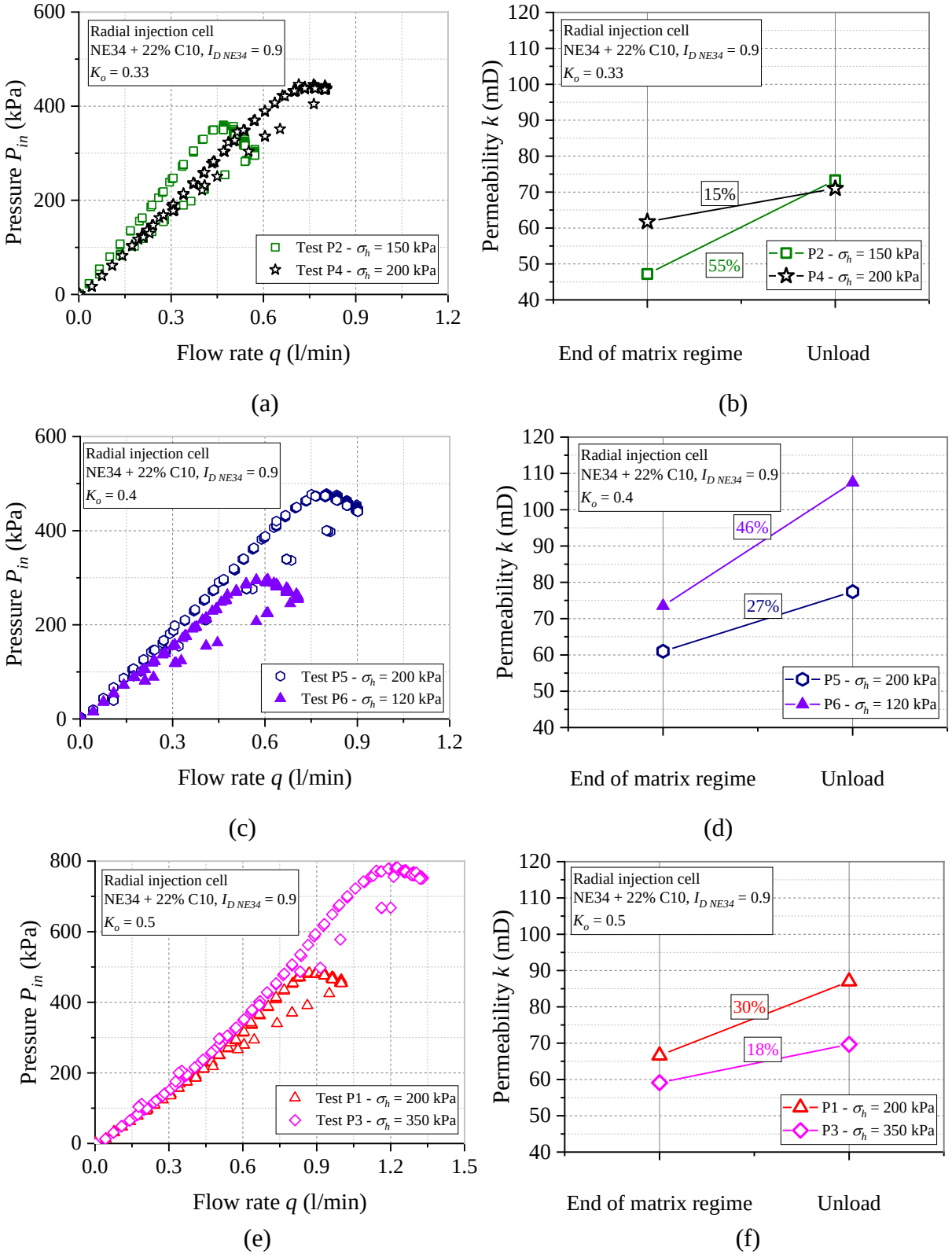

Figure 3.22: Effect of confining pressure on the pressure vs flow rate curves and the increase of the overall permeability for different values of K₀: (a), (b) K₀ = 0.33; (c), (d) K₀ = 0.4; (e), (f) K₀ = 0.5.

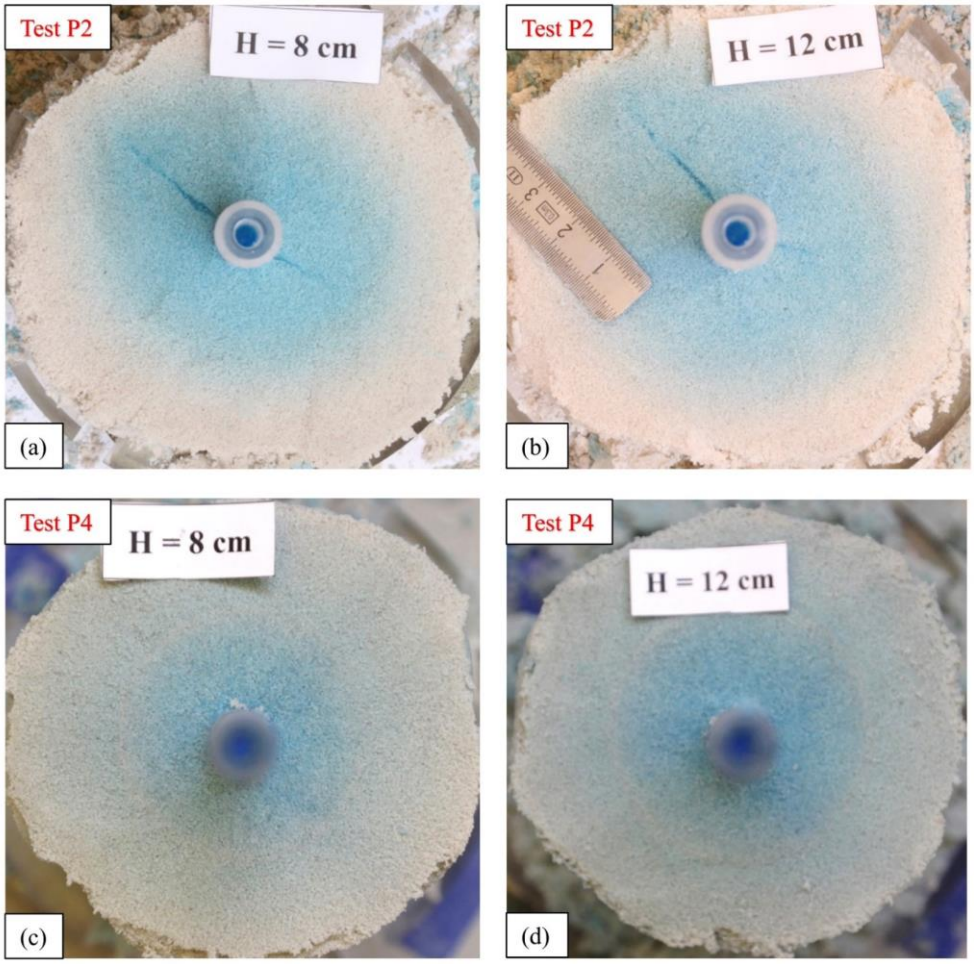

Figure 3.23: Photos of the horizontal cross-sections corresponding to different depths of excavation in the case of K_0 = 0.33 : (a), (b) test P2; (c), (d) test P4.

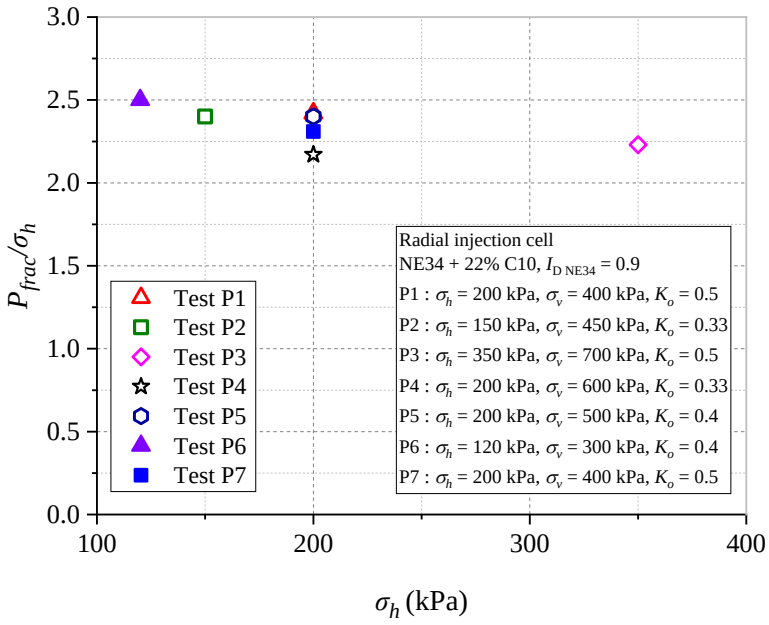

Figure 3.24: Effect of the confining pressure on the normalized fracturing pressure (P_{frac}/σ_h).

❖ *Stress ratio coefficient K_0*

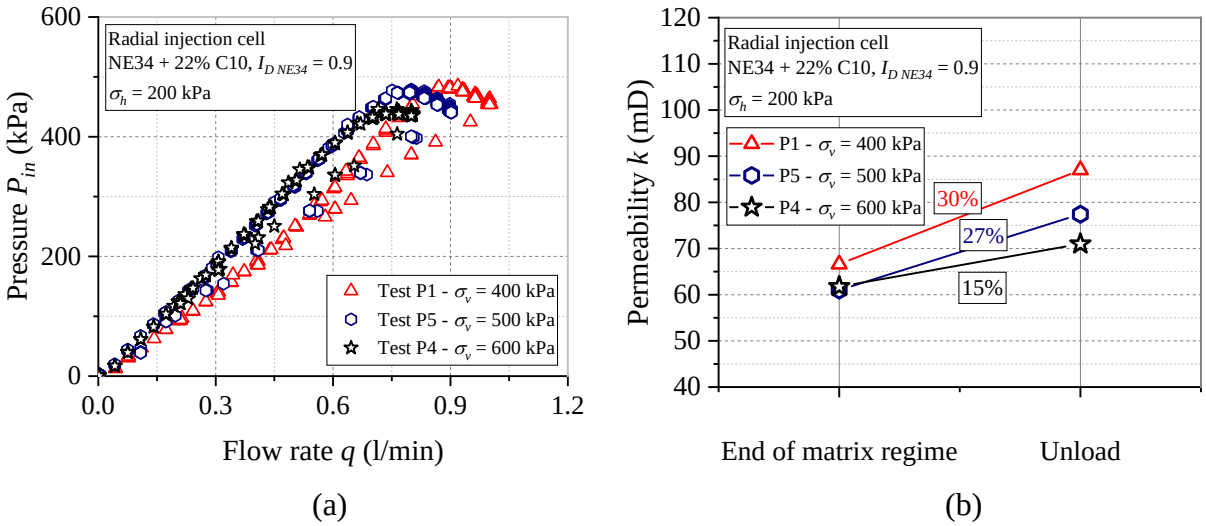

Figure 3.25: Effect of the stress ratio coefficient K_0 on: (a) the pressure vs flow rate curves; (b) the increase of the overall permeability in the different cases.

To investigate the effect of K_0 on the fracturing process, three tests with different values of the axial stress values σ_v (400, 500 and 600 kPa) while keeping the same confining pressure constant (σ_h =200 kPa) have been performed. The results are shown in Figure 3.25, and show that the stress ratio coefficient has a negligible effect on the fracturing pressure P_{frac}. A slight difference of this ratio is within the repeatability of the test. Test P4 with a higher axial stress presents the smallest fracturing pressure and increase of the overall permeability.

❖ *Effect of stress conditions on suffusion during matrix regime.*

As mentioned in the validation test Q6 and the typical test P1, the gradual decrease of the overall permeability during the matrix regime is caused by the mitigation and the subsequent retention of fine particles at the pore throats. Marot and Benamar (2012) have presented in detail the process of detachment and transport of the fine particles within the porous network due to the seepage. The term “suffusion” is used to describe the above phenomenon, according to the consensus of several researchers and experts of various countries at a workshop on the topic of internal erosion in April 2005 in Aussois (France) (Fell and Fry, 2007). This terminology will be used in our work. According to Marot and Benamar (2012), when suffusion occurs, a fraction of detached particles can resettle or be filtered at the center of the porous network which leads to a local clogging of the specimen, and consequently, a decrease of the hydraulic conductivity. The dominant parameters that govern the suffusion process are the geometry of the porous medium (grain size distribution, grain angularity and fabric), the hydraulic criteria (hydraulic gradient, fluid velocity and drag forces) and the applied stress conditions. Lafleur et al. (1989) distinguished three main curves of the grain size distribution: linearly graded (1 and 2), gap graded (3) and internally unstable (4) in which the types (3) and (4) are susceptible to suffusion and induce an unavoidable decrease of the overall permeability (see Figure 3.26). In our work,

the grain size distribution of the specimen is likely in the fourth class (internally unstable) (see Section 2.2.1.1), which explains why the increase of the injection pressure (equivalent to the permeability decline) was observed during the matrix regime in almost all tests.

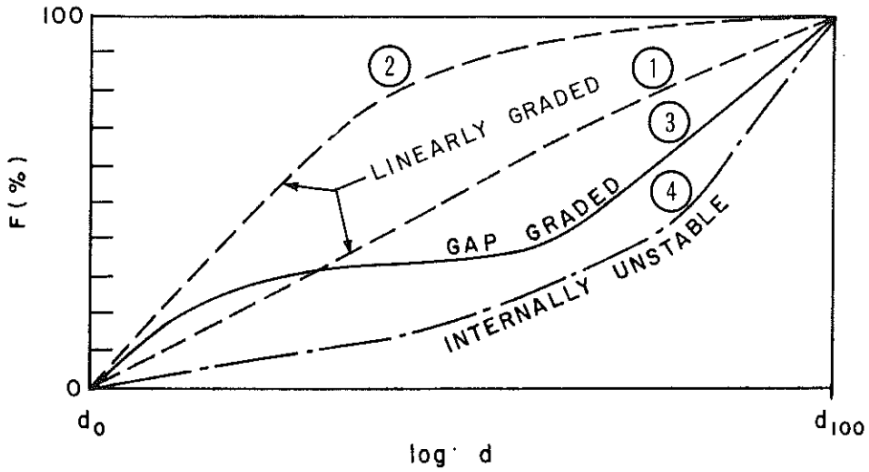

Figure 3.26: Different grain size distribution curves (Lafleur et al., 1989).

As one of the main types of internal erosion which cause the failures and the damage to embankment dams and dikes, suffusion has been widely studied in the literature (Bendahmane et al., 2008; Chang and Zhang, 2013; Skempton and Brogan, 1994). However, due to the complexity of the processes of detachment, transport and deposition of the particles, the prediction of suffusion initiation and development is difficult and strongly dependent on the granular structure studied (Bendahmane et al., 2008; Marot and Benamar, 2012). In this part, we investigate the effect of stress conditions on the erosion rate in the specimen of a mixture of sand and 22% of fine particles having a very dense structure (global porosity of 0.23) and a low permeability (in the range of 80 mD). As observed in the preliminary test Q6 (see Appendix B.4), a change of the stress conditions, within the range studied, does not affect the overall permeability of the specimen. However, it may affect the contact between fine particles and the sand skeleton at the grain scale. Figure 3.27 presents the evolution of the permeability during the tests in radial injection cell during the loading phase. The first stage with a continuous permeability decrease corresponds to the matrix regime, whereas the further increase of the permeability corresponds to the fracturing regime.

Based on the experimental results during the matrix regime, we observed that the confining pressure change does not have a significant impact on the erosion rate for the various values of the stress ratio coefficient K_0 imposed in the tests (0.33, 0.4 and 0.5) (Figure 3.27a,b,c). The effect of this parameter was also investigated in previous research. By performing tests with glass beads specimens, Tomlinson and Vaid (2000) have found that the confining pressure has only a minor effect on the internal erosion. Bendahmane et al. (2008) have carried out an experimental study on the specimen containing a mixture of Loire sand (D_{50} = 440 µm) and kaolinite clay. The authors concluded that an increase of the confining pressure results in a decrease of the erosion rate of the clay fraction. The authors explain that the increase of the confining pressure will increase the inter-granular contact bonds and improve resistance to

internal erosion. Similar results were obtained by Chang and Zhang (2013) on the effect of confining pressure on the critical hydraulic gradient to initiate suffusion in the specimen containing a mixture of gravel and sand. The higher the confining pressure, the higher the initiation hydraulic gradient. This is mainly because the porosity decreases as the confining pressure increase, and consequently, also the pores size. However, it should not be the case in our tests, because of the very dense structure of the sand pack.

On the other hand, at the same confining pressure of 200 kPa, we observe a higher permeability decrease for a higher value of the stress ratio K_0. This indicates that a higher axial stress leads to a stronger erosion rate.

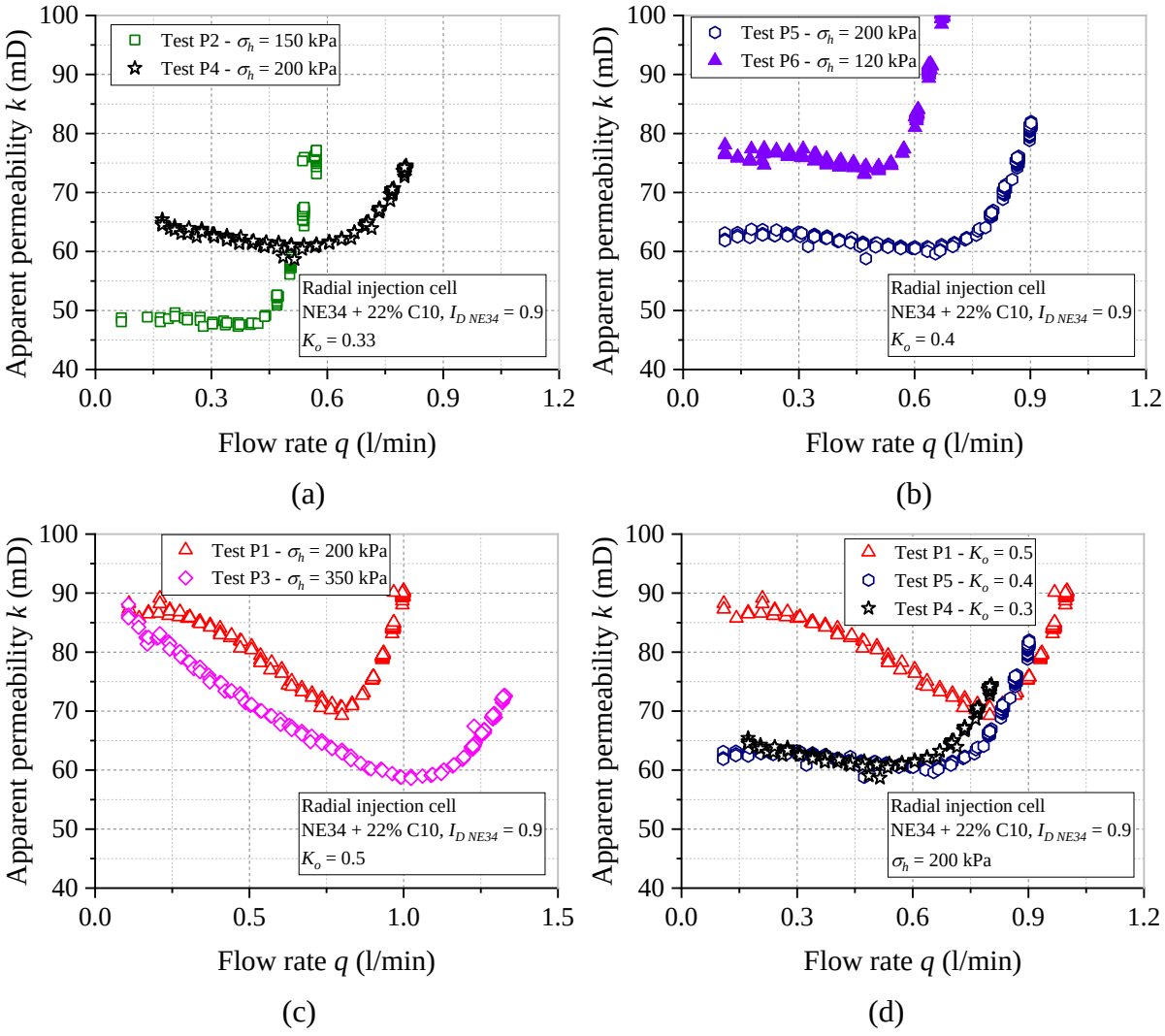

Figure 3.27: Effect of stress conditions on the erosion rate during the matrix regime.

3.4.2.3 *Effect of initial permeability*

Different scenarios of the extension and the nature of the clogged area due to PWRI can lead to different values of the permeability around the injection point. To investigate the effect of the permeability of the specimen, test P8 with a specimen containing only 19% of C10 fines (as compared to 22% for the reference test) was performed. The stress conditions are similar to

test P6 (σ_h = 120 kPa and σ_v = 300 kPa, K_0 = 0.4). The injection rate is gradually increased by a step of 0.066 l/min (instead of 0.033 l/min for the other tests with 22% C10), in order to have the same pressure steps in the specimen during each corresponding flow rate step. Figure 3.28a&b present the results in the matrix regime of tests P6 and P8, respectively. Each increase of the flow rate corresponds to an increase of about 20 kPa of the injection pressure for both tests. Figure 3.28c shows a comparison of the two tests in terms of pressure – flow rate curves. The critical fracturing pressures P_{frac} are very close (about 2.4 to 2.5 times the confining pressure). A higher increase of the permeability is observed in the case of lower concentration of C10 fines (higher initial permeability) (see Figure 3.28d). However, it should be noted that test P8 was performed with a higher increase of each flow rate step (to provide a similar increasing amplitude in the injection pressure) which may also contribute to a higher increase of the permeability. The observation of the fracture shape during excavation allows to confirm the change of the overall permeability during injection (Figure 3.29). Higher increase of the permeability after fracturing corresponds to longer and wider fractures.

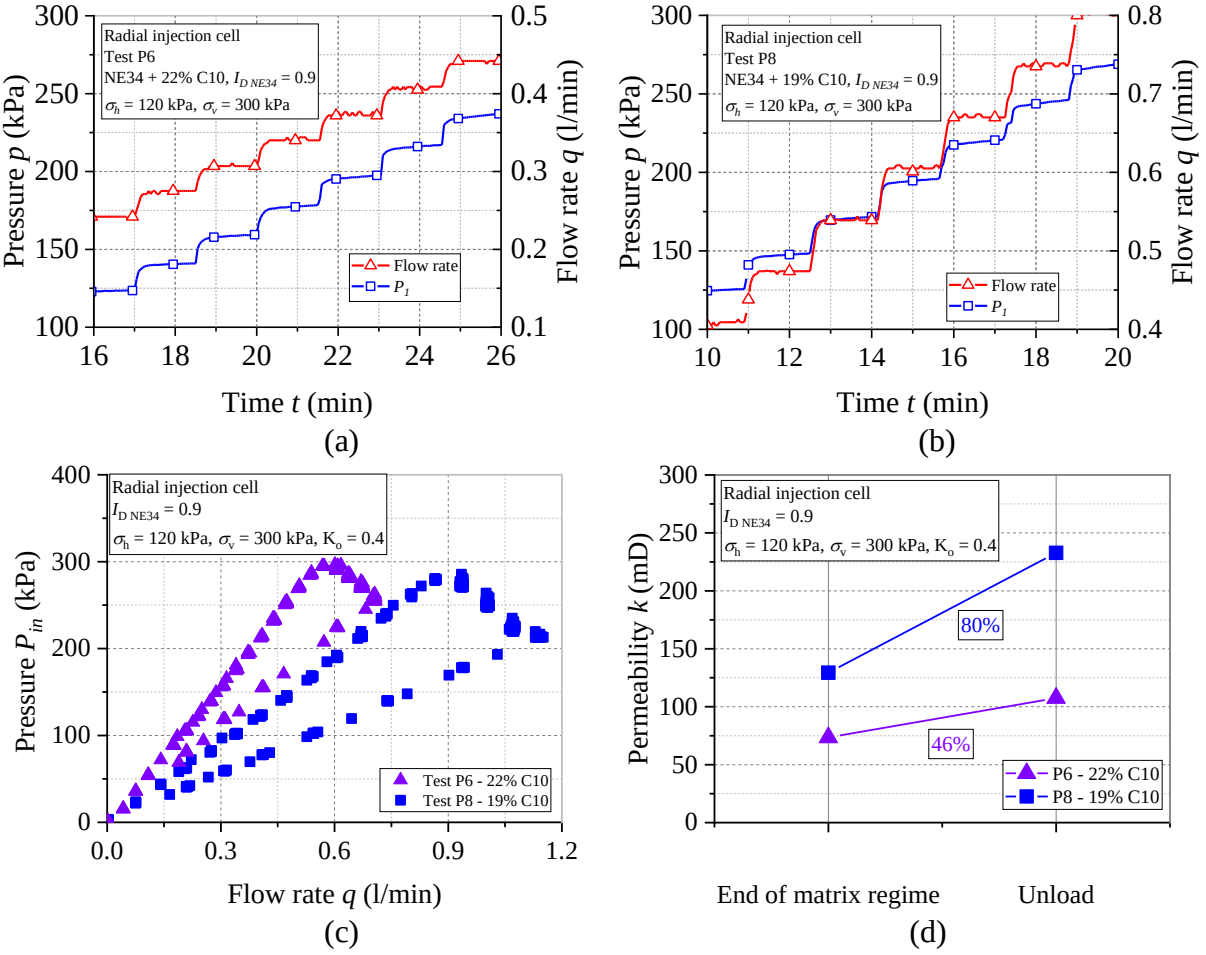

Figure 3.28: Effect of the initial permeability: (a), (b) pressure – flow rate – time curves during matrix regime of tests P6 and P8, respectively; (c) pressure vs flow rate curves; (d) increase of the overall permeability.

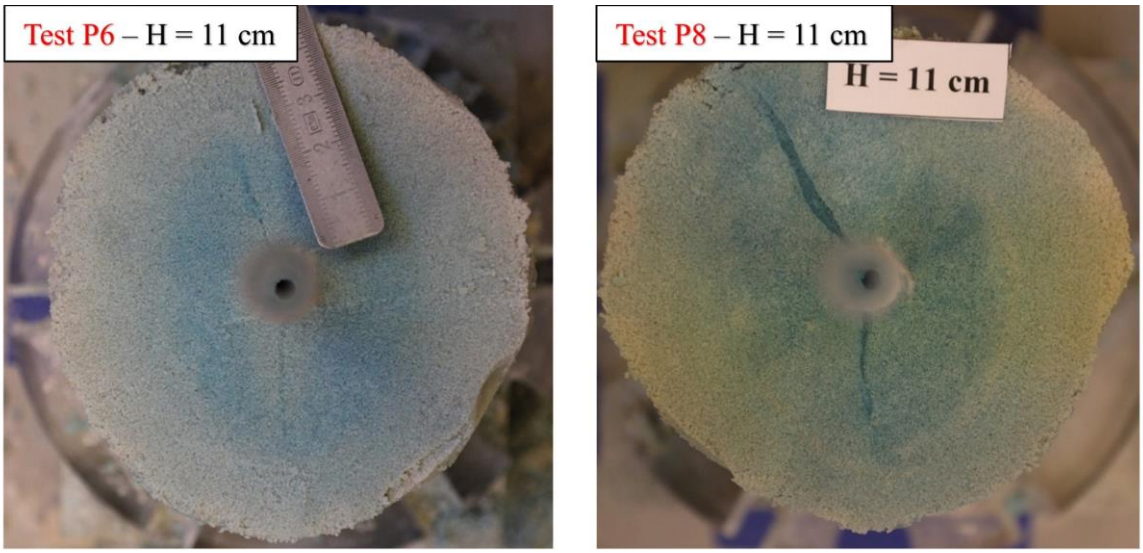

(a) (b)

Figure 3.29: Effect of the initial permeability on the fracture morphology: (a) specimen P6; (b) specimen P8.

3.4.3 Conclusion

Typical results in the radial injection cell have been described in detail (Test P1). During the water injection, we observed that fracturing occurs when the injection pressure exceeds about 2.4 times the confining pressure. After fracturing, the overall permeability of the specimen increases. During disassembly, the results show the effectiveness of the mixture of MasterRoc MP320 silica gel and Basacid Blue for performing post-mortem observations of the specimen. X-ray CT allows to obtain 3D images of the fractures formed along the injection tube and the fractures observed from X-ray CT coincide with those observed during excavation. These fractures are short with multiple small branches formed around the injection tube which can be associated with the pressure drops identified during the water injection phase. Furthermore, the scanning optical microscopy allows to identify the inter-granular structure of the fracture which contains fewer C10 fine particles and larger porous space compared to the surrounding medium which favors the injectivity surrounding the injection point.

The experimental results show that the magnitude of the confining stresses is an important factor affecting the fracturing pressure. The critical fracturing pressure is mainly controlled by the confining pressure (radial stress) and does not change significantly with the stress ratio K_0. An increase in confining pressure results in a higher critical fracturing pressure, shorter fractures as well as a smaller increase of the overall permeability. Fracturing occurs when the injection pressure reached about 2.35 times the confining pressure.

The flow rate has an important impact on the increase of the permeability and the propagation of the fracture in the fracturing regime. The study of permeability has shown no

significant effect on the critical fracturing pressure while changing the specimen initial permeability by changing the concentration of C10 fines.

Another phenomenon observed during these tests is suffusion of particles present in the specimen which results in a decrease of the permeability in the matrix regime. A higher axial stress (lower K_0) results in a lower rate of suffusion whereas the effect of confining pressure within the testing range is insignificant.

3.5 EXPERIMENTAL RESULTS IN THE RADIAL INJECTION CHAMBER

3.5.1 Typical test results

In this part, we present in detail the results of a typical test, called N33, performed in the radial injection chamber. First, the water injection phase and the colored gel injection are presented. Then, the observation of the sand pack during the horizontal excavation is shown. In addition, we present an analysis of the granular structure of some typical cylindrical samples containing fractures, using X-ray CT and optical microscope observations. Note that these observations have been performed on another test, called N32, which exhibits a similar fracture pattern as the typical test N33.

3.5.1.1 *Water injection phase*

The injection protocol used in the injection chamber is quite similar to the one used in the injection cell. During this phase, a loading-unloading cycle of the flow rate (i.e., increasing the flow rate to reach the fracturing regime, then decreasing it to zero) has been performed (Figure 3.30a). In the matrix regime, each step at constant injection rate was maintained for approximately 5 minutes. The choice of this time step allows satisfying some of the following criteria: reaching a quasi-steady-state condition of the injection pressure, minimizing the effect of suffusion (as observed in the validation test N29 presented in Appendix E.1) and permitting a suitable injection time as compared to the radial injection cell. This value is higher than in the protocol of the injection cell because of the larger dimension of the sand pack. Due to suffusion of C10 particles, a slight continuous increase in injection pressure was observed when imposing a constant flow rate (Figure 3.30b) in the matrix regime. At 4 l/min, the injection pressure was instantly stabilized at 510 kPa whereas the two previous steps at 3.6 and 3.8 l/min showed an increase in injection pressure (Figure 3.30c). This step seems to be a sign of the transition from the matrix to the fracturing regime. A decrease in the slope of the pressure – flow rate curve, instead of a continuous increase due to suffusion, is also observed from this transition point as shown in Figure 3.31. The definition of the transition point will facilitate the comparison of results between single and several injection phases that will be discussed later in Section 3.5.2.3 . The first pronounced pressure drop, denoted by P_{frac}, was 524 kPa (4.36 σ_h) at a flow rate, Q_{frac}, of 4.4 l/min. This point is identified as the fracturing point. The loading phase was continued with three more steps of 15 minutes at flow rates of 4.6, 4.8 and 5.0 l/min, then gradually decreased by steps of about 1.2 l/min until stop pumping.

Figure 3.31 presents the results in terms of injection pressure – flow rate curve which is similar to the results obtained in the radial injection cell (see Section 3.4.1). Due to suffusion, the overall permeability decreased from an initial value k_{int} of 92 mD to 80 mD until reaching a transition point of the injection regime at a flow rate of 4l/min. The last value is defined as the overall permeability at the end of the matrix regime, denoted $k_{end,\,m}$. The overall permeability during the unloading, denoted as k_{unload}, was about 106 mD which is 32% higher than $k_{end,\,m}$.

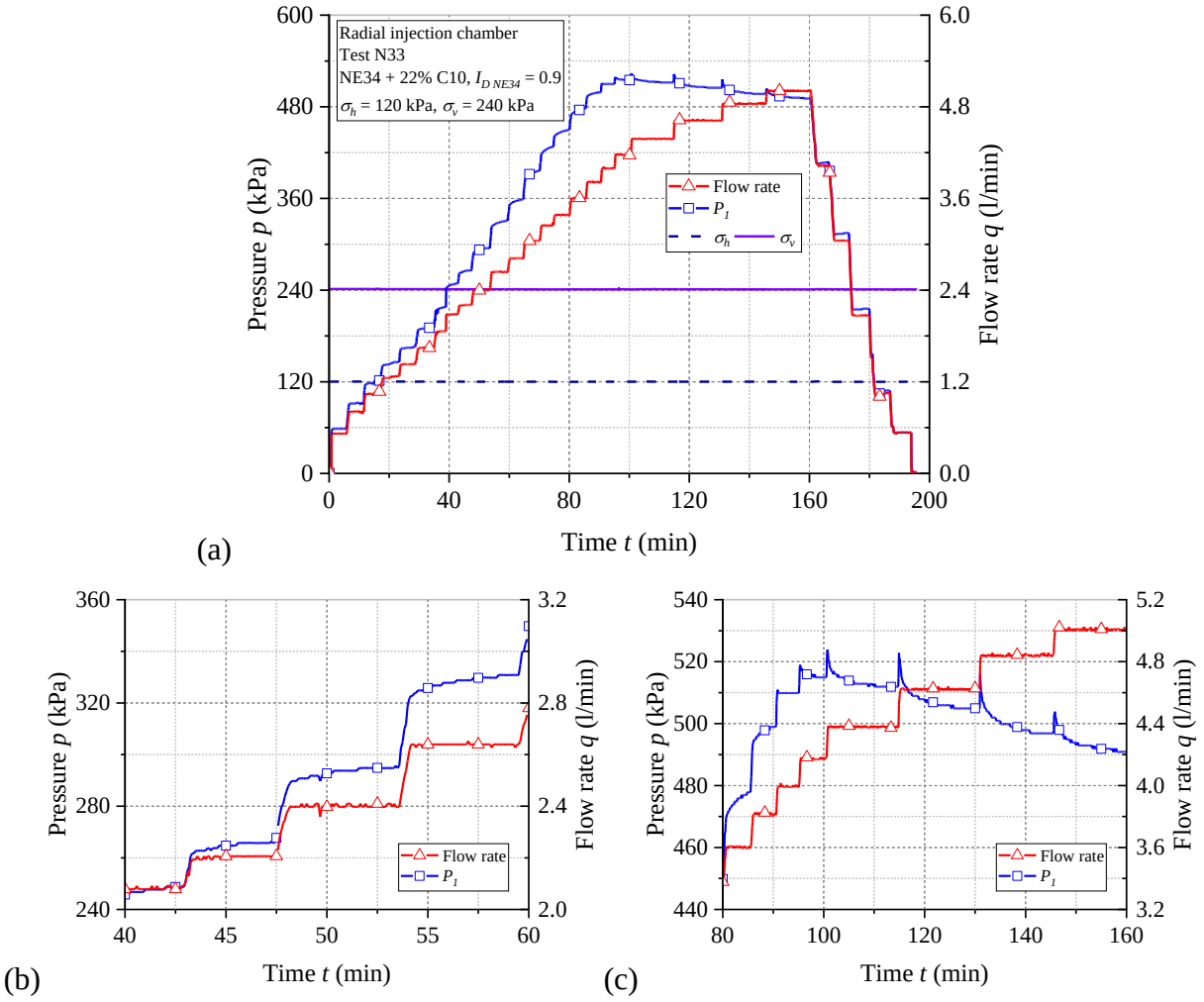

Figure 3.30: Results of typical test N33: (a) evolution of the injection pressure and flow rate versus time during water injection phase; (b) zoom between 40 to 60 minutes during the matrix regime; (c) zoom between 80 to 160 minutes showing significant pressure drops during the frac-regime.

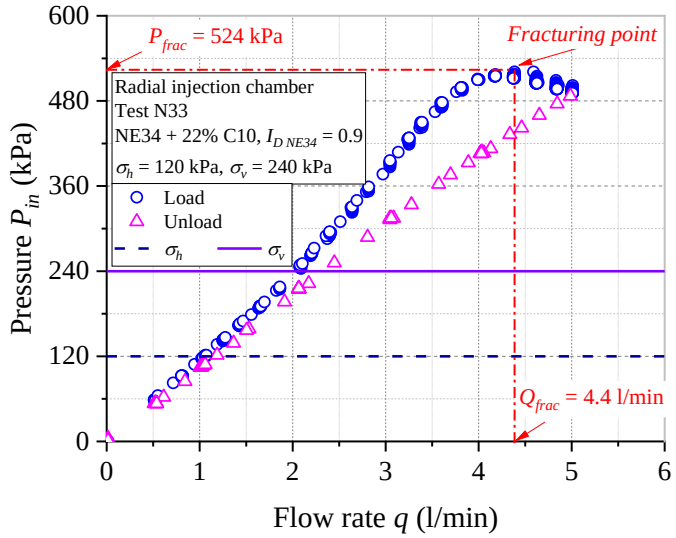

Figure 3.31: Test N33 - Evolution of injection pressure versus flow rate.

3.5.1.2 *Colored gel injection*

Similar to the tests in the radial injection cell, a small volume of mixture of MasterRoc MP320 gel + 0.2% Basacid Blue 762, corresponds to approximately 50 % of the void volume of the inner ring was injected. Figure 3.32 presents the test results of this phase. Before injecting the colored gel, two reloading steps were carried out at 2 l/min and 3.5 l/min to confirm the change in permeability after fracturing (Figure 3.32a). The reloading result matched with that of the unloading phase, showing a permanent increase of the permeability after fracturing. To reach the maximum pressure during the water injection phase (524 kPa), the colored gel was injected at a flow rate of 3.5 l/min for approximatively 25s. The maximum pressure recorded during this step was about 539 kPa (Figure 3.32b)

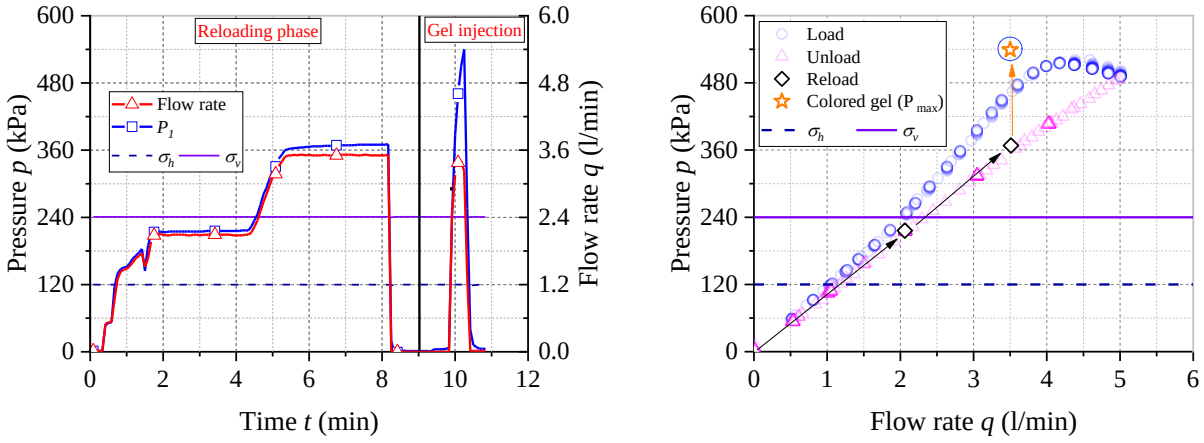

(a) (b)

Figure 3.32: Test N33 - Colored gel injection: (a) pressure – flow rate – time curves; (b) pressure versus flow rate.

3.5.1.3 *Disassembling phase*

The disassembling phase consists in excavating the first low permeability layer and then excavating the outer ring which contains only pure Fontainebleau NE34 sand. The membrane and lateral drainage system had been removed before the horizontal excavation of the inner ring was performed

Figure 3.34 presents some views of the sand pack during excavation of the low permeability layer and of the outer ring. No trace of blue is observed in these layers. The disassembling of the inner ring consists of a horizontal excavation from top to bottom of the specimen. A camera was placed above the specimen, allowing photos to be taken every 5 mm of excavation. As the injection tube has a diameter of 7 cm and it is higher than the specimen, it does not allow to see a small area of the specimen around the tube (obscured zone). To limit this effect, the camera lens needs to be fixed exactly at the center of the injection tube. The setup of the camera is shown in Figure 3.33. Figure 3.35 shows the horizontal cross-sections of the inner rings at different heights. When the excavation reached the low part of the inner ring, the obscured zone became larger and the fracture length observed was shorter, therefore a smartphone was used to take the photos for the rest of the sand pack (Figure 3.36).

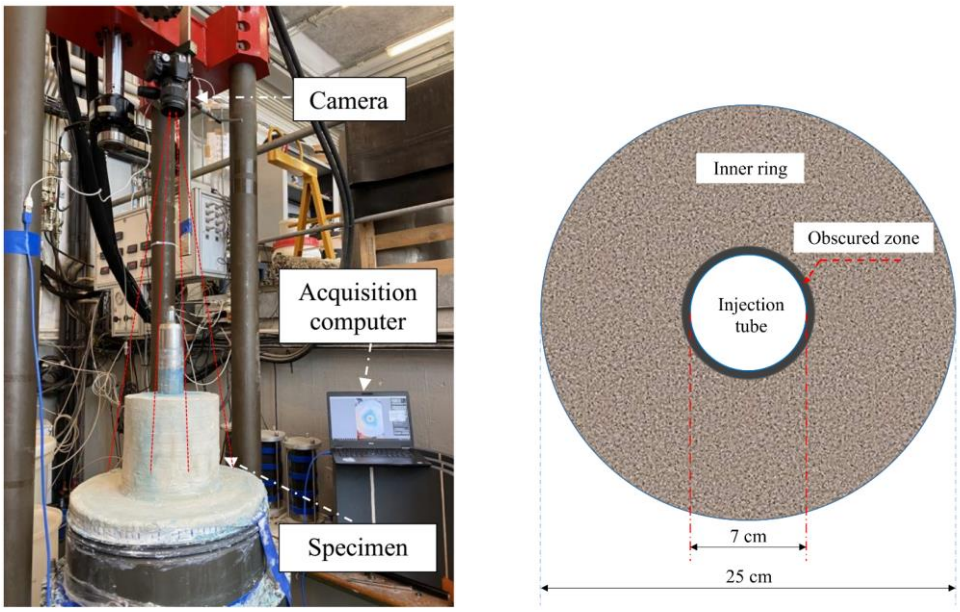

(a) (b)

Figure 3.33: (a) installation of the camera; (b) photo representative of an horizontal cross-section taken by camera

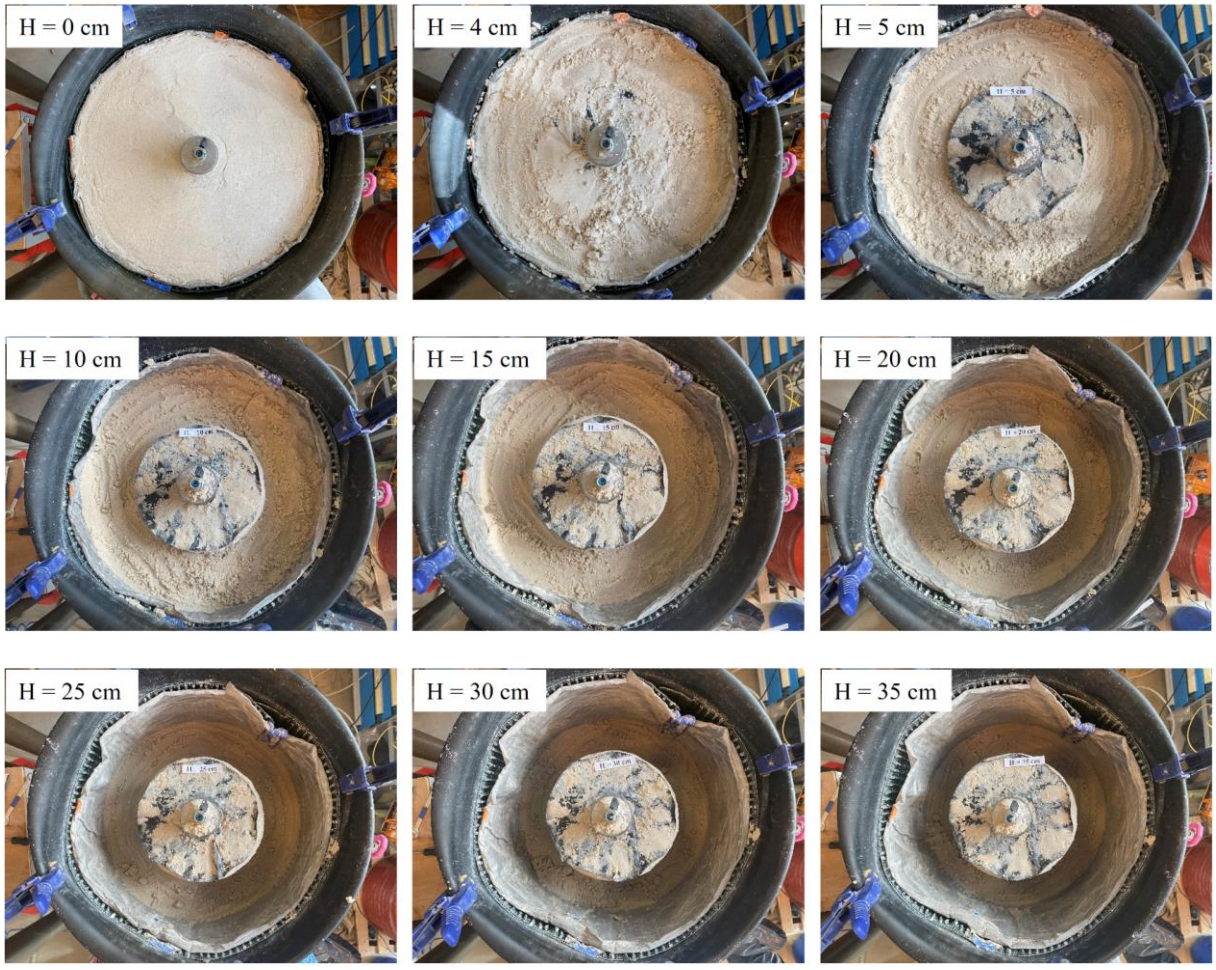

Figure 3.34: Excavation of the upper low permeability (H = 0 to 4 cm) and the outer ring at different heights of the sand pack N33.

When excavating the internal ring, three vertical fractures were clearly observed which propagated nearly perpendicular to the strainer tube (Figure 3.35). The fracture length varies up to 6 cm, depending on the height level of the sand pack. The longest was observed at H = 12 cm (Figure 3.37). Some other small fractures were also identified around the strainer (Figure 3.36). The photos make evidence of a non-symmetric distribution of the colored gel. The colored zone was more important in the area containing fractures. It can be concluded that fracturing favors the flow, therefore, the overall permeability of the specimen increases.

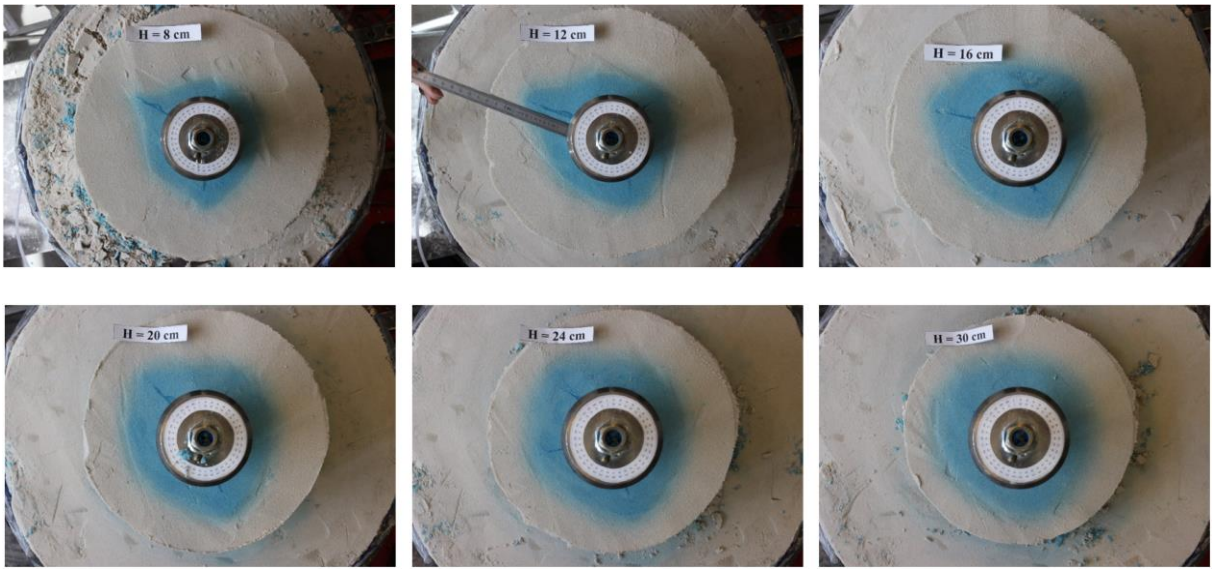

Figure 3.35: Test N33 - Transversal cross-sections of the inner ring at different heights (photos taken by a camera).

Figure 3.36: Test N33 - Transversal cross-sections of the inner ring at different heights (photos taken by a smartphone)

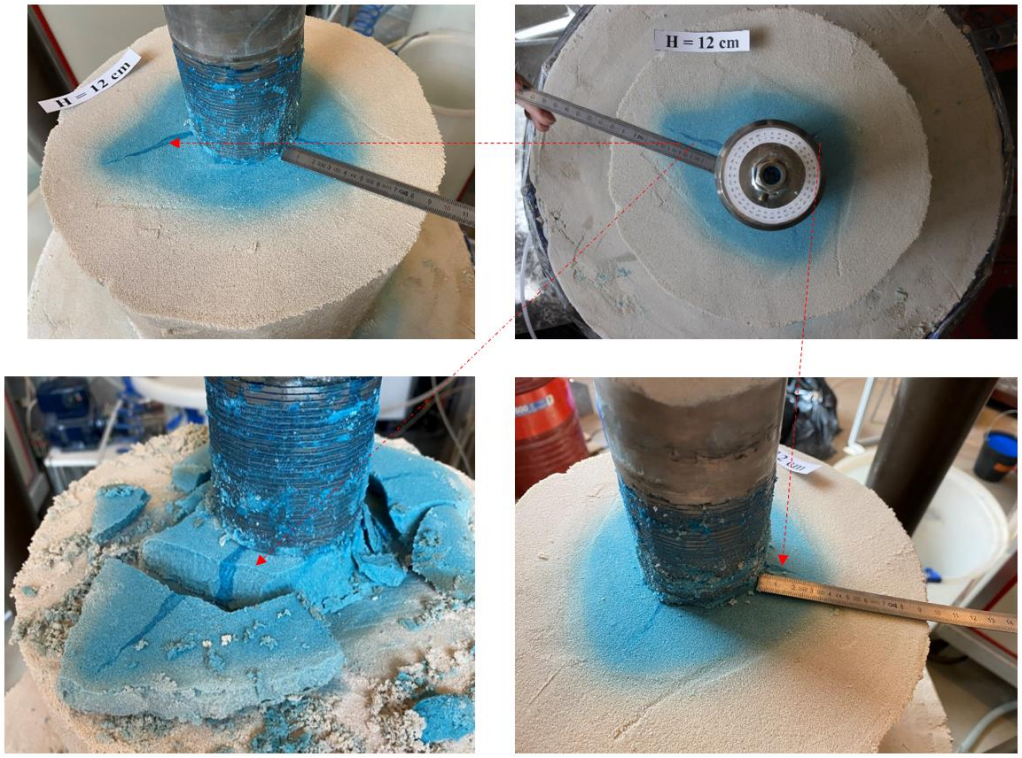

Figure 3.37: Test N33 - Different views of the horizontal cross-section at H = 12 cm.

The fracture morphology is quite complex as shown in Figure 3.38. However, in general, the fracture width is in the range of 1 mm to less than 1 cm and it gradually decreases from the tube to the fracture tip.

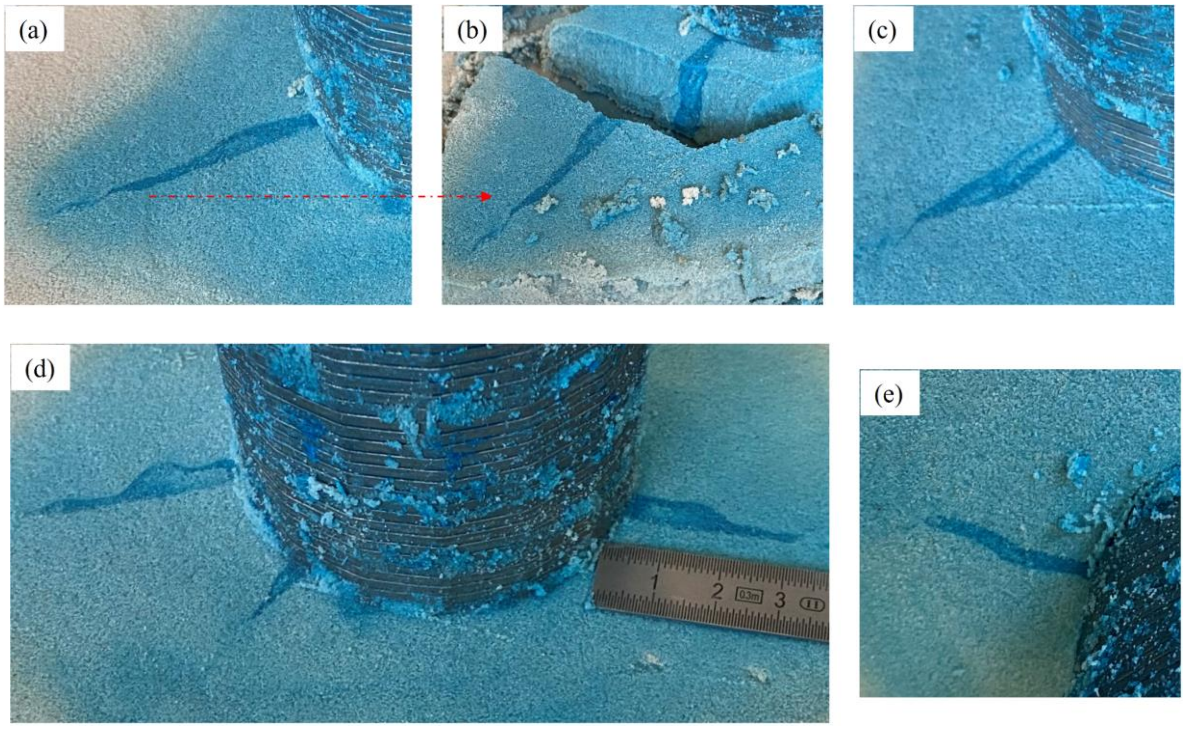

Figure 3.38: Test N33 - Typical fracture morphologies observed.

3.5.1.4 *Analysis of the induced fractures using X-ray CT and optical microscope (Test N32)*

In this part, we present the observation of the inter granular of fractures by using X-ray CT and the additional optical microscope observation. This analysis was performed on another test called N32 in which the induced fractures were similar to those of the typical test N33. Three cylinders were carefully extracted at the middle of the sand pack N32 (Figure 3.39). The detail of this test N32 is presented in Appendix E.3. These cylinders have a diameter of 2 cm and a height of 3 cm (Figure 3.39). Two of them contain the fractures (Sample 1 and Sample 2). In order to provide a higher spatial resolution, local computed tomography was performed (local CT) which allows a more detailed view of the grains. The reconstructed volume was a cylinder of 1.4 cm in diameter centered in the sample. The image has a voxel size of 6 µm. Figure 3.40 shows the typical cross-sections of these three samples. The fracture is a darker band at the middle of the image and only appears in the case of Sample 1 and Sample 2 which is similar to visual observation. A enlarged image of Sample 1 is presented in Figure 3.41

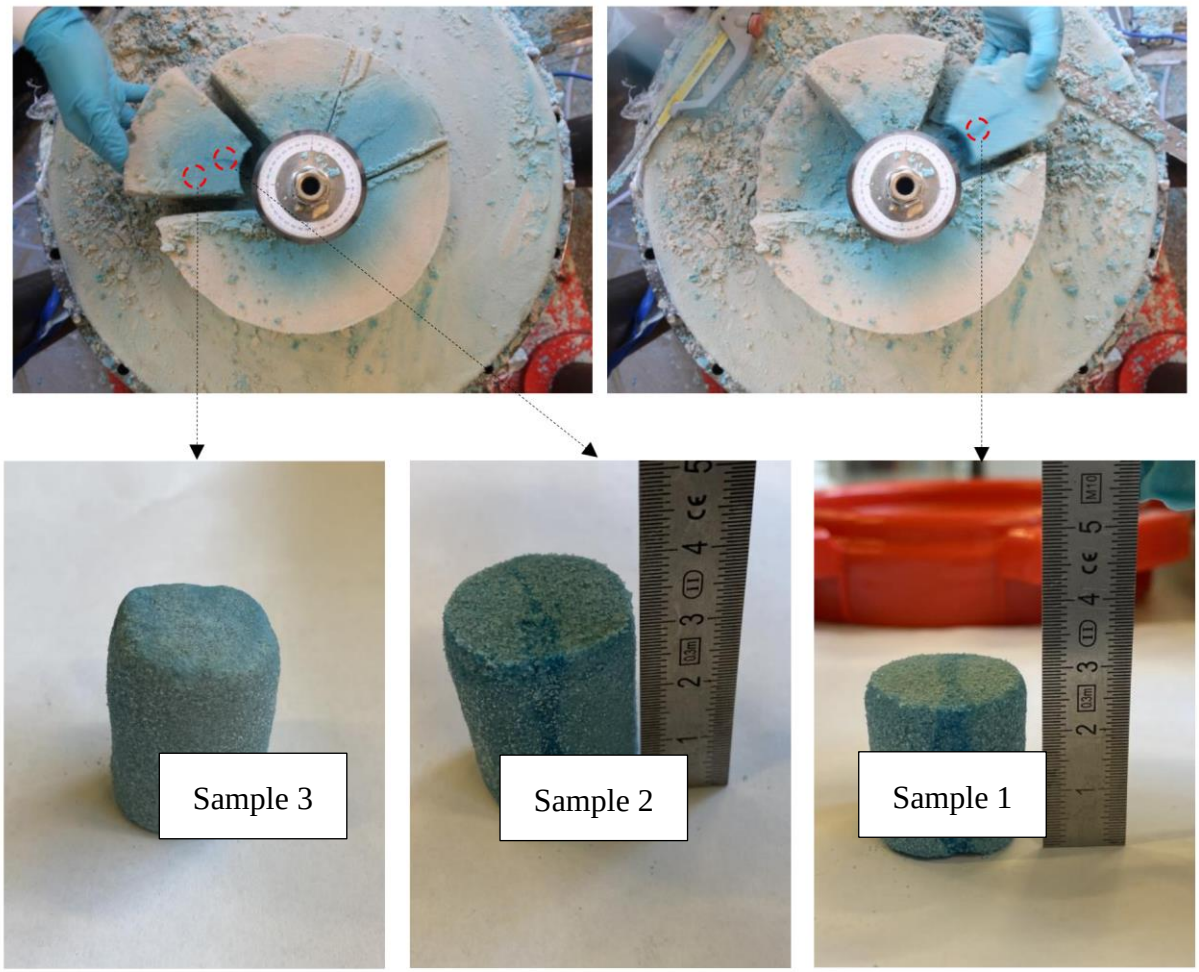

Figure 3.39: Three cylinders taken at the inner ring from H = 20 cm to H = 23 cm of the sand pack NE32.

By applying a filter " median " from FIJI, the noise of the image was reduced while keeping sharp boundaries between different phases (Figure 3.41c). Figure 3.41d presents a profile of the grey level evaluated over a typical line inside the fracture. Grain and air phases can be easily identified both by visual observation (brightness and darkness zone) and by the grey levels (highest and lowest grey levels). The existence of the air phase might come from the sampling process (manual extraction) and/or evaporation of water inside the sample. Note that the silica gel contains more than 60% by mass of water. Because of the limited resolution of the scanning images, C10 fine particles cannot be detected on the image.

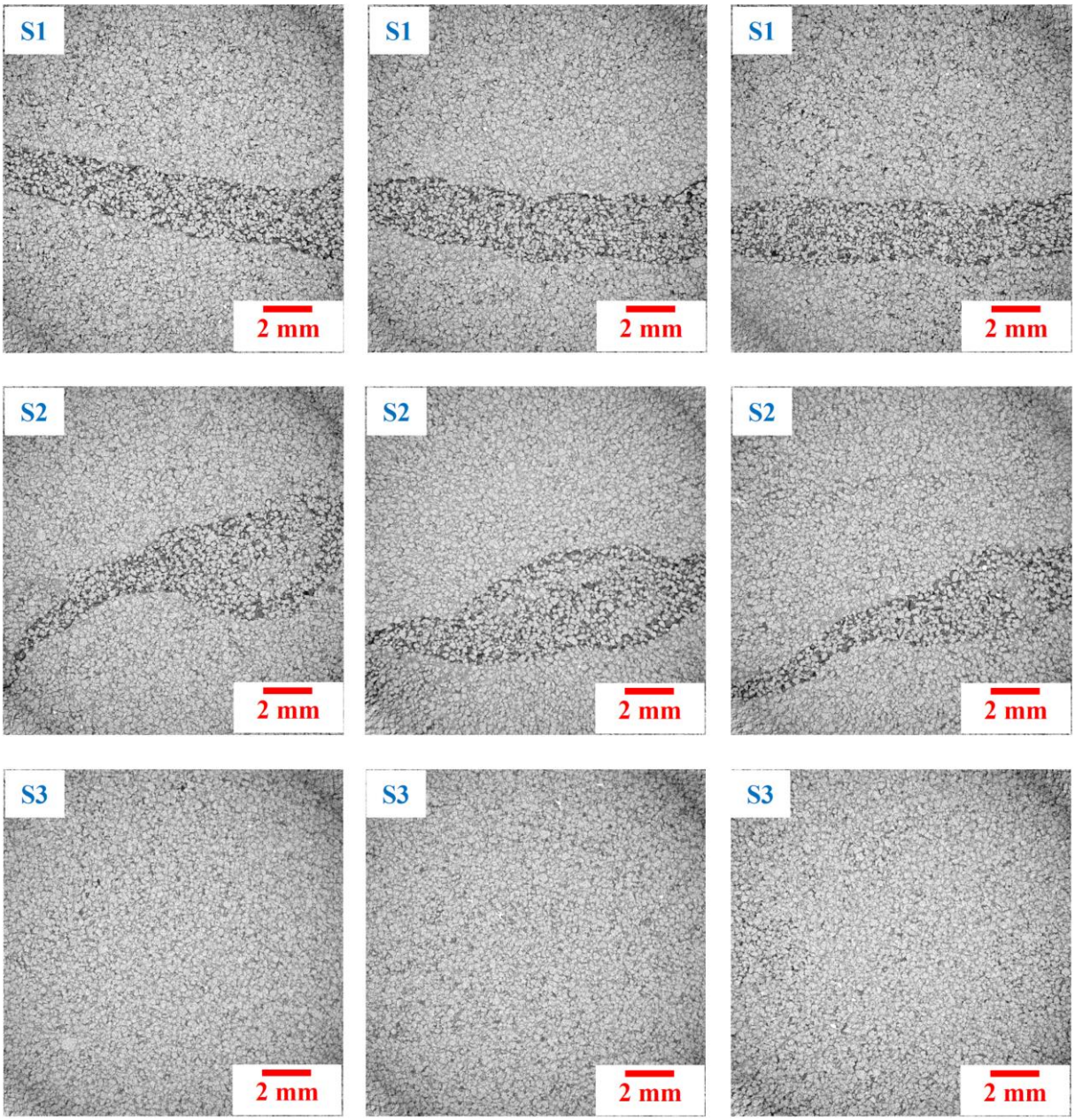

Figure 3.40: Transversal cross-sections of the XRCT image recorded on the different samples (Sand pack N32; Sample 1 - S1, Sample 2 - S2, Sample 3 - S3).

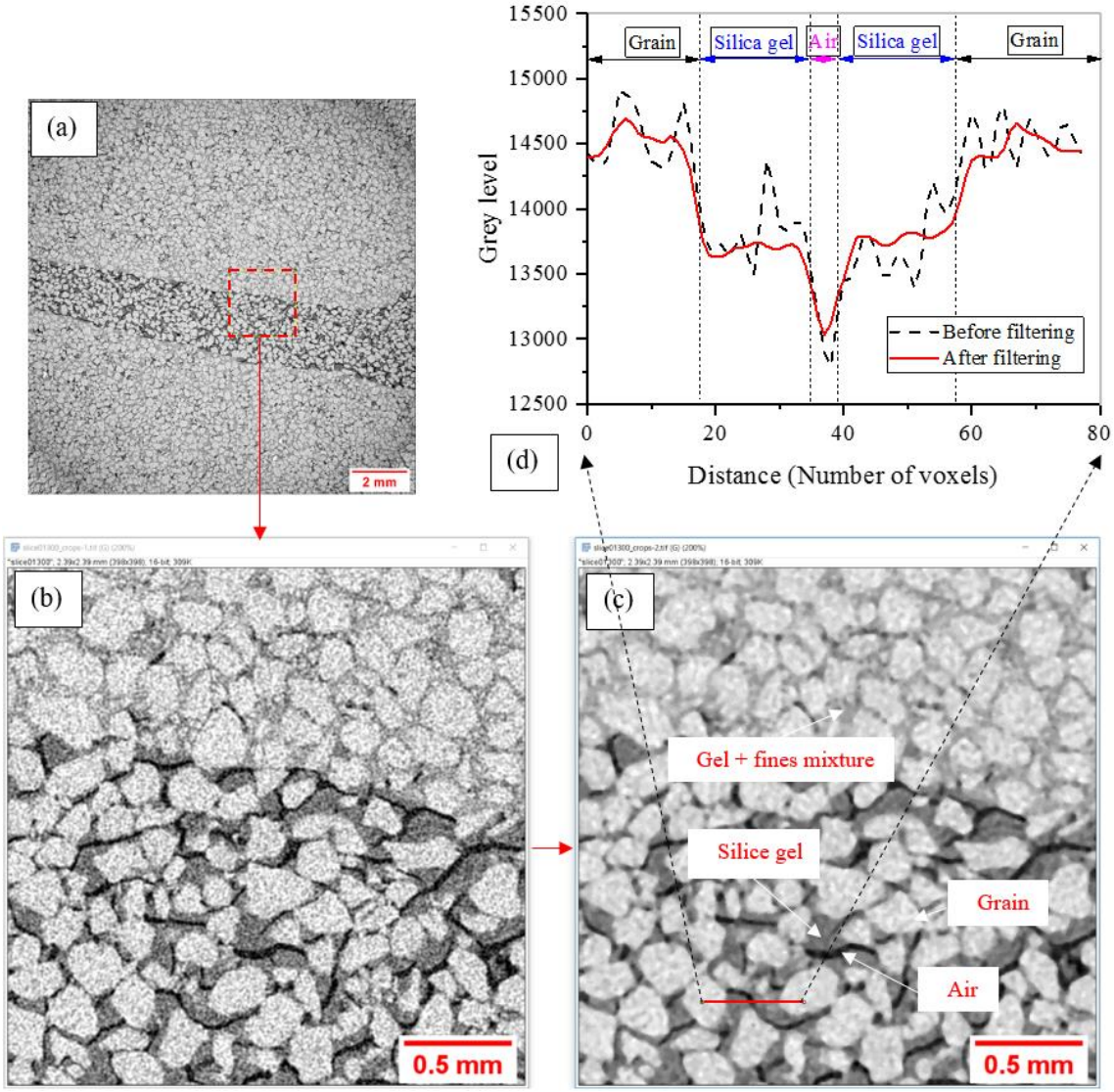

Figure 3.41: Magnified image showing grains structure and intergranular pores of a typical cross-section (Sand pack N32): (a) typical cross-section of Sampe 1; (b) zoomed image of a section; (c) zoomed image after filtering, (d) profile of the grey level evaluated over the red line shown in figure c.

Moreover, in order to complete the characterization, a transversal cross-section in the middle of Sample 1 was observed with an optical microscope (Figure 3.42). The image was enlarged up to the grain scale. The zone of localized fracture is clearly identified with a darker blue visible to the naked eye. The observation of the surrounding medium also confirms the homogeneity of the mixture of NE34 sand and of C10 fine particles during sample preparation in which fine particles filled the void space of the sand matrix (Figure 3.42). At the grain scale, we can clearly observe that the fracture presents fewer C10 fine particles and more porous space as compared to the surrounding medium. It can be seen that during fracturing when the injection pressure and drag force locally become greater than a critical threshold, the dilation of the sand matrix occurred at some localized zones around the injection point where the injection pressure was highest. This phenomenon was attributed to a higher pore network within these zones,

consequently, C10 particles were detached from the sand matrix and transported with the fluid flow. Therefore, a preferential path (fracture) of high porosity was created favoring the injectivity as illustrated in Figure 3.43. These structures look quite similar to dilation bands as described by Du Bernard et al. (2002). They are characterized by a localized increase in porosity and dilation within a thin band of localized deformation. Note that pure dilation bands correspond to zones of localized dilatant volumetric deformation with negligible shear strain. It is not possible here to have quantitative local strain measurements that would permit to distinguish between pure dilation bands and dilating shear bands.

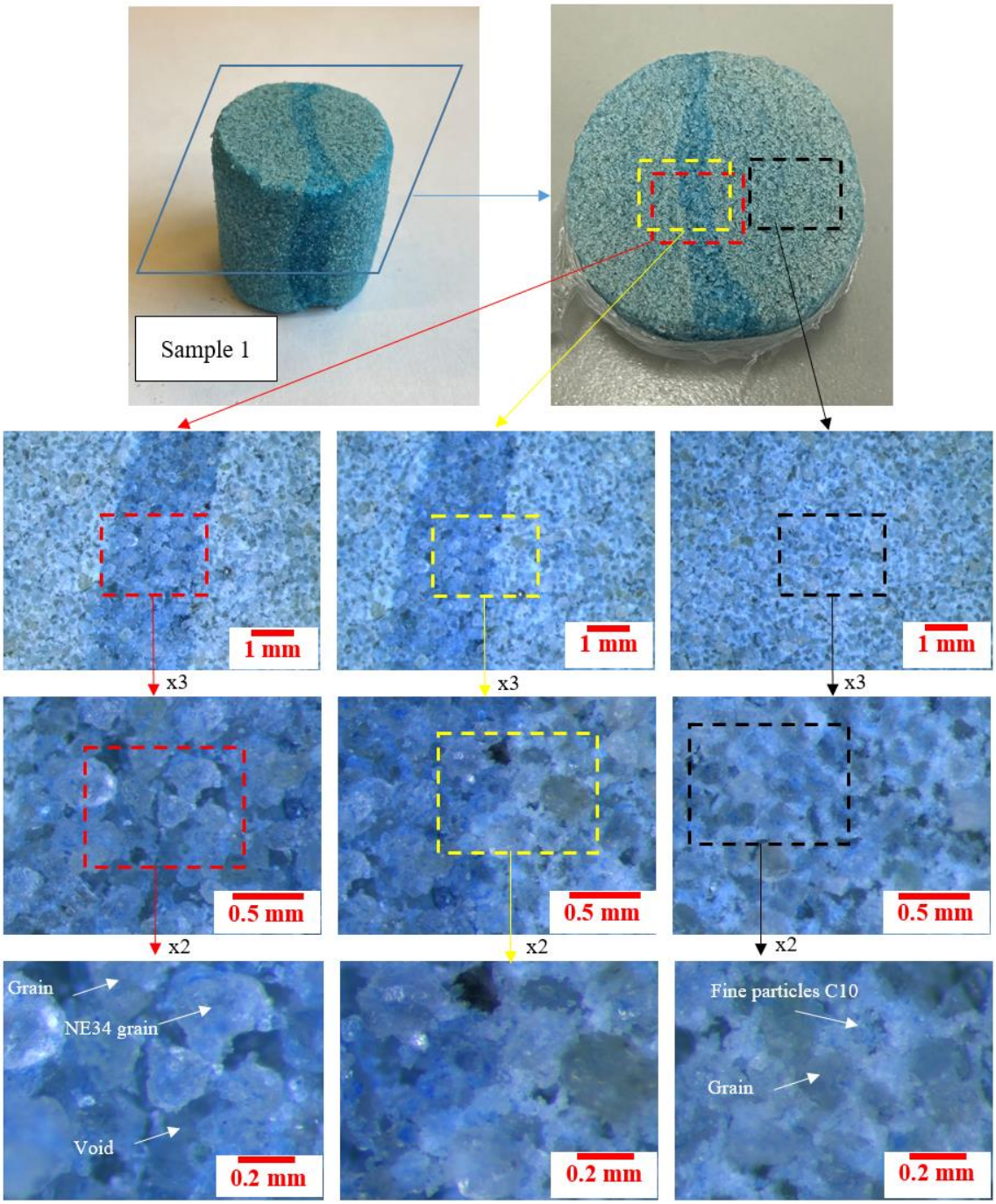

Figure 3.42: Optical microscopy observation of a typical transerval cross-section of the sample (Sand pack N32).

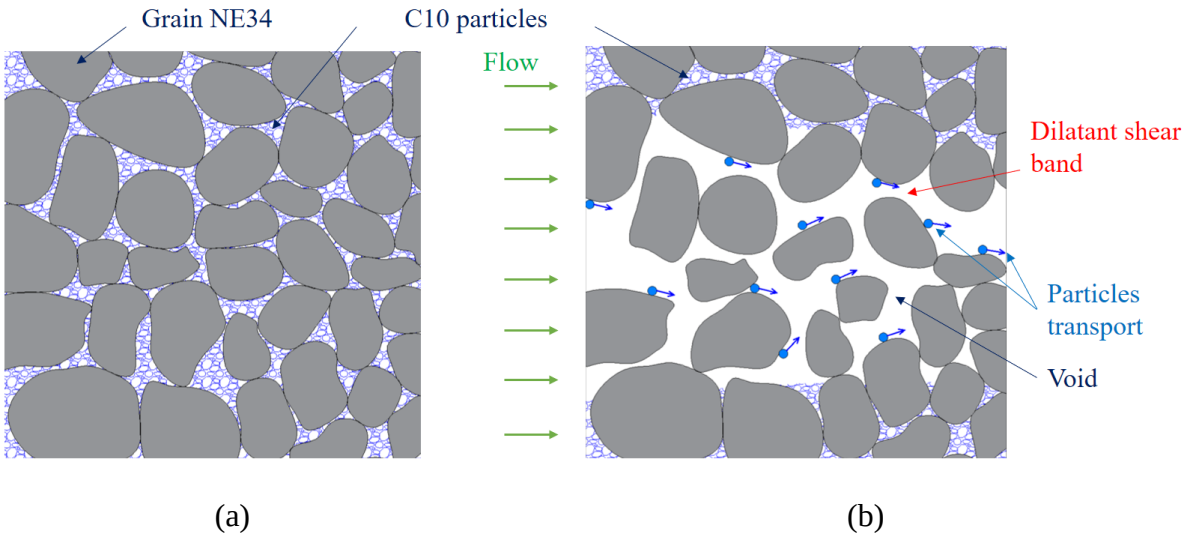

Figure 3.43: Schematic illustration of the fracturation process: dilatant shear band and particles transport (a) initial structure; (b) changing of the medium after fracturing.

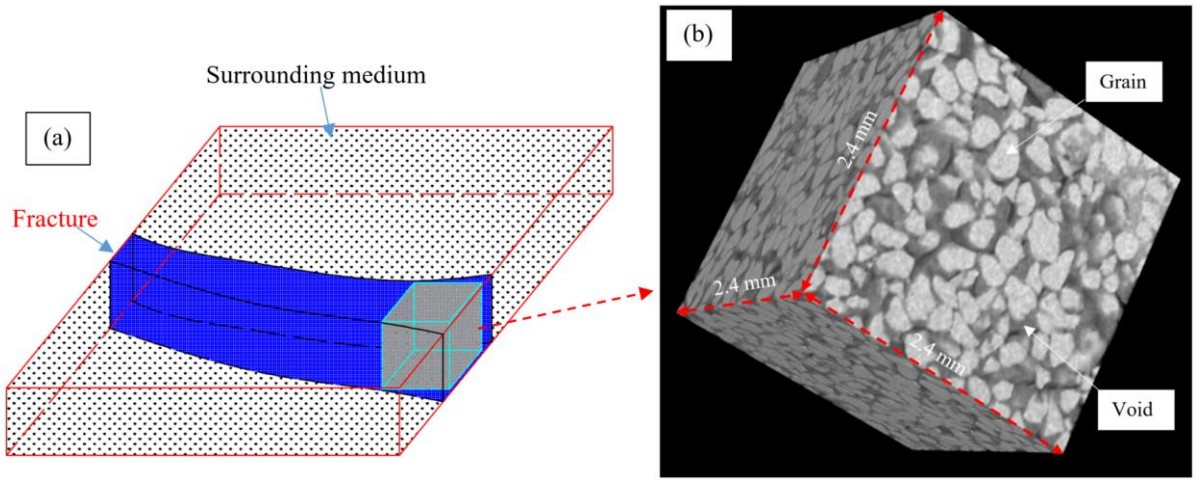

Figure 3.44: (a) Image representative of the volume extracted from the X-ray CT images of the Sample 1; (b) Volume rendering of the cube inside the fracture.

To estimate the global porosity of the fractured zone, image processing was performed on a volume extracted inside the fracture (Figure 3.44). This volume was a cube of a side length of 2.4 mm corresponding to 400 voxels. By imaging, a simple method can be applied to calculate the porosity of a given volume of sample. The treatment process usually consists of the three following next steps:

- Filtering: reduce the noise of images while keeping sharp boundaries between different phases.
- Thresholding: create binary images (white voxels corresponding to the grain phase whereas black voxels corresponding to the void phase).
- Analysing: measure the volume fraction of each component based on the number of voxels.

The following section presents the treatment process applied to a typical transversal cross-section of the cube.

❖ *Step 1: Filtering*

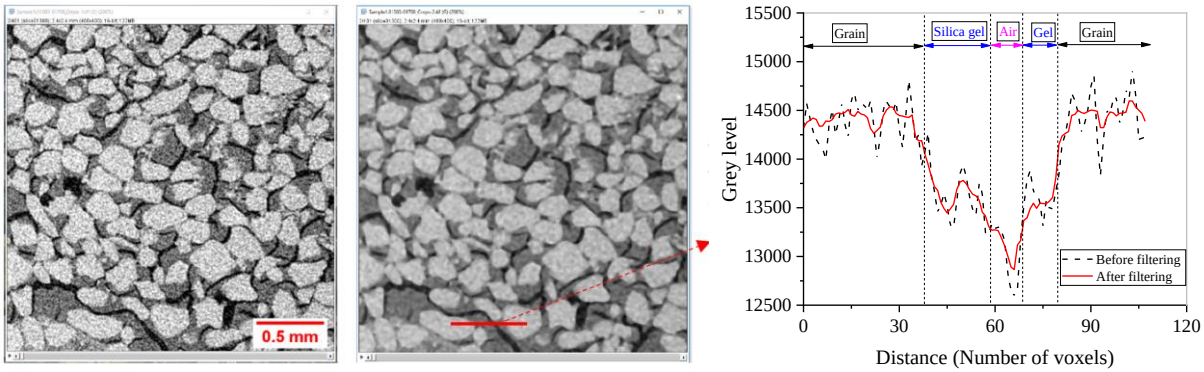

(a) (b) (c)

Figure 3.45: Filtering results of a typical section of the fracture (Sand pack N32): (a) original image; (b) filtered image; (c) grey values profiles before and after applying the median filtering. Image dimensions: 2.4 mm x 2.4 mm. Voxel size: 6 µm.

As presented above, a standard median filter using a radius of 2 voxels was applied on the original X-ray CT image (Figure 3.45). Based on the optical microscopy observation, we assume that there are no fine particles inside the fracture, hence, the fracture contains only three phases: air, silica gel and grain. The void volume was defined as the sum of the air phase and the gel phase whereas the solid volume was defined as the grain phase.

❖ *Step 2: Thresholding*

After the filtering step, a global threshold was applied to obtain binary volume that separates two different phases (void and solid). Figure 3.46a shows a histogram of the image after median filtering of a radius of 2 voxels. Only two distinguishable peaks are observed (gel and grain phase) because the volume of the air phase is quite small as compared to that of gel and grain phase. The selection of the threshold point is based on the lowest peak on the histogram and by visual observation from the binary image corresponding to a grey level equal to 13925. Figure 3.46c shows the binary image after thresholding. The grain-filled volumes shown in white voxels and black voxels represent the void phase.

❖ *Step 3: Analyzing*

After thresholding, it is easy to calculate the volume fraction of each phase by using the equations below:

$$f_v = \frac{n_v}{n_t} = \frac{n_v}{n_v + n_s} \tag{3.2}$$

$$f_s = 1 - f_v \tag{3.3}$$

where f_v is the volume fraction of the void phase; f_s is the volume fraction of the solid phase. n_v, n_s, n_t are respectively the number of voxels corresponding to the void phase, solid phase and total voxels of a selected image.

As the analyzed image (Figure 3.46c) is a square of 2.4 mm x 2.4 mm with a voxel size of 6 µm, the total number of voxels n_t corresponding to this section is 16 x 10^4 voxels. The number of voxel of void phase is counted directly using FIJI that is 69 x 10^3 voxels. By using Equation (3.2), the volume fraction of the void phase is 43.1%.

Applying this treatment process for the entire cube (Figure 3.44b), the global porosity can be calculated which corresponds to the fraction volume of the void phase of the entire cube. This value is 43% which is much higher as compared to the initial porosity of the medium (23%).

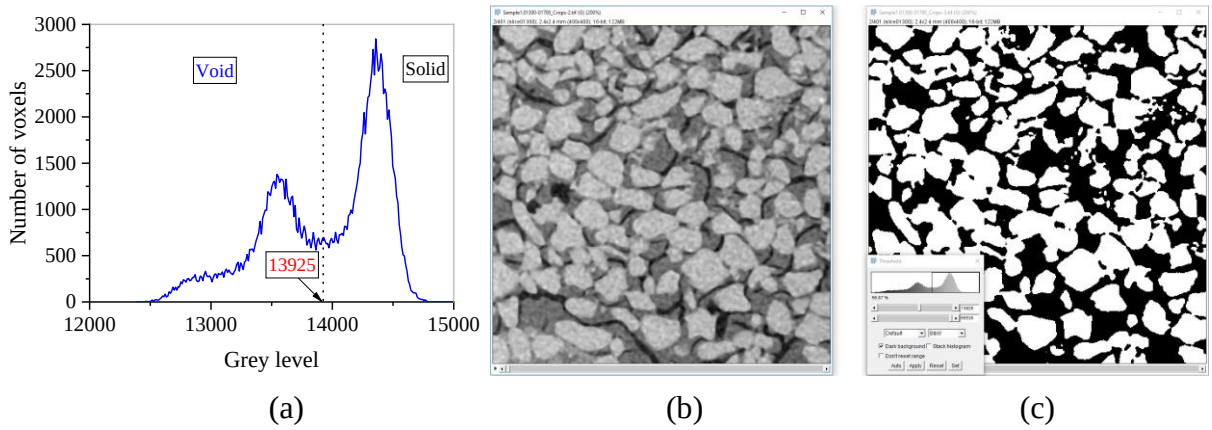

Figure 3.46: Thresholding steps (Sand pack N32): (a) histogram of the filtered image; (b) filtered image; (c) binary image after thresholding with the solid phase shown in white. Image dimensions: 2.4 mm x 2.4 mm. Voxel size: 6 µm.

3.5.2 Parametric study

3.5.2.1 *Effect of the confining pressure*

Three tests have been performed under different confining pressures (120 kPa, 150 kPa and 200 kPa) while keeping a constant stress ratio coefficient K_0 of 0.33. The results are presented in Figure 3.47. Test N32 under 200 kPa of confining pressure was injected up to a flow rate of 7 l/min (maximum pump capacity) and the corresponding maximum pressure was 700 kPa (3.5 σ_h). However, the results showed an almost linear relationship between injection pressure and flow rate without any pressure drops, which indicates that the fracturing regime has not reached yet (Figure 3.47a). Test N31 under 150 kPa of σ_h exhibited a higher critical fracturing pressure as well as a higher magnitude of the pressure drop during the fracturing phase as compared to N32 (120 kPa) which explained a higher increase of the overall permeability obtained during unloading (Figure 3.47e). Note that test N31 was performed with time-steps of 10 minutes which is twice higher as compared with the typical injection protocol. Longer injection time may increase suffusion within the sand pack, therefore decrease the overall permeability. However, the results of test N31 exhibit a similar slope of pressure – flow rate curve during the

matrix regime as test N32 (Figure 3.47a), showing a negligible effect of this difference in the time-step on the sand pack response.

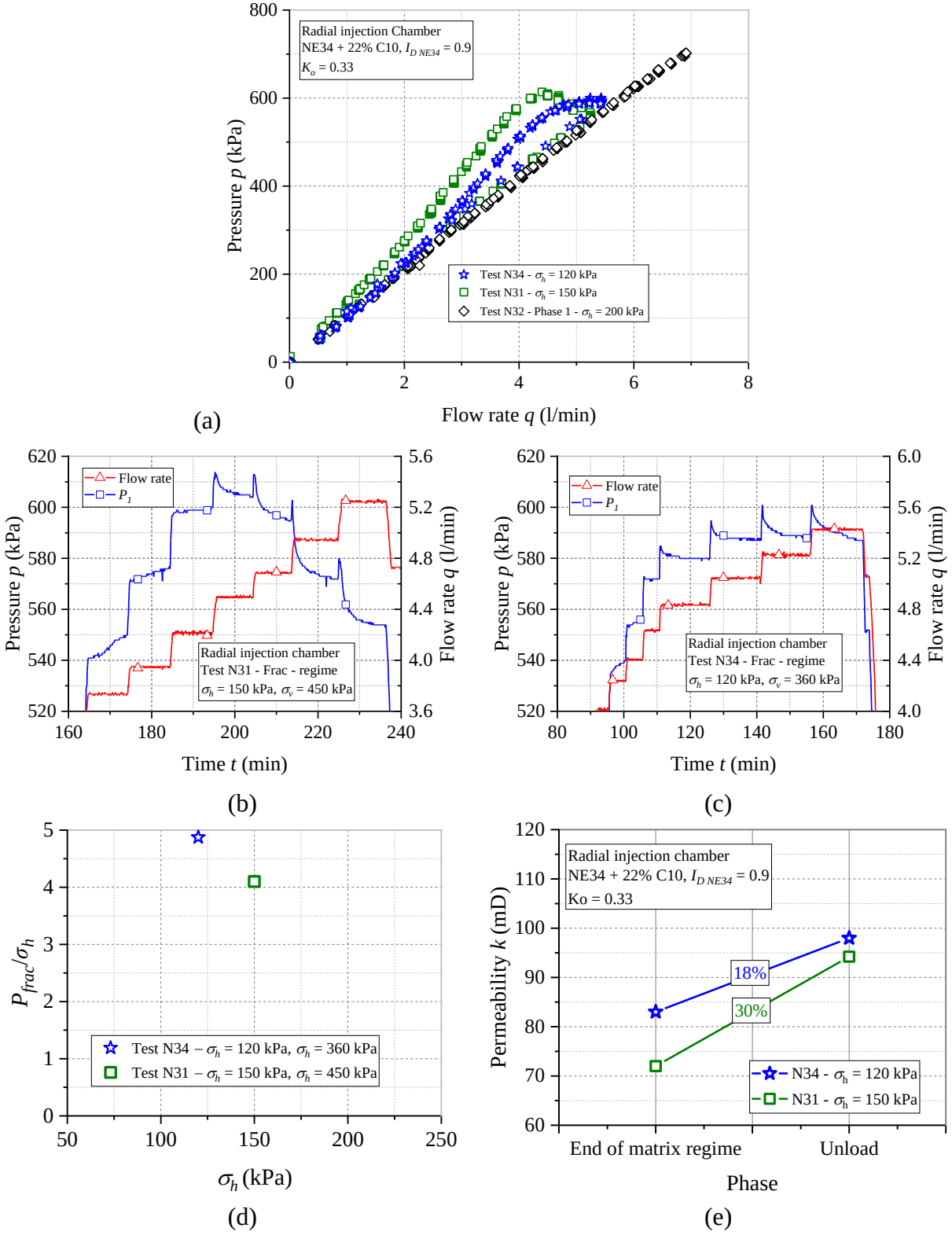

Figure 3.47: Effect of the confining pressure: (a) injection pressure vs flow rate; (b), (c) frac-regime during tests N31 and N33, respectively; (d) normalized fracturing pressre (P_{frac}/σ_h) vs confining pressure; (e) increase of the overall permeability.

Similar to the typical test N33, suffusion occurred during the matrix regime, identified by a gradual increase in pressure at a constant flow rate until it reached the transition point at which the injection pressure stabilizes immediately (N31: Q_{tr} = 4.2 l/min, P_{tr} = 598 kPa and N34: Q_{tr} = 4.2 l/min, P_{tr} = 572 kPa). The first pressure drop was detected right after this point. As can be seen in Figure 3.47d, a lower confining pressure results in a higher value of normalized fracturing pressure.

Figure 3.48 presents some typical photos of corresponding to tests N31 (a,b,c) and N34 (d,e), showing the fracture pattern within the specimen. Longer fractures obtained in test N31 confirm the higher increase of the permeability after fracturing.

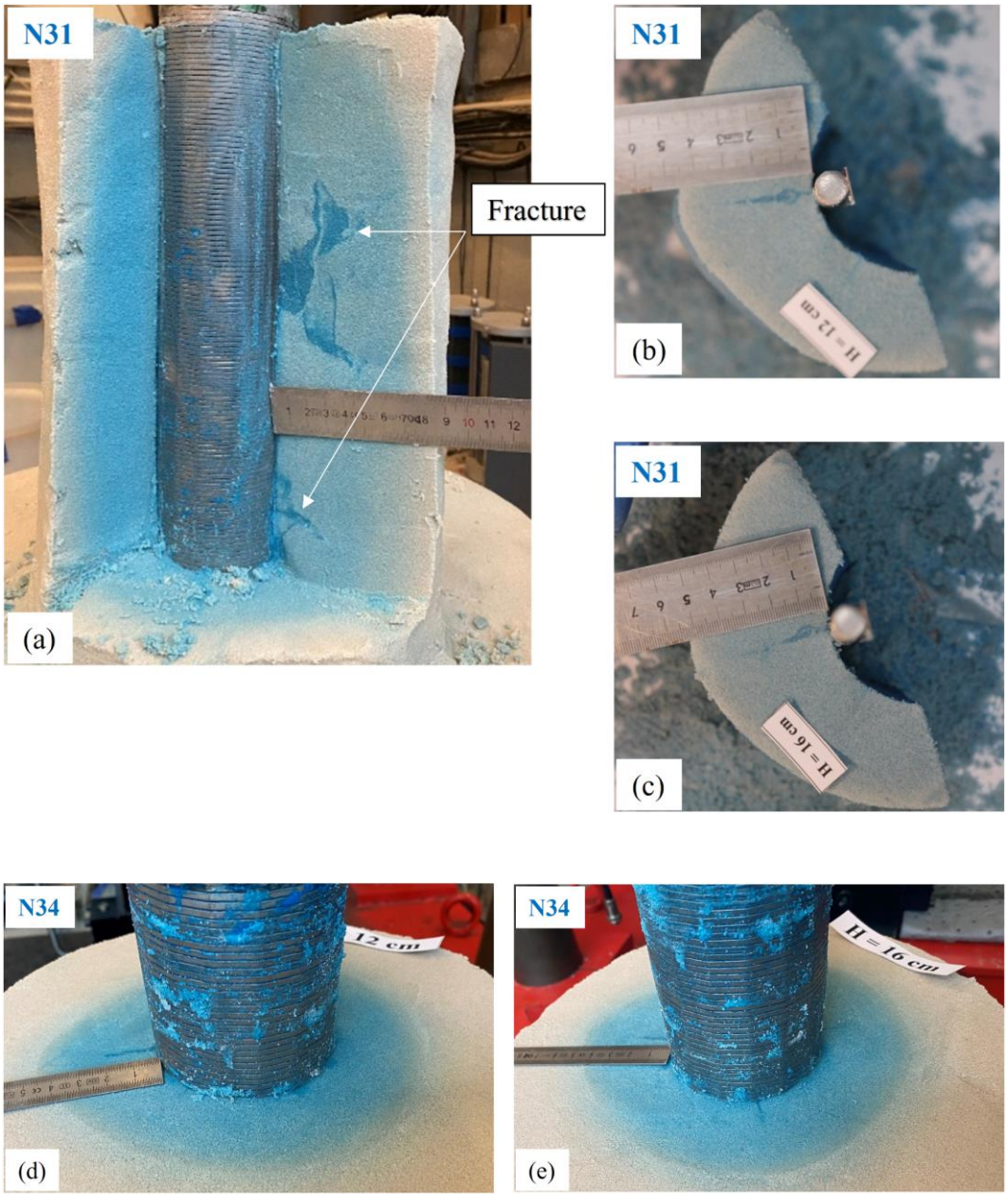

Figure 3.48: Effect of the confining pressure on the fractures morphology: (a),(b),(c) test N31; (d),(e) test N34.

3.5.2.2 *Effect of the stress ratio coefficient K_0.*

In this part, we evaluate the effect of K_0 on the fracturing response. These tests were performed under the same confining pressure of 120 kPa and the different axial stresses (240 and 360 kPa) (Figure 3.49a). The test under a higher axial stress (i.e., lower K_0) shows a higher fracturing pressure, equivalent to a higher value of normalized fracturing pressure (Figure 3.49b) and a lower increase of the permeability (Figure 3.49c). However, because of the limited number of tests carried out, we do not have at this point a clear basis for drawing conclusions on this parameter. Therefore, further studies of the effect of K_0 should be performed at higher confining pressures in the future.

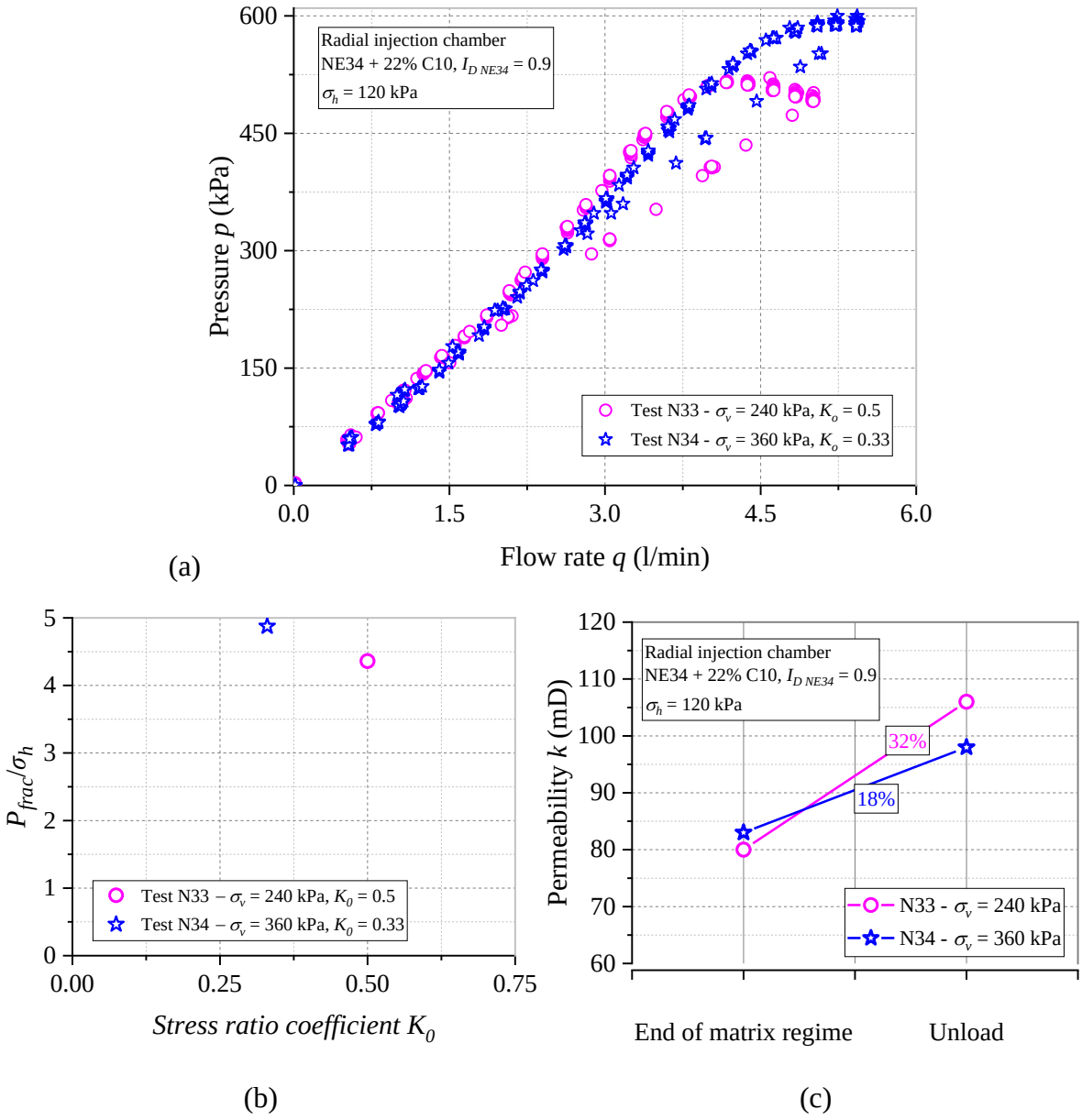

Figure 3.49: Effect of stress ratio coefficient: (a) injection pressure vs flow rate; (b) normalized fracturing pressure (P_{frac}/σ_h) vs stress ratio coefficient K_0; (c) Evolution of the permeability.

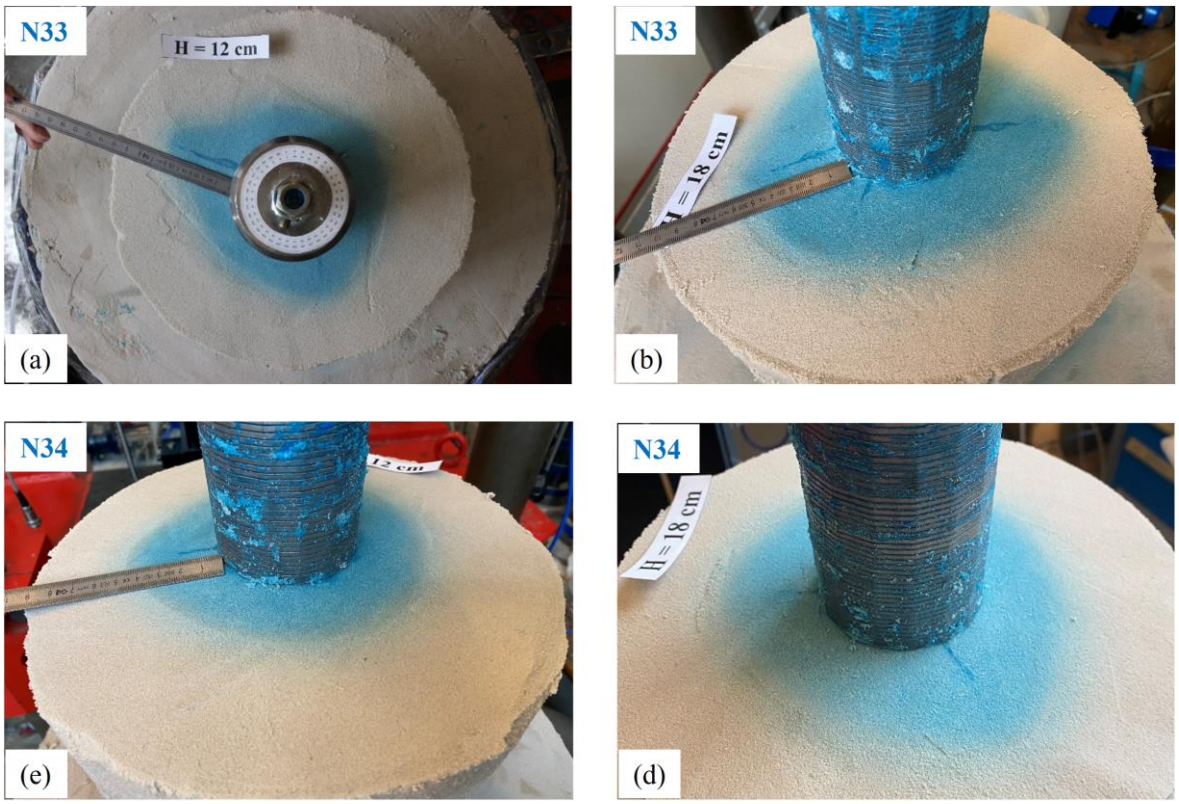

Figure 3.50: Effect of confining pressure on the fractures morphology: (a),(b) test N33; (d),(e) test N34.

3.5.2.3 *Effect of several injection phases*

Few tests have been also performed under several injection phases of pure water. Test N30 is the first successful test in the radial injection chamber in which fracturing has occurred. The injection has been performed under three injection cycles of flow rate. The maximum flow rates are 3.15, 3.6 and 5.l l/min, respectively for these phases (Figure 3.51). Note that during this test, a flowmeter having a maximum measurement of 3.15 l/min was used. Beyond this value, the flow rate is calculated based on the calibration curve of the pump. The detailed description of test N30 is presented in Appendix E.2. An important increase of the pressure due to suffusion was observed during phase 1 and phase 2 when maintaining the injection for a few hours at a constant flow rate (phase 1 at 3.15 l/min, phase 2 at 3 l/min). Similar to the injection cell, to minimize the effect of suffusion, the injection time of each step during the matrix regime is fixed to 5 minutes for further tests in the injection chamber. As shown in Figure 3.51b, fracturing occurred during phase 3 at a flow rate of 4.75 l/min, corresponding to the first pressure drop P_{frac} = 520 kPa (2.6 σ_h) (Figure 3.51c). The value of the normalized fracturing pressure in this test is much smaller than those obtained in the tests with only one injection cycle (Figure 3.47d and Figure 3.49b), showing a significant effect of the previous injection stages on the fracturing initiation. On the other hand, unlike the pressure response in the tests with only one injection cycle, the transition point (i.e., the step at which a change in the slope of the pressure – flow rate curve is observed) appeared much earlier compared to the fracturing point (i.e., the step at which the first pressure drop is observed). During the disassembling, small

vertical fractures were detected along the strainer (Figure 3.52), confirming the pressure drops during injection.

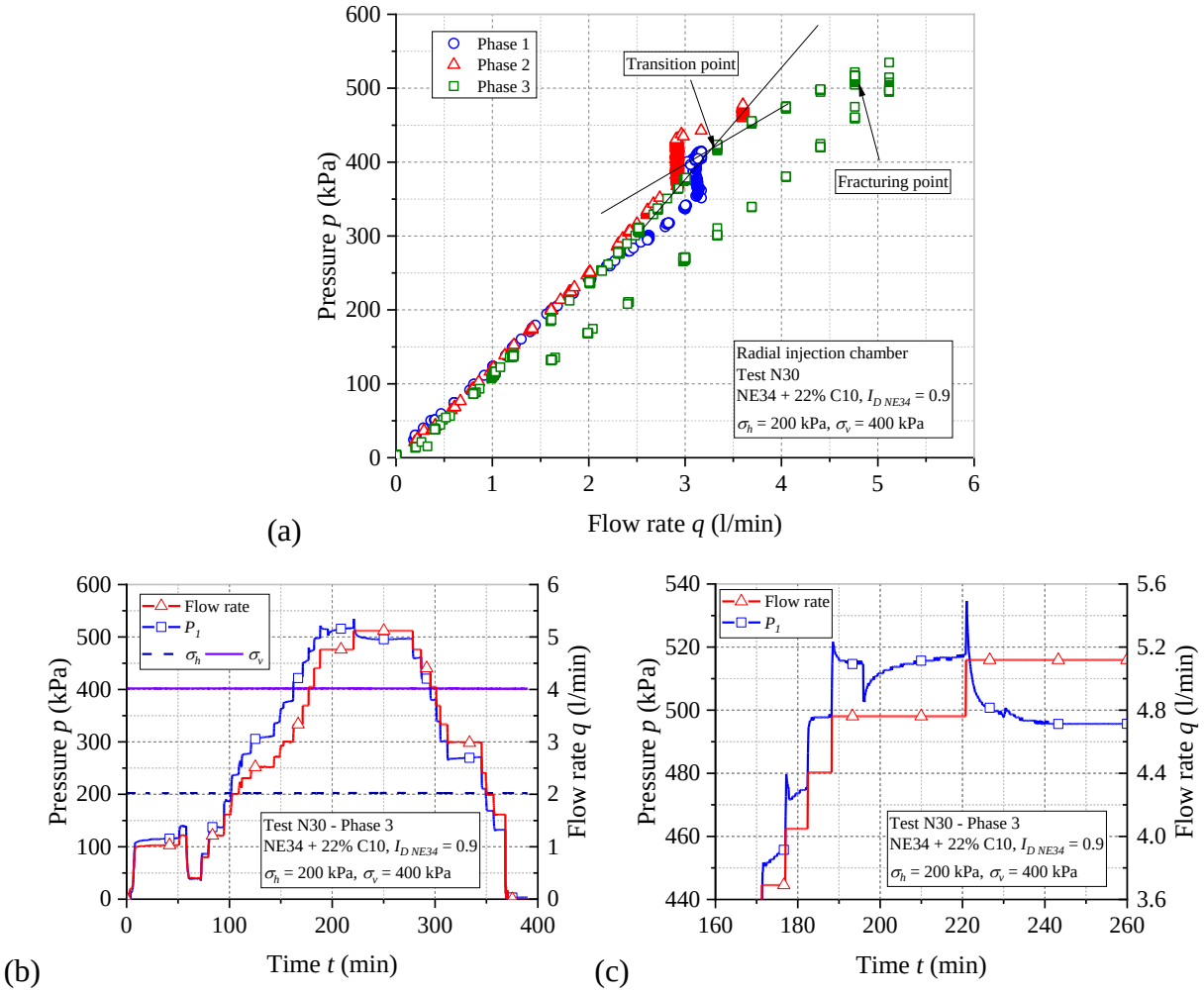

Figure 3.51: Results for test N30: (a) full response corresponding to three injection phases: (b) results for phase 3; (c) phase 3 during the fracturing regime.

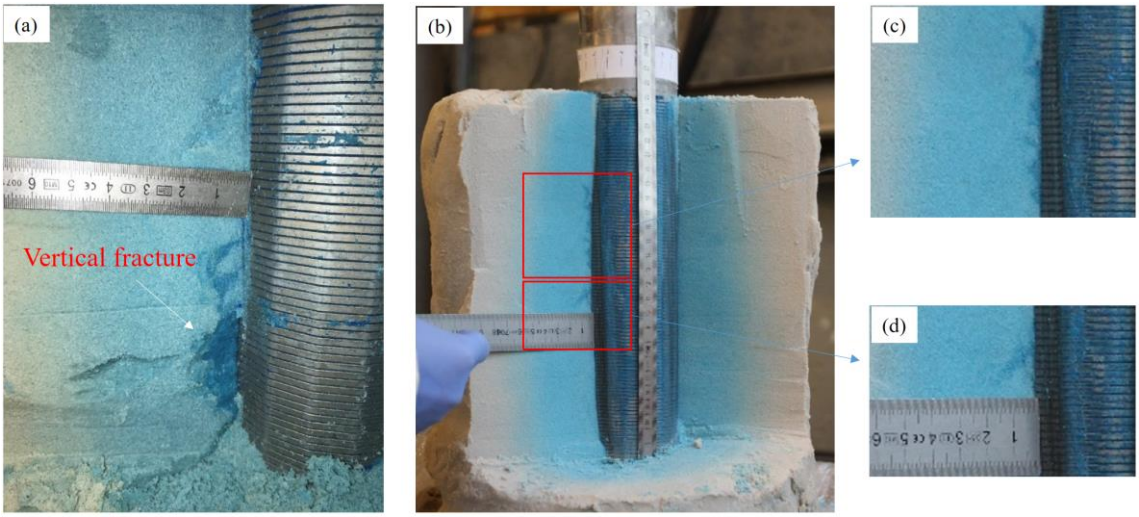

Figure 3.52: Observation of the fractures along the trainer tube in the sand pack N30.

Test N32 has been also carried out with four injection cycles (Figure 3.53). The first and the second phases were performed under 200 kPa confining pressure and 600 kPa axial stress (K_0 = 0.3) and the third phase at a lower axial stress of 500 kPa. However, no fracture occurred during these phases even at a maximum flow rate of the pump of 7l/min and the highest recorded pressure of 702 kPa (≈ 3.5 σ_h). Therefore, the stress conditions were reduced to a confining pressure of 120 kPa and an axial stress of 360 kPa (K_0 = 0.3) to be able to break the sand pack within the flow capacity of the pump. Finally, pressure drops were detected during the fourth phase (Phase 4 – see Figure 3.53c). The results of test N32 are detailed in Appendix E.3. Similar to test N30, the transition point is far away from the fracturing point (Figure 3.53b).

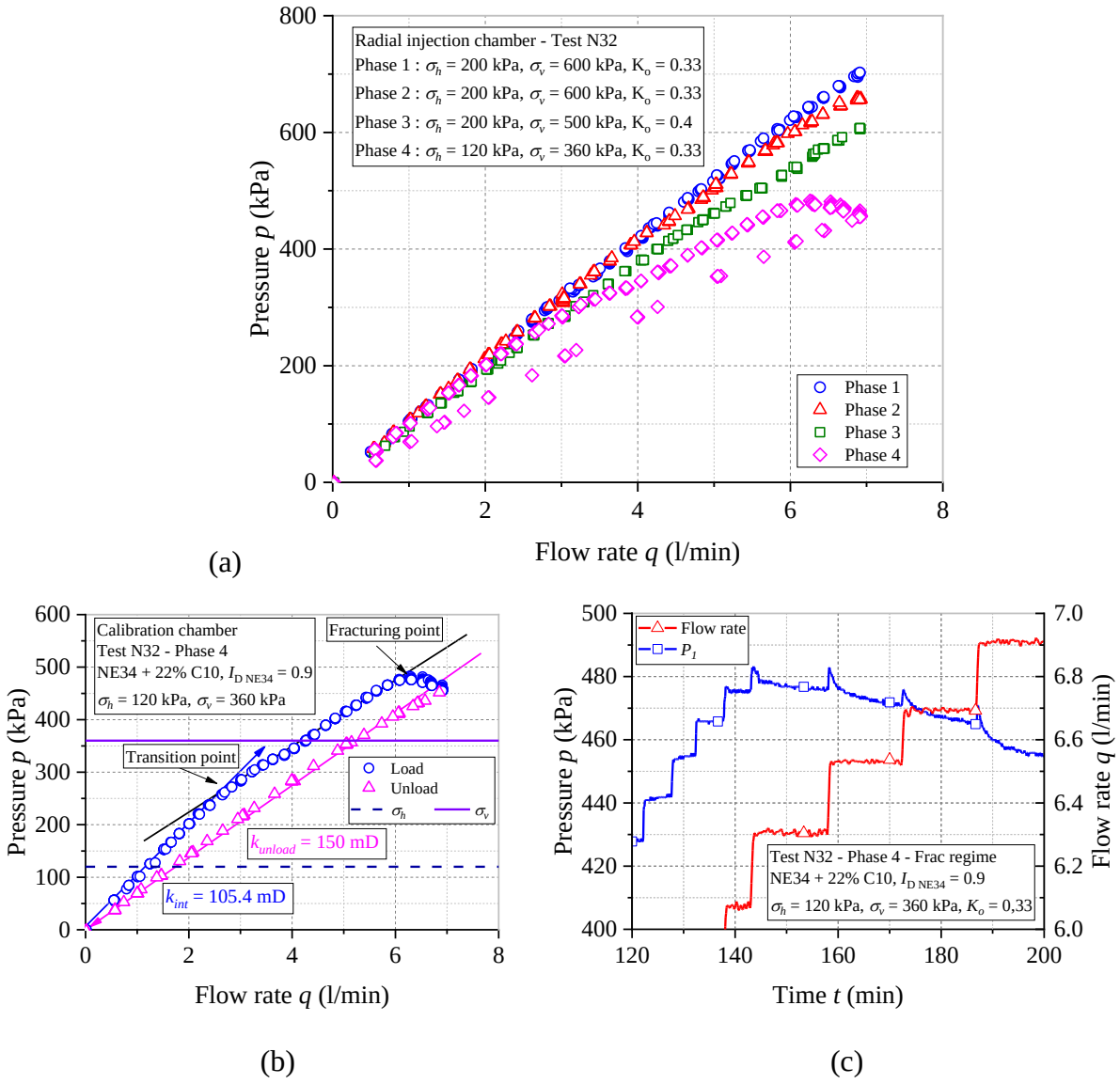

Figure 3.53: Results for test N34: (a) pressure – flow rate curves during four injection phase; (b) results for phase 4; (c) fracturing regime during phase 4.

Benahmed (2001) has explored the effect of applied confining pressure on the void ratio of sand specimens (Figure 3.54). The effect of the confining pressure becomes less important

when the sample is denser. Test N32 was performed at a very dense state (density index of the sand matrix $I_{D\ NE34}$ of 0.9). Moreover, in the inner ring that is constituted by the mixture of NE34 + 22% C10 fines, the corresponding void ratio is only 0.3. Therefore, according to Benahmed (2001), the effect of applied stress conditions on a modification of the initial void ratio can be considered as negligible.

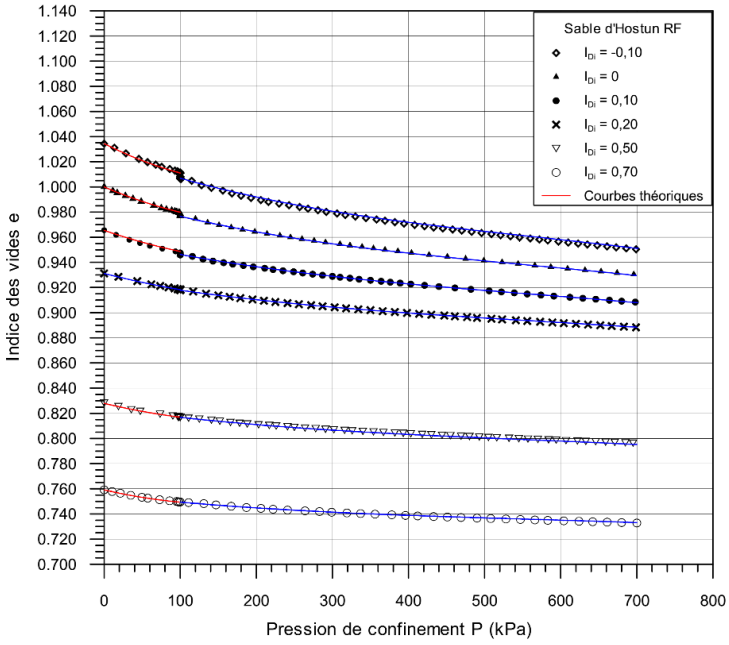

Figure 3.54: Experimental results of the variation of void ratio depending on the applied confining stress conditions (Benahmed, 2001).

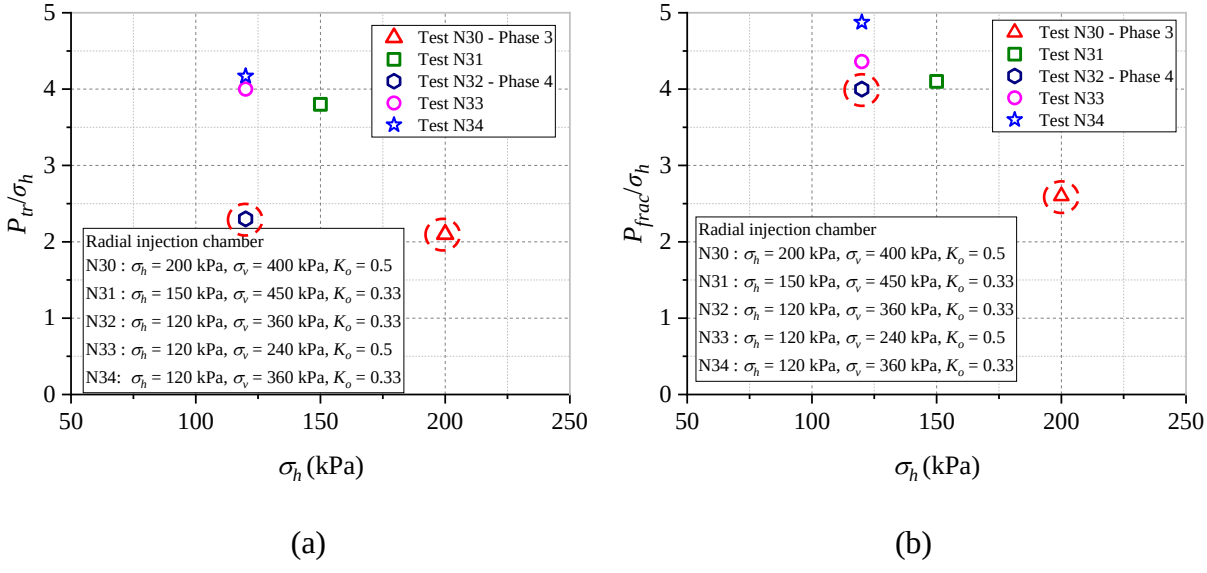

Figure 3.55: Tests in the injection chamber: (a) normalized transition pressure (P_{tr}/σ_h); (b) normalized fracturing pressure (P_{frac}/σ_h).

Figure 3.55 shows an important effect of subsequent injection phases on the results of the normalized transition pressure and of the normalized fracturing pressure. These values are smaller than those in the tests with only one injection phase, showing that fracturing is generated at a smaller injection pressure if the sand pack experiences a high injection pressure in a previous injection stage. This phenomenon would need to be further explored by performing additional tests. However, in an attempt to understand the underlying mechanisms, we can assume that two competing processes occur during the previous injection stages: dilation and accumulation of fines in pore throats. Both processes modify the internal packing of the specimen which could be responsible for earlier fracturing. If confirmed with additional tests, these observations could have interesting consequences in oil industry. Imposing pressure pulses in the matrix regime could allow to lower the fracturing pressure.

3.5.2.4 *Conclusion*

During the typical test N33, fracturing initiates at a critical fracturing pressure corresponding to 4.4 times the confining pressure. Four frac steps of 15 minutes each allowed an increase of 32% of the overall permeability comparing to the apparent permeability calculated at the end of the matrix regime. During disassembling phase, vertical fractures have been observed all along the strainer tube which confirms the pressure drops identified during injection. The diffusion of the colored gel was more important in the area containing the fractures, showing that a stronger flow occurred at these locations. Additional observations from X-ray CT and optical microscopy on some typical samples containing fractures permit not only to identify a change of the granular structure inside the fracture but also to calculate the evolution of the local porosity. The fracture presents a local porosity value of 43% which is much higher as compared to the initial state (23%). This analysis was not performed for the tests in the radial injection cell because of a small fracture width (in the range of millimeters) and a low scanning resolution corresponding to the size of the specimen.

For the tests with only one injection phase, fracturing occurs when the injection pressure reaches about 4 to 5 times the confining pressure and a higher increase of the permeability is linked to longer and wider fractures induced around the strainer tube. An increase of the confining pressure leads to an increase of the fracturing pressure. An important effect of the cyclic injection on the response of the injection pressure is also observed. Fracturing is generated at a smaller injection pressure if a high pressure is applied on the sand pack in the previous injection stages.

3.6 COMPARISON OF THE RESULTS OBTAINED WITH TWO INJECTION SETUPS

As presented in detail in Section 2.3.1, the sand pack of the injection chamber represents a damaged reservoir with the formation of an internal cake around the strainer tube due to the particles filtration (i.e., the inner ring of a mixture of NE34 sand and 22% of C10 fines) and the outer ring of the sand pack is prepared with pure sand. The specimen of the injection cell, on the other hand, is homogenous using the same mixture as the inner ring of the sand pack in the injection chamber. The configuration and its corresponding dimensions are illustrated in Figure 3.56. The permeability of the outer ring is negligible as compared to that of the inner ring (see Figure 3.57), so that the two setups provide the similar pressure distribution within the cell specimen and inner ring of the sand pack. Therefore, we could compare the results obtained in the injection cell with those in the injection chamber. The overall permeability is calculated using Equation (3.1). The parameters of the device in this equation consist of r_0, r_1 and H, where r_0 is the radius of the injection tube; r_1 is the radius of the specimen (cell) or the inner ring (chamber) and H is the height of the injection zone.

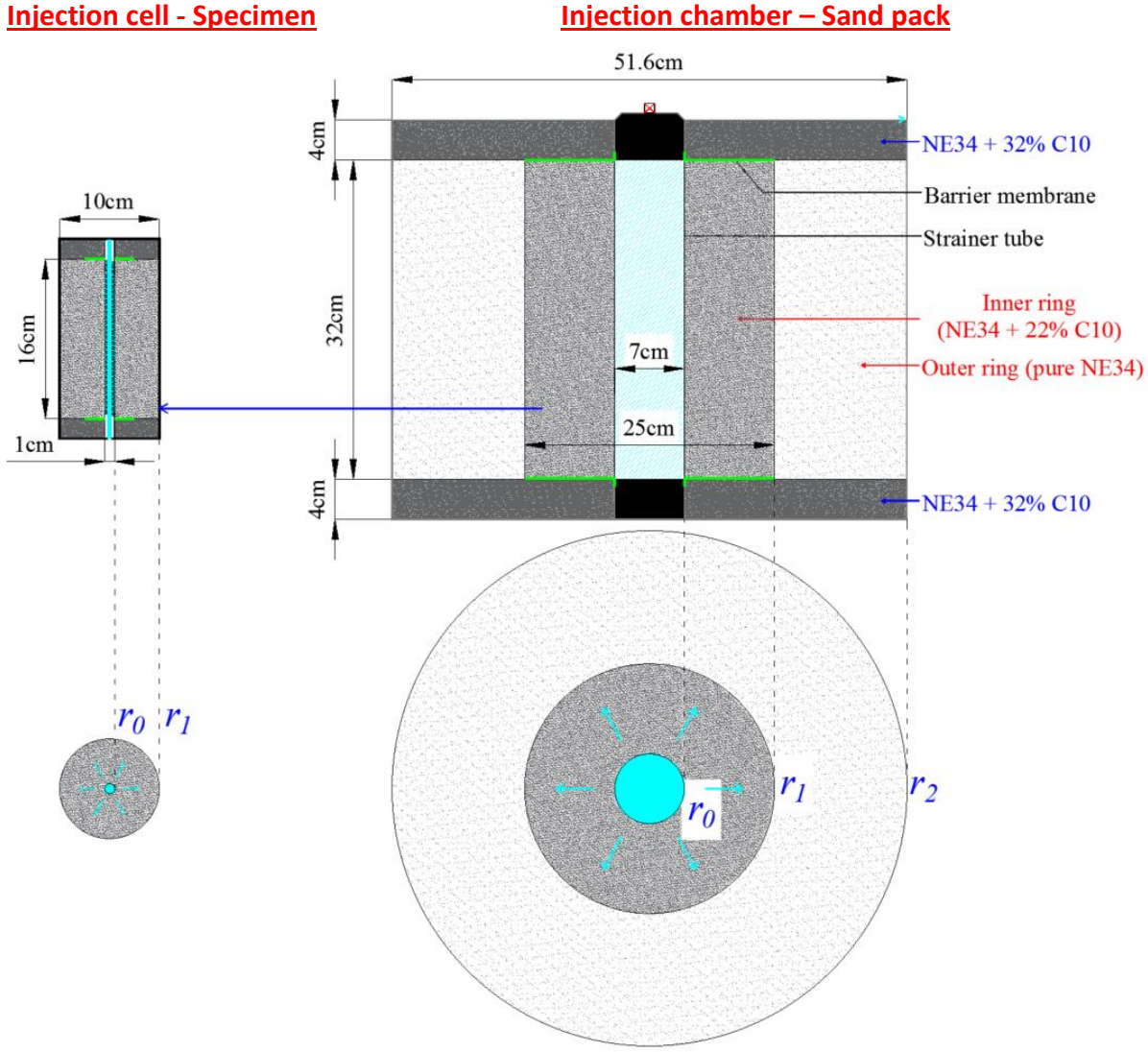

Figure 3.56: Configuration of the specimen/sand pack in the two injection setups.

As the injection height and the radius of these specimens are different, we use the radial flow velocity at the entrance of the specimen ($r = r_0$) denoted by v_{r0} instead of the flow rate q in order to compare these setups. The radial flow velocity v_{r0} is calculated as:

$$v_{r0} = \frac{Q}{2.\pi.r_0.H} \tag{3.4}$$

Note that the further away from the injection tube, the slower the radial velocity, which is inversely proportional to the radius.

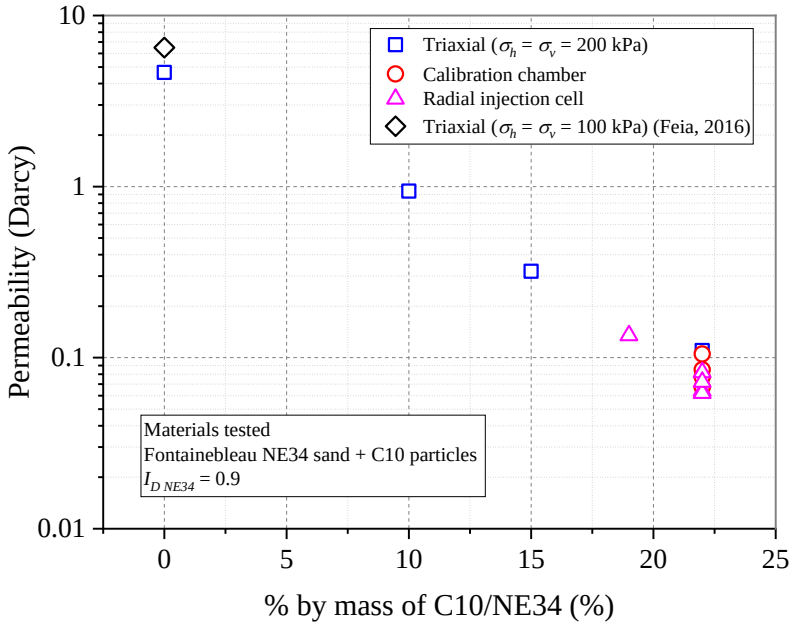

Figure 3.57: Evolution of permeability depending on the percentage by mass of C10 particles to NE34 sand (combining the results of several studies and setups).

Figure 3.58 presents a comparison of the test results obtained in two injection setups under the same applied stresses. When performing under the same stress conditions of 150 kPa in confining pressure and of 450 kPa in axial stress, test N31 in the injection chamber results in a higher fracturing pressure than test P2 in the cell (Figure 3.58a).A similar result is observed in the case of 150 kPa confining pressure (Figure 3.58b). Note that the applied axial stress is different between these tests, however, it is evident that the chamber tests exhibit a higher fracturing pressure than those of the injection cell. For the injection chamber, fracturing occurs at a smaller value of the entrance radial flow velocity than that in the cell (Figure 3.58). This may be a reason why the chamber requires a higher injection pressure to fracture the sand pack. Another reason is that the inner ring of the sand pack is twice as thick as the cell specimen which could also play a role for a higher fracturing pressure in the injection chamber (Figure 3.56).

No matter what stress conditions are, fracturing is observed at about 2.35 of the normalized fracturing pressure (P_{frac}/σ_h) in the radial injection cell and this value is about 4 to 5 in the injection chamber (Figure 3.59).

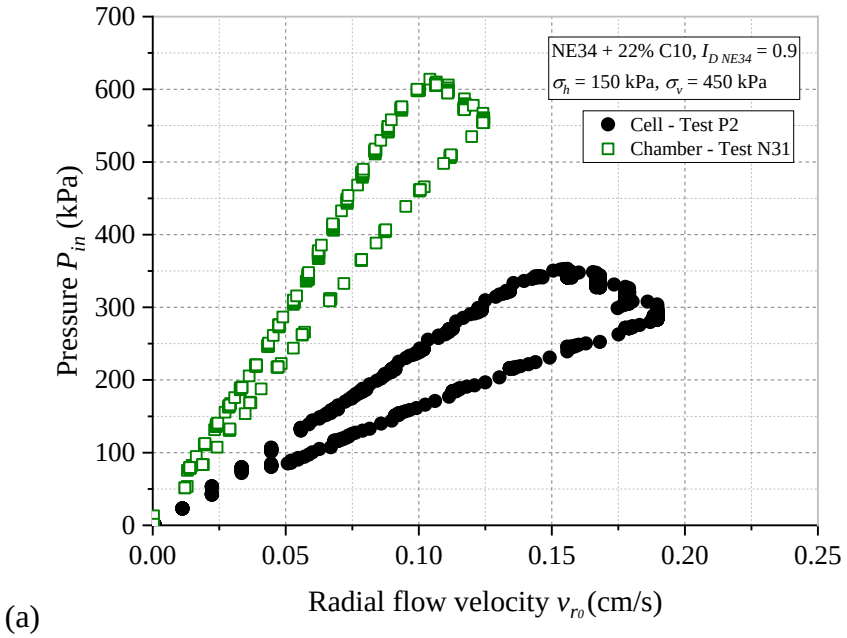

(a)

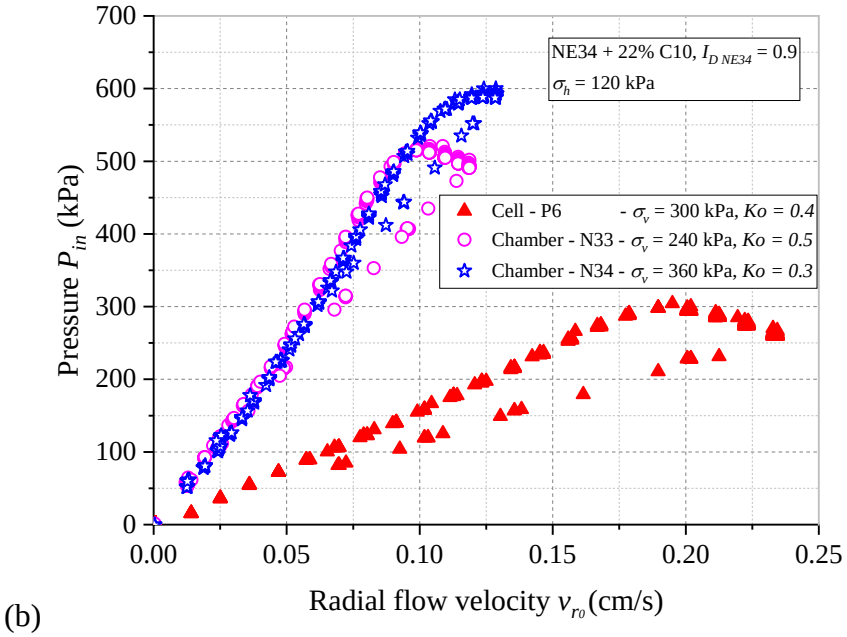

(b)

Figure 3.58: Comparison of the results in terms of injection pressure versus radial flow velocity under the same stress conditions: (a) σ_h = 150 kPa, σ_v = 450 kPa; (b) σ_h = 120 kPa.

When comparing the fracture mophology induced around the injection tube for the two setups, the observation shows a similar fracture pattern with some main vertical fractures propagating relatively perpendicular to the injection tube as shown in Figure 3.60. Small fractures are also induced around the injection tube for both test setups as shown in the sections above, which contributes to the increase of the overall permeability after fracturing as well.

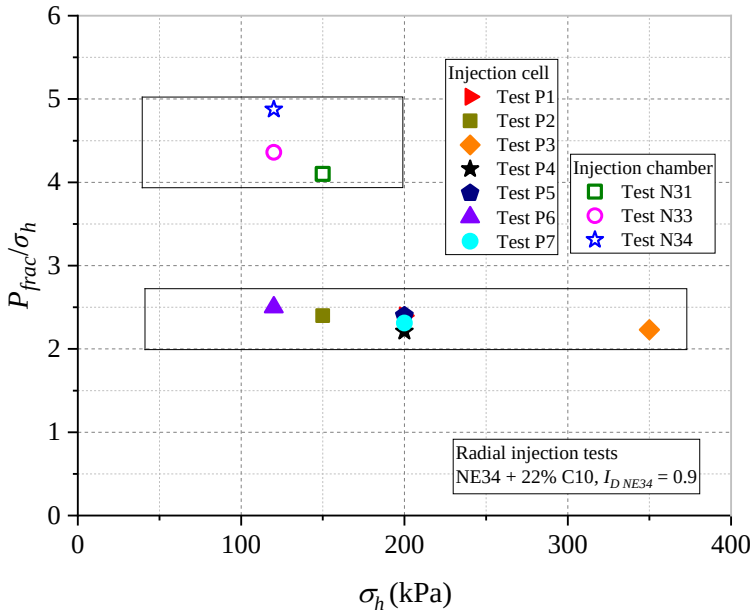

Figure 3.59: Synthesis of the normalized fracturing pressure of tests performed in both setups.

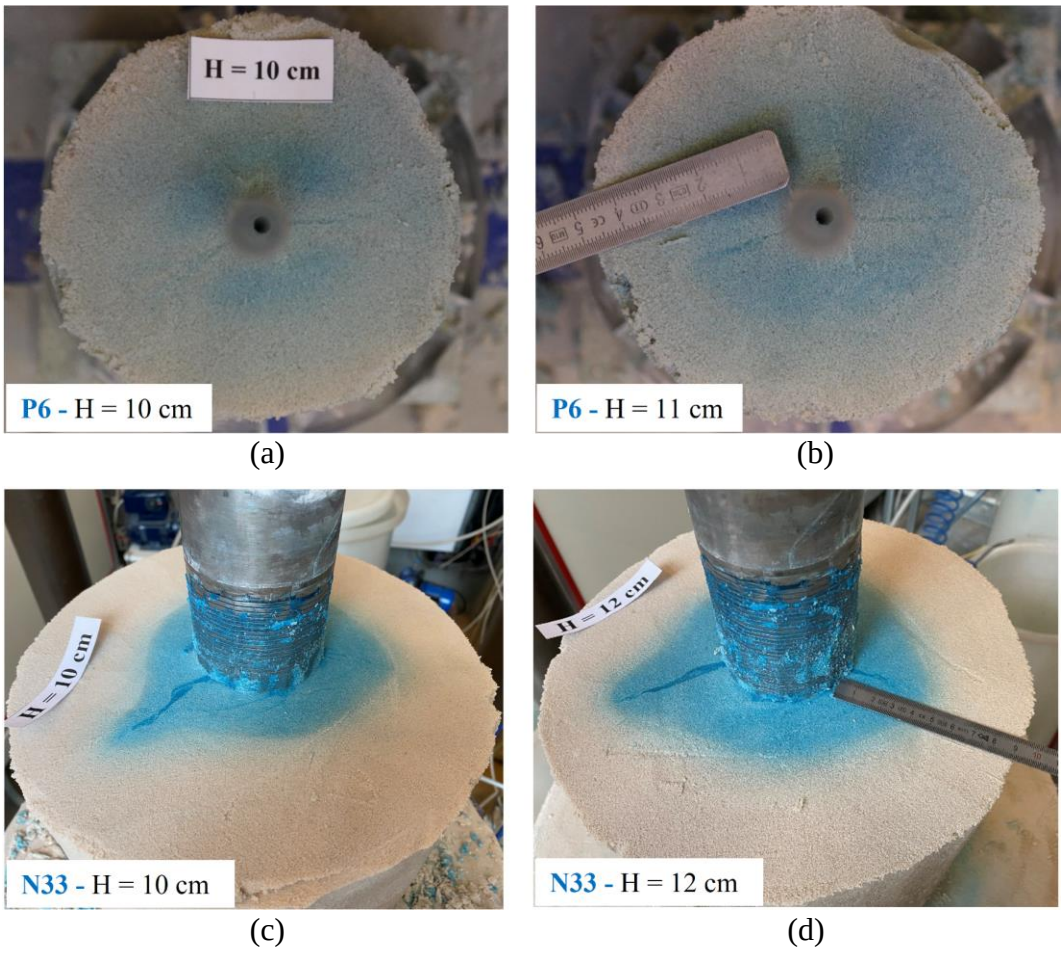

Figure 3.60: Typical fractures induced during the tests under the same confining pressure of 120 kPa: (a), (b) specimen P6 in the injection chamber; (c),(d) sand pack N33 in the injection chamber.

Some important conclusions can be made based on the results of the two series of tests performing on these two setups (i.e., the injection cell and the injection chamber), giving a better understanding of the fracturing mechanisms and of the conditions to reach the fracturing regime in the unconsolidated sand medium. The experimental results in both setups shown that suffusion during the matrix regime results in a decrease of the initial permeability. The transition point (i.e., the step at which the slope of the pressure – flow rate curve starts to decrease) is close to the fracturing point (i.e., the step at which the first pressure drop is observed). A similar fracture pattern and a similar granular structure of the fracture are observed for both setups. One of the biggest difference between these setups is the critical value of the fracturing initiation as expressed as the normalized fracturing pressure (P_{frac}/σ_h). Two main assumptions are proposed to explain this result, which are a lower flow velocity at the entrance and a longer radius of the injection zone. Additional tests with a smaller radius of the inner ring should be performed in the future to validate this assumption. Comparing to the sensitivity study in the radial injection cell, the effect of the stress conditions in the radial injection chamber is less evident because of the limited number of tests and the reduced stress range, in particular for the effect of the stress ratio. More injection tests under higher confining pressures while changing K_0 are needed to better explore the effect of this parameter.

3.7 CONCLUSION

This chapter has presented an extensive experimental investigation of fracturing within the granular medium due to the injection of the high pressurized fluid. The objective of this study was to investigate the condition for the fracture initiation and the mechanisms that can explain the fracturing propagation in unconsolidated sand reservoirs. The effect of various parameters (confining pressure, stress ratio coefficient, flow rate, permeability) have been investigated to encircle the main factors controlling the initiation of the fracturing regime, the restore of the permeability as well as the fracture morphology. Two radial injection setups (the injection cell and the injection chamber) were used during this experimental campaign.

Typical results of two tests, performed in the injection cell and on the injection chamber, have been described. The experiments show a fairly good consistency in terms of the pressure response and the fracture morphology induced around the injection points between these tests. Fracturing occurs when the injection pressure reaches about 2.35 times the confining pressure for the tests in the radial injection cell whereas in the radial chamber, this critical value is much higher and is in the range of 4 to 5 times the confining pressure. This difference may be attributed by a lower radial flow velocity around the injection point when fracturing occurs and by a larger size of the sand pack in the injection chamber as compared to those in the injection cell.

During disassembly, the results show the effectiveness of the mixture of MasterRoc MP320 silica gel and Basacid Bleu 762 for analyzing the change of the inter granular of the induced fractures and for visualizing the flow pattern after fracturing as well. X-ray CT allows to obtain the 3D images of the fractures formed within the specimen in the injection cell and the fractures observed from X-ray CT coincide with those observed during excavation. Fractures appear vertically along the injection tube, which confirms the pressure drops during the fracturing

injection regime. The diffusion of the colored gel is more important in the area containing the fractures, which attests that these fractures favor the flow. The fracturing mechanisms are the coupling between the dilation bands of the sand matrix and the subsequent transport of particles present within these bands to form the preferential paths (fractures) of high porosity around the injection point. This conclusion is validated by the analysis of the cored samples containing fractures using the X-ray CT and the optical microscope observation.

The sensitivity analysis in the radial injection cell indicates that the magnitude of the confining pressure is a main factor affecting the fracturing pressure as well as the increase of the permeability after fracturing. The critical fracturing pressure is mainly controlled by the confining pressure (radial stress) and does not change significantly with the stress ratio K_0. An increase of confining pressure results in a higher critical fracturing pressure, shorter fractures as well as a smaller increase of the overall permeability.

The flow rate has an important impact on the increase of the permeability and the propagation of the fracture during the frac-regime whereas the study of permeability has shown no significant effect on the critical fracturing pressure while changing the specimen initial permeability by changing the concentration of C10 fines. The effect of the several injection cycles on the critical fracturing pressure has also been studied in the injection chamber. A smaller normalized fracturing pressure (P_{frac}/σ_h) is observed for the test in which the sand pack experiences a high injection pressure in the previous stage.

For all tests carried out in the injection cell, the normalized fracturing pressure is about 2.35 ± 0.1 which is relatively twice smaller than that for the tests in radial injection chamber (in a range of 4 to 5), showing an important impact of the specimen size on the critical fracturing pressure. For all tests in both setups, a higher increase of the overall permeability after fracturing always corresponds to the detection of longer and wider fractures around the injection point.

In the next chapter, the experimental study is extended to the injection of water containing suspended particles in order to investigate the effects of transport, deposition and clogging on the fracturing mechanisms.

CHAPTER 4. EXPERIMENTAL RESULTS WITH SUSPENDED PARTICLES IN WATER INJECTION

4.1 INTRODUCTION

The re-injection of produced water is a continuous process during the production of hydrocarbons even when the formation damage occurs and the reservoir permeability gradually decreases due to filter cake formation. Pure water injection or other treatment methods are just temporary solutions in short periods due to the cost efficiency and the environmental impact of discharging produced water into the environment (Mainguy et al., 2020). Therefore, the injection of produced water in the frac-regime could be an option for restoring and maintaining the injectivity of the well.

For this purpose, an experimental protocol has been established where suspended particles are continuously injected into the specimen in two phases. The first one (phase 1 - plugging phase) consists of injecting water containing suspended particles at a low constant flow rate (in matrix regime) to reproduce the formation damage process (internal cake formation), then raising the flow rate until fracturing of the medium (phase 2 – fracturing phase). The suspended particles are still injected in the frac-regime to test the recovery of injectivity.

In this chapter, we present the experimental study with suspended particles injection which was performed in the radial injection cell as well as in the injection chamber.

4.2 EXPERIMENTAL PROGRAM

This study started by a series of preliminary tests to establish and validate the test protocol when injecting water containing suspended particles. The main characteristics of these tests are presented in Table 4.1. They were all performed under the same stress conditions of 200 kPa in confining pressure and 400 kPa in axial stress and the same density index of the sand matrix ($I_{D\ NE34}$ = 0.9). The concentration of particles and the particle size in the injection fluid (water) were firstly chosen according to Feia et al. (2015). C500 silica fines with D_{50} = 4.5 µm were selected as the suspended solids in the injected fluid. The first test was performed with a concentration of suspended particles of 200 mg/l and the fluid was injected in a pure NE34 sand specimen with a permeability of about 6 Darcy. However, this high concentration of the particles in the injected fluid caused plugging of the injection tube. Consequently, the specimen could not be fractured even at a very high injection pressure. Note this concentration is much higher than the one measured in the practice of PWRI (Ochi and Oughanem, 2018). Finally, a low concentration between the range of 10 and 50 mg/l was selected to perform the tests in both setups. The specimens were prepared as a mixture of NE34 + 10% C10 which provide a reasonable injection time when injecting at a low particles concentration.

For the sensitivity analysis in the radial injection cell, four tests have been performed to study the effect of the concentration of suspended particles and of the confining pressure

(Table 4.2) on the formation damage by deposited particles and the fracturing mechanisms of sand specimens as well. The injection protocol consists of first injecting water containing particles at a constant flow rate to partially plug the sand pack specimen (phase 1) and then increasing the flow rate until fracturing of the medium (phase 2).

Table 4.1: Characteristics of the preliminary tests with suspended particles injection in the radial injection cell.

Test	Materials		Fluid		Stress conditions			Injection protocol
	% C10	k (mD)	μ (cP)	% C500 (mg/l)	σ_h (kPa)	σ_v (kPa)	K_0	
Q7	0	≈ 6 x 10^3	1	200	200	400	0.50	Constant flow rate q = 0.3 l/min.
Q11	10	≈ 600	1	50	200	400	0.50	Injecting at a constant q = 0.2 l/min to form an internal damaged specimen.
Q12	10	≈ 600	1	50	200	400	0.50	Injecting at a constant q = 0.2 l/min to reproduce the plugging process, then gradually increase the flow rate until fracturing.
Q13	10	≈ 600	1	10	200	400	0.50	Stage 1: Pure water injection by increasing the flow rate steps up to 2 l/min. Stage 2: Suspended particles injection with the same injection protocol as the stage 1.

Table 4.2: Characteristics of parametric tests in the radial injection cell.

Test	Parameters	Materials		Fluid		Stress conditions			Density index $I_{D\ NE34}$	Injection protocol
		% C10	k (mD)	μ (cP)	% C500 (mg/l)	σ_h (kPa)	σ_v (kPa)	K_0		
SP1 (*)	Effect of particles concentration	10	≈ 600	1	10	200	400	0.50	0.90	- Phase 1 (plugging phase) Injecting at q = 0.2 l/min
SP2		10	≈ 600	1	10	200	400	0.50	0.90	
SP3 (*)		10	≈ 600	1	20	200	400	0.50	0.90	- Phase 2 (fracturing phase) Gradual increasing the flow rate until fracturing of the specimen
SP4 (*)	Effect of the confining pressure	10	≈ 600	1	10	120	240	0.50	0.90	

Note: (*) Scan of X-ray CT

Two tests have also been performed in the radial injection chamber to simulate injection at a larger scale and explore size effects. The test characteristics are similar to the ones realized in the radial injection cell (see Table 4.3). These tests were performed under the same stress conditions (σ_h = 120 kPa, σ_v = 240 kPa), with the same density index of the sand matrix (0.9) as well as the concentration of suspended particles (10 mg/l). The injection protocol was similar to the one in the radial injection cell. The sand pack consisted of a double ring as in the reference configuration: an inner ring of a mixture of NE34 + 10% C10 and an outer ring of the pure NE34 sand. The height of the sand pack for test N37 was chosen twice smaller than the one for test N36 to provide a higher fluid velocity for the same flux rate imposed by the pump.

Table 4.3: Characteristics of the tests with suspended particles injection in the radial injection chamber.

Test	Sand pack	Fluid		Stress conditions			Density index of the matrix
	H (cm)	μ (cP)	% fine C500	σ_h (kPa)	σ_v (kPa)	K_0	$I_{D\ NE34}$
N36	32	1	10 mg/l	120	240	0.50	0.90
N37	16	1	10 mg/l	120	240	0.50	0.90

4.3 PRELIMINARY TESTS FOR DEVELOPING THE INJECTION PROTOCOL

A series of 4 injection tests has been performed (Table 4.1) to develop a new injection protocol for the injection of water containing suspended particles. These tests were carried out at the same stress conditions (σ_h = 200 kPa, σ_v = 400 kPa) and density index of the sand matrix ($I_{D\ NE34}$ = 0.9). These tests are detailed in Appendix F.

The first test called Q7, was performed in a pure sand specimen of 6 Darcy in permeability. Water containing 200 mg/l of particles C500 was injected at a constant flow rate of 0.3 l/min. Two pressure response trends are observed: a gradual increase in pressure up to the confining pressure value followed by an unstable stage of the pressure pulsation (Figure 4.1). The first stage may represent the formation of the internal cake. When injection pressure reached a critical value close to the confining pressure, pressure pulses were observed. Many drops and rises of the injection pressure were identified, however, the injection pressure always tends to increase. This phase may correspond to the formation of the external filter cake. During the disassembling, no fracture has been detected in the specimen whereas the injection tube was completely plugged due to particles deposition (Figure 4.2). An external cake has been also formed at the surface of the sieve. This explains why the injection pressure increased dramatically during injection. Pressure drops are the signs of the breakdown of some plugging areas of the injection tube, which were filled up again right after by the injected suspended particles.

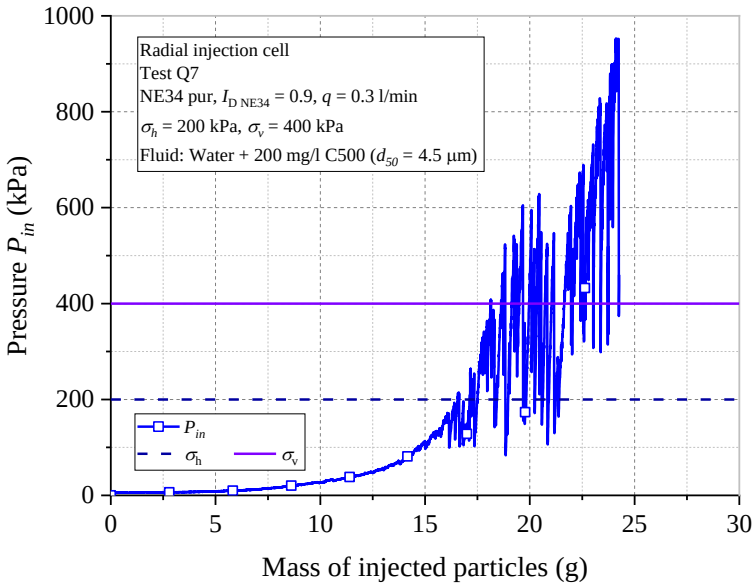

Figure 4.1: Test Q7 – Evolution of the injection pressure versus mass of injected particles.

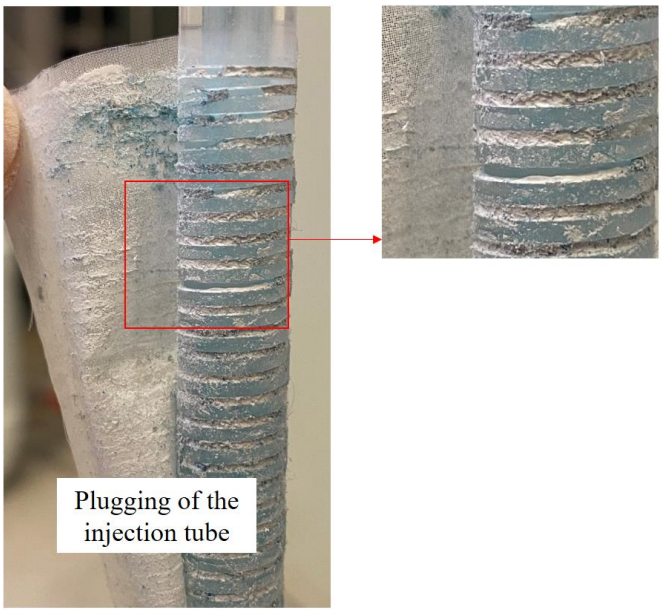

Figure 4.2: Test Q7 - Plugging of the injection tube by deposited particles.

As can be observed on test Q7, fracturing of the specimen could not be achieved because the injection of water at a high concentration of suspended particles and a constant low flow rate leads to the plugging of the tube. Furthermore, water injection with a low concentration of suspended particles can significantly increase the time duration of the whole test. A successful injection protocol should cope with the following objectives:

- Obtain a damaged specimen due to the deposition of injected particles;
- Do not plug the injection tube;
- Fracture the specimen in a reasonable injection time (for practical reasons, a duration of maximum one day for the test is searched);

To do so, the following injection protocol is proposed. Firstly, water containing suspended particles will be injected at a constant flow rate to plug the specimen (phase 1), and then the flow rate is increased quite quickly until fracturing (phase 2). Two tests, called Q11 and Q12, have been performed to validate this protocol. A concentration of 50 mg/l of C500 particles was selected in these tests. The specimen was prepared as a mixture of NE34 sand and 10% of C10 particles, instead of pure sand to decrease the permeability of the specimen and minimize the injection time.

Test Q11 aims at reproducing a damaged specimen due to deposited particles without clogging the injection tube (only phase 1). Injection of the suspension at a constant flow rate leads to an increase of the injection pressure due to progressive clogging of the specimen. The injection rate was maintained constant at 0.2 l/min during 2.5 hours to reach a target pressure of 100 kPa (Figure 4.3). This value corresponds to an apparent permeability of 80 mD which is similar to the initial permeability of the reference specimen containing 22% of C10 particles (see Section 3.4.1). Although it is expected that the internal structure of the obtained partially clogged sample and that of the homogeneous samples used in Chapter 3 are different, we have chosen this reference initial apparent permeability for easier comparison of the fracturing pressures of the various tests.

During disassembling, a small sample was carefully excavated in a zone close to the injection tube and was observed using an optical microscope in order to visualize the profile of deposited particles at the interface between specimen and injection tube. As shown in Figure 4.4, injected particles are captured in the porous medium to form the internal cake, consequently, reducing the overall permeability of the specimen. At this damaged level, the external cake has not been formed yet. The results obtained satisfy the purpose of this test in which a filter cake was formed by deposited particles and the injection tube was not plugged. A more detailed description of this test is given in Appendix F.2.

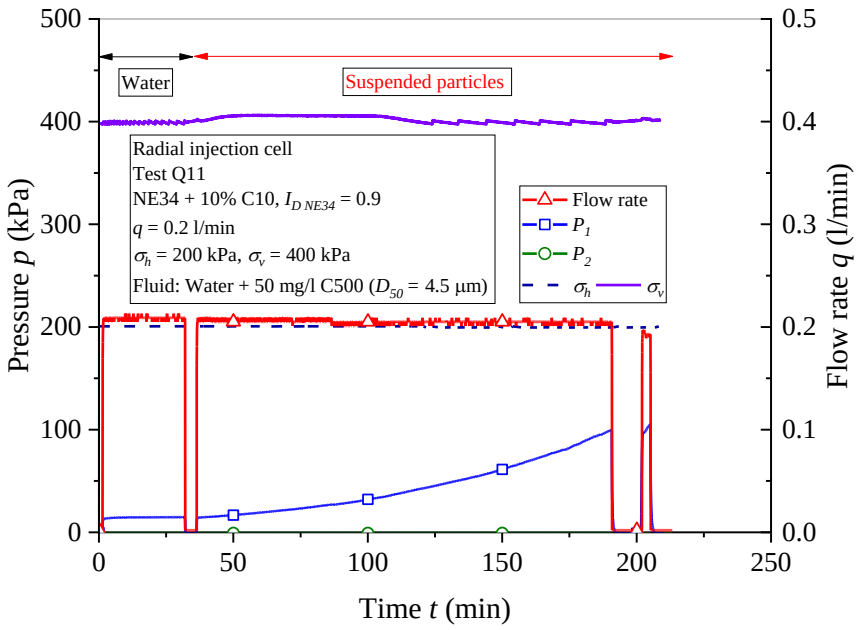

Figure 4.3: Injection results for test Q11.

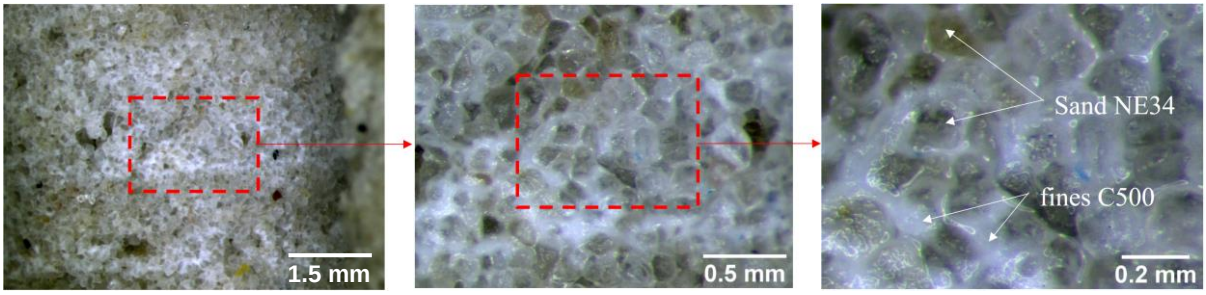

Figure 4.4: Test Q11 - Optical microscope observation of the interface between specimen and 80 µm sieve covered the injection tube.

Test Q12 was performed under the same testing conditions as test Q11. The suspended particles were firstly injected at a constant flow rate of 0.2 l/min until reaching an injection pressure of 100 kPa. Then, the flow rate was increased right after to fracture the specimen. As shown in Figure 4.5a, a very good repeatability of the test was observed during the plugging phase in terms of the overall permeability evolution. Note that the calculation of the apparent permeability is based on the relation between the pressure loss within the specimen ΔP_S and the corresponding flow rate q over time using Darcy's law with an assumption of homogeneity of the specimen as presented in Equation 3.1. However, once the filter cake starts forming within the specimen, calculating permeability as simple as Darcy's law is no longer accurate because of the heterogeneity of the sand structure due to deposited particles. In geo-petroleum studies, a parameter so-called "Injectivity Index (II)" is used to evaluate and monitor the evolution of the injectivity during injection (Bayona and Saudi, 1993; Souilah et al., 2014; Mainguy et al., 2020) which is conventionally defined as the ratio between the injection flow rate q and the applied pressure differential (i.e., pressure loss within the specimen ΔP_s). The evolution of II during tests Q11 and Q12 is also presented in Figure 4.5a. This evolution is proportional to the evolution of the apparent permeability. In this chapter, the apparent permeability will be used instead of II to unify the concept of changing permeability/injectivity used throughout this thesis.

After reaching the target pressure, the flow rate was increased by steps of 0.033 l/min as the test protocol with pure water (Figure 4.5). Some remarkable pressure drops were also identified which are similar to those obtained during test Q7. When excavating, no fracture was detected inside the specimen and the suspended particles filled the helical groove and the open holes of the tube, creating a barrier that impedes the inlet flow (Figure 4.6). This proves that during the phase 2 of increasing the flow rate, the injected particles were captured by the filter cake formed during the phase 1 and then gathered on the tube. In order to avoid this phenomenon, the flow rate should be increased faster to reach the frac-regime.

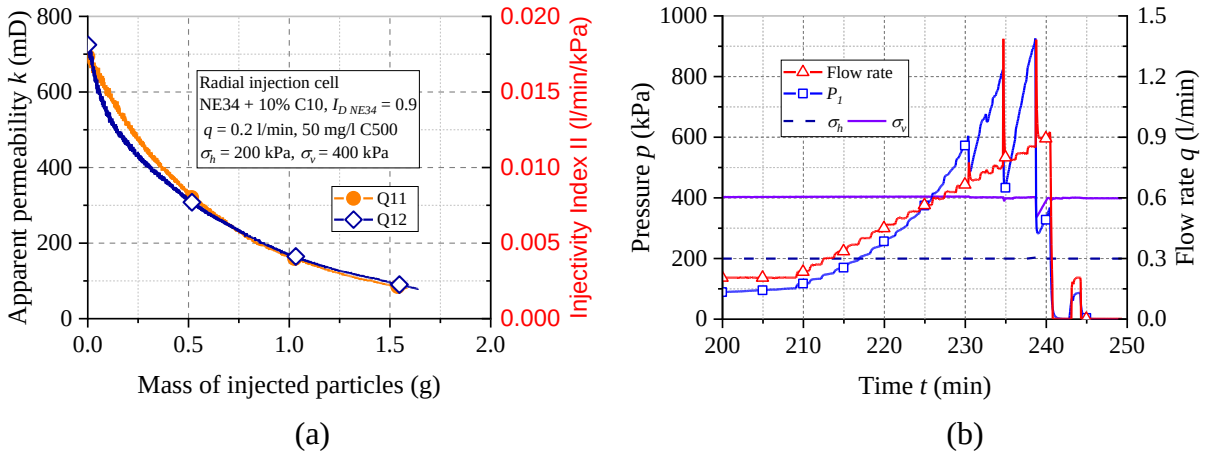

Figure 4.5: Results of test Q12: (a) evolution of the permeability/injectivity index during phase 1 as compared with test Q11; (b) phase 2 when increasing the flow rate.

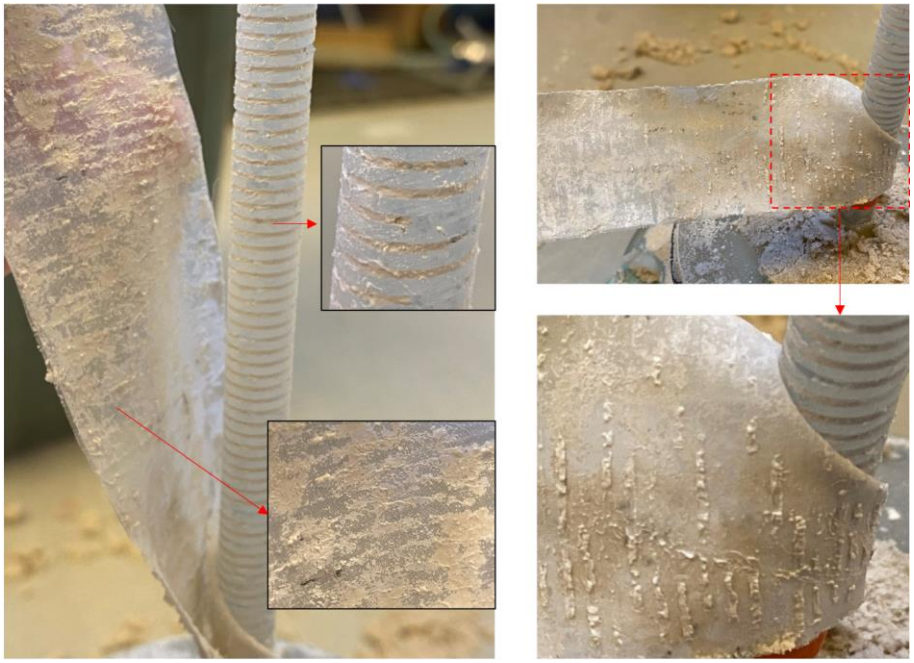

Figure 4.6: Observation of the injection tube post-test Q12.

Another unexpected phenomenon that should be minimized during the experiment is the effect of increasing the pressure in the matrix regime due to suffusion as mentioned in the previous chapter. With the less dense specimen containing a smaller concentration of particles in the mixture, this phenomenon has even a stronger effect as seen in the preliminary test Q13 (see Appendix F.4). Figure 4.7 presents a comparison of two testing particles concentration (10 and 22%). A higher concentration of particles results in a lower rate of suffusion, consequently, a lower decrease of the overall permeability. A similar result has been observed by Bendahmane et al. (2008).

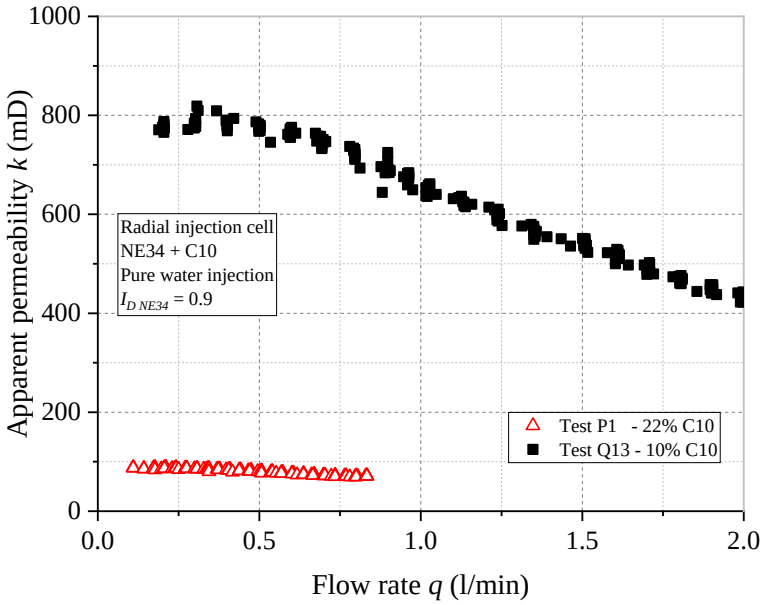

Figure 4.7: Effect of particles concentration present in the specimen on the suffusion rate.

Therefore, during the matrix regime of phase 2, the flow rate will be increased by a higher step of flow rate (0.2 l/min instead of 0.033 l/min) until reaching the first pressure drop. Thus the duration of this phase is reduced which minimizes the effect of suffusion.

As mentioned in test Q13 (see Appendix F.4), in order to minimize the effect of the pressure loss due to the driving lines, a new PVC pipe of the cell of 6 mm in internal diameter was installed, replacing the current PVC pipe of 4 mm, in the subsequent experiments. This diameter selection is based on the calculation of the pressure loss presented in Appendix C and the suitability to the size of the setup.

❖ *Final injection protocol for the scenario of suspended particles injection.*

The various phases of the injection process are illustrated in Figure 4.8. The experiment is performed under controlled flow rate. The plugging process is simulated by first injecting water containing suspended particles at a constant flow rate in the matrix regime to partially plug the sand specimen (Figure 4.8b), then the flow rate is increased rapidly in order to fracture this damaged specimen and to retrieve (partially) the injectivity loss (Figure 4.8c). Suspension is prepared in a 20l water tank (see Section 2.3.2.1) using an efficient mixer to ensure the homogeneity of suspension in water. Figure 4.9 presents a schematic diagram of the injection program with the two injection phases: plugging and fracturing. The final state of the plugging phase (Phase 1) is chosen to provide a reference permeability of 80 mD before starting the fracturing phase. This permits a comparison of the critical fracturing pressure P_{frac} with that obtained in the tests with injection of pure water in a specimen containing 22% of C10 particles as described in Chapter 3. Nevertheless, it is expected that the internal structure of the obtained partially clogged specimen is different from that of a homogeneous specimen prepared with 22% of C10 particles. During the fracturing phase (Phase 2), the flow rate is increased by steps of 0.2 l/min (1.5 minute for each step) until reaching the initiation of the frac-regime which is defined as first sharp pressure drop recorded at the entrance pressure transducer.

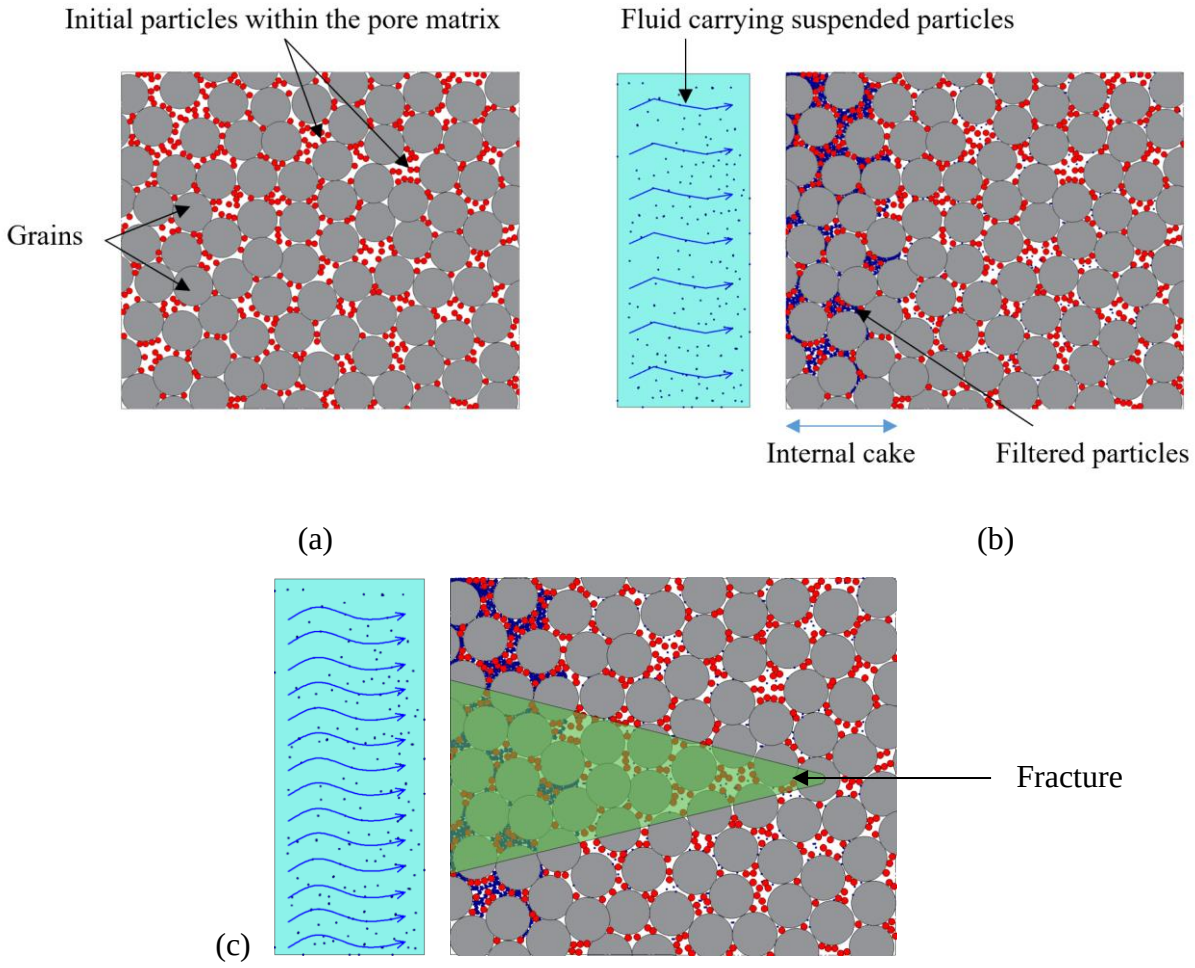

Figure 4.8: Various phases of the injection process: (a) initial state of the specimen; (b) plugging of the medium due to the deposition of suspended particles; (c) fracturing of the clogged specimen under high injection pressure.

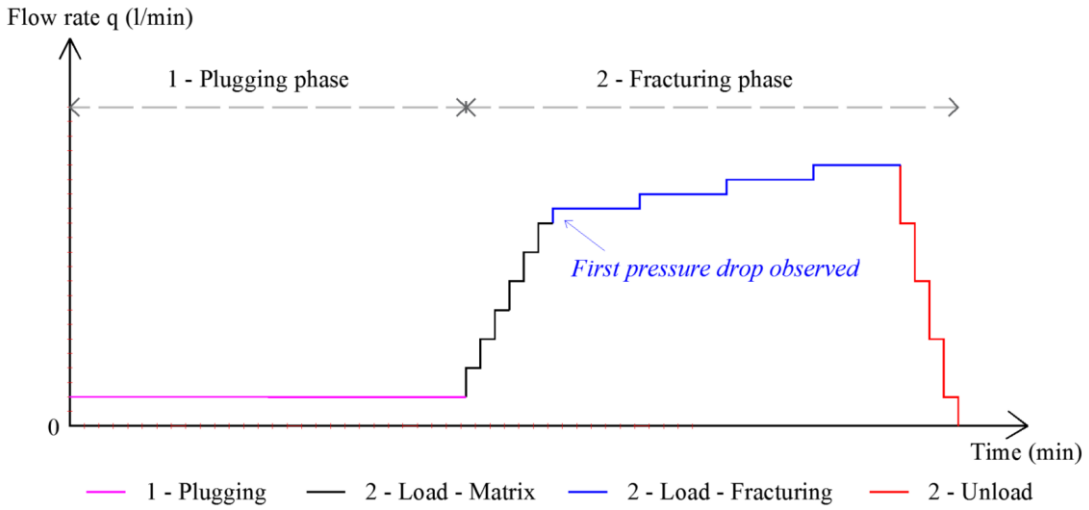

Figure 4.9: Scheme of the injection program with two injection phases: plugging and fracturing.

Four injection steps (10 minutes for each step) are carried out in the frac-regime with the same increasing magnitude of the flow rate of 0.033 l/min as the cell tests performed in Section 3.4 in order to compare the increase of the permeability obtained in different injection scenarios. The injection steps in the frac-regime last longer than those in the matrix regime to track the evolution of the injection pressure after a sudden drop. At the end of the injection, a bleu dye (Basacid® Blue 762) is injected from the central tube to visualize the flow pattern within the specimen after fracturing.

4.4 EXPERIMENTAL RESULTS IN THE RADIAL INJECTION CELL

4.4.1 Typical test results

4.4.1.1 *Suspended particles injection*

Figure 4.10 presents the results during injection for the typical test SP1. Pure water was initially injected at 0.2 l/min to measure the initial permeability of the specimen (Figure 4.10b). The measured pressure P_1 stabilized quickly at a value of 13 kPa, corresponding to an initial permeability of 670 mD. The suspended particles were injected in two phases: (1) plugging and (2) fracturing. The first one was performed at a constant flow rate of 0.2 l/min for about 6 hours until the injection fracture reached 100 kPa (Figure 4.10c). The choice of this value was based on two arguments: having a similar apparent permeability as the initial permeability of the reference specimen (22% C10) and assuring that the plugging of the injection tube does not occur at the end of phase 1.

Figure 4.11 presents the results obtained during phase 2. The fracturing state (i.e., the first pressure drop) was identified at a flow rate Q_{frac} of 2.23 l/min and a pressure P_{frac} of 706 kPa (3.5 σ_h). Injection was carried out with three more steps of 10 minutes each corresponding to a flow rate of 2.26, 2.29 and 2.33 l/min (maximum pump capacity) before decreasing the injection flow rate to zero. Figure 4.12a presents the evolution of the injection pressure and the overall permeability versus flow rate. At a constant flow rate of 0.2 l/min, we observe a progressive increase of the pressure up to 100 kPa (plugging phase). Then, when increasing the flow rate, a quasi-proportional increase of the injection pressure is observed. A lower slope of pressure – flow rate curve during unloading indicates an increase of the overall permeability after fracturing. However, the permeability is only slightly increased as compared to the permeability loss during the plugging phase (Figure 4.12b).

To estimate the gain in permeability, denoted by g, the average values of the permeability between the matrix regime of the phase 2 $k_{av,mat}$ and at the end of the test $k_{av,unload}$ (when the flow rate is decreased) are compared based on the linear fit of the pressure – flow rate curve:

$$g = (k_{av,unload} / k_{av,mat} - 1) \text{ x } 100 \text{ (\%)} \qquad (4.1)$$

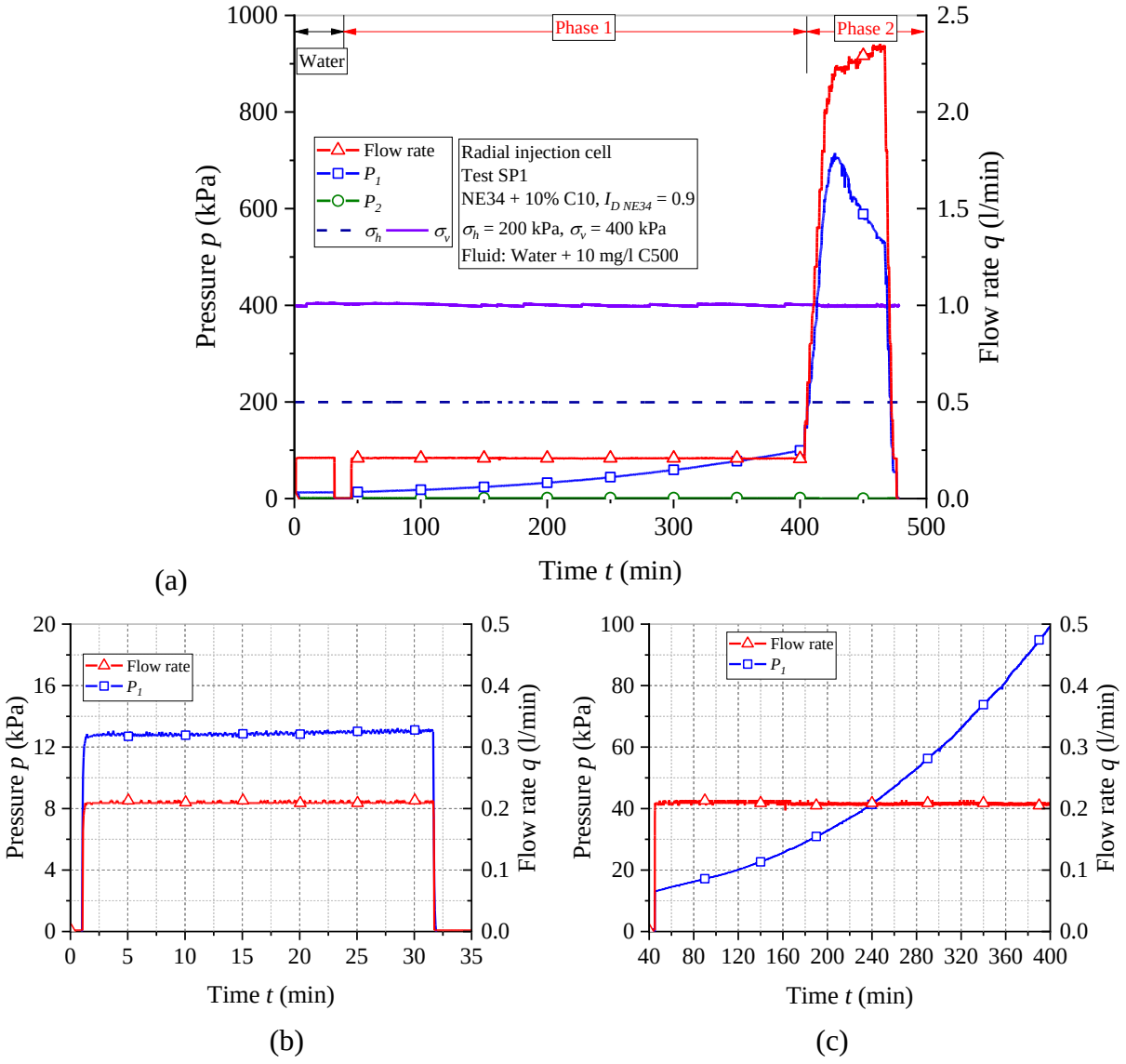

Figure 4.10: Results of typical test SP1 : (a) evolution of pressure and flow rate versus time; (b) initial pure water injection step; (c) phase 1 of suspended particles injection at a constant flow rate of 0.2 l/min.

For test SP1, fracturing of the medium permits a gain of 41% of the overall permeability. Figure 4.13 presents the accumulative mass of the injected particles during injection. About 0.75g of C500 injected during the plugging phase leads to a loss of 87% of the permeability. During the frac-regime, more suspended particles (about 0.9g) were injected than during the plugging phase. However, these particles did not cause a decrease of the permeability. This is mainly because of the high flow rate and of the occurrence of fractures, allowing the particles to penetrate into the medium without any further deposition on the filter cake. This observation confirms the effectiveness of the injection of produced water in the fracturing regime, even if a filter cake has been formed at the wellbore.

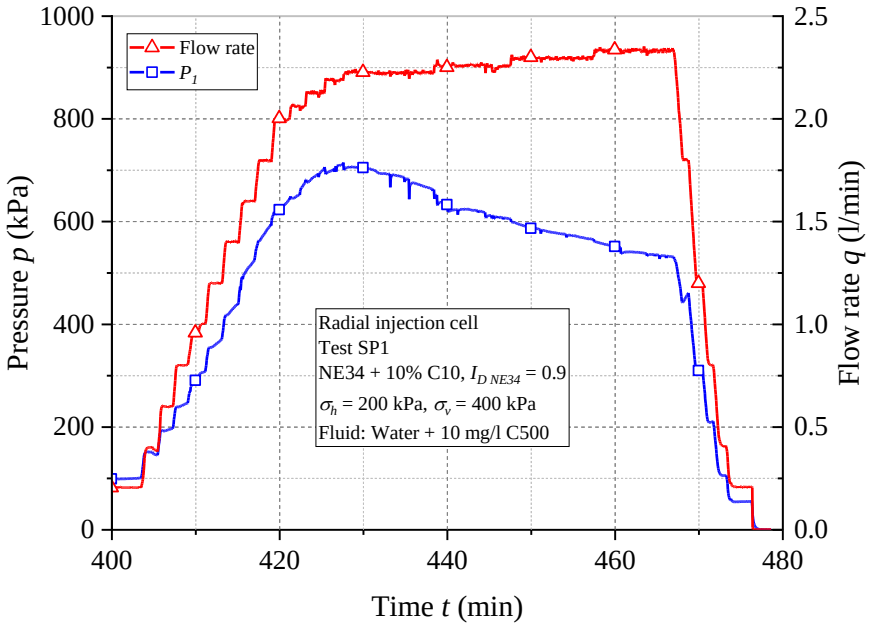

Figure 4.11: Evolution of pressure and flow rate versus time during phase 2 (Test SP1).

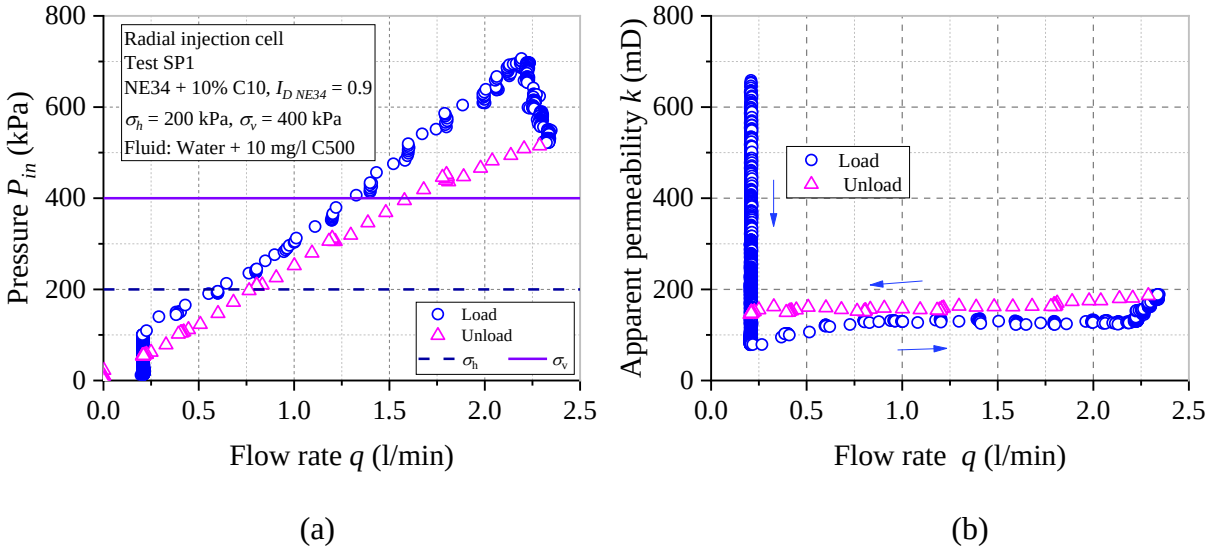

Figure 4.12: (a) evolution of pressure; (b) apparent permeability over time (Test SP1).

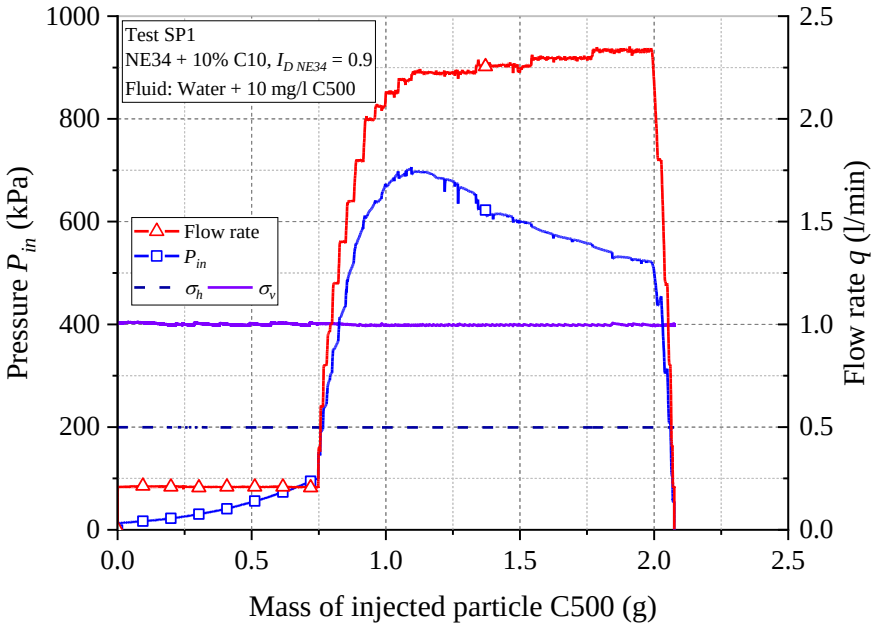

Figure 4.13: Mass of injected particles over time (Test SP1).

4.4.1.2 *Disassembling phase*

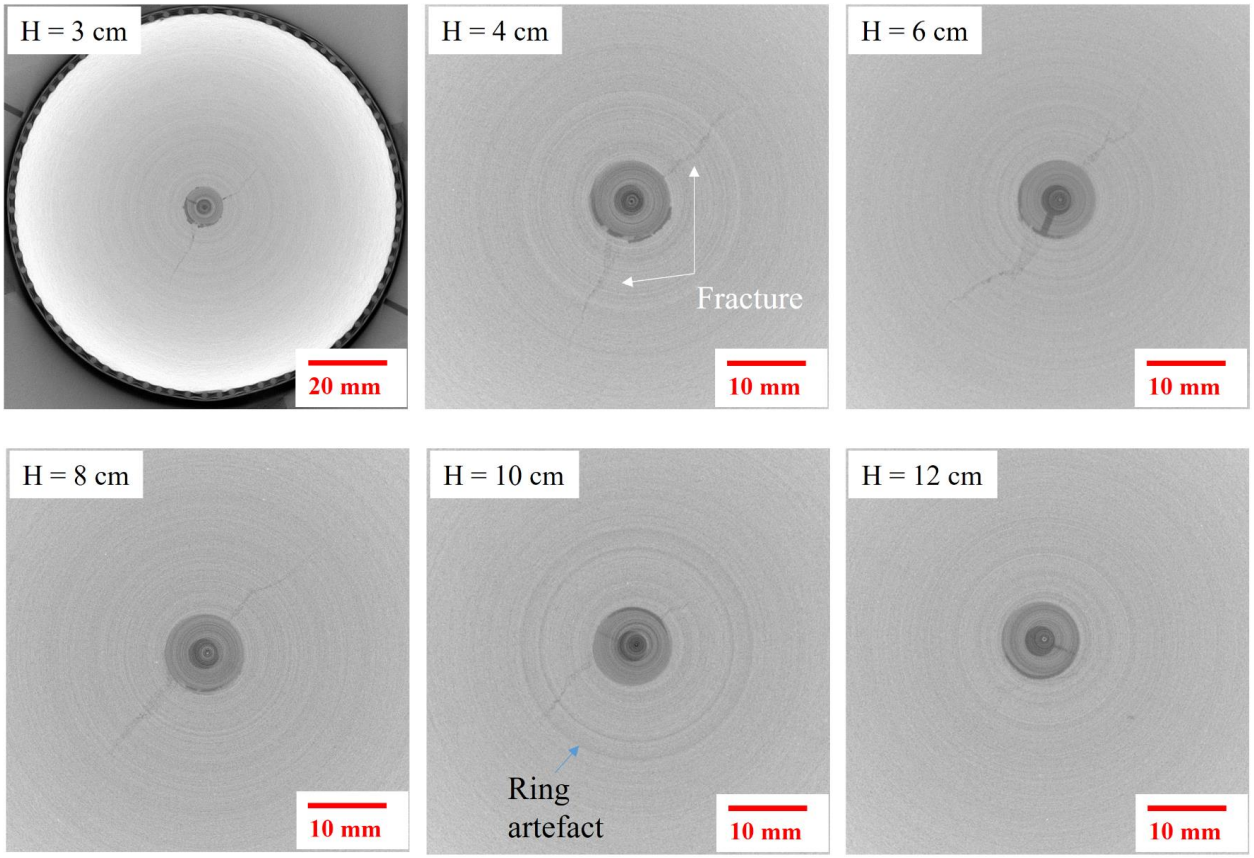

Figure 4.14: Typical X-ray CT images at different heights within specimen SP1.

At the end of the injection phase, a small volume of a mixture of water and 0.2% blue Basacid was injected to visualize the flow pattern within the specimen. Before excavating, the specimen was scanned using X-ray CT. As shown in Figure 4.14, two vertical fractures were detected near the injection tube in the upper part of the specimen (from H = 2 to H = 10 cm). These fractures are short and tortuous. To display a 3D view of fractures, image processing was applied to the scanning images. This process was presented above in Section 3.4.1. The 3D views of two typical sections containing fractures are shown in Figure 4.15. From the front view of fractures, we see that these fractures are quite curvy in the vertical direction.

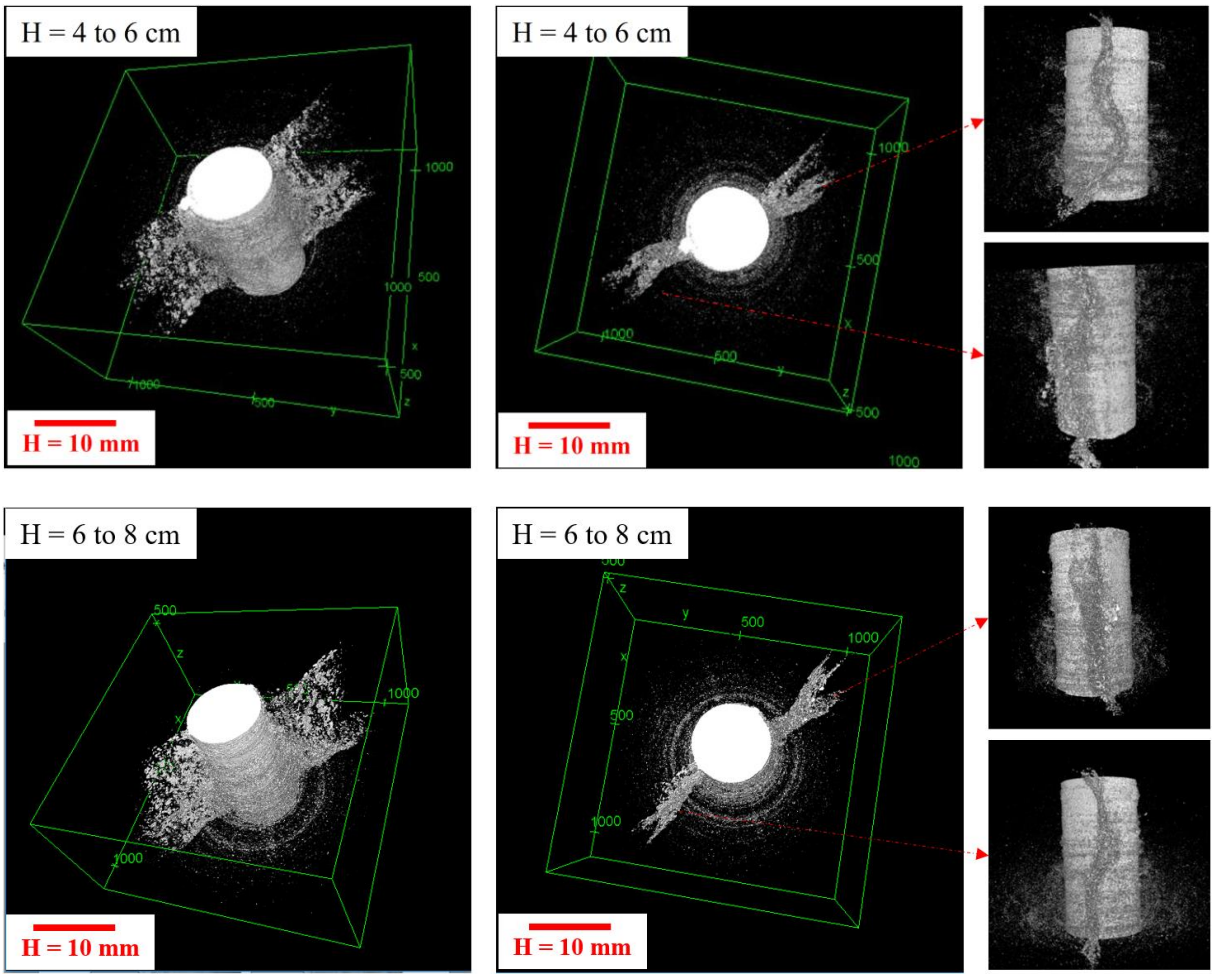

Figure 4.15: 3D views of fractures developped along two different sections of specimen SP1: from H = 4 to 6 cm and from H = 6 to 8 cm.

Figure 4.16 shows some photos of the specimen when removing the drainage system and the latex membrane. The invasion of the injected blue dye is observed only in the upper part which indicates that a higher flow occurs in this area. The fractures observed during excavation coincide with those detected in the images of the scanned specimen (Figure 4.17 and Figure 4.18).

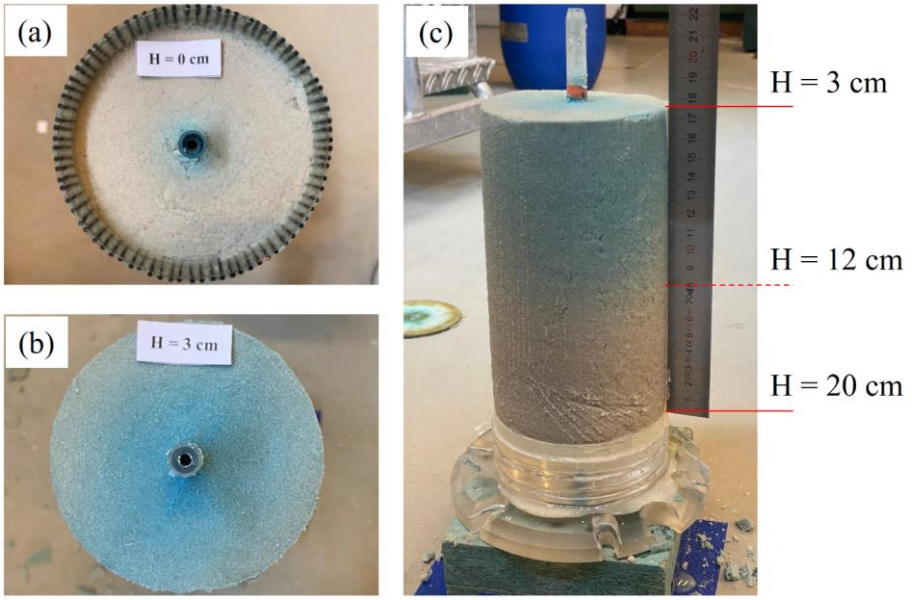

Figure 4.16: (a) upper surface of the low permeability layer; (b) horizontal cross-section at H = 3 cm; (c) view of specimen SP1.

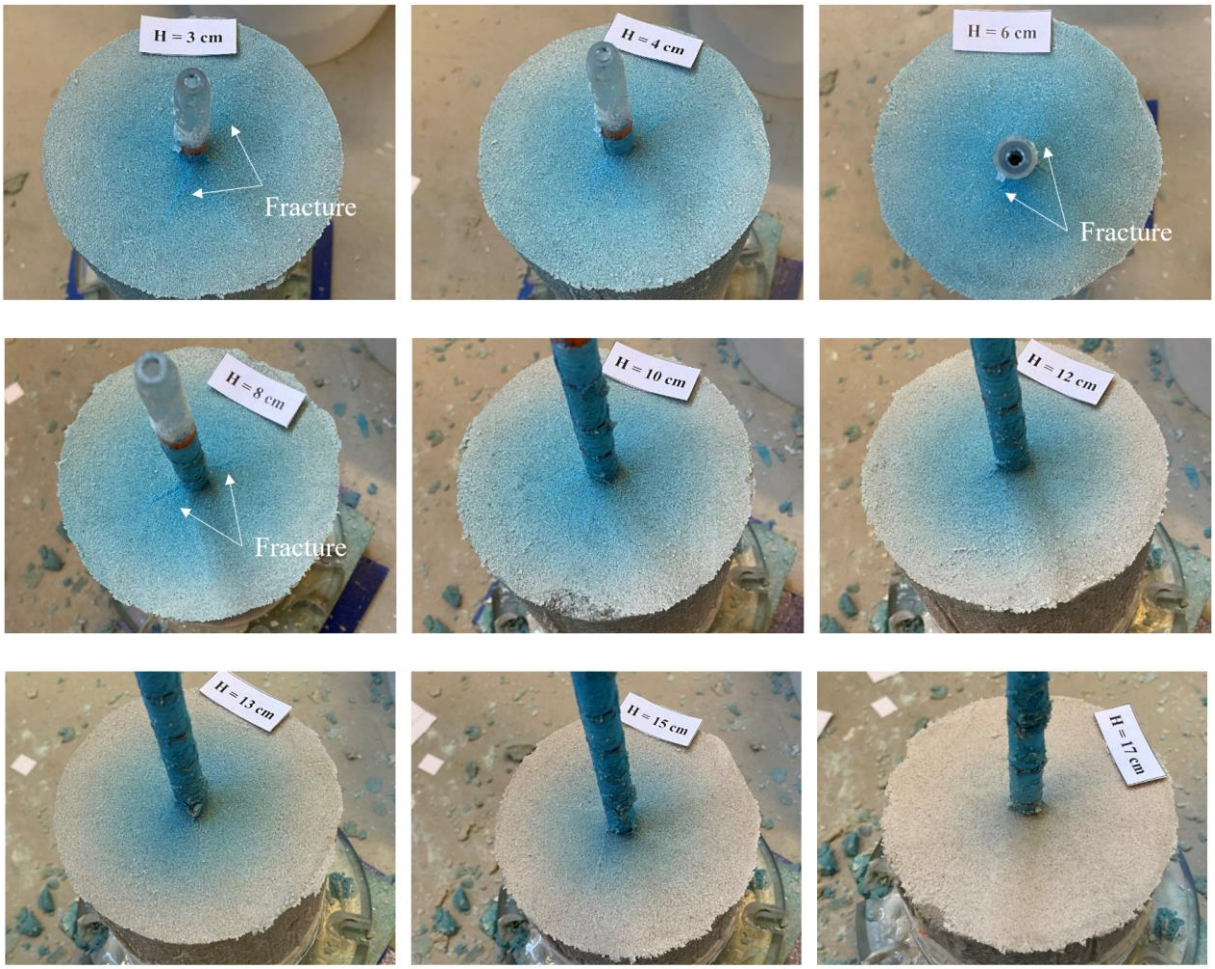

Figure 4.17: Photos of the horizontal cross-section at the different heights during excavation of specimen SP1.

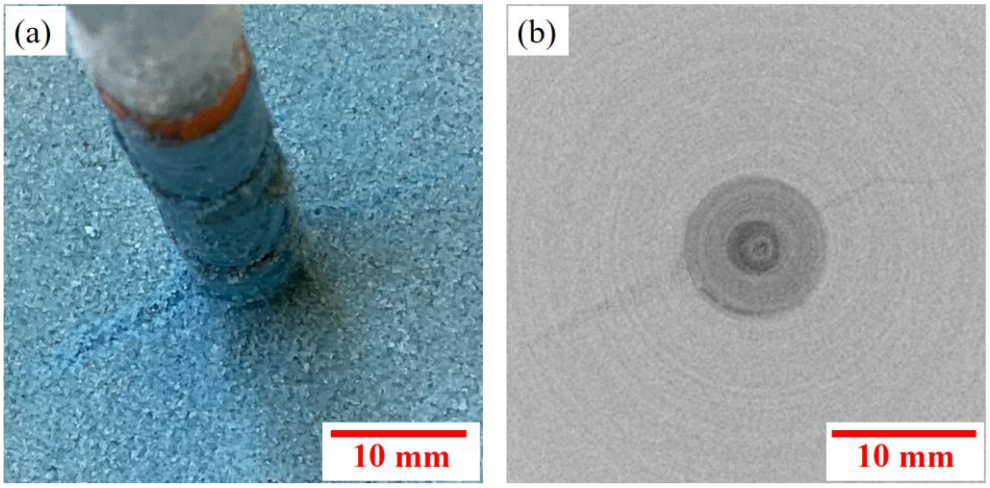

Figure 4.18: Observation of the fracture at H = 8 cm from (a) excavation and (b) X-ray scanning image (specimen SP1)

When removing the 80 µm sieve, we observed the deposition of particles at the sieve surface (external cake formation) (Figure 4.19) which contributes to the decrease of overall permeability during phase 1. Note that 2.1 g of particles has been injected during this test in which 0.75 g was injected in the first phase (plugging phase) and the rest was injected during phase 2.

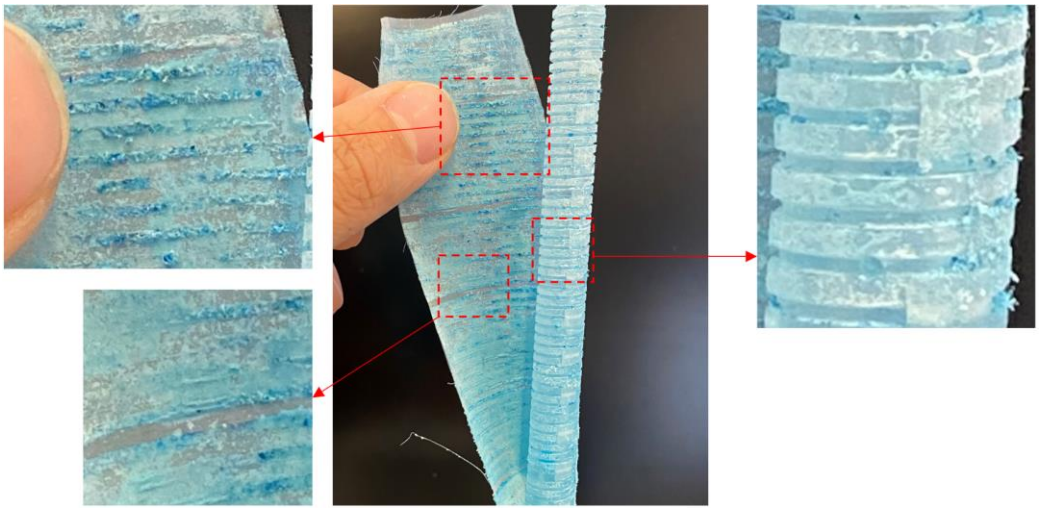

Figure 4.19: Observation of the injection tube of specimen SP1.

4.4.2 Parametric study

4.4.2.1 *Test repeatability*

For every new experimental protocol, it is always important to evaluate the repeatability of the test. To do so, a test called SP2 has been performed under the same testing conditions as the typical test. Figure 4.20 shows a comparison of these tests during the plugging phase in terms of pressure and apparent permeability evolution. This phase was carried out at Q = 0.2 l/min. A

slight difference of the initial permeability was observed, depending on the initial structure of the mixture of NE34 sand and C10 particles (Figure 4.20). We also observe that test SP1 exhibited a faster increase of the inlet injection pressure, corresponding to a faster decrease of the overall permeability. It was mainly due to the complexity of the deposition, transport and rearrangement of particles during injection.

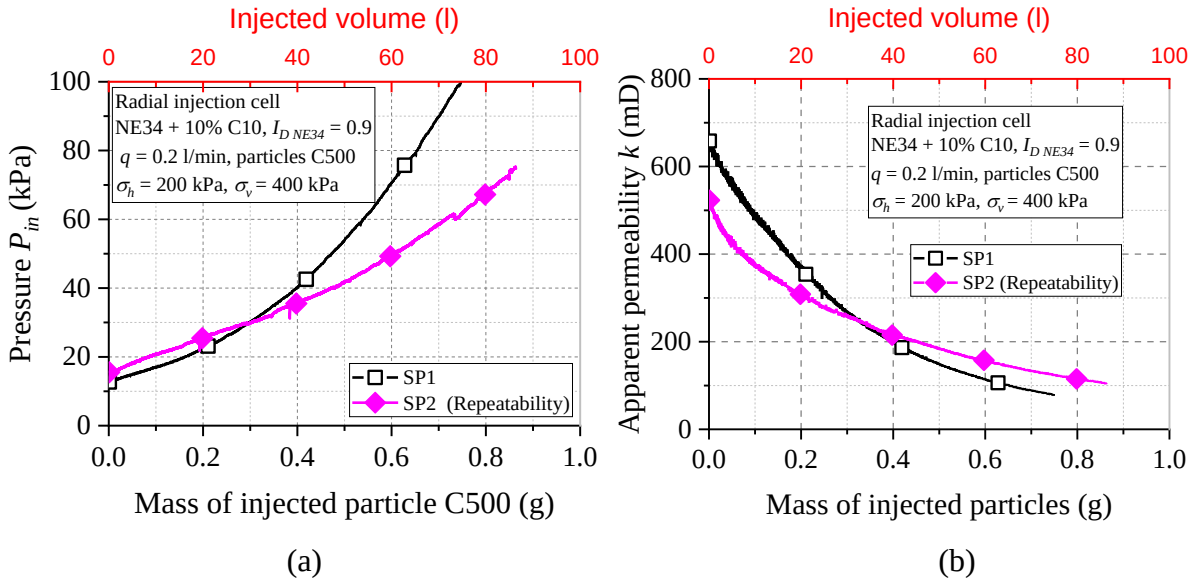

Figure 4.20: Repeatability tests during the plugging phase:(a) evolution of the injection pressure (b) apparent permeability.

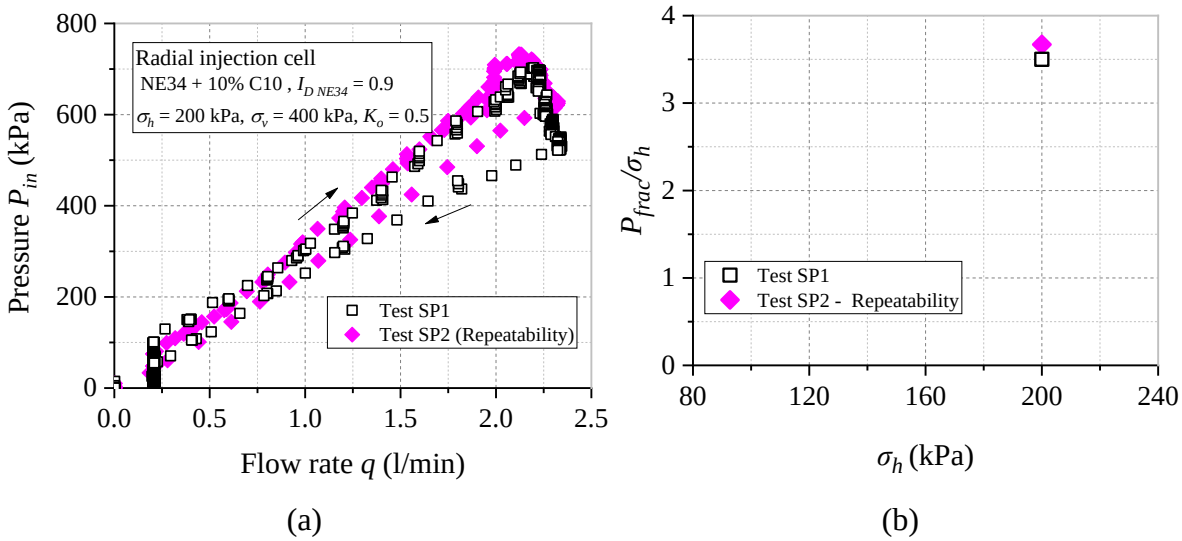

Figure 4.21: Repeatability tests during fracturing phase: (a) pressure – flow rate curve; (b) normalized fracturing pressure (P_{frac}/σ_h).

As the typical test, the flow rate was gradually increased by steps of 0.2 l/min until fracturing occured. A fairly good repeatability in terms of pressure – flow rate curve is observed (Figure 4.21a). In these tests, fracturing initiates when the injection pressure reached about 3.5 times the confining pressure (Figure 4.21b). During the further fracturing steps, test SP1 shows a stronger drop of the injection pressure as compared to SP2 – repeatability, which indicates a

slightly higher increase of the overall permeability after fracturing for SP1 (a gain of 41% for SP1 as compared to 22.5% for repeatability test SP2).

4.4.2.2 *Effect of suspended particles concentration*

In this part, we first evaluate the impact of suspended particles concentration on the plugging phase and then, we discuss the effect of this parameter on the fracturing process.

a. Plugging phase

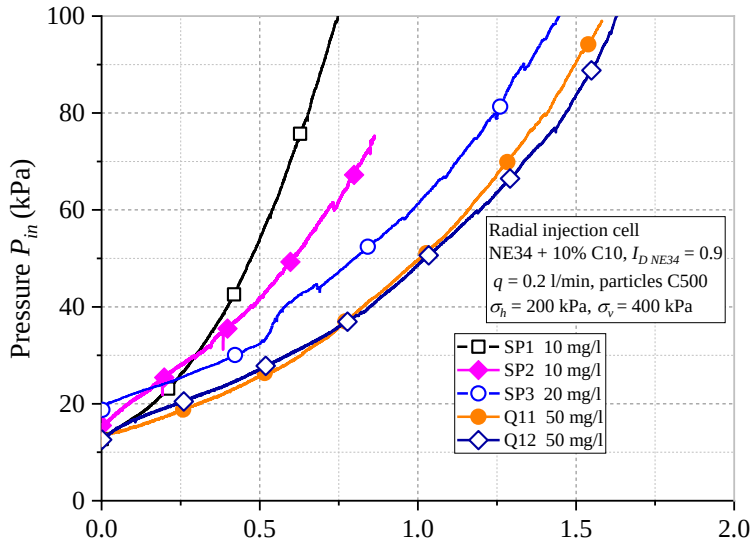

(a)

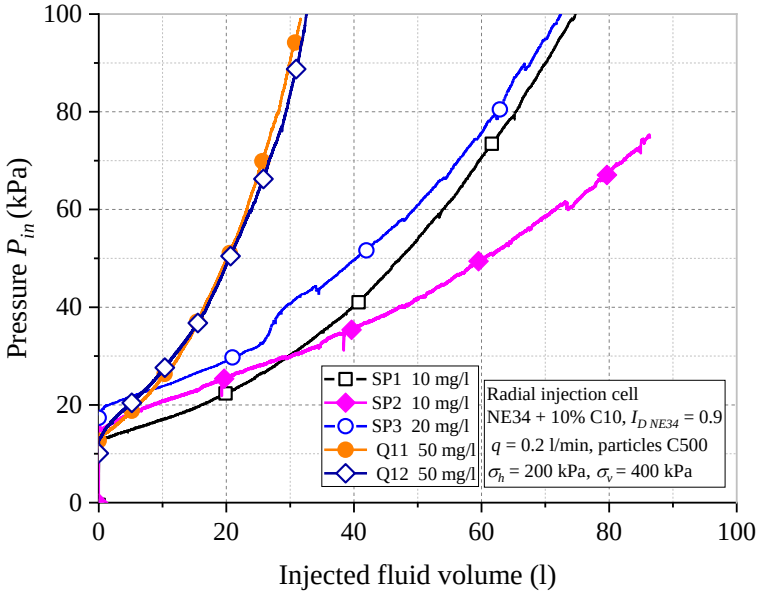

(b)

Figure 4.22: Effect of the particles concentration on the plugging damage: (a) injection pressure versus mass of injected particles; (b) injection pressure versus injected fluid volume.

Five tests have been performed under the same testing conditions while changing only the concentration of suspended particles in the injected fluid (10, 20 and 50 mg/l). These specimens contained a mixture of NE34 sand and 10% of C10 particles, compacting at a density index of the sand matrix of 0.9. The stress conditions are 200 kPa in confining pressure and 400 kPa in axial stress. The injection was maintained constant at 0.2 l/min until the injection pressure reached a target value of 100 kPa. The results in terms of injection pressure versus injected particles mass are shown in Figure 4.22a. We observe that the increase of injection pressure is more pronounced (in terms of the quantity of injected particles) with a lower concentration of suspended particles. Similar results have been obtained by Feia et al. (2015) when studying the effect of particles concentration (Figure 4.23) on permeability impairment of a sand sample under axial injection flow. However, when plotting the results in terms of pressure versus injected volume, it is observed that a higher concentration results in a faster increase of the injection pressure, and consequently, a faster decrease of the overall permeability. Similar results were also obtained by Ochi and Oughanem (2018). Following Feia et al., 2015, this could be explained by the fact that, at a relatively low injection rate, when injecting at a lower particles concentration, the particles have time to be deposited on sand grains with little re-entrainment, therefore less deposited particles are needed to plug the medium. On the other hand, because of the lower concentration, a larger volume of the injected fluid is needed to provide enough deposited particles.

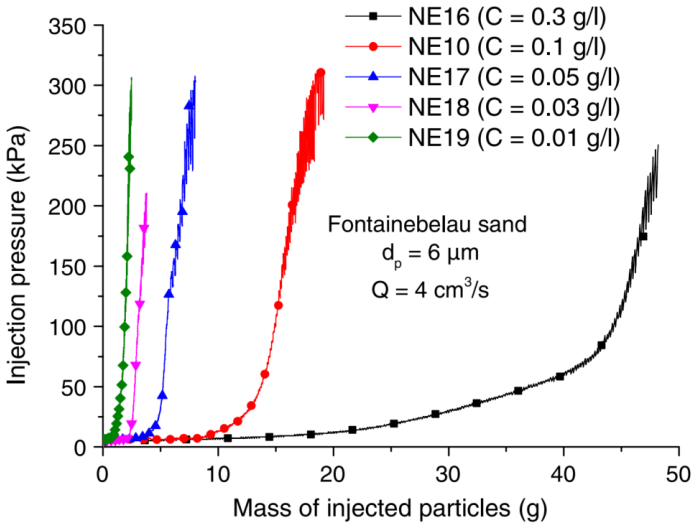

Figure 4.23: Effect of the particles concentration on the plugging damage (Feia et al., 2015)

b. Fracturing phase

Changing the particles concentration may affect the formation of filter cake during the plugging phase. Therefore, it may give different structures of the clogging zone, especially, around the injection point. To investigate the effect of this parameter on the fracturing process, three different concentrations have been tested (10, 20 and 50 mg/l). However, test Q12 with 50 mg/l of particles did not generate fractures, although the maximum measured pressure

reached 4.6 times the confining pressure, due to the plugging of the injection tube. Therefore, we compare the results obtained in the tests with a concentration of 10 and 20 mg/l (Figure 4.24). Il can be observed that the particles concentration, within the range tested, has no significant effect on the critical fracturing pressure (Figure 4.24b). Fracturing occured when the injection pressure reached about 3.45 to 3.65 times the confining pressure. Due to a sudden stop of the pump at the end of injection, test SP13 (20 mg/l) was performed with only 3 steps in frac-regime (Figure 4.25a), thus the increase of the apparent permeability is smaller than for the two other tests with 10 mg/l.

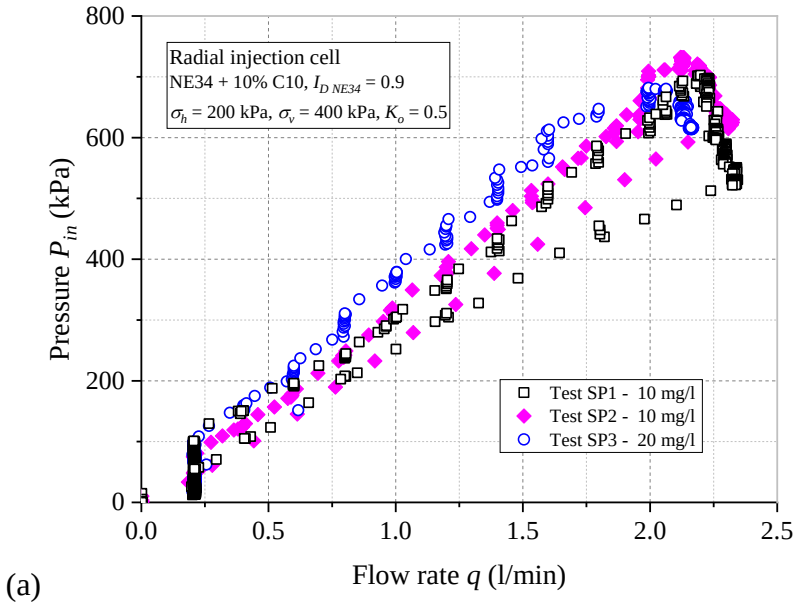

(a)

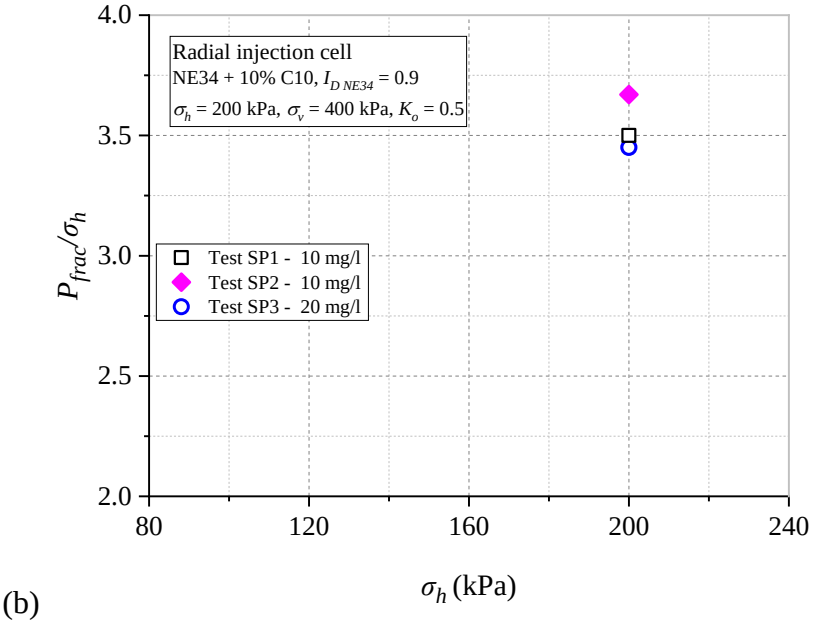

(b)

Figure 4.24: Effect of the particles concentration on the fracturing response: (a) injection pressure versus flow rate; (b) normalized fracturing pressure (P_{frac}/σ_h).

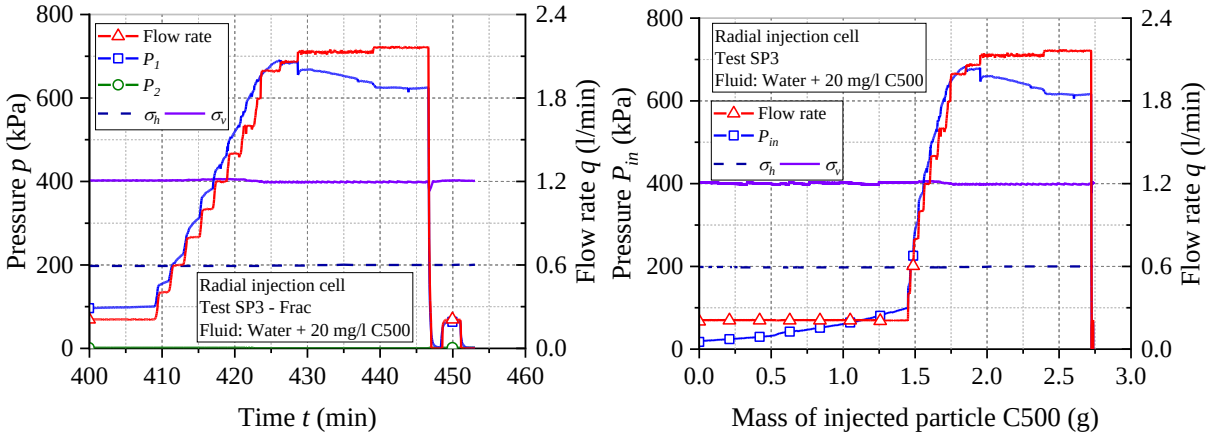

Figure 4.25: Results obtained for test SP3: (a) pressure evolution during phase 2; (b) pressure and flow rate versus the particles mass during the test.

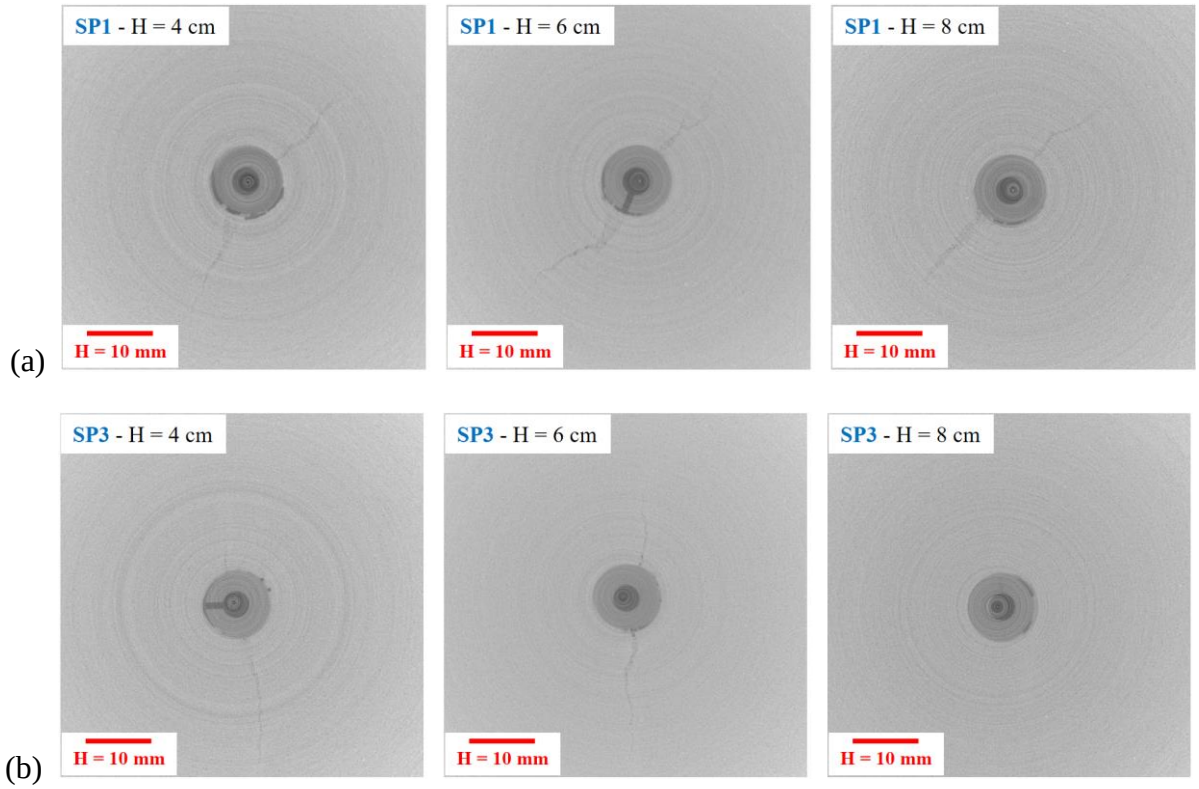

Figure 4.26: Typical X-Ray CT images at different heights of the specimens: (a) SP1; (b) SP3.

In test SP3 (20 mg/l), fractures were generated only in the upper part of the injection zone from H = 2 cm to H = 8 cm (Figure 4.26b). Comparing to the typical test SP1 (10 mg/l), this fracturing zone is shorter and the fractures' width is smaller (Figure 4.26). This observation can explain the smaller increase of the overall permeability after fracturing during test SP3.

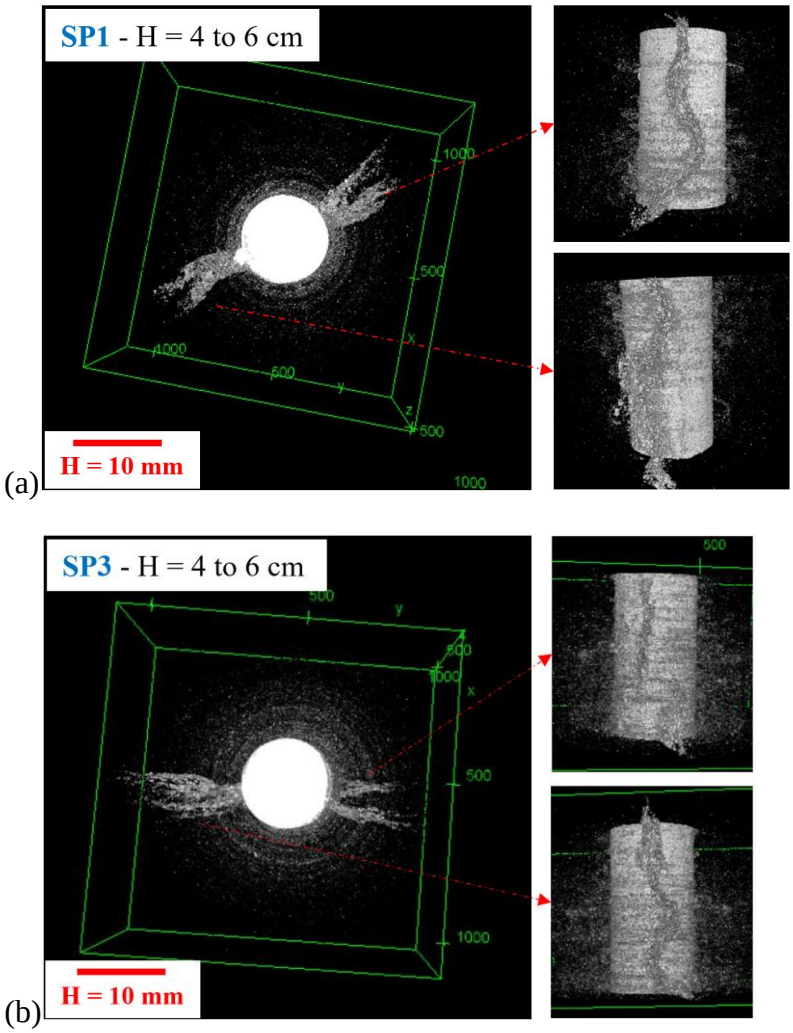

Figure 4.27: 3D views of the fractures developped along a section between H = 4 cm and H = 6 cm post-tests: (a) SP1 and (b) SP3.

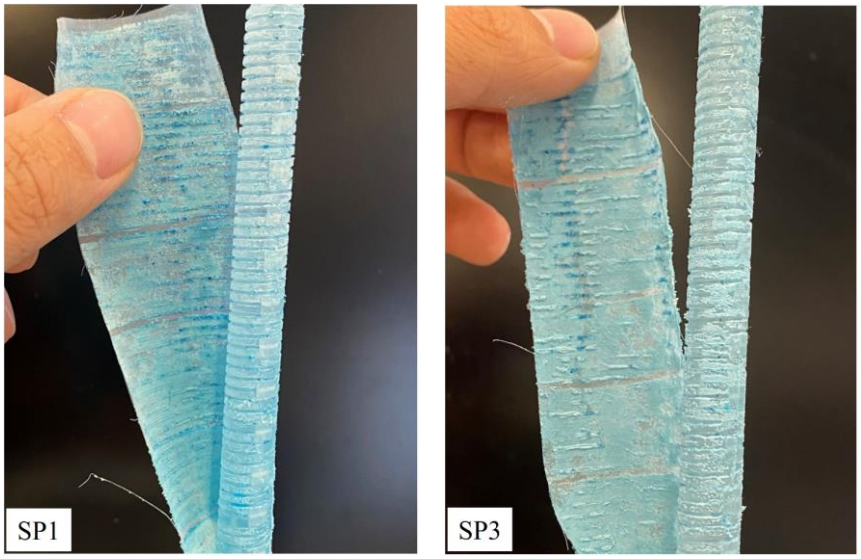

Figure 4.28: Deposited particles on the 80 µm sieve and on the injection tube observed after tests SP1 (10 mg/l) and SP3 (20 mg/l).

Figure 4.27 presents the 3D views of fractures along a section between H = 4 and H = 6 cm. The fracture morphology is similar between these tests. When observing the profile of deposited particles on the 80 µm sieve, test SP3 with a higher particles concentration exhibits a higher deposition of particles on the sieve (Figure 4.28). It should be noted that 2.7 g of suspended particles were injected for test SP3 (Figure 4.25b) as compared to 2.1 g for test SP1.

4.4.2.3 *Effect of confining pressure*

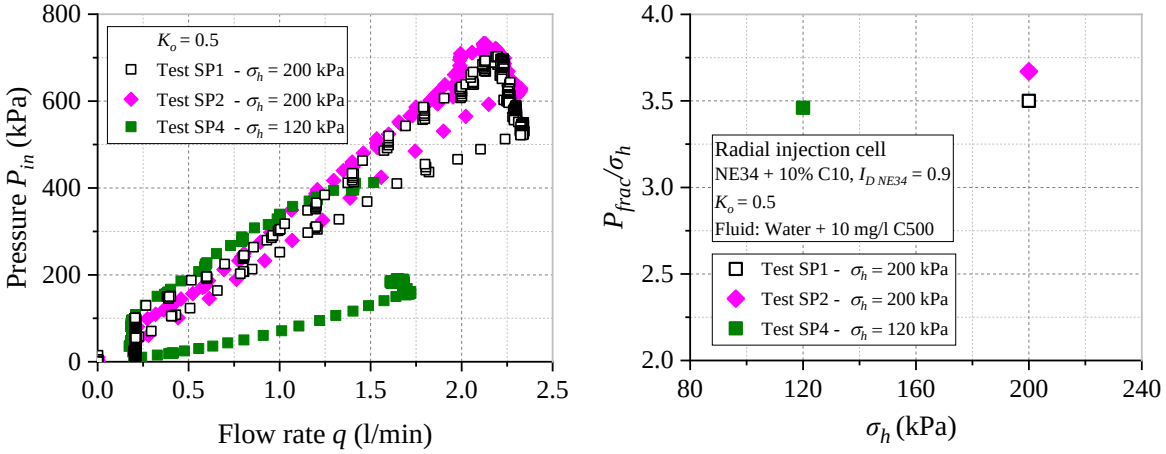

Figure 4.29: Effect of the confining pressure on the fracturing response: (a) injection pressure versus flow rate; (b) normalized fracturing pressure.

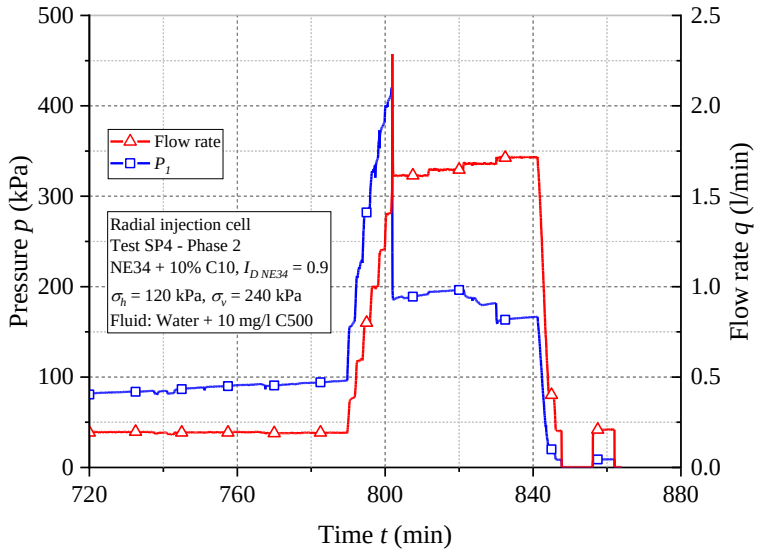

Figure 4.30: Results of test SP4 in terms of pressure and flow rate during phase 2 of the test.

The experimental results during pure water injection showed that the confining pressure is the primary factor controlling the fracturing pressure. It is thus interesting to investigate the effect of this parameter when injecting water with suspended particles. To do so, test SP4 was carried out at a lower confining pressure (120 kPa) as compared to the reference test (200 kPa) while keeping the same stress ratio K_0 of 0.5. The comparison is shown in Figure 4.29. The

higher the confining pressure, the higher the fracturing pressure and the lower the increase in permeability. Interestingly, fracturing occurs when the injection pressure reaches about 3.5 times the confining pressure for both tests. During test SP4 with 120 kPa of confining pressure, a remarkable drop of the injection pressure was observed when increasing the flow rate from 1.4 to 1.6 l/min and the inlet measured pressure suddenly decreased from 420 kPa to 180 kPa (Figure 4.30).

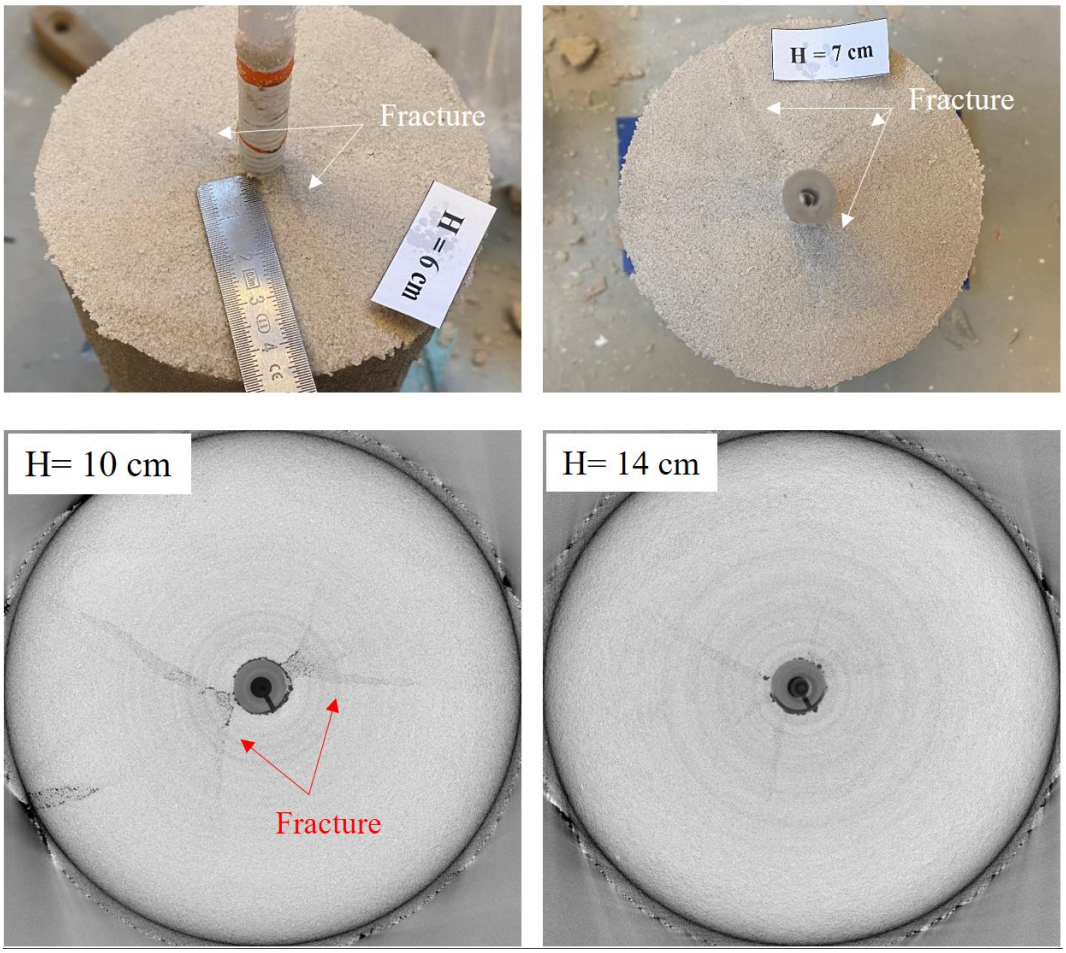

Figure 4.31: Horizontal cross-sections of the specimen SP4 observed during manual excavation and X-ray CT scan.

The observation of fractures after the test allows to confirm the results obtained during the injection phase. As shown in Figure 4.31, a larger and more complex network of fractures is observed in specimen SP4 as compared to specimen SP1 under 200 kPa of σ_h (Figure 4.14). During the SP1, fractures were only generated in the upper part of the specimen (Figure 4.17) whereas fractures propagated all along the injection tube during test SP4. Figure 4.32 shows the typical 3D views of fractures developed at the center of the specimen. This observation is in accordance with the first noticeable fracturing point and a higher increase of the apparent permeability in test SP4 (200% of the permeability gain g for test SP4 as compared to 41% for SP1).

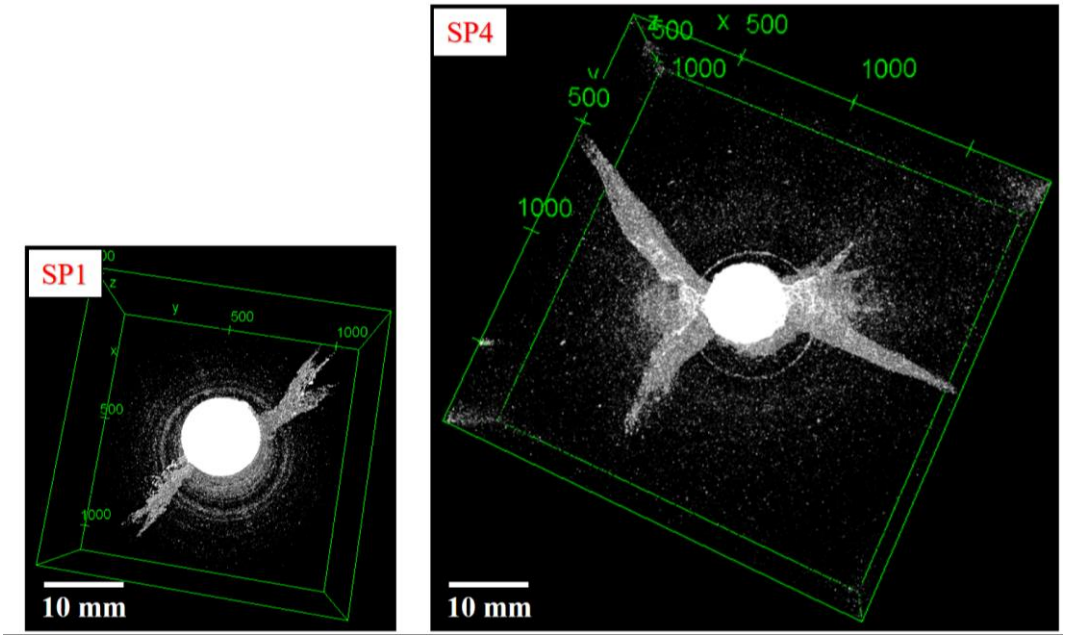

Figure 4.32: 3D views of the fractures developed at the center of the specimens SP1 and SP4

4.4.3 Comparison of the results obtained in two injection scenarios (water injection with and without suspended particles)

Each scenario of injection has its own benefits. The main objective is to study the fracturing mechanisms in unconsolidated sand specimens by injecting fluid under high injection pressure. For the first experimental campaign with pure water, the reference specimen is a mixture of NE34 sand and 22% of fine particles which provides an adequate permeability of the specimen to reach the critical pressure of fracturing within the range of the pump capacity. This injection scenario allows to investigate fracturing mechanisms in a homogeneous medium of a mixture sand + fine particles which represents an internal cake induced during PWRI. In the second scenario, the study is more complicated with two continuous phenomena: formation damage due to the transport and deposition of injected particles and then fracturing of this plugged formation. However, the second scenario gets closer to the reality of PWRI operations in practice.

In this part, we present a comparison of the results obtained for two injection scenarios, which are obtained during the radial injection cell tests. Two tests series with two different magnitudes of confining pressure (120 kPa and 200 kPa) are evaluated. Figure 4.33 shows the case of 200 kPa of confining pressure. The injection tests with suspended particles need a higher pressure to reach the frac-regime (Figure 4.33a). The ratio between the fracturing pressure and the confining pressure is about 3.5 for the suspended particles scenario and 2.5 for pure water (Figure 4.33b). With the same number of steps in the frac-regime, the suspended particles injection tests exhibit a higher recovery of permeability (compared to the apparent permeability before fracturing). Because in the second scenario, the overall permeability of the specimen is determined by that of the filter cake.

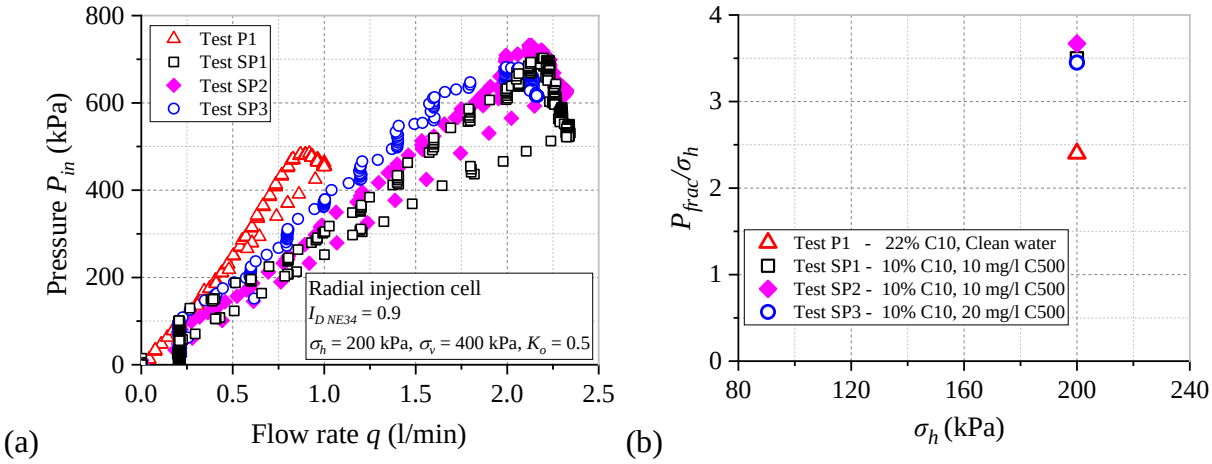

Figure 4.33: Results comparison of two scenarios (pure water and water containing suspended particles) at the same stress conditions (σ_h = 200 kPa, σ_v = 400 kPa): (a) injection pressure versus flow rate; (b) normalized fracturing pressure (P_{frac}/σ_h).

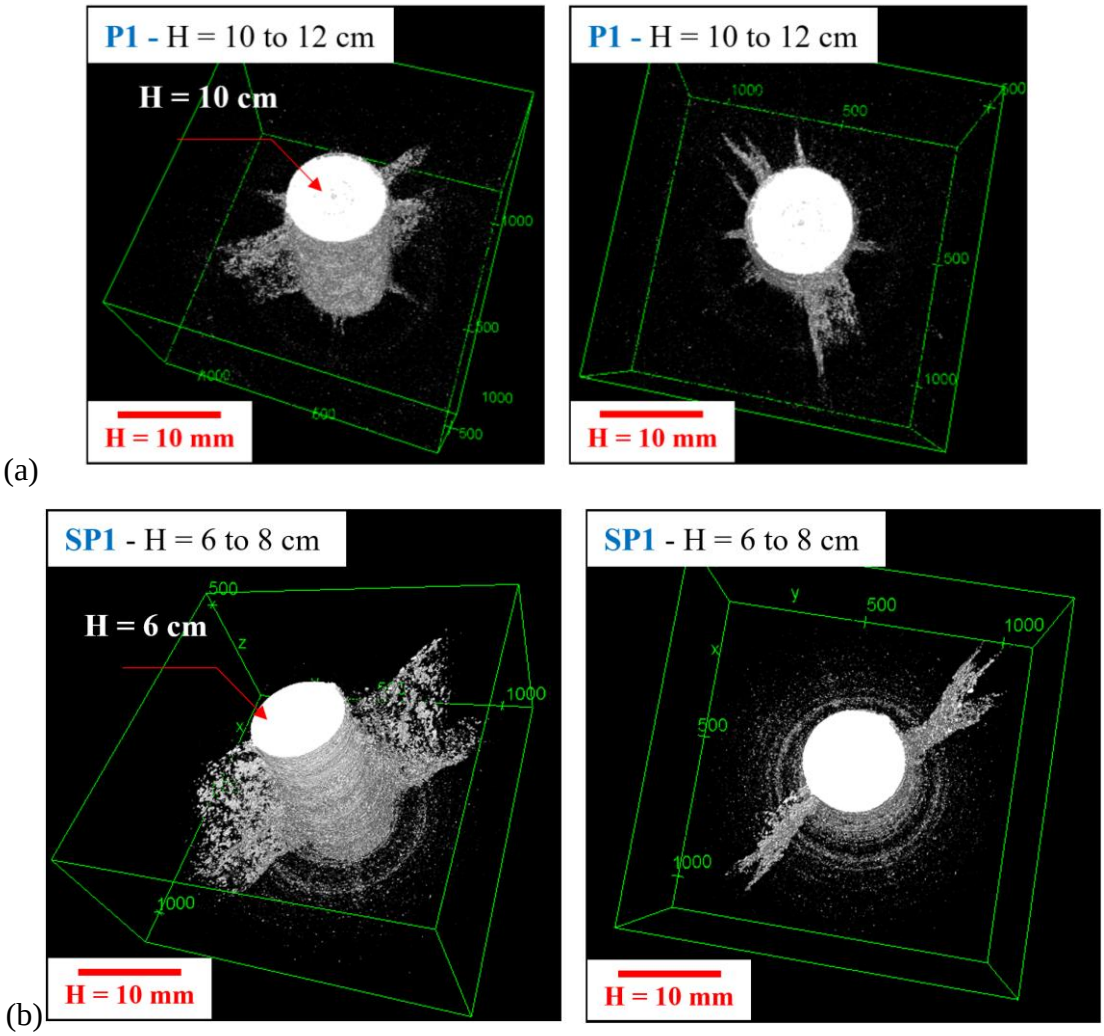

Figure 4.34: 3D fracture views of the typical tests of two scenarios at the same stress conditions (σ_h = 200 kPa, σ_v = 400 kPa): (a) pure water – Specimen P1; (b) suspended particles (specimen SP1).

This result is also confirmed by the appearance of longer fractures around the injection tube as shown in Figure 4.34. Other views and photos of these tests can be seen in Section 3.4.1 and Section 4.4.1.

Similar results were obtained in the case of 120 kPa of confining pressure (Figure 4.35 and Figure 4.36). A higher fracturing pressure, a longer fracture as well as a higher increase of the permeability after fracturing were observed in the scenario of suspended particles. These tests were performed for different values of K_0 (0.4 for P6 and 0.5 for SP4), however, as concluded above in Section 3.4, this parameter has no significant impact on the fracturing pressure (at least, for this specimen configuration).

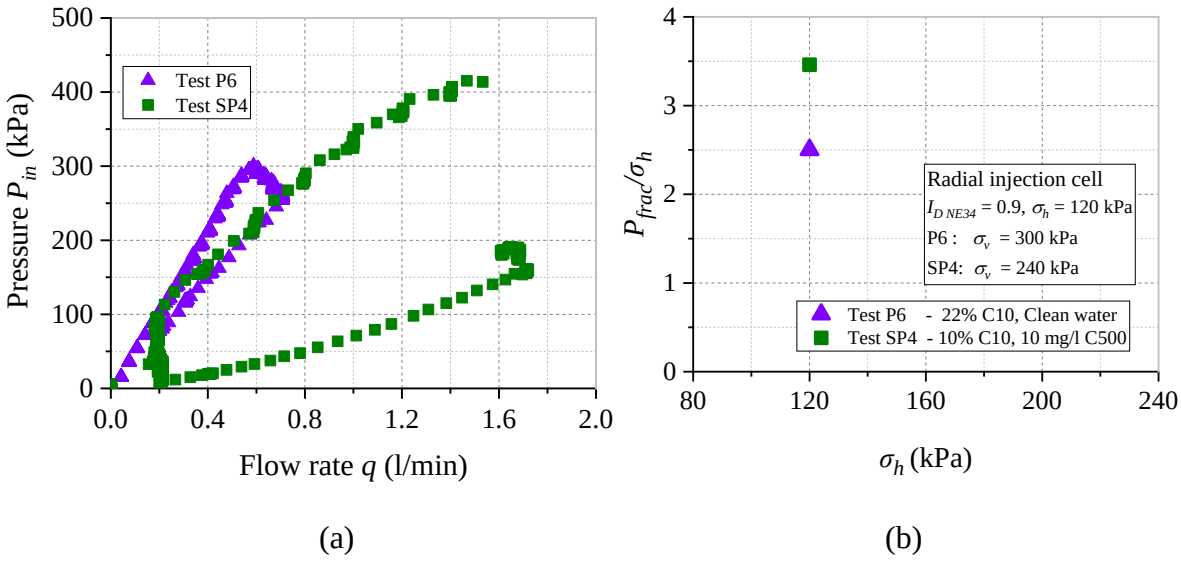

Figure 4.35: Comparison of results for the two scenarios at the same confining pressure of 120 kPa: (a) injection pressure versus flow rate; (b) normalized fracturing pressure (P_{frac}/σ_h).

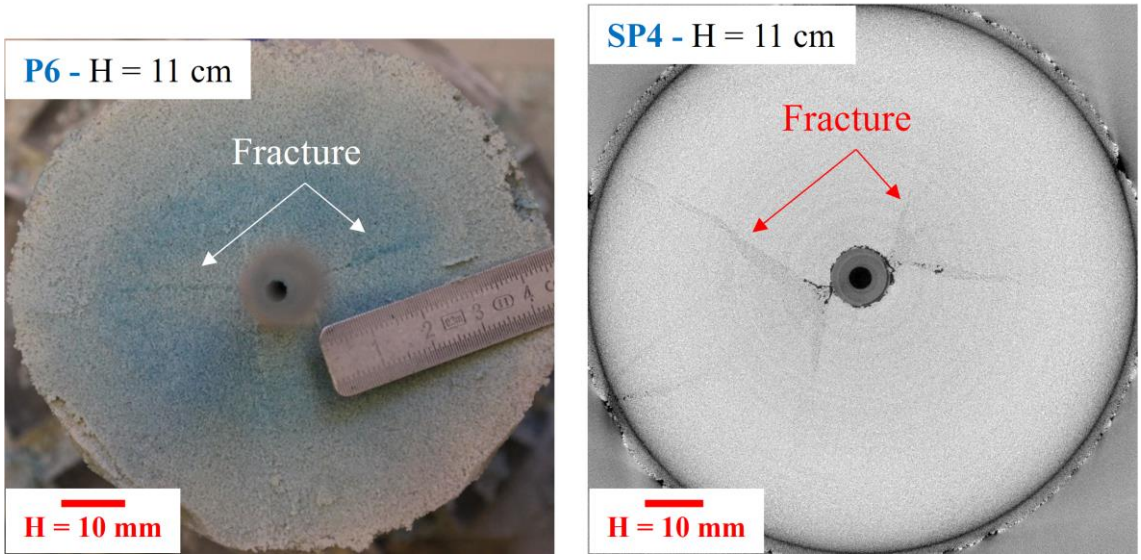

Figure 4.36: Typical fracture pattern observed in two scenarios at the same confining pressure of 120 kPa.

For both scenarios, an increase of the confining pressure leads to a higher critical fracturing pressure, shorter fractures and a smaller increase of the overall permeability. Based on the experimental results, we found that the specimens injected with suspended particles require a higher critical injection pressure to reach the frac-regime as presented in Figure 4.37. To better understand this result, it is interesting to analyze the effect of the filter cake on the critical pressure required for fracturing. Similarly to our results, different previous works (Farajzadeh, 2004; Feia et al., 2015; Ochi and Oughanem, 2018; Wong and Mettananda, 2010) have shown that, during the plugging process, only the deposition of particles at the first layer (filter cake) affect the overall permeability decline of the specimen (equivalent to the increase of inlet pressure measured at the entrance of the specimen) whereas the pressures measured at different positions within the specimen do not exhibit any significant change. The presence of this cake may require a higher injection pressure to firstly break or destabilize this zone before creating fractures within the specimen. Besides the occurrence of fracturing of the specimen, the break/unclogging of the filter cake in the second injection scenario (suspended particles) plays also an important role on the increase of the permeability during the frac-regime. This explains why a higher increase of this value is observed in the second protocol. Figure 4.38 illustrates the pressure distribution within the specimen of two specimens at the end of the matrix regime (i.e., just before the first pressure drop appears). As the initial permeability of a specimen containing 10% C10 is much smaller than that with 22% C10, pore pressures within the non-plugging zone are smaller than those at the same radius of the specimen with 22% C10. The value of the normalized fracturing pressure (P_{frac}/σ_h) was not affected by the change in confining pressure (Figure 4.37). The fracture pattern inside the plugging specimen was much more complicated, especially in the case of the longer fracture induced. Instead of propagating radially in the flow direction from the injection tube, the fracture extended to different branches as observed in the specimen SP4 (more details are given in Appendix G.2).

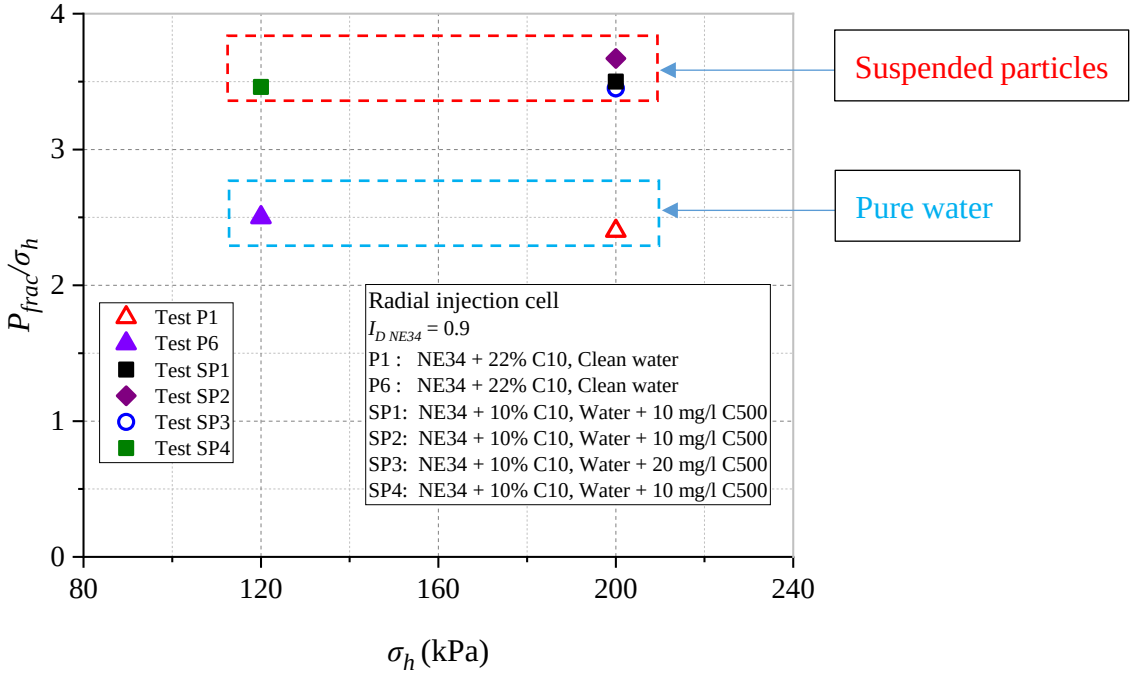

Figure 4.37: Synthesis of the normalized fracturing pressure with the two scenarios in radial injection cell: pure water and suspended particles injection.

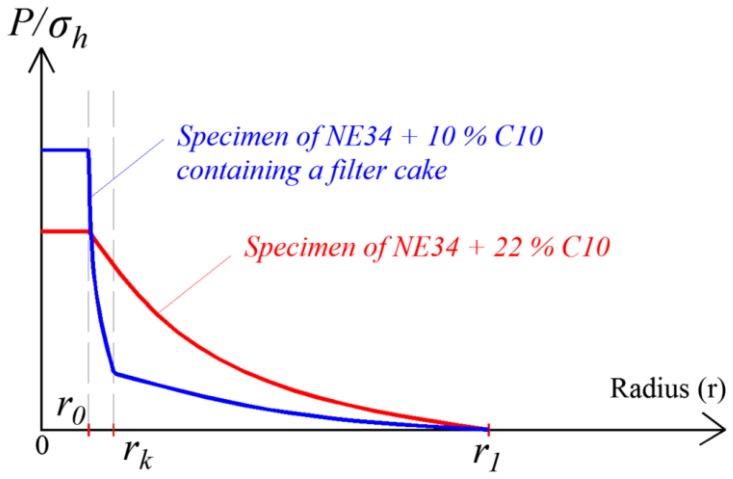

Figure 4.38: Schematic representation of the pressure distribution within the specimen just before fracturing in the two scenarios studied (r_0, r_k and r_1 are the radius of injection tube, filter cake and specimen, respectively).

4.5 EXPERIMENTAL RESULTS IN THE RADIAL INJECTION CHAMBER

4.5.1 Test N36

4.5.1.1 *Injection of water with suspended particles*

Figure 4.39a presents the results of water injection with suspended particles for test N36. The test characteristics are presented in Table 4.3. The injection lasted for 2 days with interruption during the night. In Figure 4.39, the beginning of the second day corresponds to 400 min of *t*. As for the tests carried out in the injection cell, the flow rate was maintained at 1.5 l/min (phase 1) and the injection pressure increased from 25 kPa to 170 kPa after approximately 500 minutes of injection. Thus, the apparent permeability decreased from an initial state of 650 mD to 80 mD. The last value corresponds to the overall permeability of the reference sand pack (NE34 + 22% C10). During phase 2, the flow rate was increased by steps of about 0.4 l/min (Figure 4.40a). In the matrix regime, the pressure response was different as compared to the tests with pure water. A sudden increase of the flow rate did not result in a corresponding increase of the pressure magnitude, instead, the injection pressure kept increasing gradually. Many noticeable pressure drops were identified for flow rates higher than 4 l/min. The first pressure drop was observed at a flow rate of about 4.25 l/min. After reaching 408 kPa, the injection pressure sudden drops to 330 kPa and then, it gradually increased right after (Figure 4.40a). This observation is similar to the preliminary tests in radial injection cell (see Section 4.3). The flow rate was increased up to 7 l/min (maximum pump capacity) then decreased to zero (Figure 4.40b). The highest pressure recorded was 610 kPa (5.1 σ_h) at a flow rate of 4.85 l/min.

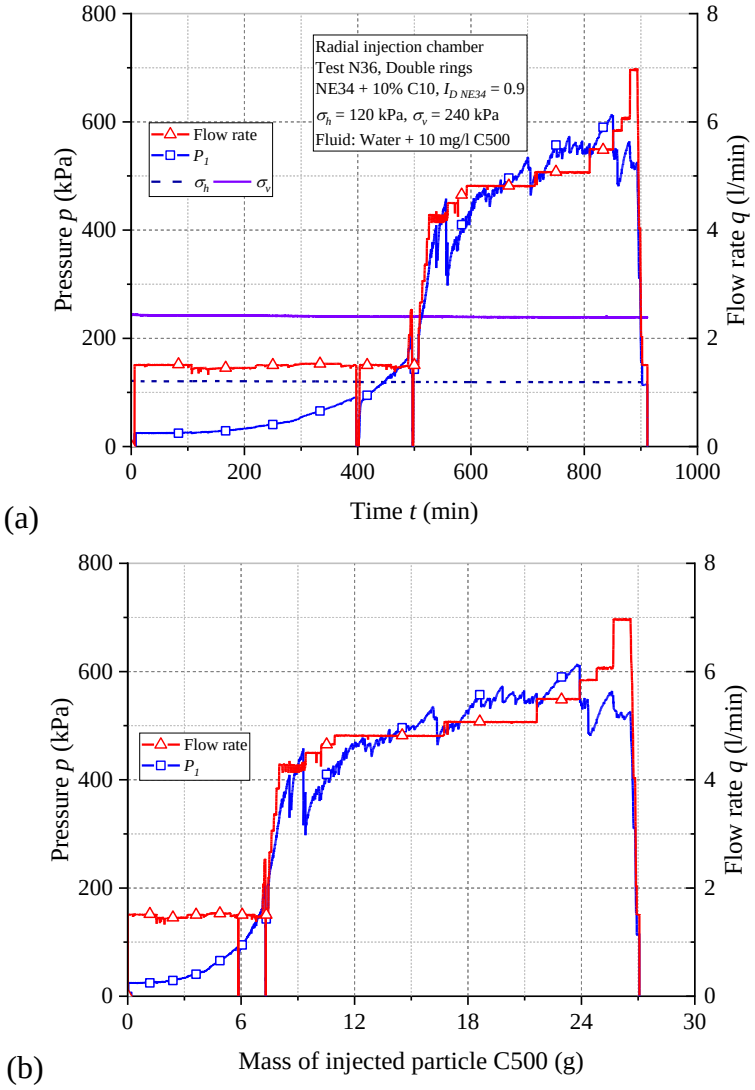

Figure 4.39: Results of test N36 during suspended particles injection: (a) pressure – flow rate – time curves; (b) pressure – flow rate – injected particles mass curves.

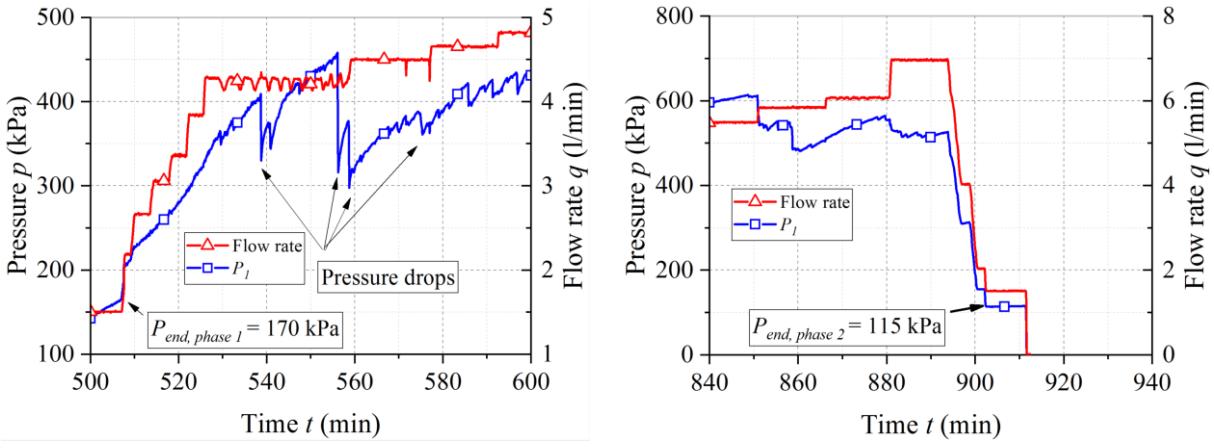

Figure 4.40: Test N36 - Different zooms during injection phase: (a) pressure drops identified (500 to 600 minutes); (b) decreasing the flow rate and stop pumping (840 to 940 minutes).

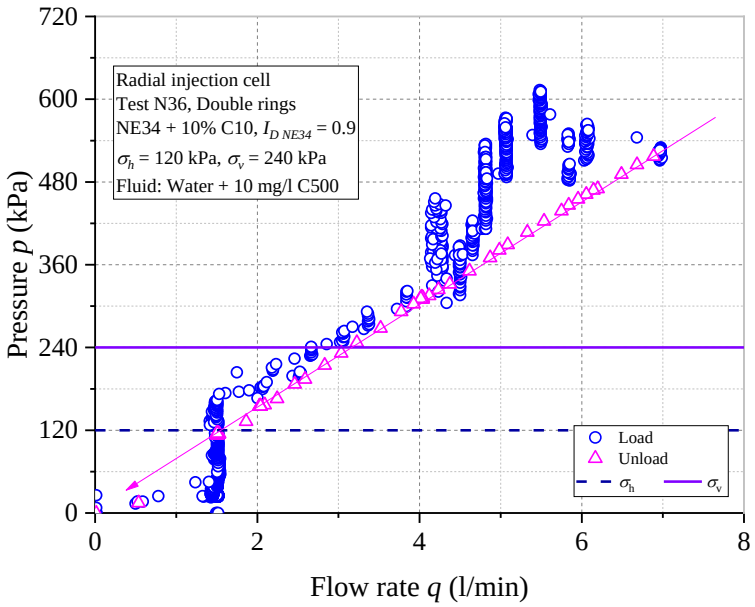

Figure 4.41: Pressure – flow rate curve of test N36.

During unloading (i.e., decreasing the flow rate), we observe that, for the same flow rate, the pressure is smaller than during loading (Figure 4.41). At a flow rate of 1.5 l/min, the injection was maintained during 10 minutes and the corresponding measured pressure was 115 kPa which is much smaller than the pressure measured before starting phase 2 (170 kPa, see Figure 4.40b). This lower injection pressure may be attributed by the unclogging of the filter cake when pressure pulses occur.

4.5.1.2 *Disassembling*

A small volume of a mixture of 0.2% Basacid Bleu 762 diluted in water was injected before disassembling. Silica gel (MasterRoc MP320) was not used in the experiment with suspended particles injection because it makes difficult to observe the deposited particles profile on the strainer tube. Figure 4.42 presents some typical photos of the sand pack during excavation. No fracture has been detected around the strainer tube and the diffusion of the blue dye was not symmetrical along the sand pack. Along the injection tube, a ring of filter cake with a thickness of several millimeters was detected (Figure 4.43).

Several samples were carefully extracted from this cake as shown in Figure 4.43 and then observed using the optical microcope Leica™ M80. Three typical structures at the surface of the filter cakes were identified: internal cake, external cake and pure sand (Figure 4.44). The observations highlight the complexity of the transport/deposition of the suspended particles in the porous medium, especially when injecting at a high flow rate as well as a high injection pressure. The pressure drops obtained during injection may correspond to the wash-out of filter cake at certain points along the length of the strainer tube and not the occurrence of fracturing in the sand pack. It should be noted that the initial sand pack has also 10% of the C10 particles (D_{50} = 20 µm). At some positions around the tube, these particles were also transported far away, so that only pure NE34 sand has been detected (Figure 4.44c). This observation of the

filter cakes around the trainer may explain the non-symmetrical distribution of the dye inside the inner ring.

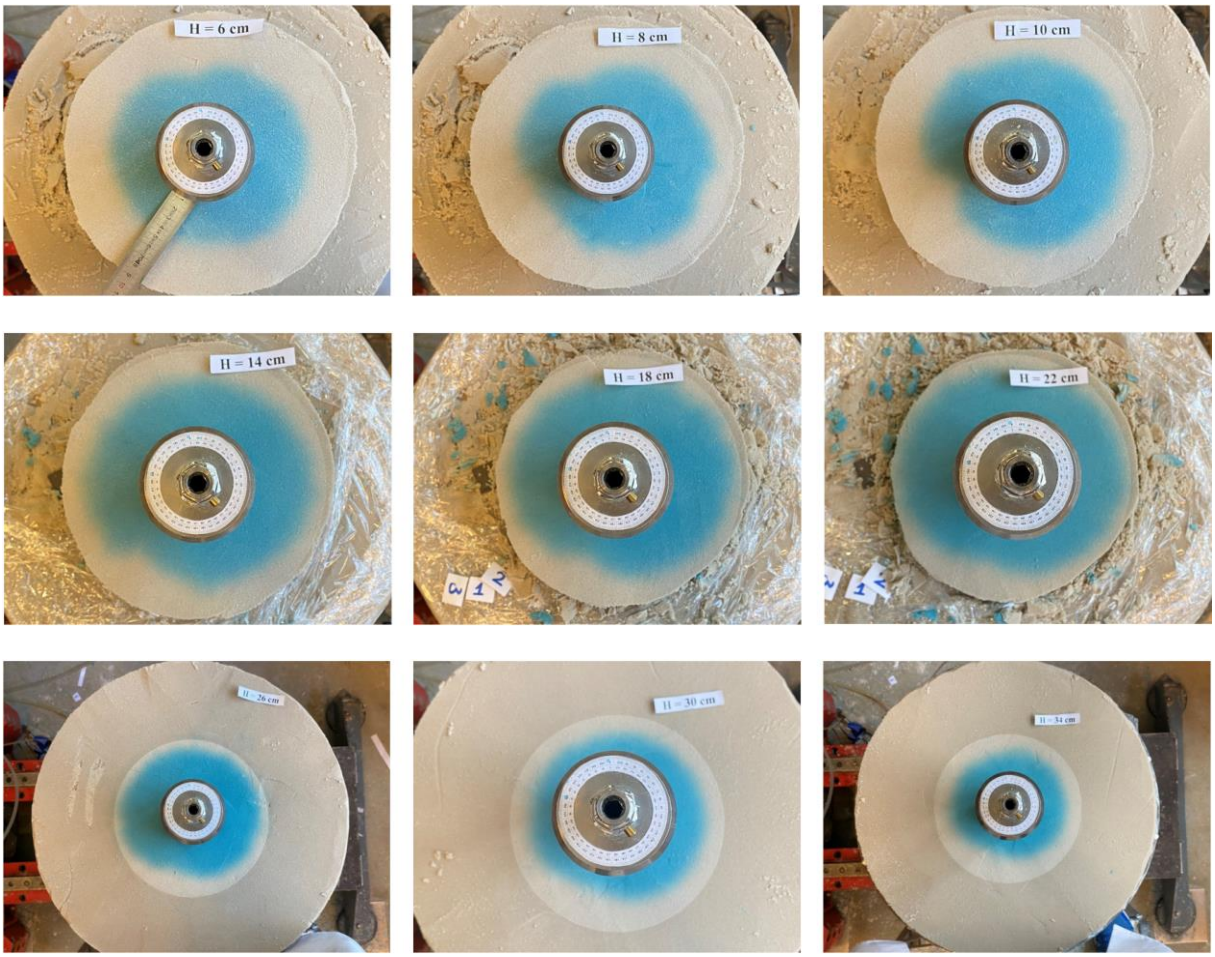

Figure 4.42: Photos of different horizontal sections during excavation of sand pack N36.

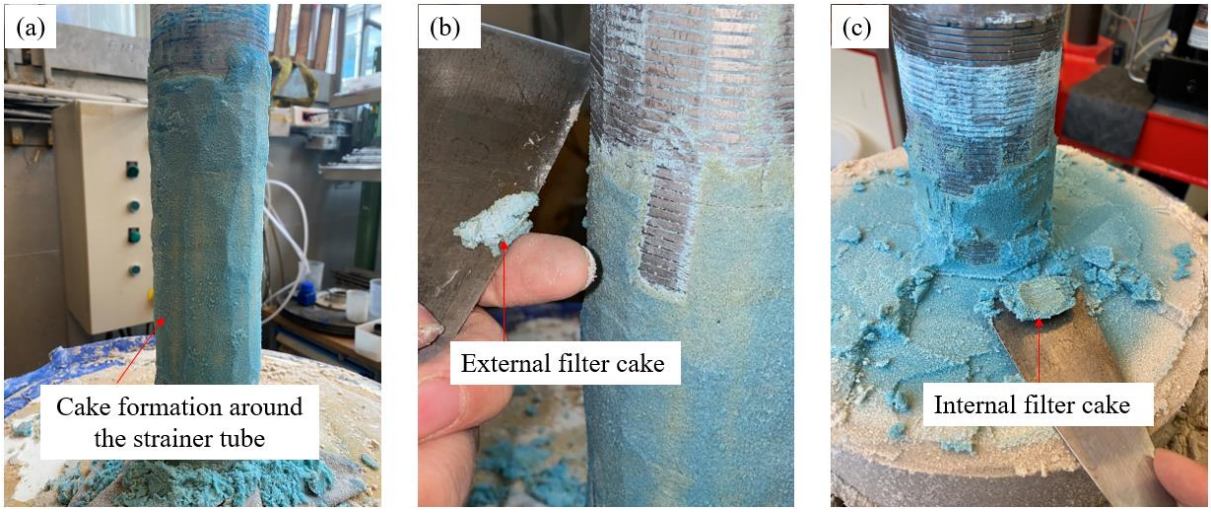

Figure 4.43: Photos of the filter cakes of sand pack N36.

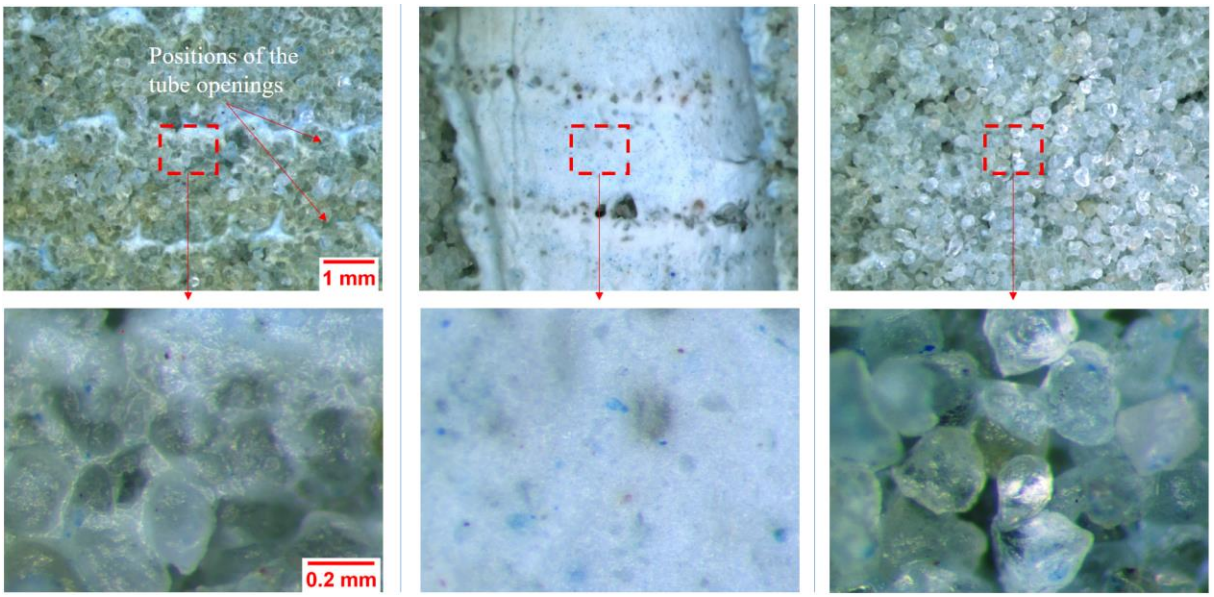

(a) (b) (c)

Figure 4.44: Typical observations of the interface between sand pack and strainer tube using optical microscope (Test N36): (a) internal cake; (b) external cake; (c) pure NE34 sand.

4.5.2 Test N37

4.5.2.1 *Injection of water with suspended particles*

During test N36, the injection pressure reached a maximum value of 610 kPa which corresponds to 5.1 times the confining pressure and 2.55 times the axial stress, however no fracture has been observed during excavation of the sand pack. This can be attributed to the formation of an external cake which prevents the fluid pressure to increase sufficiently within the sand pack in order to reach fracturing. To be able to perform a test at a higher injection pressure and considering the limits of the pump (Q_{max} = 7 l/min), we reduced the height of the injection zone from 32 cm (reference configuration) to 16 cm, so that, with the same flow rate imposed by the pump, the flow velocity in the sand pack can reach values twice higher. To do so, a half-height of the strainer tube was prevented using two adhesive tapes: one for sealing (orange adhesive) and other one for strengthening it (blue adhesive) (Figure 4.45). The injection zone of 16 cm is located at the center of the sand packs with two lower permeability layers of 12 cm each below and above (Figure 4.45b). The configuration of sand pack N37 is presented in Figure 4.46.

Figure 4.47 presents the results for test N37 during the injection phase. Several flow steps of pure water injection were performed to measure the initial permeability (Figure 4.47b). At 0.75 l/min, the measured pressure was nearly constant for 20 minutes. When increasing the flow rate to 2.5 l/min, the pressure started to increase gradually due to the detachment and re-arrangement of the C10 particles inside the sand pack. This corresponds to a slight decrease of the initial permeability. Then, suspended particles were injected at a flow rate of 0.75 l/min which provides the same fluid velocity in the sand pack as phase 1 of test N36. After about 150 minutes of injection, the pressure has increased from 20 to 170 kPa. Before increasing the

flow rate, pumping is stopped, then re-increased right after to 0.75 l/min to confirm the permeability decrease observed during phase 1. As can be seen in Figure 4.47c, when the injection restarted, the pressure values reached 170 kPa after a few minutes of injection, which could indicate the formation of a filter cake within the sand pack. Pulses of pressure were observed from a flow rate of 2.4 l/min corresponding to a pressure of about 2.7 σ_h (Figure 4.47d). The first significant pressure drop which seems to be the sign of fracturing of the sand pack was observed at a flow rate of 3.8 l/min and corresponding pressure, before dropping, of 470 kPa (3.92 σ_h) (see Figure 4.47e). This flow rate was maintained during 10 minutes before increasing the flow rate to 4.4 l/min. However, at a flow rate of 4.4 l/min, we observed that particles were flowing at the outlet. Injection was pursued with a last further step of the flow rate up to 4.7 l/min and then decreased to zero.

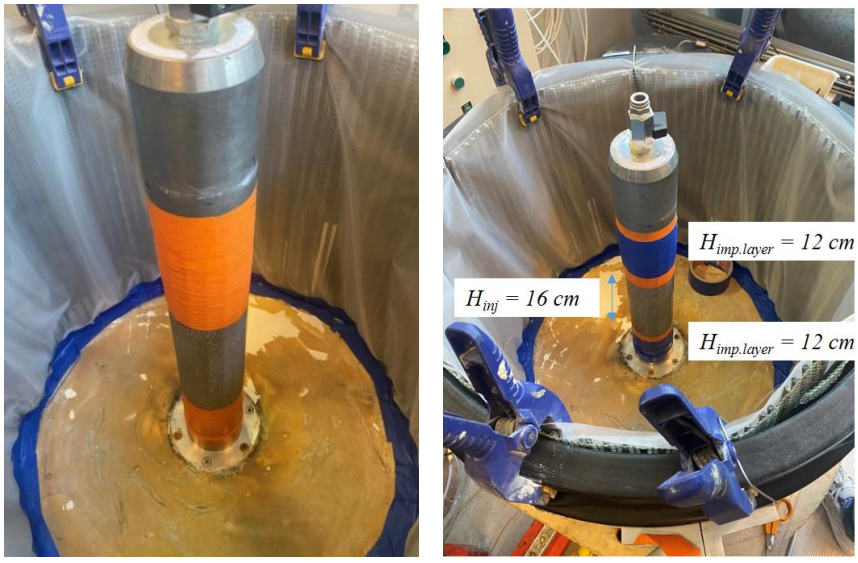

Figure 4.45: Test N37 – Reducing the height of the injection zone from 32 cm to 16 cm using the adhesive tapes to cover the non-injection zone of the strainer tube.

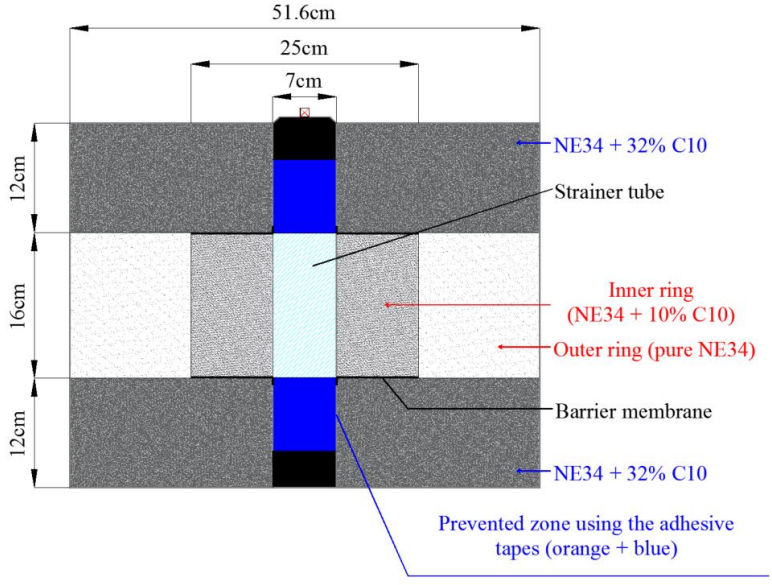

Figure 4.46: Configuration of sand pack N37.

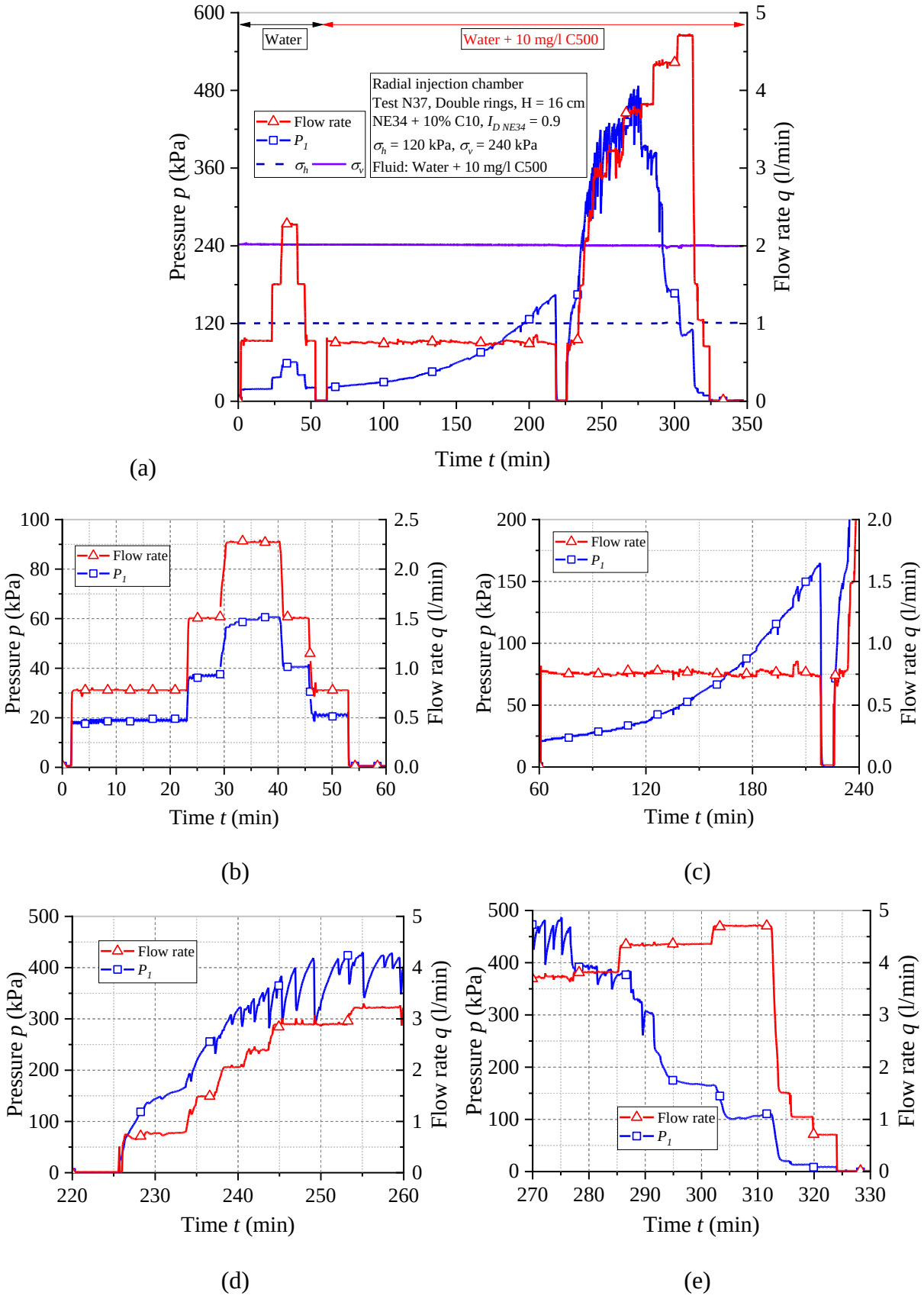

Figure 4.47:Test N37: (a) full response; (b) pure water injection (t = 0 to 60 minutes); (c) plugging phase at Q = 0.75 l/min; (d) phase 2 - increasing the flow rate (t = 220 to 260 minutes); (e) pressure drops during phase 2.

4.5.2.2 *Disassembling*

During the excavation of the specimen after the test, we observed a cavity formed at the boundary of the sand pack (Figure 4.48a). After removing the membrane, eroded sand and particles were detected in the drainage system (Figure 4.48b). Note that the drainage system is a flat sheet and is rolled to form a cylindrical drainage system and the two ends are joined together using adhesive tape. It this test, a polyamide fabric sieves of 80 µm in opening mesh as the one used in the radial injection cell was used to replace the old metallic sieve in the previous test due to its degradation (Figure 4.45). During injection at a high flow rate, the double face adhesive tape was peeled off at the upper part of the drainage system which created an opening for the material to be washed out of the sand pack. Piping was observed at the interface between injection zone and upper low permeability layer due to the loss of materials (Figure 4.48d,e).

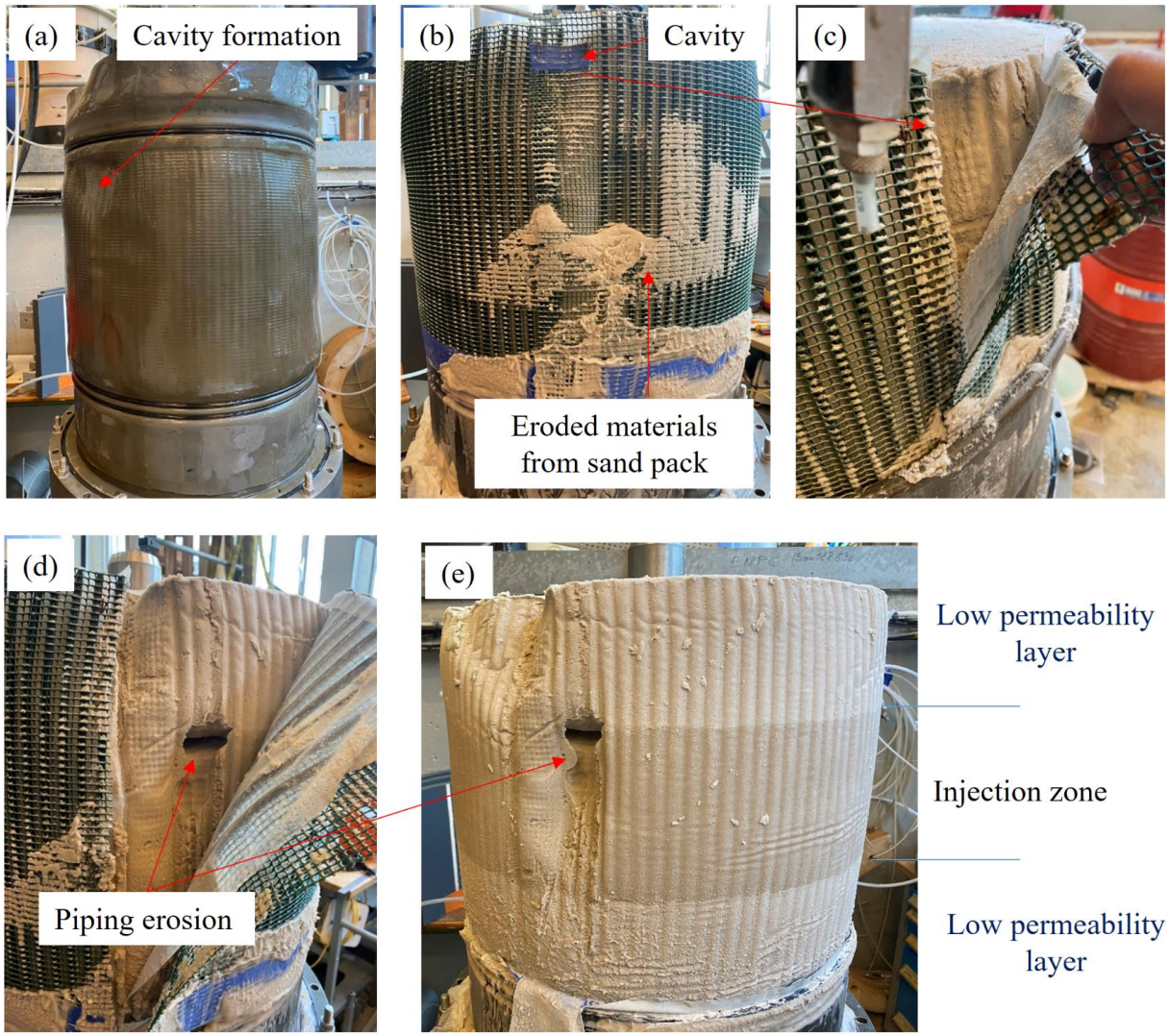

Figure 4.48: Cavity formation due to the removal of sand particles in test N37.

Figure 4.49 shows the photos of the upper surface of the sand pack with the appearance of the cavity around the strainer tube. This cavity was potentially due to the vertical parasitic flow along the strainer tube. During the excavation of the upper low permeability layer, no trace of the blue dye was detected (Figure 4.50a,b) which confirms that the vertical parasitic flow occurred only at the surface of trainer tube. Using adhesive tape is not a really effective solution for sealing, especially when injecting at a high injection pressure. Piping started from the strainer tube at a point under the barrier membrane (Figure 4.50c,d,e).

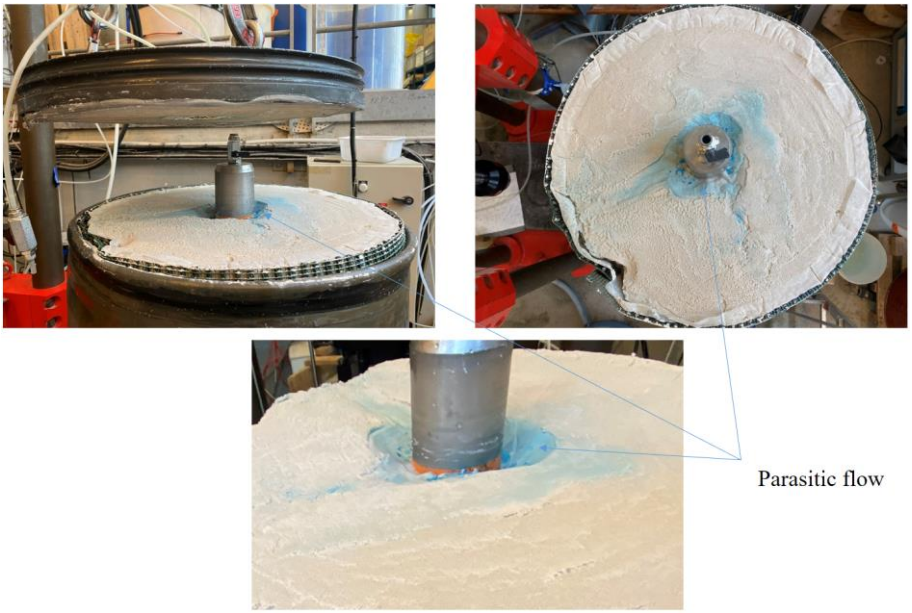

Figure 4.49: Parasitic flow toward the interface between sand pack and upper baseplate (Sand pack N37).

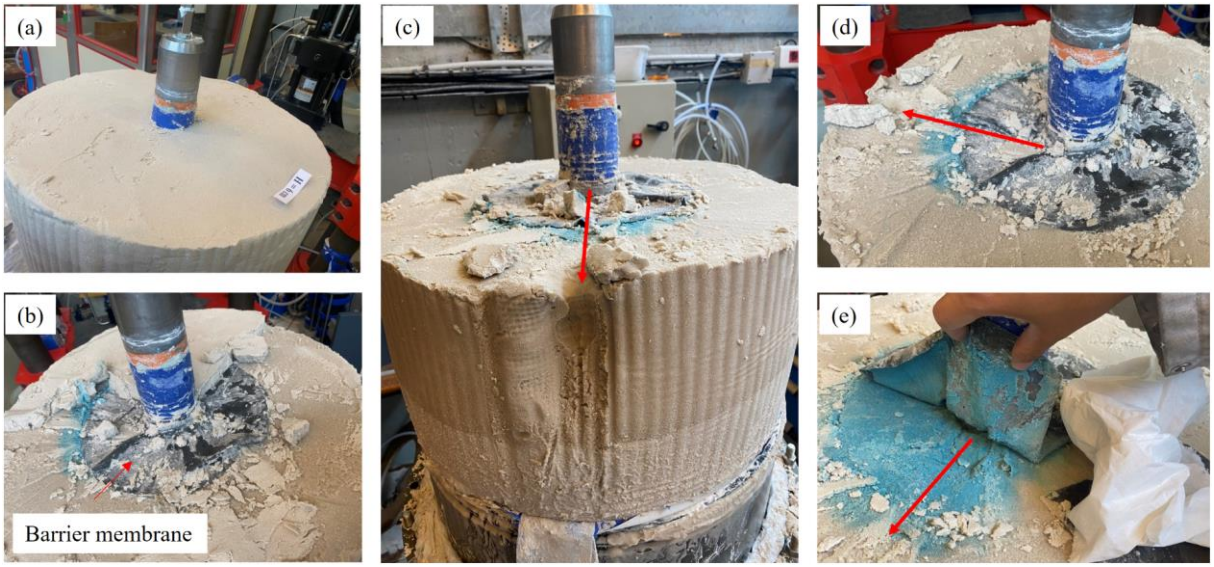

Figure 4.50: Excavation of the upper low permeability layer (H = 0 to 12 cm): (a) horizontal transversal-section at H = 6 cm; (b) upper view of the barrier membrane; (c),(d),(e) different views of the piping position (Test N37).

An interesting observation is that the injected dye did not only flow through the piping hole (Figure 4.51). Only the upper part of several centimeters of the injection zone shows a larger invasion of the blue dye in the direction of the piping position (H = 12 to 15 cm). At the height of 16 cm (4 cm below the injection surface), a darker blue band was detected from the injection tube which is similar to the fracture observed in the tests with pure water injection. The invasion of the dye was more important on this side as well. This fracture observed along the strainer tube can be linked to the first pronounced pressure drop during injection before piping erosion occurs.

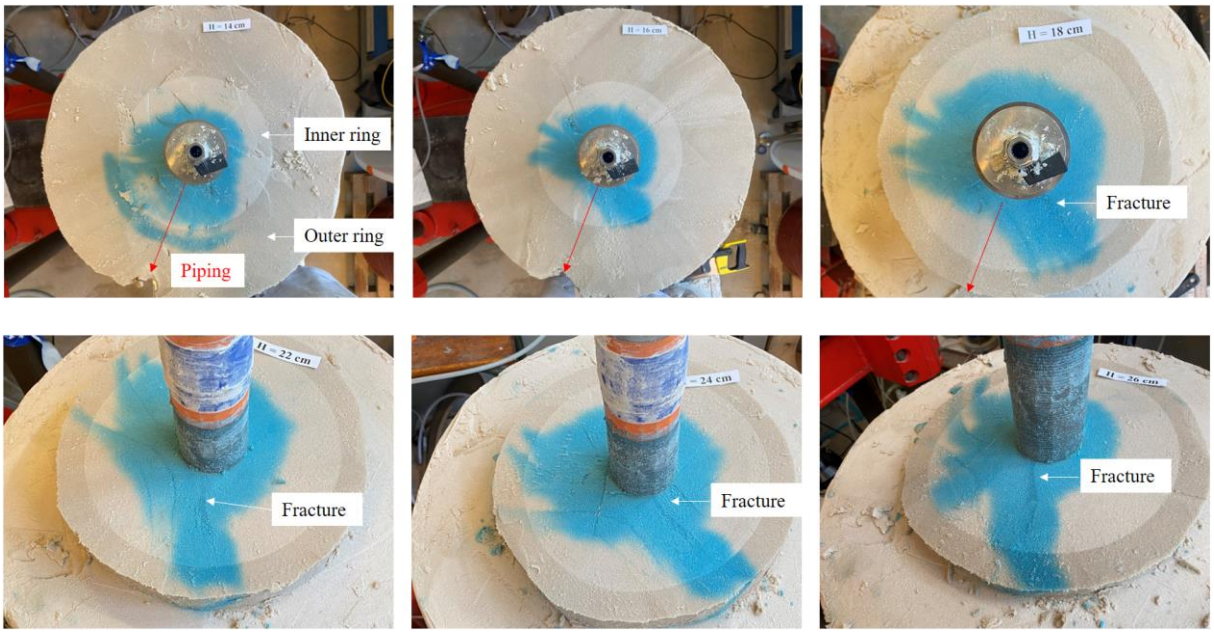

Figure 4.51: Horizontal cross-sections of the injection layer at different heights (H = 12 to 28 cm) (Test N37).

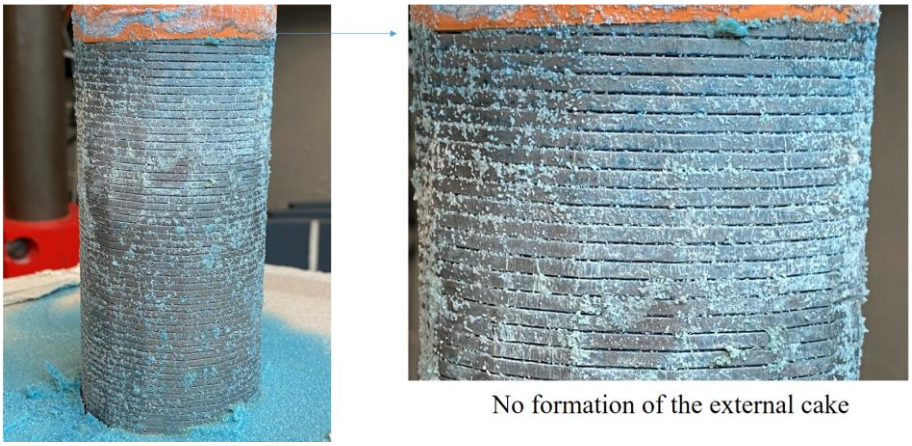

Figure 4.52: Observation of the strainer tube after injection (Test N37).

When observing the strainer tube, no external cake has been detected at the surface (Figure 4.52). The dominated damage during the first phase was the formation of the internal cake. In

absence of external cake, it is reasonable to consider the maximum pressure of 470 kPa (3.92 σ_h) at a flow rate of 3.8 l/min (Figure 4.47e) as the critical value of fracturing. This value can be compared to those obtained in the cases of pure water injection (in the range of 4 to 5 times of confining pressure). More tests should be performed to confirm this result.

4.6 CONCLUSIONS

In this part, an experimental study has been designed and performed in both radial injection setups, aiming to mimic the process of re-injection of produced water in sand reservoirs under both matrix and frac regimes. Injection of suspended particles in the matrix regime resulted in a decrease of the overall permeability due to the formation of internal cake and/or external cake at the nearest layer of the specimen. The sensitivity analysis in the radial injection cell showed that when injecting at a lower particles concentration, a smaller amount of injected particles is needed to induce the same plugging level in terms of pressure increase, however, a higher injected volume is needed to provide a sufficient quantity of particles for plugging. In this cell, fracturing could only be induced when the injection tube was not completely damaged (i.e., plugging by deposited particles). In all the tests performed in the injection cell with suspended particles, fracturing occurred when the injection pressure reached about 3.5 times the confining pressure. The effect of the particles concentration in the injection fluid and of the confining pressure on the fracturing mechanisms were explored as well. In the range of particles concentration studied here, no clear effect of this parameter was observed whereas a pronounced effect of the confining pressure was identified which is similar to the observation in the pure water scenario. Comparing the results of two injection scenarios in the cell (i.e., the 1st scenario - pure water vs the 2nd scenario - suspended particles injection), the second exhibits a higher normalized fracturing pressure, a higher increase of the permeability and longer fractures induced. In both scenarios, an increase of the confining pressure leads to an increase of the critical fracturing pressure, a lower increase of overall permeability as well as a shorter fracture induced within the specimen.

Two tests have also been performed in the radial injection chamber to investigate fracturing under suspended particles injection. During phase 1 at a constant flow rate, a gradual increase of the injection pressure confirmed the formation of the filter cake in the sand pack. A long vertical fracture was also detected in test N37 which could be a sign of fracturing, however, due to the parasitic formation of a cavity, further tests should be performed to better understand fracturing in the radial injection chamber.

More generally, more tests in the injection chamber are needed and will be performed in the future for comparing the response of the two setups.

GENERAL CONCLUSION AND PERSPECTIVES

The objective of this Ph.D thesis was to explore experimentally in the laboratory the conditions for switching from the matrix injection regime to the fracturing regime (frac-regime), to highlight the factors controlling the initiation of the frac-regime as well as to understand the fracturing mechanisms in unconsolidated sand reservoirs. The injection tests have been carried out on dense sand specimens containing a mixture of Fontainebleau NE34 sand and C10 silica fines, under anisotropic stress conditions, in which water with and without suspended particles is radially injected from a central injection tube. The experimental study has been performed in the two radial injection setups (i.e., radial injection cell and radial injection chamber).

The first step of this work was to develop a new injection setup, called radial injection cell, for reconstituting a smaller specimen than the one in the radial injection chamber and for allowing the whole specimen to be scanned using X-ray CT. The tests in the radial injection cell are simpler to perform compared to those in the injection chamber, therefore, this setup allows to perform an extensive parametric analysis with very good control of the experimental conditions. The setup has been developed on the basis of the function scheme of the radial injection chamber and the design of the confining cell is basically a classical triaxial cell using the transparent materials with X-Ray. A series of preliminary tests has been carried out to qualify this new injection setup and to validate the injection protocol.

The observation of the granular structure's change after fracturing is also an important aspect of this work. To do so, the sand structure must be solidified before the disassembling, in particular for the tests in the radial injection chamber without the possibility of scanning the sand pack by X-ray CT. The silica gel has been selected because of its advantages as compared to other substances presented in the bibliographic review (i.e., similar viscosity and similar absorption of X-ray as water, adjustable gel time, no volume change after gelification, excellent durability characteristics, easy to clean). To better visualize the fractures within the specimen during the manual disassembling, a dye was added into the colloidal silica before injection. After performing a series of validation tests, a mixture of the silica gel "MasterRoc MP320" and of dye "Basacid® Blue 762" is chosen as the reference colored gel because of a good efficiency of solidification and visualization of the invaded zone as well as a reasonable gelling time.

Two sets of the experimental program have been established and performed based on the two injection scenarios with pure water (Scenario 1) and with water containing suspended particles (Scenario 2). Scenario 1 permits to explore fracturing mechanisms of the medium containing a homogeneous mixture of sand and fine particles which represents the final state of an internal cake induced by PRWI. In this scenario, the testing conditions can be well controlled and a homogeneous specimen allows to avoid unexpected results or preferential flows within the sand specimen. Scenario 2, on the other hand, gets closer to the phenomena that occur during PWRI operations in practice with the coupling phenomena: formation damage due to the formation of a filter cake on the sand surface during the matrix regime and fracturing of the

medium during the frac-regime. However, the physical processes associated with Scenario 2 are more complicated with the superposition of numerous phenomena such as filtration, deposition, detachment, transport of fine particles and formation of dilating strain localization bands in the sand matrix.

Tests have been performed in both radial injection setups (i.e., injection cell and injection chamber). In addition, the imaging analysis using X-ray CT and optical microscopy has been used which allows to access and explore the change of the granular structure due to fracturing. The effect of various parameters, including confining pressure, stress ratio coefficient, flow rate, permeability, particles concentration in injection water on the fracturing process and plugging formation (only for Scenario 2) have been investigated. The comparison has been established on the results obtained with two different injection setups to study the effect of the specimen size. In addition, the comparison of the results of two different injection scenarios allows to explore the effect of a previous plugging phase (only for Scenario 2) on the fracturing response of the medium.

The main experimental results obtained for Scenario 1 with the injection of pure water are summarized in the following:

- Fracturing occurs when the injection pressure reaches a critical threshold which is about 2. 35 times the confining pressure for the tests in the radial injection cell and is in the range of 4 to 5 times for those in the radial injection chamber. The pressure drops during the frac-regime correspond to the formation of vertical fractures along the injection tube which are observed during the disassembling phase. The analysis of the granular structure's change inside the induced fractures and the visualization of the flow pattern after fracturing can be easily made thanks to the efficiency of the colored gel. Fractures observed from X-ray CT images coincide with those detected during excavation. Moreover, 3D images of fractures within the specimen in the radial injection cell can be reconstituted. These vertical fractures are generally perpendicular to the injection tube. The invasion of the colored gel is more important in the direction of the induced fractures, demonstrating that these fractures favor preferential flow paths within the sand specimen. From image analysis, made on cored samples containing fractures using X-ray CT and optical microscopy, the fracturing mechanisms can be identified. They involve the formation of dilation bands in the sand matrix and the subsequent transport of small particles present within these bands to form the fractures (i.e., the preferential path of high porosity) observed around the injection tube. The sensitivity analysis performed in the radial injection cell has permitted to investigate the effect of four main parameters: confining pressure, stress ratio, flow rate and permeability (which is controlled by the concentration of C10 particles in the sand specimens). The experimental results show that the confining pressure is the main factor affecting the initiation of the frac-regime. The critical fracturing pressure is mainly governed by the confining pressure (radial stress) and does not change significantly with the change of the stress ratio K_0. Higher confining pressure leads to a higher critical fracturing pressure, shorter fractures as well as a smaller permeability increase after fracturing. In the frac-regime, an increase of the flow rate leads to the extension of fractures, and

consequently, to an increase in overall permeability. The comparison of the tests with different concentrations of particles in the specimen shows a negligible effect of the initial permeability on the critical fracturing pressure. The impact of the subsequent injection cycles on the initiation of frac-regime has been also explored in the injection chamber. A smaller normalized fracturing pressure (P_{frac}/σ_h) is observed for the tests in which the sand pack experiences a high injection pressure in a previous stage.

- Comparing the obtained results with the two different injection setups, the experiments show a similar tendency of the pressure – flow rate curve and a similar fracture morphology induced along the injection tube. For all tests in the radial injection cell, fracturing occurs when the injection pressure reaches 2.35 ± 0.1 times the confining pressure which is about twice smaller than the fracturing pressure obtained in the radial injection chamber (in a range of 4 to 5). This size effect (larger size of the sand pack in the injection chamber) is associated with a lower radial flow velocity around the injection point when fracturing occurs as compared to that in the injection cell. In general, a higher increase of the overall permeability after fracturing always corresponds to the detection of longer and wider fractures within the medium.

Concerning Scenario 2 with the injection of water containing suspended particles, the main conclusions are the following:

- In this scenario, the key idea was that water containing suspended particles is first imposed at a constant flow rate in the matrix regime to partially plug the sand specimen, then the flow rate is increased rapidly in order to fracture this damaged specimen. The obtained results show that injection of suspended particles in the matrix regime leads to a decrease of the overall permeability because of the filter cake formation at the nearest layer of the sand specimen. Injection in the fracturing regime otherwise permits to partially restore the permeability loss by the unplugging of the filter cake and fracturing of the medium. Continued injection of suspended particles in the frac-regime did not lead to further loss of permeability because of the presence of fractures and a high injection rate, allowing particles to penetrate into the medium.
- The sensitivity analysis in the radial injection cell shows an important effect of particles concentration carried in water on the plugging mechanisms. A lower particles concentration leads to a faster plugging in terms of the amount of injected particles (i.e., the mass of injected particles). However, a higher volume of injection fluid is needed to provide a sufficient quantity of particles for plugging. For the fracturing conditions, a higher confining pressure exhibits a higher fracturing pressure, a lower permeability increase as well as longer and wider fractures. For the range of particles concentration studied here, no clear effect of this parameter was observed on the fracturing response. In all performed tests, the frac-regime initiates when the injection pressure reaches about 3.5 times the confining pressure.
- Comparing the obtained results of two injection scenarios in the injection cell (i.e., Scenario 1 - pure water and Scenario 2 - suspended particles), the second requires a higher injection pressure to reach the frac-regime because of the presence of filter cakes.

Moreover, the tests under this scenario present a higher increase of the permeability and longer fractures induced at the same stress state. In both scenarios, an increase of the confining pressure leads to an increase of the critical fracturing pressure, a lower increase of overall permeability as well as shorter fractures induced within the specimen.

- As for the injection cell setup, the two tests performed in the radial injection chamber present a continuous decrease of the overall permeability during the injection of suspended particles at a constant flow rate in the matrix regime, confirming the formation of a filter cake in the sand pack. Pressure pulses when injecting at higher flow rates may correspond to the unclogging of filter cakes rather than fracturing of the sand pack which also contribute to an increase of overall permeability of the damaged sand pack.

The extensive experimental results explored during this Ph.D work can provide additional important insights for production engineers to understand the underlying mechanisms of fracturing in unconsolidated sand reservoirs during the PWRI operation. Furthermore, this work can provide practical rules for identifying the critical pressure need for fracturing and a number of experimental data to validate predictive injectivity softwares.

Suggestions for future research

The experimental study presented in this thesis can be pursued and extended by performing further tests to better explore the effect of parameters on the fracturing response in unconsolidated sand specimens, in particular for the radial injection chamber.

❖ Concerning the experiments with the injection of pure water in the radial injection chamber:

- The injection pressure remains limited because of the capacity of the pump in terms of the injection rate and the configuration of the sand pack (height of the injection zone, permeability of the medium). We could be able to reach the state of fracturing with the tests under a confining pressure below 200 kPa. However, the effect of this parameter remains poorly understood in the calibration chamber compared to those performed in the radial injection cell. Additional tests under higher confining pressure are needed in an attempt to understand the effect of this parameter on the critical fracturing pressure and the fracture morphology.
- The effect of the damaged zone's thickness, for the radial injection chamber, (i.e., the internal ring containing a mixture of sand and particles) on the normalized fracturing pressure should be investigated in order to better understand the difference in the results in the two injection setups.
- Further tests with several injection phases will help to get a better understanding of the impact of subsequent injection cycles on the critical fracturing pressure.
- Increase in viscosity of the injection fluid could permit to fracture the medium at a lower flow rate and to increase the sweep efficiency of oil production as

compared with water. Therefore, it would be interesting to investigate the effect of the viscosity of the injected fluid, in both setups, on the critical fracturing pressure, the extension of fractures as well as the permeability increase.

❖ Concerning the experiments with the injection of water containing suspended particles:

- Further tests in the radial injection chamber should be performed to first study the profile of the deposited particles along all strainer tube and to further investigate the fracturing mechanisms as well as the effect of parameters on the fracturing process in the sand pack.
- This experimental work can be extended by studying injection of a fluid containing a mixture of oil droplets and fine particles. Ochi and Oughanem, 2018 have observed more aggressive formation damage when injecting this mixture compared to the one with fine particles only. The deposition of oil droplets within the specimen and between the deposited particles leads to a reduction of the pore-access size, and consequently, to a higher overall permeability decrease. To reach the fracture regime in a damaged specimen by the deposition of both oil droplets and particles may require a higher fracturing pressure than the one with particles only.

Another important future step of the study will be the modelling of the experimental tests presented in this thesis. The extensive results obtained in the experimental campaign performed during this thesis can thus be used to validate the predictive models of PWRI design. Furthermore, numerical modelling of the tests would permit to simulate the evolution of the stress and pressure fields inside the specimen and better understand the effect of the various parameters of the tests.

REFERENCES

Adachi, J.I., 2001. Fluid-driven fracture in permeable rock. University of Minnesota.

Adachi, J.I., Detournay, E., 2008. Plane strain propagation of a hydraulic fracture in a permeable rock. Eng. Fract. Mech. 75, 4666–4694. https://doi.org/10.1016/j.engfracmech.2008.04.006

Agarwal, K., Sharma, M.M., 2011. A new approach to modeling fracture growth in unconsolidated sands, in: SPE Annual Technical Conference and Exhibition. OnePetro.

Ahmadun, F.-R., Pendashteh, A., Abdullah, L.C., Biak, D.R.A., Madaeni, S.S., Abidin, Z.Z., 2009. Review of technologies for oil and gas produced water treatment. J. Hazard. Mater. 170, 530–551. https://doi.org/10.1016/j.jhazmat.2009.05.044

Al-Abduwani, F.A.., Shirzadi, A., van den Broek, W.M.G.T., Currie, P.K., 2005. Formation damage vs. solid particles deposition profile during laboratory-simulated produced-water reinjection. SPE J. 10, 138–151. https://doi.org/10.2118/82235-pa

Al-Abduwani, F.A.H., Hime, G., Alvarez, A., Farajzadeh, R., 2005. New experimental and modelling approach for the quantification of internal filtration, in: SPE European Formation Damage Conference. OnePetro. https://doi.org/10.2118/94634-ms

Alsiny, A., Vardoulakis, I., Drescher, A., 1992. Deformation localization in cavity inflation experiments on dry sand. Geotechnique 44, 395–410. https://doi.org/10.1680/geot.1994.44.2.365

Ameen, S., Taleghani, A.D., 2015. Dynamic modeling of channel formation during fluid injection into unconsolidated formations. SPE J. 689–700.

Amer, A.M., Awad, A.A., 1974. Permeability of Cohesionless Soils. J. Geotech. Eng. Div. 100, 1309–1316.

Bahrainian, S.S., Nabati, A., Hajidavalloo, E., 2018. Improved rheological model of oil-based drilling fluid for south- western Iranian oilfields. J. Pet. Sci. Technol. 8, 53–71. https://doi.org/10.22078/jpst.2017.2706.1459

Barenblatt, G.I., 2003. Scaling. Cambridge University Press.

Barkman, J.H., Davidson, D.H., 1972. Measuring water quality and predicting well impairment. J. Pet. Technol. 24, 865–873. https://doi.org/10.2118/3543-PA

Bautista, J.F., Taleghani, A.D., 2018. Prediction of formation damage at water injection wells due to channelization in unconsolidated formations. J. Pet. Sci. Eng. 164, 1–10. https://doi.org/10.1016/j.petrol.2017.12.073

Bayona, H.J., Saudi, A., 1993. Review of well injectivity performance in Saudi Arabia's Ghawar field seawater injection program, in: Middle East Oil Show. OnePetro, pp. 201–214. https://doi.org/10.2523/25531-ms

Benahmed, N., 2001. Comportement mécanique d'un sable sous cisaillement monotone et cyclique : application aux phénomènes de liquéfaction et de mobilité cyclique. Marne-la-vallée, ENPC.

Bendahmane, F., Marot, D., Alexis, A., 2008. Experimental parametric study of suffusion and backward erosion. J. Geotech. geoenvironmental Eng. 134, 57–67.

Bohloli, B., de Pater, C.J., 2006. Experimental study on hydraulic fracturing of soft rocks: Influence of fluid rheology and confining stress. J. Pet. Sci. Eng. 53, 1–12. https://doi.org/10.1016/j.petrol.2006.01.009

Bunger, A.P., Detournay, E., Garagash, D.I., 2005. Toughness-dominated hydraulic fracture

with leak-off. Int. J. Fract. 134, 175–190. https://doi.org/10.1007/s10704-005-0154-0

Carrier, B., Granet, S., 2012. Numerical modeling of hydraulic fracture problem in permeable medium using cohesive zone model. Eng. Fract. Mech. 79, 312–328. https://doi.org/10.1016/j.engfracmech.2011.11.012

Chang, D.S., Zhang, L.M., 2013. Critical hydraulic gradients of internal erosion under complex stress states. J. Geotech. Geoenvironmental Eng. 139, 1454–1467. https://doi.org/10.1061/(asce)gt.1943-5606.0000871

Chang, H., 2004. Hydraulic fracturing in particulate materials. Georgia Institute of Technology.

Chudnovsky, A., Shulkin, Y., Golovin, E., Zhang, H., Dudley, J.W., Wong, G.K., 2015. Observation and modeling of fluid flow under matrix and fracturing injections in unconsolidated sand, in: 49th US Rock Mechanics / Geomechanics Symposium 2015. OnePetro.

Cnudde, V., Boone, M.N., 2013. High-resolution X-ray computed tomography in geosciences: A review of the current technology and applications. Earth-Science Rev. 123, 1–17. https://doi.org/10.1016/j.earscirev.2013.04.003

Dal Ferro, B., Smith, M., 2007. Global onshore and offshore water production, in: Oil & Gas Review OTC Edition.

de Pater, C.J., Dong, Y., 2009. Fracture containment in soft sands by permeability or strength contrasts, in: SPE Hydraulic Fracturing Technology Conference. OnePetro, pp. 685–693. https://doi.org/10.2118/119634-ms

de Pater, C.J., Dong, Y., 2007. Experimental study of hydraulic fracturing in sand as a function of stress and fluid rheology, in: SPE - Hydraulic Fracturing Technology Conference. OnePetro. https://doi.org/10.2118/105620-ms

Detournay, E., 2016. Mechanics of Hydraulic Fractures. Annu. Rev. Fluid Mech. 48, 311–339. https://doi.org/10.1146/annurev-fluid-010814-014736

Detournay, E., Cheng, A.H.D., 1993. Fundamentals of poroelasticity, in: Analysis and Design Methods. Pergamon, pp. 113–171. https://doi.org/10.1016/b978-0-08-040615-2.50011-3

Dong, Y., 2010. Hydraulic fracture containment in sand. Delft University of Technology.

Du Bernard, X., Eichhubl, P., Aydin, A., 2002. Dilation bands: A new form of localized failure in granular media. Geophys. Res. Lett. 29, 1–4. https://doi.org/10.1029/2002GL015966

Dupla, J.C., 1995. Application de la sollicitation d'expansion de cavité cylindrique à l'évaluation des caractéristiques de liquéfaction d'un sable. Ecole Nationale des Ponts et Chaussées.

Economides, M.J., al., E., 2007. On the problem of fluid leakoff during hydraulic fracturing. Transp. Porous Media 67, 487–499. https://doi.org/10.1007/s11242-006-9038-7

Farajzadeh, R., 2004. Produced Water Re-Injection (PWRI): An experimental investigation into internal filtration and external cake build up. Delft Univ. Technol.

Feia, S., 2015. Effet de l'injection d'eau de production sur la perméabilité des réservoirs pétroliers non cimentés. University Paris Est.

Feia, S., Dupla, J.C., Canou, J., Ghabezloo, S., Sulem, J., Chabot, B., Aubry, E., Mainguy, M., 2017a. An experimental setup with radial injection for investigation of transport and deposition of suspended particles in porous media. Geotech. Test. J. 40. https://doi.org/10.1520/GTJ20160032

Feia, S., Dupla, J.C., Ghabezloo, S., Sulem, J., Canou, J., Onaisi, A., Lescanne, H., Aubry, E., 2015. Experimental investigation of particle suspension injection and permeability impairment in porous media. Geomech. Energy Environ. 3, 24–39.

https://doi.org/10.1016/j.gete.2015.07.001

Feia, S., Sulem, J., Dupla, J.C., Ghabezloo, S., Canou, J., Muhammed, R.D., 2017b. Injection d'eau chargée en particules solides dans les réservoirs de sable. Internal report: Unpublished work.

Fell, R., Fry, J.-J., (eds), 2007. Internal erosion of dams and their foundations: selected and reviewed papers from the workshop on internal erosion and piping of dams and their foundations, Aussois, France, 25-27 April 2005. CRC Press.

Fjar, E., Holt, R. M., Raaen, A. M., & Horsrud, P., 2008. Petroleum related rock mechanics, Elsevier.

Francis, R., 1997. Etude du comportement mécanique de micropieux modèles en chambre d'étalonnage. Application aux effets de groupe. Ecole Nationale des Ponts et Chaussées.

Gallagher, P.M., Lin, Y., 2009. Colloidal Silica Transport through Liquefiable Porous Media. J. Geotech. Geoenvironmental Eng. 135, 1702–1712. https://doi.org/10.1061/(asce)gt.1943-5606.0000123

Garagash, D.I., 2006. Plane-strain propagation of a fluid-driven fracture during injection and shut-in: Asymptotics of large toughness. Eng. Fract. Mech. 73, 456–481. https://doi.org/10.1016/j.engfracmech.2005.07.012

Geertsma, J., de Klerk, F., 1969. Rapid Method of Predicting Width and Extent of Hydraulically Induced Fractures. J Pet. Technol. 21, 1571–1581. https://doi.org/10.2118/2458-pa

Germanovich, L.N., Hurt, R.S., Ayoub, J.A., Siebrits, E., Norman, W.D., Ispas, I., Montgomery, C., 2012. Experimental study of hydraulic fracturing in unconsolidated materials, in: SPE International Symposium and Exhibition on Formation Damage Control. OnePetro, pp. 931–945. https://doi.org/10.2118/151827-MS

Gieg, L.M., Jack, T.R., Foght, J.M., 2011. Biological souring and mitigation in oil reservoirs. Appl. Microbiol. Biotechnol. 92, 263–282. https://doi.org/10.1007/s00253-011-3542-6

Gil, I., 2005. Hydraulic fracturing of poorly consolidated formations: Considerations on rock properties and failure mechanisms. The University of Oklahoma.

Golovin, E., Chudnovsky, A., Dudley, J.W., Wong, G.K., 2011. Injection rate effects on waterflooding mechanisms and injectivity in cohesionless sand, in: 45th US Rock Mechanics / Geomechanics Symposium. OnePetro.

Golovin, E., Jasarevic, H., Chudnovsky, A., Dudley, J.W., Wong, G.K., 2010. Observation and characterization of hydraulic fracture in cohesionless sand, in: 44th US Rock Mechanics Symposium and 5th US-Canada Rock Mechanics Symposium. OnePetro.

Hurt, R.S., 2012. Toughness-dominated hydraulic fractures in cohesionless particulate materials. Georg. Inst. Technol. Georgia Institute of Technology.

Hurt, R.S., Germanovich, L.N., 2012. Parameters controlling hydraulic fracturing and fracture tip-dominated leakoff in unconsolidated sands, in: SPE Annual Technical Conference and Exhibition. OnePetro, pp. 1–19. https://doi.org/10.2118/160140-MS

Igunnu, E.T., Chen, G.Z., 2014. Produced water treatment technologies. Int. J. Low-Carbon Technol. 9, 157–177. https://doi.org/10.1093/ijlct/cts049

Jaeger, J., Cook, N.G., Zimmerman, R., 2007. Poroelasticity and thermoelasticity, in: Fundamentals of Rock Mechanics. Blackwell Publishing. https://doi.org/10.1111/j.1468-8123.2009.00251.x

Jasarevic, H., Golovin, E., Chudnovsky, A., Dudley, J.W., Wong, G.K., 2010. Observation and modeling of hydraulic fracture initiation in cohesionless sand, in: 44th US Rock Mechanics Symposium and 5th US-Canada Rock Mechanics Symposium. OnePetro.

Khodaverdian, M., McElfresh, P., 2000. Hydraulic fracturing stimulation in poorly consolidated sand: Mechanisms and consequences, in: SPE Annual Technical Conference and Exhibition. OnePetro. https://doi.org/10.2118/63233-MS

Khodaverdian, M.F., Sorop, T., Postif, S.J., Van den Hoek, P.J., 2010. Polymer flooding in unconsolidated-sand formations: fracturing and geomechanical considerations, in: SPE Production & Operations. pp. 211–222. https://doi.org/10.2118/121840-PA

Khristianovic, S.A., Zheltov, Y.P., 1955. Formation of vertical fractures by means of highly viscous liquid, in: 4th World Petroleum Congress Proceedings. OnePetro, pp. 579–586.

Lafleur, J., Mlynarek, J., Rollin, A.L., 1989. Filtration of broadly graded cohesionless soils. J. Geotech. Eng. 115, 1747–1768.

Le Kouby, A., 2003. Etude du comportement mécanique de micropieux sous chargements monotones et cycliques verticaux. Application aux effets de groupe. Ecole Nationale des Ponts et Chaussées.

Le Thiet, T., 2005. Étude du processus de vibrofonçage d'inclusions cylindriques en chambre d'étalonnage. Application au pieux. Ecole des Ponts ParisTech.

Li, Z., Wong, R.C.K., 2008. Estimation of suspended particle retention rate and permeability damage in sandstone from back analysis of laboratory injection tests, in: Canadian International Petroleum Conference. OnePetro.

Mahadevan, A., Orpe, A. V, Kudrolli, A., Mahadevan, L., 2012. Flow-induced channelization in a porous medium. EPL (Europhysics Lett. 98. https://doi.org/10.1209/0295-5075/98/58003

Mainguy, M., Perrier, S., Buré, E., 2020. Produced-Water Reinjection in Deep Offshore Miocene Reservoirs, Block 17, Angola. SPE Prod. Oper. 35, 292–307. https://doi.org/10.2118/197061-PA

Marot, D., Benamar, A., 2012. Suffusion, transport and filtration of fine particles in granular soil, Erosion of Geomaterials. https://doi.org/10.1002/9781118561737.ch2

Montgomery, C.T., Smith, M.B., Jr, C., Dollarhide, F.E., Elbel, J.L., Robert Fast, C., Hannah, R.R., Harrington, L.J., Perkins, T.K., Prats, M., van Poollen, H., 2010. Hydraulic fracturing: history of an enduring technology. J. Pet. Technol. 62, 26–40.

Muhammed, R.D., 2015. Etude en chambre d'étalonnage du frottement sol-pieu sous grands nombres de cycles. Application au calcul des fondations profondes dans les sols fins saturés. Université Pierre et Marie Curie-Paris VI.

Nordgren, R.P., 1972. Propagation of a vertical hydraulic fracture. Soc. Pet. Eng. J. 12, 306–314. https://doi.org/10.2118/3009-pa

Ochi, J., Dexheimer, D., Corpel, P. V., 2014. Produced-water-reinjection design and uncertainties assessment, in: SPE Production and Operations. pp. 192–203. https://doi.org/10.2118/165138-PA

Ochi, J., Oughanem, R., 2018. An experimental investigation of formation damage induced by PWRI in unconsolidated sands, in: SPE International Symposium on Formation Damage Control. https://doi.org/10.2118/189513-ms

Oliveira, E.P., Santelli, R.E., Cassella, R.J., 2005. Direct determination of lead in produced waters from petroleum exploration by electrothermal atomic absorption spectrometry X-ray fluorescence using Ir-W permanent modifier combined with hydrofluoric acid. Anal. Chim. Acta 545, 85–91. https://doi.org/10.1016/j.aca.2005.04.030

Onaisi, A., Ochi, J., Mainguy, M., Souillard, P., 2011. Modeling non-matrix flow and seals integrity in soft sand reservoirs, in: SPE European Formation Damage Conference. Society of Petroleum Engineers, pp. 1371–1387.

Papanastasiou, P., 1999. The effective fracture toughness in hydraulic fracturing. Int. J. Fract. 96, 127–147. https://doi.org/10.1023/A:1018676212444

Papanastasiou, P., 1997. The influence of plasticity in hydraulic fracturing. Int. J. Fract. 84, 61–79. https://doi.org/10.1023/A:1007336003057

Papanastasiou, P., Thiercelin, M., 1993. Influence of inelastic rock behaviour in hydraulic fracturing. Int. J. rock Mech. Min. Sci. Geomech. Abstr. 30, 1241–1247. https://doi.org/10.1016/0148-9062(93)90102-J

Papanastasiou, P.C., 1997. A coupled elastoplastic hydraulic fracturing model. Int. J. rock Mech. Min. Sci. 34, 431. https://doi.org/10.1016/S1365-1609(97)00132-9

Perkins, T.K., Kern, L.R., 1961. Widths of Hydraulic Fractures. J. Pet. Technol. 13, 937–949. https://doi.org/10.2118/89-pa

Persoff, B.P., Apps, J., Moridis, G., Whang, J.M., 1999. Effect of dilution and contaminants on sand grouted with colloidal silica. J. Geotech. Geoenvironmental Eng. 125, 461–469.

Reynolds, R.R., Kiker, R.D., 2003. Produced water and associated issues, Oklahoma Geological Survey.

Saada, Z., Canou, J., Dormieux, L., Dupla, J.C., 2006. Evaluation of elementary filtration properties of a cement grout injected in a sand. Can. Geotech. J. 43, 1273–1289. https://doi.org/10.1139/T06-082

Sarris, E., Papanastasiou, P., 2013. Numerical modeling of fluid-driven fractures in cohesive poroelastoplastic continuum. Int. J. Numer. Anal. Methods Geomech. 37, 1822–1846. https://doi.org/10.1002/nag

Savitski, A., Detournay, E., 2002. Propagation of a penny-shaped fluid-driven fracture in an impermeable rock: asymptotic solutions. Int. J. Solids Struct. 39, 6311–6337.

Schindelin, J., Arganda-Carreras, I., Frise, E., Kaynig, V., Longair, M., Pietzsch, T., Preibisch, S., Rueden, C., Saalfeld, S., Schmid, B., Tinevez, J.Y., White, D.J., Hartenstein, V., Eliceiri, K., Tomancak, P., Cardona, A., 2012. Fiji: An open-source platform for biological-image analysis. Nat. Methods 9, 676–682. https://doi.org/10.1038/nmeth.2019

Schmid, B., Schindelin, J., Cardona, A., Longair, M., Heisenberg, M., 2010. A high-level 3D visualization API for Java and ImageJ. BMC Bioinformatics 11.

Sharma, M.M., Pang, S., Wennberg, K.E., Morgenthaler, L.N., 1997. Injectivity decline in water-injection wells: An offshore Gulf of Mexico case study, in: SPE European Formation Damage Conference. OnePetro. https://doi.org/10.2118/60901-PA

Shell, I.E., 2009. Integrated water flood training.

Shutong, P., Sharma, M.M., 1997. A model for predicting injectivity decline in water-injection wells, in: SPE Formation Evaluation. pp. 194–201.

Skempton, A.W., Brogan, J.M., 1994. Experiments on piping in sandy gravels. Géotechnique 44, 449–460.

Souilah, R., Brocart, B., Ourir, A., Onaisi, A., Pourpak, H., Ochi, J., Lescanne, H., 2014. Produced water re-injection in a deep offshore environment-Angola block 17, in: SPE - European Formation Damage Conference, Proceedings,. OnePetro. https://doi.org/10.2118/168216-ms

Tali, B., 2011. Comportement de l'interface sols-structure sous sollicitations cycliques : application au calcul des fondations profondes. Université Paris-Est.

Todd, A.C., Kumar, T., Mohammadi, S., 1990. Value and analysis of core-based water-quality experiments as related to water injection schemes. SPE Form. Eval. 5. https://doi.org/10.2118/17148-pa

Tomlinson, S.S., Vaid, Y.P., 2000. Seepage forces and confining pressure effects on piping erosion. Can. Geotech. J. 37, 1–13. https://doi.org/10.1139/t99-116

Van Dam, D.B., Papanastasiou, P., De Pater, C.J., 2000. Impact of rock plasticity on hydraulic fracture propagation and closure, in: SPE Annual Technical Conference and Exhibition. OnePetro, pp. 531–543. https://doi.org/10.2523/63172-ms

van Oort, E., van Velzen, J.F.G., Leerlooijer, K., 1993. Impairment by suspended solids invasion. Testing and prediction. SPE Prod. Facil. 8, 178–183. https://doi.org/10.2118/23822-pa

Wong, G.K., Dudley, J.W., Golovin, E., Zhang, H., Chudnovsky, A., 2017. Injector completion performance under hydraulic fracturing and matrix flooding conditions into a sand pack, in: 51st US Rock Mechanics / Geomechanics Symposium 2017. OnePetro.

Wong, R.C.K., Mettananda, D.C.A., 2010. Permeability reduction in Qishn sandstone specimens due to particle suspension injection. Transp. porous media 81, 105–122. https://doi.org/10.1007/s11242-009-9387-0

Wu, R., 2006. Some fundamental mechanisms of hydraulic fracturing. Georgia Institute of Technology.

Xiao, M., Shwiyhat, N., 2012. Experimental investigation of the effects of suffusion on physical and geomechanic characteristics of sandy soils. Geotech. Test. J. 35, 1–11. https://doi.org/10.1520/GTJ104594

Xu, B., Wong, R.C.K., 2010. A 3D finite element model for history matching hydraulic fracturing in unconsolidated sands formation. J. Can. Pet. Technol. 49.

Yew, C.H., Weng, X., 2014. Mechanics of Hydraulic Fracturing, 2nd ed.

Zhai, Z., Sharma, M.M., 2005. A new approach to modeling hydraulic fractures in unconsolidated sands, in: SPE Annual Technical Conference and Exhibition. OnePetro.

Zhou, J., Dong, Y., de Pater, C.J., Zitha, P.L.J., 2010. Experimental study of hydraulic fracturing caused by polymer injection in unconsolidated heavy oil reservoirs, in: Society of Petroleum Engineers - International Oil and Gas Conference and Exhibition in China 2010, IOGCEC. OnePetro. https://doi.org/10.2523/131261-ms

Zhou, K., Hou, J., Sun, Q., Guo, L., Bing, S., Du, Q., Yao, C., 2018. A Study on Particle Suspension Flow and Permeability Impairment in Porous Media Using LBM–DEM–IMB Simulation Method. Transp. Porous Media 124, 681–698. https://doi.org/10.1007/s11242-018-1089-z

LIST OF TABLES

LIST OF FIGURES

APPENDICES

Appendix A Preliminary tests of the dyes in uniaxial cell

The characterizes of these tests are presented in Tab. A-1 below.

Tab. A-1: Validation tests of the dye using the uniaxial device.

Test	Dye	% by mass of the dye diluted in water	Confining pressure (kPa)	Flow rate (l/min)
C1	Puricolor® Red	0.3%	300	0.14
C2	Puricolor® Red	0.07%	300	0.14
C3	Basacid® Blue 762	0.2%	300	0.14
C4	Dispers® Blue 6900	0.2%	300	0.14

Fig. A-1 shows the results of test C1 in which Puricolor® Red (0.3 %) was injected. The initial permeability of the specimen is approximately 132 mD. When injecting the Puricolor® Red dye, a gradual increase of injection pressure was observed ($\Delta P \approx 10$ kPa/min) at constant flow rate of 0.14 l/min. It is caused by the filtration of Puricolor® Red particles. After injecting for about 12 minutes, a large amount of Puricolor was deposed at the entrance of the specimen (Fig. A-2). However, the whole specimen is well colored using this dye. The second test (C2) was carried out with the same dye by reducing its concentration by a factor of 4 (0.07% instead of 0.3% by mass). The results are presented in Fig. A-3. During the injection of the dye, the pressure increased by approximately 5 kPa/min (2 times smaller than test C1). Higher concentration of the Puricolor dye results in a higher increase of the injection pressure. Fig. A-4 shows a good coloring of the specimen.

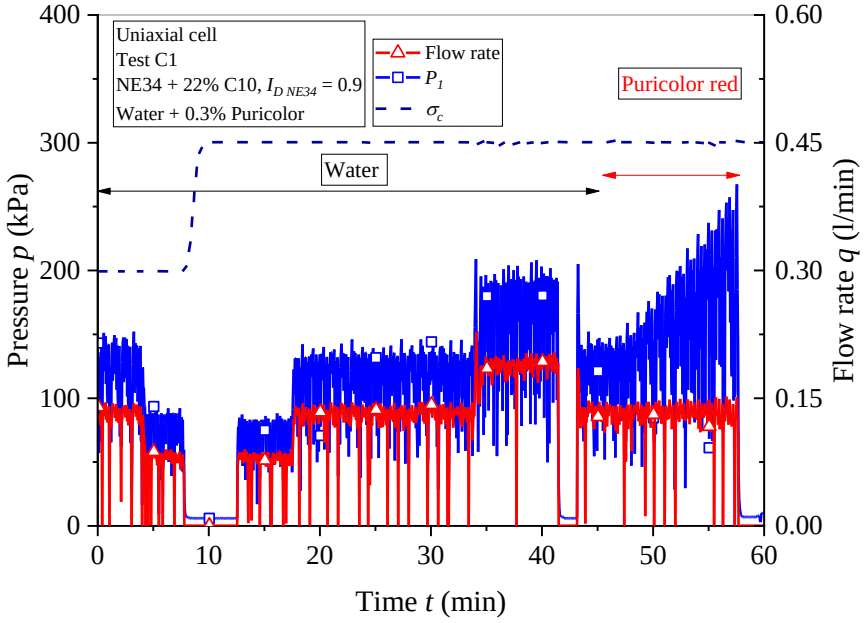

Fig. A-1: Test C1 with Puricolor® red (0.07%) in the uniaxial cell.

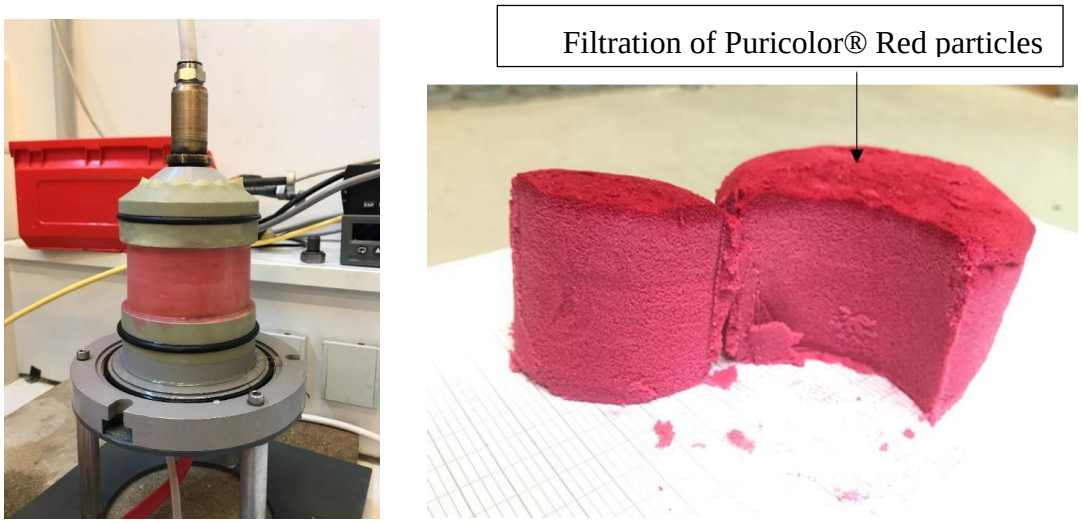

Fig. A-2: Disassembling of test C1.

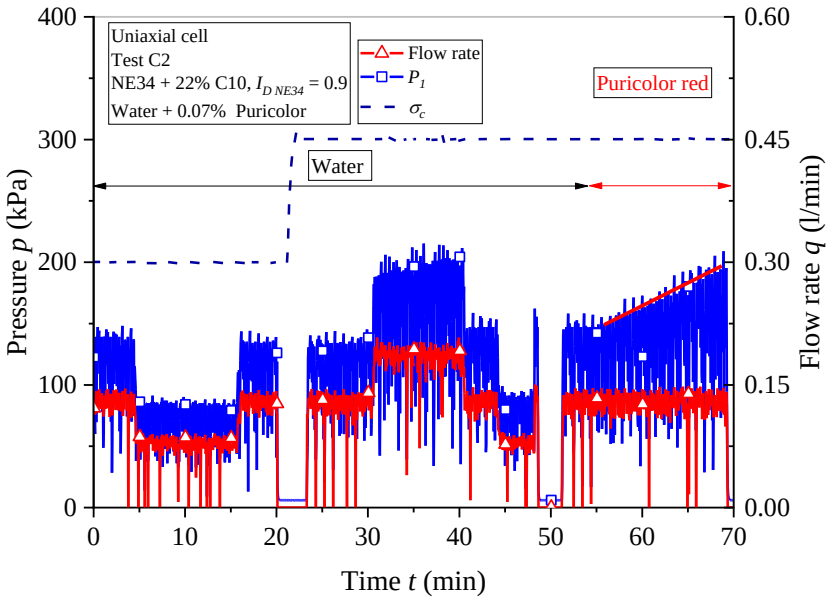

Fig. A-3: Test C2 with 0.07% of Puricolor® red.

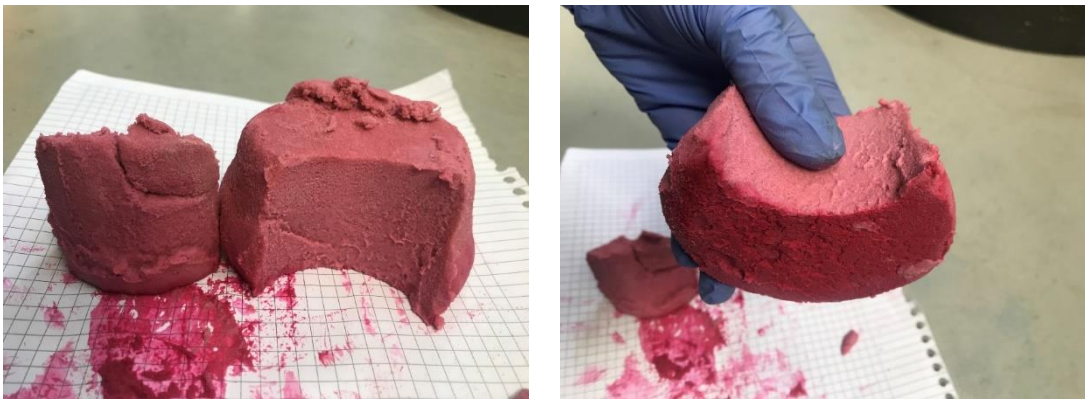

Fig. A-4: Disassembling of test C2.

The injection test (C3) with Basacid Blue 762 (0.2 %) was performed by repeating the protocol as two previous tests. When injecting this dye, the pressure kept constant over time (Fig. A-5). During the disassembling, good penetration of this dye without filtration was observed (Fig. A-6). In addition, the entire device (sensor, pipes, injection pump, etc.) can be easily cleaned with water. An injection test (Q4) with the third dye (Dispers Blue 9600) was also performed (Fig. A-7). Even this dye is an aqueous solution and only 0.2 % by mass of the injection fluid (water + 0.2 % Dispers), a high filtration of this dye at the entrance of the sample is identified (Fig. A-8). During disassembling, it was very difficult to clean because it adheres to the inner surface of the flexible connection tube.

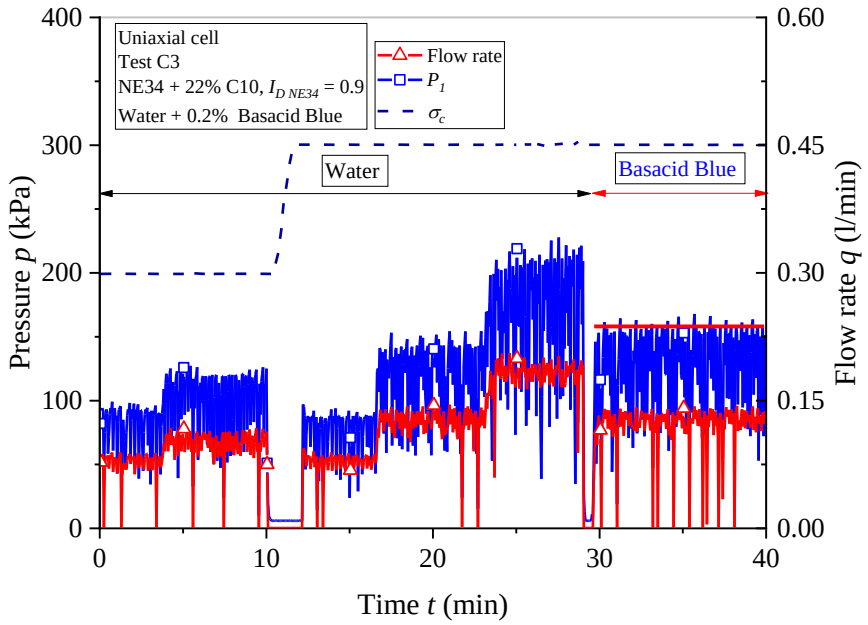

Fig. A-5: Test C3 with 0.2% of Basacid Blue 762.

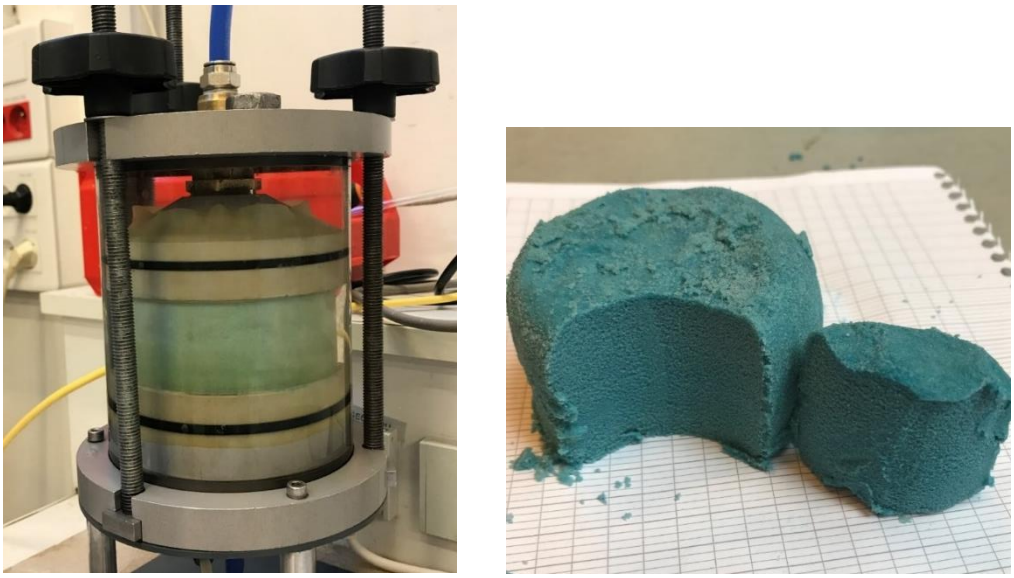

Fig. A-6: Disassembling of test C3.

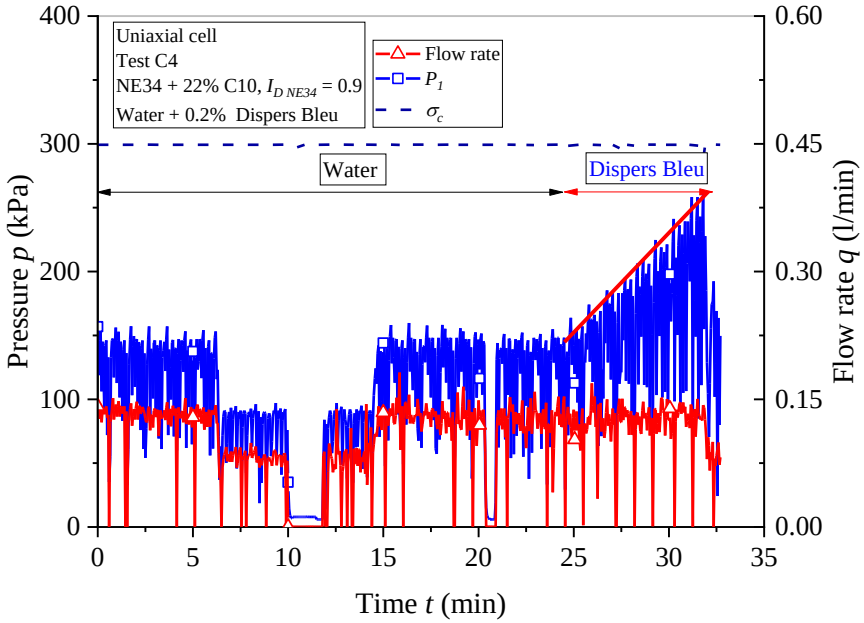

Fig. A-7: Test C4 with 0.2% of Dispers Bleu 9600.

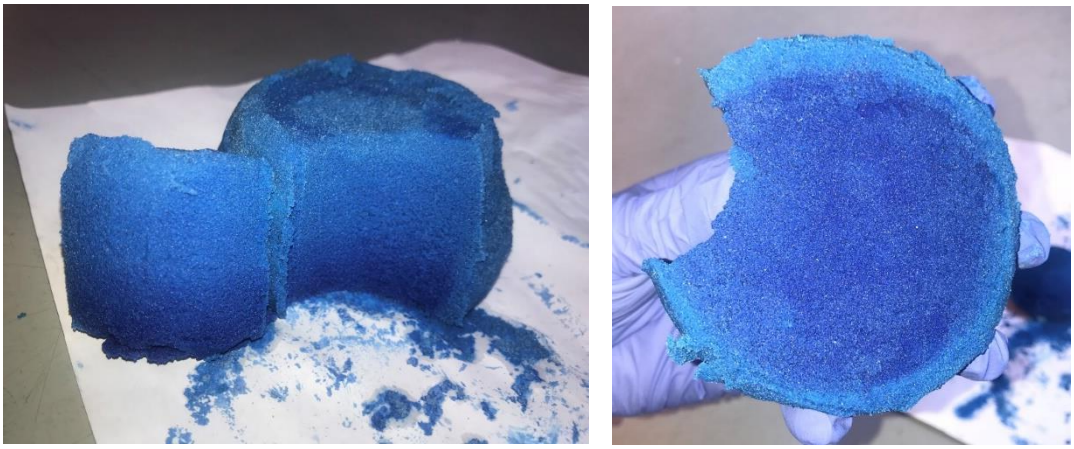

Fig. A-8: Disassembling of test C3.

Appendix B Preliminary tests with water injection in the radial injection cell

B.1 Results of the tests Q1, Q2 and Q3

The first three preliminary tests were performed using the first configuration of the injection tube. The outer diameter of the tube is 10 mm, and its inner diameter is 6 mm. Several 1 mm diameter holes are made along the tube. The distance between these holes is 15 mm with 6 diametrically opposed holes punched at each level of the height (Fig. B-1). To prevent grains entering into the tube, we covered it with an 80 µm polyamide sieve. The tube is made of PPMA to prevent absorption of X-rays during scanning of X-ray CT. Fig. B-2 presents the results obtained in test Q1. The characteristic of the test is presented in Table 3.1. An isotropic confining pressure of 200 kPa was applied. During the test, an important fluctuation was observed in all measurement data. At a flow rate of about 0.83 l/min, we identify a fluctuation of about 20 kPa in measured pressure. This fluctuation may be caused by noise from the electrical system, pump pulsation and the accuracy of the data acquisition system. In the second test, modifications were made to the device, a pulsation dampener and a multi-meter were installed (Fig. B-3).

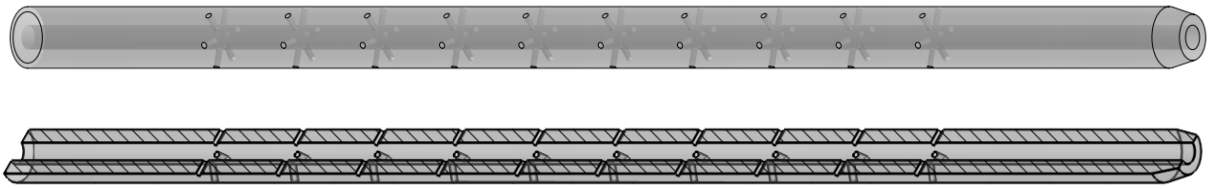

Fig. B-1: 1st configuration (Tube 1) of the injection tube used in the tests Q1, Q2, Q3.

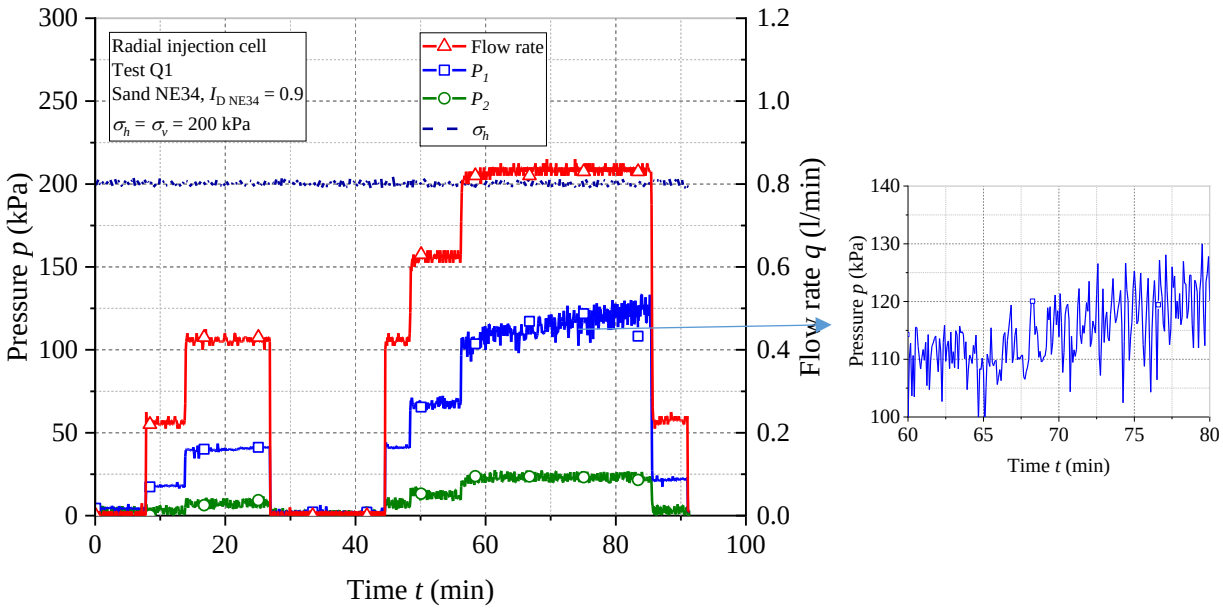

Fig. B-2: Results of test Q1.

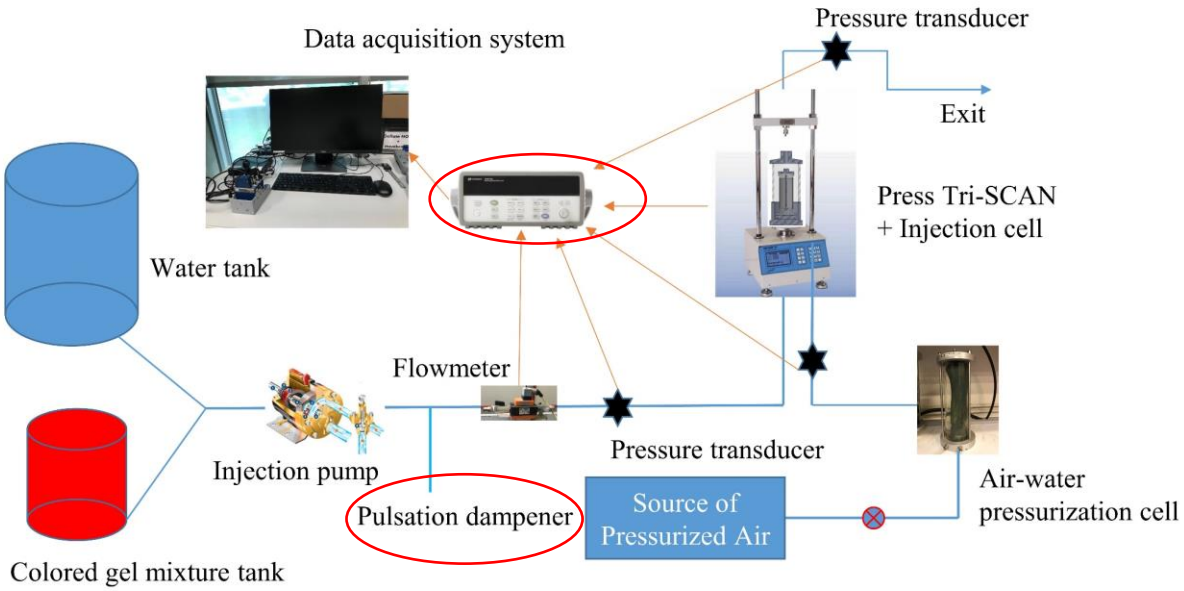

Fig. B-3: Modification made to the radial injection cell setup.

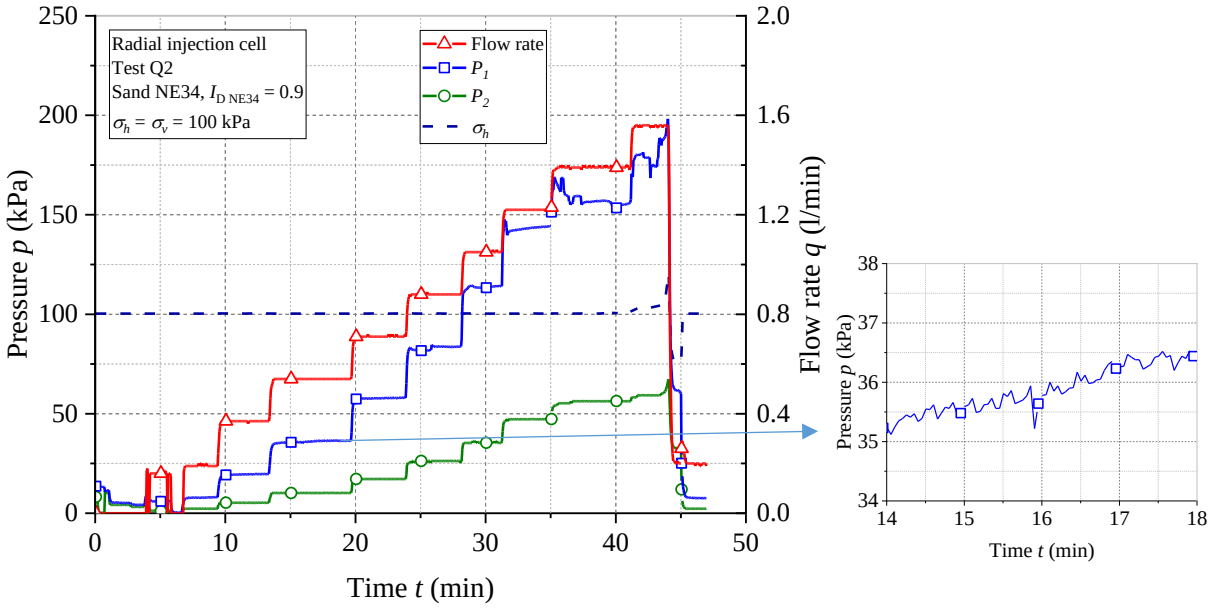

Fig. B-4: Results of test Q2.

The results of test Q2 are shown in Fig. B-4, there is no longer any fluctuation in the measurement data. This confirms the effectiveness of the changes made. At a flow rate = 0.54 l/ min, the pressure fluctuation is less than 1 kPa which is the accuracy of the pressure sensor. At the end of test Q2, Basacid blue 762 dye (0.2% diluted in water) was injected in order to visualize the flow within the specimen under the condition of the matrix injection regime. Fig. B-5 shows the disassembling of the specimen. No trace of Basacid Blue was observed in the two low permeability layers (Fig. B-5b, c and h). The diffusion of the blue in the injection zone remains radial and relatively symmetrical around the injection tube.

After two validation tests on Fontainebleau NE34 sand specimen, test Q3 was carried out on the mixture of NE34 + 22% C10. This is used as the reference mixture in this research. However, the density index of the NE34 sand matrix reached only $I_{D\ NE34}$ = 0.6 (corresponding to a porosity of 27%) instead of 0.9 as the reference case (corresponding to a porosity of 23%) due to the difficulty of compaction. Noted that the central tube is made by PMMA which is a fragile material and it could be broken during the specimen preparation. Fig. B-6 shows the results of test Q3. The injection pressure increased gradually without stabilizing during test. This increase can be caused by the accumulation of C10 fines at the outlet of the specimen which relates to the clogging of the lateral drainage system (Fig. B-7). Note that the current number of O-rings in the lateral drainage system is not sufficient. Indeed, when the confining pressure is applied (200 kPa), the membrane is pressed against the specimen, and the flow space is reduced to small conduits around the O-rings. A new drainage system is going to be fabricated by adding more O-rings in order to overcome this problem.

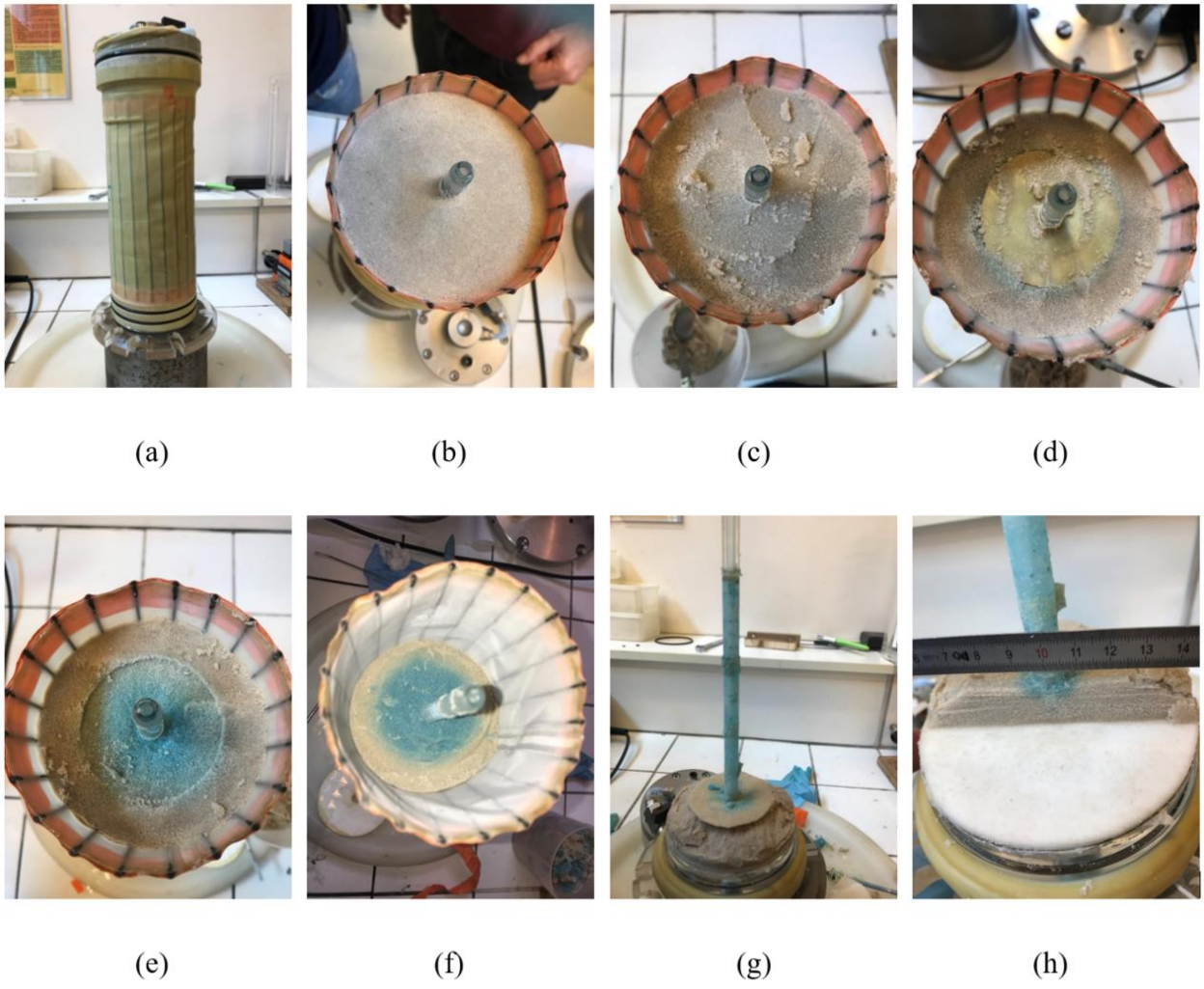

Fig. B-5: Disassembling of specimen Q2 : (a) view of the specimen ; (b) upper surface of the lower permeability layer; (c),(d) above the small membrane; (e) below the membrane ; (f) mid-height of the injection area; (g) view of the injection tube; (h) lower permeability layer.

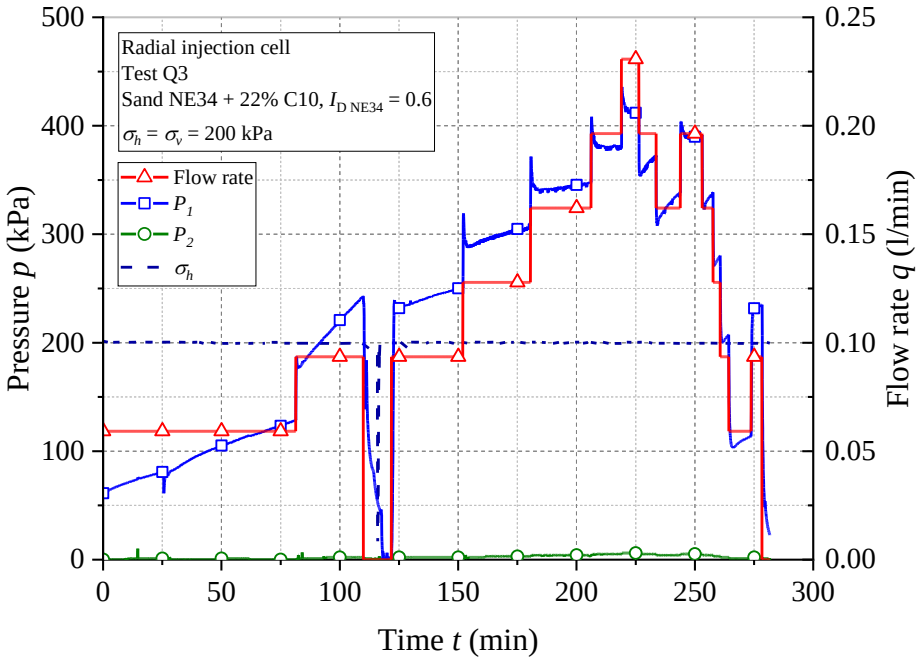

Fig. B-6: Results of test Q3.

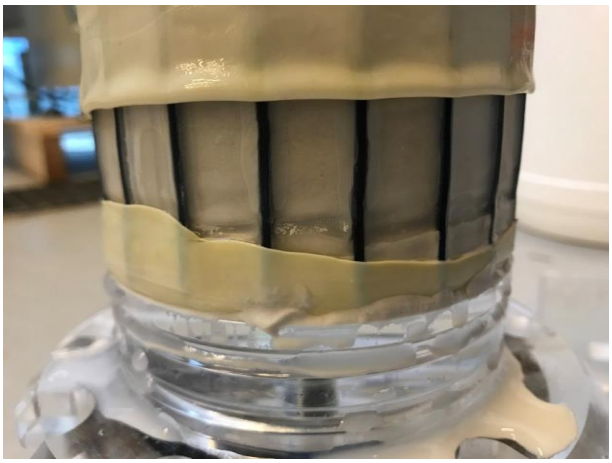

Fig. B-7: Fine particles out of the specimen and accumulate in the lateral drainage system (Test Q3).

B.2 Test Q4

Fig. B-8 shows the 2nd configuration of the injection tube which is used as the Q4. More open holes as well as the bigger holes (1.5 mm) are made in the tube as compared to the those in 1st configuration. The distance between these holes is 6 mm. The third configuration is shown in Fig. B-9. The open holes are made at the helical groove with the same number of holes as in the second configuration, but the diameter is smaller (D_{hole} = 1 mm). The third configuration allows, a priori, a more uniform injection than the first and the second.

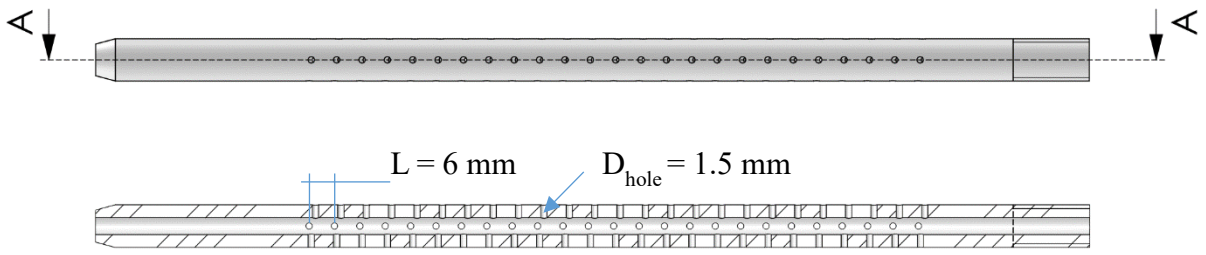

Fig. B-8: 2nd configuration (Tube 2) of the injection tube used in test Q4.

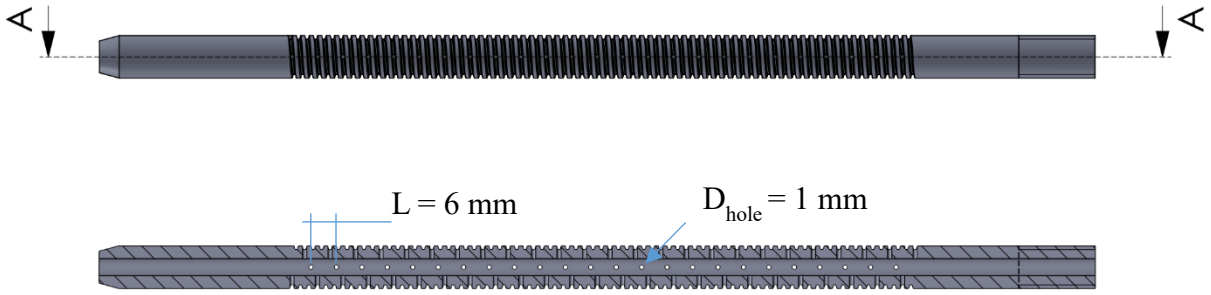

Fig. B-9: 3nd configuration (Tube 3) of the injection tube used in test Q5.

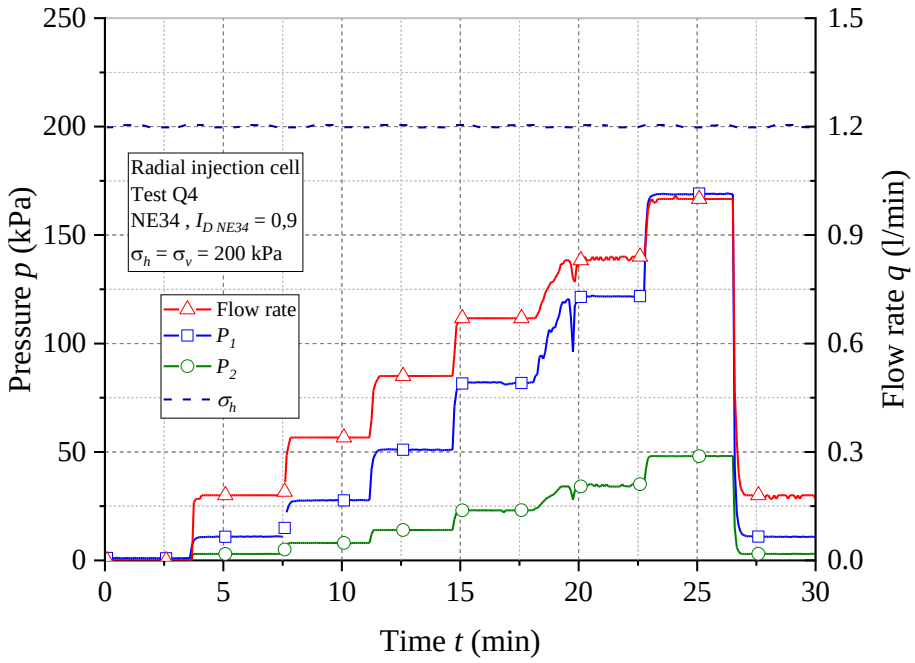

Fig. B-10: Results of test Q4

Fig. B-10 shows the results of test Q4. The flow rate is increased in successive steps up to 1 l/min. At each step, not only an increase in the pressure at the injection inlet is observed, but also an increase in the pressure measured at the outlet of the specimen. Fig. B-11 shows the flow-pressure curves for test Q4. The value of ΔP is the pressure difference between the two

pressure measuring sensors (inlet pressure - outlet pressure). It makes evident in Fig. B-11 a nonlinear relation of the flow-pressure curve in the matrix regime.

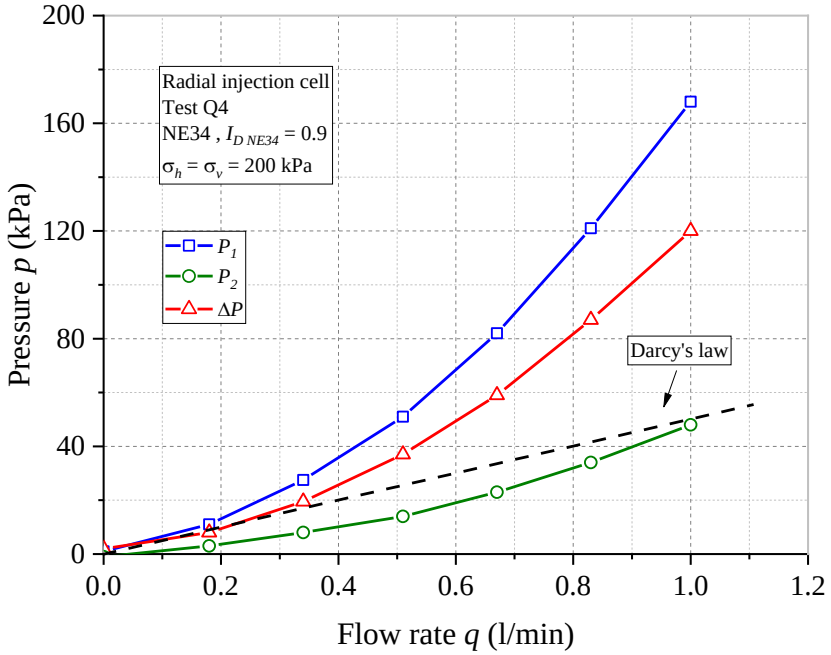

Fig. B-11: Pressure – flow rate curve of test Q4

When the permeability remains constant (matrix regime), there must be a linear relationship between the injection flow rate and the corresponding pressure (black dotted line in Fig. B-11). However, the measured values of the pressure are higher than the theoretical values.

B.3 Test Q5

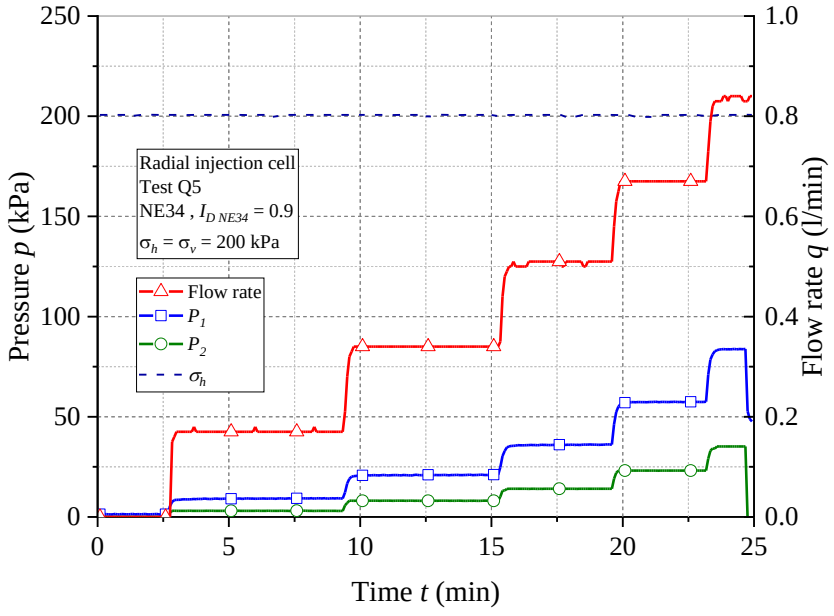

Fig. B-12: Results of test Q5.

Test Q5 was carried out with the same characteristics of test Q4, but changing the type of injection tube. This allows studying the effect of the tube configuration on the injection pressure response. The results of test Q5, presented in Fig. B-12, show the same trends as those observed in test Q4, with a significant increase in the pressure measured at the outlet.

The injection with the third configuration of the tube (test Q5) decreases the inlet pressure compared to the measurement of test Q4 (Fig. B-13). This confirms that this configuration (helical groove) allows for a more uniform injection along the tube.

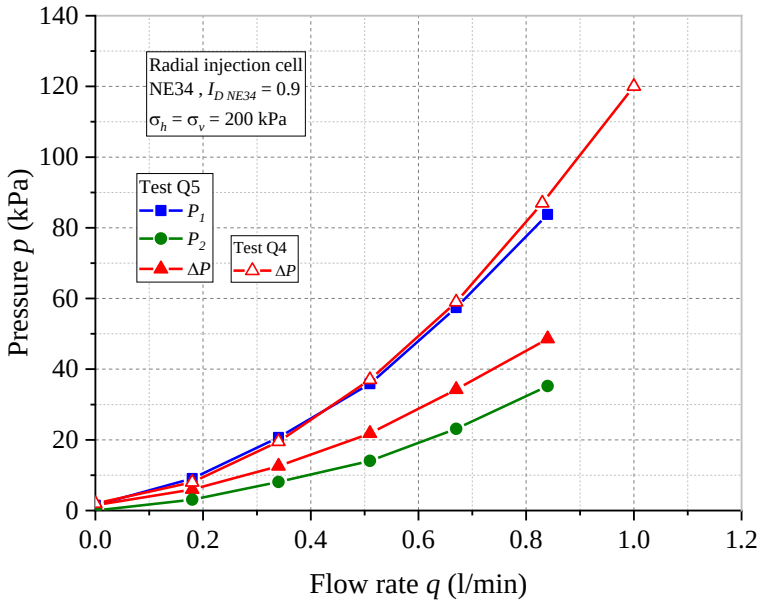

Fig. B-13: Flow rate - pressure curve of test Q5 comparing with the result of the Q4.

Fig. B-14 shows the position of the pressure transducers installed on the setup. During tests Q4 and Q5, a long Connection tube was connected to the outlet of the pressure sensor to discharge injected water (Fig. B-15). This pipe causes a very high pressure loss on the pressure measurement. In fact, during a second injection phase, carried out on the Q5 test without the outlet pipe, a reduction in the measured pressure values was observed (Fig. B-16). In particular, the outlet pressure P_2 is close to atmospheric pressure even at a high flow rate. On the other hand, the value of ΔP remains similar in both cases.

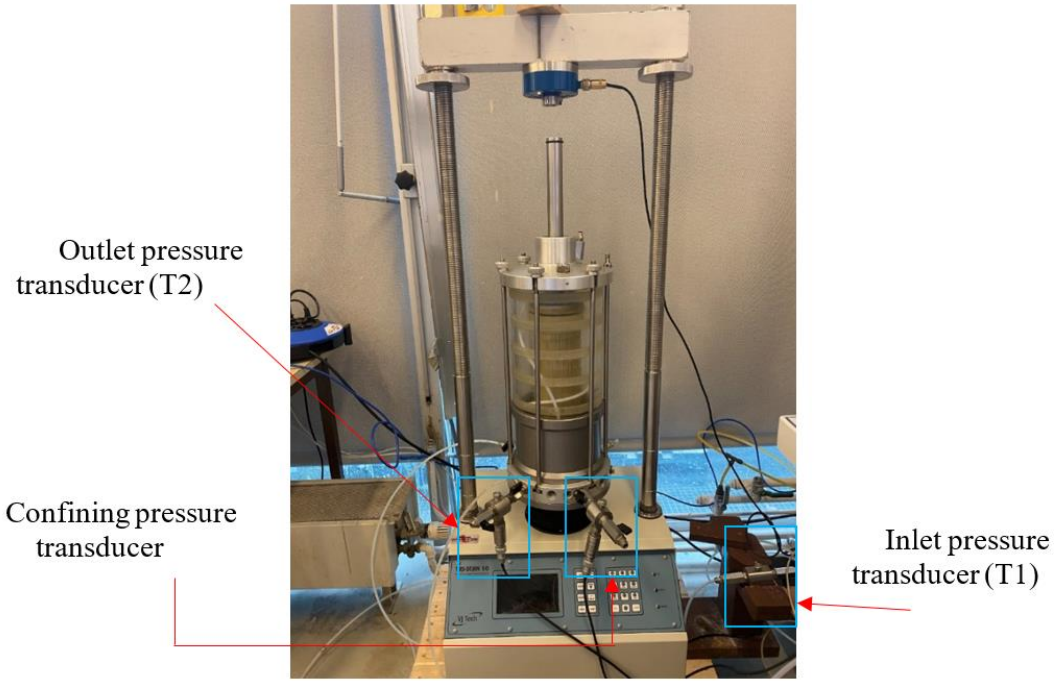

Fig. B-14: Position of the pressure transducers in the device setup.

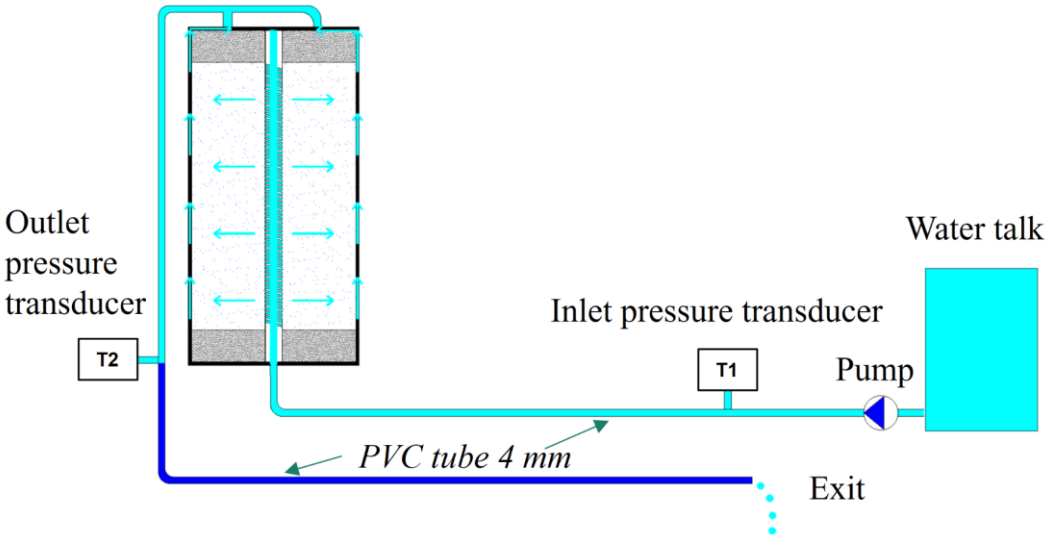

Fig. B-15: Schema representation of the fluid flow during injection.

As the pressures transducers are installed outside of the specimen, at a given flow rate, the total pressure drop (difference in pressure measured between two pressure transducers T1 and T2) is the sum of pressure loss (loss of hydraulic head) in the driving line (flexible connection tube, valve, hydraulic tee fitting) and pressure loss in the specimen. A detailed study of the pressure loss due to the device will be presented later in Appendix C. A representative diagram of the pressure drop of test Q5 is shown in Fig. B-17 based on the measured data. In the case of Q4 and Q5, since the permeability of the specimen is high (specimen of the NE34 pure sand), the pressure loss by the flow though the specimen is small compared to the pressure loss due to

the driving line. This may explain the non-linear shape of the pressure-flow curve observed in tests Q4 and Q5.

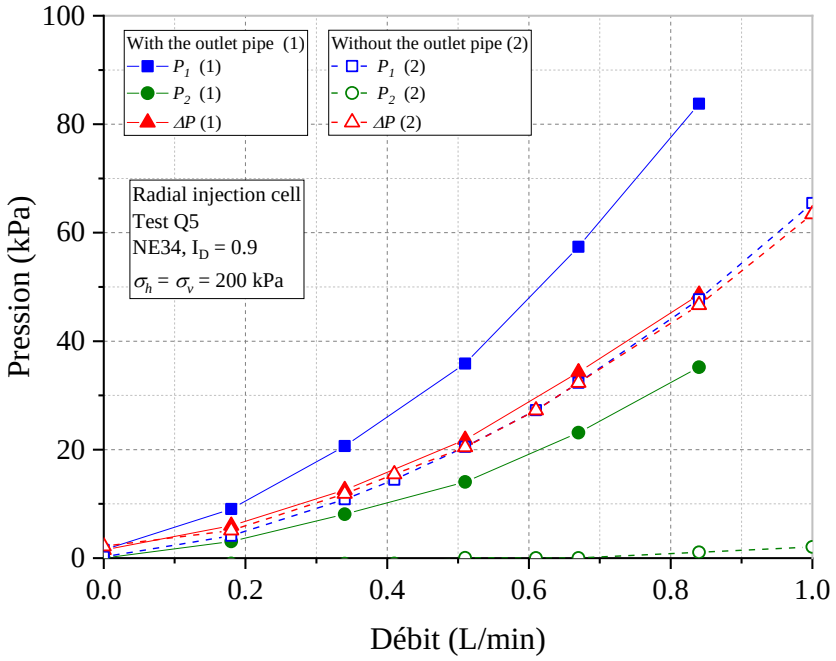

Fig. B-16: Results of test Q5 with and without the outlet pipe connected to the outlet of sensor T2.

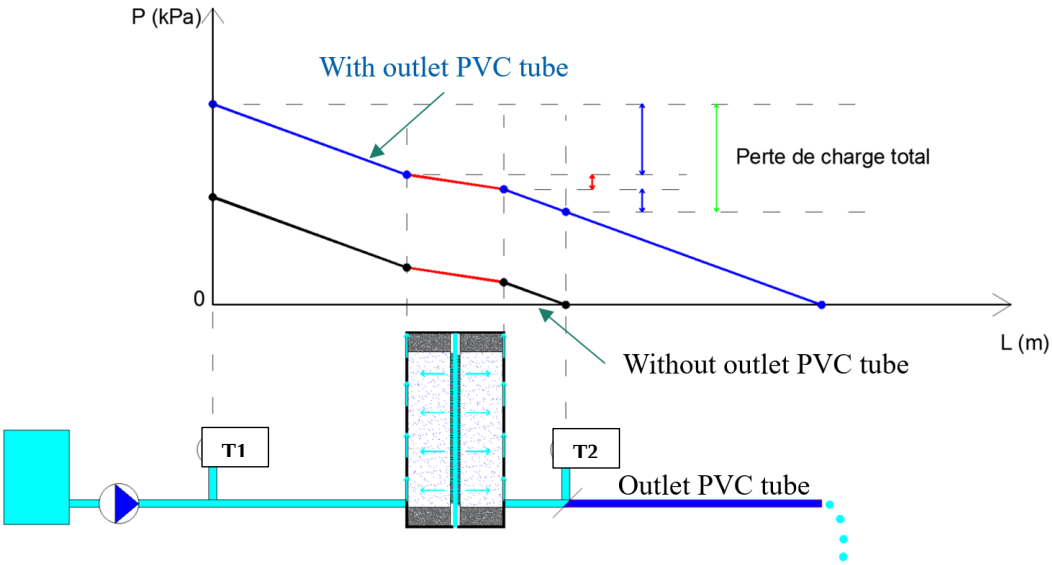

Fig. B-17: Schema diagram of the pressure loss in test Q5 at an imposed flow rate.

In this study, the specimen is reconstituted with a mixture of N34 sand and 22% of C10 fines. The permeability tests in Section 2.2.1.3 show that the addition of 22% of C10 fines reduces the permeability by a factor of 50 to 60 times compared to the case without fines (pure

NE34). Therefore, the pressure drop will be much higher in the case of mixing with 22% fines compared to the case without fines. Fig. B-18 shows a representative diagram of the effect of permeability on the pressure drop measured at a given flow rate. In the case of the N34 + 22% C10 mixture, the pressure loss by the driving line is negligible as compared to that due to the specimen.

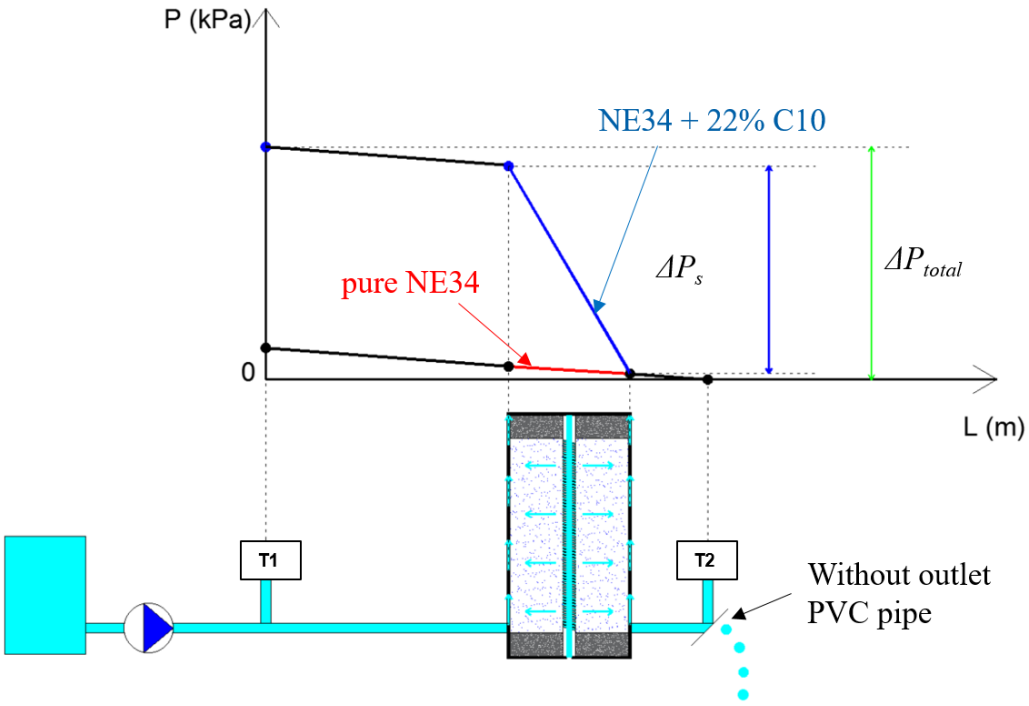

Fig. B-18: Schema diagram of the pressure loss with different specimen permeability at a same imposed flow rate.

At the end of the Q5, we injected the dye Basacid Blue to visualize the flow through the specimen in the matrix regime. A small amount of the water + 0.2% Basacid Bleu 762 mixture, corresponding to half the void volume of the specimen, was injected. During excavation, a symmetrical distribution of blue was observed along the central tube (Fig. B-19). This observation validates the configuration of the tube used in test Q5 (helical groove). Among the injection tube tested (Fig. B-20), the third configuration (Tube 3) is selected for the parametric study in radial injection cell.

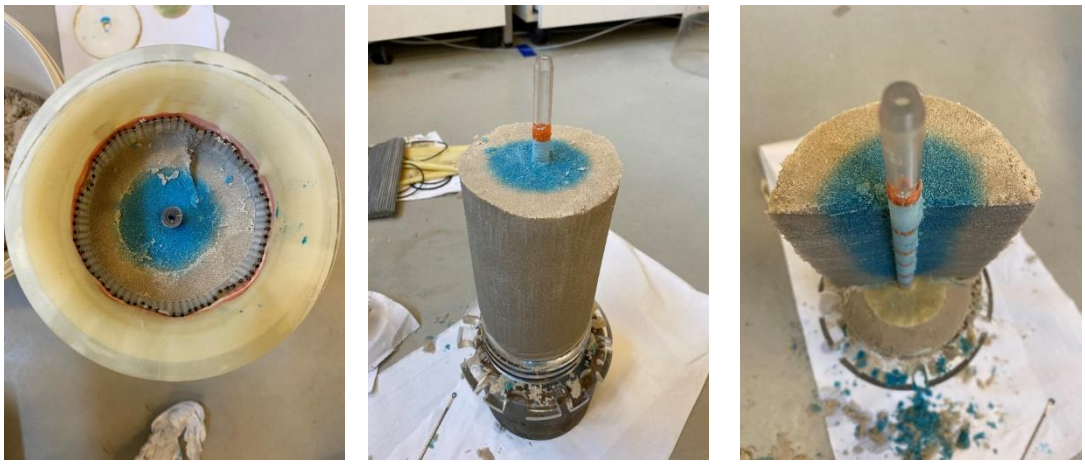

Fig. B-19: Views of the specimen during disassembling.

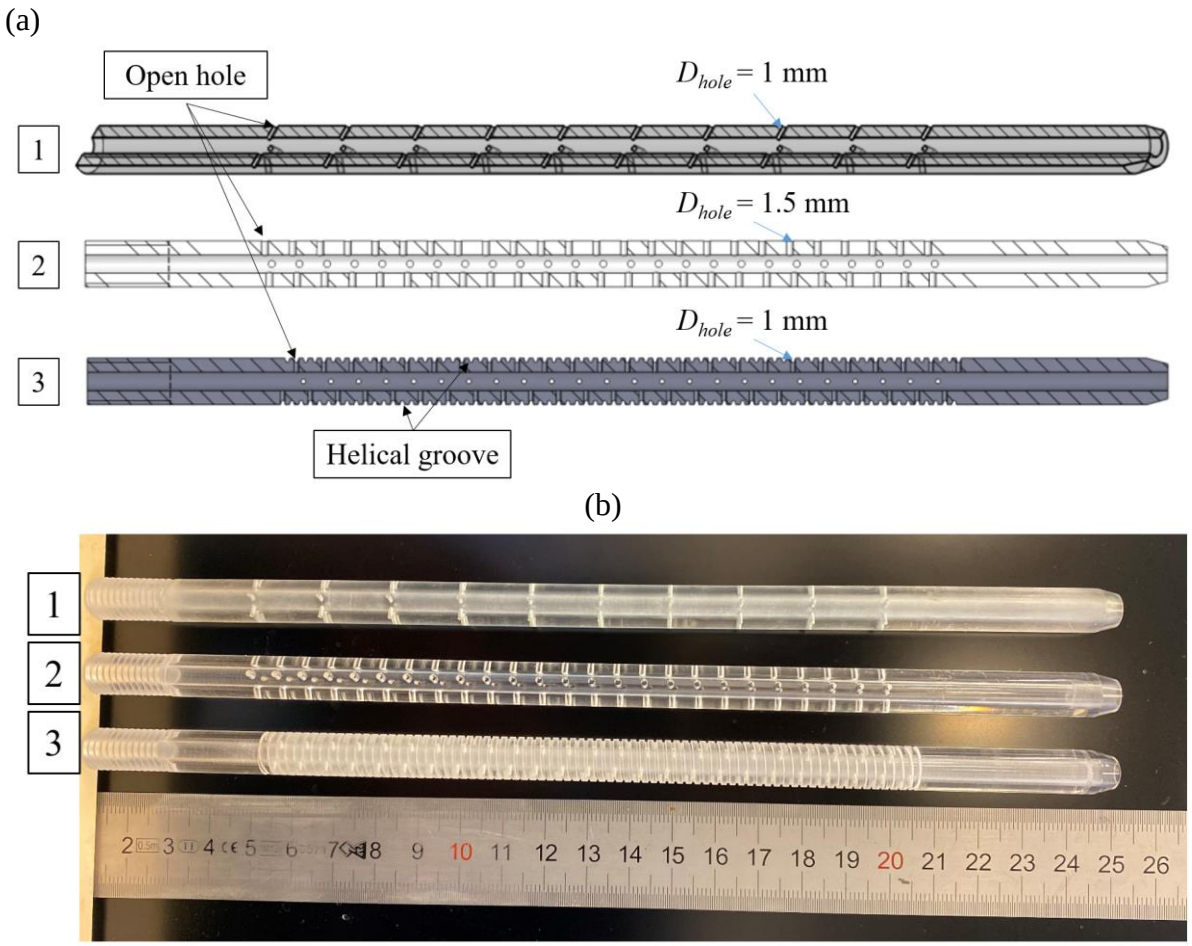

Fig. B-20: Three configurations of the injection tube used in the preliminary tests: (a) design; (b) view.

B.4 Test Q6

B.4.1 Results of the test during the injection phase

Fig. B-21 shows all 5 phases of test Q6. Phase 1 consists of a gradual increase by steps of the flow rate step to 0.21 l/min at an isotropic stress condition of 200 kPa to calculate the initial permeability of the specimen. During this phase, the phenomenon of gradually increasing pressure over time at a constant imposed flow rate was observed. The increase in pressure corresponds to a decrease in the permeability of the specimen. In phase 2, an anisotropic stress state (σ_h = 200 kPa, σ_v = 400 kPa) was applied to study the effect of this parameter on the permeability of the specimen. In phase 3, the flow rate was gradually increased to reach the frac regime. However, for a flow rate of about 0.66 l/min, corresponding to an initial pressure of about 380 kPa, a rapid pressure increase was identified. This step was maintained for approximately 2 hours, with no stabilization observed. Phase 4 corresponds to the continuation of phase 3, but with a higher maximum flow rate of 0.8 l/min. In this phase, the first pressure was observed at a flow rate of about 0.7 l/min, corresponding to a fracturing pressure of about 460 kPa (2.3 σ_h). At the end of the test, the mixture of the silica gel with the dye was injected (Phase 5) in order to freeze the specimen. The results obtained during these five phases are described in more detail below.

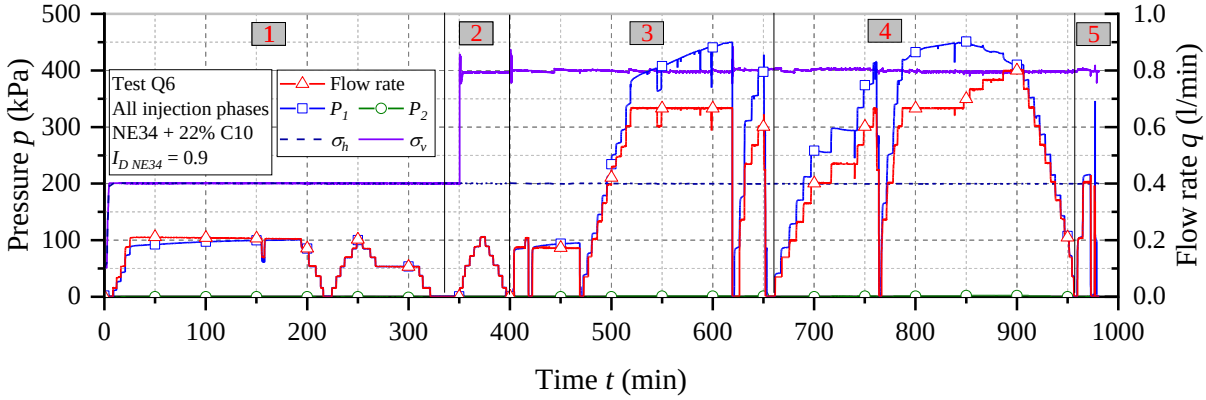

Fig. B-21: Injection results of test Q6.

a. Phase 1

Fig. B-22 shows the results of phase 1. The flow rate was gradually increased in increments to approximately 0.21 l/min. During the injection, it was observed that the pressure gradually increases during a constant flow rate. For this reason, the injection at the last loading step (flow rate = 0.21 l/min) is maintained until stabilization, which corresponds to a duration of about 3 h. The pressure increased from 89 to 100 kPa. Unloading was then carried out, followed by a second recharge/discharge cycle. During these stages, the pressure stabilizes very quickly after a few minutes of injection. Fig. B-23 shows the pressure-flow curve for phase 1. It is identified that the increase in pressure during the last loading stage affected the overall permeability of the massif. The permeability decreased about 12% from its initial value (about 89 mD). During the second reload/unload cycle, the permeability hardly changed (Tab. B-1). In Fig. B-23, we

also present an estimation of the pressure drop due to the flexible driving tube that is taken from the calibration test. It is highlighted that this value is much smaller than the total pressure drop (about 5%), so the pressure drop due to the driving line could be neglected in the calculation of the permeability of the specimen.

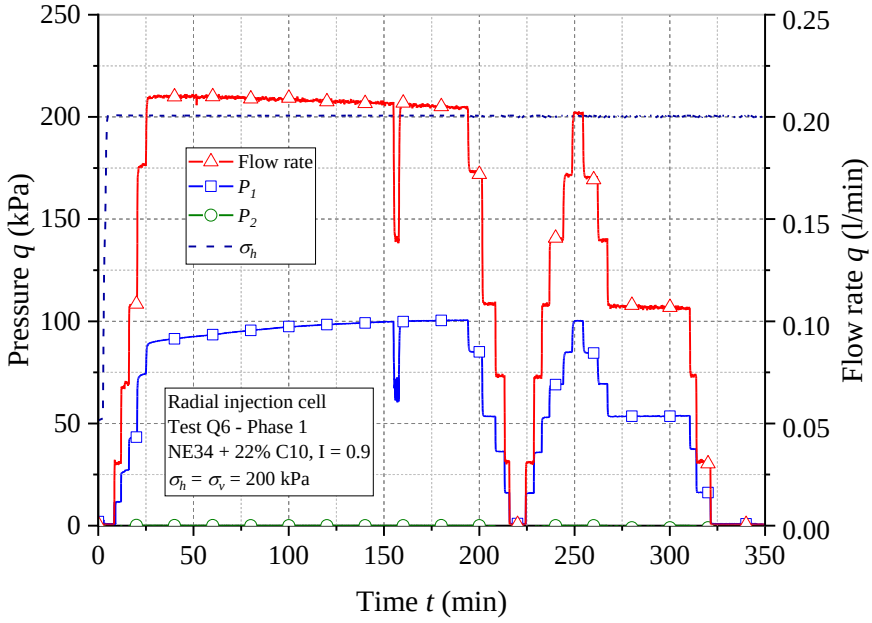

Fig. B-22: Results of the phase 1 (Test Q6).

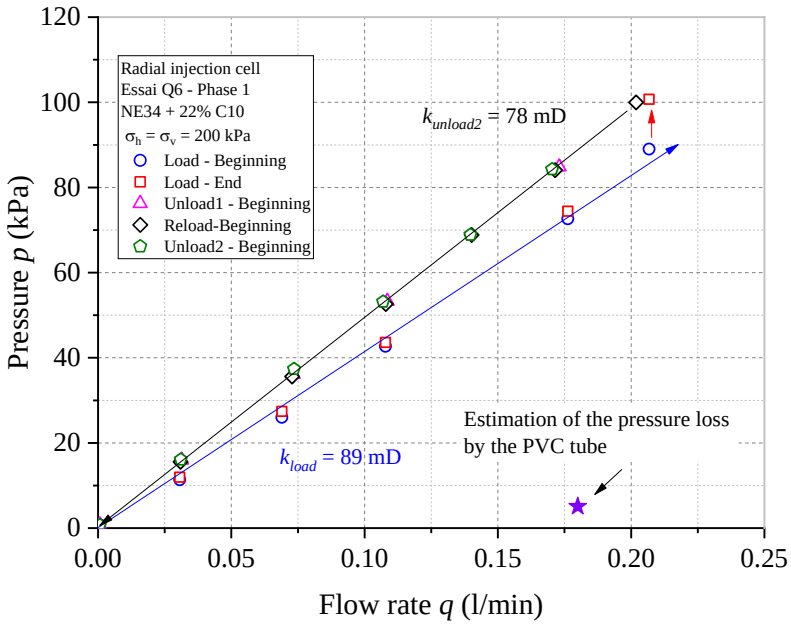

Fig. B-23: Pressure – flow rate curves. The plotted pressures are the measured values at the beginning and at the end of each flow rate step (Phase 1 – Test Q6)

Tab. B-1: Evolution of the permeability during phase 1

Step	Load (1)	Unload 1 (1)	Reload (1)	Unload 2 (1)
k (mD)	89.3	78.4	77.4	77.9

b. Phase 2

This phase was performed on the same day as phase 1. It consists in applying the vertical stress (σ_v) with the press TRI-SCAN, then injecting at the same flow rate steps as in phase 1. An additional vertical stress of 200 kPa was applied to reach the final vertical stress of 400 kPa (initially: $\sigma_{vo} = \sigma_h = 200$ kPa). The results during injection are shown in Fig. B-24. During this phase, the pressure stabilizes rapidly during all injection steps. The evolution of the permeability is presented in Tab. B-2. Compared to phase 1, the permeability keeps unchanged. It can be concluded that for the range of stresses considered, there is no effect of the applied stress change on the permeability of the specimen.

Tab. B-2: Evolution of the permeability during phase 2

Step	Load (2)	Unload (2)
k (mD)	76.9	76.4

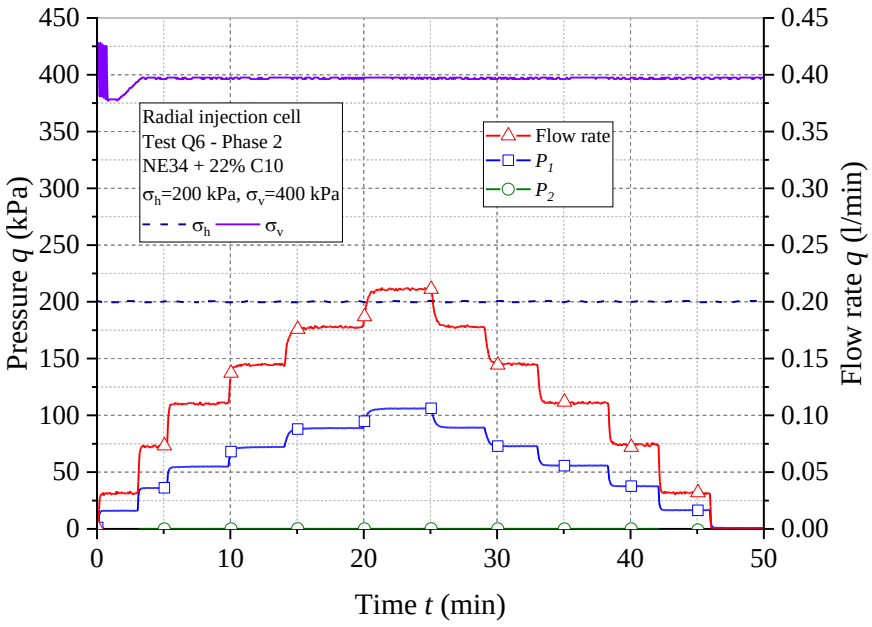

(a)

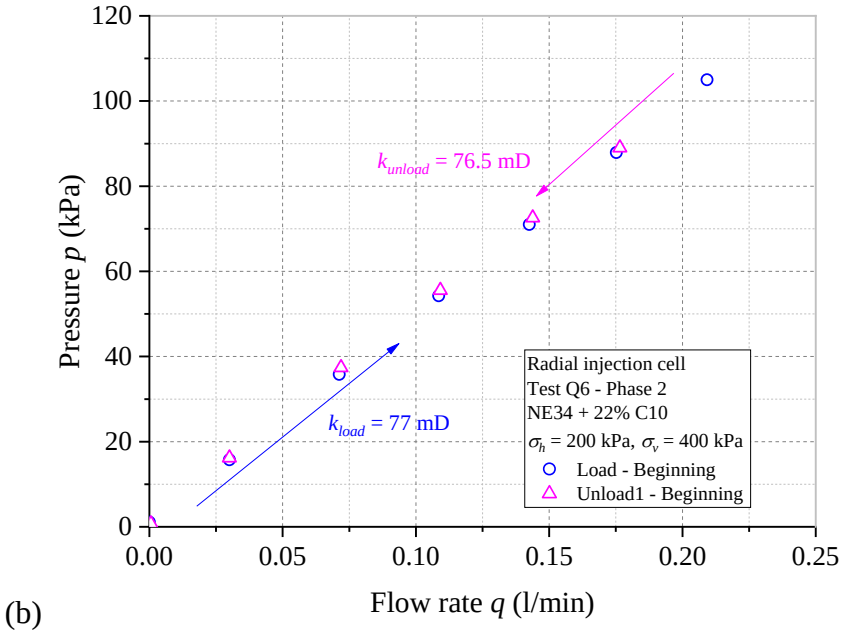

(b)

Fig. B-24: Test Q6 - Phase 2: (a) Evolution of the pressure and the flow rate versus time; (b) pressure – flow rate curve.

c. Phase 3

The specimen was maintained under stresses for a weekend before continuing with Phase 3. The results of this phase are shown in Fig. B-25. To verify the pressure stabilization, injection was maintained for approximately one hour at a flow rate of about 0.17 l/min. As in phase 1, the pressure increased gradually with a rate $\Delta P \approx 0.16$ kPa/min. This increase corresponds to a decrease in the permeability of the specimen.

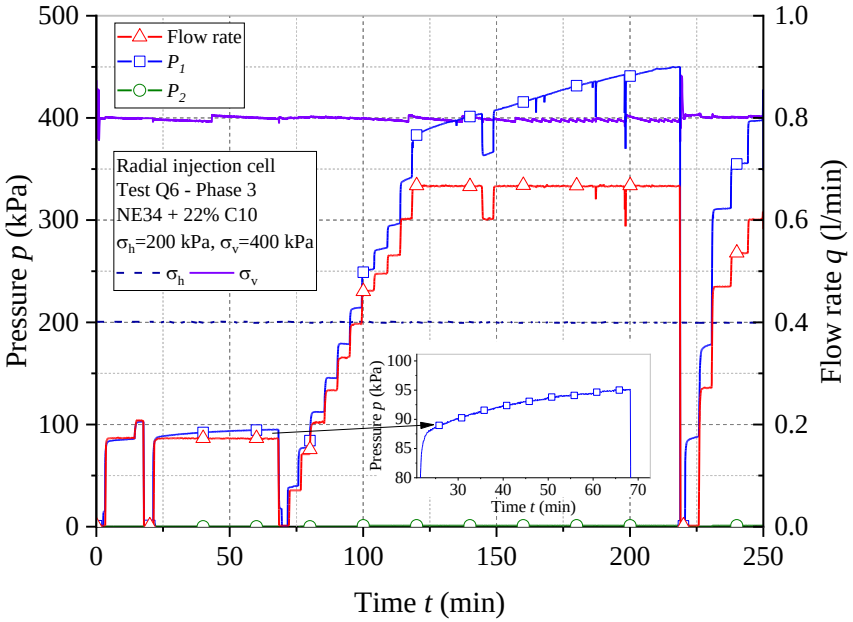

Fig. B-25: Results of Phase 3

To avoid the decrease of the permeability during injection, each step is maintained for only 5 minutes. For the maximum flow rate of 0.66 l/min, corresponding to an initial pressure of 380 kPa, no change in the slope of the pressure-flow curve is identified (Fig. B-26).

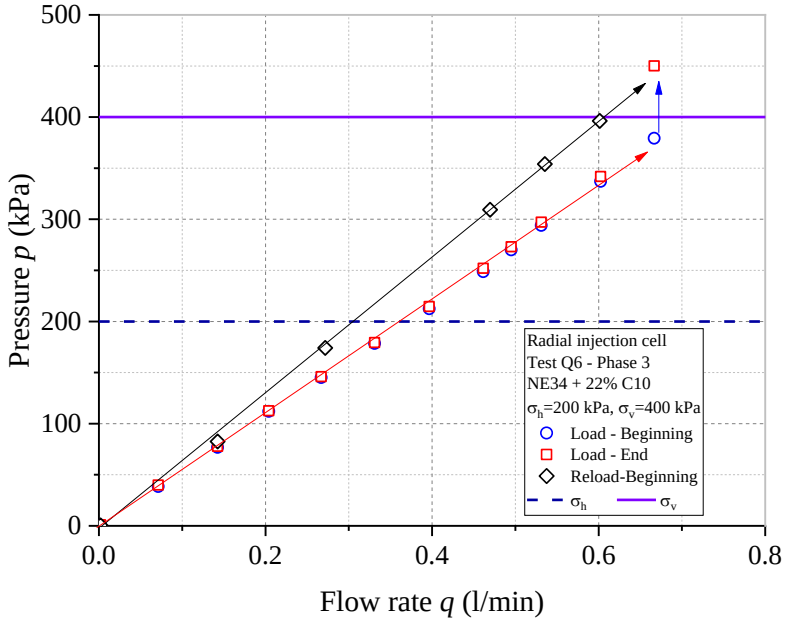

Fig. B-26: Injection pressure – flow rate curve (Phase 3 – Test Q6).

At a flow rate of 0.66 l/min (Fig. B-27), a rapid increase of injection pressure ($\Delta P \approx 1.5$ kPa/min) is observed. This step was maintained for approximately 1.7 h and the rate of pressure increase tended to decrease with time. Small drops in the pressure and the flow rate was also observed, but they returned to their initial value very quickly. These drops were likely the pulses of the pump.

At the end of phase 3, we proceeded to some reloading steps up to 0.6 l/min. A decrease in the permeability of the specimen is observed during reloading (Tab. B-3). This phenomenon can be explained by the effect of the internal erosion (suffusion) which corresponds to a redistribution/migration of certain fraction of fine particles (C10) in the specimen. These accumulate in the accesses to the pores, which leads to a local clogging of the specimen, and consequently a decrease in the global permeability. Xiao and Shwiyhat (2012) conducted an experimental study on the effects of suffusion on physical properties (permeability, volume change, compressive strength, ...) of sandy soils. The tests were performed using a modified triaxial device. The specimens were prepared with a mixture of sand and 10% kaolinite clay. Fig. B-28 shows the change in permeability during suffusion in the specimen. The authors observed a decrease in permeability for all specimens tested. This study allows confirming our observation.

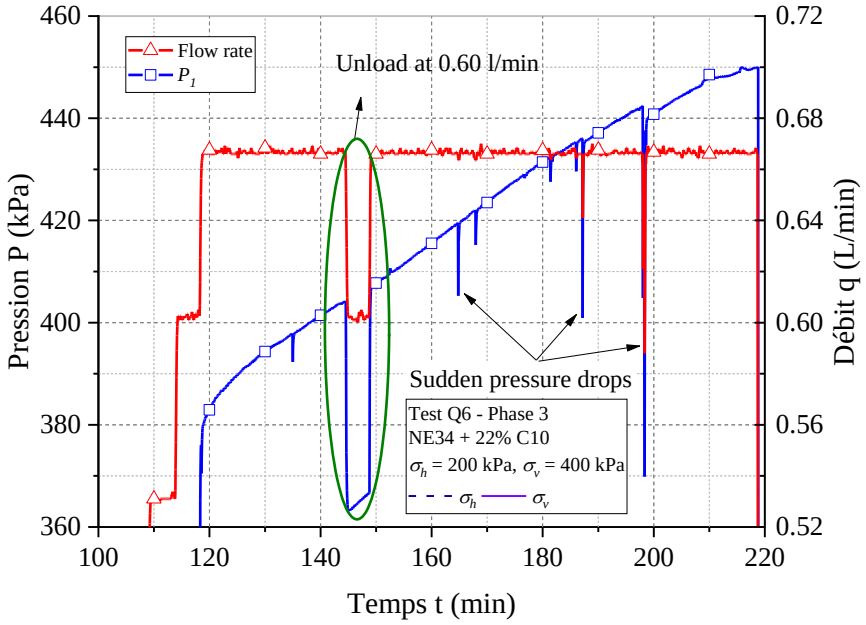

Fig. B-27: Augmentation progressive de la pression à un débit de 0.66 l/min (Phase 3)

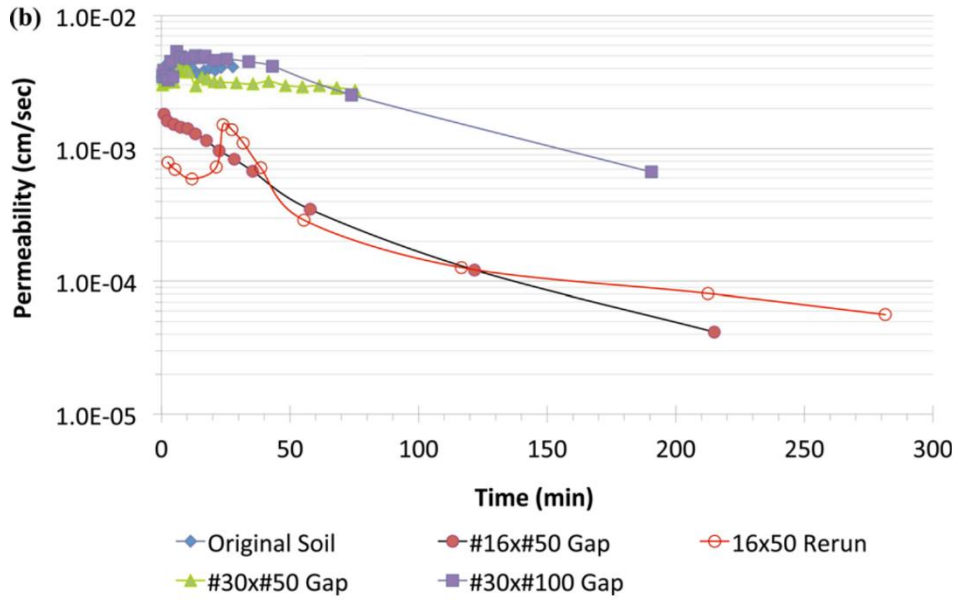

Fig. B-28: Evolution of the permeability due to suffusion (Xiao and Shwiyhat, 2012)

Tab. B-3: Evolution of the permeability during phase 3

Etape	Charge (3)	Recharge (3)
k (mD)	68	57

d. Phase 4

Fig. B-29 shows the results of Phase 4. The injection rate was gradually increased to 0.8 l/min. To verify the results obtained in Phase 3, injection at a flow rate of 0.66 l/min was maintained for approximately one hour (Fig. B-30) and the injection pressure again increases rapidly, especially at the beginning of the injection step. Pressure drops are also observed during this step which are mainly the pulses of the pump (see zooms in Fig. B-30)

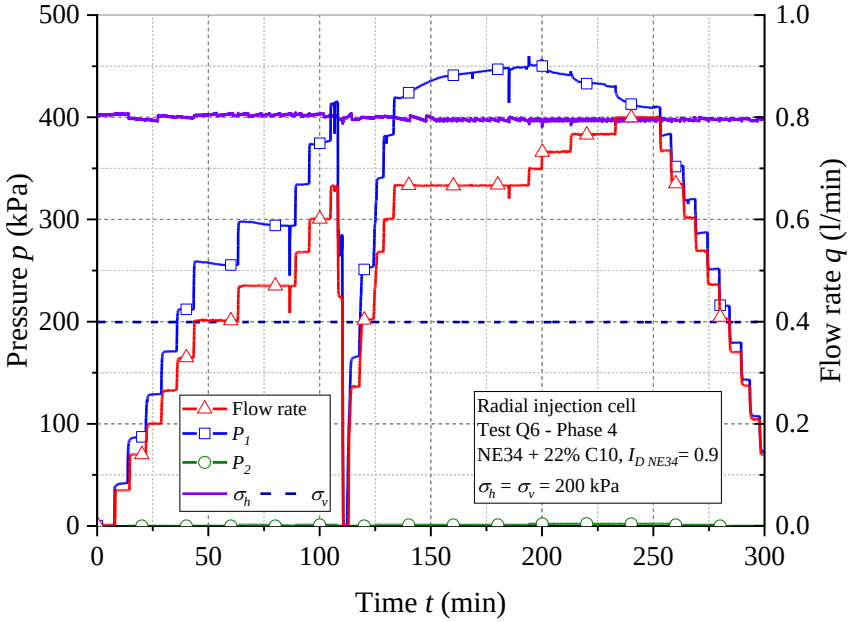

Fig. B-29: Test Q6 – Results of Phase 4.

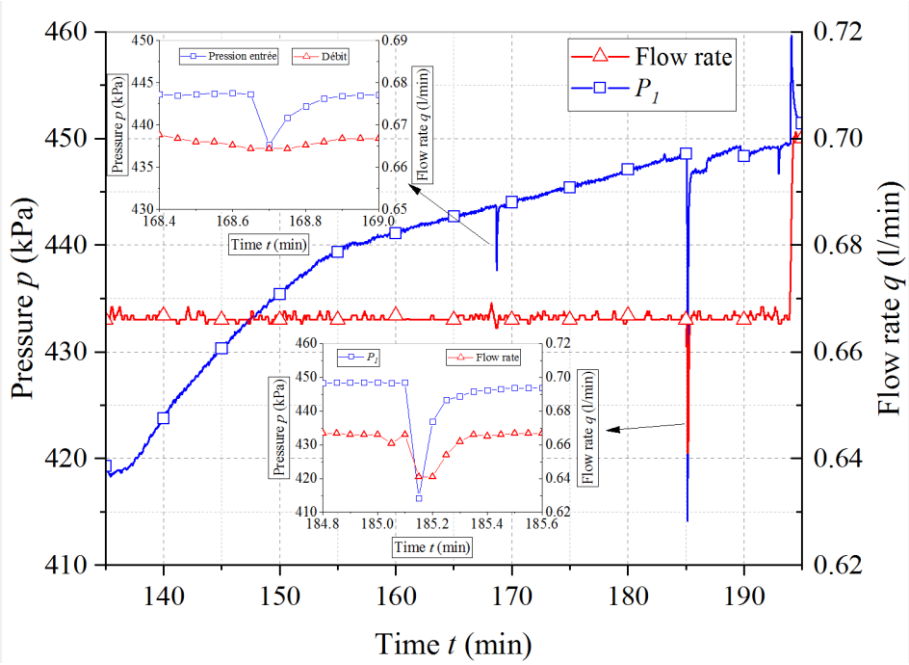

Fig. B-30: Gradual increase of the injection pressure at a flow rate of 0.66 l/min (Phase 4).

When increasing the injection rate beyond 0.66 l/min, significant drops in pressure are observed (see Fig. B-31) followed by a gradual decrease in pressure over time. At the end of phase 4, full unloading is performed in steps. Fig. B-32 shows the pressure-flow curve for Phase 4. After fracturing, the overall permeability increased approximately 26%.

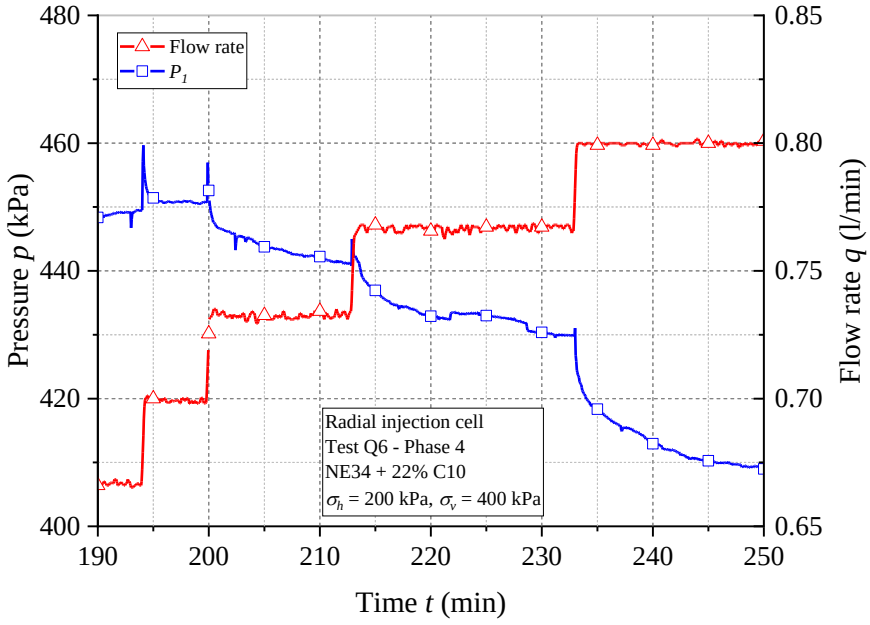

Fig. B-31: Significant pressure drops during the frac regime.

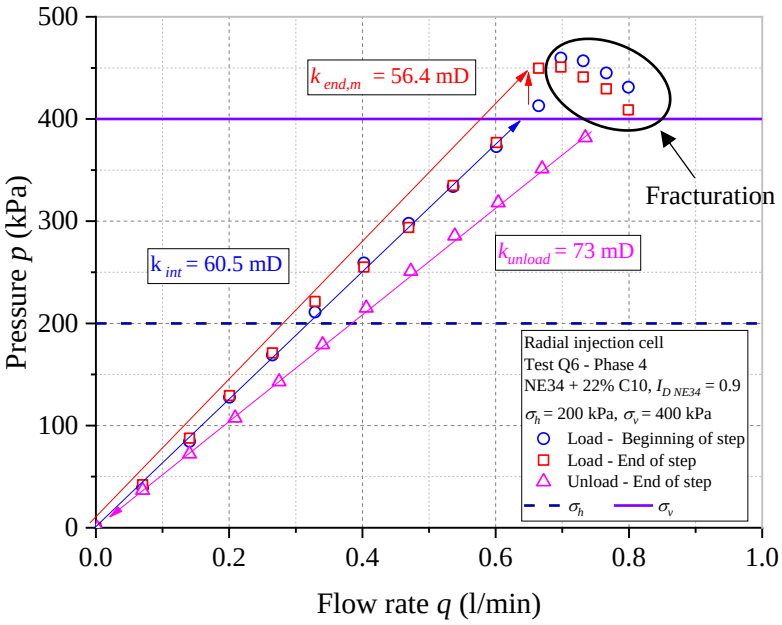

Fig. B-32: Injection pressure versus flow rate (Phase 4 – Test Q6).

Fig. B-33 shows the evolution of the permeability during all injection phases. Two distinct phenomena are highlighted: suffusion and fracturing. During suffusion, the global permeability

of the specimen decreases progressively, on the contrary, an increase in permeability is observed during fracturing

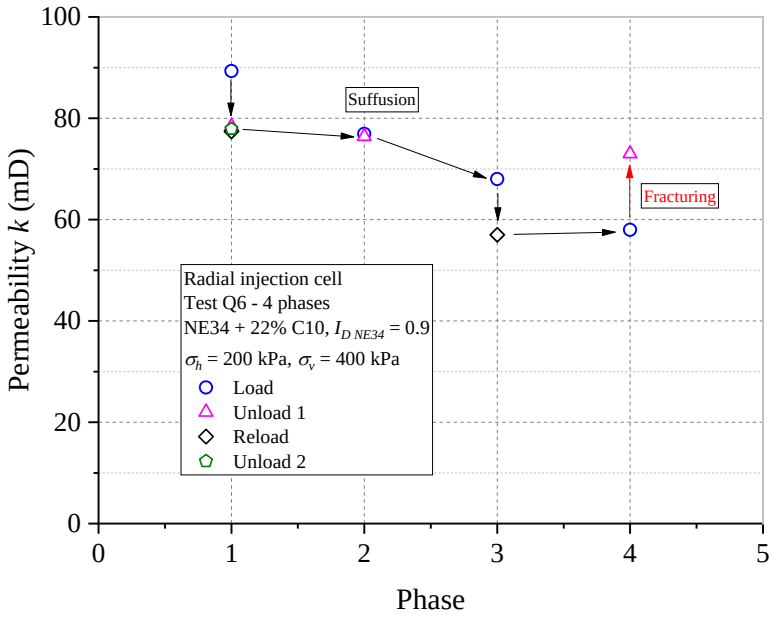

Fig. B-33: Synthesis of the permeability evolution during test Q6.

e. Phase 5 - Colored gel injection

Before injecting the colored gel, two reloading steps was performed at 0.2 l/min and 0.4 l/min (Fig. B-34). We highlight that the pressure values are superimposed on those of the unloading. Due to the difference in viscosity between silica gel and water, the injection of the colored gel was planned at a flow rate of about 0.4 l/min so as not to exceed the maximum pressure in the previous phase (460 kPa). This step was maintained for only about 22 seconds in order to inject a small quantity of the mixture. However, for an actual flow rate of about 0.35 l/min, the maximum pressure measured is 350 kPa, which is still well below the theoretical pressure (460 kPa).

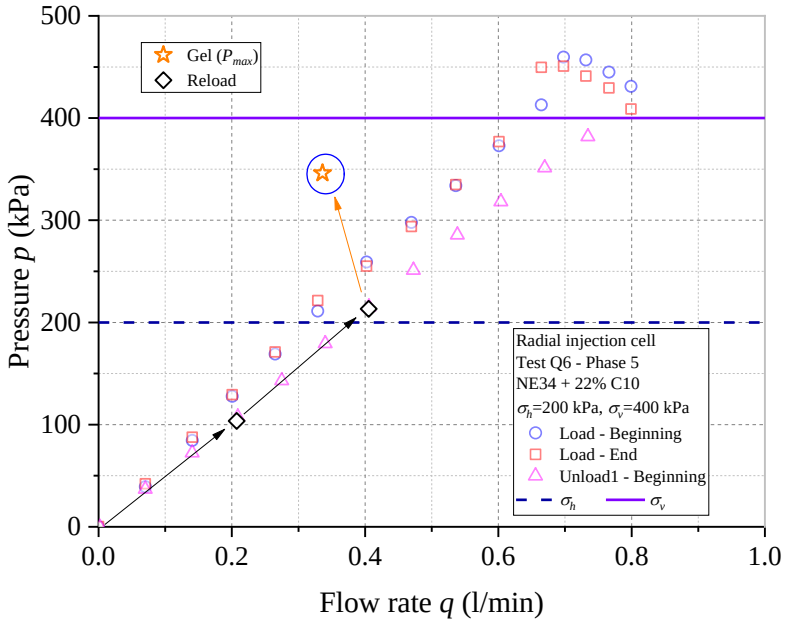

Fig. B-34: Phase 5 – Colored gel injection (Test Q6).

B.4.2 Disassembling phase

Fig. B-35: Excavation of the upper low permeability.

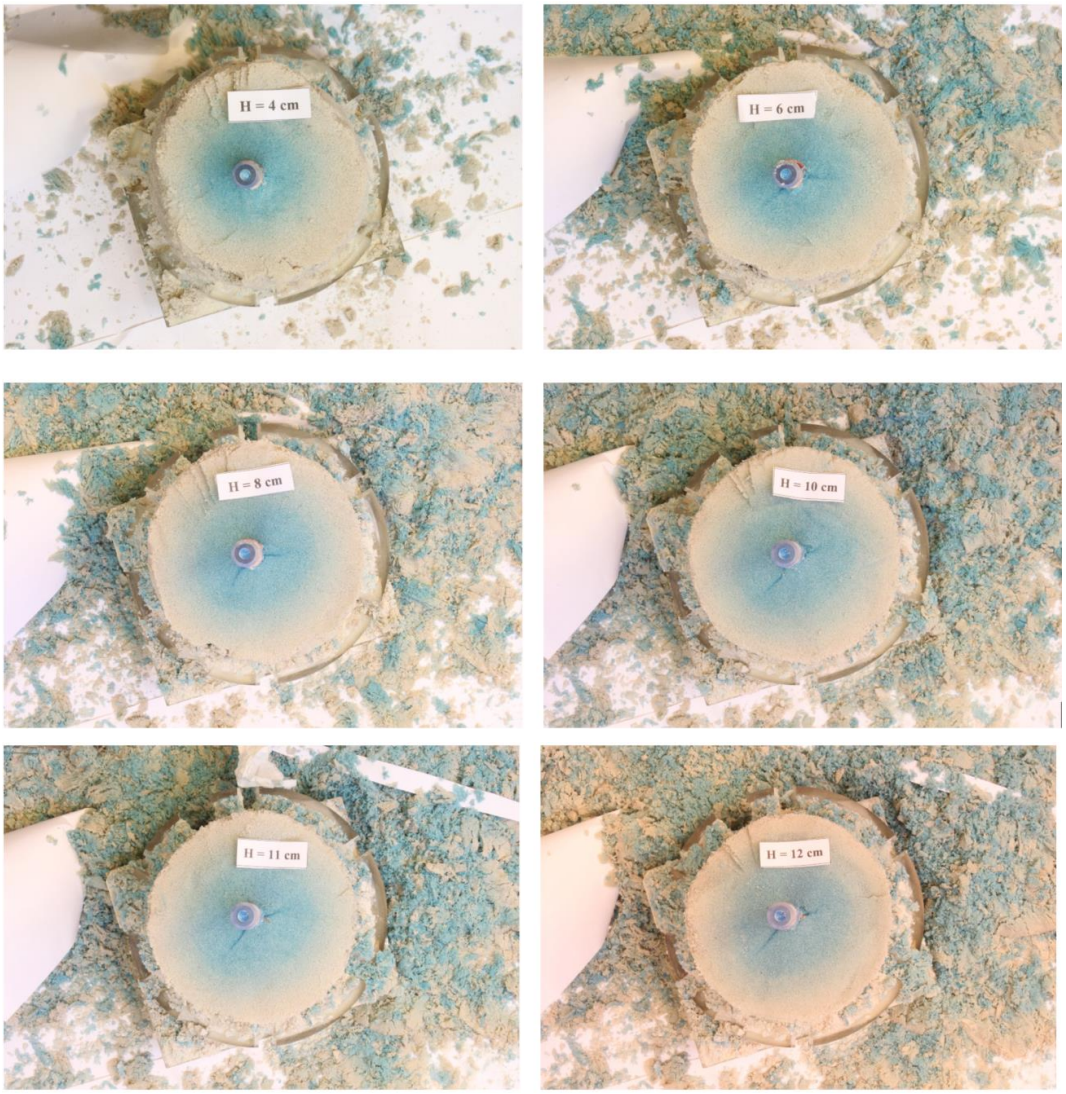

Fig. B-36: Test Q6 – Horizontal excavation of the specimen.

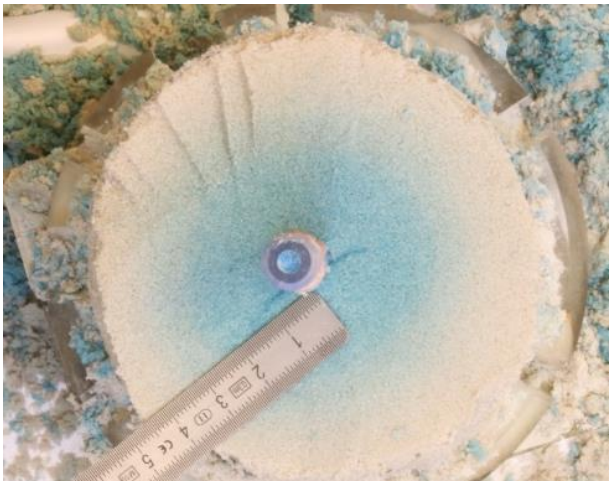

Fig. B-37: Fractures around the injection tube.

The disassembling phase consists of a horizontal excavation from top to bottom of the specimen. A camera is placed above the specimen and allows to take pictures every 2 mm of excavation. Fig. B-35 shows the different views during the excavation of the first low permeability layer. No trace of blue is observed in this layer, confirming the effectiveness of the test protocol. Fig. B-36 shows the excavation of the injection zone. It can be seen that the blue dye invaded symmetrically around the injection tube. Two vertical fractures are also detected (darker path of the blue) along the injection tube. The length of these fractures is approximately 1 to 1.5 cm (Fig. B-37).

B.4.3 Synthesis of the principal observations.

- At a low flow rate (injection pressure below the confining pressure value), the pressure increases gradually, but stabilizes after a certain injection time,

- At a high flow rate (injection pressure higher than the confining pressure), the pressure tends to increase very rapidly at the beginning of the stage. The increase in pressure corresponds to an equivalent decrease in overall permeability. This phenomenon can be explained by the effect of internal erosion (suffusion) of fine particles present in the specimen,

- Fracturing occurs at a critical fracture pressure of about 460 kPa. Four injection steps during the frac regime allow increasing 20% of the overall permeability.

- The fractures observed during excavation confirm the results obtained during the injection phase.

Appendix C Calibration tests to determine the pressure loss due to driving line of the device

As mentioned in the Appendix B.3, the pressure loss due to the driving line needs to be taken into account when interpreting the pressure loss in the specimen. To do so, a series of calibration tests has been performed. In fluid mechanics, a pressure loss occurs when frictional forces, caused by the resistance to the flow, act on a fluid as it flows through the driving line. The pressure loss is defined as the difference in the pressure between two considered points of fluid. In our research, the pressure loss is calculated by the measurement of two pressure transducers T1 and T2. The sources of the pressure loss can be separated by two classifications: regular pressure loss or linear pressure loss (connection tube - Fig. C-1) and singular pressure loss (valves, hydraulic tee fitting, central injection tube and drainage system of the injection cell) (Fig. C-2).

Fig. C-1: Regular pressure loss – flexible connection tube of 4 mm in internal diameter used in the radial injection cell setup.

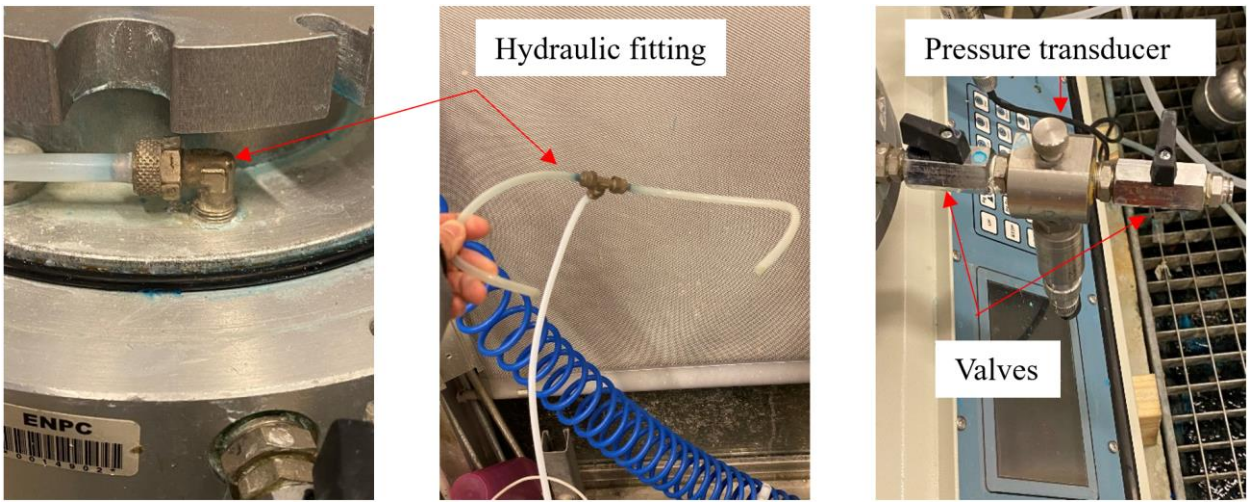

Fig. C-2: Singular pressure loss – hydraulic fittings and valves.

C.1 Calibrations tests to determine the linear pressure drop by the flexible connection tube

The flow velocity, viscosity of fluid, pipe diameter, pipe length and roughness of the pipe surface are the main factors that affect the total pressure loss of the flow in the pipe. Fig. C-3 presents the schematic diagram of 4 calibration tests with different lengths of the flexible tube connected at the outlet of the pressure transducer T1 (without tube, 0.5 m, 1 m and 2 m).

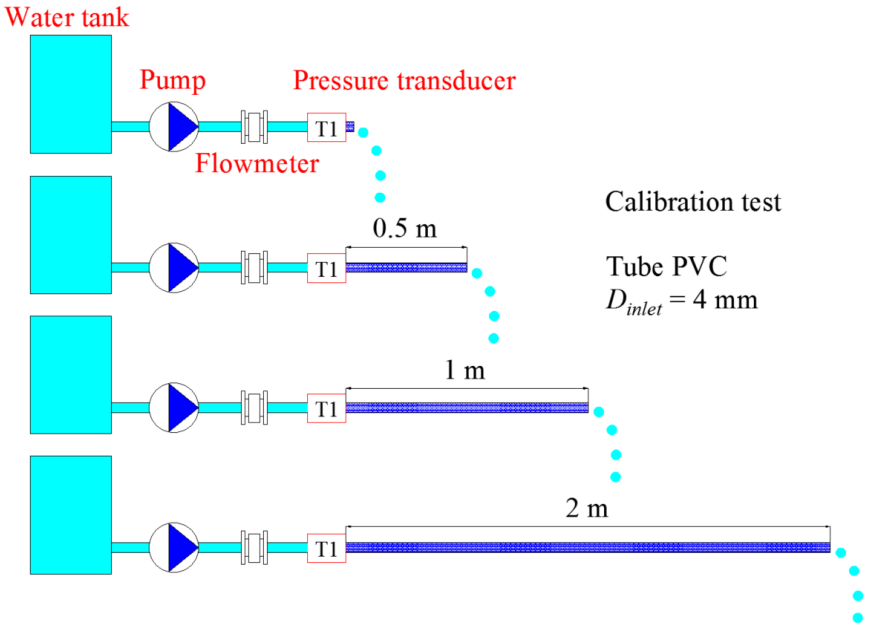

Fig. C-3: Schematic diagram of the calibration tests with the connection tube of 4 mm in internal diameter.

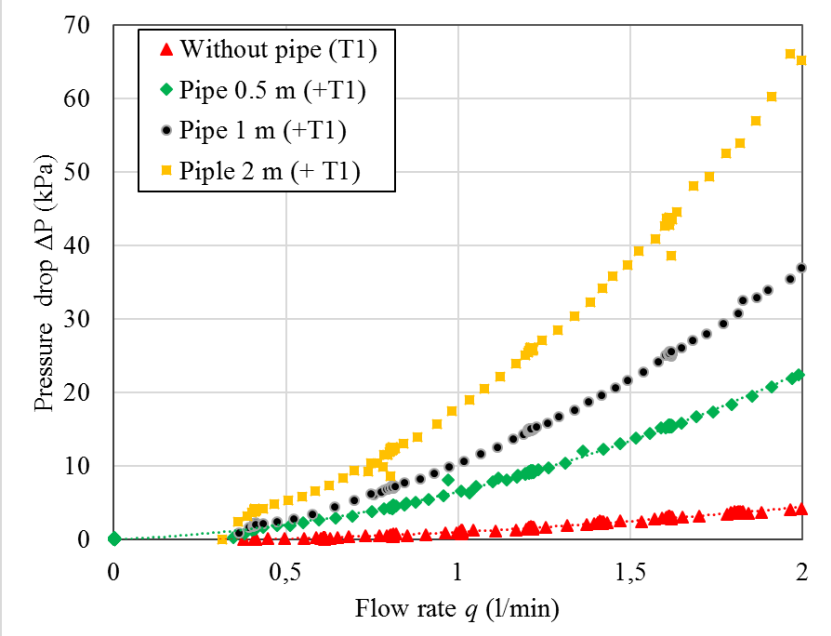

Fig. C-4: Results of the calibration tests with difference lengths of the connection tube.

The results in terms of the pressure flow - rate curve are presented in Fig. C-4. During these tests, the flow rate was increased by steps up to 2 l/min. The measured pressure by T1 is the pressure loss due to the connection tube. Even without the connection tube, the valve of the pressure transducer generates a singular pressure loss (red line). It is evidence that longer pipe results in higher pressure loss. Fig. C-5 presents the corrected pressure loss by the connection tube only.

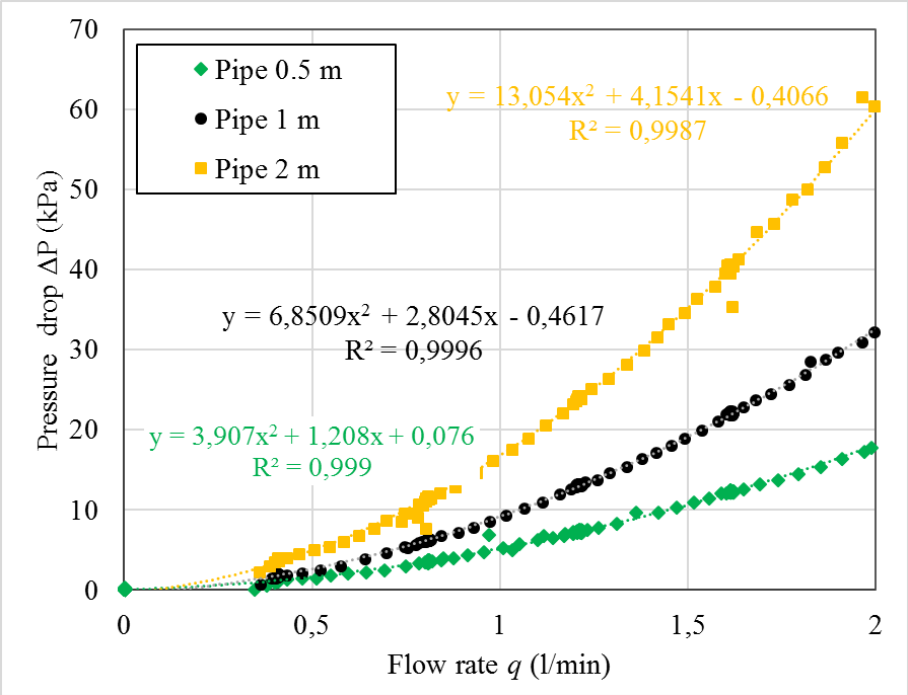

Fig. C-5: Corrected results without pressure drop by pressure transducer.

The pressure loss along a length of pipe can also be calculated using the empirical equation of Darcy – Weisbach below:

$$\Delta P = \lambda . \frac{L}{D} . \frac{\rho . v^2}{2} \qquad \text{(C-1)}$$

where ΔP is the pressure drop (Pa), λ is Darcy friction factor (-), L is the tube length (m), D is the tube diameter (m), ρ is the density of fluid (kg.m^{-3}), v is the flow velocity (m.s^{-1}).

The friction factor λ is calculated by following equation:

- For laminar flow (Reynolds number Re < 2000):

$$\lambda = \frac{64}{Re} \qquad \text{(C-2)}$$

- For turbulent flow (Reynolds number Re > 2000), the empirical Colebrook equation can be used:

$$\frac{1}{\sqrt{\lambda}} = 2\,.\log\left(\frac{\varepsilon}{3.71\,.\,D} + \frac{2.51}{Re\,.\,\sqrt{\lambda}}\right) \quad \text{(C-3)}$$

The Reynolds number Re can be calculated by:

$$Re = \frac{\rho\,.v\,.\,D}{\mu} \quad \text{(C-4)}$$

where μ is the dynamic viscosity of the fluid (kg.m/s).

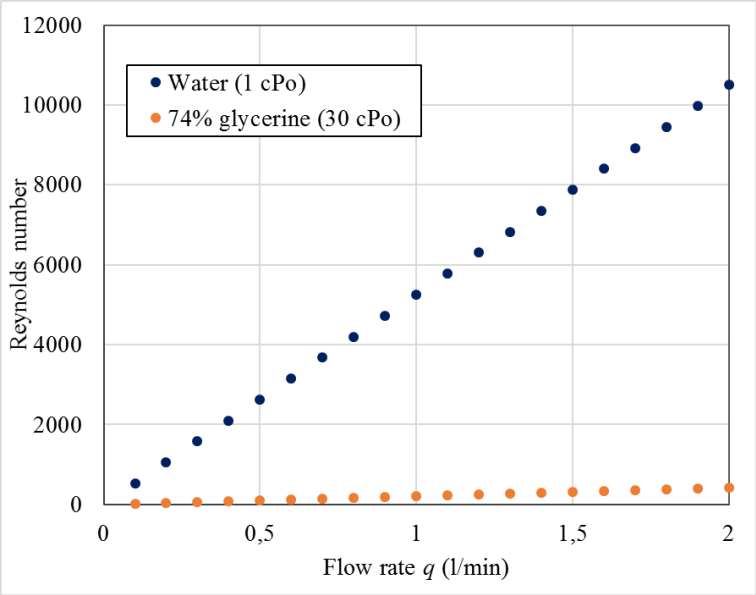

Fig. C-6: The Reynolds number of different fluids

Fig. C-6 presents the Reynolds number of different fluids that flow through a section of 4 mm in diameter. In the case of water injection, the flow is in the laminar regime. By applying Equation (C-1, the pressure loss of the driving pipe can be calculated. The selected diameter of the pipe is 4 mm. A good consistency between calculation and experiments is observed (Fig. C-7).

The effect of the viscosity on the pressure loss in the pipe was also investigated. An injection test with the glycerin of 30 cP in a tube of 4 mm in internal diameter and 1 m in length was performed. The results are show in Fig. C-8. It is evidence that increase of the fluid viscosity will increase the pressure loss.

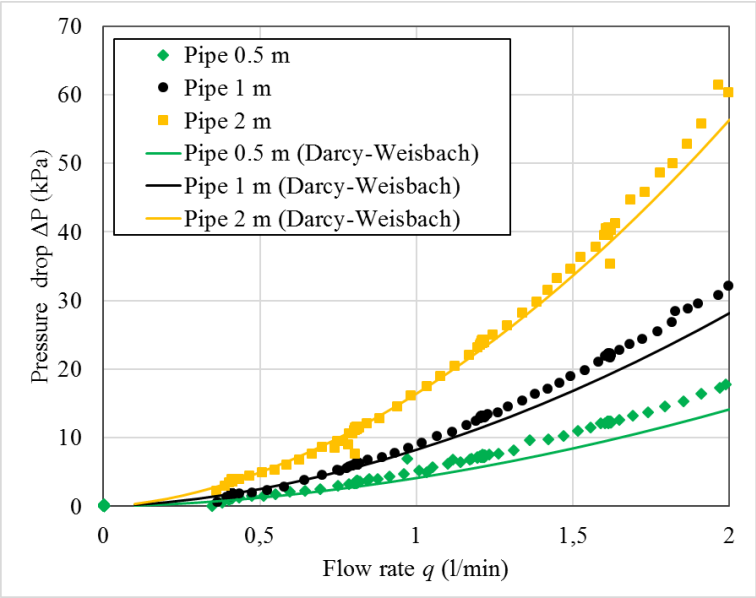

Fig. C-7: Comparison between theory (full line) and experiments (dots).

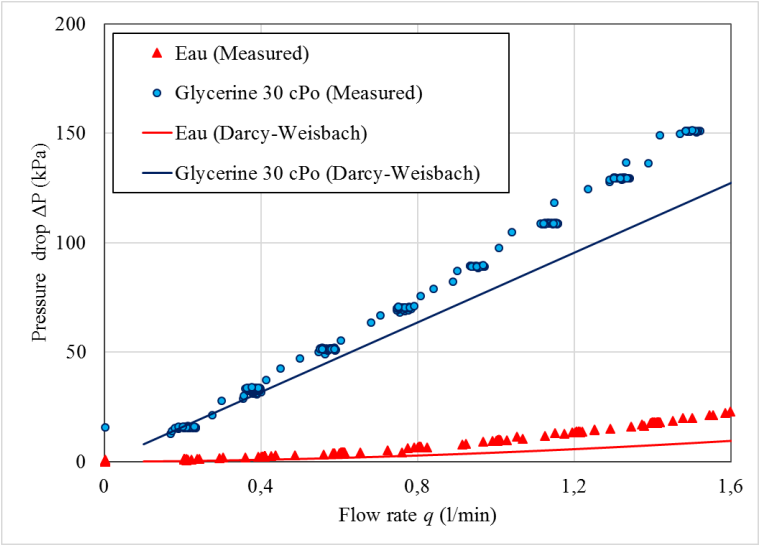

Fig. C-8: Effect of the viscosity (D = 4 mm, L = 1 m).

Fig. C-9 presents an important effect of the tube diameter on the pressure loss of the fluid using the empirical equation of Darcy – Weisbach. Reducing the tube diameter will increase the pressure loss.

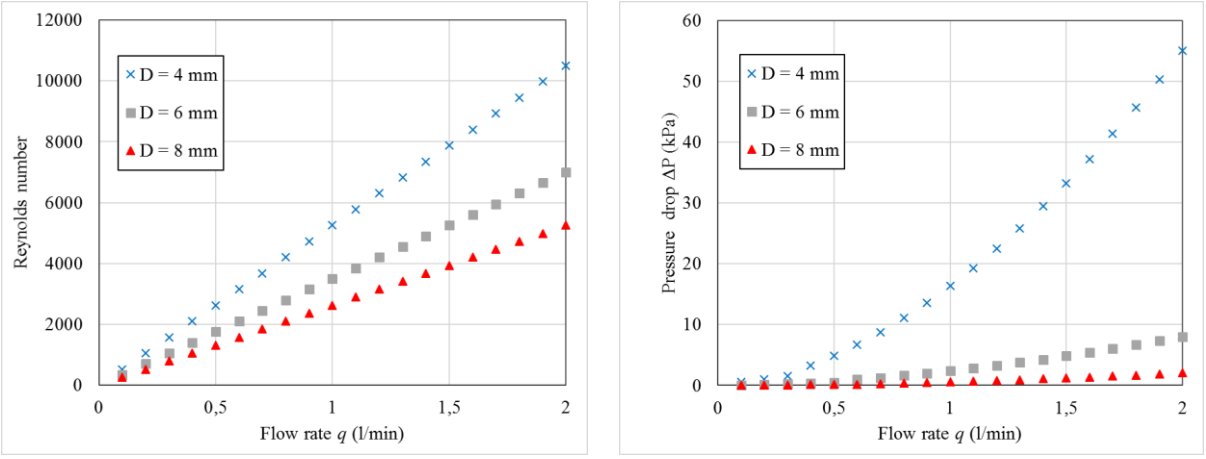

(a) (b)

Fig. C-9: (a) Reynolds numbers and (b) Pressure drops corresponding to difference pipe diameters (Values: water μ = 1 mPa.s, ρ = 1000 kg/m^3 L = 2 m).

C.2 Calibration tests with the driving line used in the radial injection cell

To quantify the pressure loss due to the driving line used in the radial injection cell, three calibration tests were performed. The characteristics of these tests are presented in Tab. C-1.

Tab. C-1: Characteristics of the calibration tests in the radial injection cell.

Test	Specimen	Fluid		Stress conditions		Density index
		μ (cP)	% fine	σ_h (kPa)	σ_v (kPa)	
CT1	Inlet + Outlet pipes only	1	0	-	-	-
CT2	Glass balls	1	0	200	200	-
CT3	Sand NE34	1	0	200	200	0,9

Test CT1 is performed with only the two pipes: inlet and outlet pipe without the injection cell. This test allows estimating the total pressure loss in these sections (connection tube + valves + hydraulic fitting). Test CT2 was performed in the glass balls specimen with a ball diameter of 6 mm (Fig. C-10). The hydraulic conductivity of the specimen can be calculated using an empirical relationship proposed by Amer and Awad (1974):

$$K = 3.5 \,.\, 10^{-4} . \left(\frac{e^3}{1+e}\right) C_u^{0.6} . D_{10}^{2.32} . \left(\frac{\rho_w}{\mu}\right) \qquad \text{(C-5)}$$

where K is the hydraulic conductivity (cm/s), C_u is uniformity coefficient, D_{10} is the effective size (mm), ρ_w is the density of water (g/cm^3), μ is the viscosity (g.s/m^2).

In the case of water injection, the hydraulic conductivity of the specimen K is about 555 cm/s which is much higher as compared to the case of NE34 specimen (6 x 10^{-5} m/s). Therefore, the pressure loss due to the balls specimen can be negligible, hence by performing the injection

test, we can quantify the total pressure loss caused by the device (driving line, central injection tube, drainage system). The test results are shown in Fig. C-11. As can be seen that the pressure loss in two tests CT1 and CT2 is very close. It confirms that the effect of the injection cell (central tube, drainage system) is negligible as compared to the connection tube (tube length, tube diameter). Test CT3 was performed with the specimen of NE34 (I_D = 0.9). The results show only a slight difference between these tests (Fig. C-11). Fig. C-12 presents a comparison of these tests with the range of the flow rate up to 1 l/min. Comparing the measurement with the theoretical curve using Darcy's law, we see that the pressure loss by the specimen is very small comparing to that of the device.

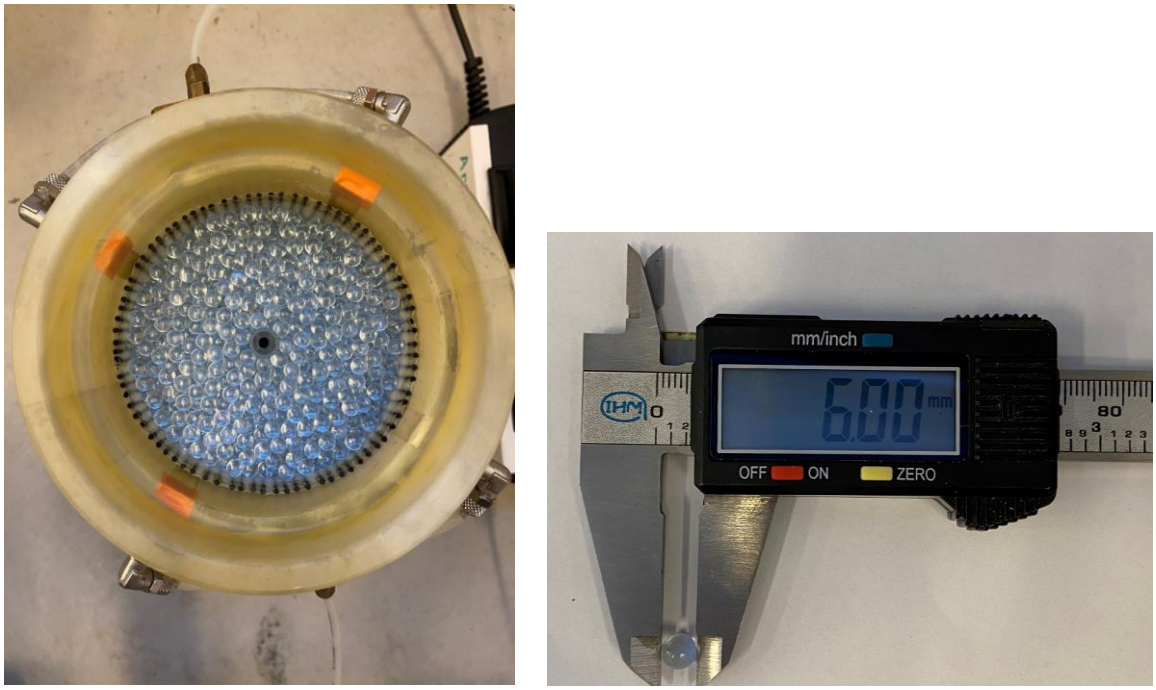

(a) (b)

Fig. C-10: (a) Glass balls specimen, (b) Measurement of the ball diameter.

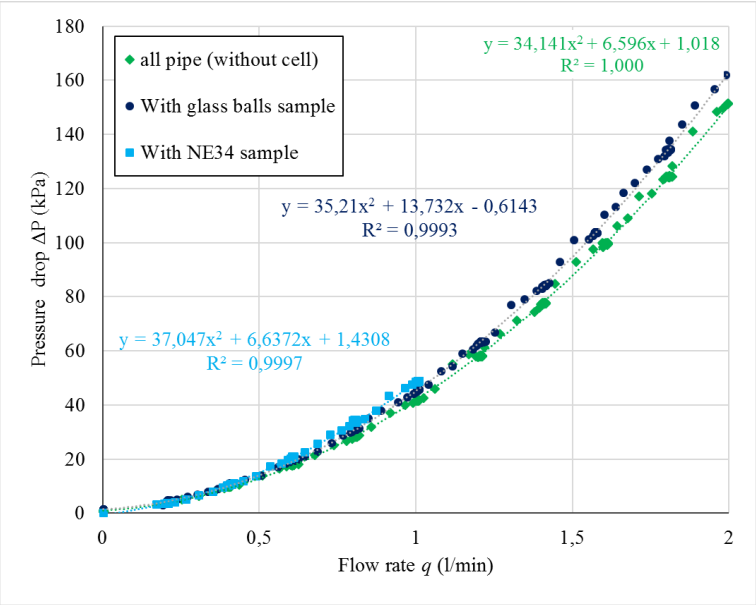

Fig. C-11: Flow rate – pressure loss curves of the calibration tests.

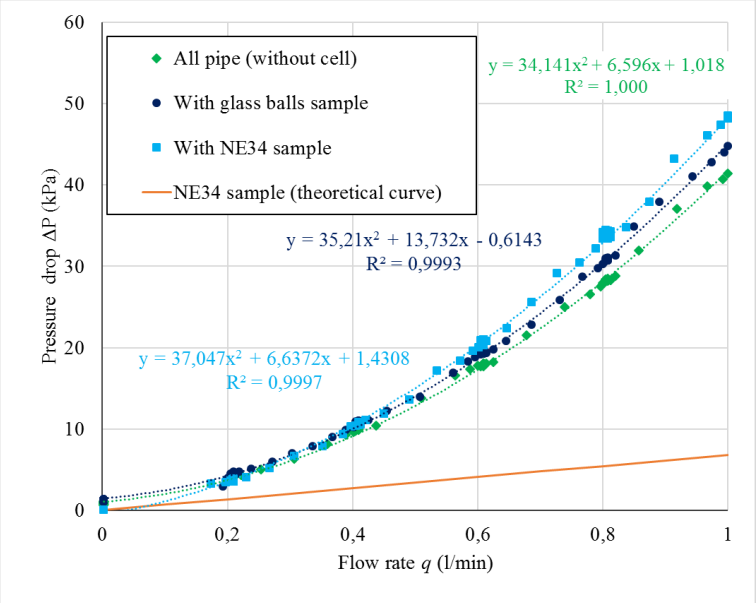

Fig. C-12: Test results within the range of the flow rate up to 1 l/min.

C.3 Corrections of pressure measurements of test P1

As mentioned in the qualification tests (see Appendix B), the hydraulic head loss due to the driving pipe must be accounted for when interpreting raw measurements. This section describes the calibration procedure for the radial injection cell.

Fig. C-13 shows the schematic representation of the fluid flow during injection. The injection pressures were measured by two pressure transducers at the inlet and outlet of the sample. Pressure drops caused by the inlet pipe and outlet pipes need to be measured for when calculating the pressure drop due to the sample. Equation (C-6) presents different parts of the

total pressure drop, whereas Equation (C-7) presents the calculation of the total drop pressure by driving pipe. These equations are schematized in Fig. C-14.

$$\Delta P_t = P_1 - P_2 = \Delta P_{p1} + \Delta P_s + \Delta P_{p2} \quad \text{(C-6)}$$

$$\Delta P_p = \Delta P_{p1} + \Delta P_{p2} \quad \text{(C-7)}$$

when ΔP_t is the total drop pressure, ΔP_{p1} and ΔP_{p2} are the drop pressure by inlet and outlet pipe, ΔP_p is total pressure drop by driving pipe, ΔP_s is the pressure drop due to sample.

The first calibration test was performed by connecting only the inlet pipe with the pump and leaving the other end in open air. The injection was performed by gradually increasing the flow rate. The drop pressure by the inlet pressure was measured by the inlet pressure transducer. By connecting the outlet pipe with the inlet pipe and repeating injection process, the total drop pressure by the driving pipe can be measured. In this experimental setup, the connection tube of 4 mm of inner diameter was used as the driving pipe. The pressure at the tube P_{in} can be calculated by equation:

$$P_{in} = P_1 - \Delta P_{p1} \quad \text{(C-8)}$$

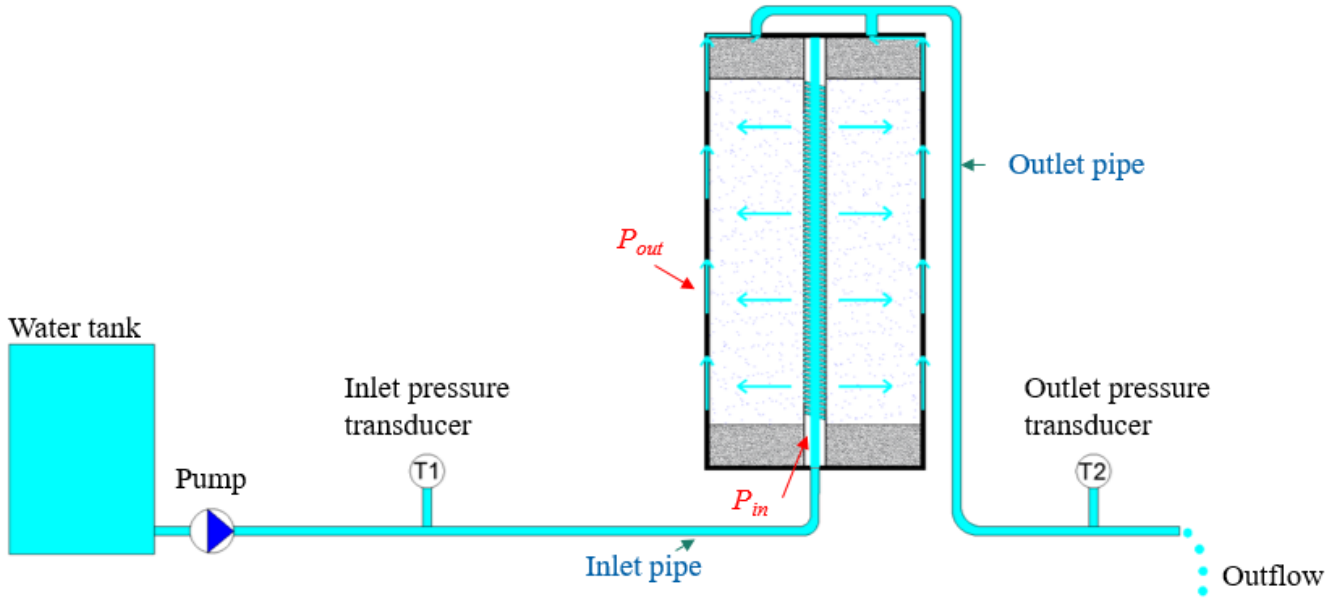

Fig. C-13: Schematic representation of the fluid flow during injection.

The results of calibration tests are presented in Fig. C-15. A simple relationship of pressure drops by driving pipe and injection rate can be obtained based on the measured values.

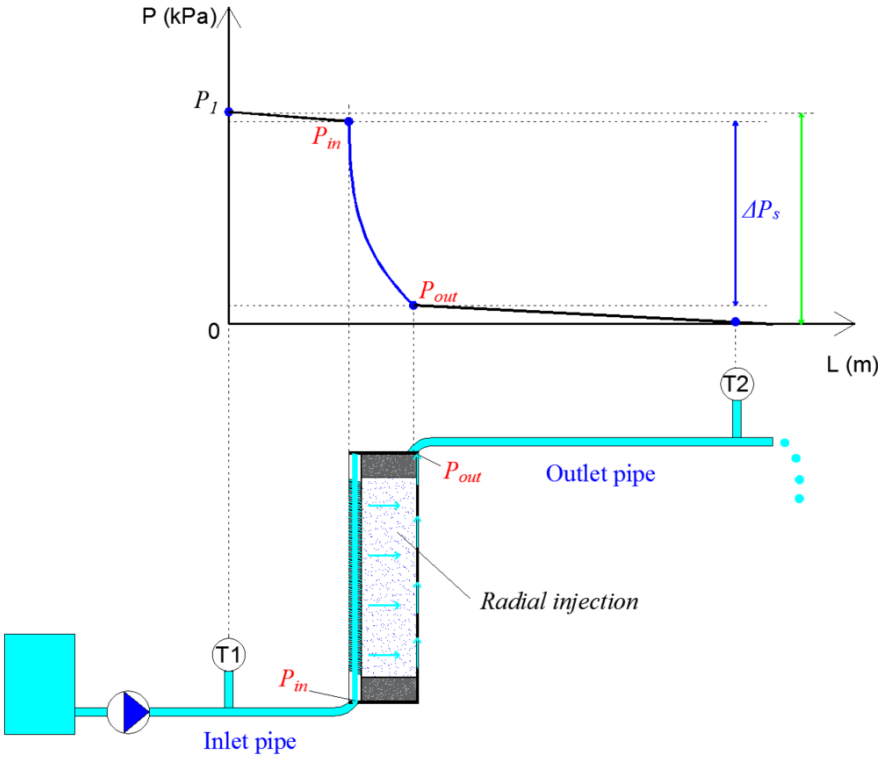

Fig. C-14: Representative diagram of the pressure drops during injection with radial injection cell.

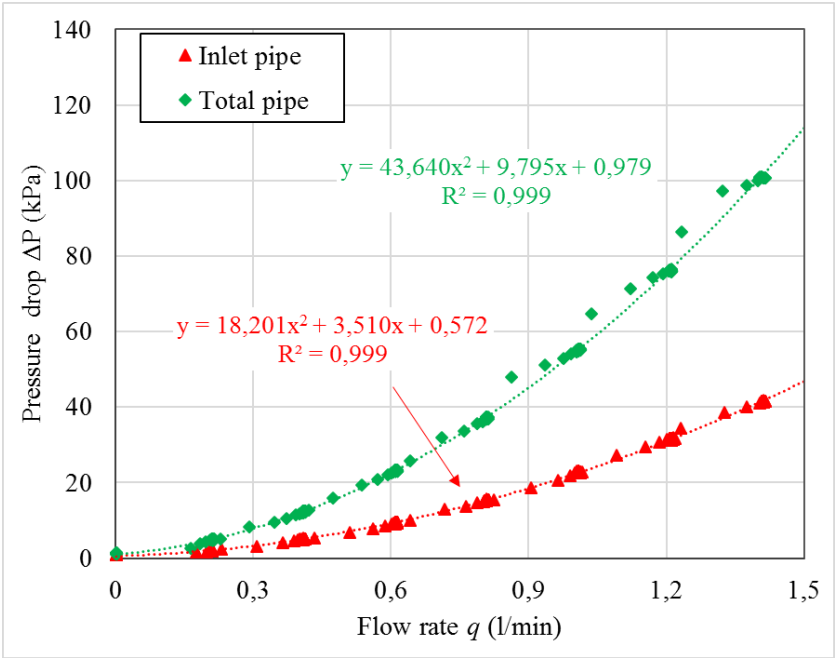

Fig. C-15: Pressure drops by driving tube corresponding to different flow rates.

a. Interpretation of raw measurements

At a given flow rate, the pressure at the inlet of tube injection P_{in} and the pressure drop inside the sample ΔP_s can be calculated by using Equations (C-7) and (C-8). In this device, the

inlet pressure transducer was installed at the same vertical position as the cell, therefore the hydrostatic pressure is negligible. Fig. C-16 presents the corrected pressures P_{in} at the injection tube and the pressure drops by the sample ΔP_s of test P1 during injection phase.

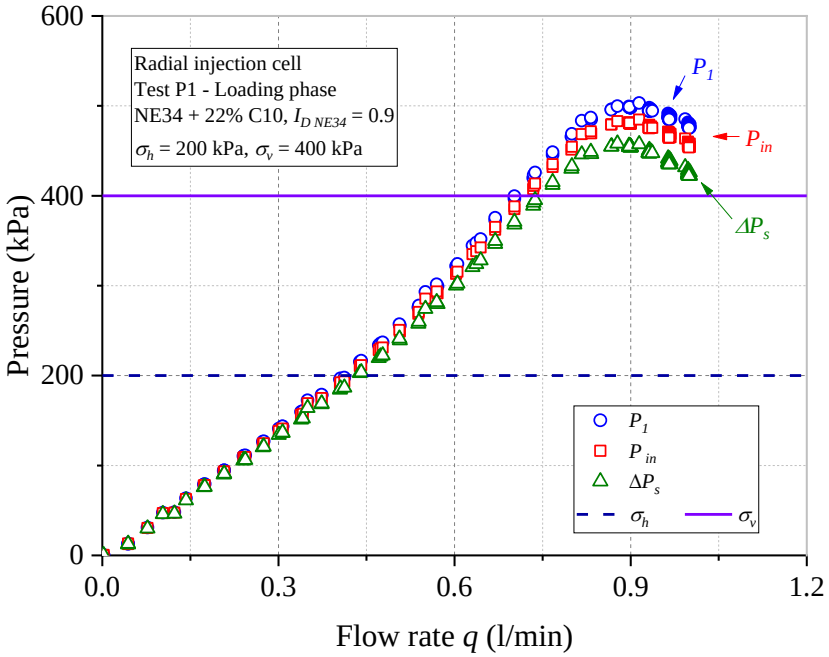

Fig. C-16: Interpretation from raw measured data of the test P1 during loading phase.

Appendix D Tests in the radial injection cell with the injection of pure water

D.1 Test P2 – (X-ray CT Scan of a half of the specimen)

D.1.1 Water injection phase

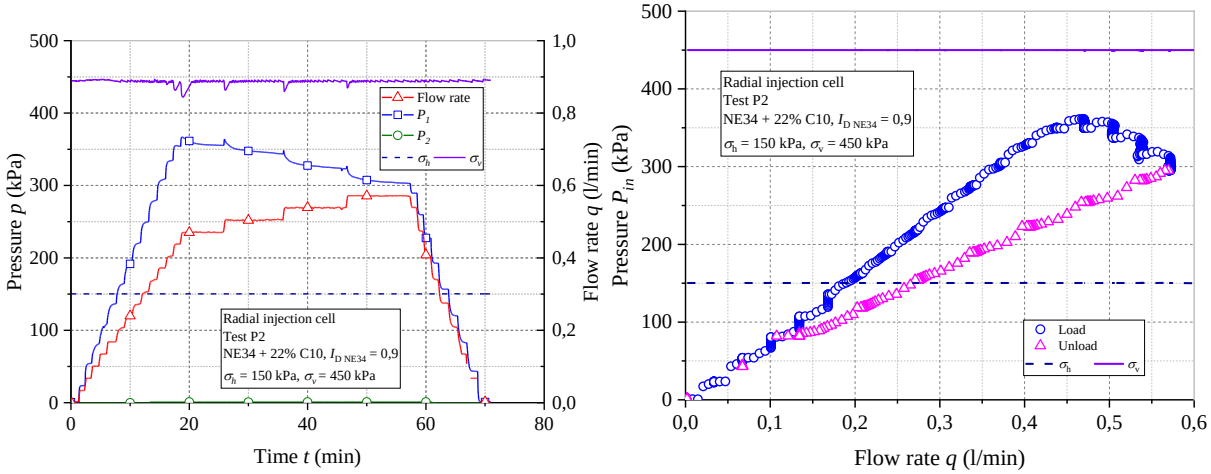

Fig. D-1: Results of test P2: (a) pressure – flow rate – time curves; (b) pressure – flow rate curve.

D.1.2 Disassembling phase

Fig. D-2 shows a schematic representation of the disassembling phase. During this phase, a half of the sample was manually excavated to visualize the fracture (from top to H = 12 cm). Then, the rest was scanned by X-ray CT. Moreover, additional observation by using optical microscopy allows to identify the change of the structure inside the fracture.

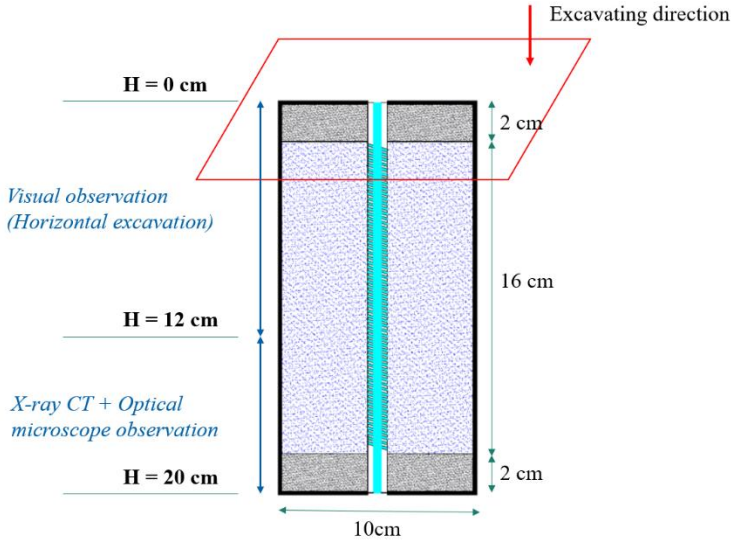

Fig. D-2: Schema showing the disassembling process (Test P2).

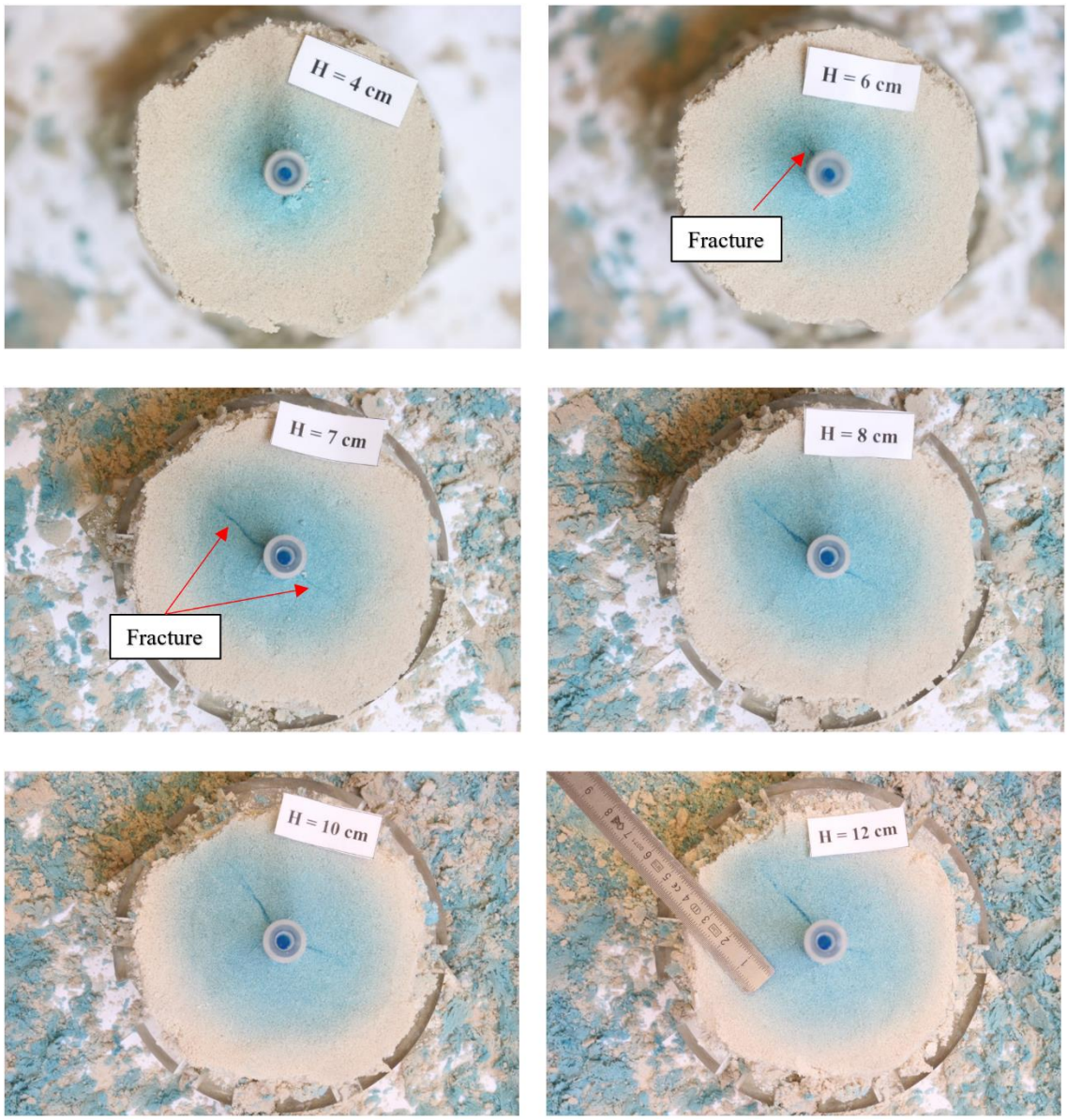

Fig. D-3:Transversal cross-sections of the top half of specimen P2.

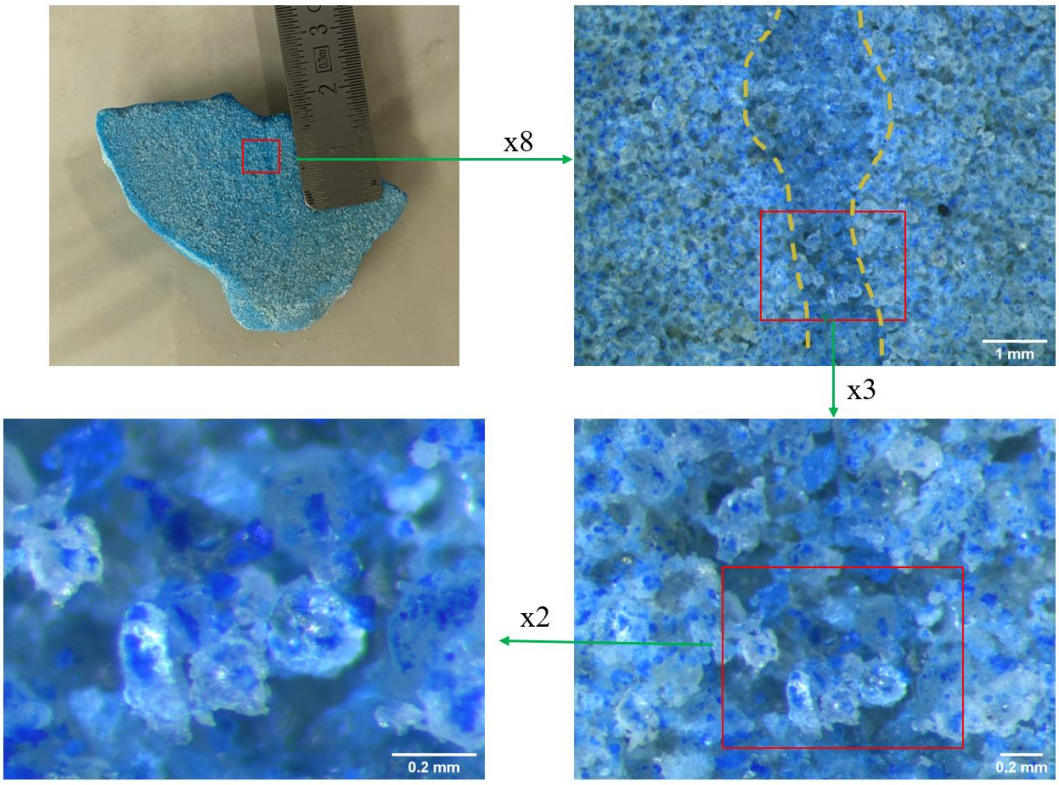

Fig. D-4: Optical microscope observation of the fracture with different zoom scales. The dashed orange line representing the edges of the fracture (Test P2).

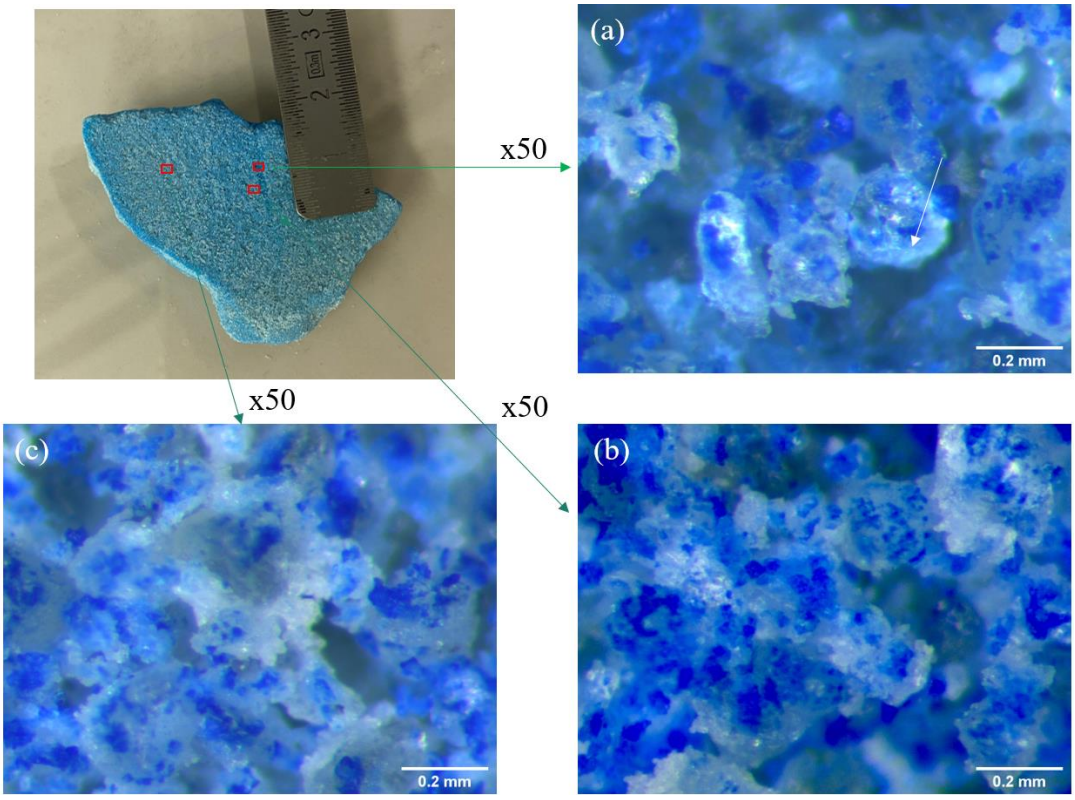

Fig. D-5: Optical microscope observation at different zones: (a) Inside the fracture; (b) Near the facture; (c) surrounding medium (Test P2).

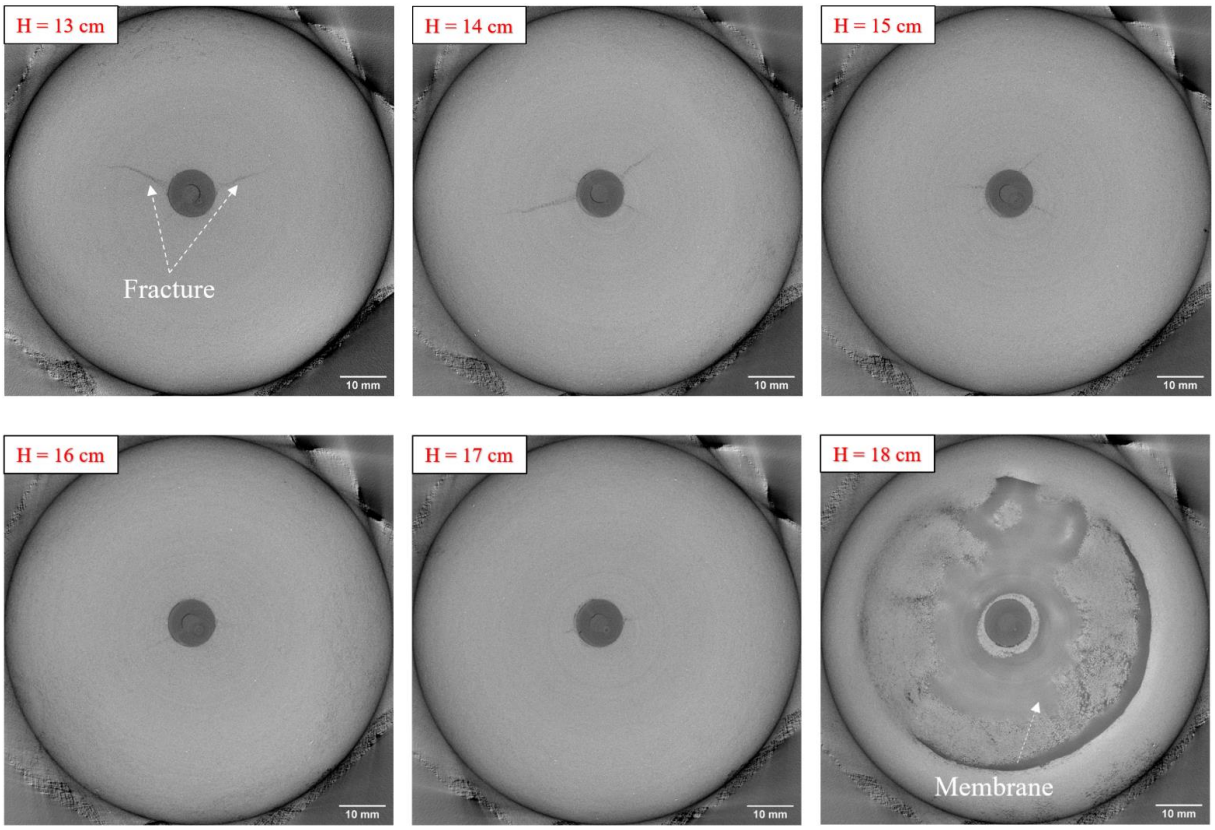

Fig. D-6: X-Ray CT images of the specimen at different heights (Test P2).

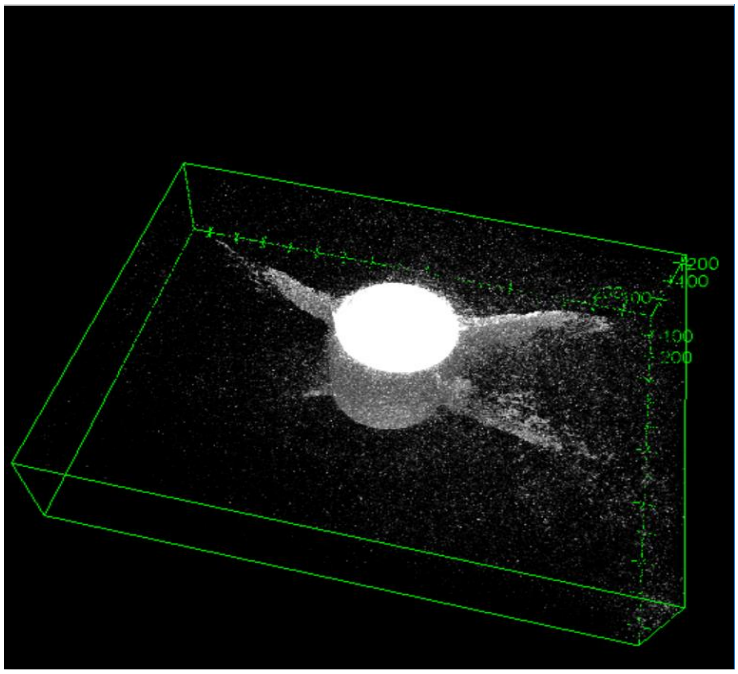

Fig. D-7: 3D image of the fracture developed at the middle of the sample (from H = 12 cm to H = 13 cm) (Test P2).

D.2 Test P3

D.2.1 Water injection phase

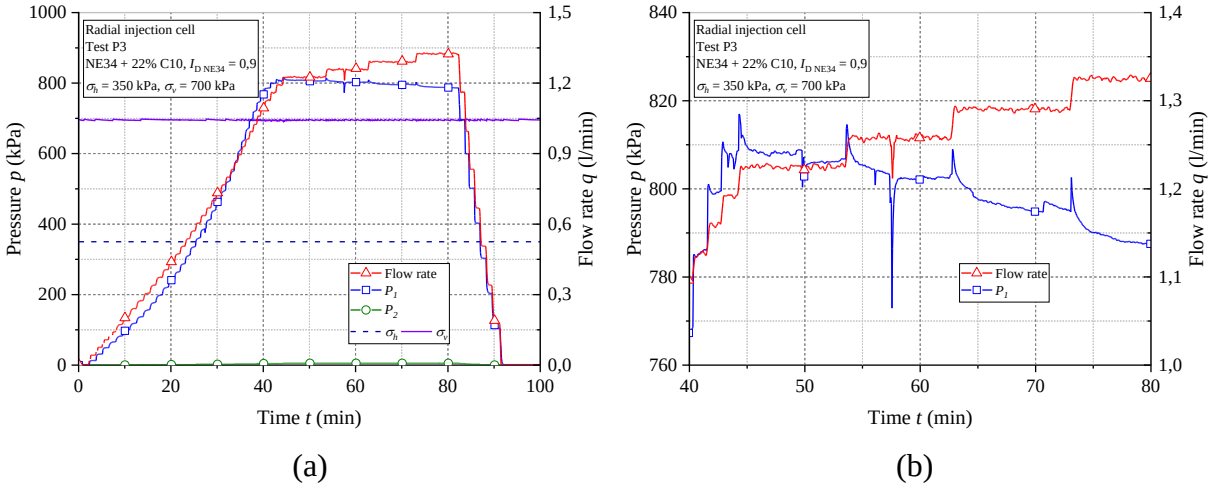

Fig. D-8: Results of test P3: (a) full response; (b) frac regime.

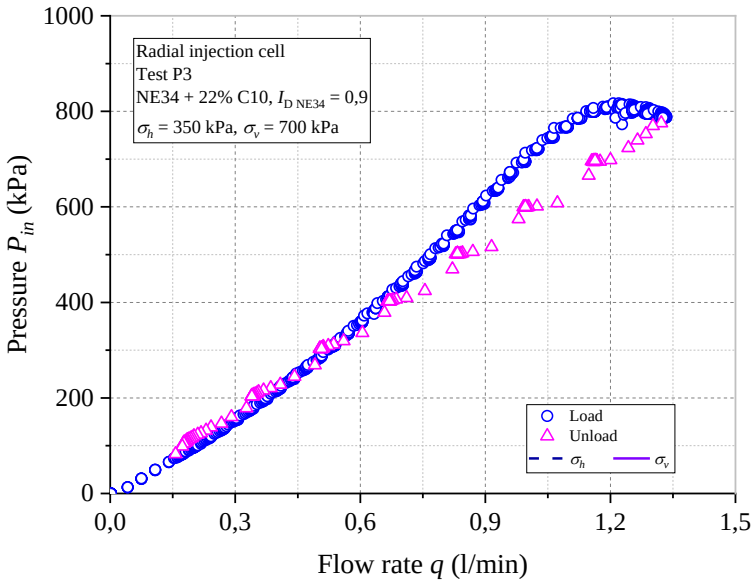

Fig. D-9: Pressure – flow rate curve (Test P3)

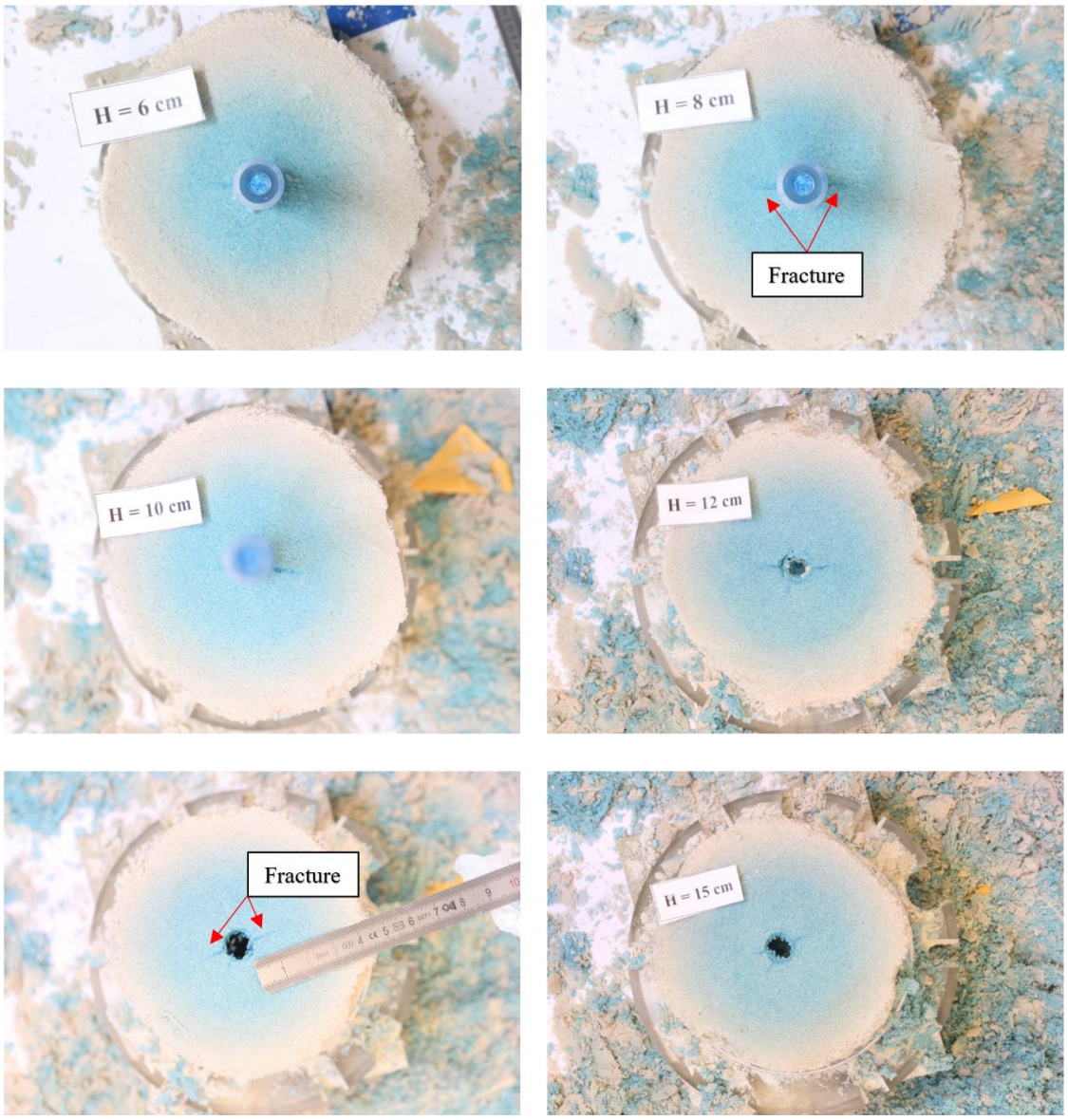

Fig. D-10: Transversal cross-sections of the sample at different heights (Test P3)

D.3 Test P4

D.3.1 Water injection phase

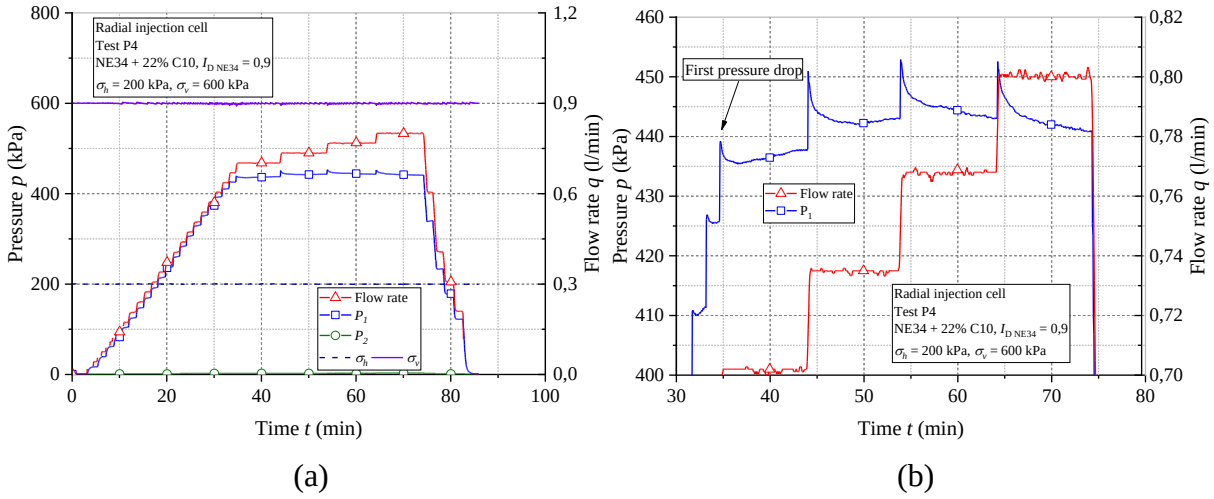

Fig. D-11: Results of test P4: (a) full response; (b) frac regime.

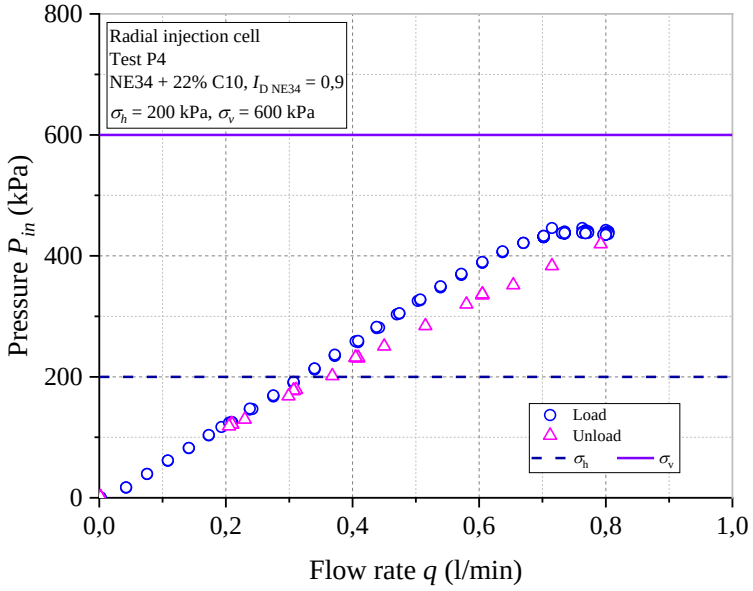

Fig. D-12: Pressure – flow rate curve (Test P4).

D.4 Test P5

D.4.1 Water injection phase

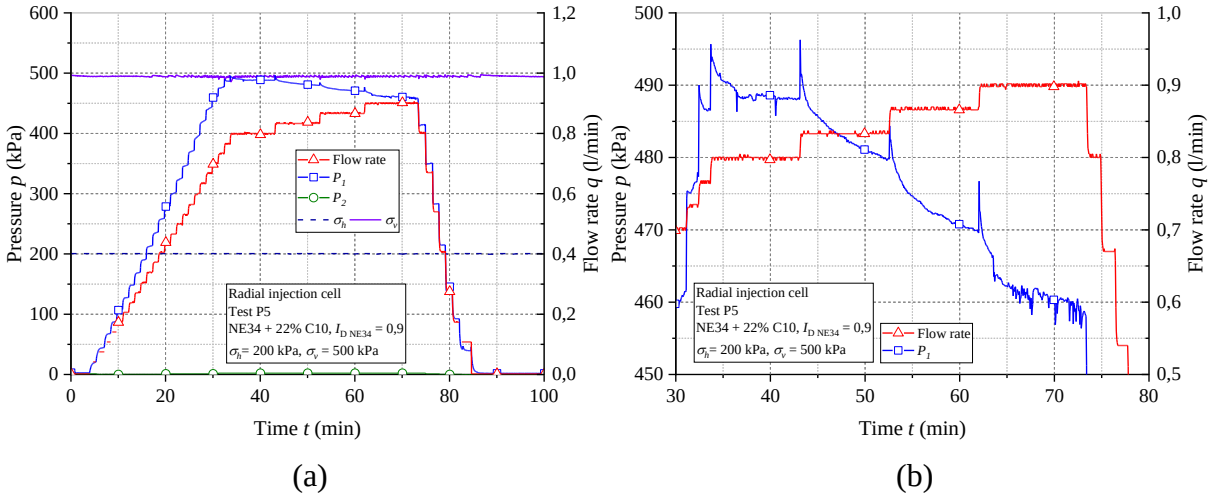

Fig. D-13: Results of test P5: (a) full response; (b) frac regime.

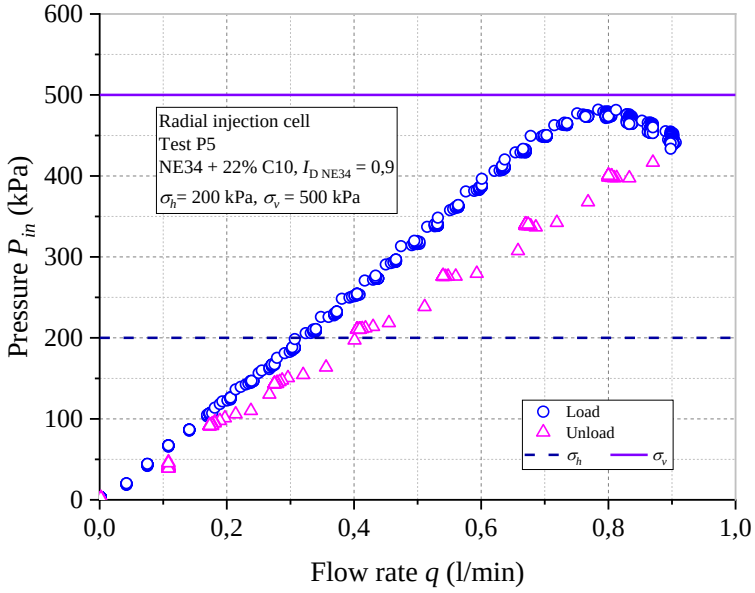

Fig. D-14: Pressure – flow rate curve (Test P5).

D.4.2 Disassembling phase

Fig. D-15: Some typical photos of the specimen during excavating (Test P5).

D.5 Test P6

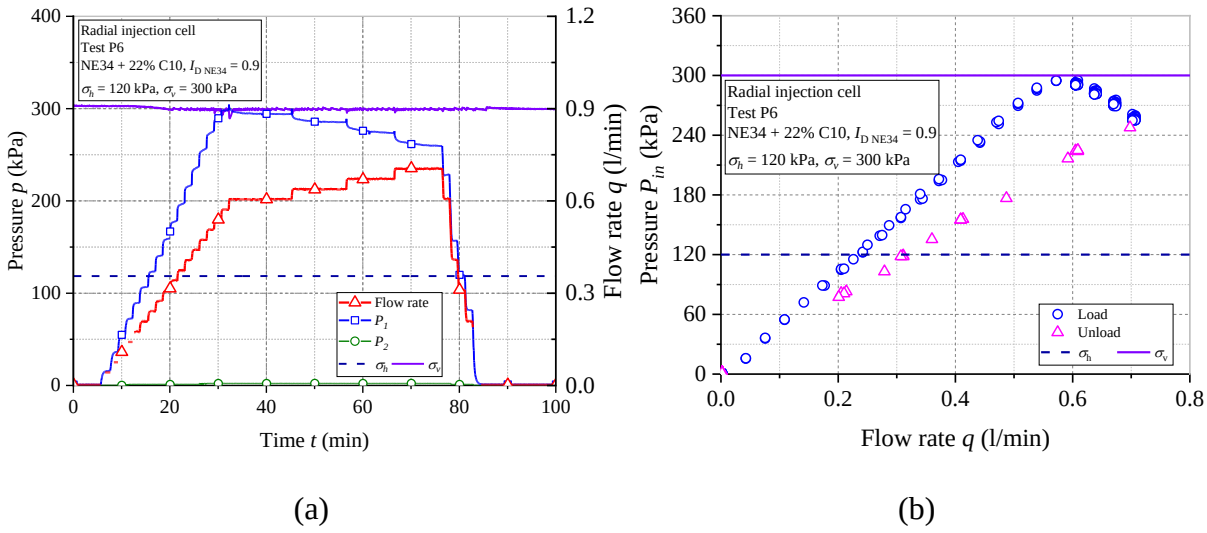

(a) (b)

Fig. D-16: Results of test P6: (a) pressure – flow rate - time curves; (b) pressure – flow rate curve.

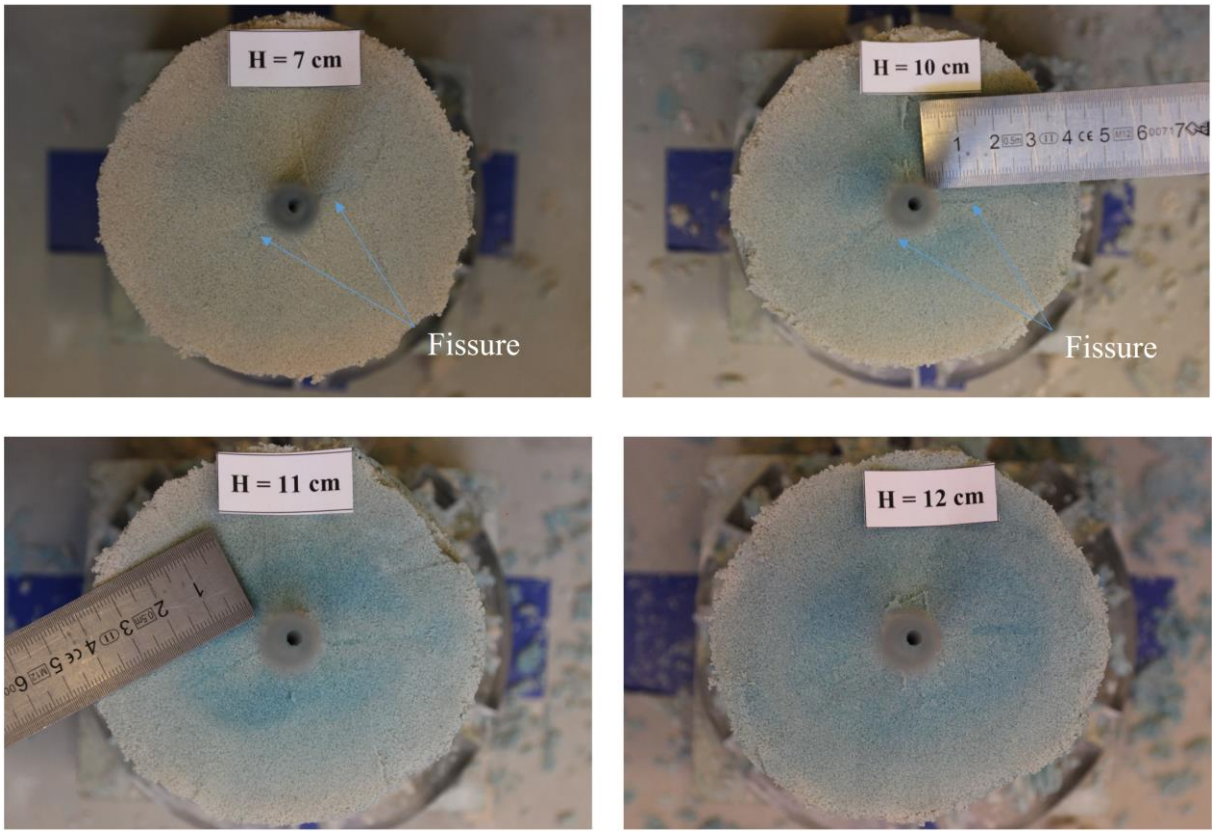

Fig. D-17: Excavation of specimen P6.

D.6 Test P8

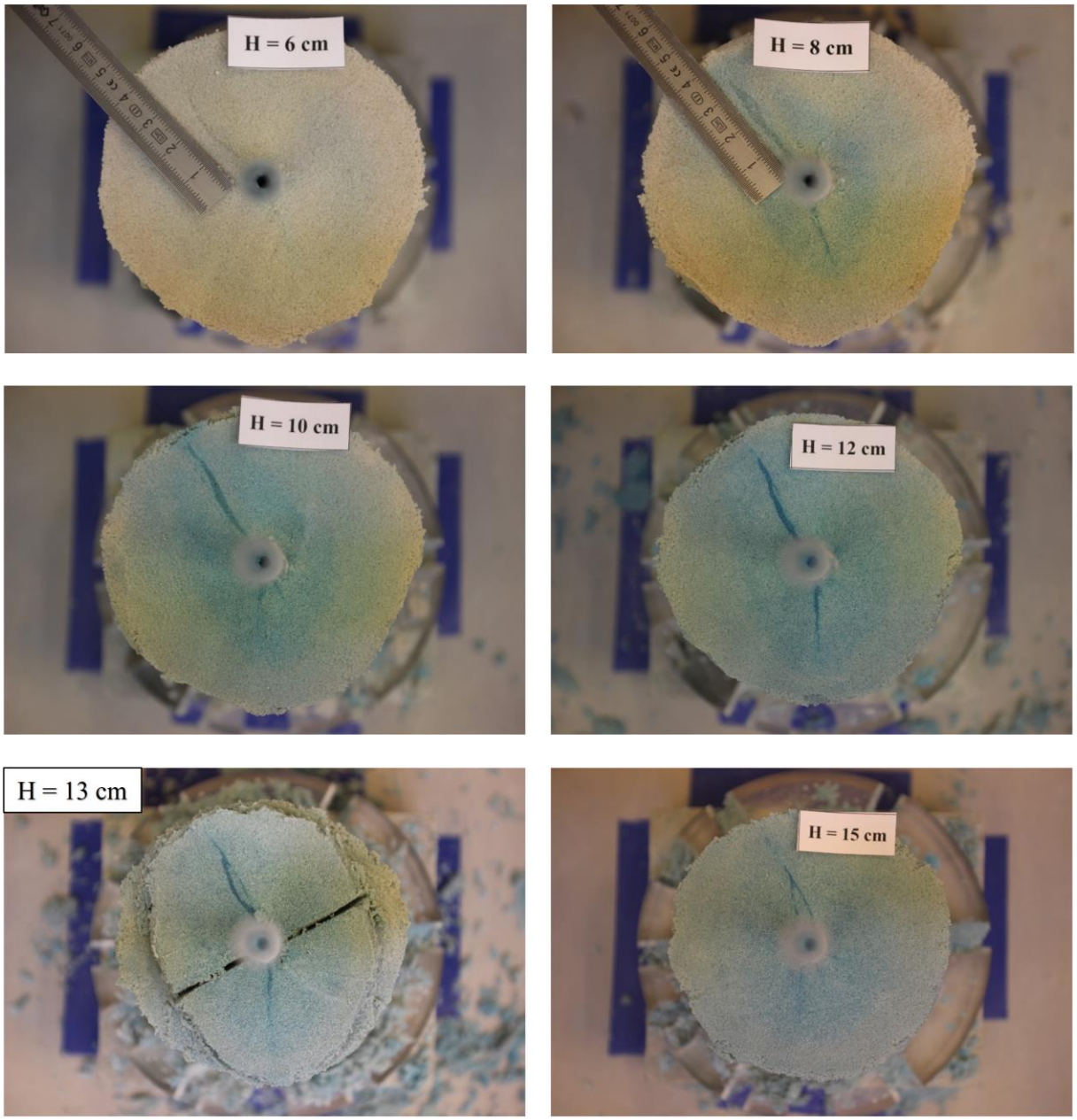

Fig. D-18: Excavation of specimen P8.

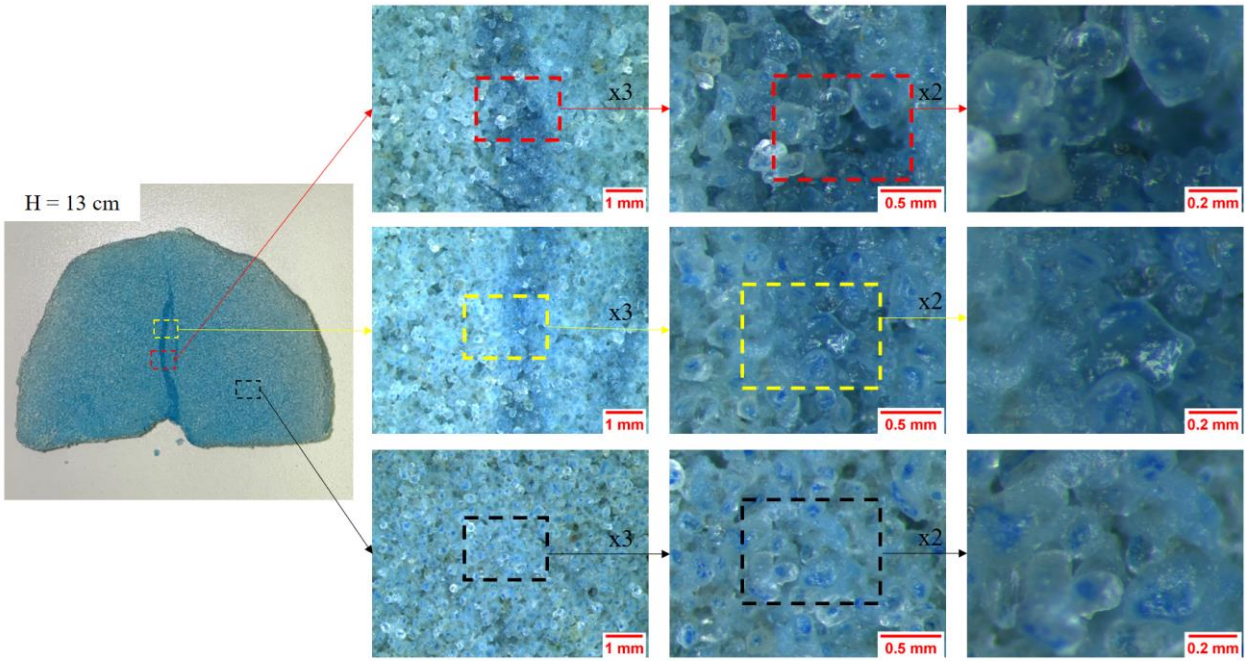

Fig. D-19: Test P8 - Optical microscope observation of a typical horizontal section containing the fracture (H = 13 cm).

Appendix E Tests in the radial injection chamber with the injection of pure water

E.1 Test N29

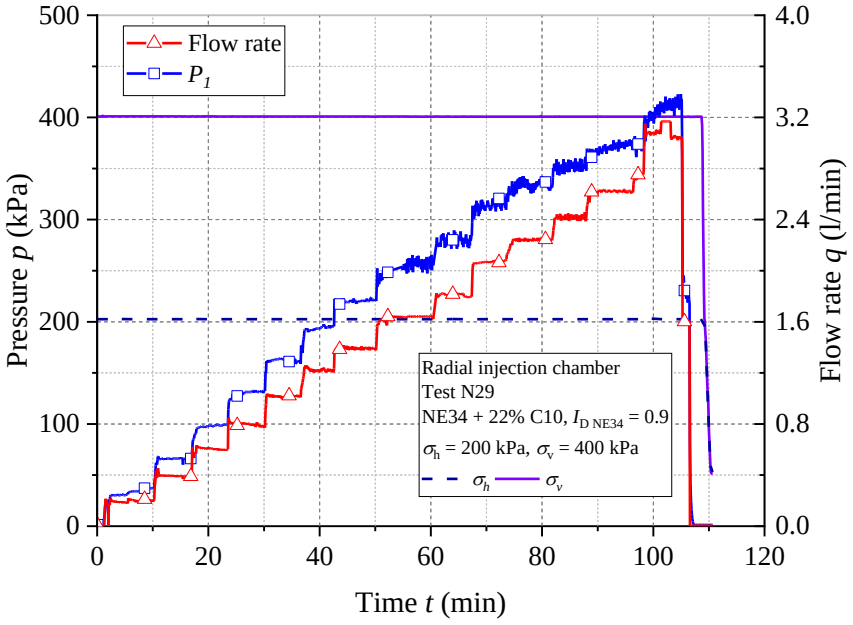

Fig. E-1: Results of test N29. Each injection step was maintained for about 5 to 7 minutes.

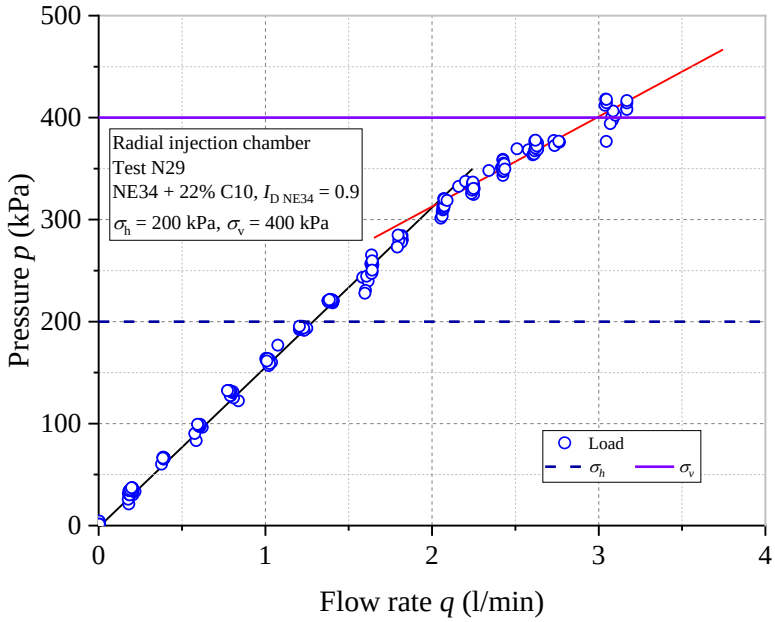

Fig. E-2: Evolution of the pressure versus flow rate (Test N29). Slight change in the slope of the pressure – flow rate curve is observed at about 320 kPa of injection pressure (1.6 σ_h).

At the end of the injection phase, a mixture of dye Basacid Bleu 762 diluted in water was injected. For this test, the injection volume of the colored water was enough to invade the whole sand pack. During the disassembling, no fracture was detected within the sand pack which matches with the results obtained during the water injection phase without any pressure drops.

As shown in Fig. E-3, the blue dye is well distributed within the sand pack, confirming the efficiency of this solution. A symmetrical zone is well observed over the entire height of the sand pack. However, the injection of such high volume does not allow to visualize the flow pattern of the fluid within the sand pack. That is why, in the following tests, only a small volume of the dye will be injected.

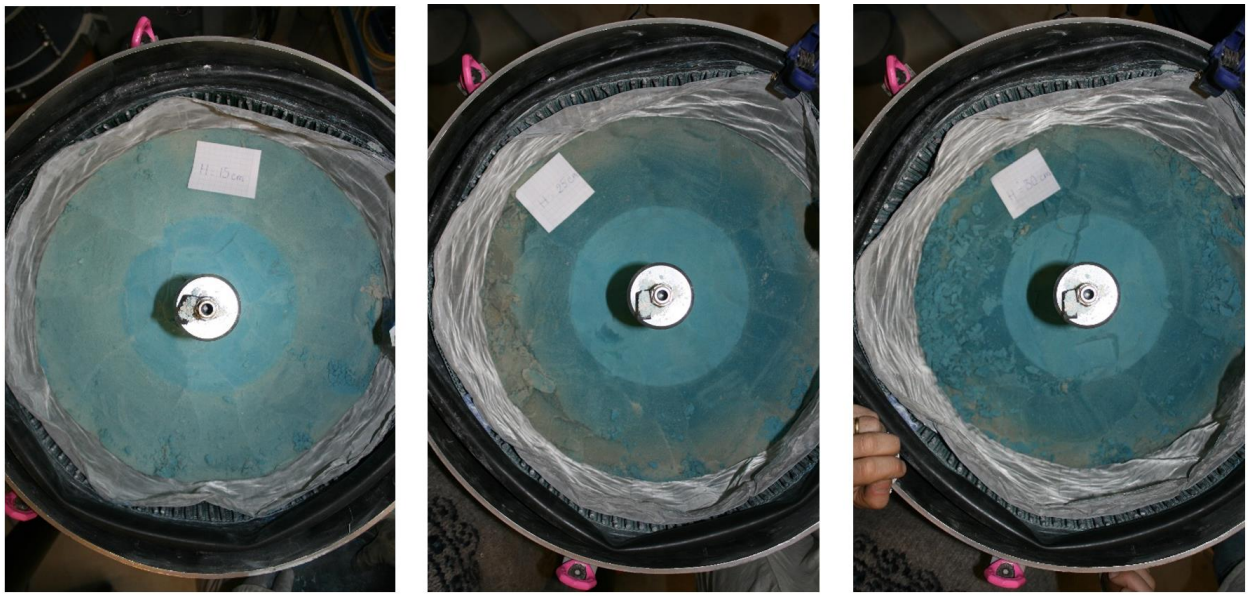

(a) (b) (c)

Fig. E-3: Some typical photos of the injection zone invaded by 0.2% of Basacid Bleu 762 diluted in water.

E.2 Test N30

E.2.1 Injection phase

The injection test was conducted in three phases (Fig. E-4). During the first phase (Phase 1), the maximum flow rate imposed was 3.15 l/min. At the last injection rate at 3.1 l/min, a progressive increase in pressure was observed without stabilization (Fig. E-5). In order to better understand this phenomenon, it was decided to perform the second phase (Phase 2) to reach a higher flow rate of 3.6 l/min (Fig. E-6). Similar to the previous phase, the injection pressure was progressively increased at a flow rate of 3.0 l/min. When the flow rate reached 3.6 l/min, the pressure curve did not show a change in slope, indicating that the frac regime has not been reached yet. Note that, during this test, a flowmeter having a maximum measurement of 3.15 l/min was used. Beyond this value, the flow rate is interpreted based on the calibration curve of the pump. The calibration test will be detailed later in this part. A new flowmeter in the range between 0.5 and 10 l/min is ordered to overcome this limitation in the following tests.

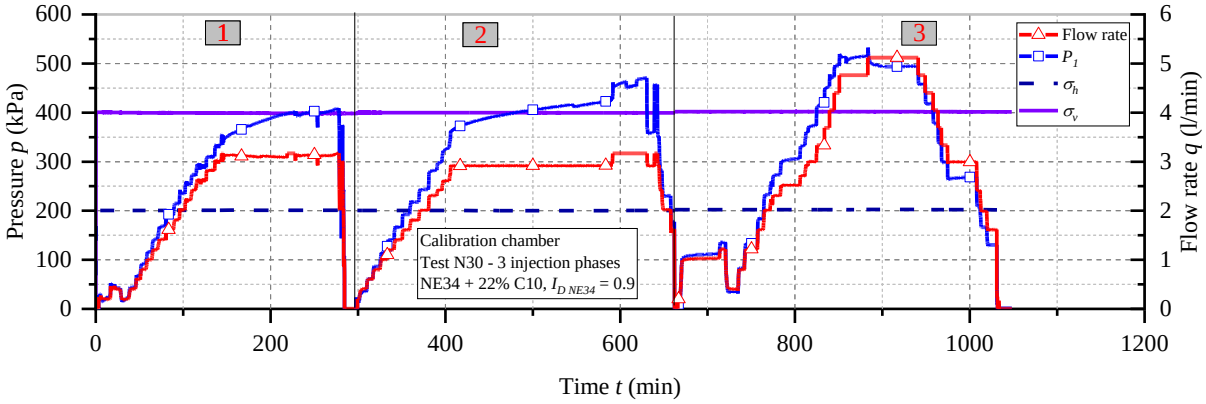

Fig. E-4: Full response of test N30.

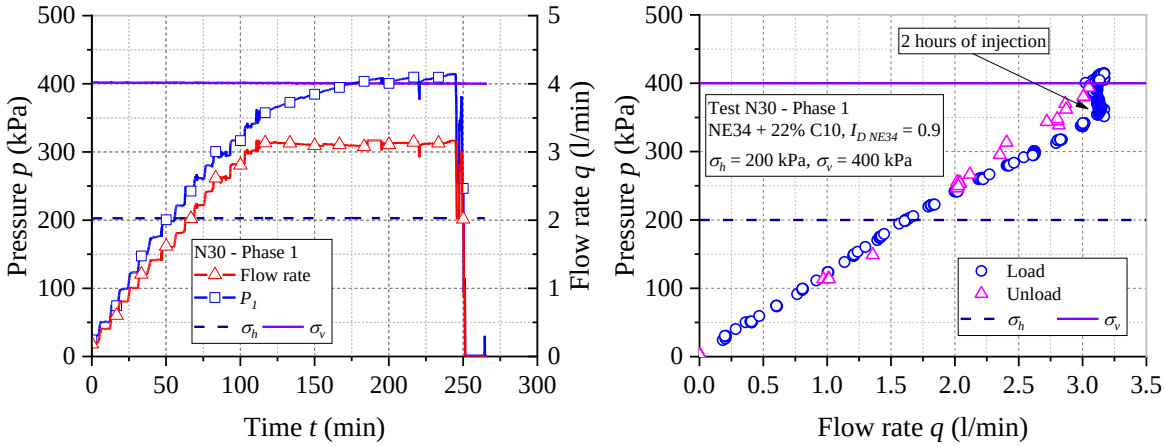

(a) (b)

Fig. E-5: Test N30 – Phase 1: (a) pressure – flow rate – time curves; (b) pressure – flow rate curve.

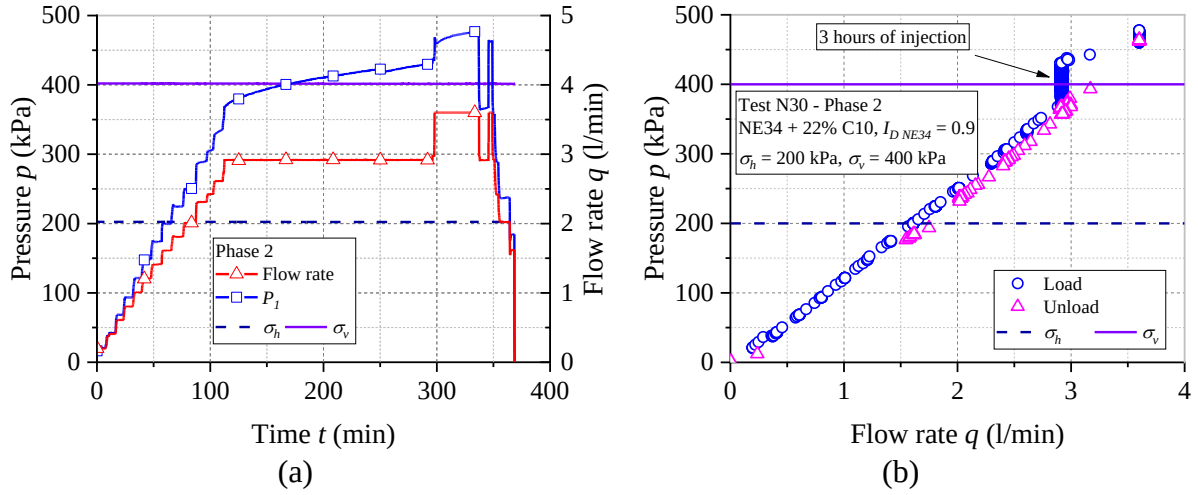

Fig. E-6: Test N30 – Phase 2: (a) pressure – flow rate – time curves; (b) pressure – flow rate curve.

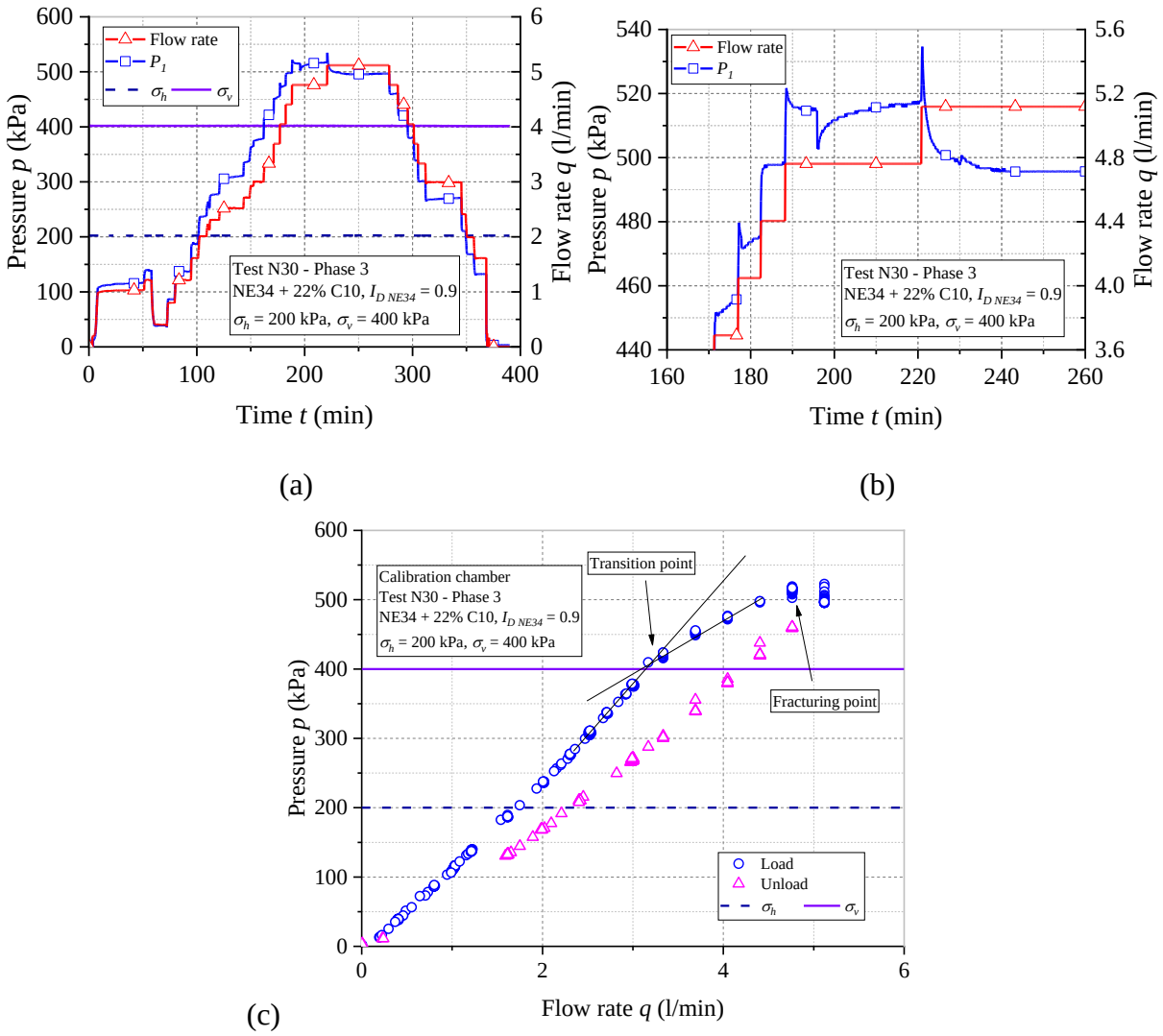

Fig. E-7: Test N30 – Phase 3: (a) full response and (b) fracturing regime in terms of pressure – flow rate –time curves; (c) pressure – flow rate curve.

The third phase then was conducted (Phase 3) by increasing the flow rate to about 5.1 l/min to reach the frac regime. A change in the slope of the pressure – flow rate curve was observed at a transition point of Q_{tr} = 3.2 l/min and P_{tr} = 420 kPa (2.1 σ_h). The first pressure drop is detected at a flow rate Q_{frac} of 4.75 l/min, corresponding to the first pressure drop P_{frac} = 520 kPa (2.6 σ_h).

❖ Calibration test of the flow rate

The flow rate is monitored using a flow control valve of the pump (Fig. E-8). Under 3.15 l/min, the flow rate is measured using a flowmeter to provide more precise data in real-time. Upper this value, the flow rate is derived from the calibration curve. The calibration test protocol consists of injecting water in steps of flow rate in the open air. In order to be in conditions close to the test, the outlet of the flow is reduced by partial clogging of an outlet valve in order to increase the injection pressure. Two injection phases are carried out with and without a flowmeter.

In the first injection phase (with the flowmeter), the flow rate was incrementally increased up to a flow rate of 3 l/min. The pressure-flow curve is shown in Fig. E-9. The flow rate corresponding to each level of the valve was measured with the flow meter. A linear relationship between the indicator on the pump valve and the measured flow rate (Fig. E-10 - blue points) is observed. By extrapolating this line (orange dots), the flow rate can be deduced with the corresponding indicator of the valve.

Fig. E-8: Flow control valve of the Wanner Hydra Cell G03 pump.

During the second injection phase, the flowmeter has been removed from the circuit. The imposed flow rate was controlled by the pump valve and was deduced from the calibration curve. The flow rate was increased to 4 l/min. Fig. E-11 shows all the results for the two injection phases, the pressure-flow curve of phase 2 is superimposed on that of phase 1, confirming that the calibration method gives satisfying results.

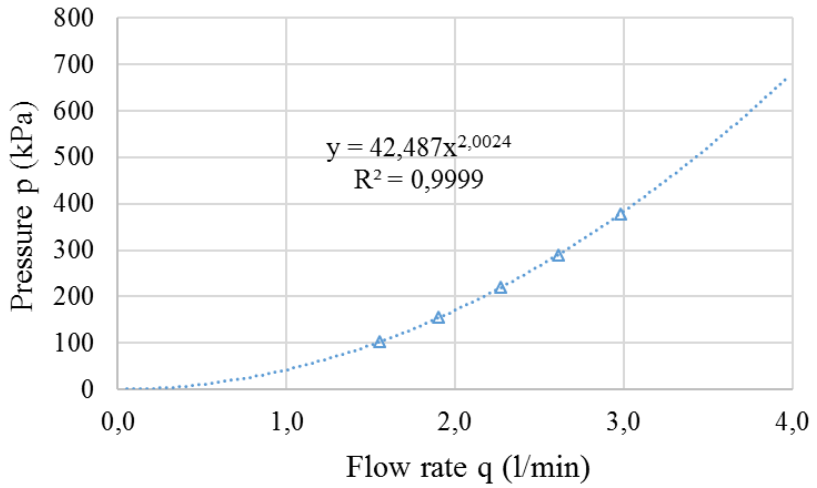

Fig. E-9: Calibration test – Phase 1 with the measurement of a flowmeter.

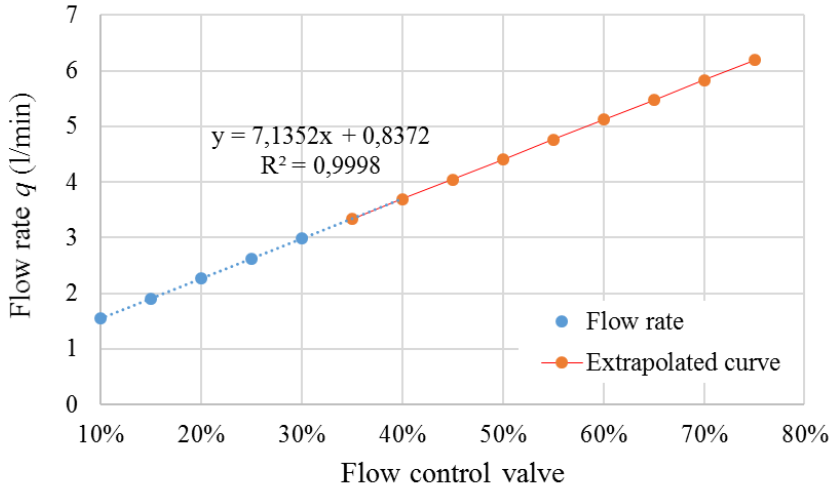

Fig. E-10: Flow rate versus valve level.

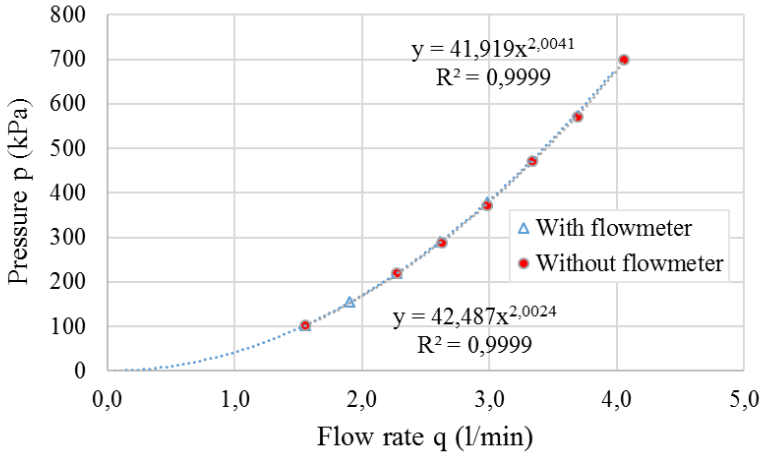

Fig. E-11: Pressure – flow curves of the calibration test.

E.2.2 Disassembling phase

As the typical test, the colored gel was injected to freeze the sand pack. Fig. E-12 presents some views of the inner ring of the mixture sand + fines. A symmetric distribution of the blue dye is observed around the injection point. The excavation of the inner ring was performed in the vertical direction. Small vertical fractures were detected around the strainer tube which confirm the pressure drops during the injection (Fig. E-13)

(a) (b) (c)

Fig. E-12: Views of the inner ring of the sand pack N30.

(a)

(b)

Fig. E-13: Small vertical fractures formed around the trainer tube (Test N30).

E.3 Test N32

E.3.1 Test characterizes

The test was carried out in four phases and the parameters of each phase are given in Tab. E-1.

Tab. E-1: Characteristics of the N32

Test N32	Test conditions			Density index of the matrix $I_{D\ NE34}$	Protocol
	σ_h (kPa)	σ_v (kPa)	K_0		
Phase 1	200	600	0.33	0.9	One loading/unloading cycle
Phase 2	200	600	0.33	0.9	One loading/unloading cycle
Phase 3	200	500	0.4	0.9	One loading/unloading cycle
Phase 4	120	360	0.33	0.9	One loading/unloading cycle + Colored gel injection

E.3.2 Water injection phase

During each phase, one loading-unloading cycle has been performed at different flow rate. Each rate was maintained for approximately 5 minutes to ensure that a quasi-steady-state condition was reached and that the injection pressure was more or less stabilized before moving to the next steps.

In the first phase (Phase 1), the injection was performed until the maximum capacity of the pump (7 l/min), without reaching the fracturing regime. At a flow rate of 7 l/min, the measured pressure was 702 kPa (≈ 3.5 σ_h). It was then unloaded with shorter flow rate-hold steps. The results showed that the permeability did not change during this phase.

In order to confirm this result, it was decided to perform a second phase (Phase 2) by repeating the same injection program. Only a slight change in the slope of pressure – flow rate curve was observed.

Then, a third injection phase (Phase 3) was carried out at an axial stress smaller than the two previous phases (500 kPa instead of 600 kPa of σ_v). A change in the slope was observed at a Q_{tr} of 4,5 l/min corresponding to injection pressure P_{tr} of 455 kPa (≈ 2.28 σ_h). Q_{tr} and P_{tr} are defined as the flow rate and the corresponding pressure at the transition point of two flow regimes (matrix and fracturing regime). The loading phase was applied until the maximum flow of the pump, again without fracturing.

The fourth phase (Phase 4) has been performed at a confining pressure of 120 kPa and an axial stress of 120 kPa (same K_0 = 0.33 as phase 1 and phase 2). We could again identify a change in the slope of the pressure – flow rate curve at a flow rate of 2.65 l/min corresponding to 256 kPa of injection pressure (≈ 2.13 σ_h). Moreover, in this phase, significant pressure drops

were observed that result in an increase of the overall permeability after fracturing. At the end of water injection phase, colored gel was injected to solidify the fracture zone.

The results obtained during each phase are described below in more detail.

a. Phase 1

The results of the first phase are presented in Fig. E-14 and Fig. E-15. The flow rate steps were stepped up to the maximum capacity of the pump (7 l/min) with an increment of 0.2 l/min without any change observed in the slope of pressure – flow rate curve. The maximum injection pressure recorded in this phase was 702 kPa which corresponds to 3.5 times the confining pressure (σ_h). In Fig. E-15, the pressures during the unloading phase, are superimposed with those of the loading phase. We can observe that the permeability was kept nearly unchanged during injection and is about 100 mD.

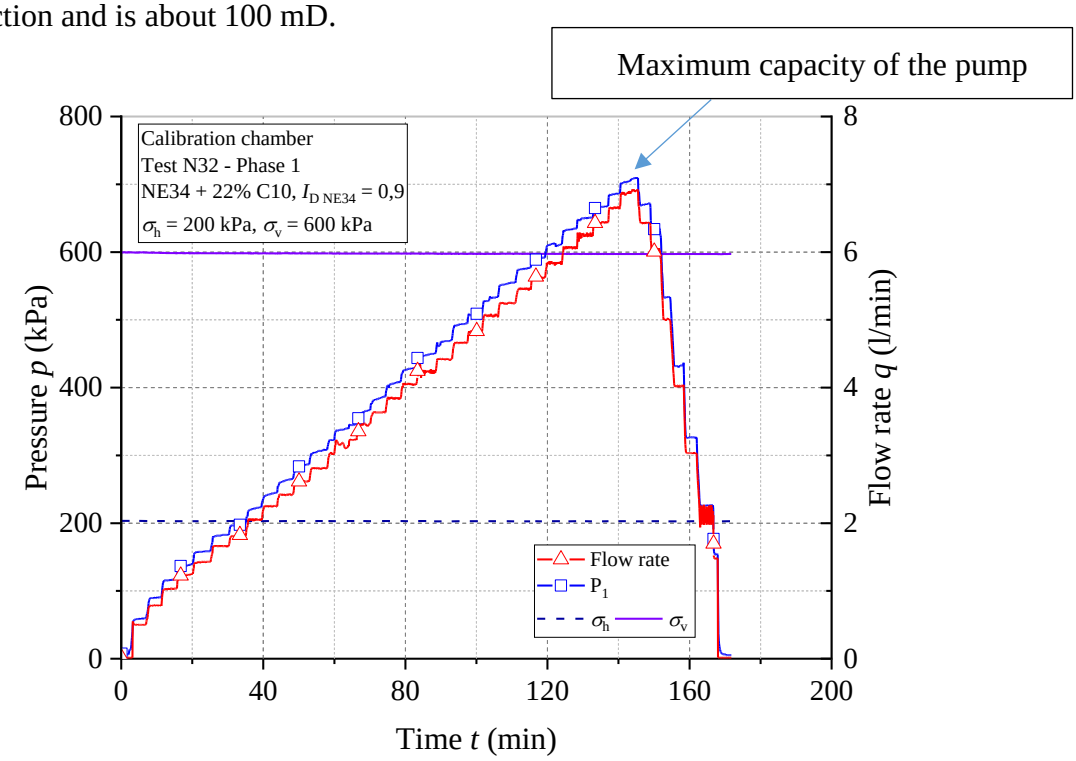

Fig. E-14: Phase 1: Pressure – flow rate – time curves (Test N32).

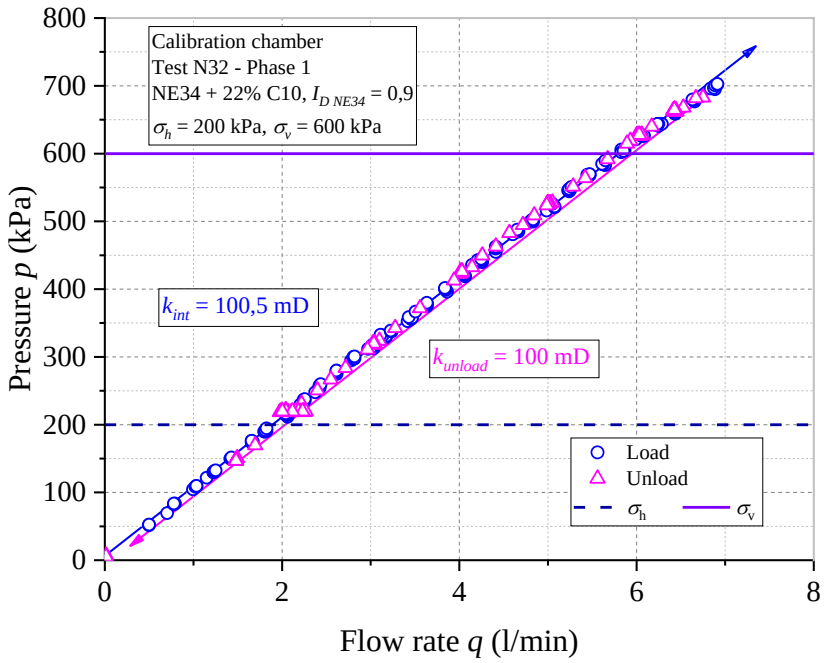

Fig. E-15: Phase 1: Pressure – flow rate curve (Test N32).

Fig. E-16 presents a comparison of the results of tests N30, N31 and N32. We observed a slight difference of the initial permeability (initial slope) between the three specimens which is 84.5 mD (N30), 77 mD (N31) and 100 mD (N32). This difference can be attributed to the variability induced by the preparation of the sand pack.

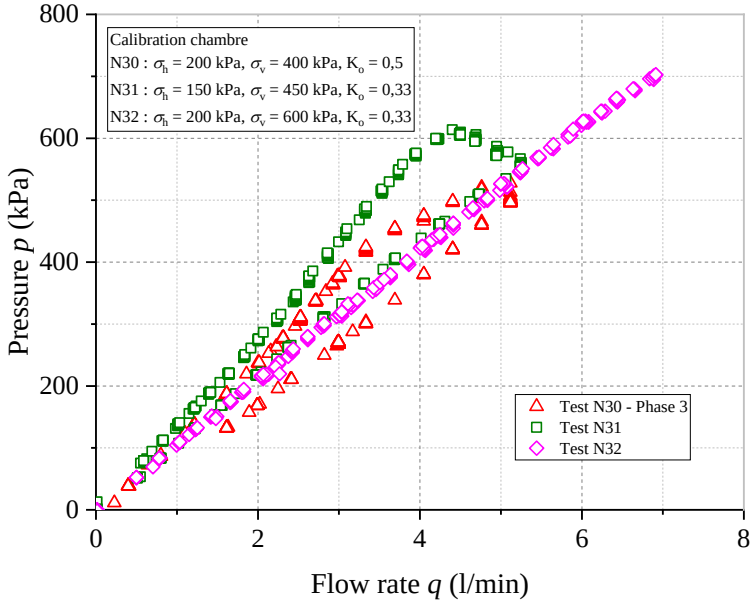

Fig. E-16: Results comparison of the tests in the radial injection chamber.

b. Phase 2

To ensure repeatability, the second injection phase was performed with the same parameters as the previous one. The results of this phase are shown in Fig. E-17. A small change in the slope of pressure - rate curve was observed (Fig. E-18) at a flow rate of 5.45 l/min, the corresponding pressure was 550 kPa (2.75 σ_h). At the maximum flow rate of 6.9 l/min, a slight drop of pressure was also identified (Fig. E-19). The injection was continued for 15 minutes at this flow rate before unloading. An increase of about 5 % of the permeability was calculated.

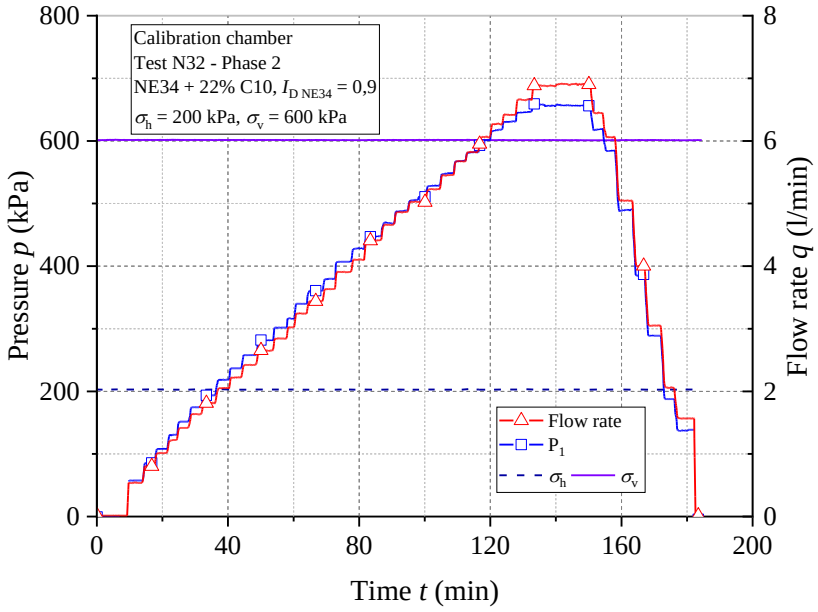

Fig. E-17: Phase 2: Pressure – flow rate – time curves (Test N32).

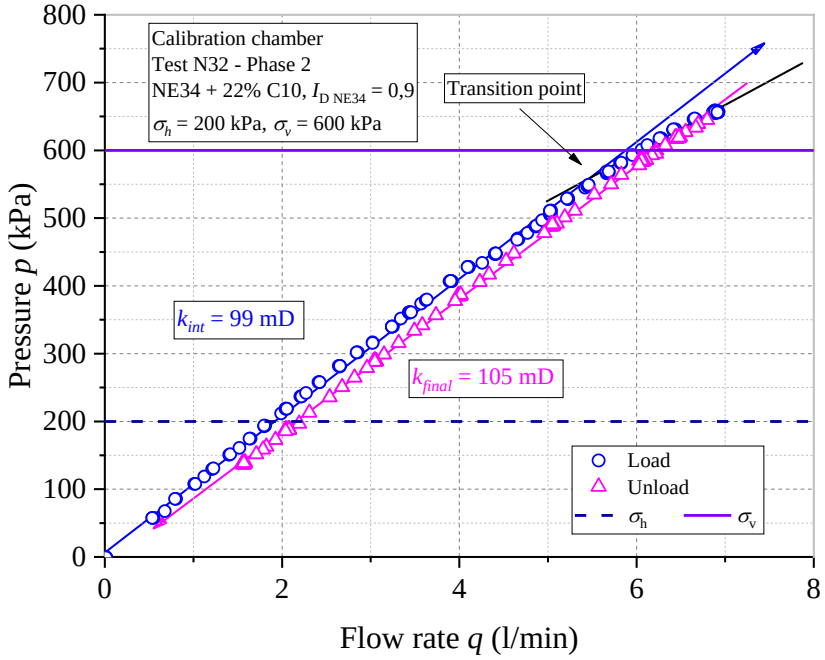

Fig. E-18: Phase 2: Pressure – flow rate curve (Test N32).

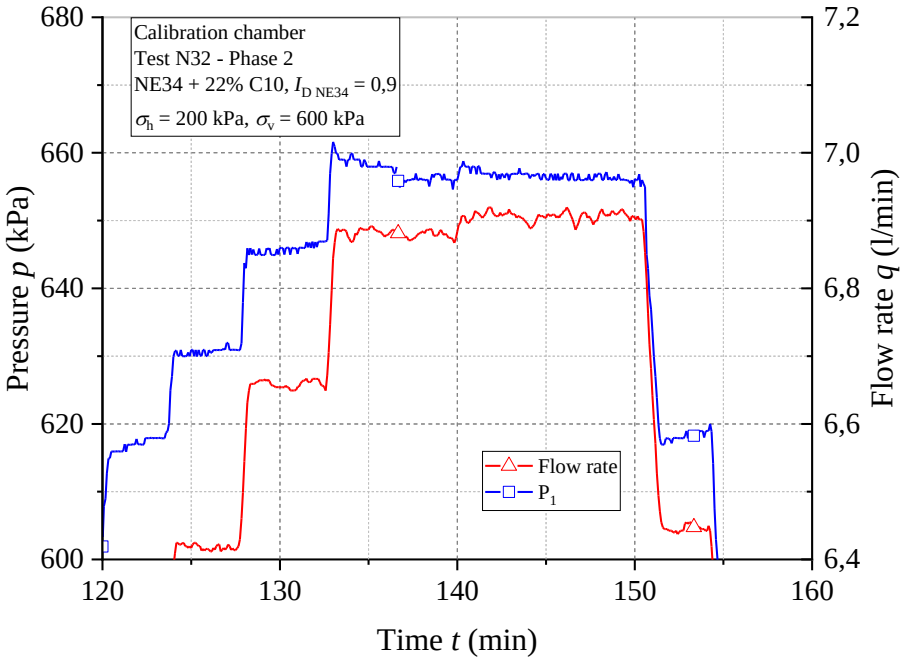

Fig. E-19: Slight drop of pressure during phase 2 (Test N32).

c. Phase 3

Based on the results of the tests N30 and N31 (Fig. E-20), it can be observed that K_0 has an important effect on the critical pressure for fracturing. The ratio P_{frac}/σ_h is higher when the deviatoric stress increases (K_0 smaller).

To reach the pressure drops state without changing the confining pressure, this phase was carried out with a value of K_0 equal to 0.4 by reducing the axial stress from 600 kPa to 500 kPa. Then, the injection program was repeated. The results are presented in Fig. E-21 and Fig. E-22. The transition regime was observed at a Q_{tr} of 4,5 l/min corresponding to P_{tr} of 455 kPa (2.3 σ_h). No pressure drop was identified during this phase and the permeability of the sample did not change.

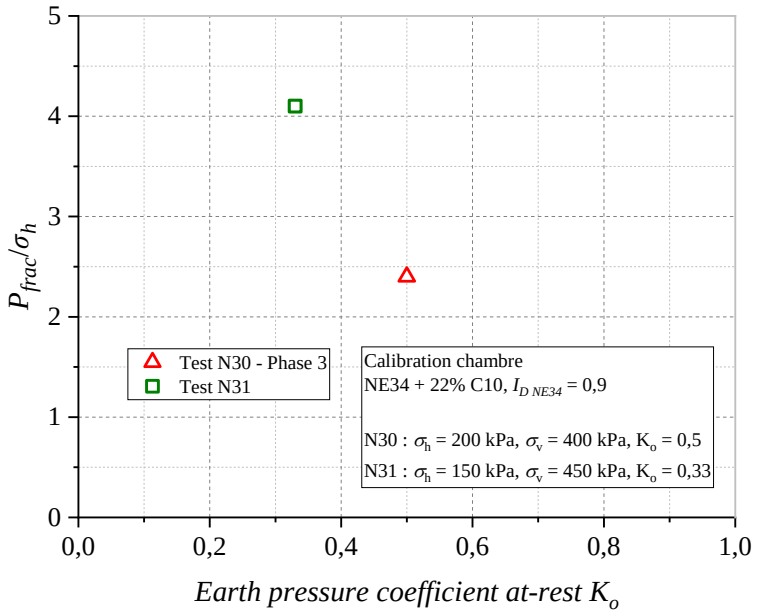

Fig. E-20: Effect of K_0 on the ratio P_{frac} / σ_h (Test N32).

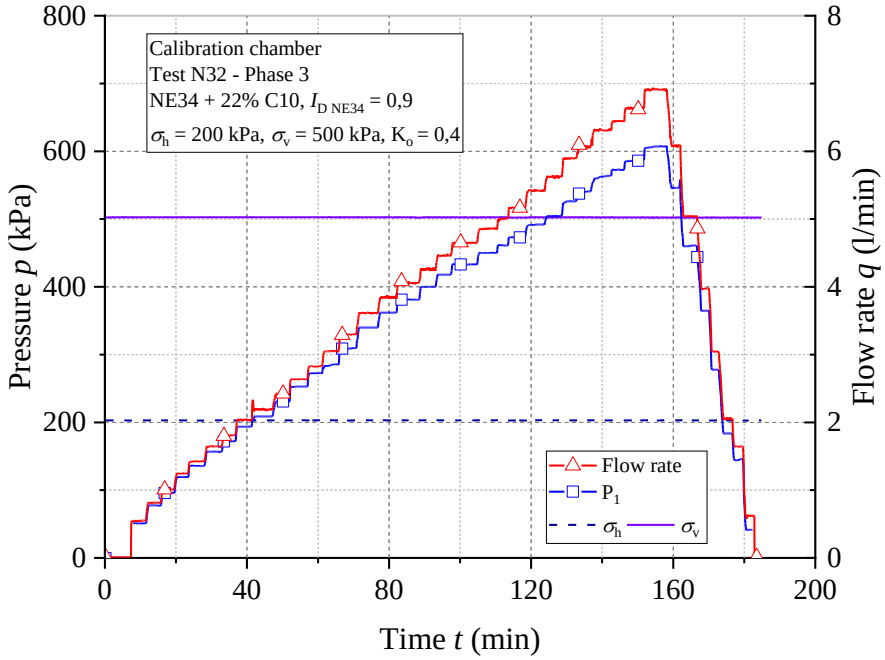

Fig. E-21: Phase 3: Pressure – flow rate vs time curves (Test N32).

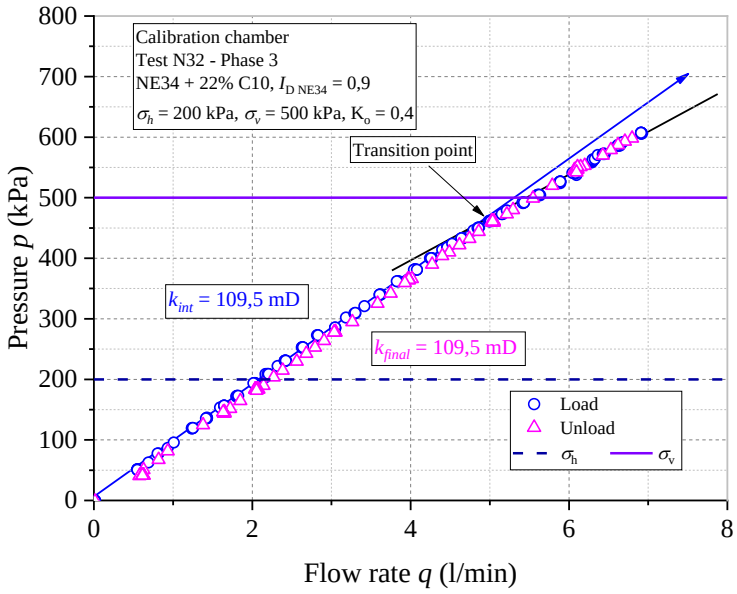

Fig. E-22: Phase 3: Pressure vs flow rate curve (Test N32).

d. Phase 4

Benahmed (2001) has explored the effect of applied confining pressure on the void ratio of sand samples (Fig. E-23). The effect of the confining pressure becomes less important when the sample is denser. Test N32 was performed with at a very dense state (density index of 0.9). Moreover, in the inner ring that is constituted by the mixture of NE34 + 22% C10 fines, the corresponding void ratio is only 0.3. Therefore, according to Benahmed (2001), the effect of applied stress conditions on a modification of the initial void ratio can be considered as negligible.

The fourth phase (Phase 4) has been performed by reducing both the confining pressure and the axial stress and keeping the K_0 = 0.33 (same as phases 1 and 2). The applied stresses are: 120 kPa for σ_h and 360 kPa for σ_v which allowed to reach the fracturing state for a flow rate compatible with the pump capacity.

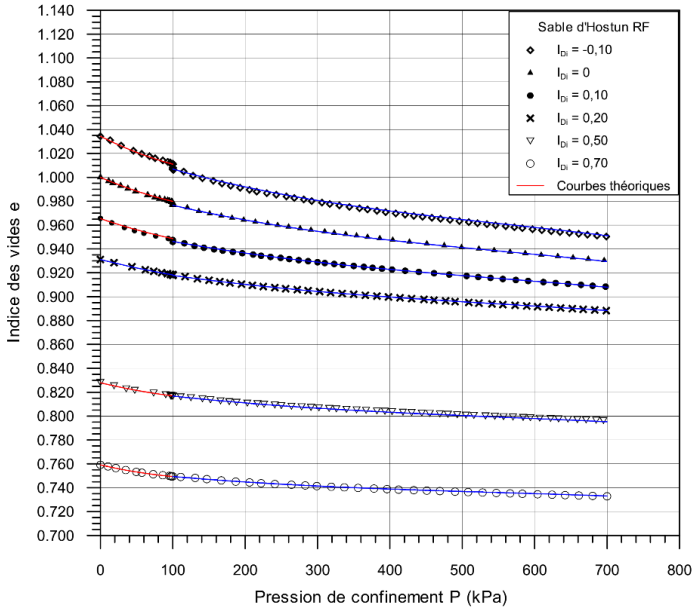

Fig. E-23: Experimental results of the variation of void ratio depending on the applied confining stress conditions (Benadmed, N., 2001).

Fig. E-24 and Fig. E-25 present the results of Phase 4. The transition point was observed at a flow rate of 2.65 l/min corresponding to 256 kPa of injection pressure (≈ 2.13 σ_h). The first visible pressure drop was observed (Fig. E-26) at a Q_{frac} of 6.3 l/min, corresponding to a P_{frac} of 484 kPa (4 times of the confining pressure). Q_{frac} is defined as the flow rate corresponding to the first drop pressure and P_{frac} is the maximum value of the pressure measured at this point. The results are similar to those observed during the test N31. The loading phase was continued with three more steps of 10 minutes at flow rates of 6.53 l/min, 6.7 l/min and 6.9 l/min before unloading. The increase in permeability is approximately 42%.

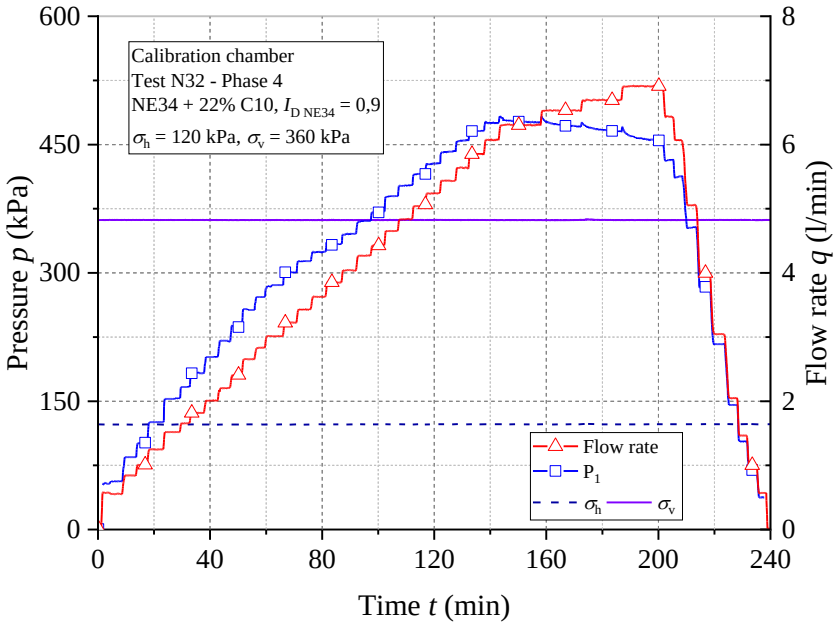

Fig. E-24: Phase 4: Pressure – flow rate – time curves

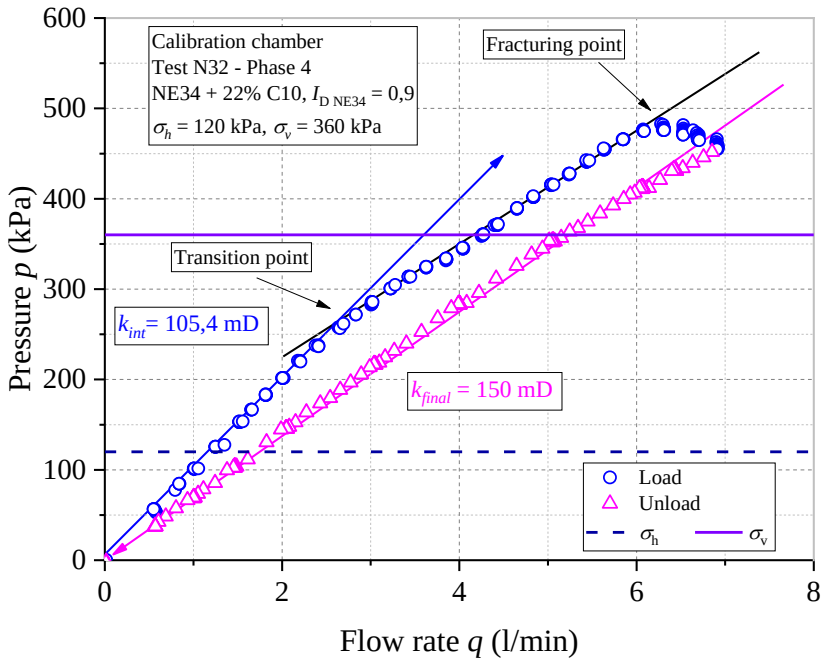

Fig. E-25: Phase 4: Pressure – flow rate curve (Test N32).

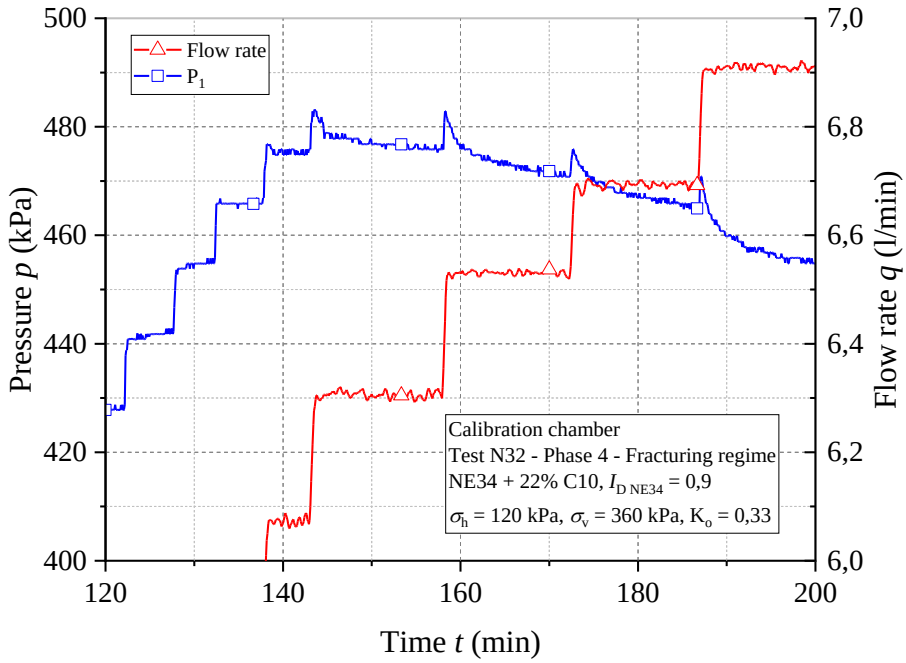

Fig. E-26: Significant drops of injection pressure during fracturing flow regime (Phase 4) (Test N32).

e. Results synthesis

Fig. E-27 presents the results synthesis of the water injection phase. The change of the applied stresses has no or very small effect on the initial permeability of the sand pack. The overall permeability varied slightly during the first three phases between 100 mD and 110 mD whereas, in phase 4, it increased significantly after fracturing (from 105 mD to 150 mD) (Fig. E-28).

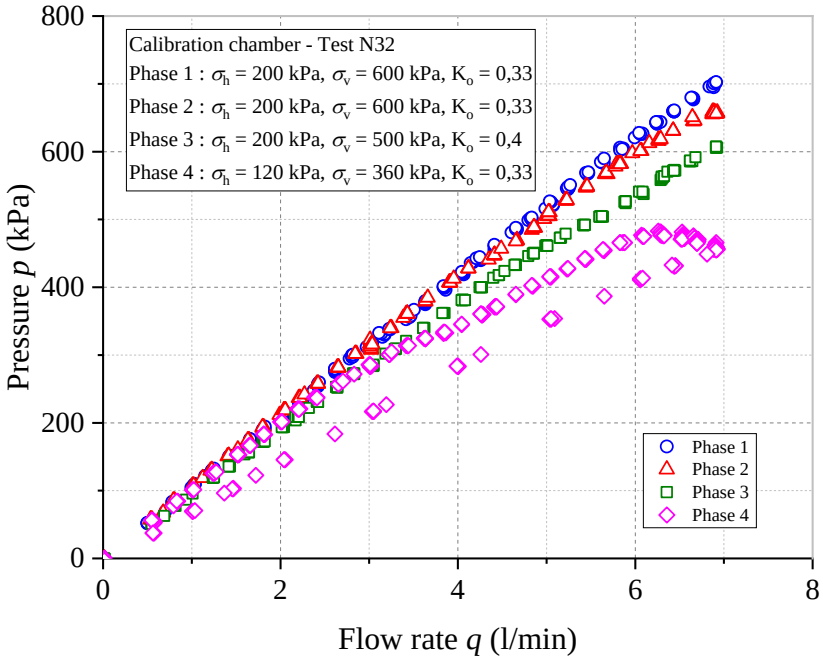

Fig. E-27: Results synthesis of water injection phase (Test N32).

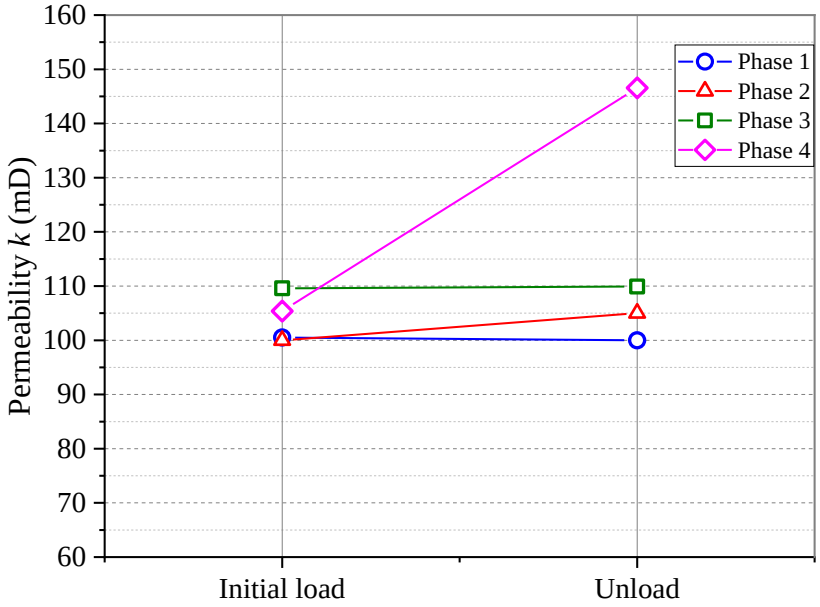

Fig. E-28: Evolution of the overall permeability during water injection phase (Test N32).

E.3.3 Colored gel injection

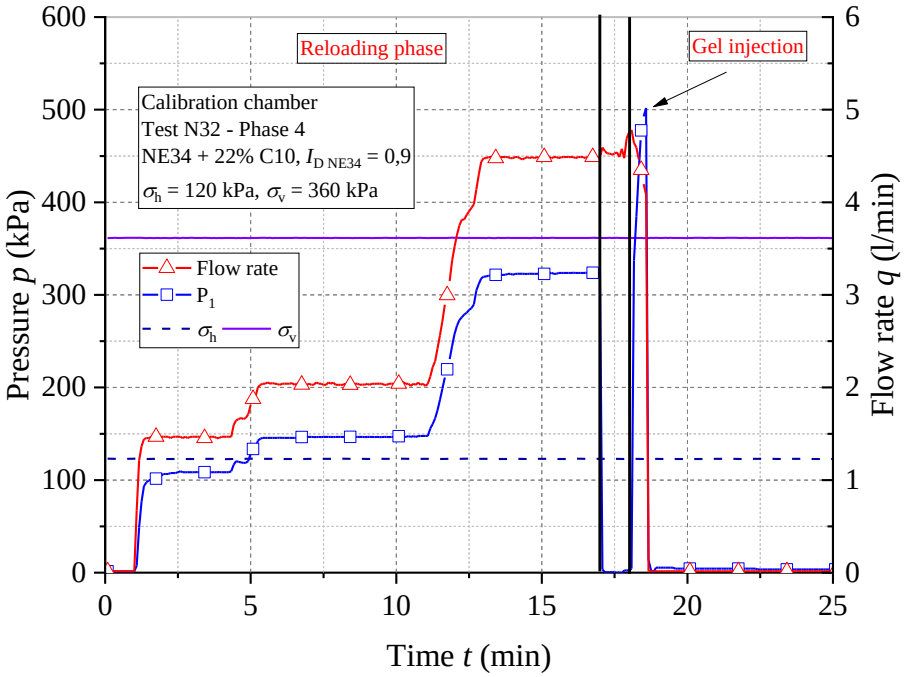

Fig. E-29: Test results during colored gel injection phase (Test N32).

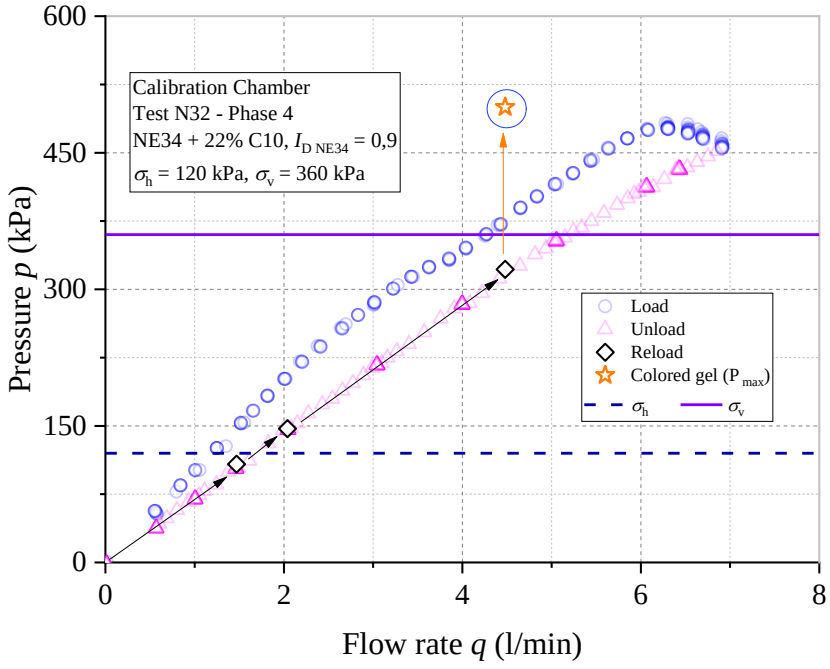

Fig. E-30: Pressure – flow rate curve (Test N32).

The colored gel injection phase was performed as the tests N30, N31. A small volume of the mixture of gel MasterRoc MP320 + 0.2% Blue Basacid 762, corresponds to 50 % of the void volume of the inner ring was injected. Fig. E-29 presents the test results of this phase. Before injecting the mixture, three reloading steps were carried out at 1.45 l/min, 2 l/min, and

4.5 l/min to confirm the change of the permeability after fracturing (Fig. E-29). To reach the maximum pressure during the water injection phase (485 kPa), this mixture was injected at a flow rate of 4.5 l/min for approx. 20s. The maximum pressure recorded was 500 kPa which is very close to the expected value (Fig. E-30).

The specimen was kept for one week under the stress conditions to solidify before disassembling.

E.3.4 Disassembling phase

The disassembling phase consists in excavating the first low permeability layer and then excavating the outer ring which contains only the Fontainebleau NE34 sand. The membrane and lateral drainage system were removed before the horizontal excavation of inner ring was performed

❖ *Manual excavation*

Fig. E-31 presents the pictures during excavating the low permeability layer and the disassembling of the outer ring is presented in Fig. E-32. No trace of blue is observed in these layers. The disassembling of the inner ring consists of a horizontal excavation from top to bottom of the specimen. A camera was placed above the specimen, allowing photos to be taken every 5 mm of excavation. Fig. E-33 shows some taken photos to make sure to the camera angle. The pictures were also taken with a smartphone, allowing to visualize the specific fracture zone around the tube. A 360-degree ruler was glued to the top of injection tube which permit to measure the angle of the fractures formed around the injection point at a given height (Fig. E-34). Fig. E-35 shows the horizontal cross-sections of the inner rings at different heights. When the excavation reached the low part of the inner ring, the obscured zone became larger and the fracture lengths observed was shorter, therefore smartphone was used to take the photos for the rest of sample (Fig. E-36).

Fig. E-31: Excavation of the low permeability layer (sand pack N32).

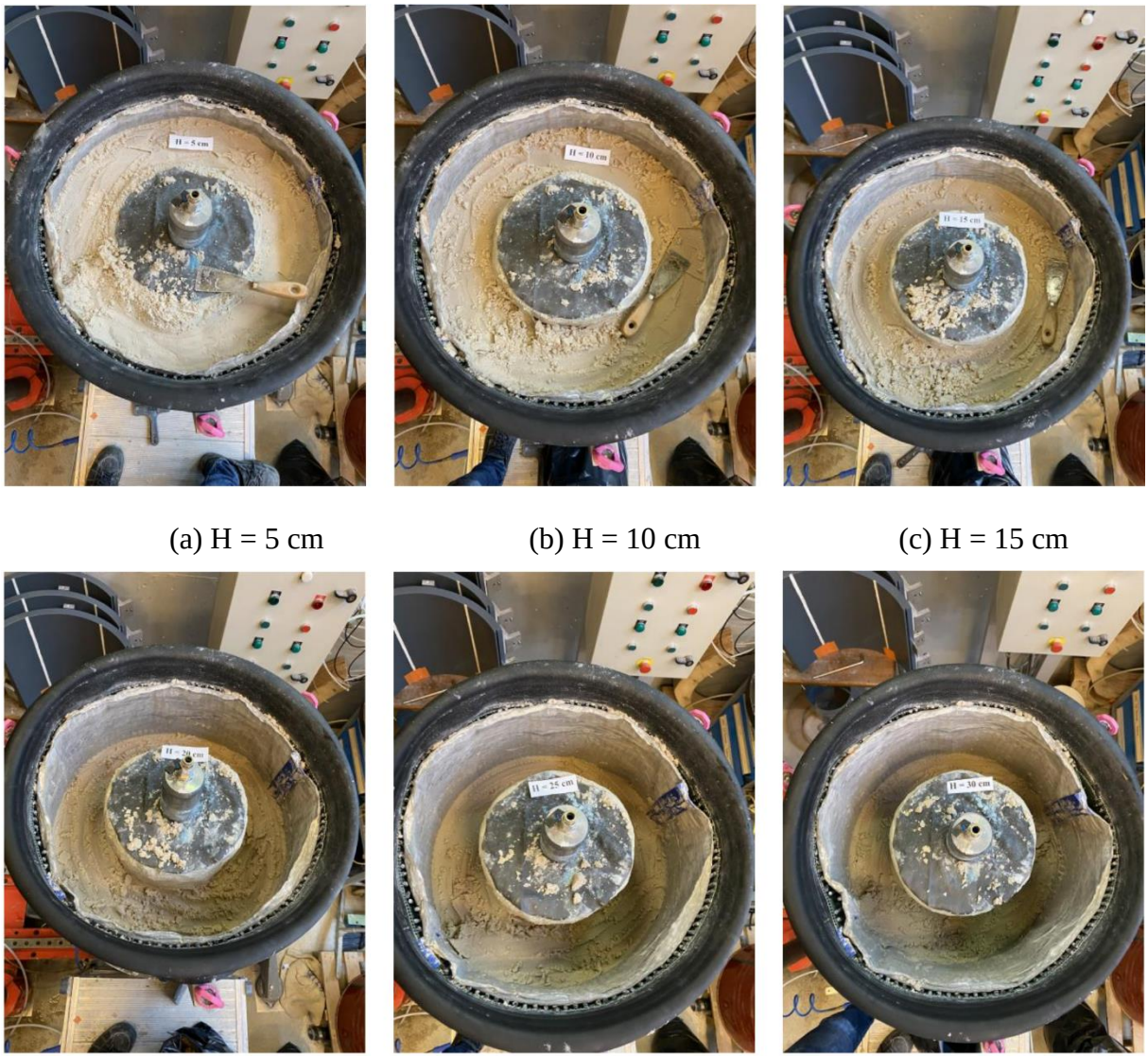

(a) H = 5 cm (b) H = 10 cm (c) H = 15 cm

(d) H = 20 cm (e) H = 25 cm (f) H = 30 cm

Fig. E-32: Sand pack N32 - Excavation of the outer ring at different heights.

Along of the injection tube, three vertical fractures were clearly observed which propagated nearly perpendicular to the injection point. Two of them developed all along the tube (Fracture 1 and Fracture 2) whereas the other (Fracture 3) stopped at the middle of the sample (Fig. E-37). The angle between these fractures varies from 90° to 145° and it only slightly changes along the tube (10 degrees). The fracture length varies between 2 and 6 cm, the longest was observed at the middle of the specimen (at H = 20 cm). The fracture width is in the range of 1 mm to less than 1 cm and it gradually decreases from the tube to the fracture tip. Some other small fractures were also identified near the two ends of inner ring (at H = 8 cm and H = 34 cm). The photos make evidence of a non-symmetric distribution of the colored gel which is similar to those observed from the test N31. The diffusion of the colored gel was more important in the area containing the fractures. It can be concluded that the fracturing favors the flow, therefore, the overall permeability of the specimen increases. A 3D image representative of the fractures formed within the inner ring after fracturing is illustrated in Fig. E-37.

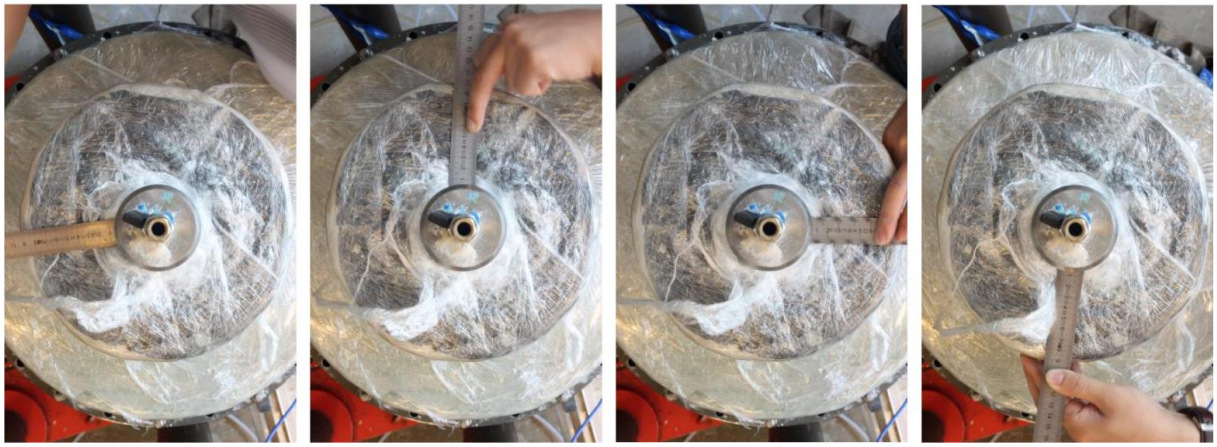

Fig. E-33: Some photos taken to verify the position of camera lens (sand pack N32).

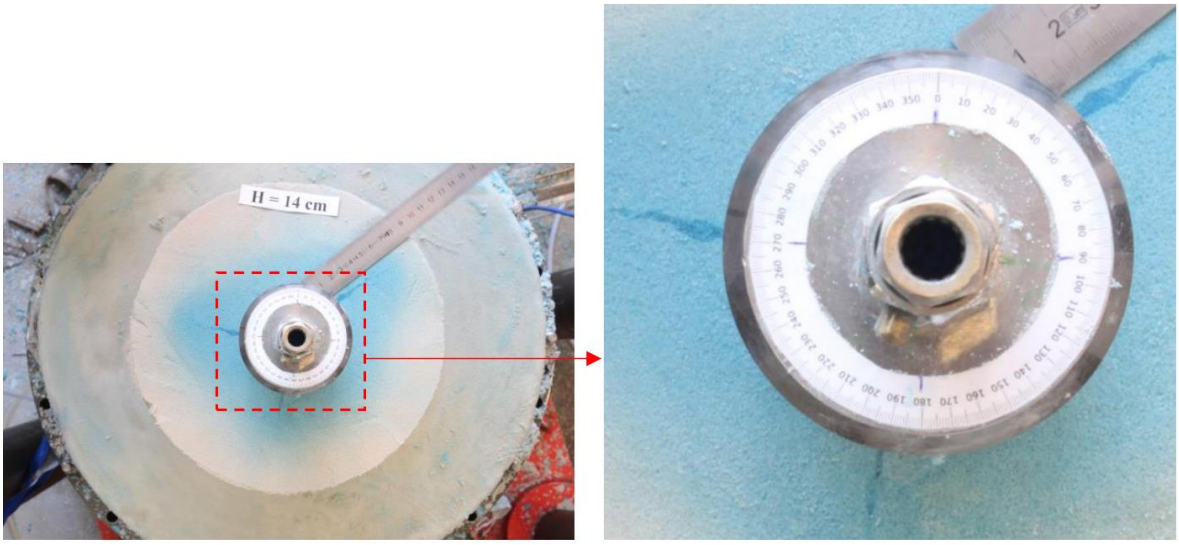

Fig. E-34: 360-degree ruler glued on the top of injection tube (sand pack N32).

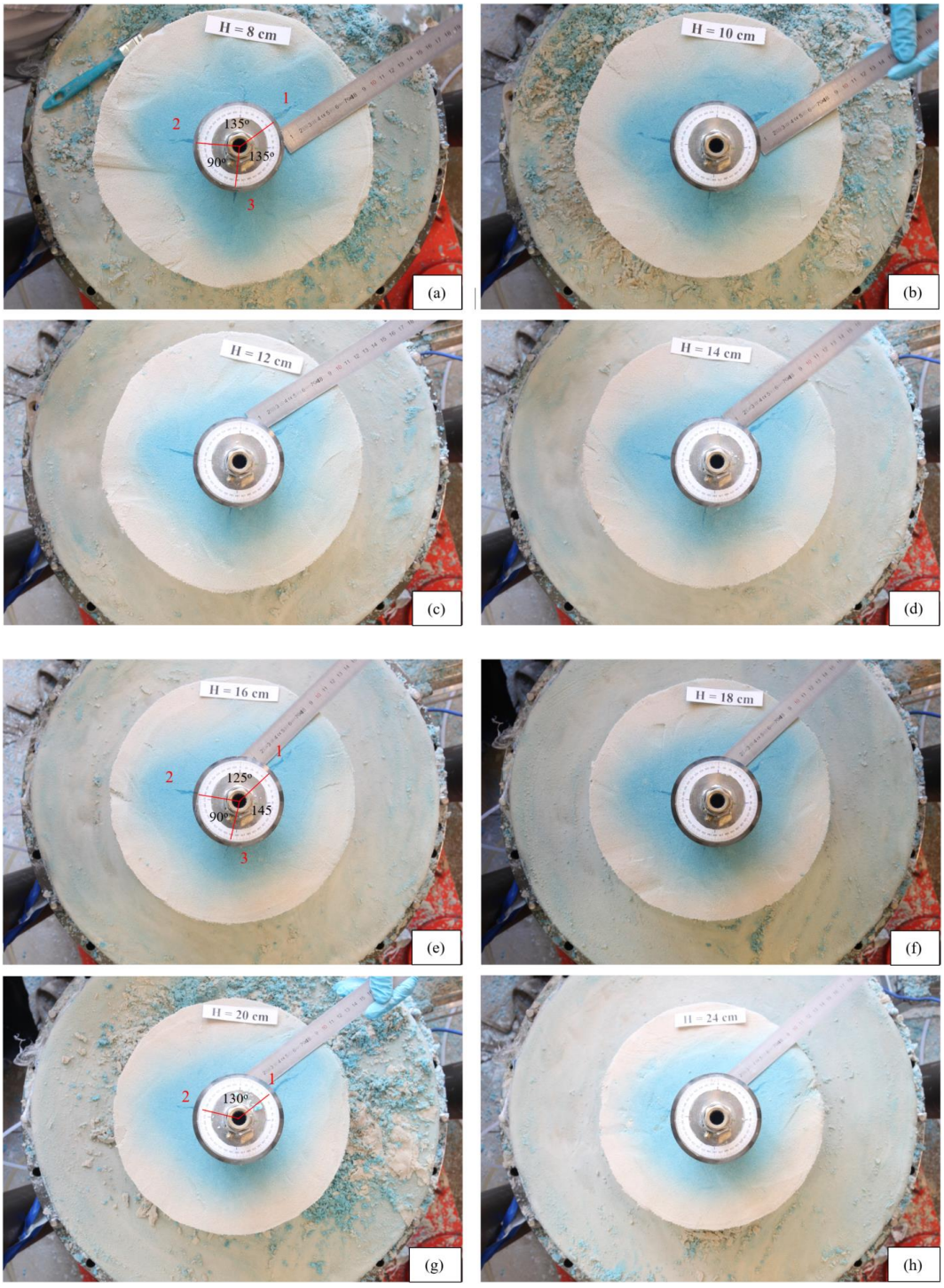

Fig. E-35: Sand pack N32 - Transversal cross-sections of the inner ring at different heights (photos taken by camera).

Fig. E-36: Sand pack N34 - Transversal cross-sections of the inner ring at different hights (photos taken by smartphone) (sand pack N32).

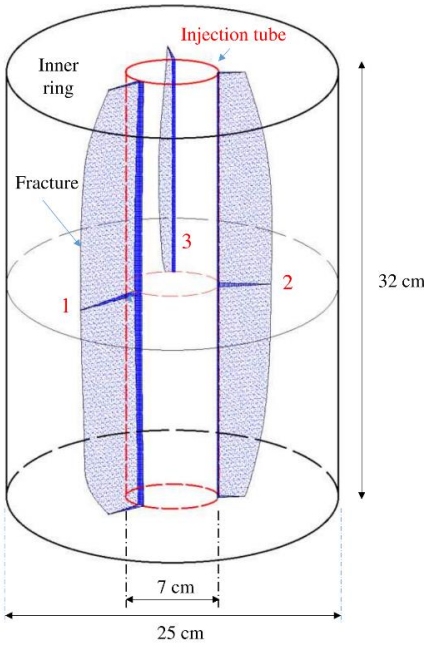

Fig. E-37: 3D image representing the fractures developed during test N32.

E.4 Test N34

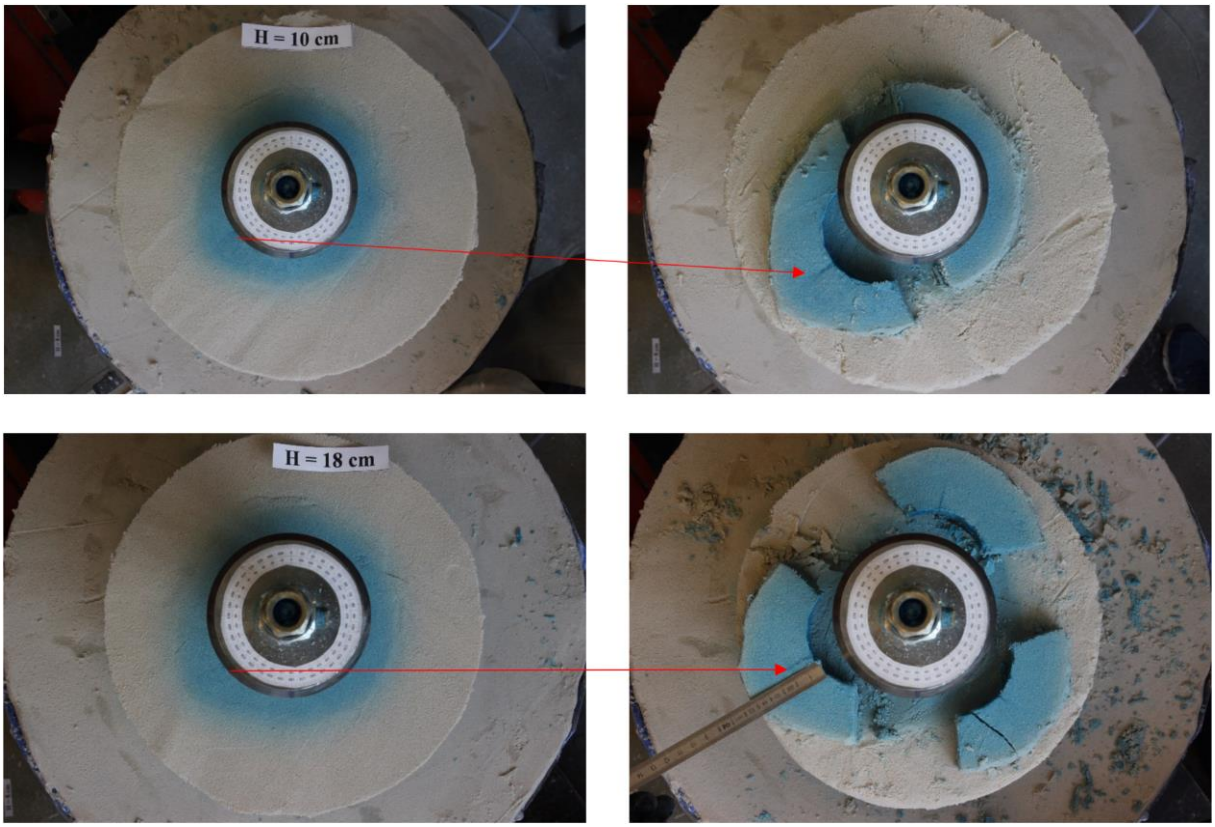

Fig. E-38: Sand pack N34 - Transversal cross-sections of the inner ring at different heights (photos taken by camera). The invasion of the colored gel is nearly symmetric around the injection point with a little longer invasion in the direction of a longest fracture.

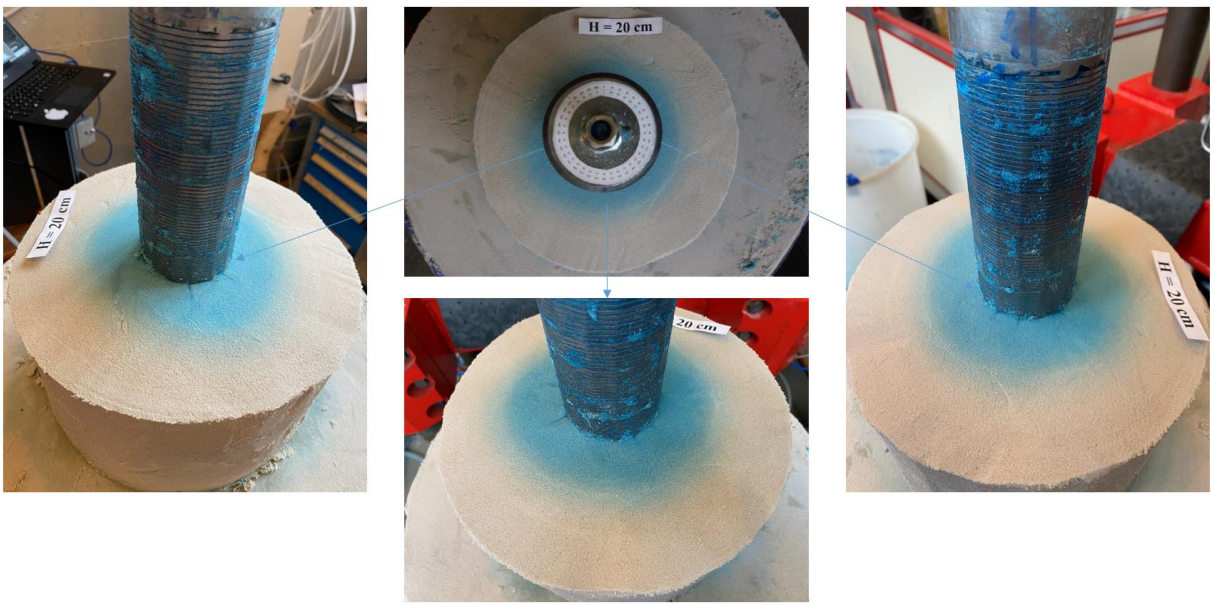

Fig. E-39: Test N34 - Small fractures induced around the strainer tube at H = 20 cm. The distribution of the blue dye is almost symmetric around the injection tube.

Appendix F Preliminary tests for developing the injection protocol with suspended particles

F.1 Test Q7

Fig. F-1 presents the results of the test Q7. The test characteristics are based on the tests in uniaxial cell performed by Feia et al. (2015). Two pressure response trends are observed: a gradual increase in pressure up to the confining pressure value followed by an unstable stage of the pressure pulsation. The first stage may represent the formation of the internal cake. When injection pressure reached a critical value close to the confining pressure, the pressure pulsation occurred (Fig. F-1c). Many increasing-decreasing loops of injection pressure were identified, however, the injection pressure always tends to increase. This phase may correspond to an important formation of an external filter cake. As shown in Fig. F-1b, we observed that, at the beginning of injection, the calculated value of pressure loss in the specimen ΔP_s was 2 kPa which is very small as compared to 7 kPa of the inlet pressure measured by the inlet sensor T1, showing an important effect of the driving line if the permeability of the specimen is very high.

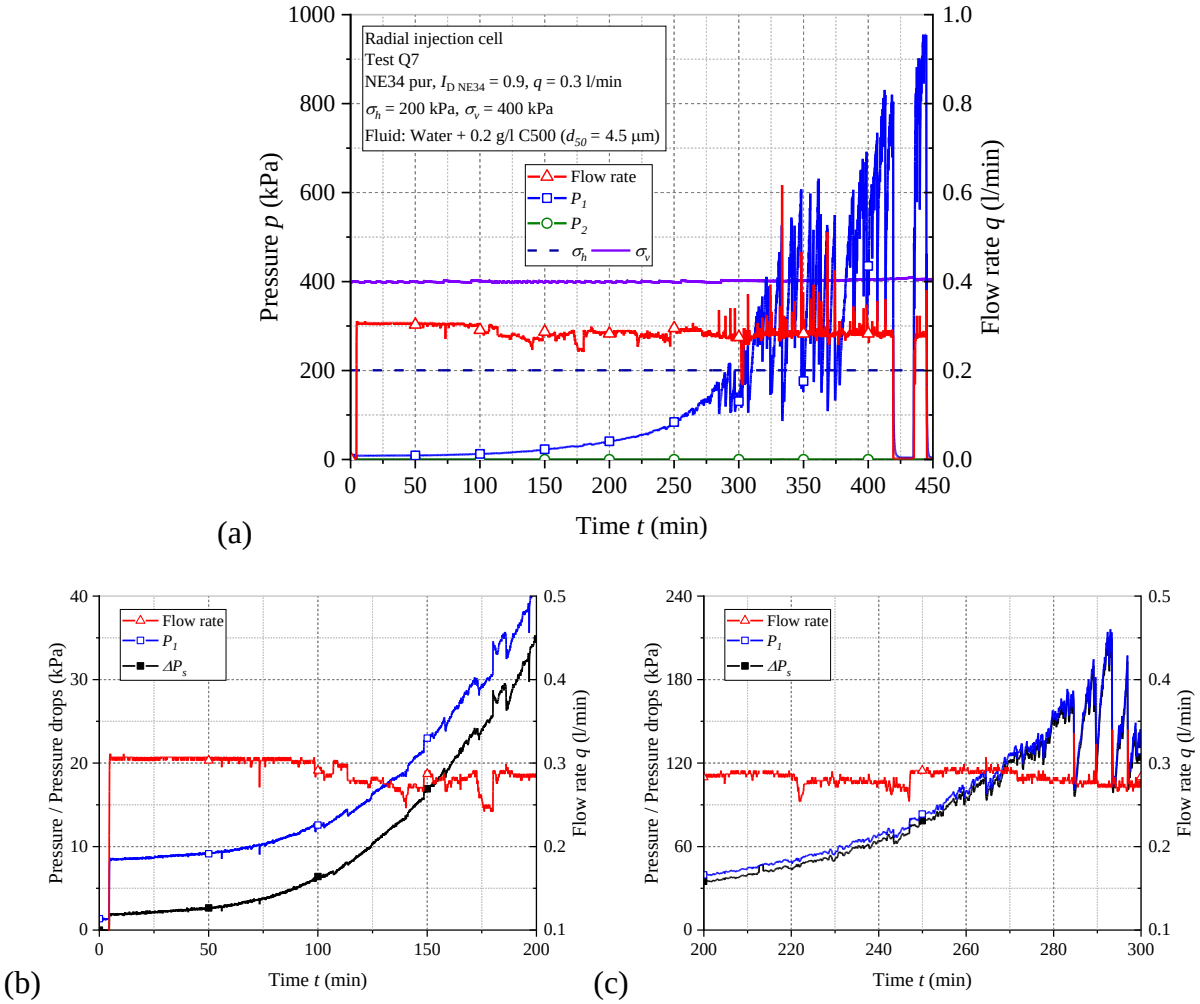

Fig. F-1: Results of the test Q7: (a) all injection results; (b) beginning of injection from 0 to 200 minutes, (c) the first noticeable pressure drops.

The evolution of the injection pressure versus cumulative mass of deposited particles during test Q7 is shown in Fig. F-2. The obtained results are very similar to those presented by Feia et al. (2015) (see Fig. F-3). Note that testing conditions between two studies are very close (specimen of pure NE34 sand, $I_{D\ NE34}$ = 0.9, suspended particles C500, flow rate in the range of 0.24 to 0.3 l/min), the major difference is the injection configuration of the cell. Feia et al. (2015) have used the uniaxial cell of the 1D injection configuration whereas the radial injection configuration is used in our study. During test Q7, the apparent permeability decreased from about 6000 mD to approximately 20 mD which are 300 times smaller than the initial value (Fig. F-4).

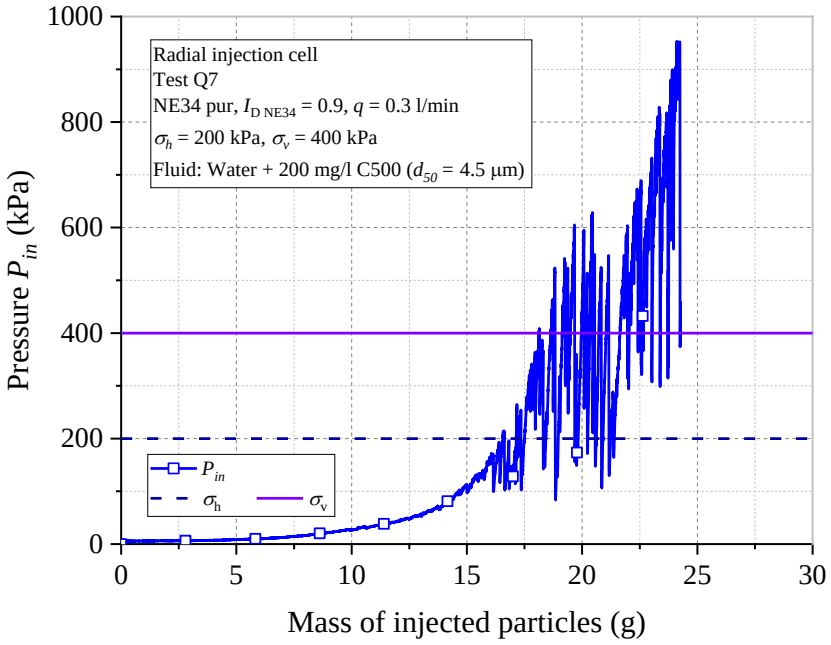

Fig. F-2: Test Q7 - Pressure evolution versus mass of injected particles.

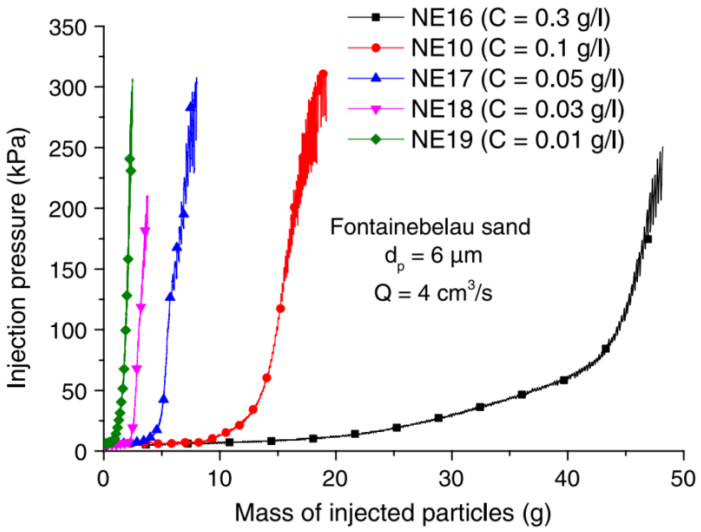

Fig. F-3: Evolution of the injection pressure at different concentrations of suspended particles. Isotropic stress σ_c = 300 kPa. Specimen of pure NE34 sand at a density index of 0.9 (Feia et al., 2015).

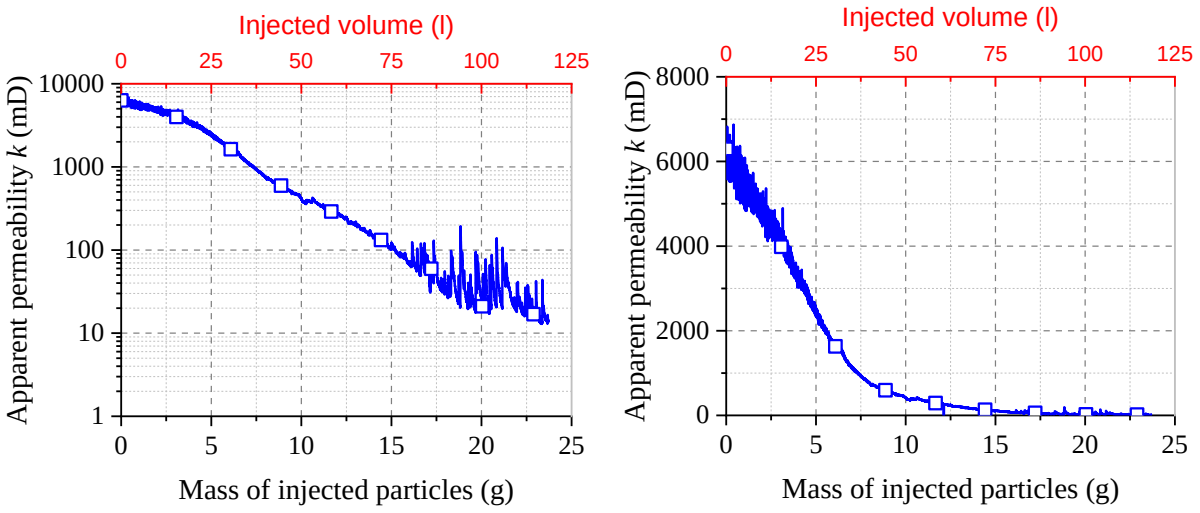

Fig. F-4: Test Q7 - Permeability decline during injection (a) logarithmic scale; (b) normal scale.

During the disassembling, no fracture has been detected in the specimen (Fig. F-6). Fig. F-5 presents the profile of deposited particles on different zones of the specimen using the dry sieve analysis. Higher particles deposition is observed near the injection source and then a rapid decrease as soon as one moves away from the center. This observation is similar to the result obtained by Feia et al. (2017). However, the low concentration of deposited particles (only 3% by mass of C500 at the nearest ring) could not be a reason that can explain such a tremendous decrease in permeability

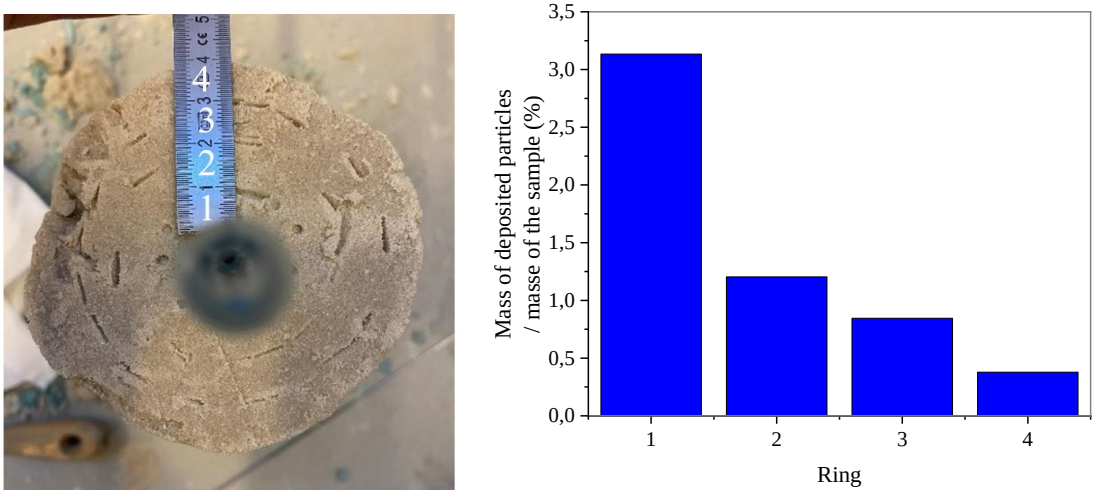

Fig. F-5: Profile of deposited particles on different rings (Analyzed samples taken from H = 6 cm to H = 10 cm): (a) view of sampling zones, (b) results of dry sieve analysis (test Q7).

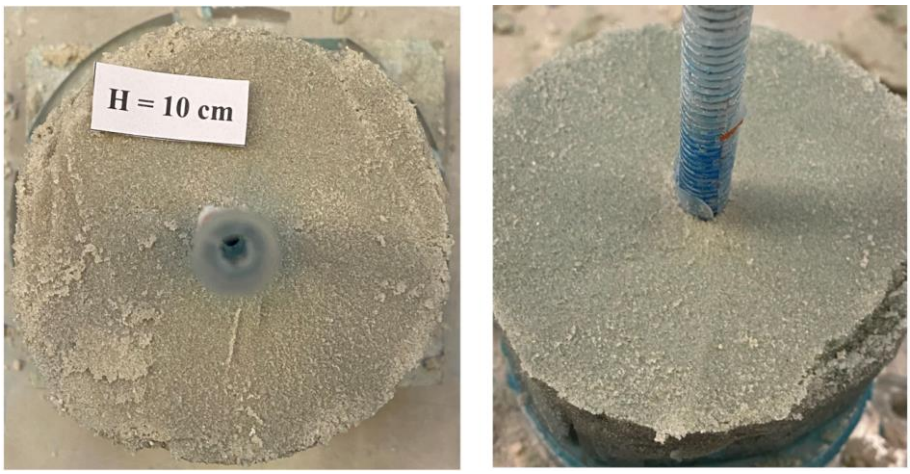

Fig. F-6: Photos of horizontal sections of the specimen Q7. No fracture detected.

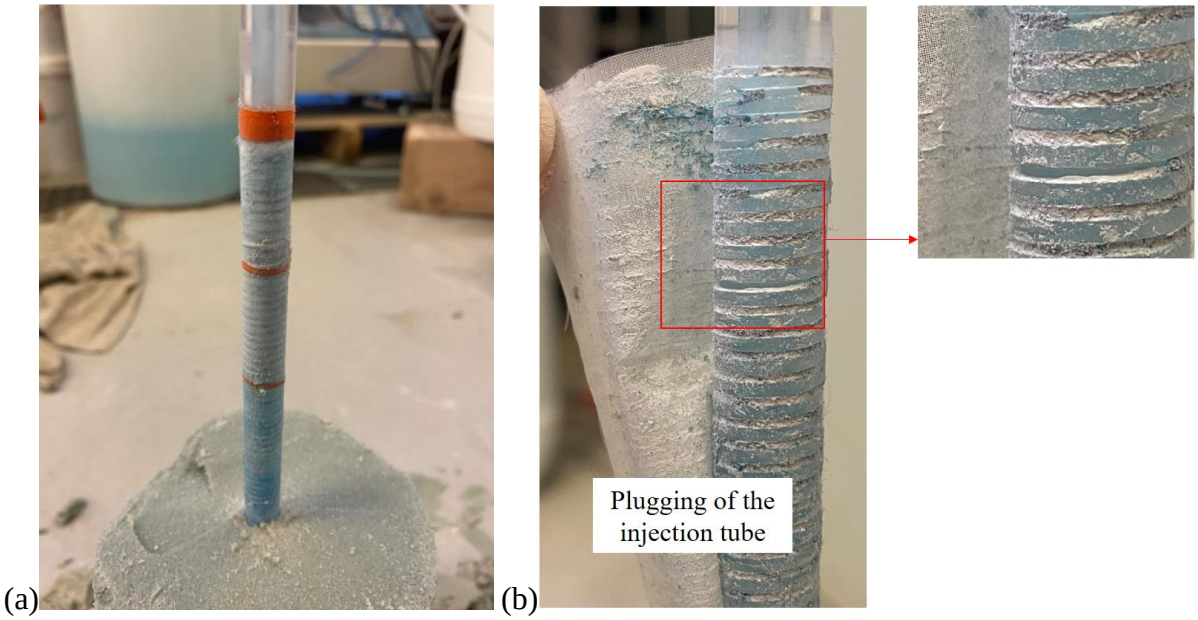

Fig. F-7: Plugging of the injection tube due to particles deposition (Test Q7): (a) outside and (b) inside views of 80 µm sieve.

During the disassembling of the injection tube, the helical groove was completely plugged due to the particles deposition (Fig. F-7). An external cake has been also formed at the sieve surface. This explains why the injection pressure increased dramatically during injection. The pressure loops may correspond to system instability after the injection tube has been completely blocked. The pressure drops are the signs of breakdown of some plugging areas of the injection tube, and then they were filled up right after by suspended particles in the fluid injection.

F.2 Test Q11

This test aims to reproduce a damaged specimen due to deposited particles in injected fluid without clogging of the injection tube. The specimen contains a mixture of NE34 sand and 10%

of C10 particles to minimize the injection time when injecting at a low particles concentration. The target increasing pressure after plugging is 100 kPa to provide the same apparent permeability as the reference specimen containing 22% of C10 particles (about 80 mD). Fig. F-8 presents the injection results of test Q11. Pure water was firstly injected at 0.2 l/min to measure the initial permeability of the specimen (Fig. F-8b). The initial permeability of the specimen was 700 mD. During the suspended particles injection, the pressure increased gradually from 15 kPa to 100 kPa for a duration of 155 minutes. At the end of injection, a reloading step of 0.2 l/min was performed to confirm the damage of the medium. As can be seen in Fig. F-8a, the injection pressure immediately reached its maximum previous value. After injecting of 1.5 g of particles, the overall permeability decreased from 700 mD to the target value of 80 mD.

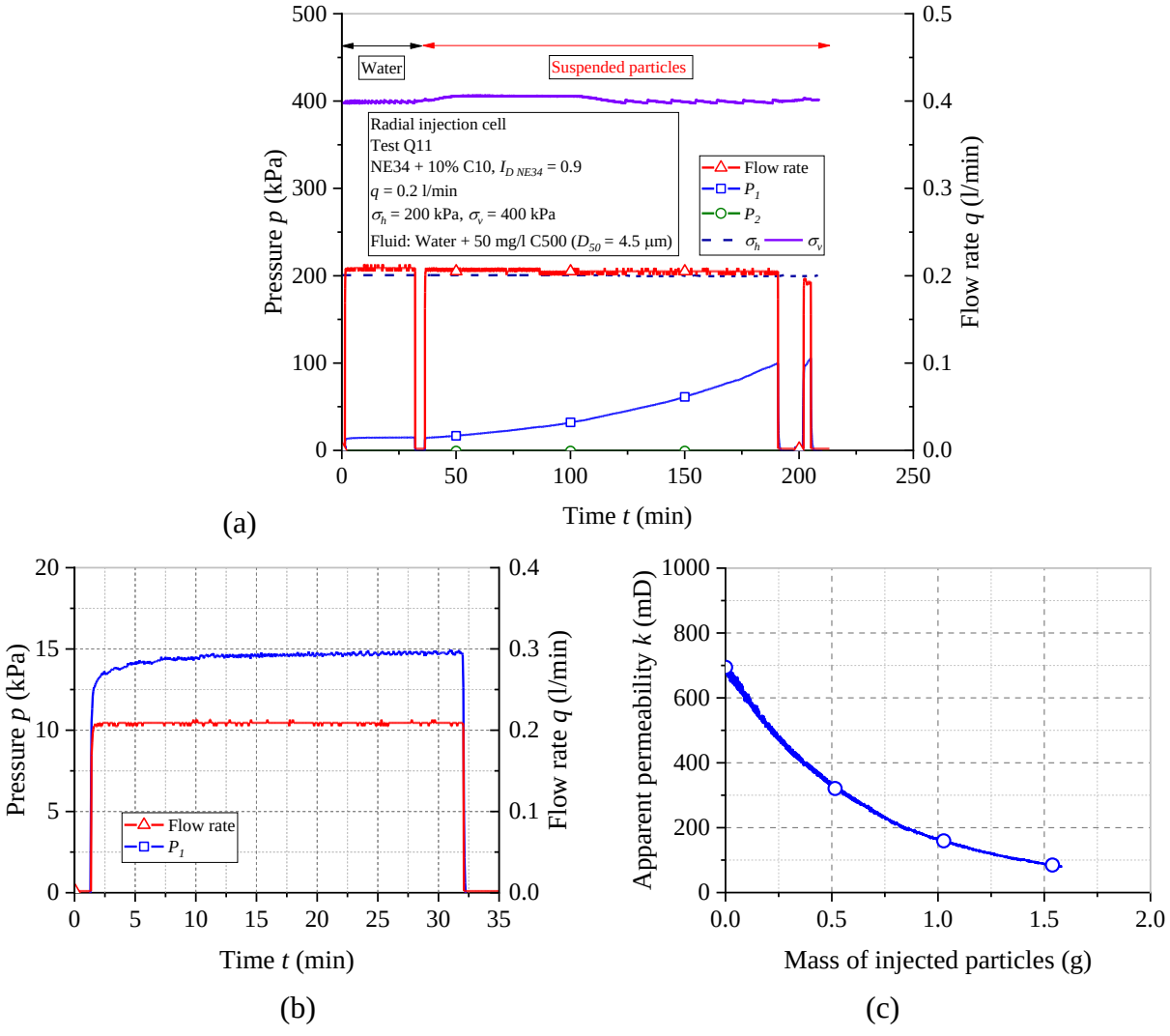

Fig. F-8: Test Q11 – (a) injection history; (b) first step of injecting pure water; (c) evolution of apparent permeability.

In this test, the disassembling was performed without colored gel injection. Fig. F-9 presents some photos of the specimen during excavation. As the maximum injection pressure was much

smaller than the confining pressure, nothing, in particular, was observed within the specimen. A small sample was carefully excavated at a zone close to the injection tube. It was then observed using an optical microscope to visualize the profile of deposited particles at the interface between specimen and injection tube. As shown in Fig. F-10, injected particles are captured in the porous medium to form the internal cake, consequently, reducing the overall permeability of the specimen. At this damaged level, the external cake has not been formed yet. When observing the injection tube, the covered sieve was partially filled by deposited particles, however, the injection tube has almost no damage (Fig. F-11). The results satisfied the purpose of this test in which the filter cake is formed by deposited particles and the injection tube is not plugged.

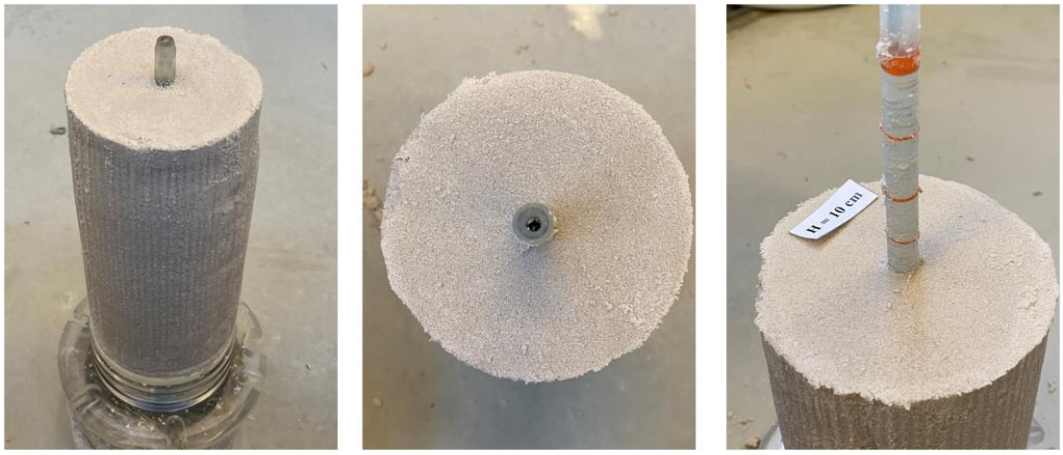

Fig. F-9: Photos of specimen Q11

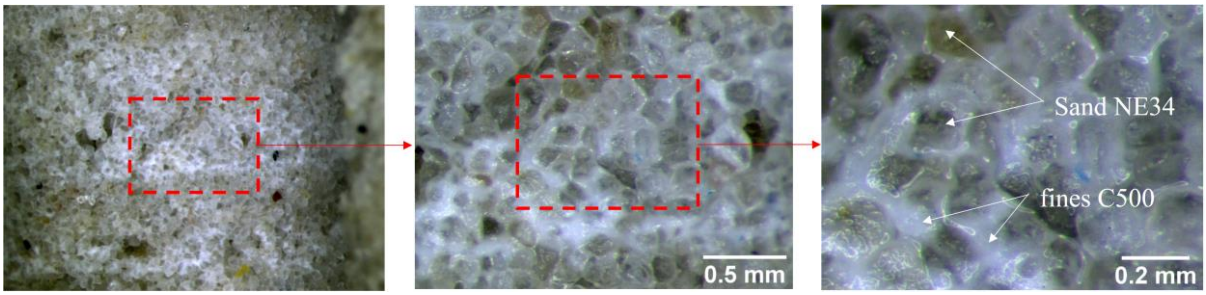

Fig. F-10: Test Q11 - Optical microscope observation of the specimen at the interface between specimen and 80 µm sieve.

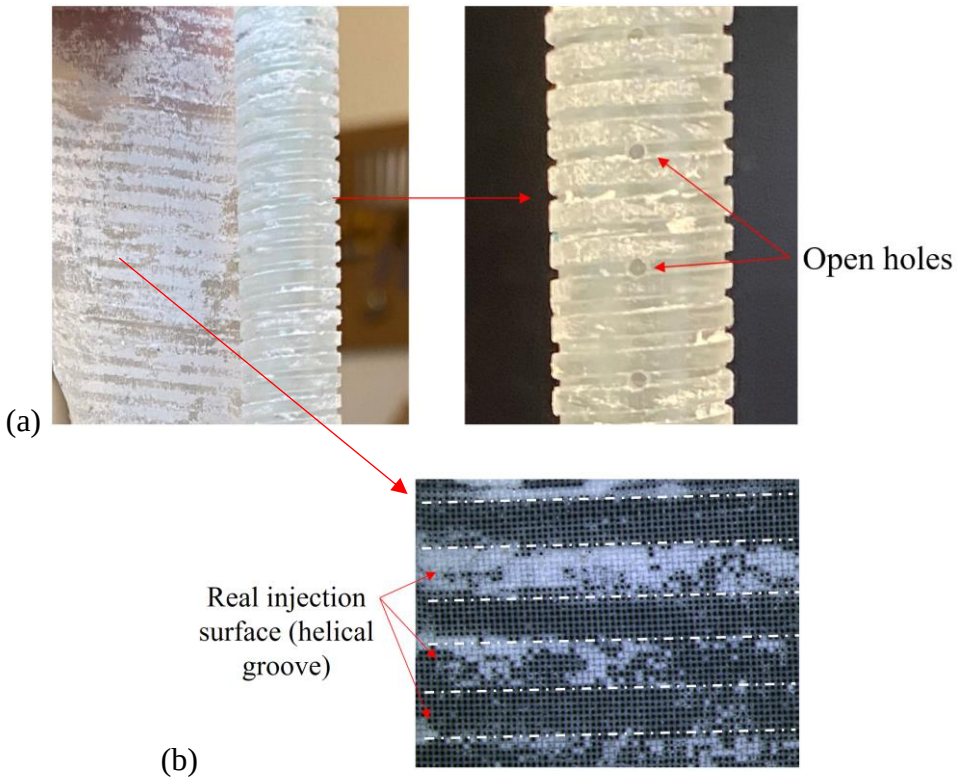

Fig. F-11: Test Q11 - Observation of the injection tube post-test (a) no plugging of injection tube; (a) no plugging of injection tube; (b) deposited particles at the 80 µm sieve (optical microscope view).

F.3 Test Q12

This test (Q12) was performed at the same testing conditions as test Q11. The suspended particles were firstly injected at a constant flow rate of 0.2 l/min until reaching 100 kPa in injection pressure as the test Q11. Then, the flow rate was increased right after to generate fractures within the specimen. The injection results are presented in Fig. F-12a. Pure water was injected at the beginning to measure the initial permeability (Fig. F-12b). As shown in Fig. F-13, a very good repeatability of the test was observed during the plugging phase in terms of the evolution of the pressure and the corresponding permeability. After reaching the target pressure, the flow rate was increased by the steps of 0.033 l/min as the injection protocol with pure water (Fig. F-12c). As can be seen in Fig. F-12d, we observe the rapid increase of the injection pressure at constant imposed flow rates. This response trend is similar to the results obtained with pure water in the previous chapter, however, this increasing magnitude is much higher at the same time period. Such fast increase may be contributed by two complementary phenomena: the mobilization of initial particles of the specimen (internal erosion) and the deposition of injected particles. The higher the flow rate, the higher the increasing rate of the injection pressure is (Fig. F-12e). During this phase, some remarkable pressure drops were also identified which are similar to those obtained during the test Q7. The pumping was stopped after obtaining a sudden pressure drop from 925 kPa to 282 kPa and this last value increased to 367 kPa after 1.5 minutes. At the end of injection, a reloading step at 0.2 l/min was injected and the measure pressure was about 85 kPa which is slightly lower than its value before starting the

phase 2 (100 kPa). During the phase 2, the apparent permeability still decreased from 80 mD to 40 mD due to above phenomena (Fig. F-14) until the pressure drop occurs.

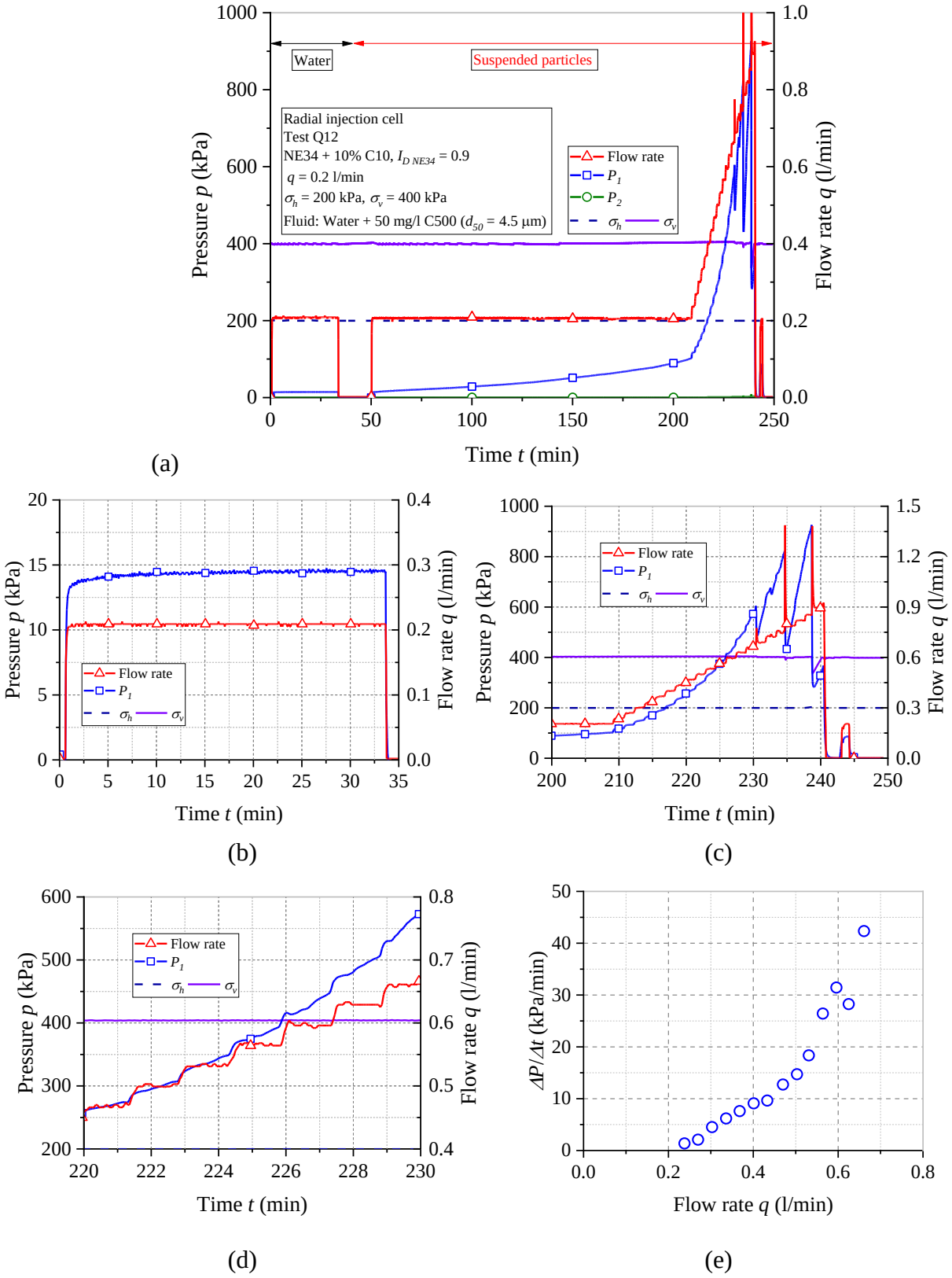

Fig. F-12: Test Q12 – (a) injection history; (b) first step of injecting pure water; (c) phase 2 of suspended particles injection; (d) rapid increase of the injection pressure; (e) increasing rate of the pressure versus its corresponding injection rate.

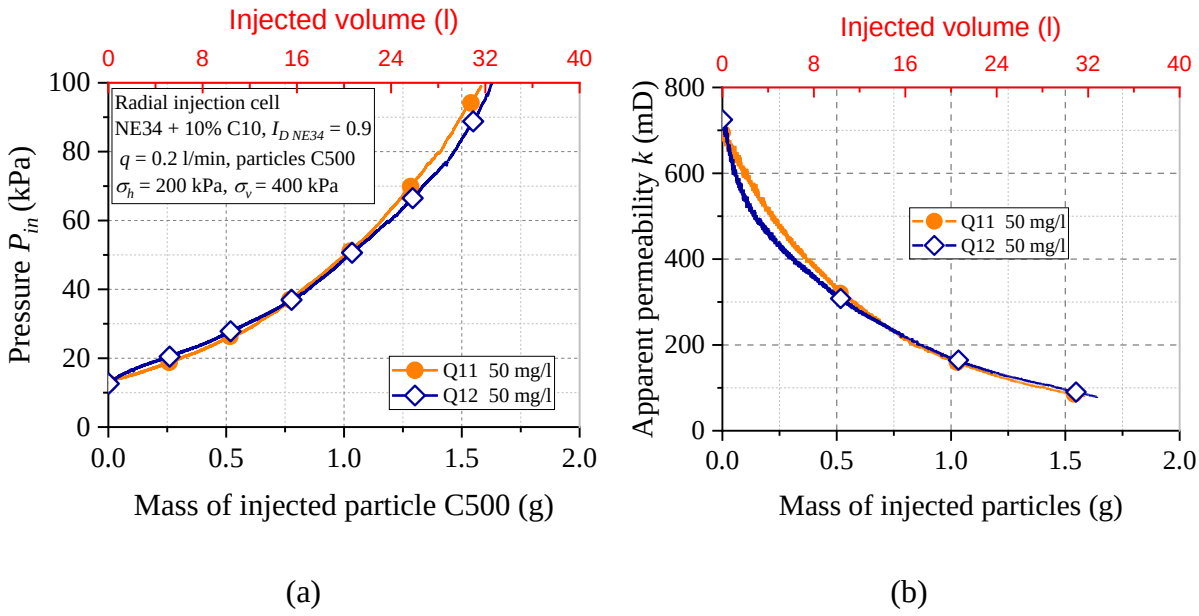

Fig. F-13: Evolution of the injection pressure (a) and the apparent permeability (b) during plugging phase (test Q12).

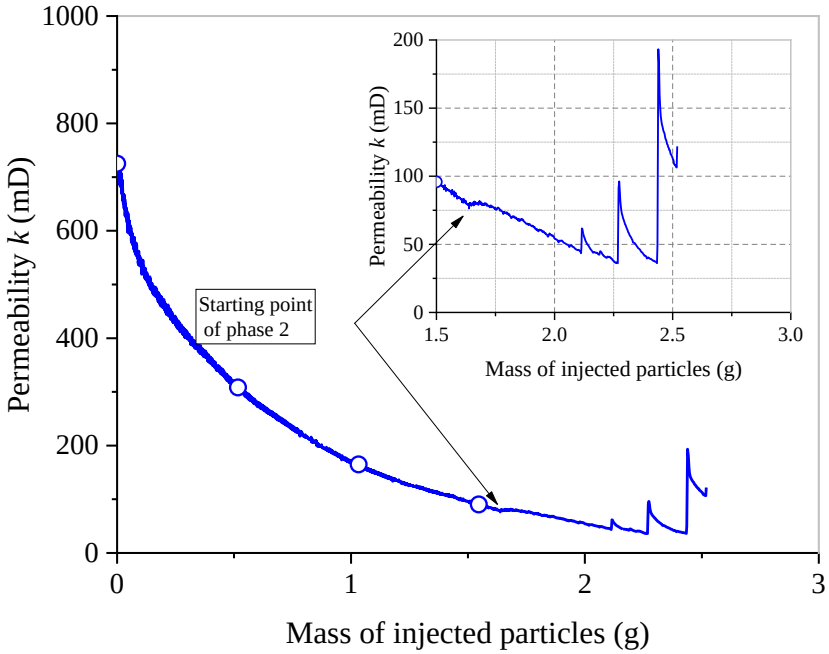

Fig. F-14: Evolution of the apparent permeability during the suspended particles injection (test Q12).

During the specimen disassembling, no fracture was detected inside the specimen (Fig. F-15), suggesting that fracturing has not occurred yet even the maximum pressure reached 4.6 times the confining pressure. The observation of the injection tube post-test permits to explain this result (Fig. F-16). The suspended particles filled the helical groove and the open holes of the tube, creating a barrier that impedes the inlet flow. The sudden pressure drops can be

explained by the unplugging of the injection tube at some positions as seen in Fig. F-16b with some open holes without damage along the injection tube.

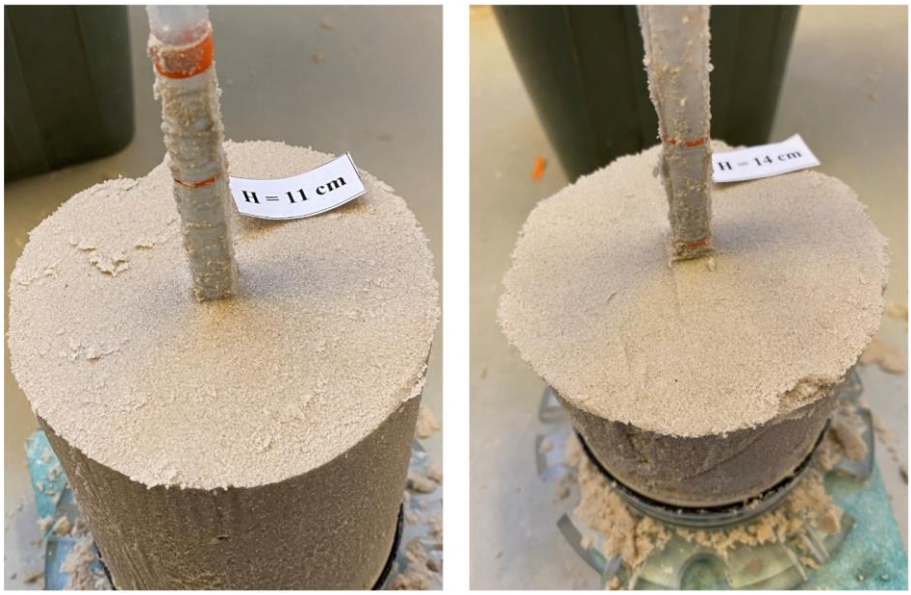

Fig. F-15: Photos of specimen Q12 during excavation.

(a)

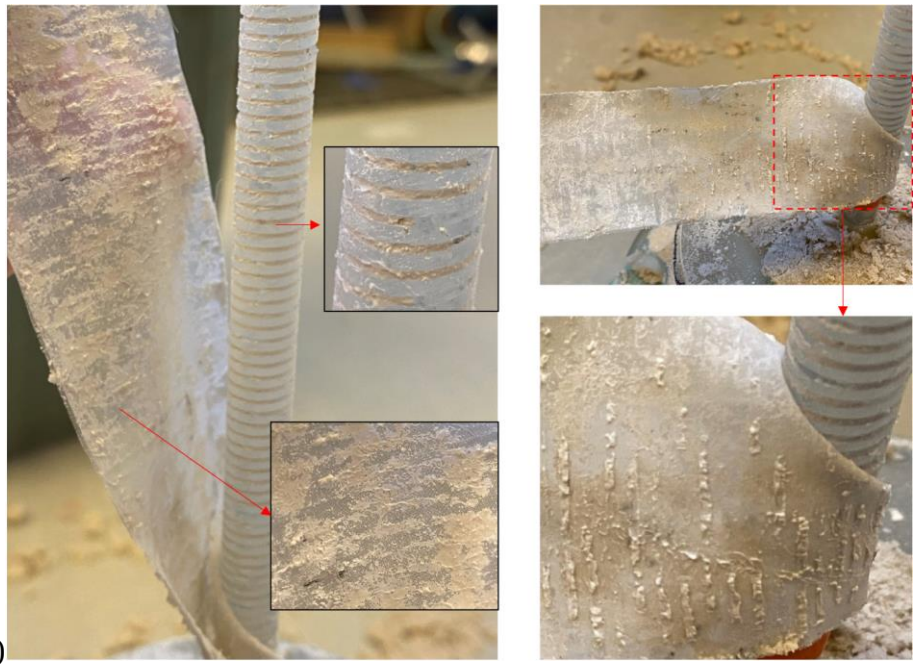

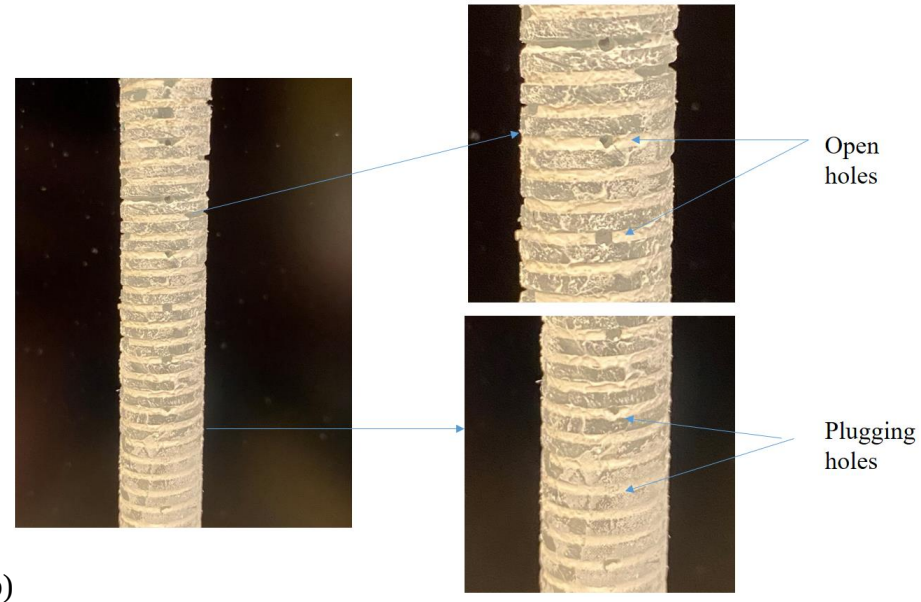

(b)

Fig. F-16: Observation of the injection tube post-test: (a) deposited particles at the injection tube and the 80 µm sieve; (b) plugging of the open holes (specimen Q12).

F.4 Test Q13

In this test, we first tried to fracture the specimen of a mixture NE34 + 10% C10 when injecting pure water up to the maximum pump rate (about 2 l/min). However, this purpose could not be achieved due to the high initial permeability of the specimen. The effect of internal erosion on the increase of the injection pressure was also analyzed in this phase. Then, injection was performed in the second stage with the suspended particles injection of 10 mg/l fines C500 by repeating the same injection protocol as the previous one. The detailed results will be presented below.

F.4.1 Phase 1 – Pure water injection

Fig. F-17 presents the results when injecting pure water. The first stage is similar to the typical test with 22% of C10 in the specimen (Fig. F-17). The flow rate was increased by steps of 0.1 l/min (1.5 minutes/step) up to 2.0 l/min. At a low flow rate of 0.2 l/min, rapid stabilization of pressure was observed around 12.5 kPa (Fig. F-17b). However, at a constant high flow rate, the pressure tended to gradually increase due to the mobilization of fine particles present in the specimen (Fig. F-17c). This phenomenon was explained in the typical test P1 of pure water (see Section 3.4.1).

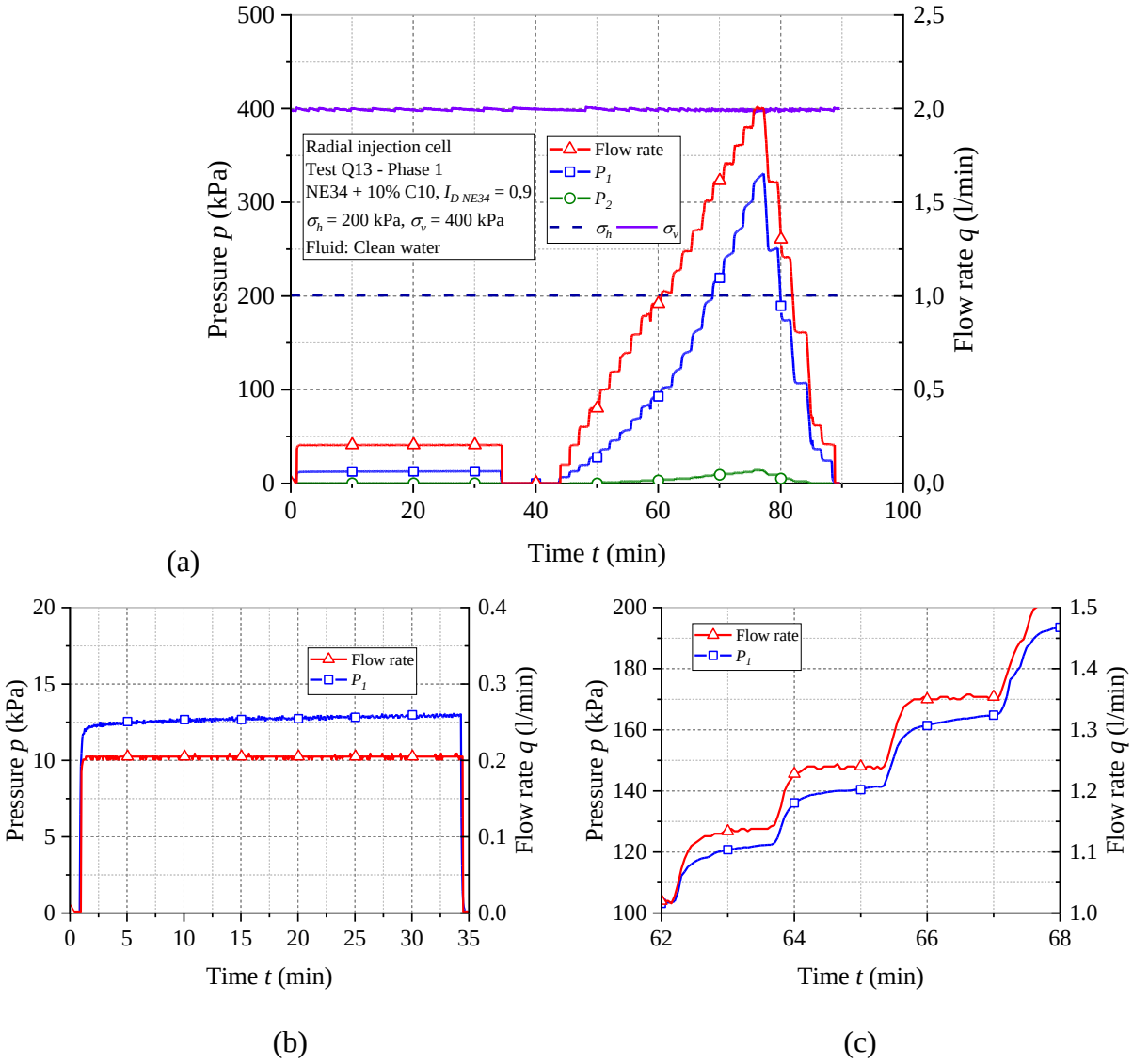

Fig. F-17: (a) Pure water injection (phase 1); (b) the first injection step at 0.2 l/min; (c) gradual increase of pressure during matrix regime (test Q13).

At high injection rate, the pressure loss due to the connection tube of 4 mm in diameter is very high. That explains the unexpected increase of outlet pressure measured at the outlet pressure transducer T2 (green curve – see Fig. F-17a). Fig. F-18 presents the measured results of the inlet pressure (P_1) by the pressure transducer T1 and the corrected pressure loss by specimen (ΔP_s). The calculation of ΔP_s was presented in Appendix C. As can be seen, the difference between two values (P_1 and ΔP_s) is bigger when increasing the flow rates which is not only reducing the accuracy of the measurement results but also reduces significantly the effective stress imposed at the boundary of the specimen. To work at a high injection flow rate, the connection tube diameter of the device need to be increased to minimize this effect. Fig. F-19 shows the evolution of the overall permeability during the phase 1. The overall permeability is calculated according to the pressure loss ΔP_s. During loading, the permeability decreased significantly, especially at high flow rate. This value dropped from 800 mD to about

400 mD (2 times smaller) at 2 l/min after nearly 35 minutes pumping. When decreasing quickly the flow rate, the values is kept stationary around 400 mD.

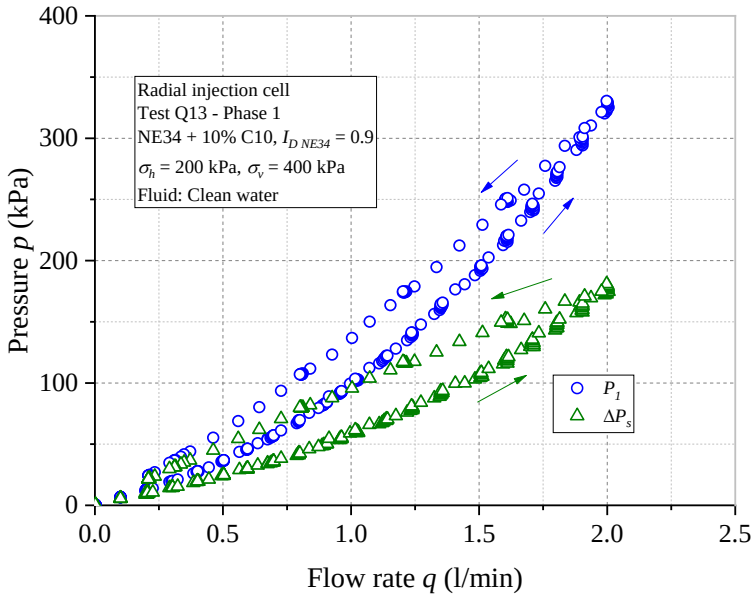

Fig. F-18: Pressure measured by the inlet pressure transducer T1 and the pressure loss by the flow though the specimen (test Q13).

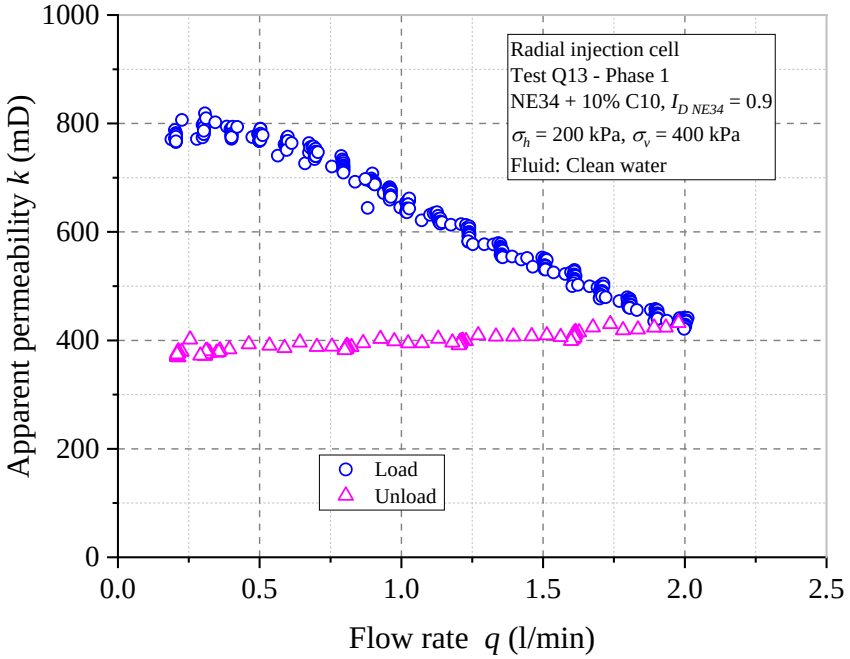

Fig. F-19: Permeability evolution during the phase 1 (test Q13).

F.4.2 Phase 2 – Suspended particles injection

The results of phase 2 are presented in Fig. F-20a. This phase started by injecting at a constant flow rate of 0.2 l/min for 30 minutes. The gradual increase of the injection pressure

was observed due to the particles deposition (see Fig. F-20b) which is different as compared to pure water. The pumping stopped and then the flow rate was increased right after by steps of 0.1 l/min. The gradual increase of the injection pressure was always observed during these steps. In particular, at 2.0 l/min, the injection was maintained for 10 minutes and the measured pressure P_1 rapidly increased from 445 kPa to 500 kPa. This trend has been explained in the test Q12. Then flow rate was then increased to 2.1 l/min and the first sudden pressure drop was identified at a maximum value of 500 kPa (measurement by pressure transducer T_1), corresponding to a fracturing pressure at the entrance of injection tube P_{fr} = 466 kPa (2.33 σ_h) (see Fig. F-20c).

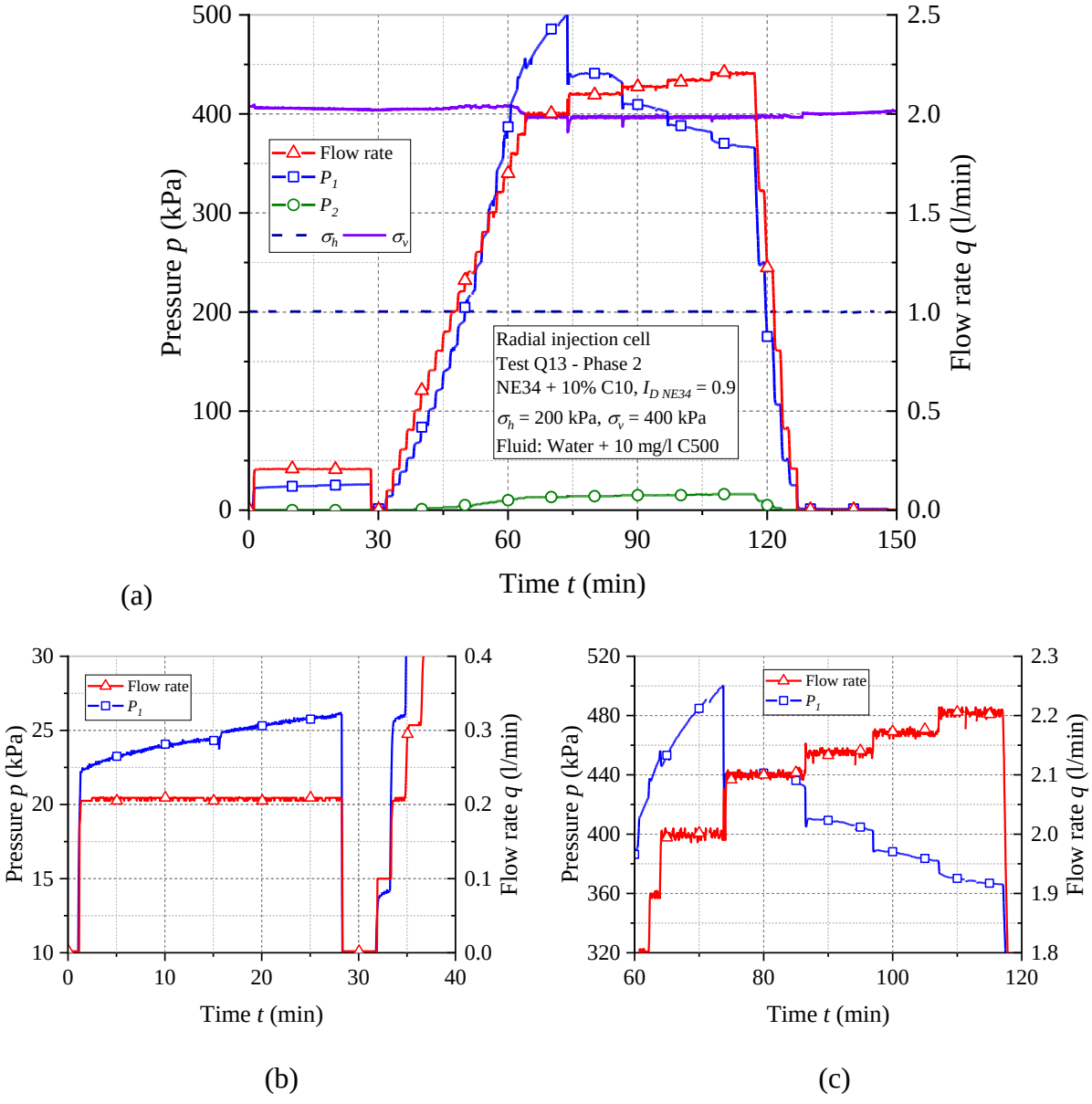

Fig. F-20: (a) Suspended particles injection (phase 2); (b) the first injection step at 0.2 l/min; (c) fracturing regime (test Q13).

Fig. F-21a presents the results in terms of pressure – flow rate curve. The slope gradually increases when the flow rate increases, corresponding to the decrease of the overall permeability

(Fig. F-21b). The injection in the first step of 30 minutes at 0.2 l/min reduced the permeability from 400 kPa to 340 mD. When pressure reached the fracturing point at about 466 kPa, fracturing occurred and the permeability restored from 218 mD to 450 mD at the end of fracturing regime.

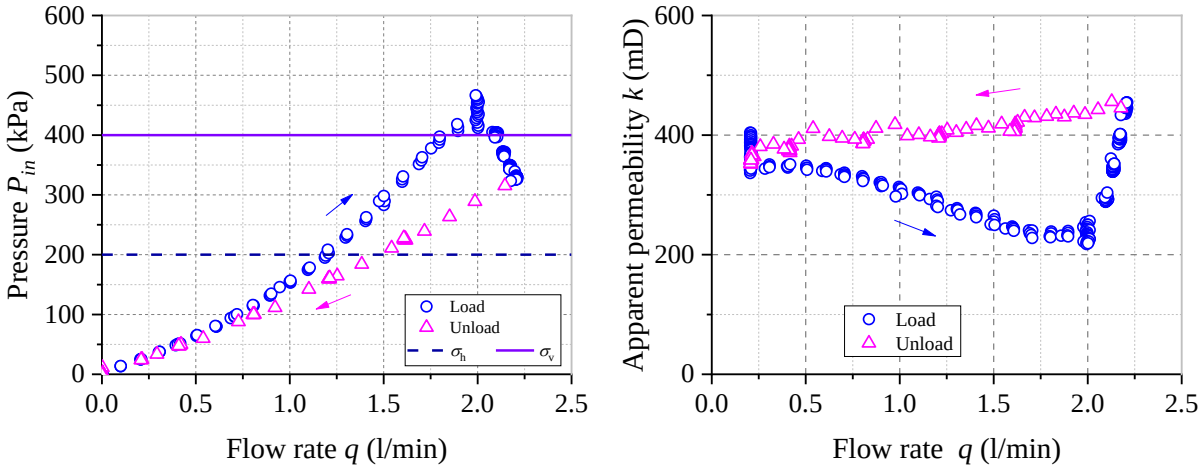

Fig. F-21: Evolution of the inlet pressure (a) and permeability (b) during the phase 2 (test Q13).

In this test, the mixture of silica gel + 0.2% Basacid Bleu 762 was used to freeze the specimen. This time, the injected volume was sufficient to invade the whole specimen. Fig. F-22 presents some photos at different heights during excavation. Similar observation as the results obtained in pure water scenario with the appearance of fractures around the tube, confirms the pressure drops during injection. However, due to the presence of the colored solid gel, we could not observe the deposition profile of the suspended at the sieve and injection tube (Fig. F-23).

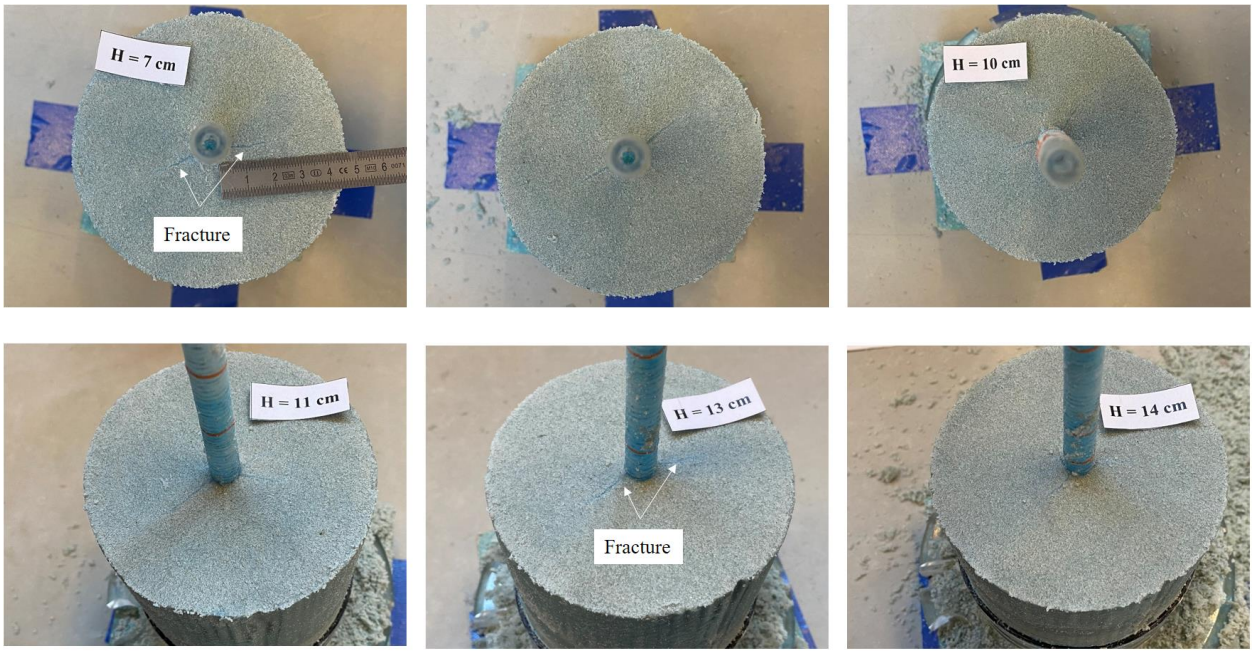

Fig. F-22: Photos of the horizontal cross-sections of specimen Q13

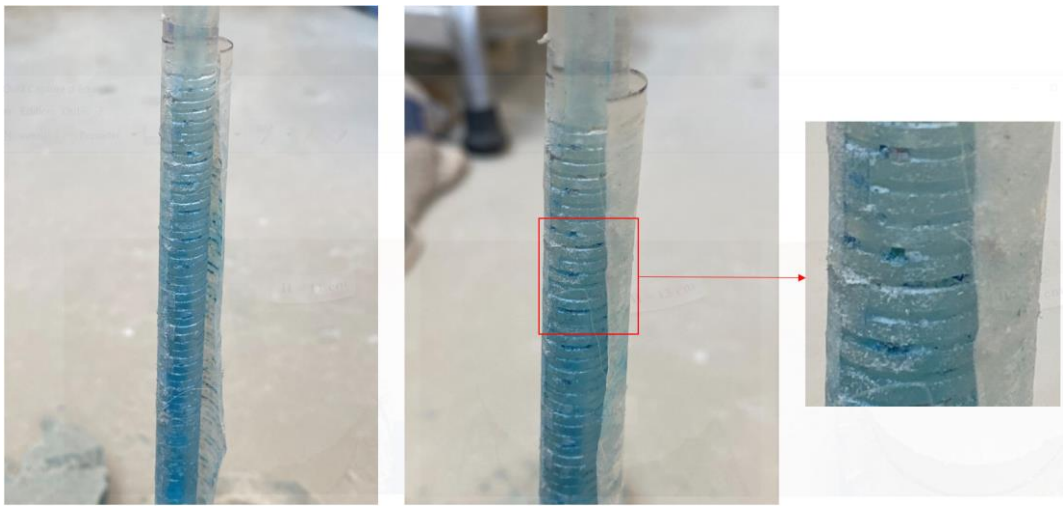

Fig. F-23: Observation of the injection tube post-test (specimen Q13).

Appendix G Tests with suspended particles in the radial injection cell

G.1 Test SP3

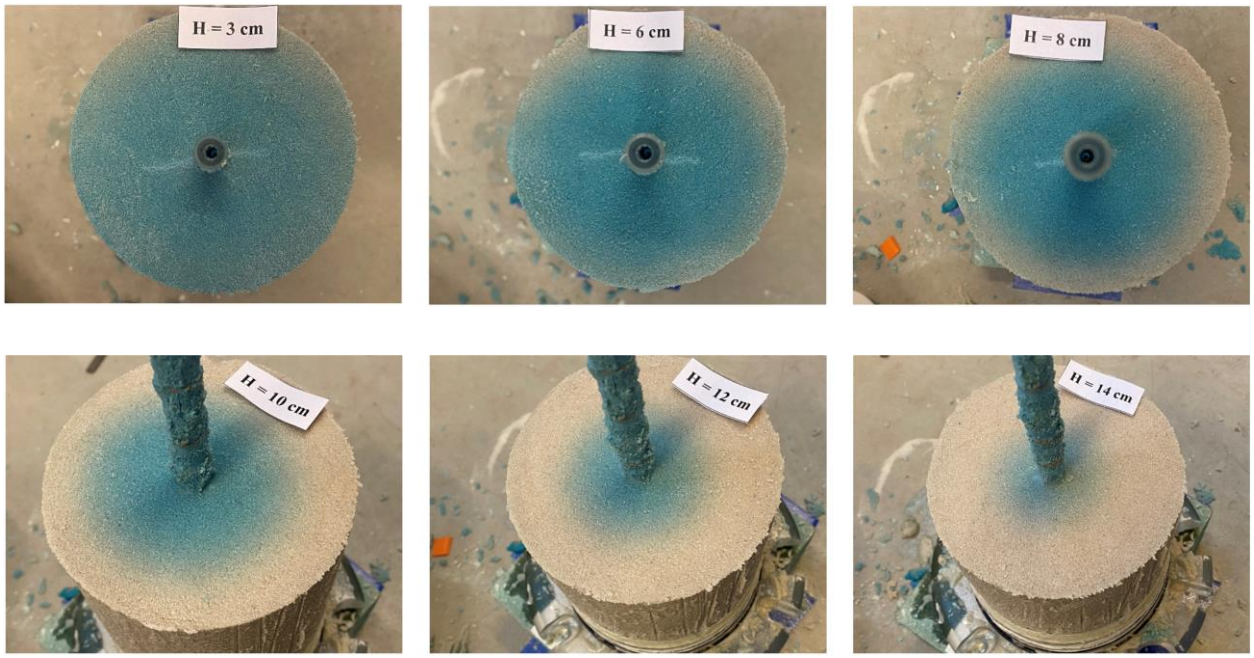

Fig. G-1: Excavation of specimen SP3. Fractures are detected only at the upper part of the specimen, consequently this part presents a higher invasion of the injected dye.

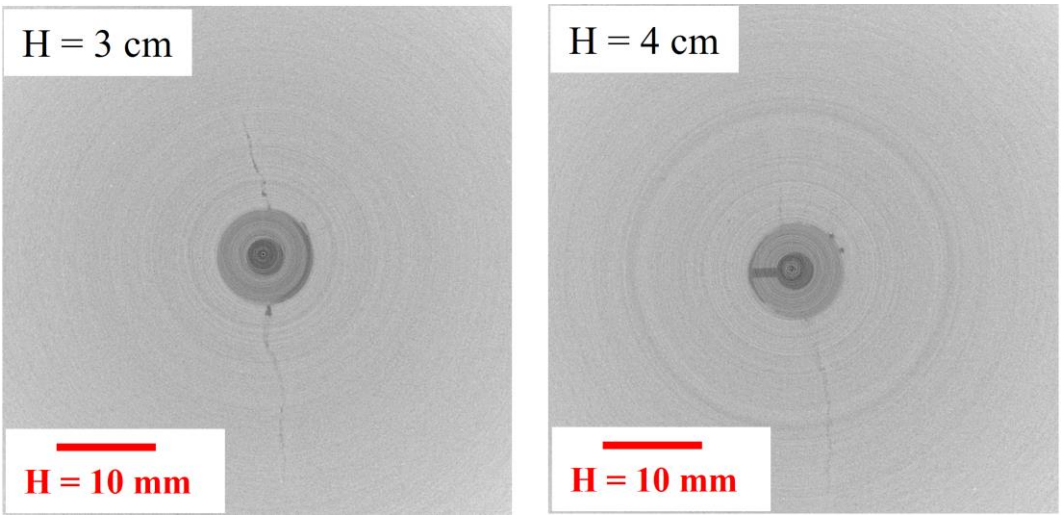

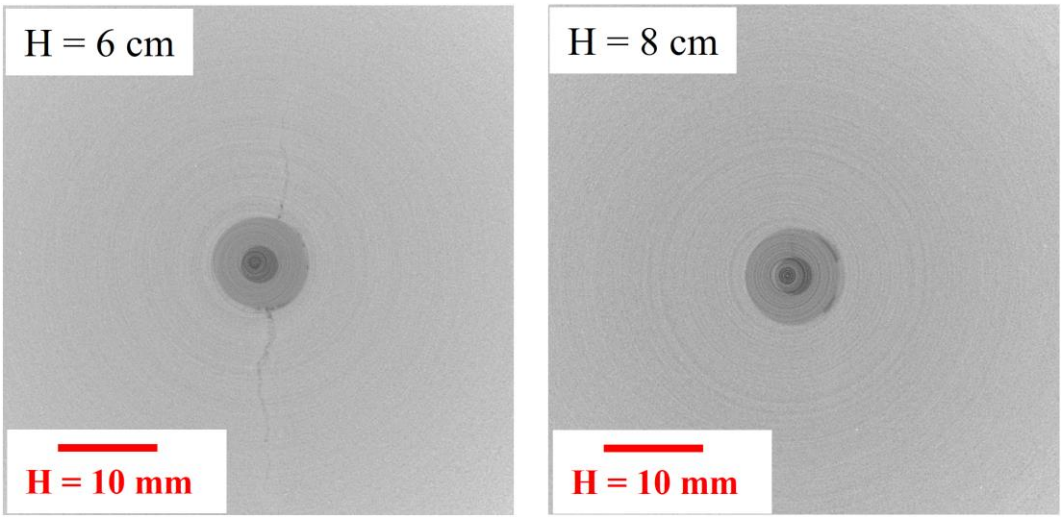

Fig. G-2: Typical X-Ray CT images at different height of specimen SP3.

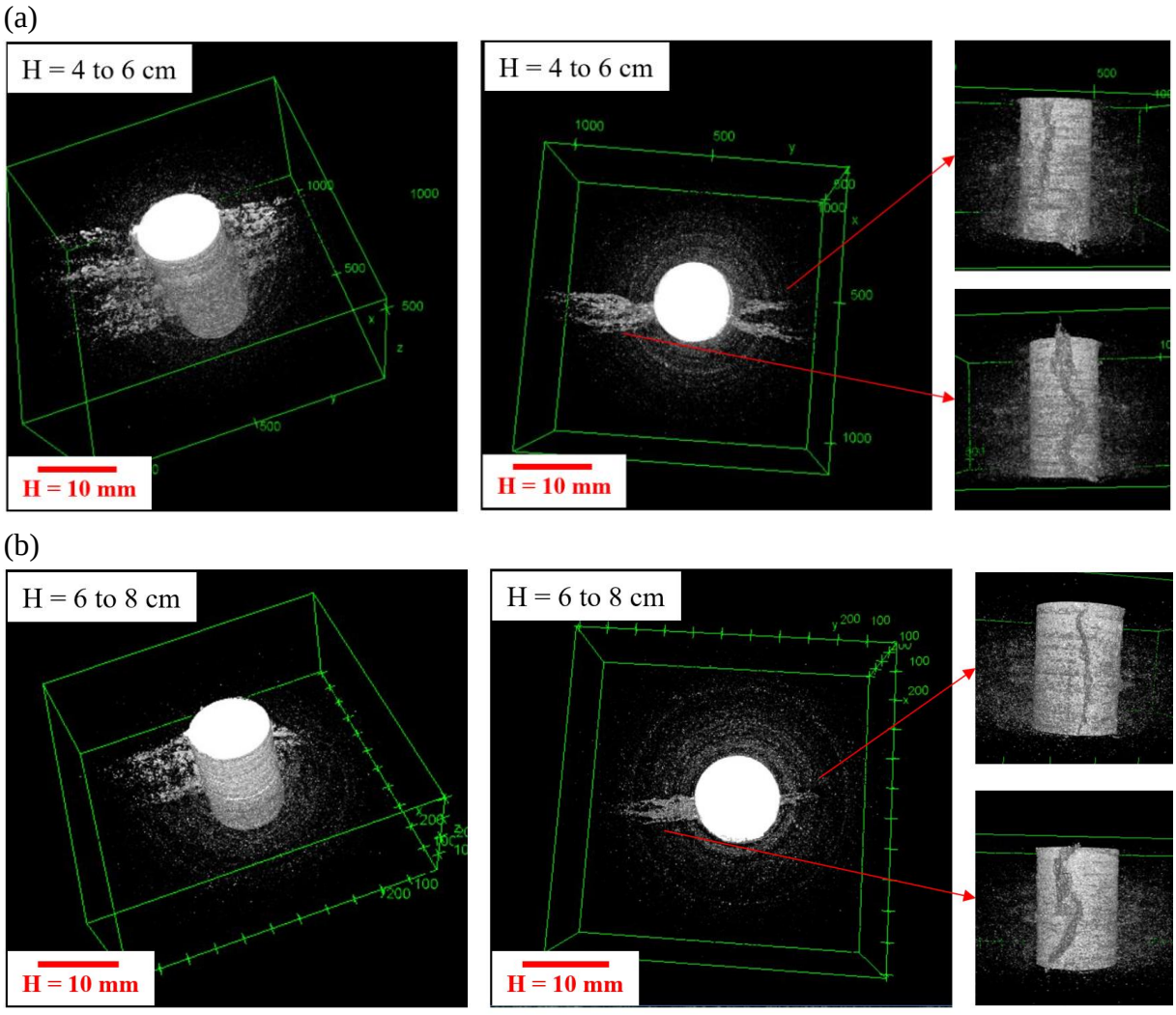

Fig. G-3: 3D views of the fracture pattern in two different section of specimen SP3 (a) H = 4 to 6 cm; (b) D = 6 to 8 cm.

G.2 Test SP4

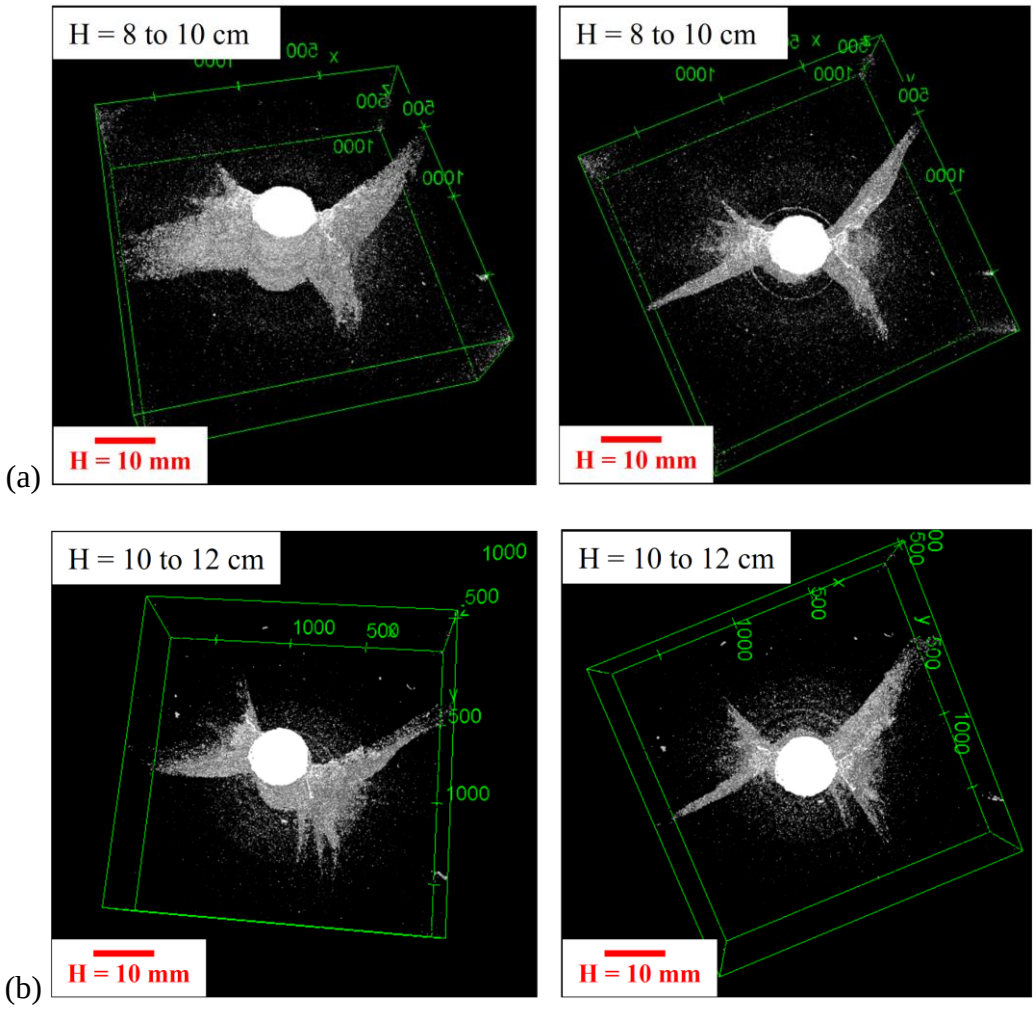

Fig. G-4: 3D views of the fracture pattern in two different section of specimen SP4: (a) H = 8 to 10 cm; (b) D = 10 to 12 cm.

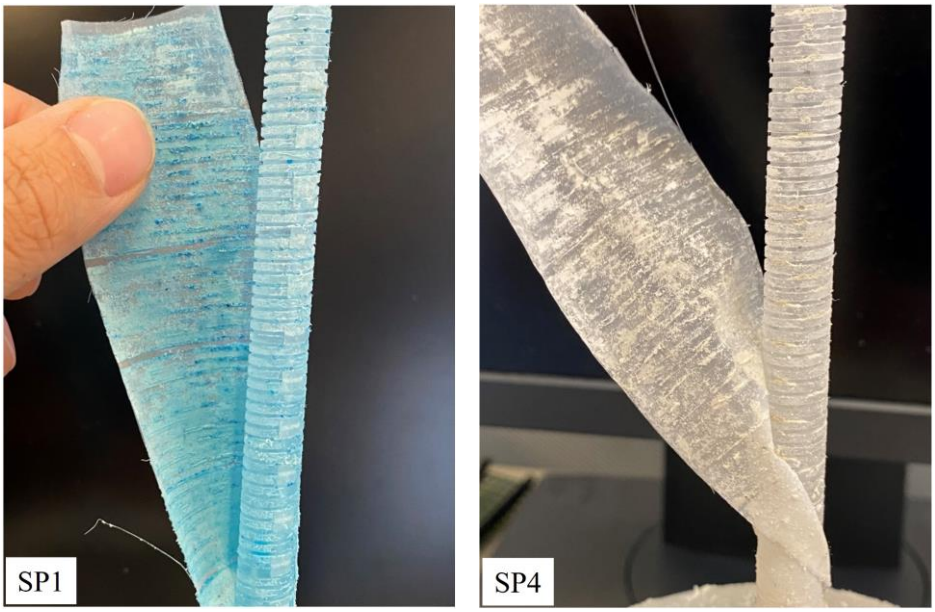

Fig. G-5: Deposited particles at the 80 μm sieve and the injection tube post-tests SP1 (200 kPa) and SP4 (120 kPa).

CHAPTER 5.